Development of a Hydrologic Characterization Technology for Fault Zones

—Final Report —

Kenzi Karasaki, Tiemi Onishi, Christine Doughty, Mark Conrad, Erika Gasperikova, Paul Cook and Craig Ulrich

Earth Sciences Division, Lawrence Berkeley National Laboratory

March 2012

NUMO-LBNL Collaborative Research Project Report

This document was prepared as an account of work sponsored by the United States Government. While this document is believed to contain correct information, neither the United States Government nor any agency thereof, nor the Regents of the University of California, nor any of their employees, makes any warranty, express or implied, or assumes any legal responsibility for the accuracy, completeness, or usefulness of any information, apparatus, product, or process disclosed, or represents that its use would not infringe privately owned rights. Reference herein to any specific commercial product, process, or service by its trade name, trademark, manufacturer, or otherwise, does not necessarily constitute or imply its endorsement, recommendation, or favoring by the United States Government or any agency thereof, or the Regents of the University of California. The views and opinions of authors expressed herein do not necessarily state or reflect those of the United States Government or any agency thereof, or the Regents of the University of California.

Executive Summary

This is the final report for the five-year program of the NUMO-LBNL collaborative project (hereafter called the Project): Development of Hydrologic Characterization Technology for Fault Zones, under a NUMO-DOE/LBNL collaboration agreement. Detailed results from the past four years of study can be found in the each year's year-end report (Karasaki et al., 2008, 2009, 2010, and 2011; Kiho et al., 2008, 2009, 2010, and 2011). In this report, we discuss the results of the studies conducted in FY2011. We also give a summary of the overall results and findings, as well as the lessons learned during the course of the Project.

In FY2011, another electrical resistivity tomography (ERT) survey was conducted parallel to the previous line, but closer to the well field. Two anomalies were detected that may be related to the faults, but this finding is not conclusive. A refraction seismic survey using both P- and S-wave sources was conducted along a line that spans wider than previous lines to cover a suspected main fault.

Further hydraulic tests were conducted in the inclined WF-4 borehole. We core-drilled another inclined borehole WF-5 to the north of the existing borehole field parallel to WF-4, with the intention of intersecting the main fault. Borehole logging and pumping tests were conducted, with the results from one of the pump tests showing that there is a good hydraulic connection between the middle of WF-5 and almost the entire length of WF-1 and the bottom of WF-4. No responses were detected in the other boreholes, WF-2 and WF-3, indicating that the main fault plane is permeable along its length and brushes by WF-1. There is a low permeability barrier along the main fault's length as well, presenting the duality of the fault-zone hydrology. Based on these findings, the fault type classification relating geologic features to hydrologic properties was modified.

Geologic analysis of the cores from WF-5 was also conducted. Zircon dating, XRD, and microfossil analyses were performed, along with a fracture-statistics analysis. Structural models of the fault zone were developed integrating all the information gathered throughout the Project. One model among these structural models assumes that the main fault plane coincides with the fault to the east, which was previously considered a separate fault.

Geochemical analysis of groundwater samples detected no water younger than 60 years, based on the tritium concentration. A ^{13}C isotope analysis suggested that the groundwater is several thousand years old. Geohydrologic models were constructed that successfully explained the observed head and temperature distribution.

The lessons learned from conducting field investigations thus far are listed in our Conclusions (Section 8). One lesson worth mentioning here is the need to prepare for Murphy's Law. Of course, all necessary and reasonable measures should be taken to prevent mishaps, but one should nonetheless assume that at least *something* will go wrong in the field. Thus, backup equipment and schedules should be in place beforehand. Another lesson learned is that investigators should not rely on existing information too heavily. Geologic maps are constructed from extrapolating/interpolating available *surface* outcrops and opportunistically obtained data, and are two dimensional. The geology at depth may be quite different, as we discovered here. It is envisaged that these lessons will be valuable pieces of information for NUMO when it conducts its own preliminary investigations at yet-to-be selected candidate sites in Japan.

The following is a list of the overall conclusions of the Project.

- Fault zones greatly affect the groundwater flow and transport
- The exact location of the main fault plane of the Wildcat Fault Zone is still in dispute among participating researchers, which highlights the fact that it is extremely difficult to uniquely characterize fault-zone geology. However, the characterization of the hydrology may be more amenable, owing to the integrating nature of the pressure field.
- Long-term monitoring and analysis of groundwater pressure over several seasons is extremely important. Large-scale through-flow permeability as well as the degree of hydrologic communication between boreholes can be estimated by analyzing the long-term pressure trend data.
- Temperature distribution along a borehole is useful for calibrating the permeability and recharge rate.

- A fault plane may not always be filled with coherent clay gauge and thus may be very permeable. The fault plane where the most recent movement is suspected may be too young to have clay gauges.
- That the exact location of the main fault plane of the Wildcat Fault Zone is still in dispute among participating researchers highlights the fact that it is extremely difficult to uniquely characterize a fault zone.
- Traditional approaches to isolating sections with ordinary packers may not be suitable for fault zone characterization.
- It is best to complete boreholes penetrating a fault zone with grouted casing and uniform perforations. It is recommended that boreholes then be packed off systematically using a newly developed sealing system with multiple daisy-chained intelligent sensors.
- Inclined drilling is an effective tool for characterizing a vertical fault zone, but also has some drawbacks.
- The Wildcat is not a single fault. It is a fault zone consisting of several fault planes that have developed over several distinct stages. This could hold true for the faults at potential candidate sites in Japan with similar tectonic settings.
- No single geophysical survey technique is almighty in every geologic condition. Electrical resistivity tomography (ERT) may be more effective than other methods in estimating subsurface structures in a complexly faulted, folded, and fractured geologic setting. But refraction seismic surveys could be better suited for a highly faulted/fractured environment.
- The hydrologic characteristics of the Wildcat Fault Zone suggest a complex, dual nature—somewhat typical of average faults with high permeability along the direction of the fault zone and low permeability across it.
- Isotopic analysis of carbonates (^{13}C, ^{18}O) from core samples may be used to estimate the location of present-day flow zones.

- Groundwater age analysis using ^{3}He may be used to infer the direction of groundwater flow and evolution.

Finally, we summarize the various recommendations for furthering the understanding and characterization methodology of fault zones and progressing to prediction of transport. We lay out the relevant approaches and mindsets that NUMO can consider employing in prioritizing and optimizing the characterization activities at preliminary investigation sites.

Table of Contents

Executive Summary iii

List of Tables xi

List of Figures xii

1 Introduction 1-1

1.1 References 1-5

2 Geophysical Surveys 2-1

2.1 Introduction 2-1

2.2 Electrical Resistivity Survey (ER-4) 2-2

2.3 Electrical Resistivity Survey (ER-5) 2-4

2.4 Seismic Refraction Survey (SF-1) 2-5

2.5 Summary 2-6

2.6 References 2-6

3 Drilling Investigation 3-1

3.1 Introduction 3-1

3.2 Drilling sequence of WF boreholes 3-1

3.3 WF-5 3-3

3.3.1 Location 3-3

3.3.2 Drilling 3-4

3.4 Borehole Logging 3-6

3.4.1 Caliper log 3-7

3.4.2 Electric logs (ELOG) 3-8

3.4.3 Borehole Televiewer (BTV) log 3-9

3.4.4 Sonic log 3-10

3.4.5 Flowing Fluid Conductivity (FFEL) log 3-11

3.5 Summary 3-11

3.6 References 3-34

4 Geologic Investigation and Analysis 4-2

4.1 Introduction 4-2

4.2 Geologic Mapping 4-3
4.3 Drilling 4-7
4.4 WF-3 Core logging and description 4-7
4.4.1 Orinda Fm/San Pablo Gr.-Claremont Fm. contact at fault zone 322-332ft 4-10
4.4.2 Claremont Fm.- Orinda Fm/San Pablo Gr. contact at 484.6-489ft – Gouge 4-11
4.5 WF-4 Core logging and description 4-16
4.5.1 Main features in WF4 4-17
4.6 Petrographic Analysis 4-28
4.6.1 Claremont Fm. chert and shale mineralogy 4-28
4.6.2 Microfossils 4-30
4.6.3 Orinda Fm. and Claremont Fm. sandstone 4-33
4.6.4 Bleached, brecciated and lithified siliceous carbonate rocks 4-37
4.6.5 Unconformity and/or Fault zone: Orinda Fm/San Pablo Gr. and Claremont Fm.. 4-39
4.7 Major fault zones in WF-4 4-42
4.7.1 WF4_18(159m/522.5ft) 4-45
4.7.2 WF4_19 (534.8ft) 4-46
4.7.3 WF4_21 (541ft) 4-46
4.7.4 WF4_22 (566.3ft) 4-47
4.7.5 WF4_10 (593.5ft) 4-48
4.7.6 WF4_20 (595.5ft) 4-49
4.7.7 WF4_31 (631.6ft) 4-50
4.7.8 WF4_23 (653.7ft) 4-51
4.7.9 WF4_24 (655.8ft) 4-52
4.7.10 WF4_25 (660.2ft) 4-53
4.7.11 WF4_26 4-54
4.8 Structural Data 4-55
4.9 3D Geologic Model 4-59
4.10 Summary 4-66
4.11 References 4-69
5 Hydrologic Investigations 5-1

5.1 Introduction 5-1
5.2 Slug tests in WF-3 5-1
5.3 Pump tests in WF-4 5-3
5.3.1 Packer configuration 5-4
5.3.2 Packer Seating 5-4
5.3.3 Gas Buildup 5-5
5.3.4 Pump Test on 1/21/2011 5-5
5.3.5 2nd Pump Test 5-7
5.4 Pressure Monitoring 5-8
5.4.1 WF Boreholes 5-8
5.4.2 SSL Boreholes 5-9
5.4.3 All Boreholes 5-10
5.4.4 Hydraugers 5-11
5.5 References 5-13
6 Geochemical Investigation 6-1
6.1 Introduction 6-1
6.2 Water Chemistry 6-1
6.3 Isotopic Analysis of Carbonates 6-2
6.4 Hexadiagram 6-3
6.5 Groundwater Ages 6-3
6.6 Groundwater Flow Direction 6-3
6.7 References 6-4
7 Hydrologic Modeling 7-1
7.1 Introduction 7-1
7.2 Data available 7-1
7.3 Numerical Simulator 7-2
7.4 Model Domain 7-2
7.5 Boundary Conditions and Sources and Sinks 7-3
7.6 Geologic Model 7-4
7.7 Grid 7-5

7.8 Simulation Results for Natural-state Head Distribution 7-5
7.9 Conclusions 7-6
7.10 References 7-8
8 Lessons Learned, Conclusions and Recommendations 8-1
8.1 Lessons Learned 8-1
8.1.1 Murphy's Law 8-1
8.1.2 Quality Assurance 8-5
8.1.3 Cost cutting 8-6
8.1.4 Pros and cons of inclined holes 8-6
8.1.5 Fault Gouges 8-7
8.1.6 Main Fault Plane 8-8
8.1.7 Environmental Protection 8-8
8.1.8 Core Recovery 8-8
8.1.9 Fault and Fault zone 8-9
8.1.10 Packer Zone 8-9
8.1.11 Take Time 8-11
8.1.12 Geophysics 8-12
8.1.13 Heterogeneity of the fault zone 8-12
8.2 Summary Conclusions 8-13
9 Recommendations 9-15
9.1 Verification study 9-15
9.2 Transport studies 9-15
9.3 Safety and environmental protection 9-16
9.4 Keep science in repository program 9-16
Appendix 1 Summary Core Logs ..... A1-1~A1-20
Appendix 2 WF-1 Core Images ..... A2-1~A2-38
Appendix 3 WF-2 Core Images ..... A3-1~A3-25
Appendix 4 WF-3 Core Images ..... A4-1~A4-22
Appendix 5 WF-4 Core Images ..... A5-1~A5-54
Appendix 6 WF-5 Core Images ..... A6-1~A6-41

List of Tables

Table 3 1 Global coordinates of WF Borehole tops 3-14

Table 3 2 Directional log results of WF-5 3-14

Table 4 1. Results from qualitative bulk XRD for Claremont chert and mudstone..... 4-27

Table 4 2 Qualitative bulk XRD for sandstone in Claremont Fm. ("◎ " denotes positive) .. 4-31

Table 4 3 Mineral composition of Orinda Fm. 4-44

Table 4 4 Summary of XRD analysis for fault rocks 4-71

Table 5 1 Calculated transmissivity and averaged permeability in WF boreholes. The low in WF-3 indicate those at some distance whereas the high are for the immediate vicinity.. 5-13

Table 5 2 Comparison of linear distances from the features in WF-4 to the intervals in WF-1 and WF-3 5-14

Table 6 1 ICP-MS results of dissolved metals in WF-1, WF-2 and SSL-1 water (□g/L)..... 6-4

Table 6 2 Other notable chemistry in WF-1, 2 and SSL-1 waters..... 6-4

Table 6 3 Major dissolved iron and 2H and 18O isotope ratios by Kiho et al. (2011) 6-5

Table 7 1 Permeability values used for the Strawberry Canyon model. The Wildcat Fault (Fd) has both a core and damage zone, whereas Fc, the Hayward Fault, and the Strawberry Creek Fault just have damage zones. Within the Moraga landslide, the permeability is the same as the permeability in the Moraga, but between the Moraga landslide and any adjacent material, permeability is three times lower..... 7-13

Table 7 2 Permeability values used for the East Canyon sub-model The anisotropic values for the fault reflect the pumping test results. The rest of the values are optimised values to match the observation data..... 7-13

List of Figures

Figure 2 1. Map showing the location of surface geophysical survey lines, trenches, boreholes and inferred trace of the Wildcat Fault by Gramer, 2000 (light blue line). Red lines at the botom left indicate the Hayward Fault. 2-10

Figure 2 2 Original electrical resistivity survey interpretation for ER-1(top), ER-2 (middle) and ER-3 (bottom). 2-11

Figure 2 3. Reanalysis results of the resistivity data by Sasaki (2009). 2-12

Figure 2 4. Resistivity reanalysis results by Korkealaakso (2009). 2-13

Figure 2 5: Original seismic reflection survey interpretation for SR-1(left), SR-2 (middle) and SR-3 (right). 2-14

Figure 2 6: Arrival time analysis of SR-2 data. The apparent velocity is faster to the east. 2-15

Figure 2 7: Location of ER-4 profile. The blue broken lines indicate potential fault trace identified in the ERT inversion. The red broken line is the previously suspected trace of the Wildcat Fault. 2-16

Figure 2 8: (a) the AGI SupeSting resistivity imaging system, (b) looking the resistivity cable laid on the ground toward the east, (c) cable laid over asphalt road, and (d) the electrode drilled into the asphalt. 2-17

Figure 2 9: (a) Scattered plot of injected current, (b) scattered plot of measured voltage for ER-4. 2-18

Figure 2 10: Two equally good resistivity inversion results, (a) and (b). 2-19

Figure 2 11: Comparison of (a) measured and (b) calculated data for the inversion model in Figure 2 10 (a). 2-20

Figure 2 12: Comparison of (a) measured and (b) calculated data for the inversion model in Figure 2 8 (b). 2-20

Figure 2 13: Inverted resistivity structure of ER-5. 2-21

Figure 2 14: (a) Scattered plot of injected current, (b) scattered plot of measured voltage for ER-5. Compared to those of ER-4 (Figure 2 9), the signals are noticeably weak. 2-21

Figure 2 15: Inverted image of ER-4 using only dipole-dipole data. 2-22

Figure 2 16: Projected faults (dark blue lines) based on ER4 and ER5 inversion images. Light blue line is the Wildcat Fault by Graymer (2000). 2-22

Figure 2 17: Surface traces of the faults by Kiho et al (2012). Superimposed is the ER-5 survey line. The anomaly at the east end of the ER-5 profile could be that caused by the Fd-main fault. 2-23

Figure 2 18: Seisimic refraction survey photos: (a) P-wave geophone, (b) seismographic station, (c) seisguns, (d) seisgun blast, (e) S-wave source. 2-24

Figure 3 1. Sattelite picture showing the location of surface geophysical survey lines,

trenches, boreholes and inferred traces of the Wildcat Fault (light blue solid and broken line). 3-16

Figure 3 2. Satellite view of the WF borehole locations compiled uising Google Earth. .. 3-17

Figure 3 3. 3-D representation of WF boreholes. Also shown are the trenches TR-1 through 3. 3-18

Figure 3 4. Geologic columns of WF boreholes. 3-19

Figure 3 5. Drilling of WF-5. Note that it is a 60□ inclined drilling..... 3-20

Figure 3 6. Comparison of drilling speed and core recovery percentage of WF-4 (left) and WF-5 (right). Massive core losses occurred between 170m ~bottom in WF-4 and 125~160m inWF-5. 3-21

Figure 3 7. Head changes in WF-1 intervals since 8/31/2011. The monitoring intervals started to respond to the drilling activity in WF-5 when the drilling reached at ~420ft indecated by the arrow..... 3-22

Figure 3 8. Fluid level changes in WF-5 as the drilling progressed. Blue line is the pressure measured by pressure transmitter converted to freshwater head. The red line is the density compensated level. Green line is the tape measured level. 3-23

Figure 3 9. Summary of faults encountered in WF-1~3 (after Kiho et al., 2012). 3-24

Figure 3 10. Summary of faults encountered in WF-4 (after Kiho et al., 2012)..... 3-25

Figure 3 11. Alterantive interpretation of Fb feature (broken pink) that intersect WF-2, 3, 4 and 5 at the TOR-TCC contact viewed from two angles. The green triangles denote the contact observed in cores. Note it does not go through TR-3..... 3-26

Figure 3 12. Alternative interpretation of the Wildcat main (light red line). It is steep and slightly east dipping, goes though the flow zones in WF-4 and WF-5 (pink diamond), brushes by WF-1, TR-1~3. 3-27

Figure 3 13. Possible interpretation of fracutre orientation statistics: More mildly dipping fractures on the west side of the suspected Wildcat Fault than on the east side, where many steeply dipping fractures are observed (stereo nets after Kiho, et al., 2012)..... 3-28

Figure 3 14. Capliper logs super imposed on geologic logs from WF boreholes. 3-29

Figure 3 15. Composite plots of BTV, caliper, fracture orientation, fracture density, natural gamma, and resistivity logs for WF-1, 2 and 3. Not apparent correlation to geology was found. 3-30

Figure 3 16. Composite plots of BTV, fracture density, orientation, SP, natural gamma, and resistivity logs fo r WF-4 and 5. 3-31

Figure 3 17. Excerpt of the ELOG results from WF-4, showing the oppsite kicks of the natural gamma and resistivity locations, marked by the blue arrows corresponding to bleached lithified brecchiated chert. A picture of the core of such rock from 607 ft (185 m) is also shown. 3-32

Figure 3 18. Borehole televiewer images from WF-3: (a) 74~77.4m (243-254ft), where the

largest inflow was observed by a FFEC log. (b) 148.7~151.7m (488~498ft), where a large fault is suspected..... 3-33

Figure 3 19. The BTV image from WF-4 at 681–684 ft (207.5 m–208.5 m). Also shown is the picture of the core from the same interval, most of which is not recovered. Note the very grainy image of the BTV, indicating that the rock is pulverized. 3-34

Figure 3 20. Flowing fluid electric conductivity log (FFEC) results (red lines) superimposed on the geologic columns of WF boreholes. Ligtht blue arrows indicate inflow locations.. 3-35

Figure 3 21. Core orientation tool. The probe attches to the core retriever and is pushed against the top of the next core at the bottom of the hole together with the tip of the red pencil. Ball bearings lock to indicate the hole bottom direction. The shape of the circular nails is matched to that of core top. Red line on the core is drawn to mark the bottom direction of the hole. 3-36

Figure 4 1 Regional stratigraphy..... 4-7

Figure 4 2 Regional geologic map of Berkeley, CA (Graymmer, 2000)..... 4-8

Figure 4 3 Map of Quaternary faults in the bay area 4-11

Figure 4 4 Map showing the WCF in the context of main faults in the San Francisco Bay Area 4-13

Figure 4 5 Aerial view of the study and surveyed area along the WCF 4-16

Figure 4 6 Location of the five trenches TR1-TR5 in relation with the Hayward Fault.. 4-17

Figure 4 7 Location of the five wells along the Calvin Road in the eastern end of LBNL 4-18

Figure 4 8 2D view of all core logs in the study area 4-20

Figure 4 9 3D view of core log distribution along the Calvin Road..... 4-21

Figure 4 10 (left) Steep dipping bedded chert in the eastern fence North of Calvin Road. Figure 4 11 (right) Gentle dipping beds. Attitude: N70E/30N. Note thin layers of inter-bedded dark mudstone..... 4-22

Figure 4 12 (left) Sub-horizontal bedding of Claremont chert in the Fire Trail 4-23

Figure 4 13 (right) Overturned fold of the Claremont chert near by Figure 1-11..... 4-23

Figure 4 14 Example of intrusive sandstone dike observed in cherts of Claremont Formation in TR3..... 4-24

Figure 4 15 Friable white sand dike in TR5 4-25

Figure 4 16 WF1_130ft (39.6m) – Foram rich laminated chert (right open nicols and left cross nicols)..... 4-28

Figure 4 17 WF2_297ft (90.5m) – Quartz and mud rich layers (right open nicols and left cross nicols)..... 4-28

Figure 4 18 Massive sandstone from WF1 4-29

Figure 4 19 Types of sandstone 4-30

Figure 4 20 Diagram showing sandstone classification 4-31

Figure 4 21 Example of sandstone from WF1_504.7ft (154m). Green grains are glauconite (open and cross nicols) 4-32

Figure 4 22 Thin section of WF4_298ft (90.8m) showing lithic fragments in sandstone (open and cross nicols) 4-32

Figure 4 23 Example of bleached material from WF1 4-33

Figure 4 24 View under microscope shows two types of carbonate cut by quartz veins. (both cross nicols) 4-34

Figure 4 25 Presence of forams in the bleached material (both cross nicols) 4-34

Figure 4 26 The graphic illustrates the XRD patterns for the Monterey Group by Pisciotto and Garisson, 1981 4-35

Figure 4 27 XRD patter for WF1_437ft (133.2m) 4-36

Figure 4 28 XRD pattern for WF1_321.6ft (98m) 4-36

Figure 4 29 XRD pattern for WF3_391ft (119m) 4-37

Figure 4 30 XRD pattern for WF4_268ft (82m) 4-37

Figure 4 31 XRD pattern for WF4_368ft (112m) 4-38

Figure 4 32 Outcrop of interbedded conglomerate and siltstone next to the cross road between the Fire Trail and Riffle Range road north of Jewel Lake in Tilden Regional Park. No evidence of fault in the creek 4-40

Figure 4 33 Intercalation of greenish fine sandstone and reddish clay rich sediments – Orinda Formation in the Fire Trail 4-41

Figure 4 34 The typical mottled green sandy to siltstone and dark mudstone in TR2 4-42

Figure 4 35 Typical greenish-gray silty to sandstone mottled with dark red mudstone-WF3_182ft (55.5m) 4-43

Figure 4 36 Contact of fine and medium coarse sandstone. WF3_497ft (151m), open and cross nicols. 4-44

Figure 4 37 Presence of white mica (muscovite) WF3_497ft (151m), open and cross nicols. 4-44

Figure 4 38 Presence of glauconite in WF3_506ft (154m), open and cross nicols 4-45

Figure 4 39 Orinda mudstone WF3_216ft (66m), open and cross nicols 4-45

Figure 4 40 Microfossil is abundant in the Orinda Fm. (open and cross nicols) 4-46

Figure 4 41 Samples from core log showing the presence of large shells preserved in the San Pablo Gr. 4-47

Figure 4 42 Typical San Pablo Group core log from WF3 4-47

Figure 4 43 WF3_262ft (80m)– Fragments of shell in coarse sandstone (both cross nicols) 4-48

Figure 4 44 Trench log of TR1 by Kiho et al, 2009 4-51

Figure 4 45 View to the west of trench NUMOTR2 near the north gate to the Fire trail.... 4-52

Figure 4 46 Main fault in TR2 showing main deformation concentrated in the Orinda Fm. 4-52

Figure 4 47 Clay gouges in faulted Orinda Formation 4-53

Figure 4 48 Mosaic of second fault observed in the middle of TR2. 4-53

Figure 4 49 Sketch of TR2 by Kiho et al, 2009 4-54

Figure 4 50 Fault contact between Orinda and Claremont Fm. 4-54

Figure 4 51 Sample of fault contact by Kiho et 2009 4-55

Figure 4 52 Sketch of trench TR3 by Kiho et al, 2009 4-55

Figure 4 53 View of TR-4 along the Panoramic Road..... 4-57

Figure 4 54 Sketch of TR4 by Kiho et al, 2010 4-57

Figure 4 55 View of the shallow trench TR5..... 4-58

Figure 4 56 Schematic drawing of Trench TR5 4-58

Figure 4 57 Dense material found in the contact between Orinda/San Pablo and Claremont. 4-59

Figure 4 58 Under the microscope the clasts and matrix are intensely cut by carbonate veins (both cross nicols) 4-60

Figure 4 59 Brecciated clasts of laminated chert cut by carbonate veins (open and cross nicols) 4-60

Figure 4 60 Conglomerate found in the contact between Orinda/San Pablo and Claremont. 4-60

Figure 4 61 Similar clasts and matrix as described in WF2. Presence of fragments of shells 4-61

Figure 4 62 Fault zone in WF3 showing the contact between Claremont Fm and Orinda Fm. 4-61

Figure 4 63 Fault contact between Orinda Fm. and Claremont Fm. in WF5 4-62

Figure 4 64 Clasts in sheared matrix of fine grained sandstone to siltstone..... 4-63

Figure 4 65 Intraclasts of dark material near the contact of granular and fine-grained material (open andcross nicols)..... 4-64

Figure 4 66 Immature sandstone with fine mica and glauconite (green mineral).Open and cross nicols. 4-64

Figure 4 67 Deformation in the Orinda Fm. in WF3 4-65

Figure 4 68 Zone of deformation in the Orinda Fm in WF5 at 148-150ft (45-46m)..... 4-65

Figure 4 69 Foliated cataclasite at 91.74m depth 4-66

Figure 4 70 Features of typical cataclasite is observed under the microscope (both open nicols) 4-67

Figure 4 71 Shear bands and dark bands are typical features of cataclastic deformation (both open nicols) 4-67

Figure 4 72 Deformation observed from 500-600ft. Location of thin section matches with location of carbonate istope sampling..... 4-69

Figure 4 73 The main zone of deformation occurs below 600ft (183m). Note increase in the number of carbonate veins. 4-70

Figure 4 74 Lamination and carbonate veins in cross-polarized views 4-71

Figure 4 75 Cataclastic flow along the dark brown zone and distribution of carbonate veins and s-c structure. All open nicols. 4-72

Figure 4 76 Red dots - 3D view of locations where gouge were described 4-75

Figure 4 77 Possible model for the fault network observed by the gouge distribution in core logs 4-76

Figure 4 78 3D regional geologic model for the study area. 4-78

Figure 4 79 Sliced view of regional model showing the well logs..... 4-78

Figure 4 80 Local borehole model illustrating the main faults in the study area. 4-79

Figure 5 1.Aerial map of the boreholes in the study area incluindg WF-1~5 and SSL-1~2. Also shown are hydraugers, Lennert-1, Quarry-1 and BG-1..... 5-18

Figure 5 2. Series of slug injection/withdrawal tests and pump tests conducted in WF-3. . 5-19

Figure 5 3. Sumperimposed plot of selected sulg test data from WF-3. 5-20

Figure 5 4. Type curve match of the slug test data in WF-3. The data are the water slug tests conducted on May 9th (red) and May 17th (blue), respectively. Broken line is the 1-D flow solution. 5-21

Figure 5 5. (a) The packer string used in WF-1~3 holes. (b) The double packer system used in WF-4 being surface tested. Soapy water is used to detect any potential leaks from the fittings and the glands..... 5-22

Figure 5 6. Packer seating in relation to fault core. (a) Packer above the fault, (b) below the fault, and (c) on the fault. Note that neither (a) or (b) isolates the zone on either side of the fault. 5-23

Figure 5 7. Mass spectroscopy results from the gas collected in WF-4..... 5-24

Figure 5 8. The head transients in three packed-off zones of WF-4 between 12/16/2010 and 2/14/2011, during which a free flow test (on January 17) and a three-day pump test in (January 22–24) were conducted. 5-26

Figure 5 9. Drawdown responses in WF-1#2~5, WF-2#2~#5, WF-3#2~5 as well as WF4#1,during the pumping in WF-4#2. Note that the pressure in the pumping interval did not recover fully to the pre-test level. The zones in WF-2 responded much stronger than those in WF-1 and 3. 5-28

Figure 5 10. Semi-log plot of the drawdown in the pumping zone during the WF-4#2 pumping test and the straight line analysis. 5-29

Figure 5 11. Horner plot of the recovery data of the pump test in WF-4#2..... 5-30

Figure 5 12. Responses in WF-1 intervals to WF-4 pumping in Jan21-24 followed by the recovery period of one week..... 5-31

Figure 5 13. Pressure response in WF-2 invervals to the pumping test on Jan. 21st and the massive packer leak on Feb 4th in WF-4#2. 5-32

Figure 5 14. Pressure response in WF-1, WF-2 and WF-4 invervals to the pumping in WF-5#2. Zones in WF-1 and WF-4#3 respond clearly. No responses in WF-2 zones are detected. 5-33

Figure 5 15. Comparison of pressure responses of WF-2 zones to WF-1#5 and WF-4#3 during the pumping in WF-5#2. Zones in WF-1 and WF-4#3 respond clearly. No responses in WF-2 zones are detected although they are closer to the pumping zone than WF-4#3... 5-34

Figure 5 16. The Wildcat Fault zone structure intersecting WF holes (Kiho et al., 2012).. 5-35

Figure 5 17. Head transients in WF-1 since January 2011. 5-37

Figure 5 18. Head transients in WF-2 since January 2011. 5-38

Figure 5 19. Head transients in WF-3 since January 2011. 5-39

Figure 5 20. Head transients in SSL-1 and SSL-2 5-40

Figure 5 21. Semi-log plot of the drawdown at SSL-1..... 5-41

Figure 5 22. Head changes since August 1st, 2011 in selected intervals from WF boreholes. The head of the zones in WF-1 holes decline at faster pace than the other zones in WF-2 and 3. The heads in WF-3 was almost constant until the end of October, when the packer configurations were changed in WF-4. 5-42

Figure 5 23. Difference in buildup behavior on opposite sides of the fault. 5-43

Figure 5 24. Locations of hydraugers and the average flow rate in the East Canyon area of LBNL. 5-44

Figure 5 25. Flow-rate fluctuations at the outfalls of the Lennert-1. It averaged 7.5 l/min

over the period with some seasonal fluctuations. 5-45

Figure 6 1. Oxygen isotope compositions of secondary carbonate minerals in fractures in Borehole WF-4. Also shown are the approximate range of □18O values for marine carbonates and for calcite in equilibrium with measured values of present-day groundwater (average □18O = -6.5‰). 6-7

Figure 6 2. Examples of the carbonates analyzed. Note that the upper one has high □18O values and has open cavities with minimal signs of shearing (from the preserved cross cutting features). The bottom two have low □18O values and have many veins in sheared chert. 6-8

Figure 6 3. Bird's eye view of the study area showing the boreholes where water samples were collected (Kiho et al., 2012). 6-9

Figure 6 4. Locations where water samples and 3He core samples were collected (Kiho et al, 2012). 6-9

Figure 6 7. Conceptualization of groundwater flow direction and ages in the WF borehole area (Kiho et al., 2012). 6-10

Figure 7 1. Shaded DEM map of the Berkeley Hills. The study area is outlined in green. The red line is the East Canyon Submodel area. 7-15

Figure 7 2. The domain of the model showing the surface relief and some of the boreholes. 7-16

Figure 7 3. DEM with model boundary and various features shown: purple squares – trenches across the Wildcat Fault; red or cyan circles – wells. 7-17

Figure 7 4. Plan view of the geologic model. 7-18

Figure 7 5. The crossections of the geology along the Wildcat Fault (Kiho et al., 2011). 7-19

Figure 7 6 Fault structure model near WF boreholes proposed by Kiho et al. (2011). 7-20

Figure 7 7. Gelogic structure model (Model #1) of 3.9 km x 2.1 km area that includes the study area proposed by Kiho et al. (2012). 7-21

Figure 7 8. Perspective view of the geologic model. 7-22

Figure 7 9. Perspective view of the geologic model showing faults and contacts between formations. Two faults are highlighted: the vertical Wildcat Fault (Fd) and the sloping Fc structure that is thought to provide good pressure communication between wells WF-2 and WF-3. 7-23

Figure 7 10. Plan view of the computational grid. 7-24

Figure 7 11. Perspective view of the central portion of the computational grid. The surface layer of inactive grid blocks is not shown. 7-25

Figure 7 12. Plan views of the central part of the grid for the top 11 layers in the numbered order, which illustrates some of the 3D features of the model including the Fc Fault. It also demonstrates that the model resolution is adequate to represent various features. The light green material in the top layer shows the landslide material. 7-26

Figure 7 13. The grid blocks representing wells extracted from the computational grid. .. 7-27

Figure 7 14. Numerical model used by Kiho et al.(2012). The bottom picture is an enlarged view of the borehole area. 7-28

Figure 7 15. Perspective view of the hydraulic pressure distribution for the base case, showing pressure isosurfaces. Topographic features such as the Strawberry Creek canyon are visible, as is the small pressure drop across the Wildcat Fault. 7-29

Figure 7 16. Perspective view of the hydraulic head distribution for the base case, showing head isosurfaces. Flow vectors are perpendiular to the head issurfaces. 7-30

Figure 7 17. Cross-sectional views of the hydraulic head distribution for the base cases. Topographic features such as the Strawberry Creek canyon are visible, as is the small pressure drop across the Wildcat Fault. 7-31

Figure 7 18. Perspective view of the gas saturation distribution for the base case, indicating the development of a vadose zone at high elevations and at places along the high-permeability structure of the Wildcat Fault. 7-32

Figure 7 19. Distribution of liquid flux out of the top surface of the model for the base case. 7-33

Figure 7 20. Comparison of modeled and observed hydraulic head measurements for the base case. 7-34

Figure 7 21. Hydraulic head profiles for a Wildcat Fault with no low-permeability fault core. 7-35

Figure 7 22. Hydraulic head profiles for a Wildcat Fault with no damage zone. 7-36

Figure 7 23. Hydraulic had profiles for the case with no Wildcat Fault. 7-37

Figure 7 24. The numerical mesh of the East Canyon sub-model. The Wildcat is modeled by two planes of low (purple) and high permeability (dark pink). The brown colored cells are the landslide material. 7-38

Figure 7 25. Comparison of simulation results with the observed head data from WF-1~3. Note that the model reproduces the deceasing head with depth very well as well as the low head anomaly in WF-1 possibly caused by the Fc fault. 7-39

Figure 7 26. Comparison of simulation results with the observed head data for WF-4 and WF-5. Solid vertical lines are observed and broken lines are simulated. The simulation underpredicts the head toward the bottom of WF-5. 7-40

Figure 7 27. Comparison of simulation results with the observed temperature data from WF-1~3. The data are solid lines and the simulation results are broken lines. The model captures the geothermal gradient well, although they are offset by a few degrees. 7-41

Figure 7 28. Flow vectors in the East Canyon sub-model and the pressure distribution at 200 m elevation. Note the flow vectors converge along the Wildcat Fault. Flow out of the Quarry-1 well also noticeable. 7-42

Figure 7 29. Saturation distribution of the East Canyon sub-model. The area south of the

WF boreholes are all saturated. In reality, the water is drained off through storm drains. 7-43

Figure 7 30. Compartion of simulation and observed head transients at WF-1#3 (blue) in response to seasonal rainfall using the best East Canyon submodel with 10% (red) and 5% (green) porosity, and isotropic Fd zone The daily precipitation (light blue) is plotted agains the right axis. Negative spikes in head in data are caused by pump tests, which were not modeled. Note that the head decline rate during the dry period is reproduced better assuming 5% average porosity. 7-44

Figure 8 1 Example readings of failing sensors. a) Noisy signal. Similar to the pressure behavior when de-gassing is present. b) Upward drift. c) Downward drift . (d) First downward and then upward drift. 8-4

Figure 8 2 Damaged packer (below) and normal packer (above). 8-5

Figure 8 3 Packer locations in relation to fault core: Packer is located either (a) below or (b) above the fault core to allow for leakage through borehole. (c) Packer is placed just right at the fault core. (d) A newly proposed continously sealing packer system. 8-12

Figure 8 4 New concept packer system that continously seal the borehole to avoid artificial short-circutting of pressure through the borehole. Their surfaces are made flush and neutraly bouyant in water..... 8-13

1 Introduction

The Nuclear Waste Management Organization of Japan (NUMO) and the Department of Energy of the United States of America (DOE) established a cooperative agreement in the field of radioactive waste management on July 10, 2002. In May 2005, NUMO and the Regents of the University of California, as the DOE Management and Operating Contractor for the Ernest Orlando Lawrence Berkeley National Laboratory (LBNL), entered into an agreement to collaborate, and for LBNL to conduct work, under the auspices of the bilateral agreement.

In 2006, ANRE (Agency for Natural Resources and Energy), jointly with JAEA (Japan Atomic Energy Agency), identified outstanding technological issues and needs regarding the research and development for geologic disposal of high-level radioactive waste (HLW) subsequent to the publication of the Second Progress Report by JNC (Japan Nuclear Cycle Development Institute) in 1999. Research organizations in Japan as well as NUMO have been conducting investigations on these issues and needs. In the area of groundwater hydrology, four R&D needs were identified and are currently being investigated: (1) improvement of groundwater flow characterization technology, (2) development of testing and characterization technology in coastal areas, (3) development of testing equipment and technology, and (4) field application of testing and characterization technology. NUMO has been incorporating the results of the outcome of these R&Ds as they become available and are deemed appropriate, and is in the process of systematizing the testing and characterization technology to form a solid technical foundation for selecting the sites for detailed investigation.

The first NUMO-LBNL collaborative project, entitled “Feature Detection, Characterization and Confirmation Methodology,” was designed to further develop radioactive waste management technologies related to an investigation strategy and technology for detection, characterization, and confirmation of key geologic features at possible nuclear waste repository sites. The project was carried out from May 2005 through March 2007. Among other important findings, the study has identified the hydrologic

properties of fault zones as one of the most important parameters that need to be evaluated during the preliminary investigation stage. Based on the lessons learned at the Mizunami and Horonobe URLs, as well as at numerous mines, dams, and tunnels—and given the geologic environment of the Japanese Islands—faults are likely to exist almost ubiquitously, which need to be assessed both at the preliminary and the detailed investigation stage (the length scale of the faults of interest would range from several kilometers in the former down to several hundred meters in the latter). However, none of the four R&D activities mentioned above sufficiently addresses the development of systematized hydrologic-characterization technology specifically tailored for fault zones. At present, it is necessary to use perhaps overly conservative values for the hydrologic parameters of fault zones for the design and performance assessment of a repository. Therefore, development of a more efficient and reliable fault-zone characterization technology is highly desirable. The geologic properties of faults and the relationships among their geometry, type, fault parameters, and internal structures are being investigated mostly overseas. Hydrologic investigation of faults of various sizes are also being conducted at foreign as well as at domestic characterization sites. However, the relationship between the geologic and hydrologic properties of faults is not yet studied sufficiently.

In light of the above, NUMO and LBNL entered an agreement for LBNL to conduct a three-year study entitled "Development of Hydrologic Characterization Technology of Fault Zones" in August 2007. For FY2007, the objectives of the study were to organize the information available from overseas to ultimately establish an efficient and systematized methodology for hydrologic investigation and characterization of faults at the scale of interest *during the preliminary investigation stage*, for more practical design and performance assessment. LBNL's study (Karasaki et al, 2008) concluded that while there is very little available in the literature that relates the geologic structure of faults to hydrology, it still may be feasible to classify faults based on geologic attributes to predict their hydrologic characteristics, and that it is critical to establish a field investigation technology for fault-zone hydrology. In July 2008, NUMO and LBNL agreed to continue the project and develop a field site to study fault-zone hydrology.

As part of the first phase of the field study program, a literature survey was conducted, which concluded that it may be possible to classify faults by indicators based on various geometric and geologic attributes that may indirectly relate to the hydrologic property of faults. The Wildcat Fault in Northern California, USA, which is a predominantly strike-slip fault and a member of the Hayward Fault system, was chosen to be the target fault of the field study. The Wildcat Fault runs through the property of the Ernest Orlando Lawrence Berkeley National Laboratory (LBNL), within and around which surface-based investigations were conducted from September of 2008 through March 2011.

Three trenches were excavated, and at least one fault was encountered in all three trenches. Some intriguing and puzzling discoveries were made that may contradict past published work. Predictions were made regarding the hydrologic properties of the Wildcat Fault based on the analysis of fault structure, and preliminary conceptual models of the Wildcat Fault were proposed. The Fault appears to have multiple splays, with some low-angled faults possibly being part of a flower structure. Surface geophysical investigations were conducted using electrical resistivity survey and seismic reflection profiling along three survey lines north and south of the LBNL site. One interpretation of the Fault generated from these investigationssuggests that the Wildcat Fault is westerly dipping; however, due to the complex geology of the Berkeley Hills, multiple interpretations of the geophysical surveys were possible. The findings are summarized in Karasaki et al (2009).

The second phase of the investigation program started in August 2009. Two more trenches were cut along the ridge of the hill that lies south of LBNL where surface geophysical surveys were conducted. The trenches encountered multiple faults. Two 150 m deep boreholes, WF-1 and WF-2, were core drilled on each side of a projected trace of the Wildcat Fault, in the East Canyon area of LBNL, during the period from December 2009 through March 2010. It was observed that the rocks were extensively sheared and fractured; gouges were observed at several depths, and a thick cataclasitic zone was also observed.

While confirming some earlier published conclusions from shallow observations about Wildcat, we made some unexpected findings. Preliminary analysis indicated that Wildcat

near the field site consists of multiple faults, with the hydraulic test data suggesting that the hydrologic structure of the fault zone had two distinct properties. A summary of these findings can be found in Karasaki et al (2010). In 2010, two additional boreholes, WF-3 and WF-4, were drilled and further investigation of the Wildcat Fault zone was conducted including geologic, hydrologic, geophysical, and geochemical studies. The results of these investigations can be found in Karasaki et al (2011).

In 2011, the last year of the five-year project, further investigation activities were conducted, including an electric resistivity tomography (ERT) and a refraction seismic survey. Another inclined borehole, WF-5, was drilled, targeting to intersect the main fault. This report summarizes the findings of these investigations, as well as overall findings made throughout the Project, which is conducted as a collaborative study between NUMO and US-DOE/LBNL. As such, the report integrates the findings by Kiho et al (2012).

It should be possible to apply/transfer the results and findings obtained in the present report, conducted at a site on the U.S. West Coast whose tectonic environment is just as active as that in Japan, to the Japanese repository program. It is expected that those results and findings would also be beneficial to the future U.S. program.

1.1 References

Karasaki, K., C.T. Onishi, Bill Black, and Sebastien Biraud, 2008, Development of Hydrologic Characterization Technology of Fault Zones, Phase I 2nd Report.

Karasaki, K., C.T. Onishi, and Y.S. Wu, 2009, Development of Characterization Technology for Fault Zones, LBNL-1635E, pp 157.

Karasaki, K., Onishi, C.T. and Zimmer, V., 2010, Development of Hydrologic Characterization on Technology of Fault Zones – Phase II Interim Report-, NUMO-LBNL-CRIEPI Collaboration Research Project.

Karasaki, K., C.T. Onishi, C. Doughty, E. Gasperikova, J. Peterson, M. Conrad and P. Cook, 2011, Development of a Hydrologic Characterization Technology for Fault Zones—Phase II 2nd Report —.

Kiho, K., Ueta, K., Miyakawa, T., Hasegawa, T., Tanaka, S., Ito, H., Hamada, M., Tsukuda, K, 2011, CRIEPI Technical Report, Survey and Analysis related to Development of Hydrologic Characterization Technology of Fault Zones

Kiho, K., Ueta, K., Miyakawa, T., Hasegawa, T., Ito, H., Hamada, M., Nakada, H., Tanaka, S., and Tsukuda, K, 2012, CRIEPI Technical Report, Survey and Analysis related to Development of Hydrologic Characterization Technology of Fault Zones IV.

2 Geophysical Investigation

2.1 Introduction

One of the challenges of conducting geophysical surveys is finding the optimum places (lines) for conducting surveys. As noted in Kiho et al. (2012), ideally some of the survey lines should be located near where boreholes will be drilled. If multiple kinds of geophysical techniques are going to be used— such as electrical, electromagnetic, and seismic surveys—it is best to conduct them all on the same line, so that the results can be compared and correlated. It is of course best to conduct all characterization activity in one location, but it is often impractical to do so. Nonetheless, as much as possible, survey lines should adhere to the following criteria. They should be:

1. Close to the site of interest
2. Straight
3. Perpendicular to the fault
4. Free of anthropogenic noise
5. Long enough to cover the depth of interest

In 2008, during the first phase of the field investigation project, surface geophysical surveys, specifically electrical resistivity and seismic reflection surveys, were conducted along the three lines shown in Figure 2-1. These lines satisfied Criteria 2 through 5 above. In addition, given our intention to bracket the fault in the north and south, we then decided to drill Wildcat Fault (WF) boreholes in the East Canyon area of LBNL. Thus, the first criterion in the list above was not met, for the following reasons (as noted in Karasaki et al. (2009):

1. The location of the Wildcat shown in the literature was believed to be accurate.
2. The truck-mounted source for the reflection surveys could not be used in the steep terrain near the WF boreholes.

3. Potential anthropogenic noise sources that may affect electrical surveys, including high voltage power lines, guard rails, and buried conduits and cables, are present along Wildcat Fault (WF) boreholes.

The results of the electrical resistivity survey are shown in Figure 2-2, and the results of the seismic reflection survey are shown in Figure 2-5. As noted in the previous report (Karasaki et al, 2009), multiple interpretations of the survey data are possible, mainly because of the highly complex geology and the inherent nature of geophysical surveys.

As part of the activities in the second phase of the project (Karasaki et al, 2010), the geophysical survey data from 2008 were reanalyzed, with the reanalysis of the electrical conductivity surveys carried out by two separate parties (Figure 2-3 and Figure 2-4), both of which showed better definition of the resistivity structure. However, there were no drastically new findings. The reanalysis of the seismic reflection data was performed by using first-arrival data only, effectively treating them as refraction survey data. The SR-2 data revealed strong evidence of a west dipping velocity discontinuity, corroborating the original analysis (Figure 2-6).

We then conducted an electrical resistivity survey in the East Canyon, which we call ER-4. The survey line is the closest ever to the WF borehole complex, marginally satisfying Criterion 1 as well as the rest of the criteria listed above. In the next section, we will describe ER-4 survey in detail.

2.2 Electrical Resistivity Survey (ER-4)

We laid out a surface electrical resistivity tomography (ERT) profile across the area of interest to image the subsurface and identify a possible fault. The profile (location as shown in Figure 2-7) was 350 m long with 6 m electrode spacing. The survey was parallel to and ~110 m north of the line that connects WF boreholes. Excellent quality data were obtained.

ERT methods use four electrodes to make each measurement: a known current is injected between two electrodes and the potential difference is measured across the other two electrodes. Electrical properties of the Earth's subsurface are related to rock types, the

presence or movement of water or other fluids, or to changes in temperature and salinity. We used a combination of dipole-dipole, Wenner and Schlumberger arrays, and an AGI SuperSting R8/IP system for data acquisition. The ERT dataset contained about 5,000 measurements. Data quality was very good—Figure 2-9(a) and Figure 2-9(b) show scattered plots of the injected current and measured voltage, respectively. For the interpretation, measurements that were below a specified minimum voltage and current were removed.

ERT data sets were inverted for resistivity variation as a function of location using an AGI inversion code (LaBrecque and Yang, 2001). Figure 2-10(a) and Figure 2-10(b) show two inversion results that fit measured data equally well. Figure 2-11 and Figure 2-12 show comparisons of calculated and measured field data for inversion results in Figure 2-10(a) and Figure 2-10(b), respectively. The warm colors indicate areas of high resistivity, while cool colors indicate areas of low resistivity. As can be seen from the figures, the measured and calculated data match very closely.

The ER-4 results appeared to show the clearest image of the subsurface structure thus far. The data were collected overnight, a relatively long time and much longer time than ER-1 through ER-3. The ER-4 data have much less noise than the previous three surveys. Furthermore, the survey line is much closer to the WF borehole complex and thus more easily relatable to the features encountered in these boreholes.

Figure 2-10 indicates that there are two discontinuities with low resistivity, at ~150 m and ~250 m from the east end of the profile. It also appears that there is a horizontal low-resistivity zone between the two vertical zones. One interpretation is that the discontinuity at 150 m is the Wildcat Fault, while the other discontinuity at 250 m could be the East Canyon Fault, whose existence has been disputed in the past. These inferred fault traces are indicated by the blue broken lines in Figure 2-7. The horizontal low resistivity zone can be interpreted as the damaged zone (with a high-water content) between the two faults.

2.3 Electrical Resistivity Survey (ER-5)

In the summer of 2011, we conducted ER-5, another ERT survey along the line approximately 75 m south and parallel to ER4 as shown in Figure 2-1. The location of the line was chosen so that it would be as close to the line that connects WF-1, 2, and 3 as permissible, but not too close because of the metal guardrail along the road and the service lines buried underneath it that would interfere with the electrical signal. Another consideration was that the line could not be parallel to or close to the high voltage power line overhead. (In retrospect, we should have elongated the line further to the east, challenging the thick poison oak infested bush.)

The inverted image of ER-5 is shown in Figure 2-13. As can be seen from the figure, the crux of the image is similar to that of ER-4: there are two somewhat vertical low-resistivity anomalies and a shallow horizontal low-resistivity anomaly. The latter could be landslide material with high saturation. Figure 2-16 shows potential faults indicated by the two ERT surveys. The fault on the west side may be the East Canyon Fault, the existence of which has recently been questioned (Jordan, 2011).

One interesting feature in Figure 2-13 is the low-resistivity anomaly at the east end. This could be an edge effect or the fault at the Claremont-Orinda contact, which, according to Kiho et al (2012), is the Fd. the main Wildcat Fault.

As for the quality of the ER-5 data, the measured signals were much smaller compared to those of ER-4. Consequently, they had larger errors in repeatability and hence larger uncertainties in the inversion estimates. One cannot compare the ER-5 and the ER-4 profile results directly because there were many factors that were different, including the profile location and electrode configurations for data acquisition. Contact resistance for most of the electrodes on ER-4 was around 1,000 ohms, all below 2,000 ohms. On ER-5, the contact resistance was less than 1,000 ohms for some of the electrodes, but most of them were in the 2,000-10,000 ohm range, with a few electrodes that did not perform well. The acquisition schedule for ER-4 contained many electrode combinations, including dipole-dipole, bipole-bipole, and Schlumberger and Wenner. The acquisition schedule for

ER-5 contained only dipole-dipole electrode configurations. A lot of measured voltage and current values were close to system accuracy levels, and so about 50% of data had to be eliminated from the data set before the inversion. While we cannot directly compare the conditions of ER-4 and ER-5, we can examine the results of ER-4 by extracting the dipole-dipole data and conduct an inversion on those data alone, as shown in Figure 2-15. As can be seen from the figure, while the other electrode combinations would yield stronger signals, deeper penetration and more robust inversion, the dipole-dipole data set did resolve most of the features. Thus, it is probably safe to conclude that ER-5 results are reasonable, although those of ER-4 are much more robust.

2.4 Seismic Refraction Survey (SF-1)

The surface geophysical survey results thus far have been inconclusive in pin-pointing the location of the main fault. One of the reasons is that the methods used may not be suitable for the highly noisy environment caused by both natural and anthropogenic reasons. Thanks to the generosity of Dr. Rufus Catchings of USGS, we recently conducted a seismic refraction survey, in which we traced the ER-4 line and extended it ~150 m to the east, as indicated by the white line in Figure 2-1. This longer survey line would allow deeper penetration of signals and wider horizontal coverage.

One of the theories that Kiho et al. (2012) propose is that the main fault intersected by WF-4 would extend to the surface and define the Orinda-Claremont contact in the east of the WF complex. This theory assumes that the main fault misses the WF-5. There is also a contradictory theory, supported by some scientists working on the project, which holds that the main fault is nearly vertical and intercepted by WF-5. The refraction survey could corroborate one of the theories.

Figure 2-18 is a collection of pictures during the survey. Seisguns were used for the P-wave source; S-waves were generated by a sledge hammer hitting the side of an aluminum block.

2.5 Summary

In the first phase of our surface geophysical surveys, we conducted three reflection seismic and electrical resistivity surveys in total, one on the northern end and two on the southern end of the study area. The results were quite inconclusive. The reflection seismic data were very noisy, which was expected given the folded, fractured, and faulted environment. These data were then reanalyzed using only refracted waves. Although inconclusive, this reanalysis corroborated the existence of a west dipping fault across SR-2. The electrical resistivity surveys were also reanalyzed by two other experts, who corroborated the previous results. Since these surveys were conducted to bracket the boundaries of the study area, it was difficult to extrapolate the results to the borehole site area. After drilling WF-1–WF-3, it was still unclear where the main fault was, so we conducted ER-4, another electrical resistivity survey, the profile from which showed two anomalies possibly related to faults. We then drilled WF-4, which intersected a large deformation zone that we now think is the main fault, and then conducted yet another electrical resistivity survey, ER-5, whose profile was quite similar to that of ER-4. However, combining the two profiles failed to produce the image of the main Wildcat. More recently, we conducted a seismic refraction survey using P-wave and S-wave sources (Catchings, 2012). At the time of submitting this report, we are still waiting for the analysis results.

2.6 References

Jordan, P., personal communication, 2011.

Karasaki, K., C.T. Onishi, W. Black and S. Biraud, 2009, Development of Hydrologic Characterization Technology of Fault Zones: Phase I, 2nd Report, LBNL-1635E-2009.

Karasaki, K., C.T. Onishi, and Valerie Zimmer, Development of Hydrologic Characterization Technology of Fault Zones —Phase II Interim Report —, March 31, 2010.

Kiho, K., K. Ueta, K. Miyakawa, T. Hasegawa, H. Ito, S. Tanaka, T. Sasaki, M. Hamada, T. Tsukuda, Survey and Analysis related to Development of Hydrologic Characterization Technology of Fault Zones III, CRIEPI, 2011.

Korkealaakso, J., Personal communication, 2009.

LaBrecque, D. J. and Yang, X., 2001, Difference inversion of ERT data: a fast inversion

method for 3-D in situ monitoring: Journal of Environmental and Engineering Geophysics, 5, 83-90.

Sasaki, Y., Personal communication, 2009.

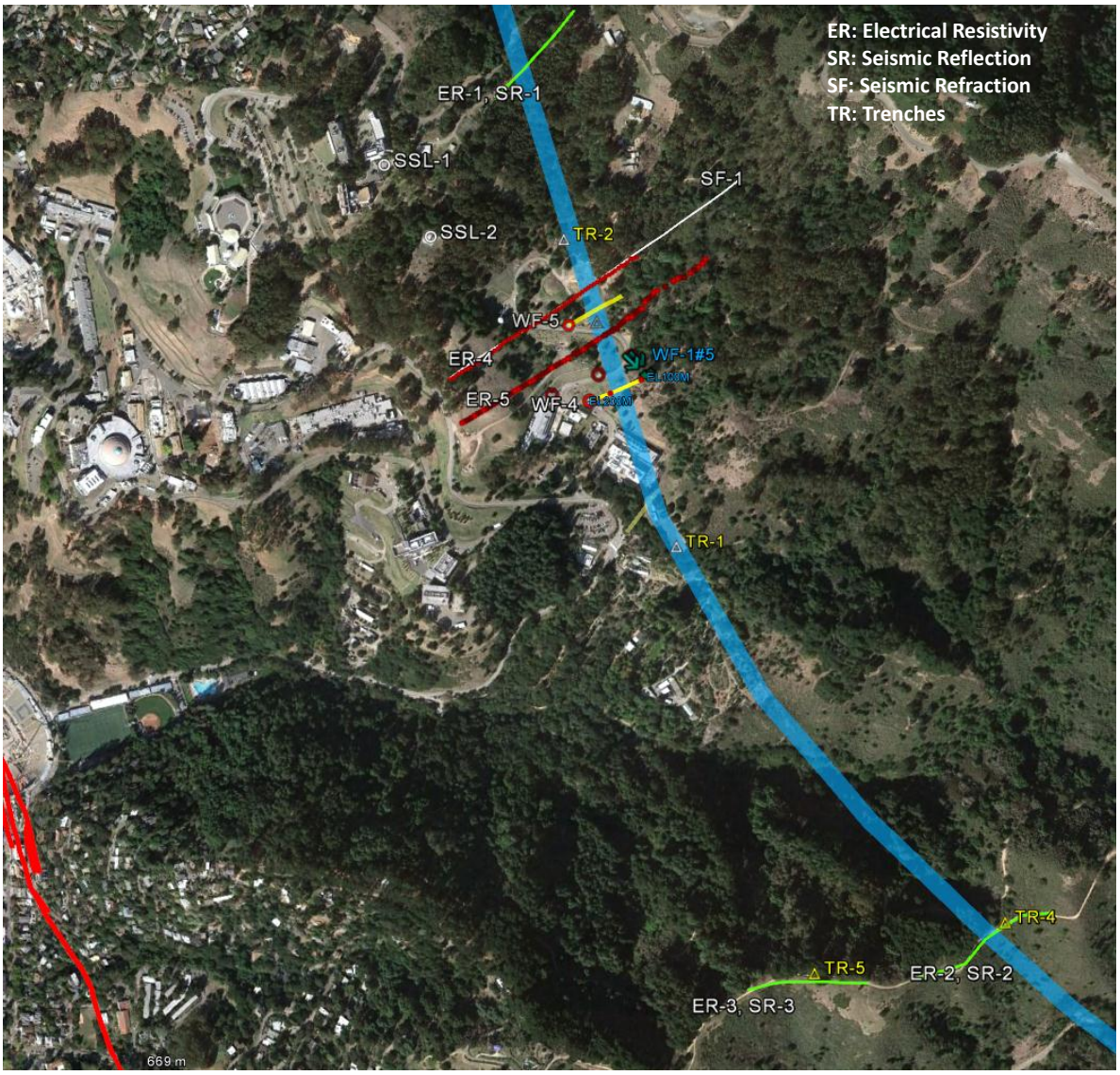

Figure 2-1. Map showing the location of surface geophysical survey lines, trenches, boreholes and inferred trace of the Wildcat Fault by Gramer, 2000 (light blue line). Red lines at the botom left indicate the Hayward Fault.

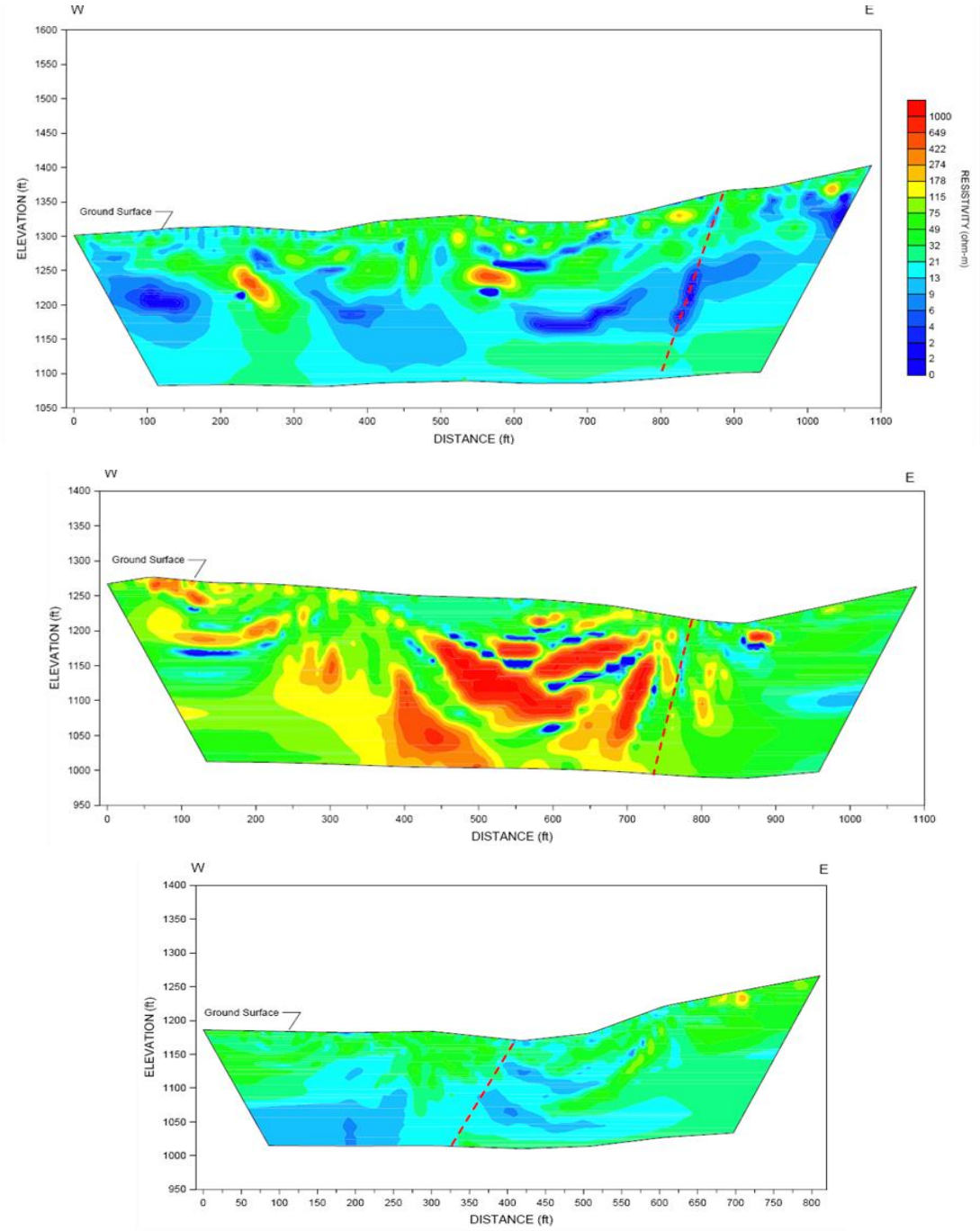

Figure 2-2 Original electrical resistivity survey interpretation for ER-1(top), ER-2 (middle) and ER-3 (bottom).

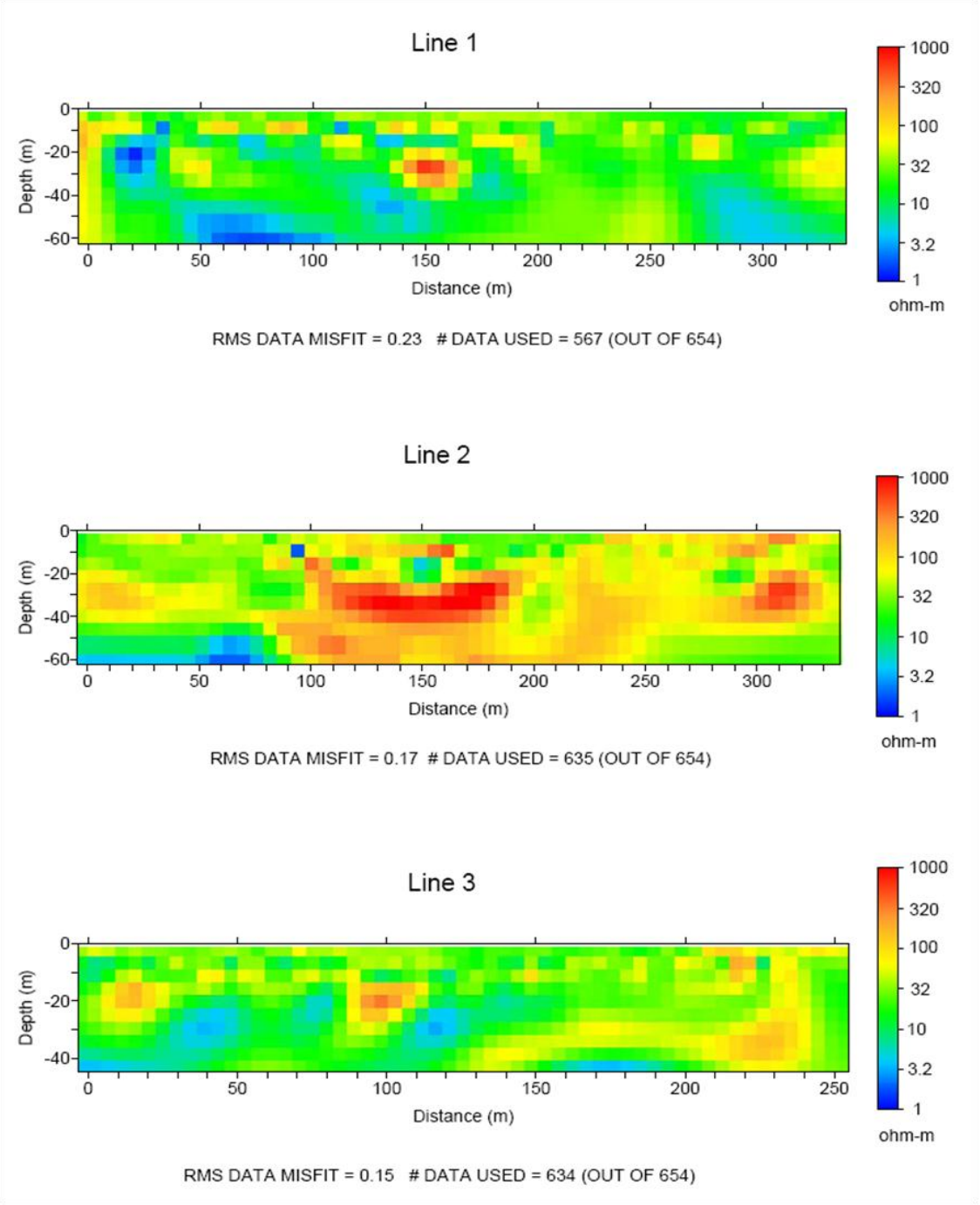

Figure 2-3. Reanalysis results of the resistivity data by Sasaki (2009).

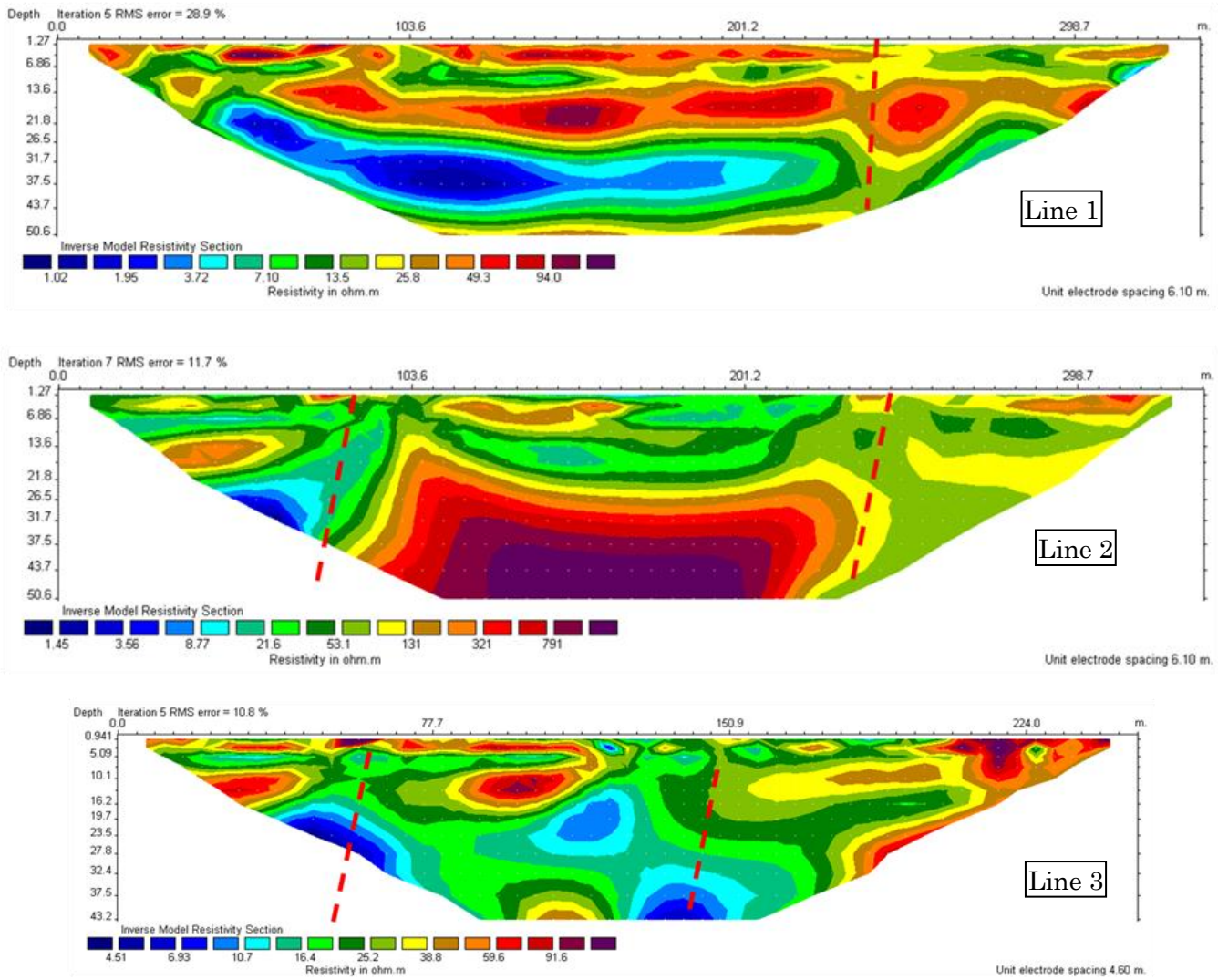

Figure 2-4. Resistivity reanalysis results by Korkealaakso (2009).

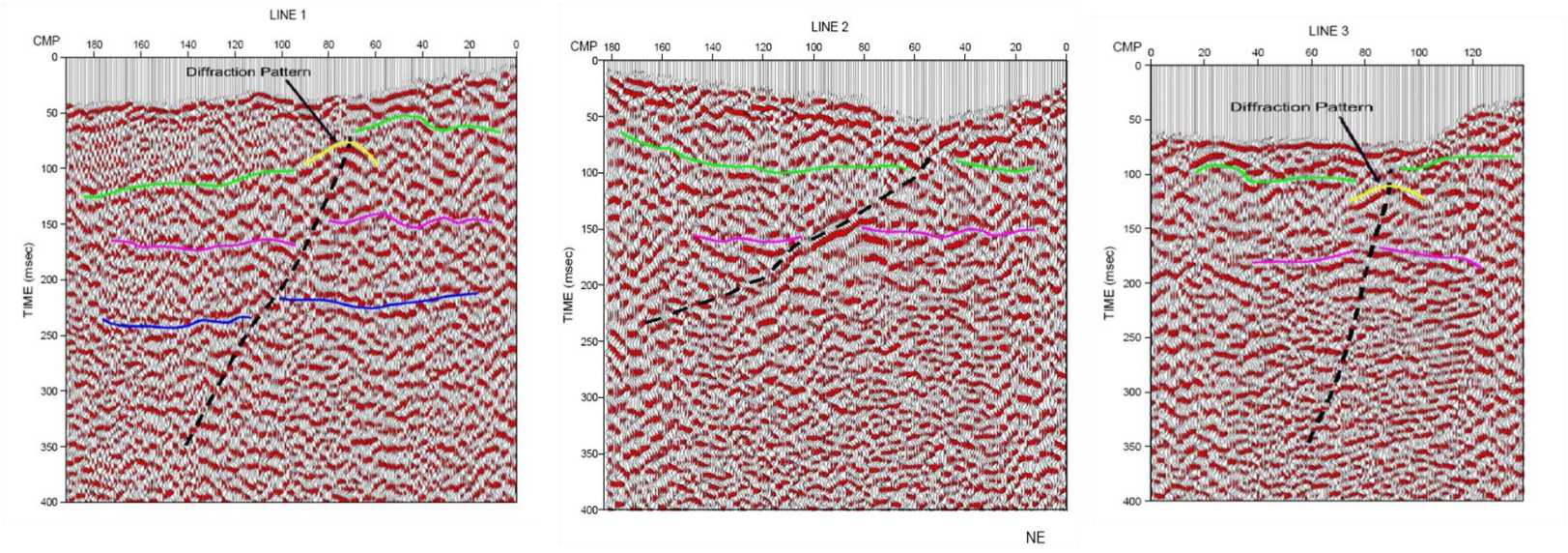

Figure 2-5: Original seismic reflection survey interpretation for SR-1(left), SR-2 (middle) and SR-3 (right).

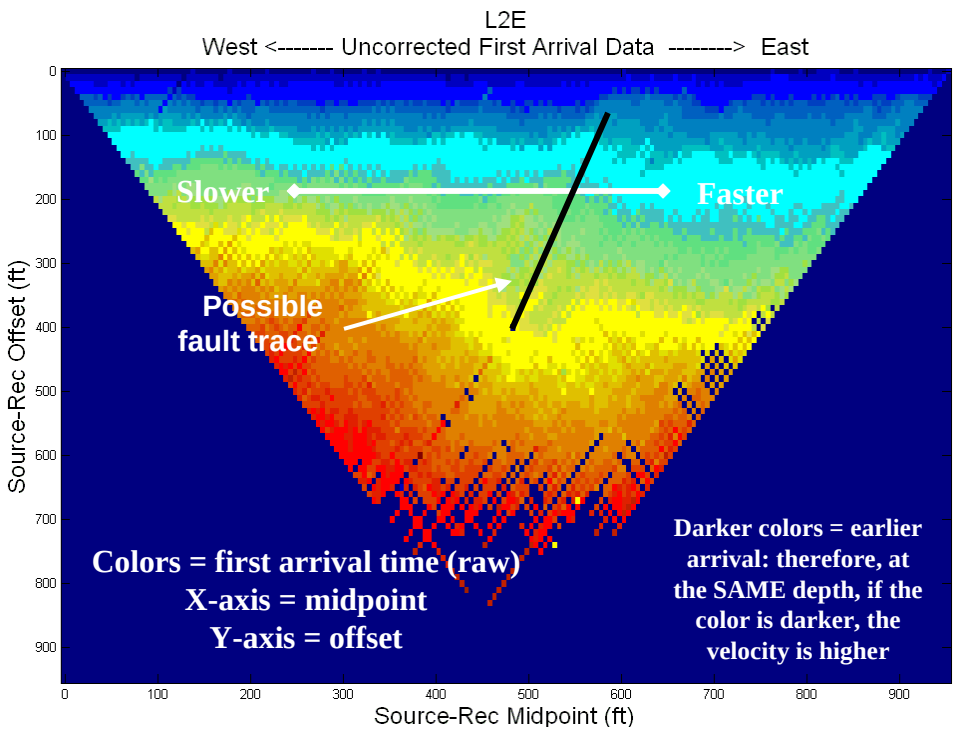

Figure 2-6: Arrival time analysis of SR-2 data. The apparent velocity is faster to the east.

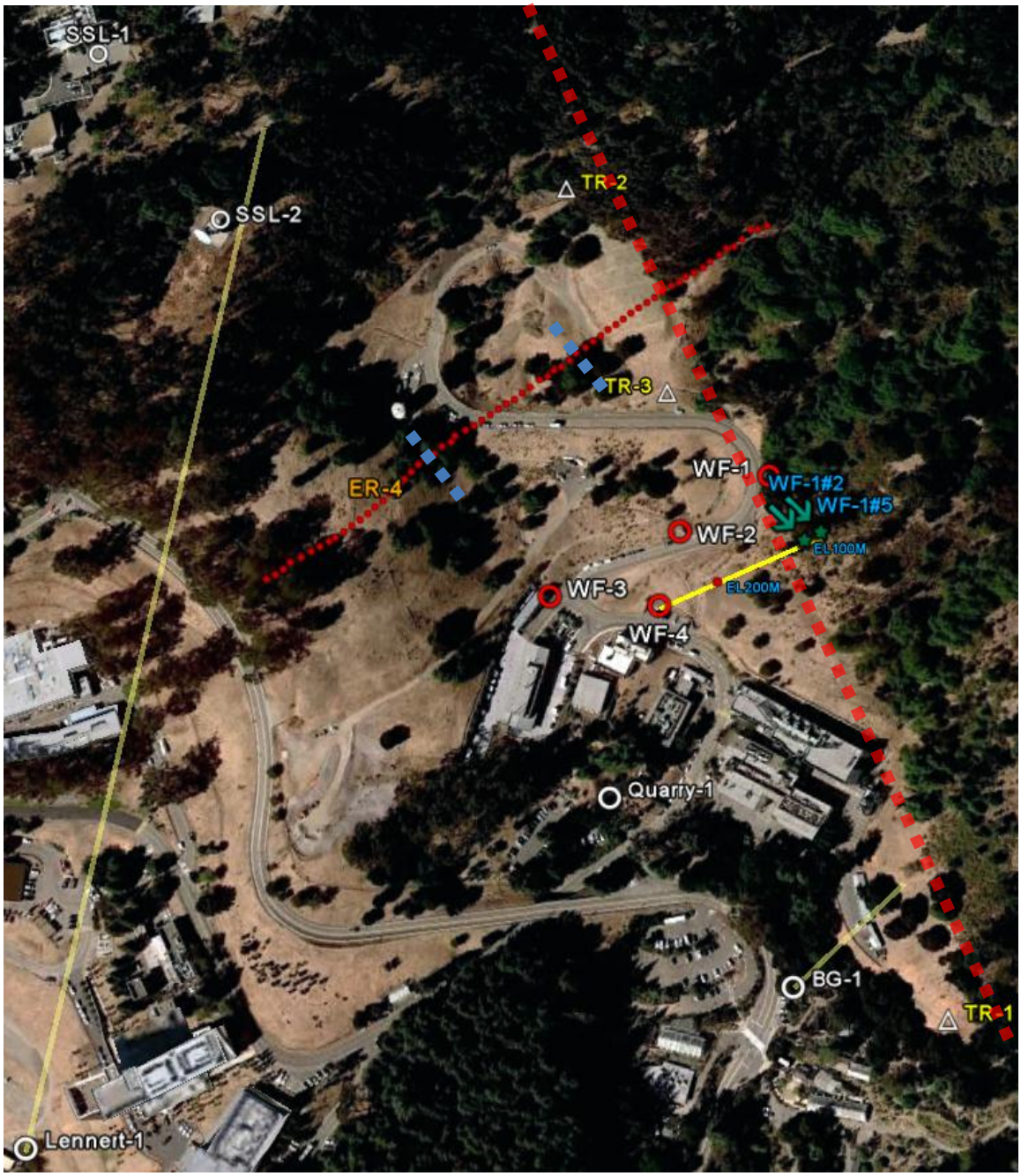

Figure 2-7: Location of ER-4 profile. The blue broken lines indicate potential fault trace identified in the ERT inversion. The red broken line is the previously suspected trace of the Wildcat Fault.

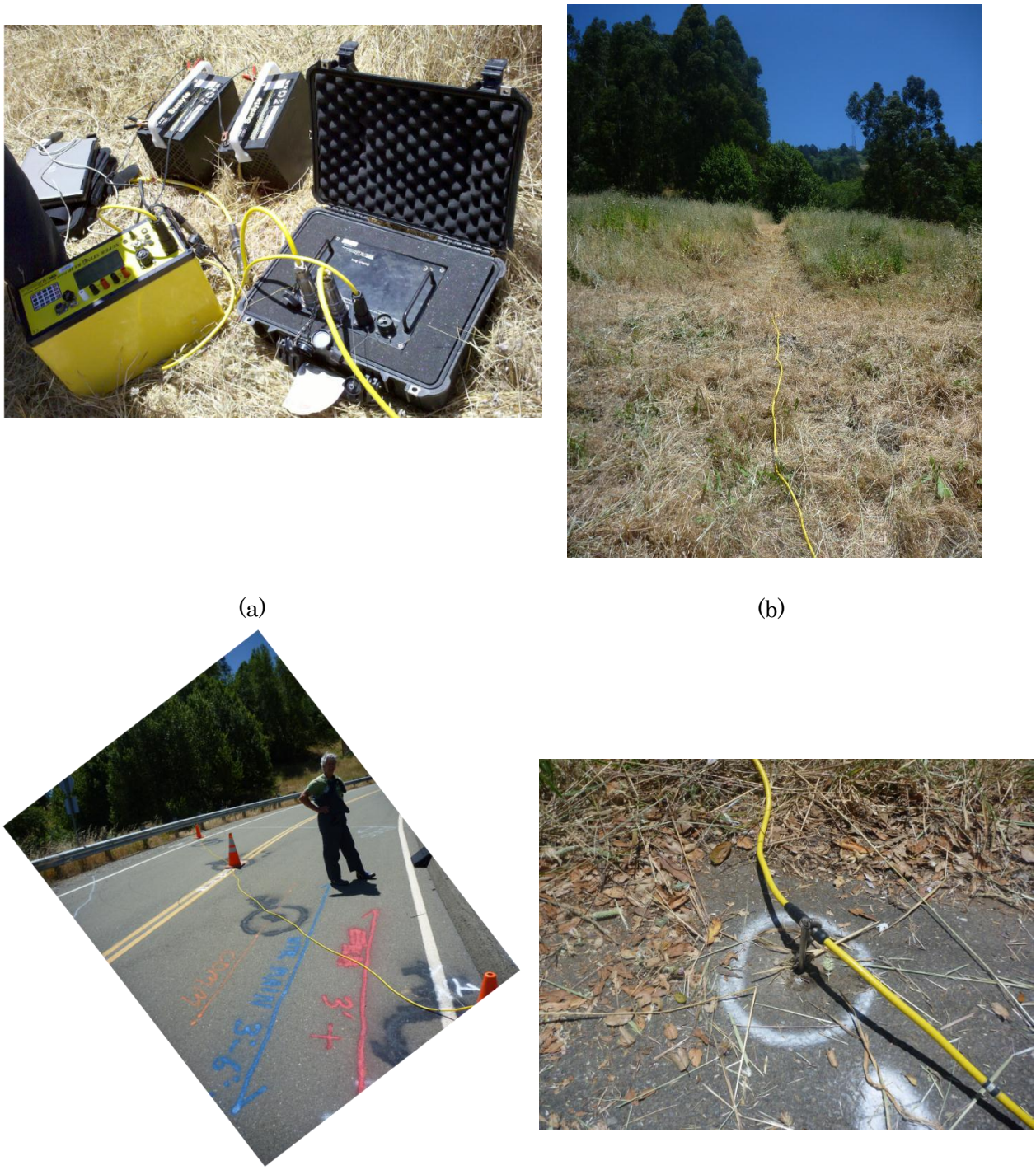

(a) (b)

(c) (d)

Figure 2-8: (a) the AGI SupeSting resistivity imaging system, (b) looking the resistivity cable laid on the ground toward the east, (c) cable laid over asphalt road, and (d) the electrode drilled into the asphalt.

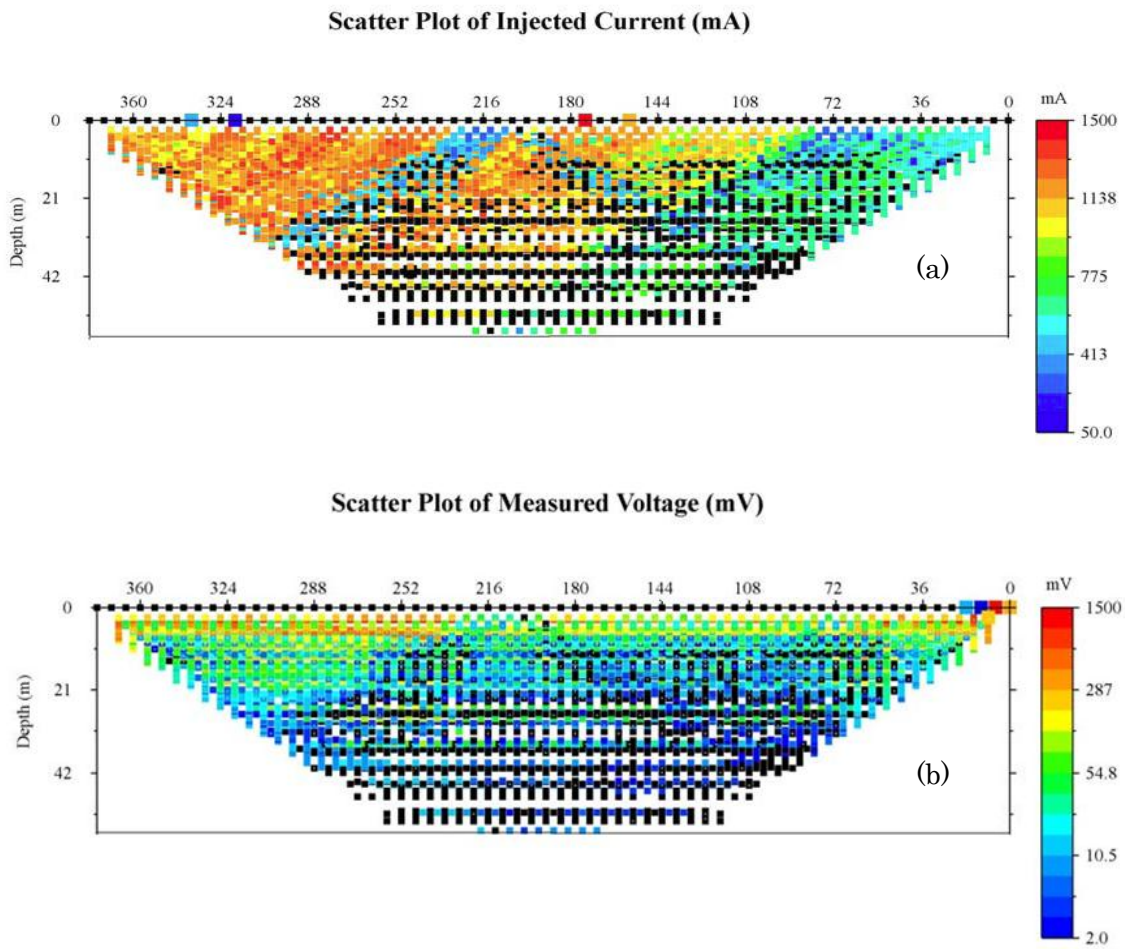

Figure 2-9: (a) Scattered plot of injected current, (b) scattered plot of measured voltage for ER-4.

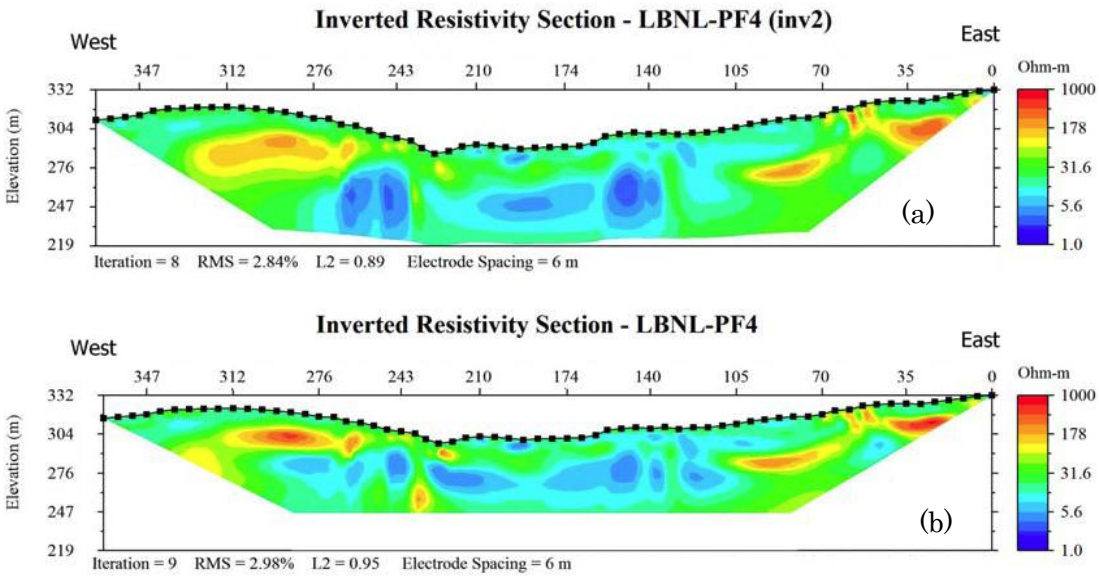

Figure 2-10: Two equally good resistivity inversion results, (a) and (b).

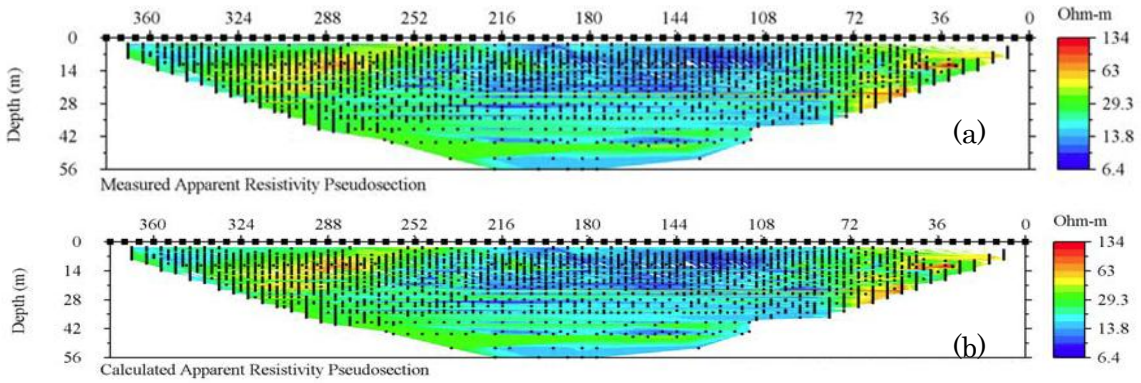

Figure 2-11: Comparison of (a) measured and (b) calculated data for the inversion model in Figure 2-10 (a).

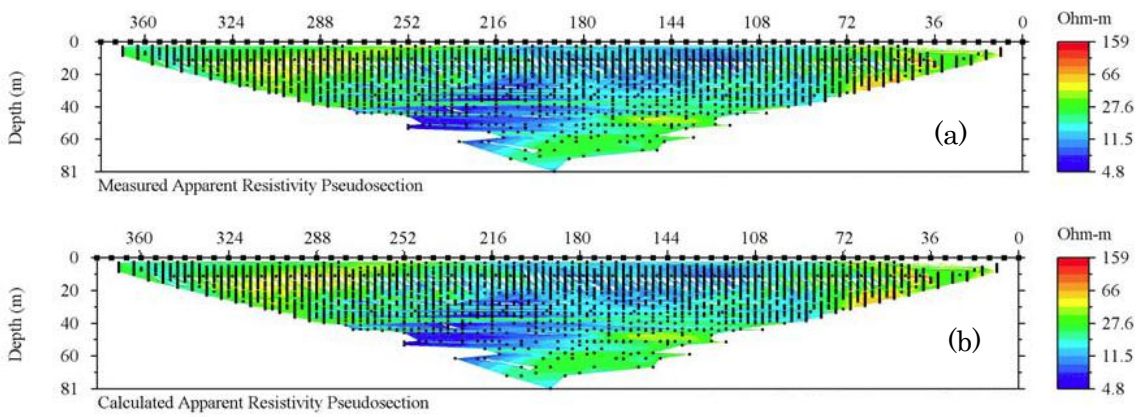

Figure 2-12: Comparison of (a) measured and (b) calculated data for the inversion model in Figure 2 8 (b).

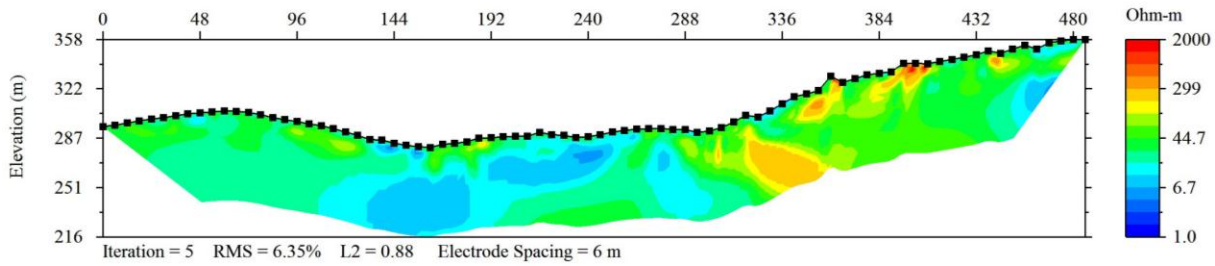

Figure 2-13: Inverted resistivity structure of ER-5.

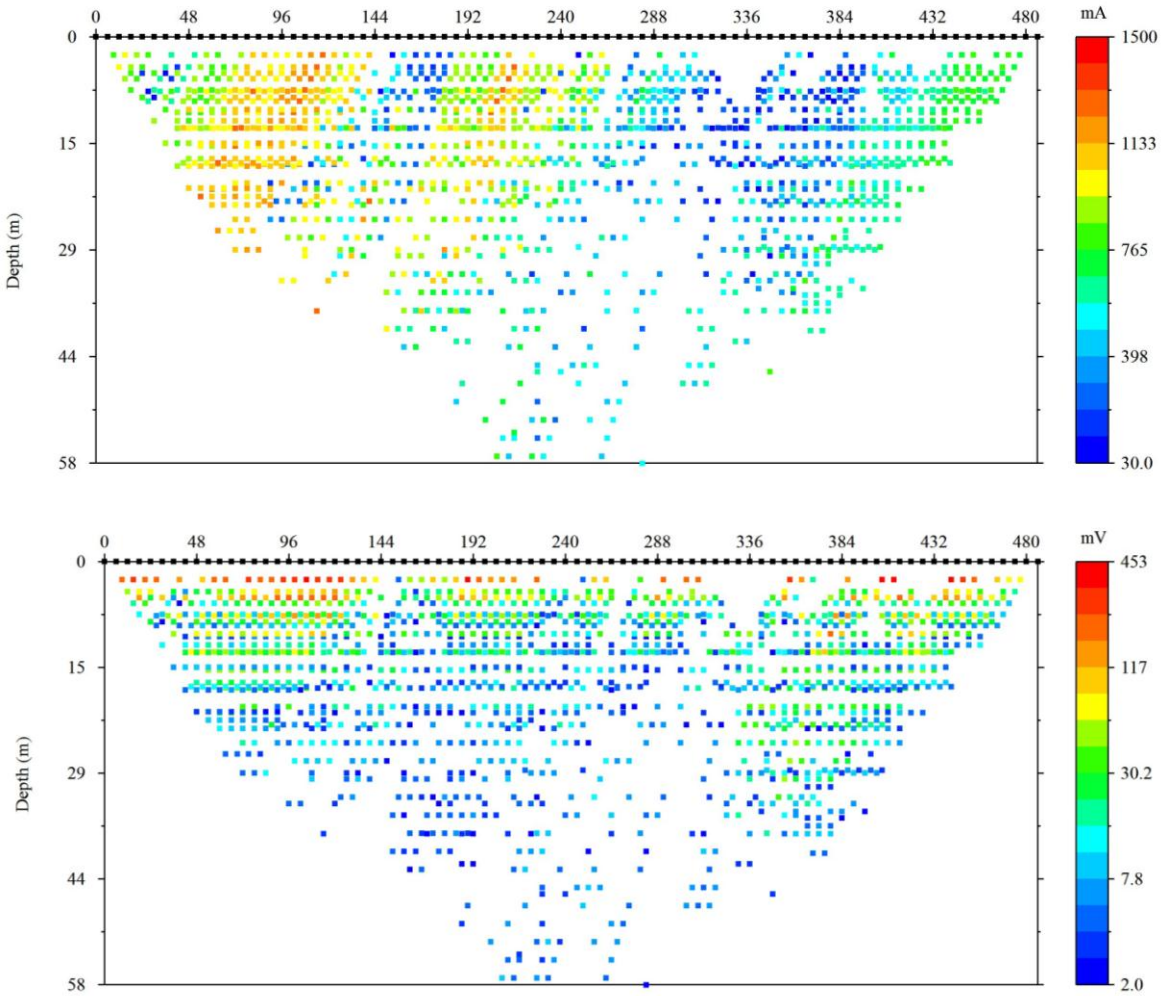

Figure 2-14: (a) Scattered plot of injected current, (b) scattered plot of measured voltage for ER-5. Compared to those of ER-4 (Figure 2-9), the signals are noticeably weak.

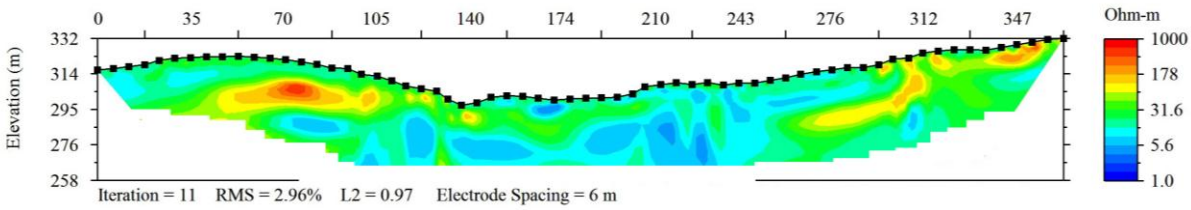

Figure 2-15: Inverted image of ER-4 using only dipole-dipole data.

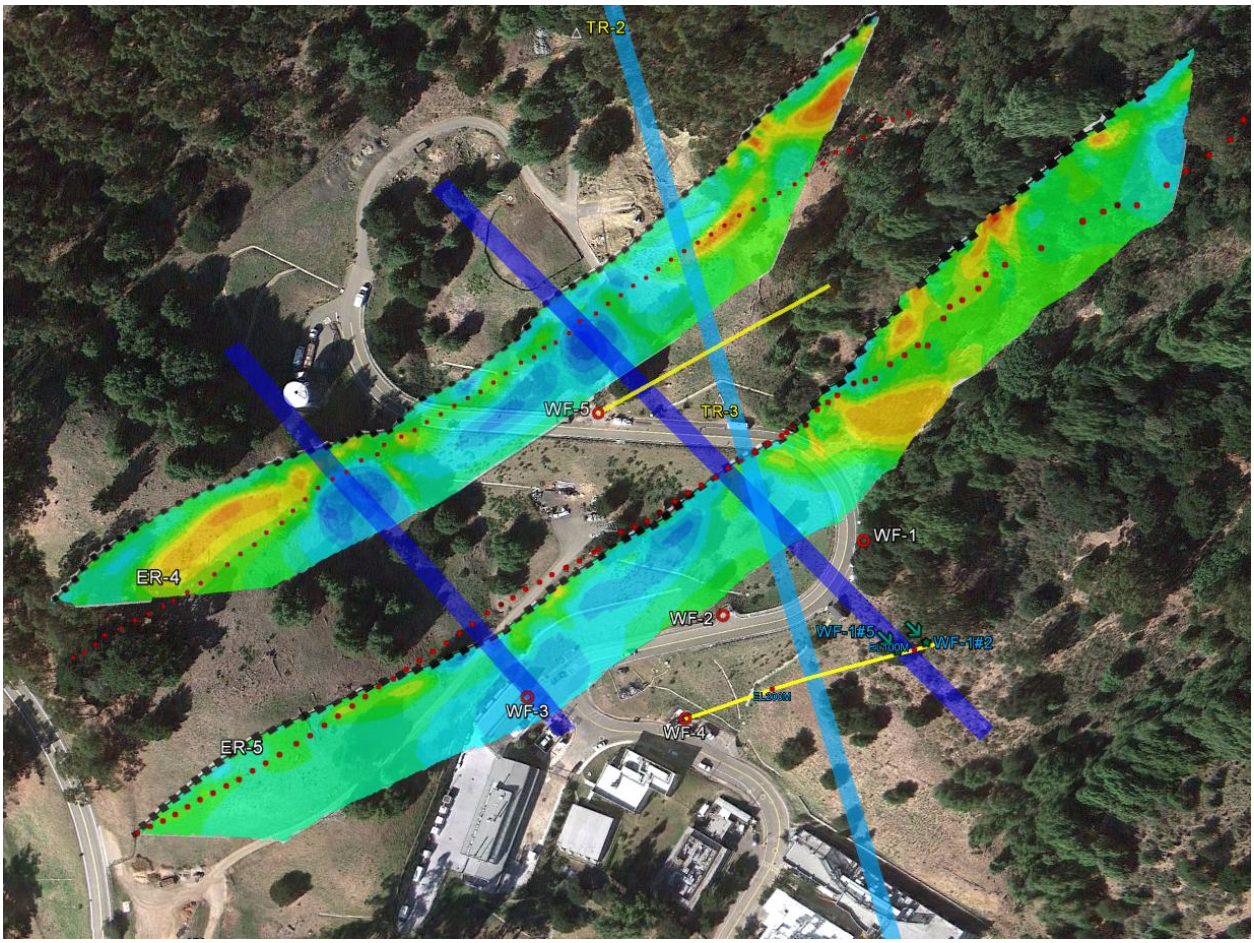

Figure 2-16: Projected faults (dark blue lines) based on ER4 and ER5 inversion images. Light blue line is the Wildcat Fault by Graymer (2000).

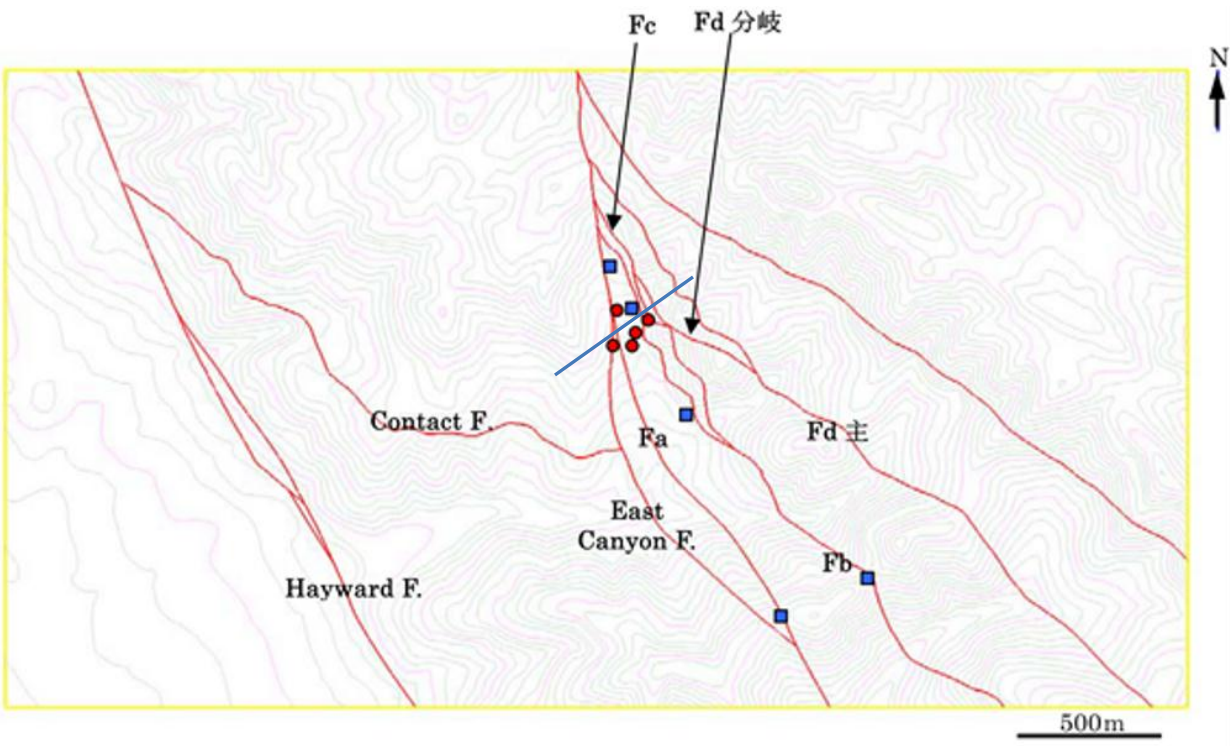

Figure 2-17: Surface traces of the faults by Kiho et al (2012). Superimposed is the ER-5 survey line. The anomaly at the east end of the ER-5 profile could be that caused by the Fd-main fault.

Figure 2-18: Seisimic refraction survey photos: (a) P-wave geophone, (b) seismographic station, (c) seisguns, (d) seisgun blast, (e) S-wave source.

3 Drilling Investigation

3.1 Introduction

Drilling is the most direct method of subsurface investigation. Although in most cases one can determine the geology or the location of a fault definitively by drilling, especially with full-core drilling, such determinations are by no means guaranteed. This is because borehole drilling is, after all, a point sampling. Furthermore, full recovery of cores is difficult in weak, fractured, or faulted zones—and borehole logging is difficult and yields uncertain interpretation in such zones. We have drilled a total of five boreholes in this project thus far, as shown in Figure 3-1, Figure 3-2, and Figure 3-3; the coordinates of the borehole tops are listed in Table 3-1. Drilling locations for the boreholes from the third one on (WF-3) were determined based on the findings from preceding holes.

From this drilling, we have thus far learned a great deal about the Wildcat Fault. We now know that the *fault* is better described as a *fault zone*. But there are some key issues remaining, one of which is the exact location of the main fault plane of the Wildcat. Below is a summary of the drilling investigation.

3.2 Drilling sequence of Wildcat Fault (WF) boreholes

In the first year of the drilling campaign, we drilled two ~150 m deep vertical boreholes (Karasaki et al, 2010) to straddle the Wildcat Fault, based on the literature (HLA 1974, 1977, 1980, 1982; Converse Consultants, 1994; WLA, 2008, Graymer, 2000). In the first hole, WF-1, we encountered the Claremont Formation, with interbeds of chert/mudstone and shale (Tcc and Tcs), and thick formations of sandstone, thicknesses (up to 100 ft) that were to some extent unexpected (Figure 3-4). According to published reports and other literature, the Wildcat Fault defines the geologic boundary between T_{CC}/T_{CS} and the San Pablo (T_{SP})/Orinda (T_{OR}) formations. Based on these reports, WF-2 was drilled on the west side of the Wildcat Fault, where we fully expected to encounter T_{SP} and/or T_{OR}. As discussed in Karasaki et al. (2010) after a mere 18 m thick T_{OR} formation, the WF-2 borehole encountered T_{CC}/T_{CS} from 18 m to the bottom of the hole, to 154 m.

The fact that we encountered the Claremont Formation at a very shallow depth in WF-2 made us wonder if we had missed the Wildcat Fault to the west. Thus, in FY2010, we drilled WF-3 at a location 86 m west of WF-2 (Figure 3-2), with the location chosen to ensure that the borehole would be on the west side of the WF, thus enabling us to bracket the western extent of the Claremont Formation. (We fully expected that we would not encounter the Claremont.) WF-3 was drilled down to 156 m. As can be seen in Figure 3-4, we initially encountered T_{OR} and T_{SP}, as expected. However, at ~100 m depth, the Claremont Formation (T_{CS}) emerged, which was totally unexpected. Unexpectedly T_{OR} appeared again near the bottom of the hole at ~150 m. These findings are quite contrary to expectations based on the existing literature, which locate the Wildcat at the geologic boundary between Orinda/San Pablo and Claremont. The detailed description of the drilling and core analysis is given in Karasaki et al (2011). Kiho et al. (2012) summarized the faults encountered in WF-1~3 as shown in Figure 3-9.

During and after the drilling of WF-3, the cores from WF-3 were examined, as well as those from WF-1 and 2. It was concluded that the main fault plane of the Wildcat Fault would probably lie between WF-1 and WF-2 after all. Thus, we decided to drill an inclined borehole from the west toward the postulated location of the fault, starting from the parking lot situated to the south west of WF-2. (See Figure 3-2 and Figure 3-3 for the exact location of WF-4 and its relation to the other boreholes.)

WF-4 was drilled in a 59NE direction with a dip angle of 59 degrees. The direction was intended to be parallel to the line that connects WF-1 and WF-2. It turned out that the casual measurement of the direction by a hand-held compass was not very accurate, and was in fact off by several degrees: the actual heading of the line connecting WF-2 to WF-1 is ~53 degrees. This difference of 6 degrees caused some inconvenience when we tried to correlate the features in each borehole. The hole was drilled relatively straight— only slightly corkscrewing. A detailed description of the WF-4 drilling and core analysis can be found in Karasaki et al (2011). Drilling speed and core recovery percentage as a function of hole length is shown in Figure 3-6, together with those of WF-5.

As opposed to vertical holes, inclined boreholes readily intersect vertical features and cover a horizontal extent. According to Kiho et al. (2012), WF-4 intersected three main features, namely Fb, Fc, and Fd faults, as shown in Figure 3-10. However, inclined drilling comes with drawbacks: Inclined boreholes take longer to drill and are more prone to have cave-ins and other operational problems.

3.3 WF-5

In this section, we will briefly describe the drilling of WF-5, the last event of the five-hole drilling campaign (Figure 3-5).

3.3.1 Location

In order to hydrologically test the main fault suspected to intersect WF-4, we decided that another inclined borehole that would intersect the fault with some horizontal distance toWF-4 would be desirable. The drilling location had to meet familiar restrictions: it needed to allow easy access for a drill-rig, it could not interfere with traffic, and it had to avoid buried services or aerial high-voltage power lines. Initially, we had three candidate sites. The first one was to be located along the line on the road that connects WF-3, 2, and 1, starting from slightly west of WF-2. This would have been a good location, because the core data from it would have directly filled the geologic information gap between WF-1 and 2. However, this location was abandoned because it would be too close for hydrologic tests to and from WF-4. Another location considered was at the midpoint between the location described above and the final location chosen. Such distance was desirable to ensure responses in the existing boreholes. However, it too was abandoned because access was awkward from inside the laboratory. We eventually decided on the location of WF-5 as shown in Figure 3-1–Figure 3-3. This location allowed relatively easy setup of a drill rig. The only concern was it might have been too far from other WF boreholes to see hydraulic communication, which later turned out to be unfounded. The coordinates of WF-5 in UTM (zone 10) and in global coordinates are given in Table 3-1.

3.3.2 Drilling

The drilling started on August 16th and was stopped on September 28th at a depth (length) of 678 ft (206.7 m), with a vertical depth of 181 m. The borehole was designed to be parallel to the line that connects the WF-1 and WF-2 boreholes, oriented 40° from Magnetic North. The dip angle of the borehole was designed to be 60° from horizontal. Because it was an inclined drilling, as was the case with WF-4, we conducted deviation surveys, using a deviation probe with a flux gate magnetometer and an accelerometer to measure the direction and inclination of the hole. The probe was lowered using the wireline after the HQ pipes were connected to the bottom before starting the day's drilling. In WF-4, we conducted orientation logging every 20 ft and found that the hole did not deviate significantly. Consequently, we conducted such a survey roughly every 100 ft in WF-5. The results are shown in Table 3-2. As can be seen from the table, the hole did not deviate appreciably, with an average orientation of 41° and inclination of 61°.

It took more than 6 weeks to drill, which was the slowest pace of all the boreholes drilled. As can be seen in Figure 3-6, the drilling speed was consistently at or less than 1 m/hr below 70 m, beneath which was the Claremont Formation. Core recovery was very poor between the depths of 80 m to 180 m. There was a sudden drill bit drop of 5 ft at a depth of ~126 m (410–415 ft), probably caused by going through a major damaged zone. Similarly in WF-4 at a depth of 180 m, the drill bit suddenly dropped 1.5 m. It is possible that these two features are closely related; Kiho et al. theorize that these features are a splay of the main Fd, whose orientation is N70 W/68°.

It is interesting to compare the drilling speed and core recovery percentage of these two inclined boreholes, WF-4 and WF-5. In WF-4, the drilling speed is ~2 m/hr above the depth of 150 m, after which the speed falls below 1 m/hr. This can be compared to the drilling speed in WF-5, where it is consistently at or below 1 m/hr throughout the entire Claremont Formation. This suggests that the properties of the Claremont Formation encountered in WF-4 change at ~150 m and become similar to those of WF-5. Admittedly, such findings are anecdotal] but drilling speed should be roughly correlated to rock properties (among other factors).

It is quite possible that the properties of the Claremont Formation are different on the opposite sides of the fault. Stereo nets of the fracture orientations from WF boreholes are shown in Figure 3-13, which is modified from Kiho et al. (2012). As can be seen from the figure, there are more moderately dipping and near-horizontal fractures in WF-2 than in WF-1. The same seems to hold true within WF-4 between the upper section (34–450 ft) and the lower section (450–695 ft). The former has more horizontal fractures than the latter. In WF-5, most fractures are steeply dipping. Although Kiho et al (2012) did not discriminate among the rock types in plotting the stereo nets, the majority of the rock is Claremont; all is Claremont in WF-1 and all but the top 60 ft is Claremont in WF-2 and WF-4. In WF-5, more than two thirds (220–678 ft) of the hole is Claremont. The Claremont dips steeply, as observed in the outcrops as close as those just north of WF-1 and as far south as in the Caldecott Tunnel (CALTRANS, 2011), which is ~3 km south of the WF complex. From gathering the data, one possible interpretation is that the main Wildcat Fault cuts though the Claremont Formation between WF-1 and WF-2, as shown in Figure 3-12.

Kiho et al. (2012) posit that Fd is cut by Fc, which is terminated by Fb, which is cut by Fa. Thus, they assume Fa is the result of a youngest fault movement, and Fd is the oldest or all concurrent. An alternative theory here is that Fd is the youngest and cuts Fb, which cuts Fc. Fa is not considered in the relationship because of a lack of data suggesting relationships to the rest of the faults. (This will be discussed in further detail in the Geology and Modeling Sections of the report.)

During the entire drilling period, a water level logger was installed in the hole at the end of every day, to monitor the water level in the hole. Also, the water level was measured by a tape at the beginning of every drilling day. Figure 3-8 shows the plot of the water level changes in WF-5 as the drilling progressed. The blue line is the pressure measured by pressure transmitter converted to the freshwater head. However, this did not match the levels measured by tape very well, since the water in the borehole is heavier than freshwater because the drilling fluid contained mud. The red line, the density compensated level, matched those from tape measurements reasonably well, with some discrepancies caused by changes in the mud density, which was not measured every day. The water level

dropped significantly overnight when the hole was drilled to 450 ft, and stayed relatively low since.

Figure 3-7 shows the head changes in WF-1 intervals during the drilling of WF-5. As can be seen in the figure, the intervals clearly started to respond to the drilling activity when the drilling length reached ~420 ft in depth. Recall that the drill bit dropped by ~5 ft at 126 m from 410 to 415 ft while drilling. We suspect that this is where the main damage zone of the Wildcat or the main fault plane itself intersects the hole. In Chapter 5 (below), we will discuss about the pumping tests conducted in this zone.

3.4 Borehole Logging

In this section, we summarize the borehole logging results from all the WF holes and discuss both the advantages and disadvantages encountered using different logging methods. While coring is the most direct way of examining subsurface geology, sometimes cores do not get recovered fully, as shown in Figure 3-6. Typically, the sections where core losses occur are where the rock is incompetent or damaged by faulting/fracturing. Borehole logging is useful in gaining some information regarding the properties of those sections. In all five boreholes, we conducted a suit of borehole logs, including caliper, natural gamma, SP, resistivity, borehole televiewer (BTV), sonic, flowing fluid electrical conductivity (FFEC), and sonic logs. In addition, we conducted a suspension log that measures the S-wave velocity as well as the P-wave in WF-1 and WF-2.

Conducting borehole logging can be very difficult in boreholes that are not stable. Weak rocks and inclined drillings make for instability. In WF-3, we had to put a steel casing in the top 30 m, because the section (made of faulted Orinda siltstone) kept on collapsing. Thus, no log data are available from there. In the inclined holes WF-4 and 5, we had extreme difficulties logging the hole. In both WF-4 and WF-5, logging was attempted four times in each borehole because of blockages caused by rock fragments falling in and bridging across the hole diameter. Each time that happened, the logging truck had to be replaced by a drill rig, and the hole had to be re-drilled. For both holes, the cost was quadruple that of the previous vertical holes.

In WF-4, the logging was done in three separate sections, with the bottom 30 m being particularly difficult. The hole was cased down to 638 ft (194 m) to complete the bottom 55 ft (16.5 m). Because the bottom 30 m intersects the main fault, we wanted to collect as much data as possible from that section. In WF-5, the top 220 ft (66 m) was weak Orinda formation, which kept collapsing. Particularly troublesome was the depth between 170 and 230 ft. Because the 220–230 ft range was a fault zone (Fc fault), we first attempted to grout the section of Orinda from 170 to 220 ft, leaving the bottom 10 ft section open. We installed a plastic wing plug at 220 ft by lowering the HQ drill pipe to the depth with the plug at the tip, and then pushing the plug out of the pipe and deployed it using plastic pipes connected down to the depth. Since the plug had a hole in the middle, we dropped bentonite pellets to plug it up—which in retrospect was probably a mistake. We subsequently poured grout into the hole, which didn't cure very well--we suspect that the bentonite prevented the grout from curing. After another attempt, the grout appeared to be set. We drilled through the grout and found that the grout was down to 235 ft. We then went in to conduct logging, but had another blockage. We finally decided to put casing down to 199 ft, leaving the section below open for logging, although it was likely that there was some grout covering the hole down to 235 ft.

Below, we summarize the borehole logging results conducted in WF-1 through WF-5. Detailed descriptions of the logging results from WF-1 and WF-2 are given in Karasaki et al. (2010); the logging results from WF-3 and WF-4 are in Karasaki et al. (2011). Results from WF-5 can be found in the Appendix.

3.4.1 Caliper log

Caliper logs yield continuous measurement of the borehole diameter as a function of depth. Most caliper probes have three spring-loaded arms that expand until one of them touches the borehole wall to measure the diameter. The tool we used had coupled arms, meaning that it gives the minimum diameter if the hole is not circular. Some caliper tools have independent arms capable of measuring a noncircular hole shape; a caliper log is

usually conducted first to test the physical condition of a borehole before using more expensive logging probes.

The results of the caliper log from the WF boreholes are shown in Figure 3-14 superimposed on the geologic columns. Caliper log anomalies correlate well with the location of faults, where the rock is generally soft, so that the borehole diameter is enlarged. As can be seen form Figure 3-10, in WF-4 below the depth of 180 m (600 ft), the borehole wall is extremely rugged. This is where the main fault plane Fd intersects the hole (Kiho et al., 2012). Other notable caliper anomalies can be seen at a depth of 67 m (220 ft) in WF-2 and at 150 m (500 ft) in WF-3, where the Fc fault intersects these holes (see Figure 3-9). The upper 30 m portion of WF-3 has several locations where the borehole diameter is quite large. According to Kiho et al. (2012) the Fa fault goes through this location.

Drill pipes vibrate and damage the hole where rock is weak, such as at the Orinda siltstone formation. Frequent pulling up and lowering down of drill pipes can damage the hole. As can be seen in Figure 3-14 every upper portion of WF-2, -3, -4 and -5 has an enlarged diameter. At the end of each day, the drill string was pulled out to prevent it from freezing in the hole due to a cave-in. This was a lesson learned from the first hole, in which the drill string was caught by a fault gouge zone and had to be overcored to release it, which significantly delayed the project and added costs.

The caliper log is thus very useful when deciding where to set packers for pump tests in a fault zone. Sometimes the ideal would be to set packers such that they straddle a zone tightly. However, if the borehole wall is not smooth, packers don't seal and even can get damaged. We had to be very careful in choosing where to place packers in WF-4 and WF-5, because they are inclined holes and intersect many faults. In one instance, a packer was pieced by a sharp chert fragment in WF-5 when setting packers for a pump test. The entire string had to be pulled and the damaged packer had to be replaced.

3.4.2 Electric logs (ELOG)

The so-called ELOG probe measures the rock resistivity with three different offsets, as well as measuring the level of natural gamma and self-potential (SP). In Figure 3-15 and

Figure 3-16, composite plots of BTV results and Elog data are shown for WF-1 through WF-3 and WF-4 through WF-5, respectively. (The entire log for WF-5 is shown in Appendix E.) ELOGs were conducted in all the five holes. However, we have not been able to correlate any significant geologic or hydrologic features to the ELOG anomalies, with the possible exception of the bleached lithified chert breccia found at several depths in some WF holes. Most notable are at 147–153 m in WF-1 (Figure 3-15), at 185 m in WF-4, and at 174 m in WF-5 (Figure 3-16). All of these occur near the suspected fault, signified by opposite kicks in natural gamma (low) and resistivity (high). Figure 3-17 shows an example of the ELOG anomalies and the picture of the core at the corresponding depth in WF-4. Note that the bleached brecciated chert near the bottom of WF-1 is the thickest. Although WF-1 does not intersect the main fault, it may be very close to it. Since the fault is near vertical, the thickness can be explained if the bleaching, brecciation, and lithification is caused by the fault.

3.4.3 Borehole Televiewer (BTV) log

Borehole televiewer (BTV) logs have been conducted in all the boreholes thus far. They have been an effective tool for determining the bedding and fracture orientations in boreholes. Optical borehole imagers generally provide better definition and color of the borehole wall, but they only work in clear water, but BTVs are effective even when the borehole is filled with drilling mud. All WF boreholes have been drilled using a mud rotary system. Drilling in the Orinda silt and Claremont mudstone formation produce fine particles, as do the fault gouges that get suspended in water even after a good washing. The use of optical viewers has not been possible.

Figure 3-15 and Figure 3-16 show BTV images superimposed on the geologic columns from WF-1~3 and WF-4~5, respectively. Detailed BTV images from WF-1 and WF-2 can be found in Karasaki et al (2010), WF-3 and WF-4 in Karasaki et al (2011). The images from WF-5 can be found in the Appendix F.

Figure 3-18 shows the borehole televiewer images from a depth of ~74–77.4 m (243–254 ft), where the largest inflow was observed by an FFEC log in the San Pablo sandstone, and a depth of 148.7–151.7 m (488–498 ft), where a large fault is suspected. The former image is very clear, and fractures can be easily identified. The latter is not so clear. Due to the presence of a fault, the borehole is enlarged and the rock is soft, so that acoustic waves reflect strongly back to the receiver. The existence of a fault is suspected, but the orientation of it is difficult to determine. The dip and orientation for the top and bottom boundaries of the darkened zone are used (with some uncertainty) to determine the orientation.

Another example of the effective use of BTV is shown in Figure 3-19, which shows the BTV image from 681–684 ft (207.5 m–208.5 m) in WF-4. Also shown is the picture of the core from the same interval, most of which is not recovered. Note the very grainy image of the BTV where the core-loss occurred, indicating the rock has been pulverized to grains.

Of all the logs conducted, BTV logs were most heavily utilized to orient the cores or determine the orientation of the features not sampled due to core-losses. To assure that the orientation of the BTV images were correct, we occasionally conducted core orientation surveys using a device that attaches to the core retriever and makes the impression of the core top when pressed against it with nails embedded in a circular fashion. It also marks the core with red pencil in relation to the vertical. It has ball bearings that rotate freely when being lowered, but lock in when making an impression of the core top. Out of more than twenty attempts, we were able to achieve three good impressions. In most cases, the probe either misfired or the nails ground the core to pieces.

3.4.4 Sonic log

Sonic velocity is a function of rock density and stiffness. Thus, sonic logs can be used to identify rock types and faults where the rock is expected to be soft, thus yielding a slower sonic velocity. The Claremont Formation appears to have within it substantial contrasts in rock density, due to fracturing/ faulting superimposed on interlayering of chert/

mudstone/ shale, as well as sandstone. We have conducted sonic logs in all the WF holes except in WF-5. Judging from the data obtained from WF-1 through WF-4, we decided that a sonic log was not necessary in WF-5. We have been unable to effectively correlate low/high velocity signatures to features of interest. Figure 3 25 shows one example of potential correlation between slow sonic velocity and a fault at 370 ft (112.7 m) in WF-4. However, this is not the case for all the faults. We found several faults below 600 ft (180 m), but the sonic log showed no distinctive anomalies (though it did show numerous moderate lows and highs that appeared noisy, which in turn may be interpreted as multiple faults). Sonic logs were initially prescribed to obtain P-wave velocity profiles along the depth of boreholes to help interpret the reflection seismic survey. In addition, suspension logs were conducted in WF-1 and WF-2 to obtain S-wave velocity profiles.

3.4.5 Flowing Fluid Conductivity (FFEL) log

FFEC logs were conducted in all WF boreholes (Karasaki et al., 2010, Karasaki et al., 2011) and proved to be effective in pinpointing the location of flowing features. When conducting FFEC logs, while it would be ideal to replace the borehole water with deionized water for maximum sensitivity, we used tap water from a nearby fire hydrant for convenience and cost saving—there is enough contrast in conductivity between the water from the fire hydrant and the formation water, FFEC logs worked reasonably well. Figure 3-20 shows the FFEC log results superimposed on the geologic columns of WF-1–WF-5. Inflow points can be identified by the high kinks in conductivity profile indicated by the light blue arrows. In WF-1, we suspect that we did not draw down the water level enough to ensure inflow from all the flow zones. Subsequent long-term monitoring revealed that the head difference between the highest top zone and the lowest bottom zone is as much as 10 m, whereas we drewdown only ~3 m. WF-4 was an artesian well, and it was challenging to conduct conductivity scans quickly enough within WF-4 before the salinity of the groundwater saturated the borehole water.

3.5 Summary

We drilled five boreholes in total: three vertical and two inclined boreholes aiming to straddle and to penetrate the Wildcat. The drilling itself was very successful overall. We found that the area we were investigating was made up of multiple faults and be better described as a fault zone. (The geologic interpretation of the drilling results will be discussed in detail in the next chapter.) Drilling is the surest way to investigate the subsurface, but it is expensive and not free of problems; in fact, it is the stage that is most problematic. The actual cost was more than twice the projected because of the problems. In particular, the inclined boreholes were very costly.

We learned many lessons and accumulated much knowledge in drilling through faults. Borehole geophysical logs can supply information lost from core losses, and it is sometimes useful in correlating hole to hole features. For example, based on fracture orientation statistics, we were able to discriminate the holes on either side of the fault. In the geology we encountered, we could not use the sonic log data effectively. The caliper logs were useful primarily for deciding packer locations. Electric logs seemed to be ineffective except for pinpointing brecciated lithified chert, which seems to be inevitably associated with a fault. However, given the limited use of borehole logging data to relate to hydrologically significant features, it is arguable if some logs are worth conducting. Especially if the funds are limited, they may be better spent on drilling additional boreholes or conducting hydraulic tests instead. Not all geophysical logs need to be conducted in all boreholes.

Table 3-1. Global coordinates of WF Borehole tops

	UTM (10)		Global Coordinate (NAD83)		Elevation (m) NAVD88
	Easting	Northing	Latitude	Longitude	
WF-1	566936.65	4192575.23	37.87820944	-122.2388631	285.8
WF-2	566886.21	4192537.39	37.8778725	-122.23944	278.1
WF-3	566812.83	4192492.57	37.87747361	-122.2402786	270.2
WF-4	566877.45	4192492.14	37.877465	-122.2395439	265.1
WF-5	566826.5	4192609.6	37.87852734	-122.24011027	300.8

Table 3-2. Directional log results of WF-5

Date	time	Depth (m)	Orientation (deg)	Inclination (deg)
8/22/2011	8:25	45.7	40.1	60.5
8/24/2011	7:40	69.5	39.5	61
8/30/2011	8:20	95.1	40	60.7
8/31/2011	9:10	102.1	39.9	61.1
9/7/2011	10:00	125.0	40.7	61.4
9/14/2011	8:30	154.6	41.8	61.3
9/23/2011	9:24	187.0	42	61.2
9/28/2011	17:00	206.7	42	60.7
Average			40.8	61

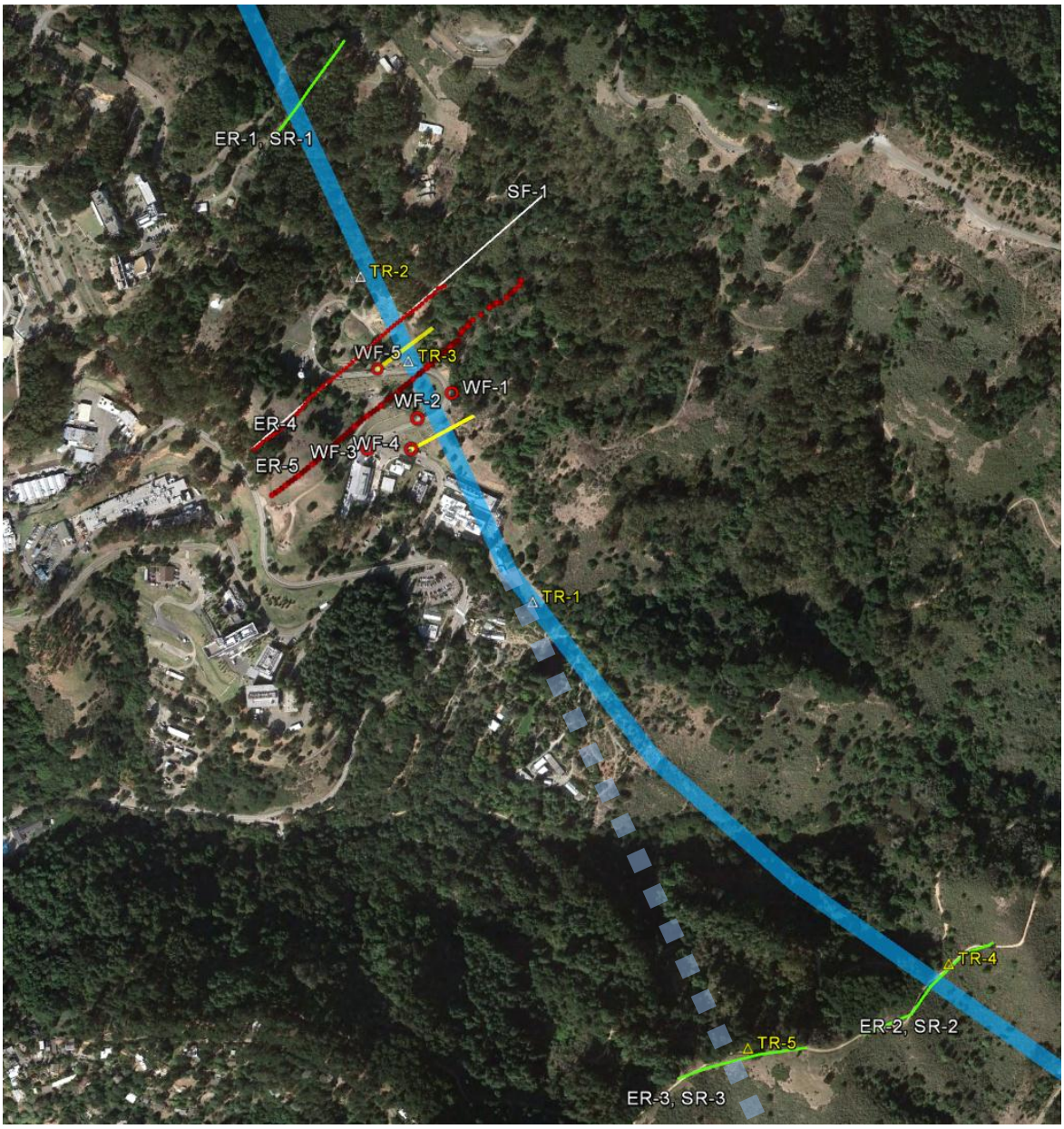

Figure 3-1. Sattelite picture showing the location of surface geophysical survey lines, trenches, boreholes and inferred traces of the Wildcat Fault (light blue solid and broken line).

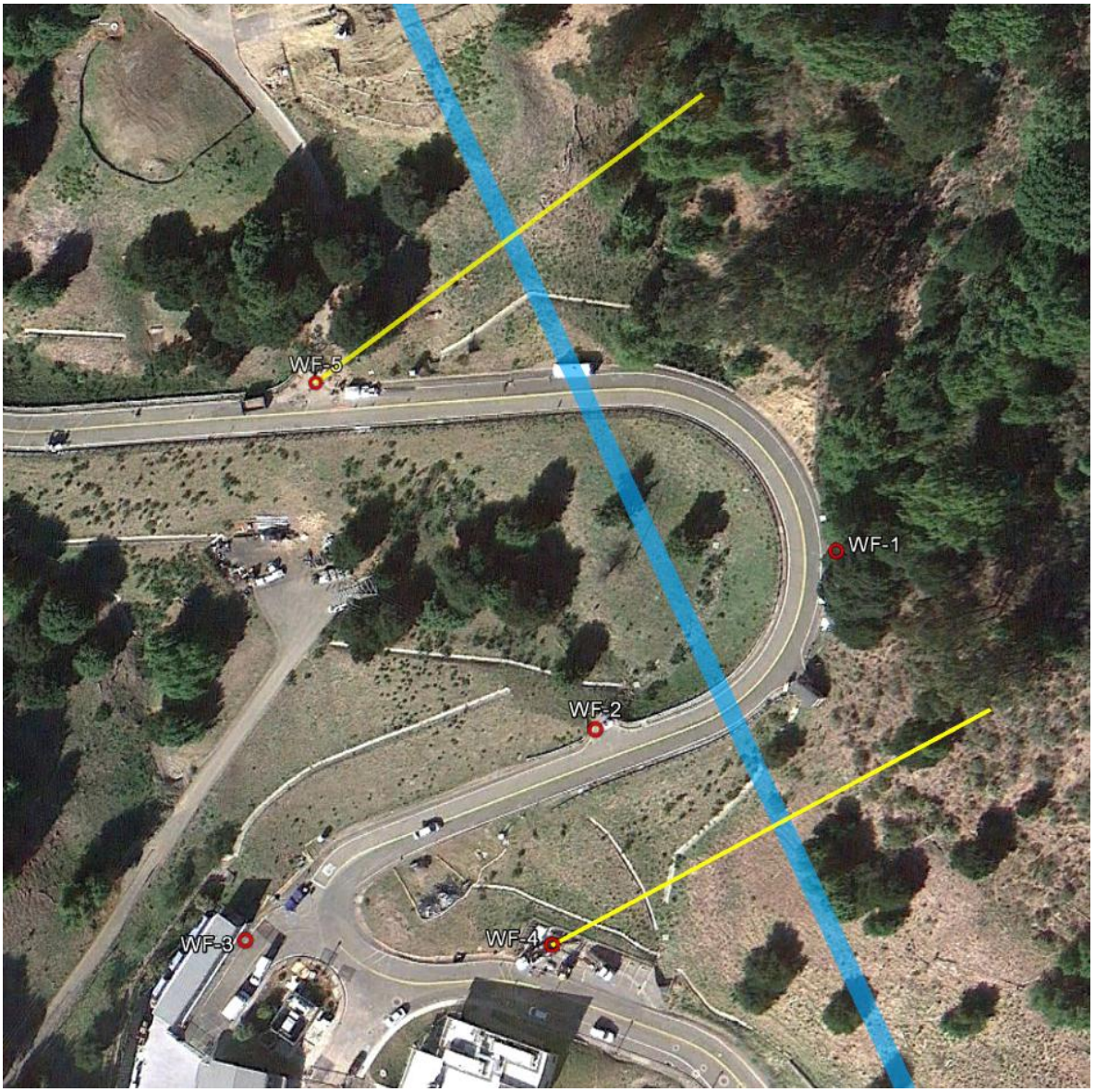

Figure 3-2. Satellite view of the WF borehole locations compiled uising Google Earth.

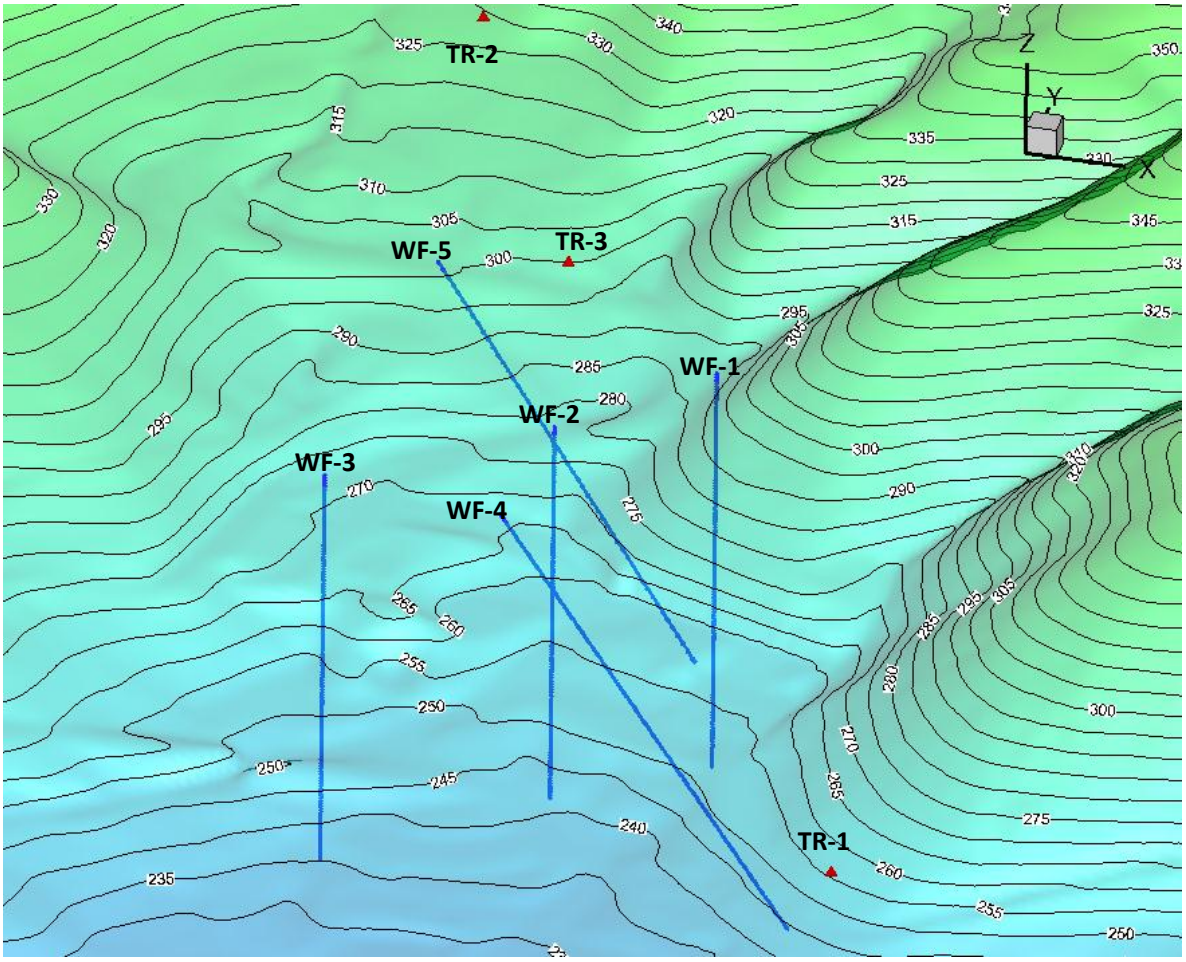

Figure 3-3. 3-D representation of WF boreholes. Also shown are the trenches TR-1 through 3.

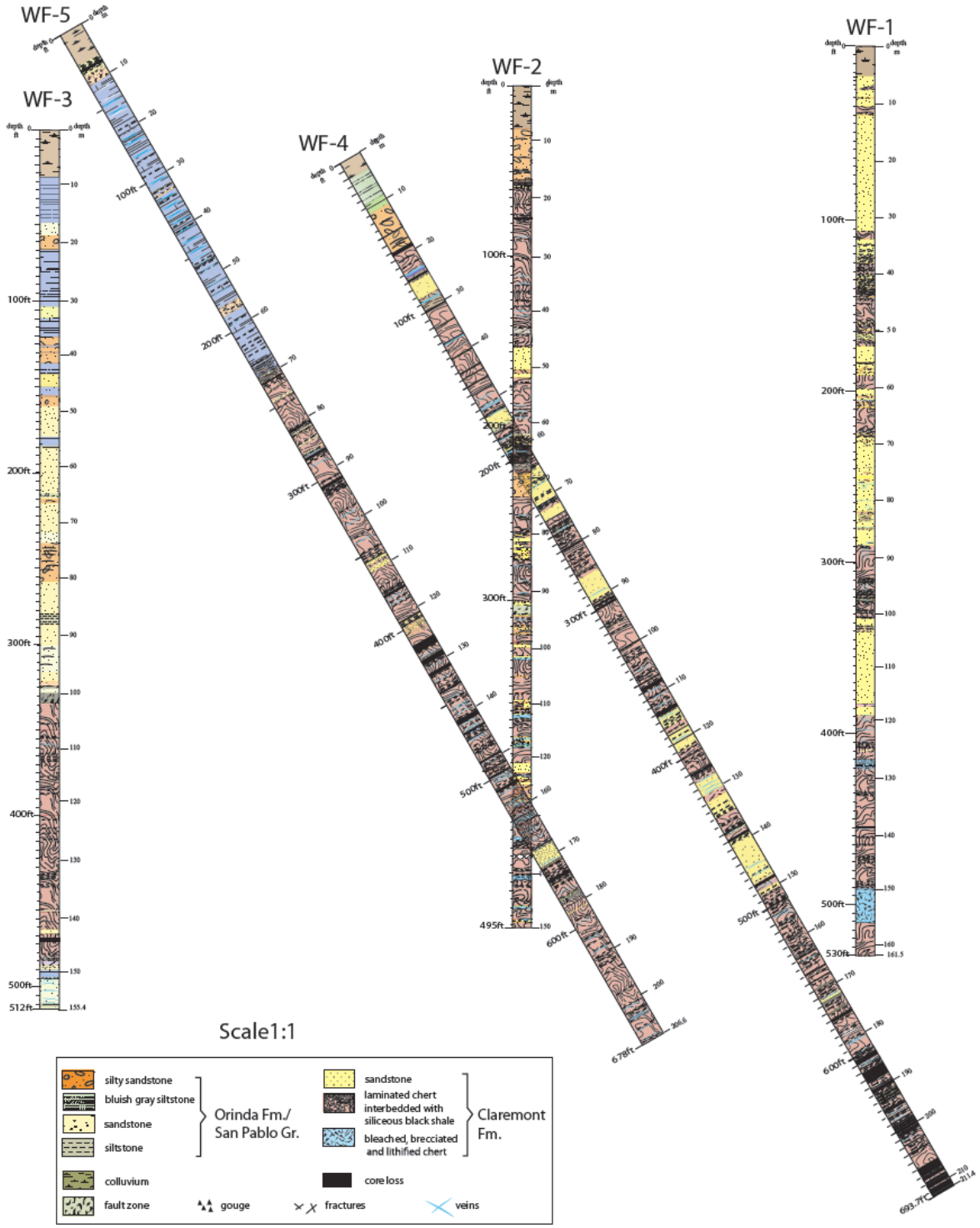

Figure 3-4. Geologic columns of WF boreholes.

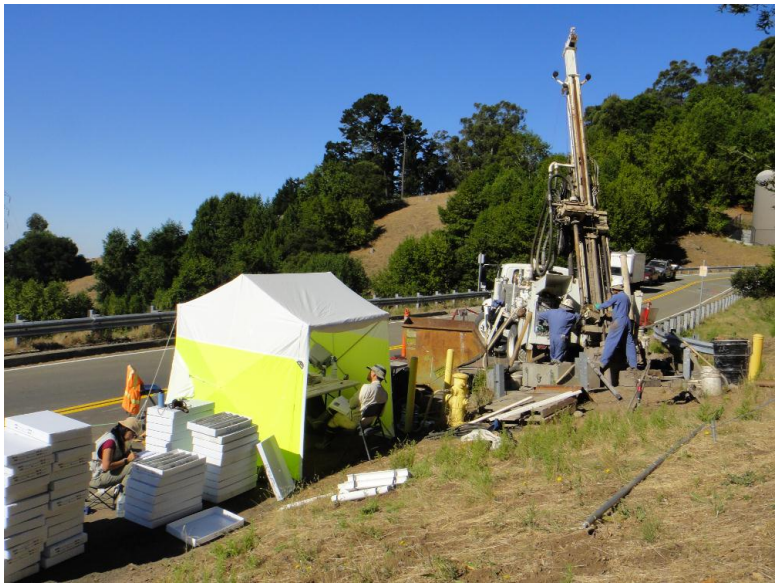

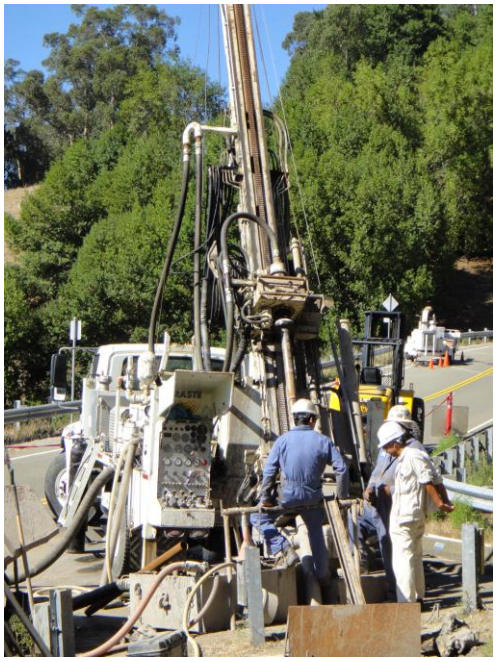

Figure 3-5. Drilling of WF-5. Note that it is a 60° inclined drilling.

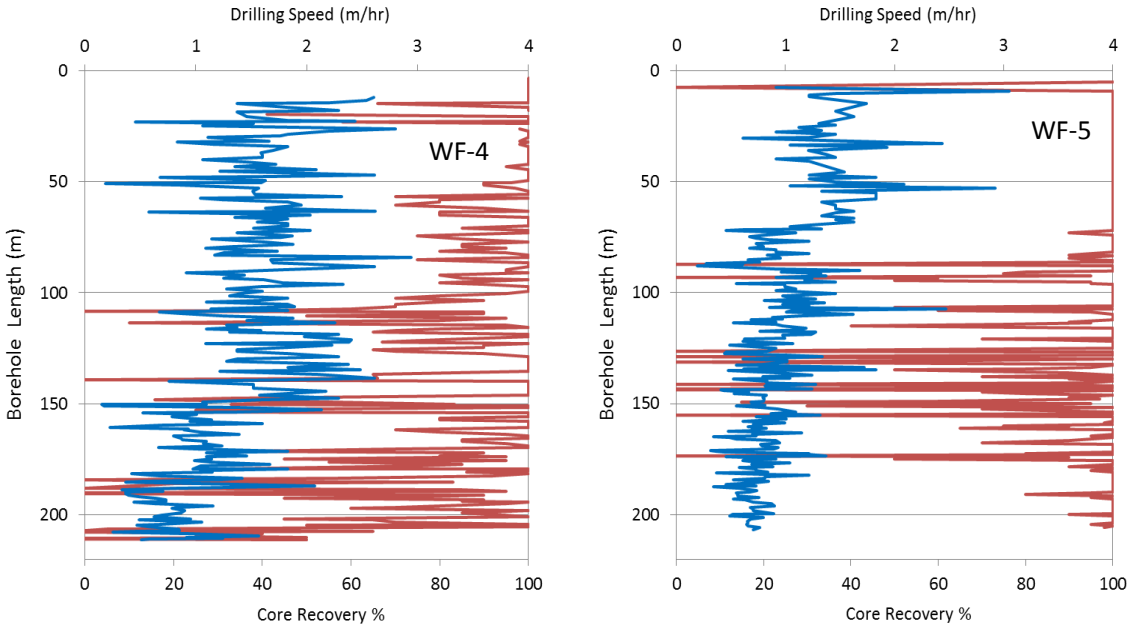

Figure 3-6. Comparison of drilling speed and core recovery percentage of WF-4 (left) and WF-5 (right). Massive core losses occurred between 170m ~bottom in WF-4 and 125~160m inWF-5.

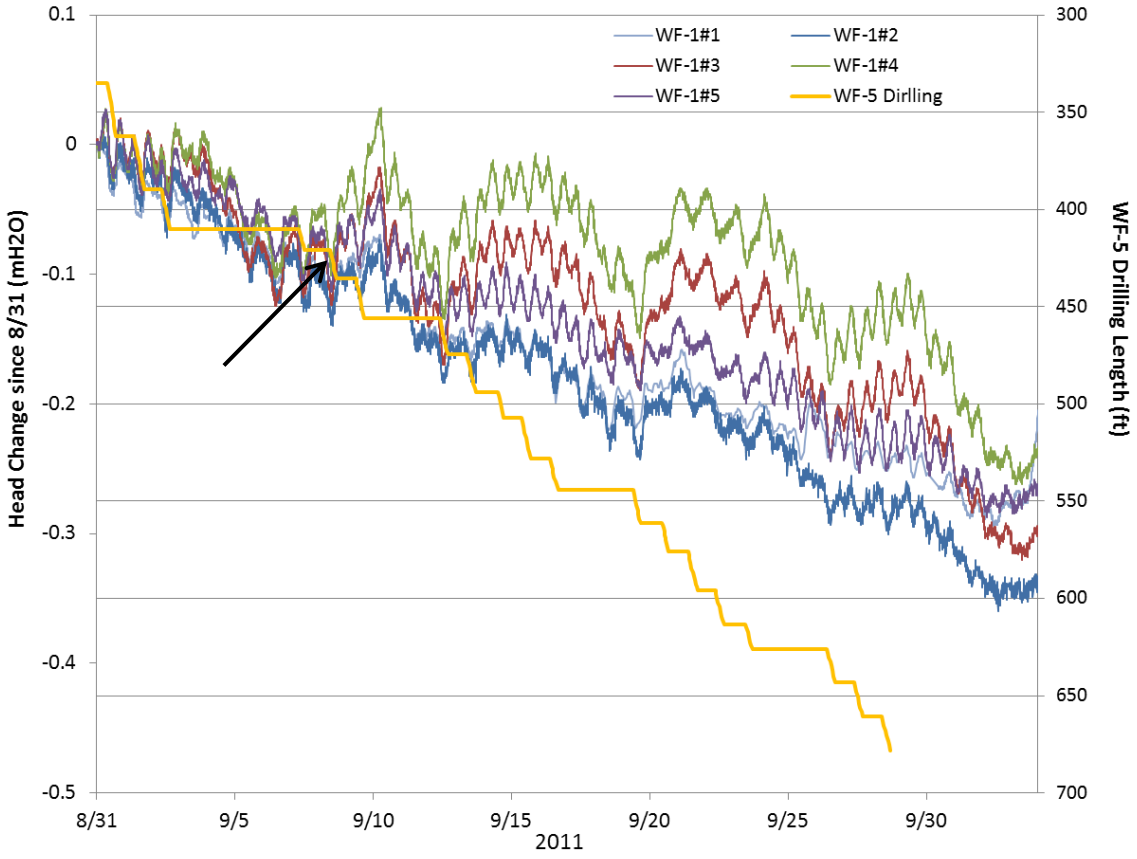

Figure 3-7. Head changes in WF-1 intervals since 8/31/2011. The monitoring intervals started to respond to the drilling activity in WF-5 when the drilling reached at ~420ft indecated by the arrow.

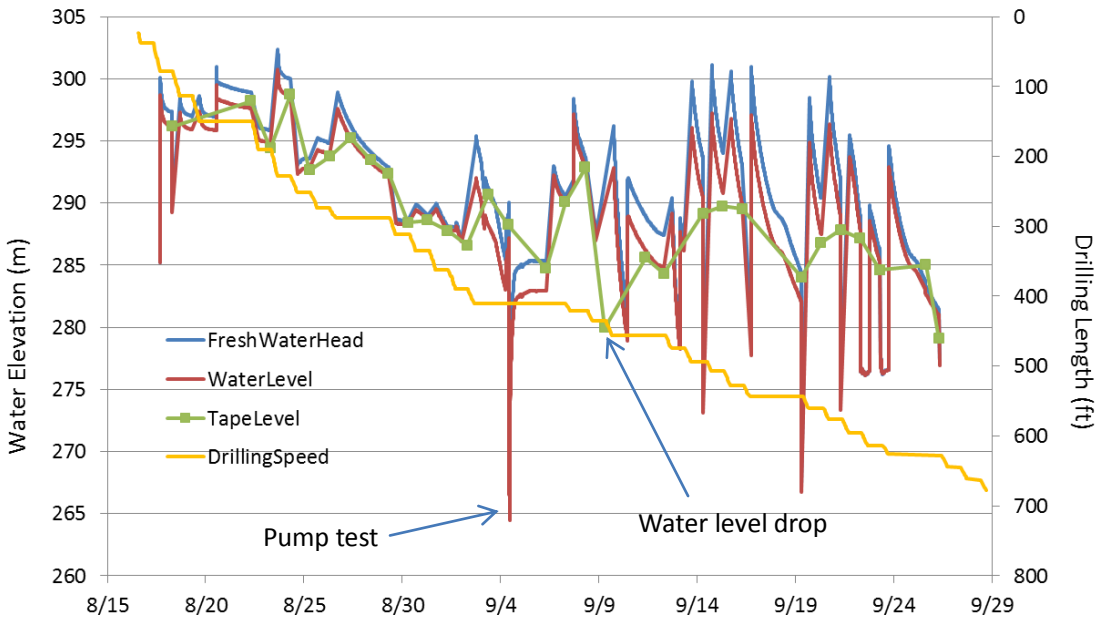

Figure 3-8. Fluid level changes in WF-5 as the drilling progressed. Blue line is the pressure measured by pressure transmitter converted to freshwater head. The red line is the density compensated level. Green line is the tape measured level.

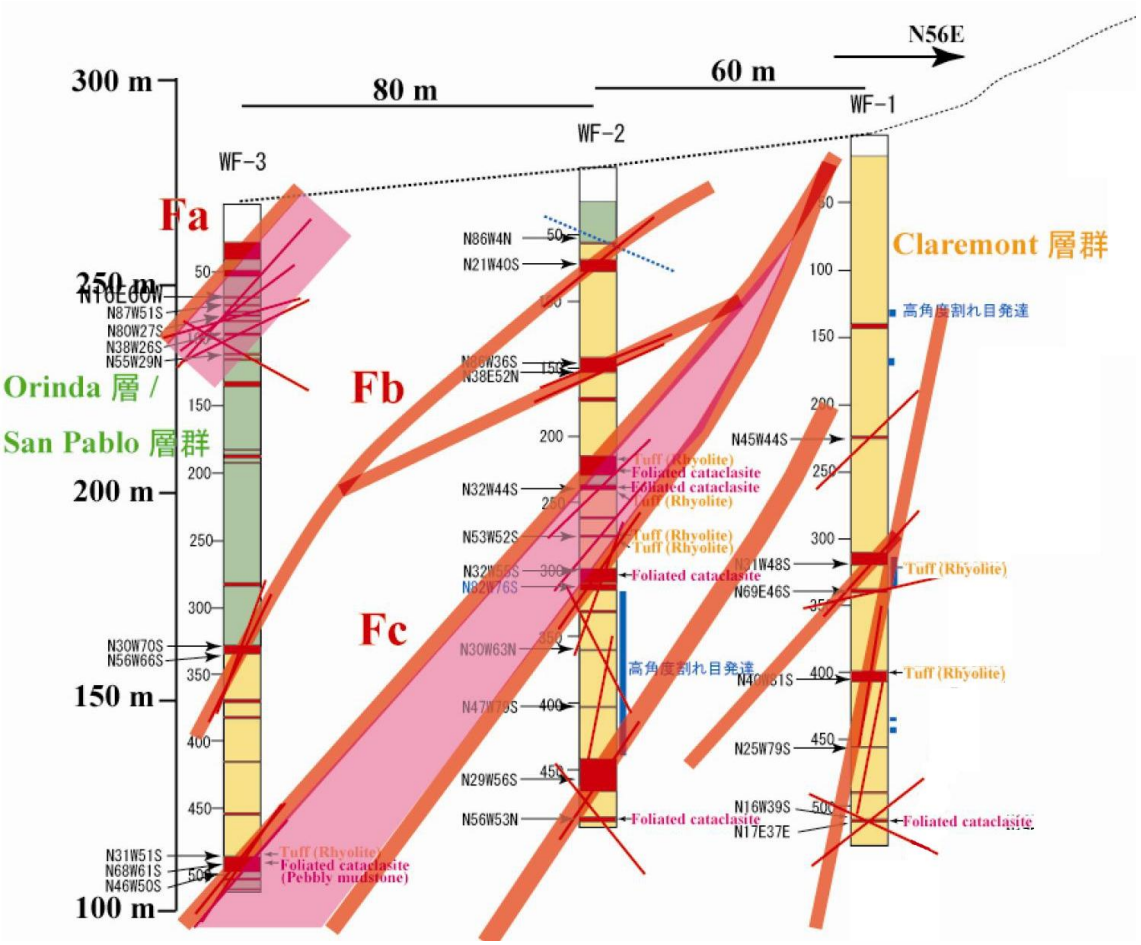

Figure 3-9. Summary of faults encountered in WF-1~3 (after Kiho et al., 2012).

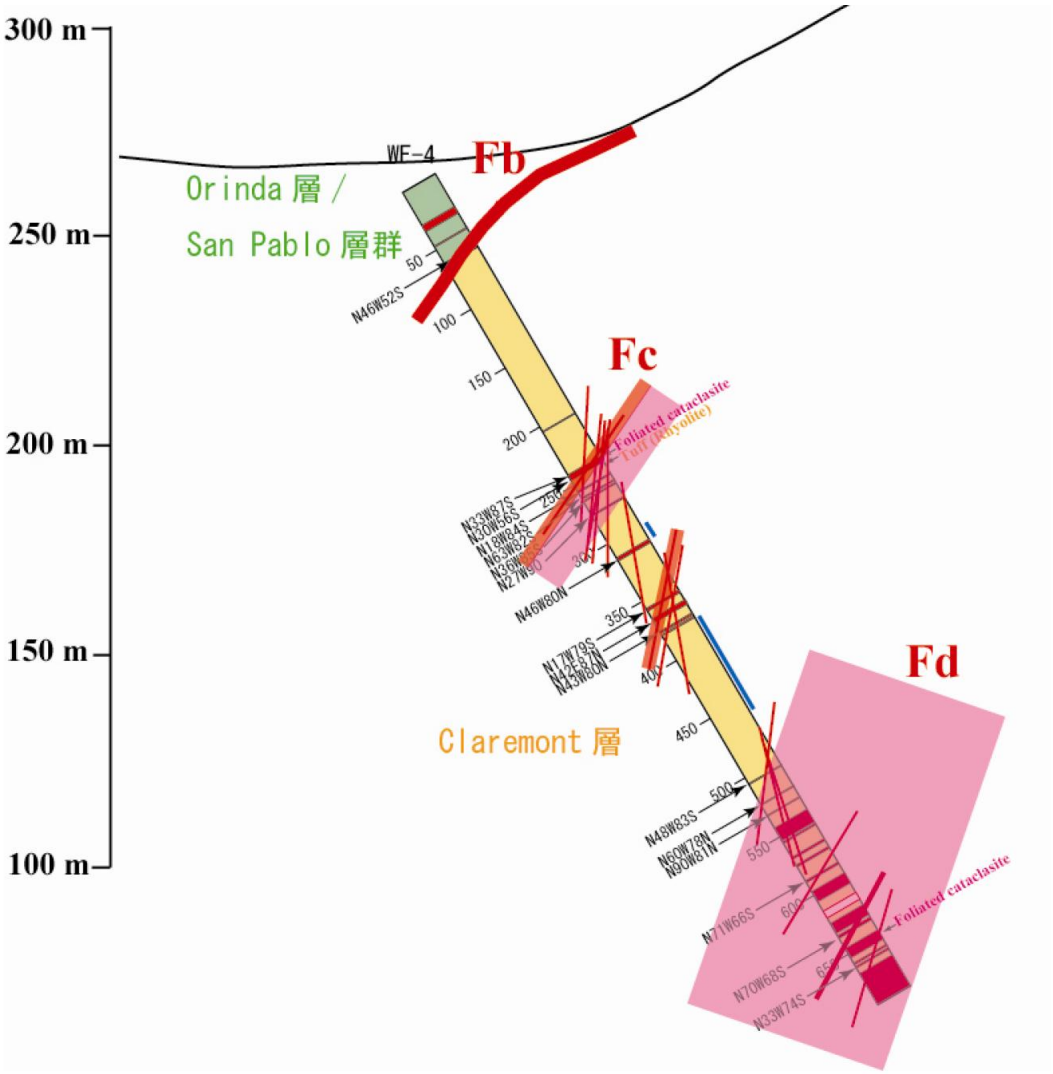

Figure 3-10. Summary of faults encountered in WF-4 (after Kiho et al., 2012).

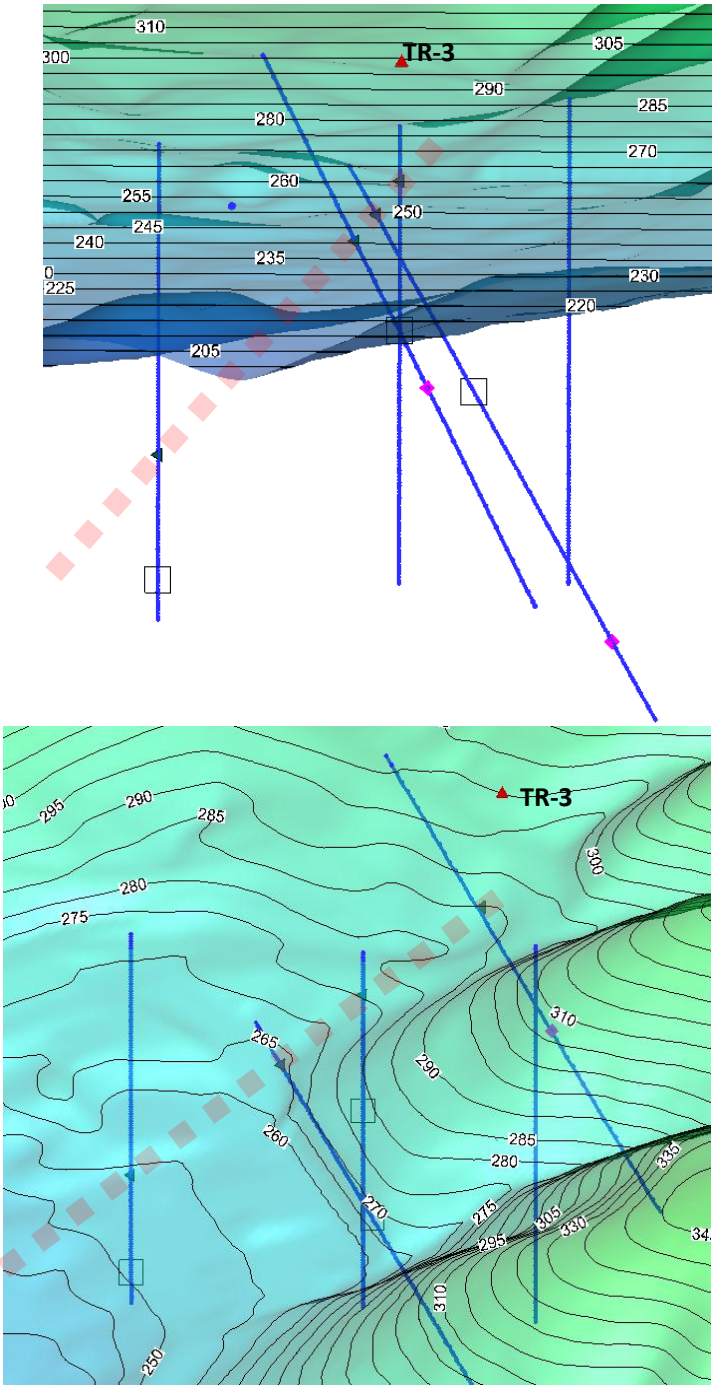

Figure 3-11. Alterantive interpretation of Fb feature (broken pink) that intersect WF-2, 3, 4 and 5 at the T_{OR}-T_{CC} contact viewed from two angles. The green triangles denote the contact observed in cores. Note it does not go through TR-3.

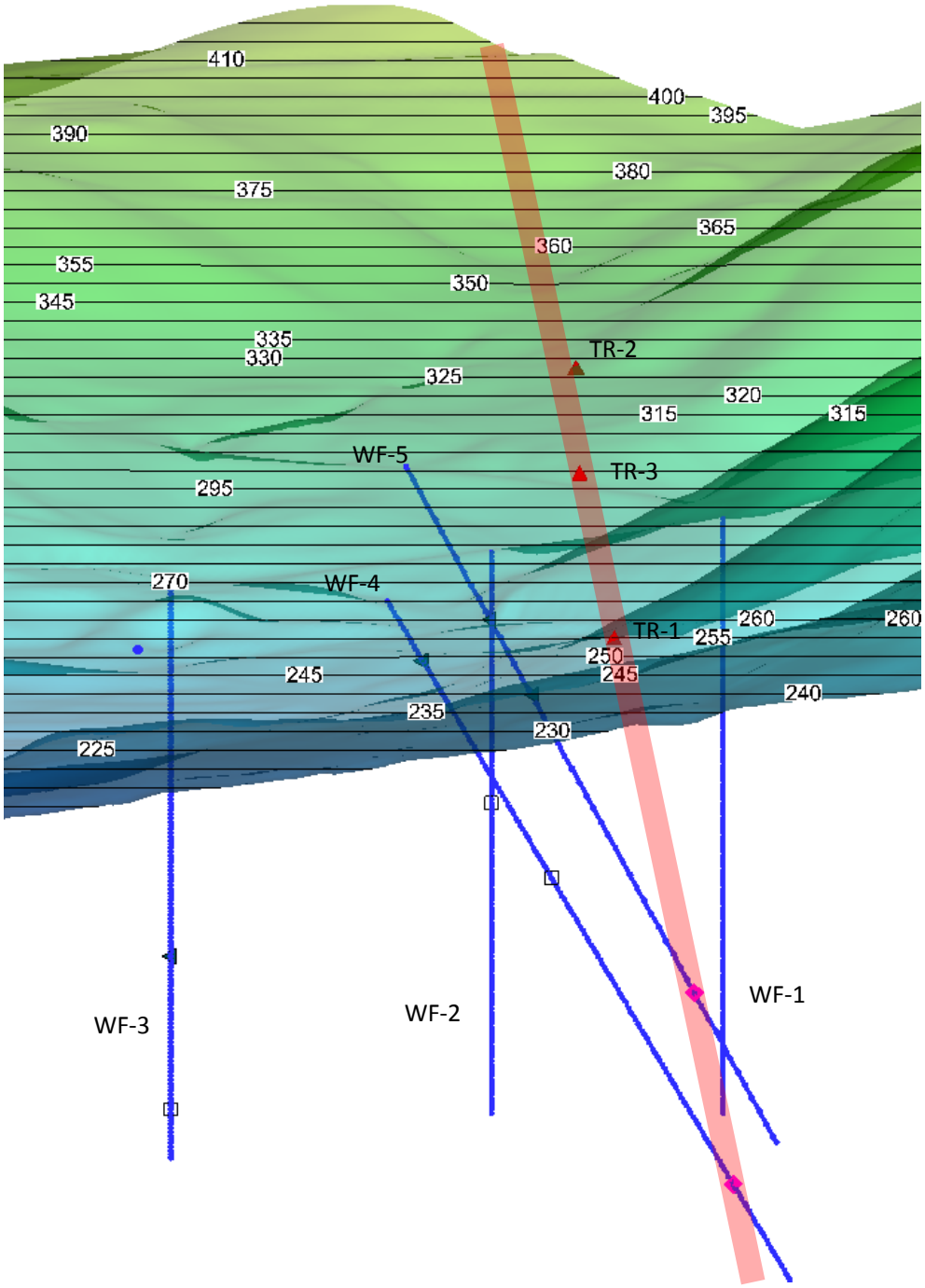

Figure 3-12. Alternative interpretation of the Wildcat main (light red line). It is steep and slightly east dipping, goes though the flow zones in WF-4 and WF-5 (pink diamond), brushes by WF-1, TR-1~3.

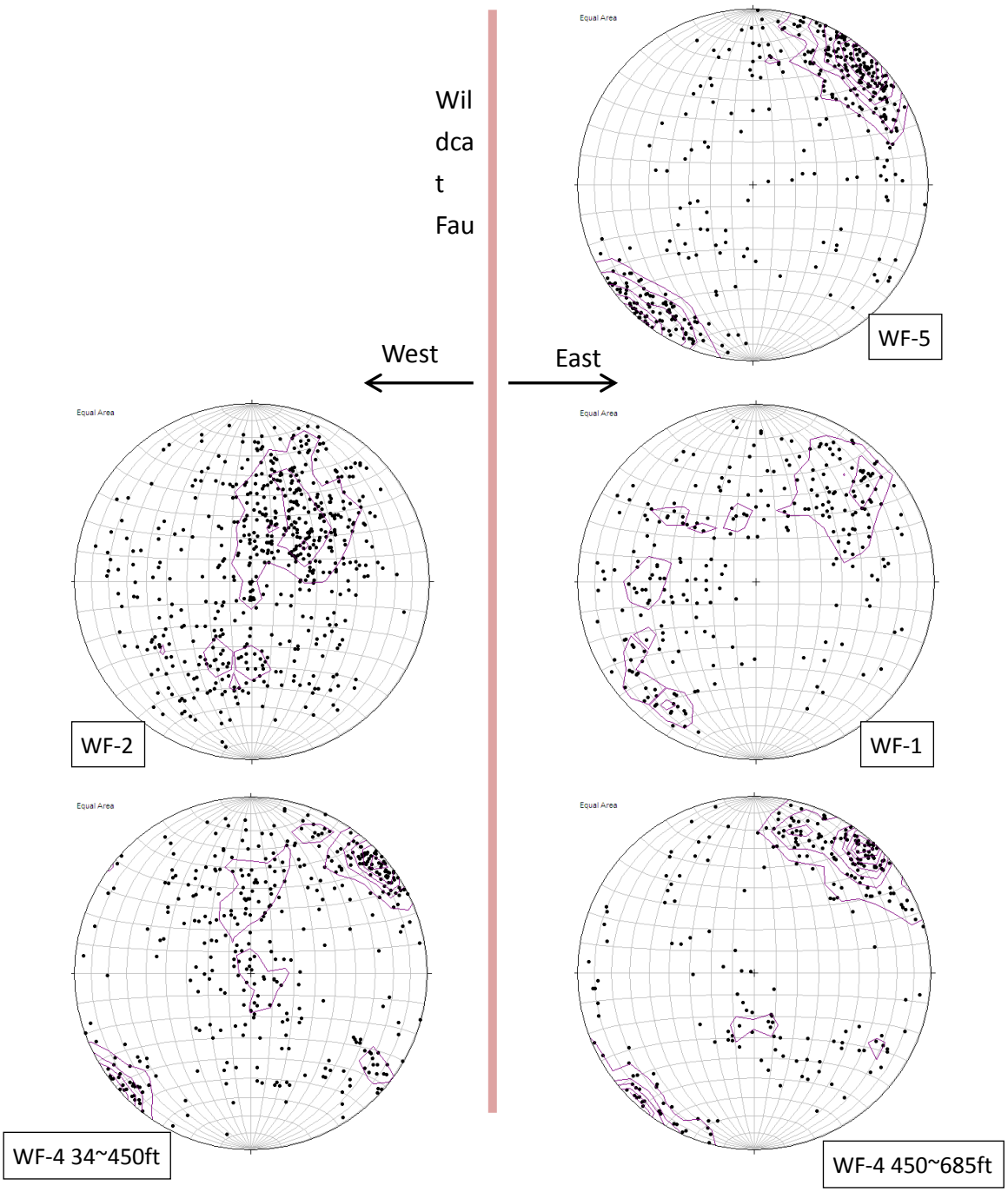

Figure 3-13. Possible interpretation of fracutre orientation statistics: More mildly dipping fractures on the west side of the suspected Wildcat Fault than on the east side, where many steeply dipping fractures are observed (stereo nets after Kiho, et al., 2012).

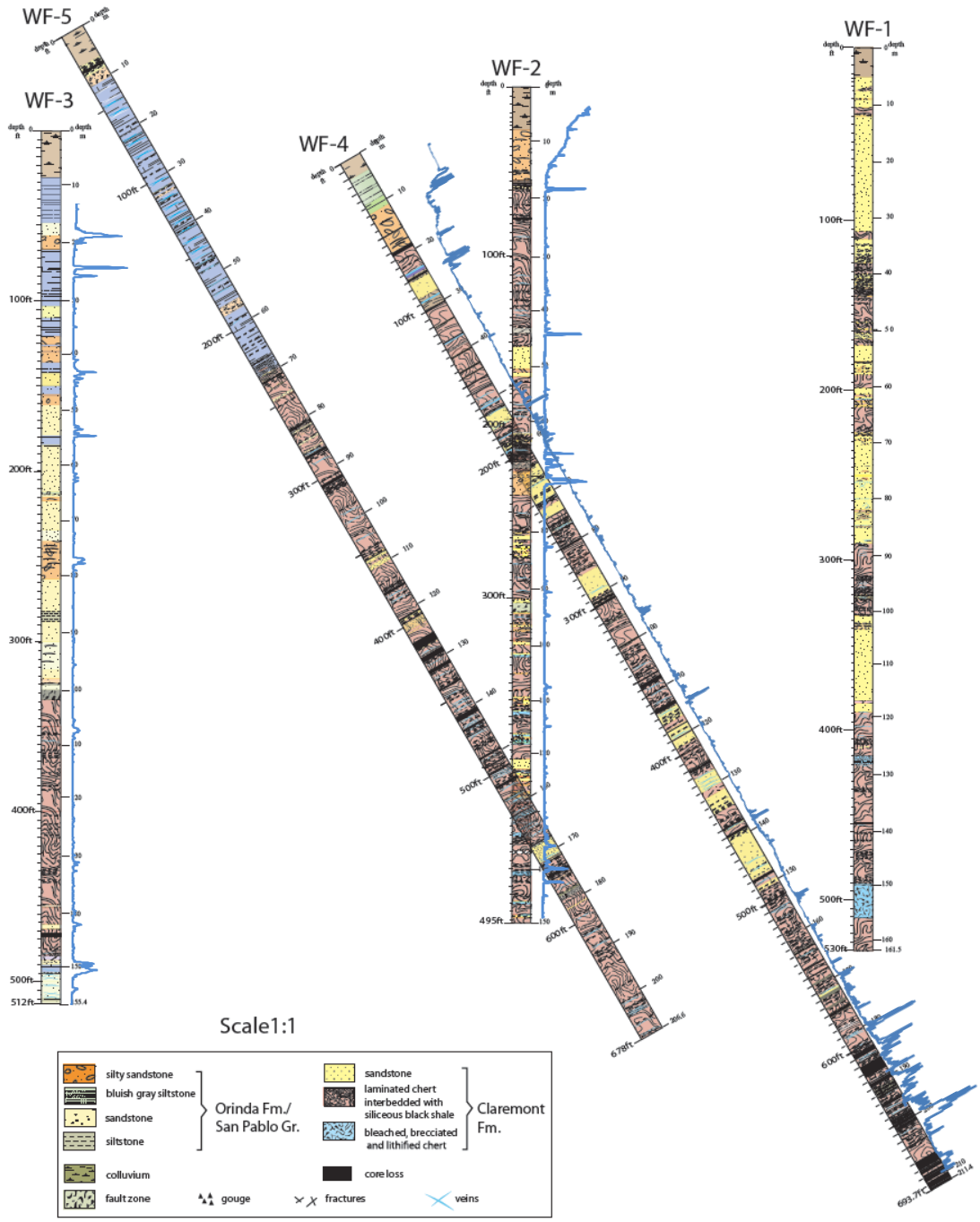

Figure 3-14. Capliper logs super imposed on geologic logs from WF boreholes.

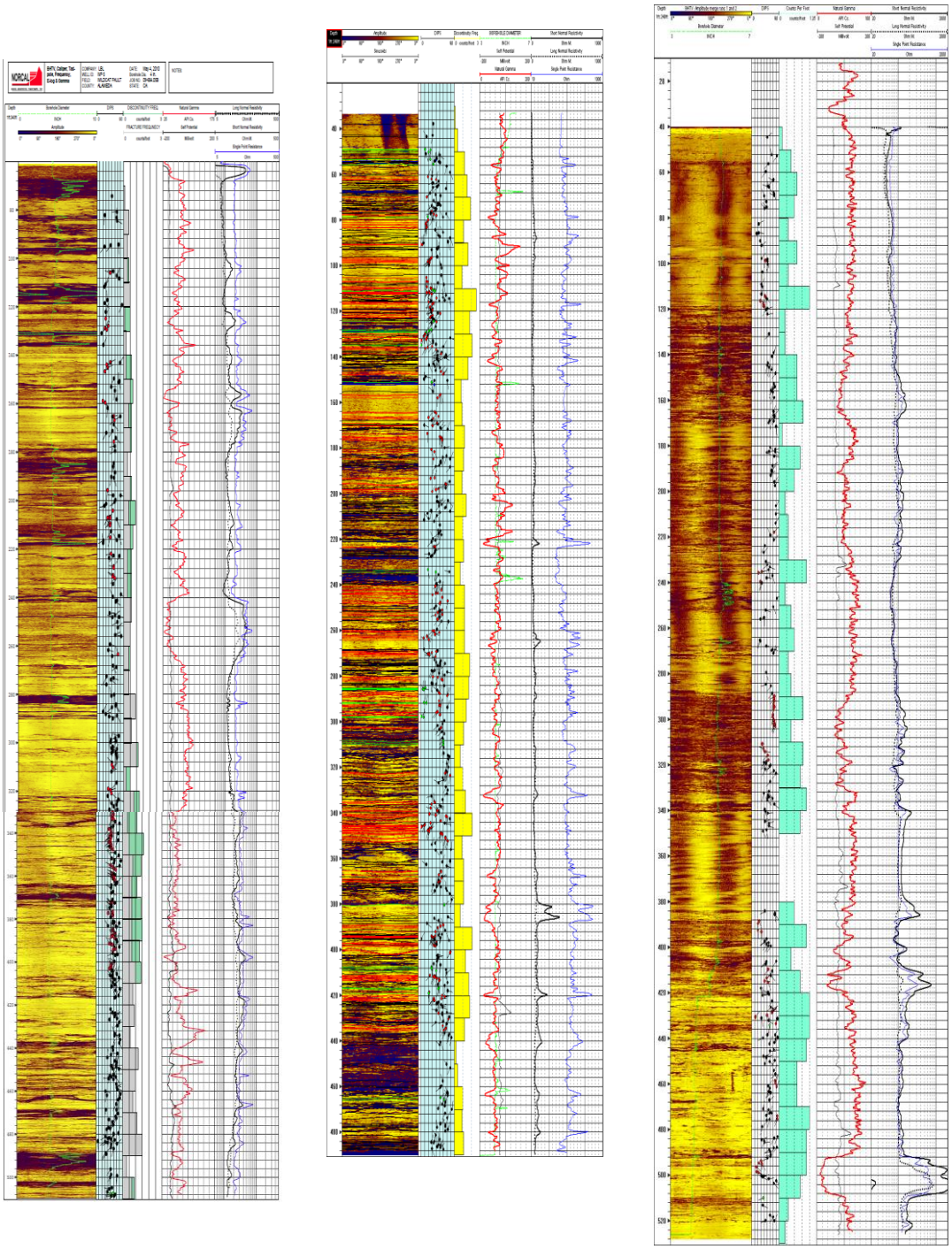

Figure 3-15. Composite plots of BTV, caliper, fracture orientation, fracture density, natural gamma, and resistivity logs for WF-1, 2 and 3. Not apparent correlation to geology was found.

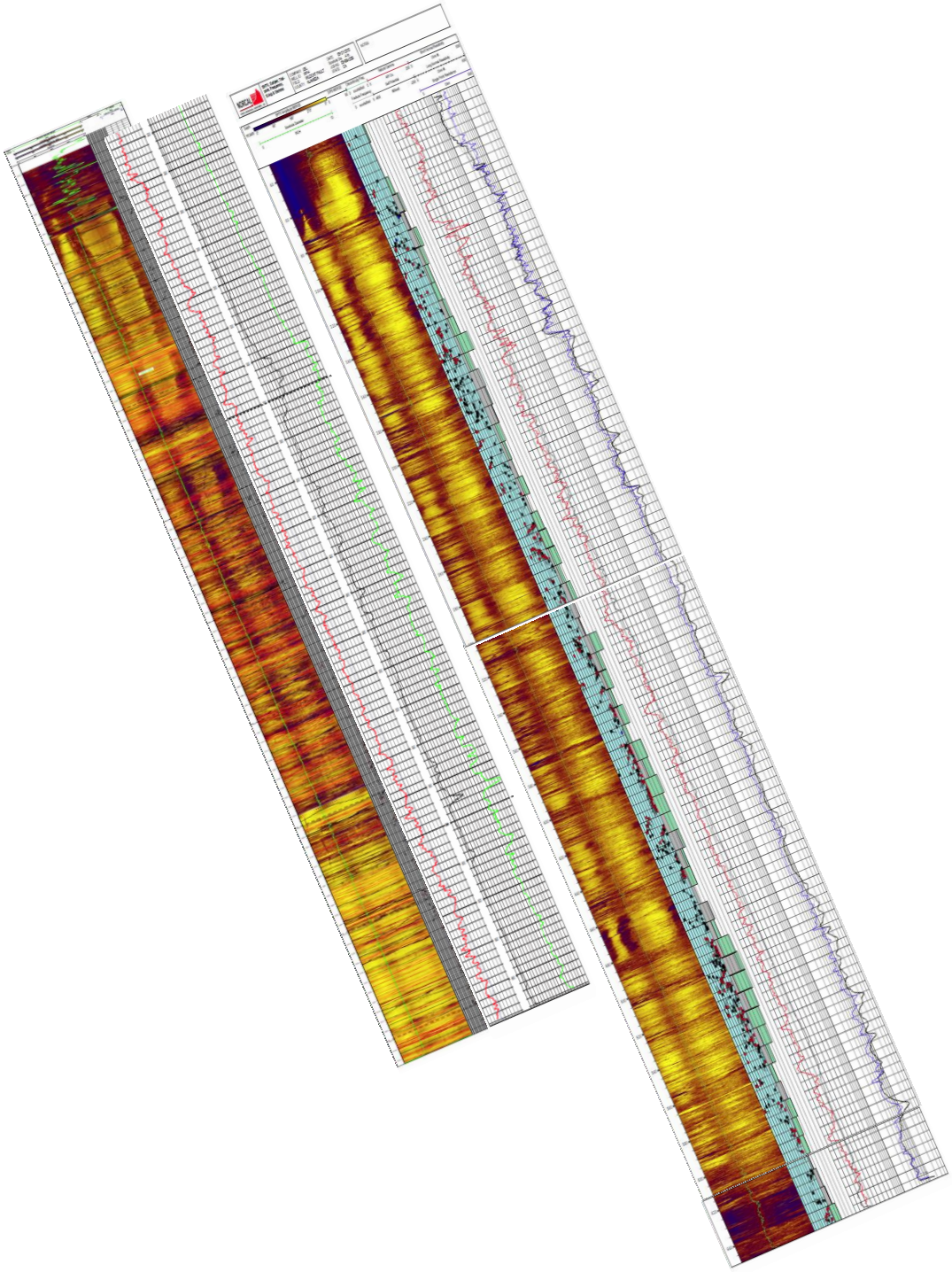

Figure 3-16. Composite plots of BTV, fracture density, orientation, SP, natural gamma, and resistivity logs fo r WF-4 and 5.

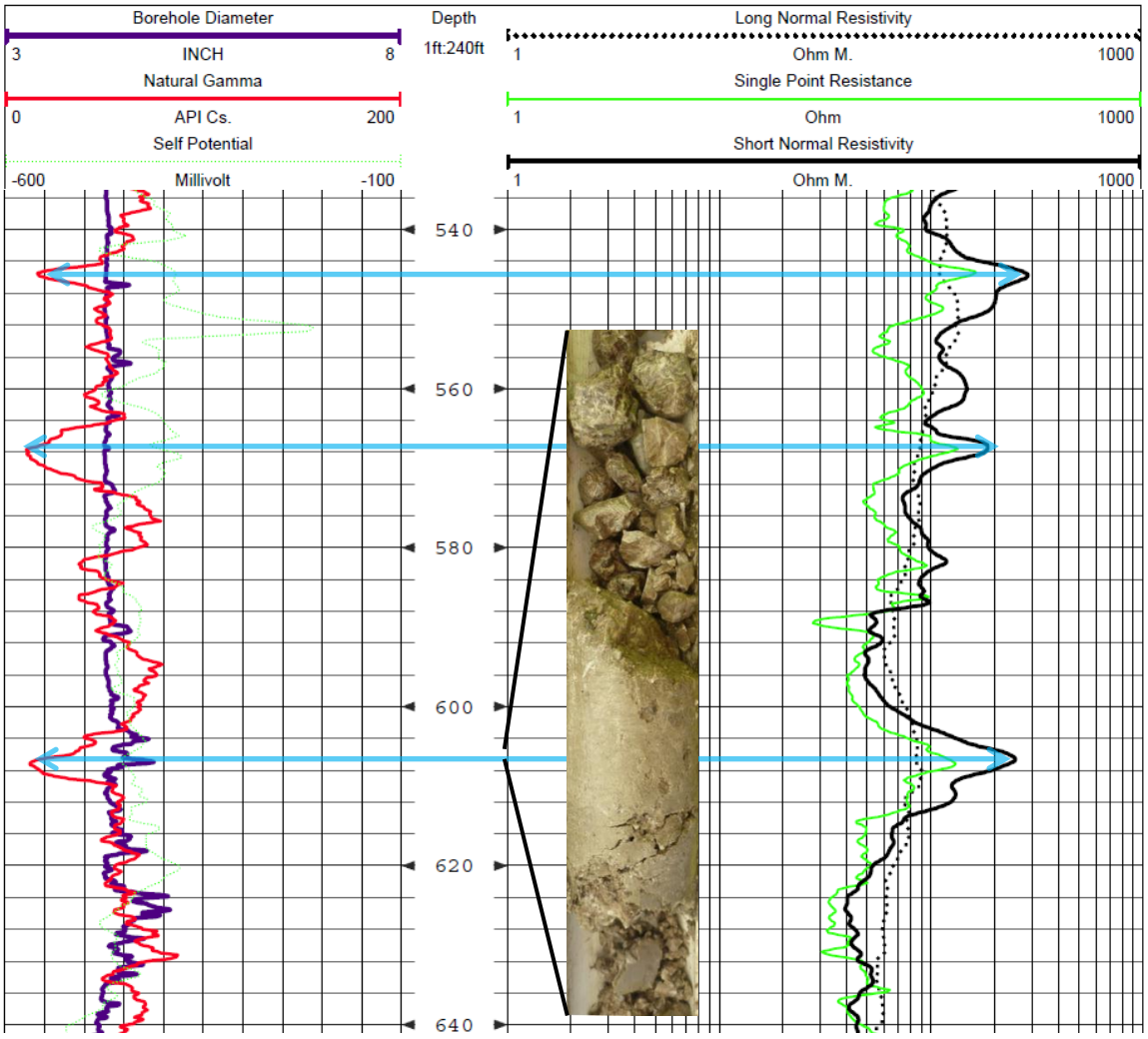

Figure 3-17. Excerpt of the ELOG results from WF-4, showing the oppsite kicks of the natural gamma and resistivity locations, marked by the blue arrows corresponding to bleached lithified brecchiated chert. A picture of the core of such rock from 607 ft (185 m) is also shown.

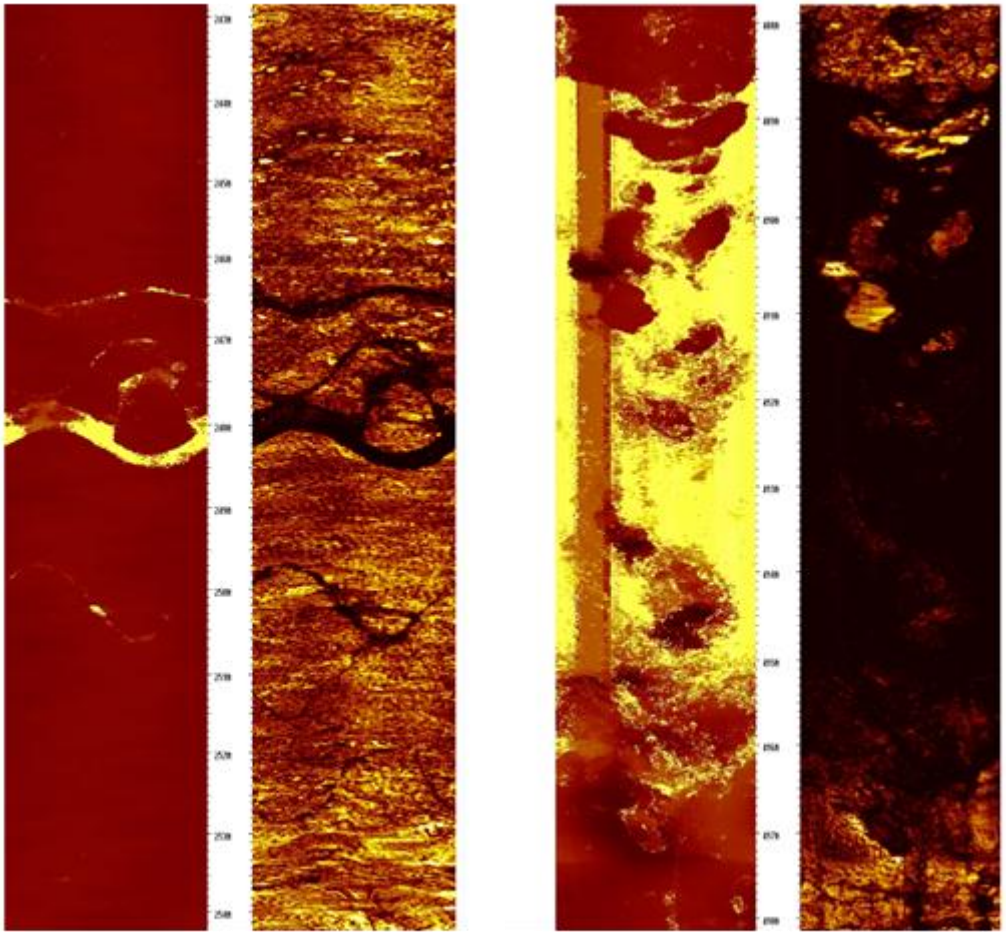

(a) (b)

Figure 3-18. Borehole televiewer images from WF-3: (a) 74~77.4m (243-254ft), where the largest inflow was observed by a FFEC log. (b) 148.7~151.7m (488~498ft), where a large fault is suspected.

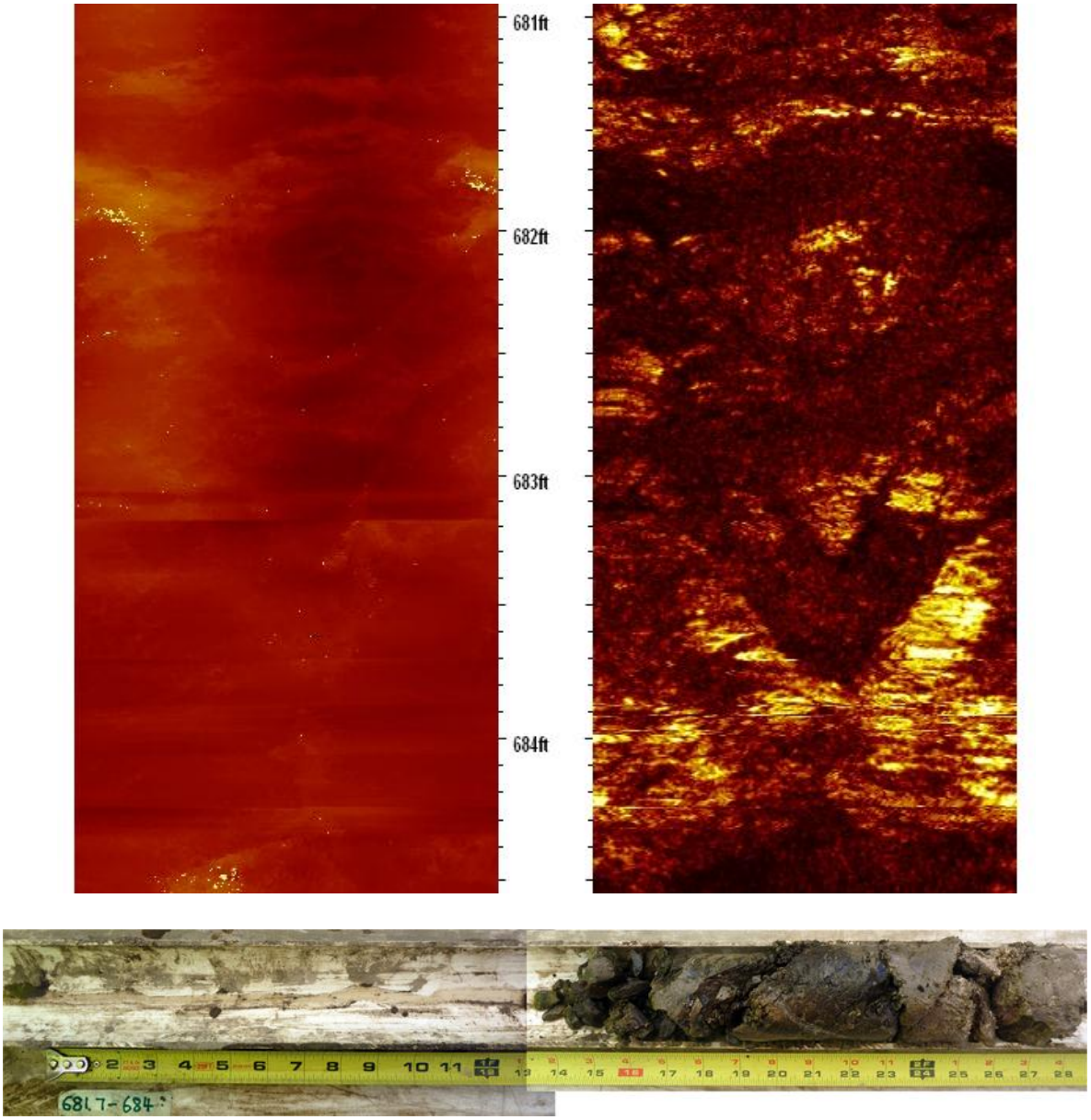

Figure 3-19. The BTV image from WF-4 at 681–684 ft (207.5 m–208.5 m). Also shown is the picture of the core from the same interval, most of which is not recovered. Note the very grainy image of the BTV, indicating that the rock is pulverized.

Figure 3-20. Flowing fluid electric conductivity log (FFEC) results (red lines) superimposed on the geologic columns of WF boreholes. Ligtht blue arrows indicate inflow locations.

Figure 3-21. Core orientation tool. The probe attches to the core retriever and is pushed against the top of the next core at the bottom of the hole together with the tip of the red pencil. Ball bearings lock to indicate the hole bottom direction. The shape of the circular nails is matched to that of core top. Red line on the core is drawn to mark the bottom direction of the hole.

3.6 References

CALTRANS, Caldecott Fourth Bore Project, http://www.caldecott-tunnel.org/index.php/home, 2012.

Converse Consultants, 1984, Hill Area Dewatering and Stabilization Studies, 82-4160.

Graymer, R.W., 2000, Geologic map and map database of the Oakland metropolitan area, Alameda, Contra Costa and San Francisco Counties, California. USGS Miscellaneous Field Studies MF3242g. Version 1.0

Harding Lawson Associates (HLA), 1974, Geologic investigation – Building 74 addition, Lawrence Berkeley Laboratory Berkeley, California. Report # 238_00001

Harding Lawson Associates (HLA), 1977, Foundation investigation - Cell Culture Facility, Lawrence Berkeley Laboratory Berkeley, California. Report # 183_00063

Harding Lawson Associates (HLA), 1980, Wildcat Fault Study Bio Medical Laboratory II Project Lawrence Berkeley Laboratory Berkeley, California. Report # 041-0020

Harding Lawson Associates (HLA), 1982, Geology of Lawrence Berkeley Laboratory. HLA Jobno. 2000,135.01. Report # 042_00

Karasaki, K., C.T. Onishi, C. Doughty, E. Gasperikova, J. Peterson, M. Conrad and P. Cook, Development of a Hydrologic Characterization Technology for Fault Zones—Phase II 2nd Report —, March 2011

William Lettis and Associates, Inc. (WLA), 2008, Surface-fault rupture hazard investigation of the Wildcat fault. roposed General Purpose Lab. Lawrence-Berkeley National Laboratory,Berkeley, California. 57.

4 Geologic Investigation

4.1 Introduction

In FY 2007, the Project started with a literature survey to develop fault classifications based on geologic and hydrologic properties. Results from this literature survey (of published peer-review journals), which focused on fault hydrology, showed that there was no clear correlation between the type of fault (e.g., normal, reverse, and strike-slip) and hydrologic properties. However, a comprehensive study of fault characteristics (such as changes in fault properties along the fault length; or variations in fault geometry, spatial heterogeneity, or internal structure) may give indications of how faults and fault zones could potentially affect local and regional hydrology.

Kiho et al. (2009) conducted a literature survey for the Japanese examples of fault hydrology. Those studies included mining and engineering constructions (dams, tunnels), which served to complement the survey conducted by Karasaki et al. (2008).

The site chosen for our fault-hydrology analogue study was the Wildcat Fault (WCF), within the property of Lawrence Berkeley National Laboratory, Berkeley, CA, USA. The WCF, located in the Berkeley Hills, is a splay of the Hayward Fault, which is part of the San Andreas Fault system. The WCF, which is inactive, shows an estimated total right-lateral displacement of 14 km based on Pliocene volcanic rock that overlies the Miocene sedimentary rock. All displacement is apparently pre-Holocene. The WCF is mapped at the regional scale as a contact juxtaposing the Miocene and Pliocene fluvial sediments of the Orinda Formation and the shallow marine San Pablo Group with the middle Miocene marine Claremont Formation.

In detail, however, the structure and stratigraphy of the WCF are rather complex. For this study, a preliminary literature and field survey were conducted. Five trenches were excavated and five vertical exploratory core logs were drilled and cored for geological investigation. Two of the core logs were drilled at an inclined angle of 30 degrees from vertical and designed to intersect the trace of the WCF.

Geological and geophysical investigations suggested the presence of a fault structure, with multiple interpretations. The faults encountered in all the excavated trenches have distinctive characteristics and attitude. Distinctive faults were also observed and described during

core logging. Although the vertical borings are only 60 to 80 m apart, no stratigraphic correlation can be found between the core logs.

Deformation within the WCF zone is widespread. At least five major faults have been intersected by the boreholes as part of the Project, as well as two dozen gouges and zones of damage (breccias to finely ground material). Analyses of cores (based on core logs) indicate that these fault traces are related to several stages and degrees of deformation, including breccia, gouge, cataclasite, and foliated cataclasite.

Petrographic and XRD results also indicate the presence of clay minerals and sometimes mica within those fault materials, suggesting low permeability. However, the brecciated and highly fractured zones may be preferred pathways for fluid movement. The most recent, yet still pre-Holocene, fault activity corresponds to a zone of intense fracturing and high fluid flow in a zone situated between 170 to 214 m in depth. Thus this study suggests that the WCF is more complex in terms of its deformation history than previously thought.

4.2 Regional Geology and Tectonics

The San Francisco Bay Area contains some of the most complex and active geology in the world. This geology is a result of plate subduction, active volcanoes, and faults along plate boundaries. The bedrock age ranges from Jurassic to Pliocene, with the oldest rocks in the region being of a Franciscan assemblage and Jurassic to Cretaceous in age (200–65 Ma). Rock was originally deposited in a deep marine environment and in trenches, then subsequently accreted during plate subduction along the coast of Northern California. Over more than 100 million years of subduction, accretion brought together the many types of Mesozoic rock that we now see in the Bay Area. Extensive tectonic activity uplifted and folded the Franciscan mélanges, which consisted of exotic blocks of basalt, chert, limestone embedded in a matrix of sheared greywacke, and shales.

To the east of the Bay Area, a thick sequence of clastic submarine fan and basin plain deposits filled the forearc basin, between the accretionary wedge of the Franciscan and subduction-related volcanic arc (the present location of the Sierra Nevada batholith). This thick sequence of over 14,000 m is the Great Valley Sequence. The contact between the Franciscan and Great Valley Sequence is defined by fault, where discontinuous and dismembered fragments of the Coast Range Ophiolite crop out.

In the Eocene, about 25–30 million years ago, there was a change in the tectonics when the Pacific plate met the North American plate. Subduction stopped along the contact of the two plates, and the Pacific plate began to slide northward past the North American plate along a transform boundary—the San Andreas Fault (Atwater, 1998; Sloan, 2006). These tectonics created shallow basins and mountain ranges. The basins were filled by marine as well as continental sediments, and many varieties of sediments—future conglomerate, sandstone, shale, and chert—also accumulated in these basins. These include the deposition of the Claremont and Orinda formations. Most of these sediments have been tightly folded. The diverse topography in the San Francisco Bay Area region has been also affected by faulting that has occurred since the Cretaceous. As the subduction continued into the Tertiary period, local faulting broke up extensive trenches, within which sediments accumulated.

During the late Tertiary, volcanic lava flows were produced by local vents associated with fault movement. These flows created most of the volcanic rock in the San Francisco Bay region, largely basalts and andesites. Examples of this volcanism are: Quien Sabe volcanic (11–13 Ma), East Bay Hills volcanic (9–10.5 Ma), Sonoma volcanic (2.6–8 Ma), and Clear Lake volcanic (2–10,000 Ma) (Graymer, 2002; Sloan, 2006)

Although the dominant movement between the Pacific and North America plates is strike-slip, a small change in plate motion occurred about 3.5 million years ago. The Pacific and North American plates began to collide at a slight angle instead of just sliding past each other, resulting in transpression (Atwater, 1998). Sloan (2006) indicated that 90% of the movement between plates is strike-slip, while 10% or less is compressional. Folding and faulting are the main processes involved in transpression. Good examples San Francisco Bay region topography resulting from transpression are Mt. Diablo and Mt. Tamalpais.

In summary, the bedrock exposed in the Berkeley Hills is highly deformed by extensive folding and faulting that has occurred since Cretaceous time, with very strong deformation occurring during the Pliocene epoch. The bedrock has been folded into a series of northwest trending anticlines and synclines, offset by faulting (Page, 1950; Graymer, 2002; HWL, 1982).

Figure 4-1 illustrates the regional stratigraphy of the Berkeley Hills.

Era	Period	Epoch	Group	Formation	Lithology	Deposition/Deformation
Cenozoic	Quaternary	Pleistocene/ Holocene		Colluvium/ Landslide deposits	Clays and silts and weathered material	Resulted from erosional process
	Late Tertiary	Late Miocene - Pliocene	Contra Costa	Moraga	Volcanic flows of basalt and andesite; tuff	Lava flow related to eruption of Bald Peak and Round Top volcanoes
		Miocene-Pliocene	Contra Costa	Orinda	Poorly consolidated sandsone, siltsone, claystone, occasional conglomerate	Flood plan or alluvial to shallow lake depositional environment. Unconformity over Claremont Fm.
		Miocene-Pliocene	San Pablo	Briones (?)	sandstones	shallow marine environment
		Middle Miocene	Monte-rey	Claremont	Siliceous shale, chert, siltstone, occasional sandsotne	Marine deposition; well interbedded, folded, fractured and faulted and overturned beds.
Mesozoic	Cretaceous to Jurassic		Great Valley Complex	Coast Range Ophiolite (CRO) and Great Valley Sequence (GVS)	CRO= rocks of upper mantle (serpentine) to basalt GVS= marine sedimentary rocks (sandstone, shale, conglomerate, volcanic eroded material)	Fore-arc basin sediments over 10 km thick over oceanic rocks.
				Franciscan	Pillow basaslts, cherts, mélanges of greywacke and shale	From ocean spread center to subduction and accretion process. Sheared and faulted.

Figure 4-1. Regional stratigraphy

4.2.1 Geology of Lawrence-Berkeley National Laboratory and surrounding areas

Lawrence Berkeley National Laboratory (LBNL) is located in the hills of Berkeley, on the eastern side of the San Francisco Bay Area, California. The bedrock at LBNL consists of Cretaceous and Miocene sedimentary rock overlain by volcanic flows (Figure 4-2). These flows are part of a homocline in the Great Valley sequence that gently dips 20–30° to the northeast. This homocline is disrupted by the WCF in the eastern part of LBNL (LBNL and Parsons, 2000).

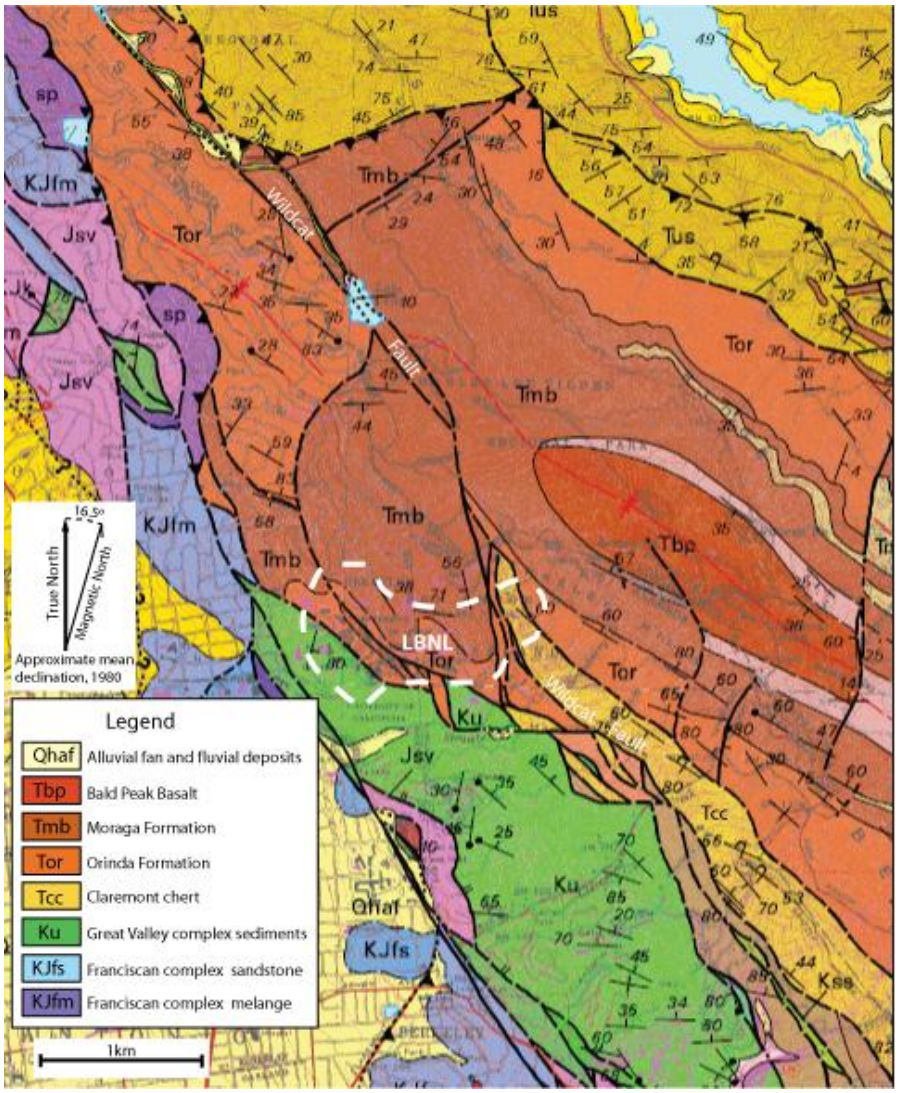

Figure 4-2. Regional geologic map of Berkeley, CA (Graymer, 2000)

4.2.1.1 Claremont Formation

The oldest rock in the study area is the Miocene age Claremont Formation, which is part of the Monterey Group. Rock from the Claremont Formation is about 14–16 million years old

and consists of well-consolidated, moderately weathered, light yellow siliceous shale and bedded chert, intercalated with thin layers of siltstone. The Claremont Formation is regionally and locally folded and commonly overturned; bedding dip varies from northeast to southwest. Compared to surrounding bedrock, cherts are generally weather-resistant, forming some of the steeply sloped hills in the area (Ultermman, 1935; Page, 1950; Graham et al, 1984).

4.2.1.2 Orinda Formation

The Orinda Formation is part of the Contra Costa Group and includes alluvial-fluvial sequences and lacustrine sequences (Graham et al., 1984). In the study area, it overlies the Claremont cherts unconformably (Jones and Curtis, 1991). The Orinda Formation comprises a succession of stacked fluvial, fining upward sequences (channelized gravel-to-cobble conglomerate, coarse grain sandstone to maroon and green-gray sandy mudstone) and lenticular conglomerate units, some of which are separated by thick mudstone intervals (Graham et al., 1984). Nonmarine, unconsolidated sediments, primarily sandstone, siltstone, and conglomerate, are interbeded with volcanic rock. The Orinda Formation was originally deposited in a shallow lake or alluvial fan environment, except for the lowest portion, which may have been deposited in a shallow marine basin. Sediments deposited in this marine environment are described as the San Pablo Group.

4.2.1.3 San Pablo Group

The San Pablo Group is characterized by fossiliferous shallow marine sandstones. As described by Graham et al. (1984), the Orinda Formation is genetically linked to the San Pablo Group as a shallow marine equivalent by widespread interfingering with the Briones sandstone (Contra Costa Group). They both display the same Franciscan provenance in the sandstone.

4.2.1.4 Moraga Volcanics

The Moraga volcanics overlies and interfingers with the Orinda Formation. It consists of alternating volcanic flows of basalt, andesite, and agglomerate, along with occasional tuffaceous sediments. The Moraga volcanics consist of up to ten basaltic volcanic flows, with interbedded volcaniclastic sediments (Curtis, 1989). It is primarily a result of Lower Pliocene (9–10.2 Ma) activity. The eruption of the Grizzly Peak volcanics constitutes the first evidence of fracturing along the Hayward trend (Graham et al., 1984). Outcrops of the Moraga are found in the north to northwest part of the study area and are typically highly fractured.

4.2.1.5 Colluviums and landslide materials

The steep topography and high hills surrounding LNBL have been extensively evaluated by geotechnical consultants. Their geological and geotechnical studies show that a large part of the LBNL property is composed of landslide and colluvium deposits. Large masses of landslide, composed primarily of the Moraga Formation, have been mapped near the study area. The masses are generally lenticular in cross section, and several are elongated in plain view (LBNL and Parsons, 2000). The thickness of colluvium/landslide material varies from 1.5 to 12 m (5 to 40 ft) deep.

4.3 Geological Structures

The San Francisco Bay Area is intertwined with active faults, which run NW-SE. They are part of the San Andreas Fault System, showing right-lateral strike slip motion. The map shown in Figure 4-3 illustrates the distribution of faults in Northern California.

Figure 4-3. Map of Quaternary faults in the San Francisco Bay Area

4.3.1 San Andreas Fault

The San Andreas Fault system of coastal California, one of the best-known transform fault systems in the world, is part of the boundary between the Pacific and North America plates. The right-lateral strike slip fault has accommodated over 330 km of displacement since Neogene. In the San Francisco Bay Area, especially in the East Bay, the San Andreas Fault splays into many subparallel fault zones. Those fault zones include the active Hayward-Rogers Creek-Maacama (commonly referred to as the Hayward Fault), Calaveras-Sunol, Concord-Green Valley, and Greenville fault zones (Graymer et al., 2002). They are characterized by northwesterly trending faults (N30–40W). The San Andreas Fault system runs approximately 15–20 miles west of LBNL.

The study area is primarily influenced by the Hayward Fault, which consists of a set of northwest-striking, right-lateral strike-slip faults. The study area is situated in a seismically active area of California, with a known history of earthquake events such as the 1906 and 1989 events along the San Andreas Fault, and the 1868 along the Hayward Fault.

4.3.2 Hayward Fault

The Hayward Fault system, which runs northward and parallel to the San Andreas Fault system, initiated about 12 million years ago. The East Bay Hills, including where Berkeley is now, are actively rising at present, squeezed upward between two major faults, the Hayward and Calaveras. The Hayward Fault is one of the main branches of the San Andreas Fault system, sharing the same relative motion, i.e., a right-lateral strike slip movement. It trends N30W and runs from an area southeast of San Jose to San Pablo Bay. The fault is around 100 km long, parts of which are either locked or creeping. The Hayward Fault crosses the eastern border of the UC Berkeley campus (which is creeping at a rate of about 5 mm/year—Simpson, 2000), interesecting the football stadium, as shown in Figure 4-4 . Most subtle geomorphic expression has been removed by development, erosion, and landslide. However, some clear geomorphic expression remains, such as a linear northwest-trending zone of geomorphic features, subtle stream offset, and beheaded channels, as observed in the LIDAR image. The last major earthquake on the Hayward fault occurred in 1868, with an estimated magnitude of 7.0. The Hayward Fault is a prime candidate for a magnitude 7 earthquake within the next 30 years (USGS, 2008).

4.3.3 Uplift of the Berkeley Hills

During the late Miocene (c.a. 12 Ma), uplift of the Berkeley Hills started with the initiation of the Hayward Fault as a result of the transition to transform-margin setting. The uplift has also changed the sedimentation patterns in the East Bay, specifically changing the deposition in the area from marine to nonmarine sediments. Paleogeographic reconstruction of the East Bay suggests changes in sedimentation patterns during the deposition of the Orinda and San Pablo groups. The eruption of the Grizzly Peak volcanics constitutes the first tangible evidence of fracturing along the Hayward Fault (Graham et al., 1984). Deformation and uplift west of the Hayward Fault spread eastward, activating the Moraga fault thrust.

4.3.4 Wildcat Fault (WCF)—Regional

The WCF is a secondary splay fault associated with the Hayward Fault. It cuts late Cenozoic strata, striking subparallel to the Hayward Fault (Figure 4-4). The WCF, which runs about one and one-half kilometers east of the Hayward Fault, has been identified as part of the San Andreas Fault system (LBNL and Parsons, 2000).

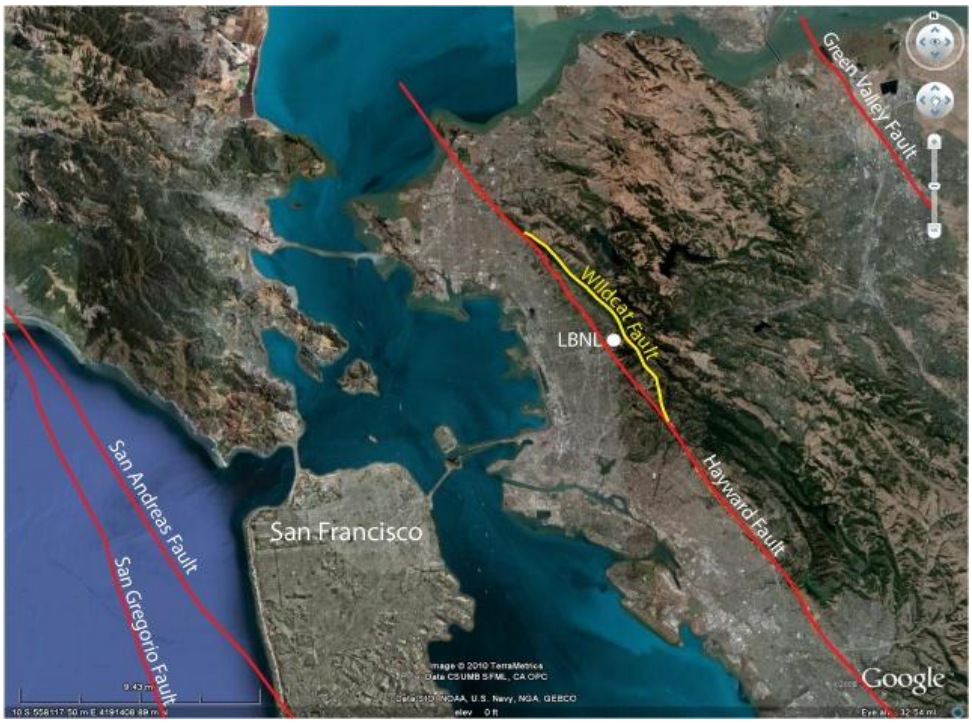

Figure 4-4. Map showing the WCF in the context of main faults in the San Francisco Bay Area

The WCF passes along the eastern margin of LBNL and runs from Oakland to Richmond. Regionally, the fault is difficult to map throughout its length and appears to be discontinuous, although it clearly truncates and offsets strata at many locations. At a regional scale, the fault shows right-lateral strike-slip movement (Curtis, 1989), and local reverse movement has also been observed and described (Jones and Curtis, 1991). The history of the WCF at regional scale is summarized below:

- The WCF has been shown on geologic maps since the early 1900s. It was originally mapped by Lawson and Palache (1900).

- Untermann (1935) named the WCF as a long break in the Berkeley Hills. Its disturbance can be one-fourth of a mile (250 m) wide in some places. According to Untermann, the WCF has a northwest-southeast trend generally dipping to SW. On his map, north of Strawberry Canyon, the fault follows the contact between cherts to the east and a series of sediments and volcanics to the west as part of the Orinda Formation. The saddles indicating the location of the fault near LBNL are the Little Grizzly Peak in the north and Sugar Loaf (named after Untermann, 1935) along the Fire Trail to the south. Shear zones, gouge, and slickensides in cherts are reported along road cuts north of Signal Hill and below Sugar Loaf, near Claremont Canyon. On the south side of Claremont Canyon, an outcrop of chert with bedding (N46W/82SW) shows horizontal striations. The disturbance zone varies from ~90 m (300 ft) to the west and a gouge zone of 45 cm to 2.4 m (18 inches to 8 ft) wide to the east. Sandstone of Sobrante (Lower Miocene) or of Cretaceous has been described south of Strawberry Canyon. The presence of older and higher beds to the east would also suggest elevation of the esst side.

  North of Strawberry Creek up to Little Grizzly Peak, Untermann reported the contact of the WCF as between the Claremont chert in the east and the sediments (conglomerate, sandstone, and shales of reddish brown and greenish color) of the Orinda Formation. Untermann also describes several locations where he observed striation in cherts (varying from vertical to horizontal), as well the presence of a secondary fault along Strawberry Canyon. Further north, Untermann describe a horizontal displacement of 1320 ft (402 m) that was measured in the lava along the Wildcat Canyon, south of Cerrito Creek. The fault follows the Wildcat Canyon merging with the Hayward Fault somewhere south of

San Pablo Bay. To the south, the fault was mapped in the Claremont Tunnel within the cherts and in the San Pablo Tunnel as a contact between Orinda and Claremont. The fault plane was reported dipping steeply to the southwest.

- A major fault zone of about 9 m (30 ft) was partially exposed during the construction of the Broadway Tunnel in Oakland (Page, 1950). The fault cuts through the Claremont Formation. The author did not identify this structure, although he noticed that strata were highly fractured, locally contorted, and cut by many irregular dikes (Page, 1950).

- The WCF runs parallel to the Hayward Fault and, according to Bishop (1973), eventually joins the Hayward Fault in the north near the San Pablo. Fault creep has been used as an indicator along the north end of the fault. The evidence consists of a slight curb offset, pavement cracks, a deflected stream, and a break-in-slope. According to Bishop (personal communication in HLA, 1980), there are no known creep features along the WCF south of the El Cerrito–Richmond line.

4.3.5 Cross Fault

The Cross Fault was originally mapped by Lawson and Palache (1900), Untermann (1935), and mentioned in Dames and Moore (1962). Untermann (1935) describes the presence of a secondary fault along Strawberry Canyon, striking N65W and steeply dipping to the NE, suggesting the possibility that the WCF had been displaced by a cross fault.

HLA (1974) reports a cross fault cutting through Building 74, although it was not observed either in borings or caissons, or exposed on the surface. It is based on the relative exposure of the Orinda to Claremont shale on the cut slope. Then, in 1980, HLA trenched across the cross fault near Building 74. The thick colluvium deposit did not expose the fault. Jordan (2008, personal communication) mapped a fault behind Building 84 that merged with the WCF instead of cutting through it (see map by LBNL and Parsons, 2000). Therefore, owing to a lack of conclusive evidence showing that the cross fault displaces the WCF, no further attempt was made to describe this fault.

4.3.6 Folding and Thrusting

Major Neogene and younger compression are recorded in the geology of the East Bay. Examples of this compression include several east-verging fold and thrust belts, such as the Moraga Fault (Aydin, 1982). In the study area, cherts of the Claremont Formation are strongly folded, generally overturned to the east, and are probably repeated several times by faulting and folding (Jones and Curtis, 1991). The age of thrusting in the Berkeley Hills is now well constrained, with evidence of the Moraga Fault displacing rock as old as 8.4 Ma (Jones and Curtis, 1991).

4.4 Geological Characterization

4.4.1 Field Work

Extensive fieldwork was conducted in 2009–2010 in the Berkeley Hills along Wildcat Creek, from Panoramic Road in the south to (and including) Alvarado Park in the north. Most of the creek cuts through Tilden Regional Park in the Berkeley Hills—detailed description and findings can be found in Karasaki et al. (2009). Evidence of the fault is nearly nonexistent in the outcrops of the surveyed area. North of the study area shown in Figure 4-5, a trace of the WCF cuts through the Moraga volcanic and then along Wildcat Creek, which lithologically cuts through the silststone and mudstone of the Orinda Formation.

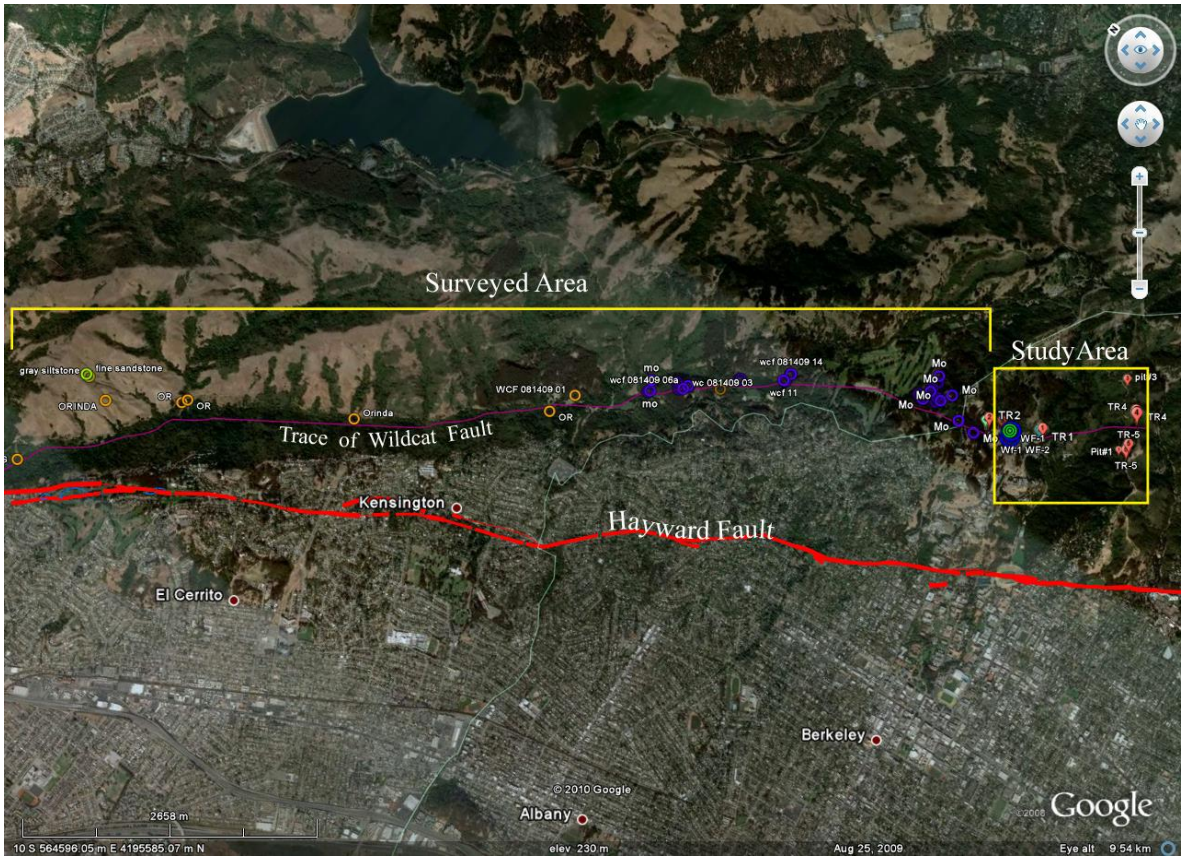

Figure 4-5. Aerial view of the study and surveyed area along the WCF

4.4.2 Trenching

After literature and field surveys were conducted, we excavated five trenches in the study area in order to identify and characterize the WCF. The location of the trenches were based on (1) proximity of the trace of the fault from geotechnical reports (for TR-1 and TR-2), (2) the field description by Ultermann (1935) (for TR4), and (3) field work evidence (for TR-3 and TR-5). Figure 4-6 show the location of the five trenches excavated in the study area.

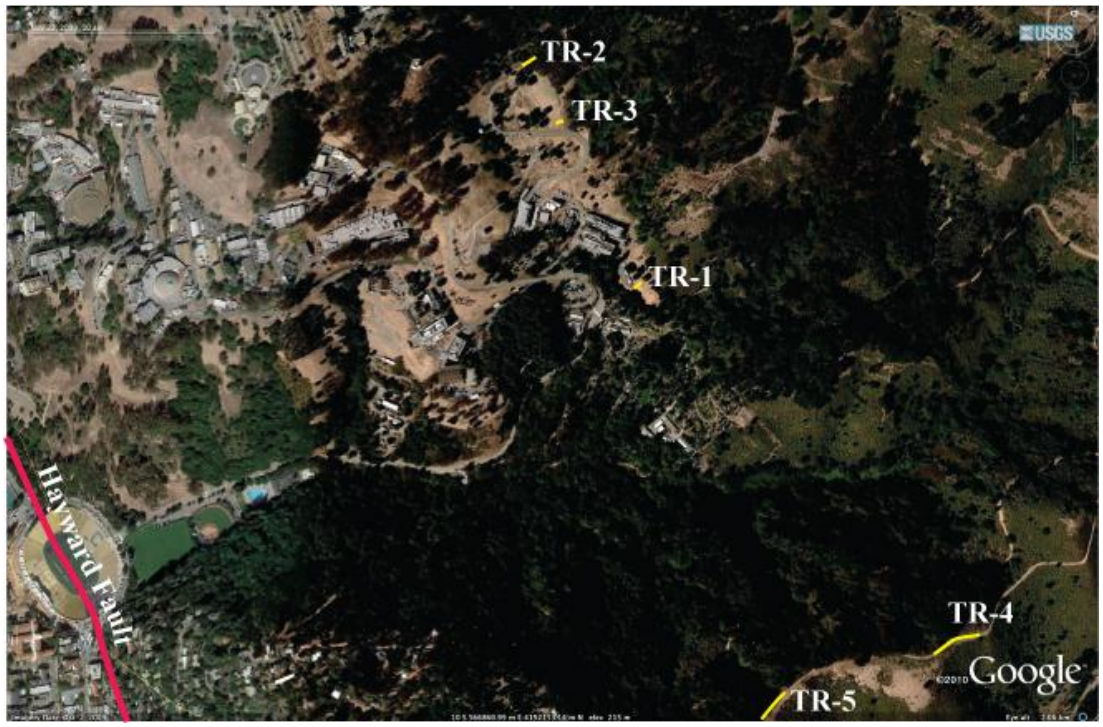

Figure 4-6. Location of the five trenches TR1–TR5 in relation with the Hayward Fault

4.4.3 Drilling and Coring

Drilling was specifically located in the Lawrence Berkeley National Laboratory property along Calvin Road. The original plan was to drill and core three boreholes up to 150 m (500 ft), two vertical on each side of the trace of the fault and one inclined to intersect the fault trace. Instead of three, five boreholes were drilled and cored for the reasons discussed in Chapter 3. Figure 4-7 illustrates the location of the boreholes within the LBNL property along Calvin Road.

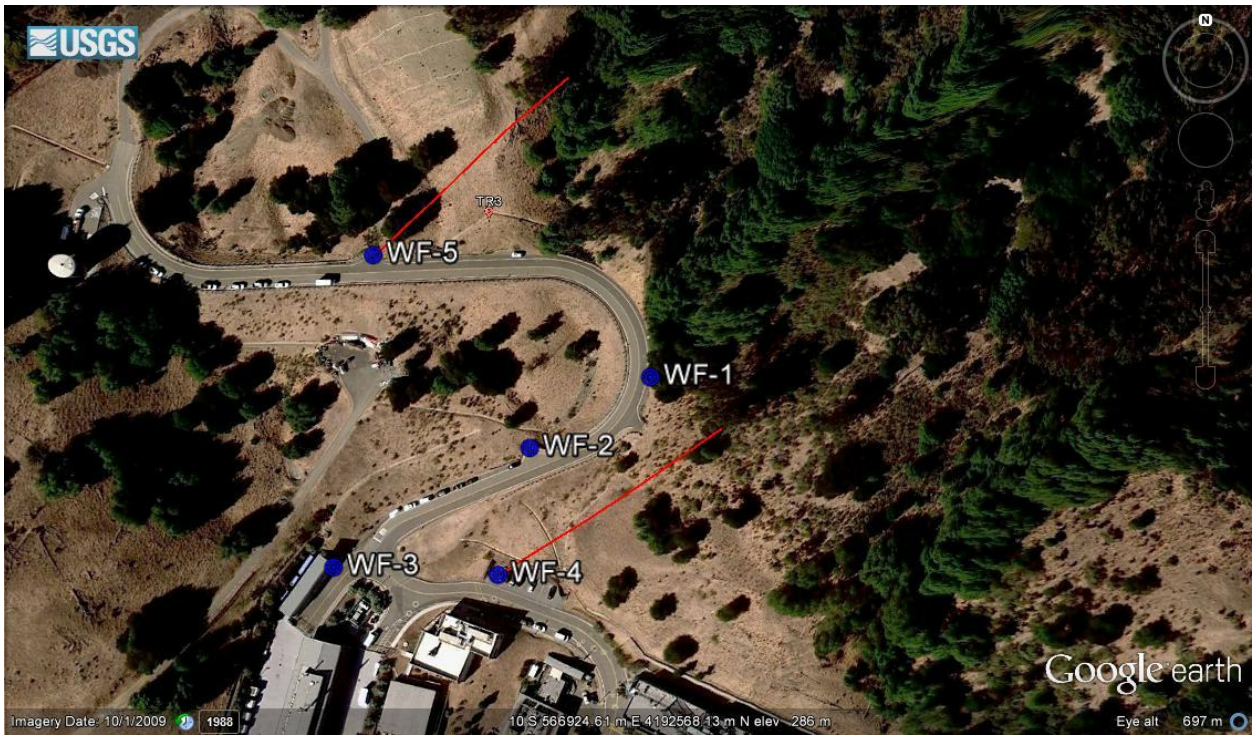

Figure 4-7. Location of the five boreholes along Calvin Road in the eastern end of LBNL

Based on the trace of the WCF, WF-1, a 530 ft (161.5 m) deep vertical borehole was drilled and cored on the eastern side of the fault trace and entirely within the Claremont Formation. It was followed by WF-2 and WF-3, both vertical boreholes 495 ft (150.8 m) and 512 ft (156 m) deep respectively, drilled and cored on the western side of the fault trace. According to the geological map, WF-2 should have been entirely within the Orinda Formation/San Pablo Group. However, only the top 35 ft (10.6 m) was composed of the Orinda Formation, with the rest being the Claremont Formation. Consequently, WF-3 was drilled further to the west so it would be, according to the geologic map, entirely within the Orinda Formation/San Pablo Group. As expected, the top 300 ft (91.44 m) of WF-3 was composed solely of sedimentary rocks of the Orinda Formation locally interbedded with coarse sediments of the San Pablo Group. A fault contact with Claremont chert and mudstones was intercepted at 320 ft (97.5 m) depth. Another fault intercepted at 495 ft (150.8 m) depth to the end of the core log suggests that the contact was with sediments of the Orinda Formation. This change in lithology indicates a complex fault system.

WF-4, an inclined borehole 693.7 ft (211.4 m) long, was drilled and cored at a middle distance between WF-2 and WF-3. The top 50 ft (15.24 m) was composed of Orinda Formation

sediment, with the rest intercepting the Claremont Formation. Although the fault could not be clearly mapped based on surface geology and geomorphology, this borehole must have intercepted the Wildcat. The rocks encountered were the most damaged of all the boreholes. Zones of core loss, brecciation, protocataclasite and gouge were encountered throughout this borehole. The main zone of deformation was encountered in the last 200 ft (60 m), with increases in core losses, deformation, and carbonate veins, as well as water losses. This evidence suggests that this zone is a major active fault zone. Borehole walls repeatedly collapsed, making the drilling operation difficult.

A new inclined borehole, WF-5, was drilled in August 2012 to intersect the fault further north and to examine the eastern side of the fault. This borehole, 678 ft (206.6 m) in length, was drilled about 120 m northwest of WF-1 along Calvin Road (Figure 4-7). The top 220 ft (67 m) of WF-5 encountered the typical siltstone and mudstone of the Orinda Formation. locally inter-fingered with conglomeratic facies, possibly a channel deposit. The contact of the Orinda Formation and the laminated cherts and mudstone of the Claremont Formation is defined by a wide zone of deformation much similar to the one described in WF3 at 480 ft (146 m). The only difference is that stratigraphy is inverted, which adds complexity to our analysis. Between 410 ft to 430 ft (125–131 m), three zones of core loss were observed. The largest core loss, a 5 ft (1.5 m) core and water loss, was encountered at 410 ft (125 m). Although the deformation around this core-loss zone is moderate compared to WF-4, it is possible that it represents one of the main faults in WF-5.

Figure 4-8 illustrates the distribution of the core logs in 2D, and Figure 4-9 the distribution in 3D. Appendix 1 summarizes the core log description for the five boreholes. Appendices 2, 3, 4, 5 and 6 include the core images for WF-1, WF-2, WF-3, WF-4 and WF-5, respectively.

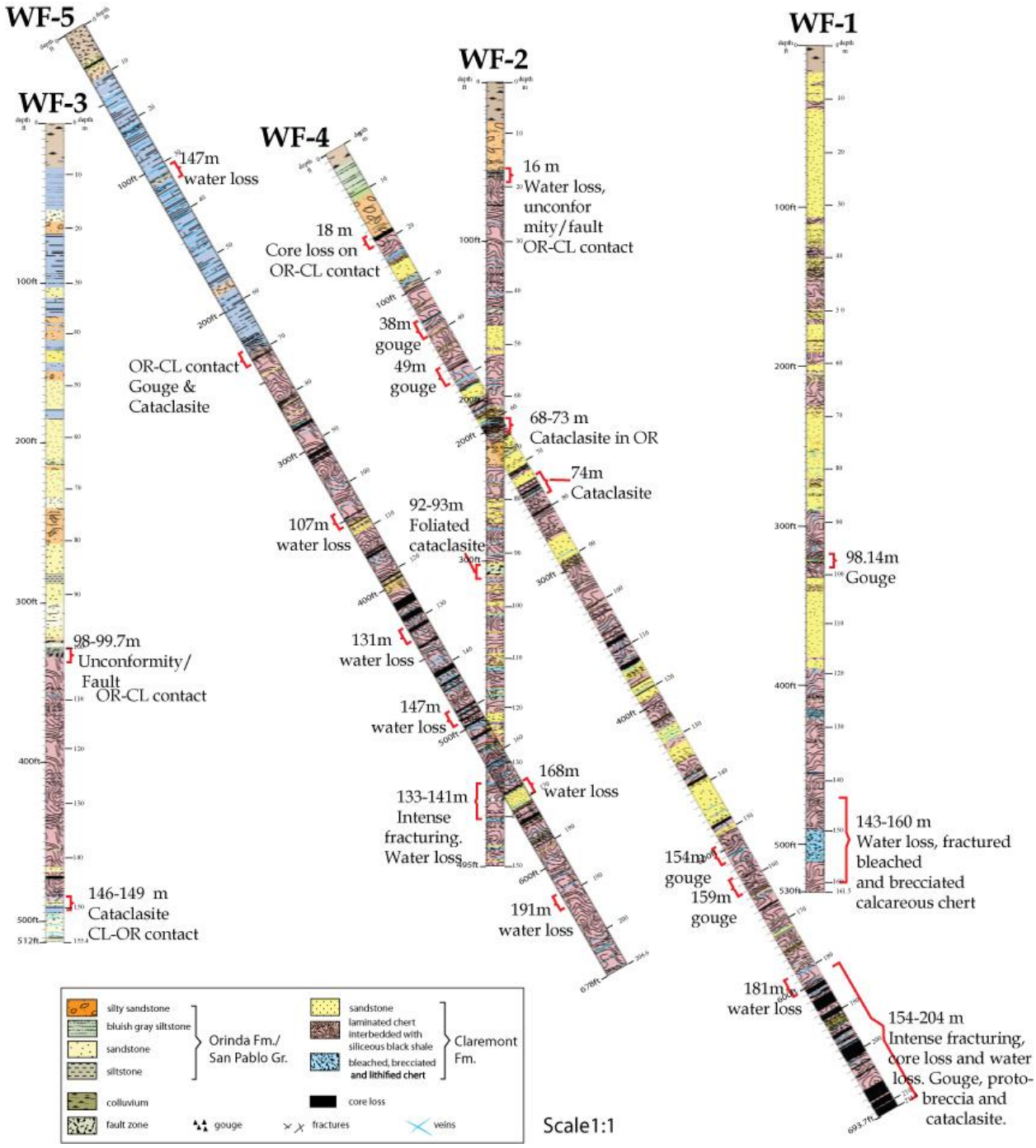

Figure 4-8. 2D view of all core logs in the study area

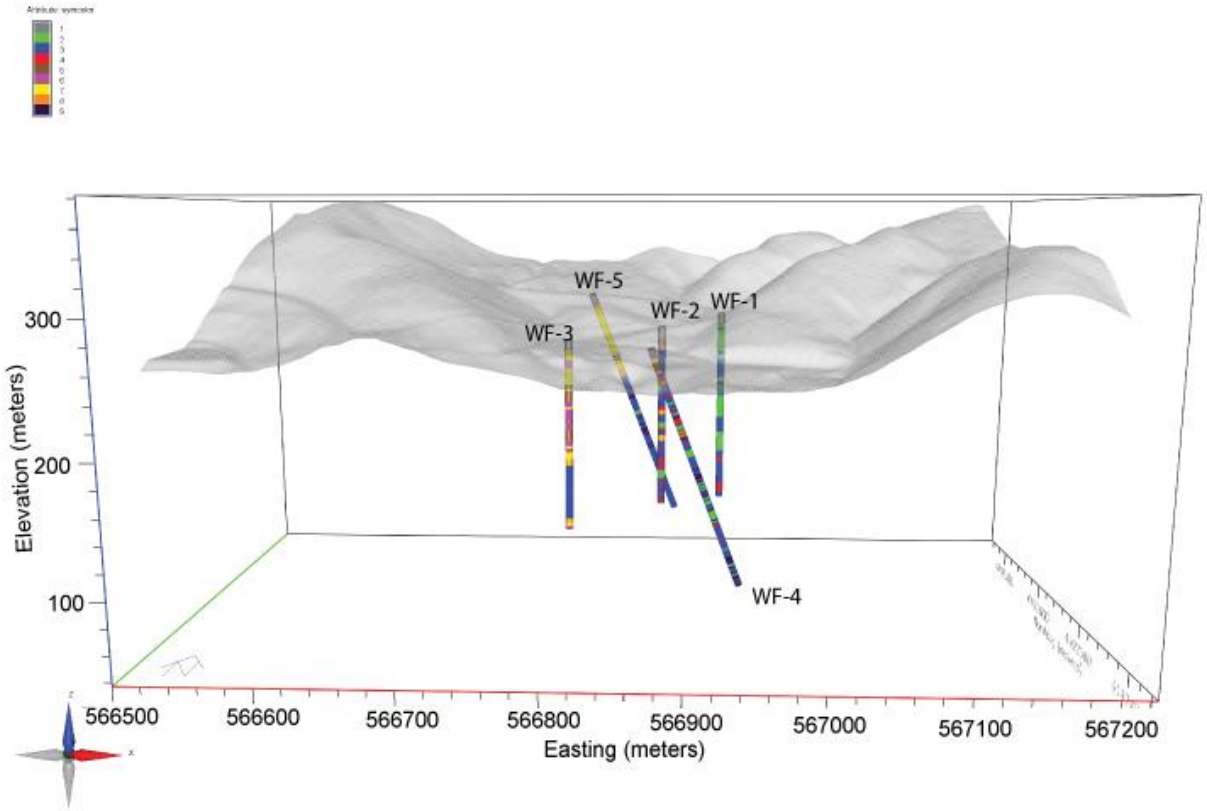

Figure 4-9. 3D view of core log distribution along Calvin Road

4.5 Claremont Formation in the Berkeley Hills

According to Graymer (2000), the Claremont chert is a combination of laminated and bedded chert, minor brown shale, and white sandstone. Chert crops out as distinct, massive to laminated, gray or brown beds as much as 10 cm thick with thin shale partings. Distinctive black, laminated chert crops out locally in the Berkeley Hills. Lawson (1914) named rocks of this unit (and coeval rocks elsewhere in and around the map area) Claremont Shale, but within the area of Assemblage I in Graymer's map, where the study area is located, including Claremont Canyon, this unit is made up much more of chert than shale.

Cherts at LBNL are described as light brown to yellow or gray and locally black silicified, thin to thick bedded to laminated, and moderately weathered. The chert is interbedded with gray to brown shale laminae and small amounts of light brown to white sandstone that

occurs as dikes, beds, and boudins. Both the cherts and sandstones are weak to strong. All lithologies are intensely to closely fractured (LBNL and Parsons, 2000; Galpin, 1994).

From borehole data elsewhere on the LBNL property, the Claremont Formation is described as:

- Laminated, hard to moderately hard, dark gray/white/yellow/black banded/laminated/silicified chert and moderated to deep weathered (Subsurface Consultants, 1994);
- Brown shale, dark brown siliceous shale, thinly bedded (HLA,1980);
- Light brown and black Claremont shale (Kleinfelder, 2001).
- Beds of chert separated by sandy to silty shale interbeds. Claremont chert derived dense sandy gravel matrix with angular to subrounded chert clasts, locally redish-brown, clay-rich weathering zone (WLA, 2008).

During field survey in the surrounding area, several exposures of the Claremont chert is found along the Fire Trail. They show the typical bedding of thin laminated siliceous chert interbedded with thin layers of dark mudstone. The thickness of the laminated chert varies from 2 to 5 cm thick. Structurally it is intensely deformed. The bedding dip varies from steep, to gentle, to almost subhorizontal. Overturned folds can also be observed in the field (Figure 4-10, . Figure 4-11, Figure 4-12 and

Figure 4-13).

Figure 4-10 (left). Steep dipping bedded chert in the eastern fence north of Calvin Road.
Figure 4-11. (right). Gentle dipping beds. Attitude: N70E/30N. Note thin layers of inter-bedded dark mudstone.

Figure 4-12. (left) Sub-horizontal bedding of Claremont chert in the Fire Trail
Figure 4-13. (right) Overturned fold of the Claremont chert near .
Figure 4-11.

The sandstone in Claremont Fm. has been described as dikes by Untermann (1935) and Graham et al. (1984, p. 1950) and is a common feature in the Claremont Formation. Unterman described the presence of sandstone dikes near the zone of disturbance associated with the WCF and observed on the west side of the fault. Those sandstone dikes occupy a variety of positions from horizontal to vertical, generally discordant to chert bedding (Unterman, 1935, p. 1950). Unterman described sandstone dikes during the Broadway Tunnel construction. In the tunnel, the dikes commonly crosscut surrounding strata, but in some instances they are sill-like, nearly parallel to beds of cherts and shales. Their sizes and shapes are variable, ranging from an inch to at least 82 ft in thickness, with some exceeding 200 ft in length. The shape varies from tabular to bizarre forms. In the Broadway Tunnel, sandstone dikes were not observed at the contact between Claremont and Orinda formations, suggesting that the dikes were formed prior to the deposition of Orinda sediments, because no clastic dikes were found in the latter (Page, 1950). Sandstone dikes were observed in trenches TR-3 and TR-5, as described in detail in Sections 4.5.1 and 4.8.1.

4.5.1 Claremont Formation – Trenches

The Claremont Formation as encountered in the trenches is described as dark-red laminated siliceous chert interbedded with dark brown mudstone, moderately to strong weathered, moderately to highly fractured. Dikes of weathered, well-sorted fine-grain sandstone were observed occupying a concordant position with respect to chert bedding in TR3. Two sandstone dikes are 10-15 cm wide. No visible planar structures were observed in the sandstone dikes (Figure 4-14).

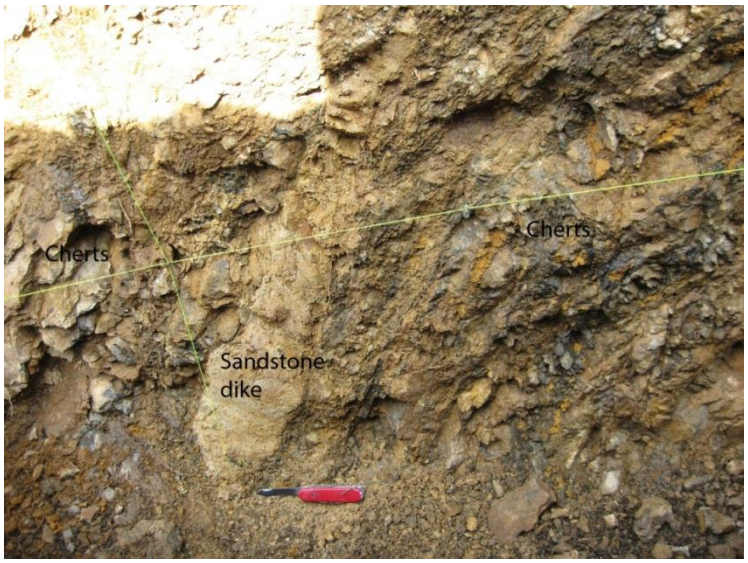

Figure 4-14. Example of intrusive sandstone dike in cherts of Claremont Formation in TR3

The main possible manifestation of the Claremont Formation in TR-2 is friable sandstone juxtaposed directly by fault with the Orinda Formation. The sandstone is weathered yellow, medium grained, and poorly sorted, with no visible structure. No cherts are observed in TR-2.

Sandstone and cherts are commonly found in TR-4 and TR-5 as described by Kiho et al. (2010). In TR-5, the sandstone dikes are narrow and white in color, friable, and found cutting through cherts and siltstones (Figure 4-15).

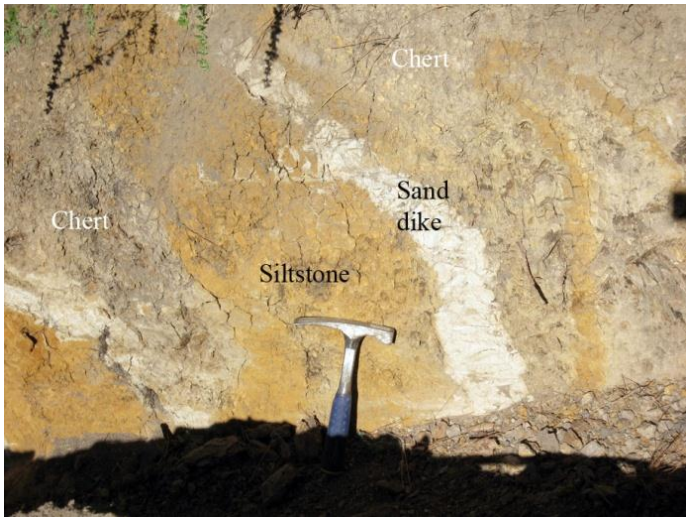

Figure 4-15. Friable white sand dike in TR5

4.5.2 Claremont Formation – Core logs

WF-1–The core log from WF-1, a vertical borehole (Karasaki et al., 2009) composed entirely of Claremont laminated chert interbedded with dark mudstone and thick layers of fine-grained gray sandstone. The sandstone makes up 35% of the core. The total length of the core is 530 ft (161.5 m). The sandstone is cored as massive and is between 15 to 20 m long. Macroscopically, sandstone does not show sedimentary texture such as sorting or grading. The grains are homogeneous and angular. Main structures observed with the naked eye are several dark seams several millimeters in length, localized brecciation, and irregular contact with black shale and chert.

Intermixing of sandstone and cherts are commonly observed between 65–170 ft (50–52 m) and 230-290 ft (70–88 m) intervals. The shale/chert fragments vary in size and shape, but they all show stretched edges, suggesting that deformation occurred before it was consolidated.

Interbedded black shale with laminated dark red chert makes up approximately 45% of WF-1. Black shale has a fissile texture and, in most open surfaces, shows a glossy surface often marked with slickensides, indicating a sheared surface. Besides slickensides, other features, such as asymmetric folds and small displacement along small shear surfaces, are observed. Several calcite veins, some with well-crystallized calcite, are observed filling fractures in the sandstone and bedded shale, as well as the chert, suggesting paleo fluid flow.

In WF-1, most of the original bedding is tilted at an angle varying from 30 degrees to subvertical. This high angle tilting suggests that drilling is directed obliquely to bedding or near parallel to the strike of bedding. Another possibility is that folding has thickened the bedding.

Localized spots of bitumen are found in planes of open fractures in the chert, suggesting localized flow paths.

WF-2—WF-2 is drilled on the western side of the trace of the WF, on the edge of Calvin Road and ~56 m west of WF-1. It is also a vertical borehole, with a total length of 496 ft (149.96 m). The site was chosen because it has been mapped as Orinda Formation by previous studies and, as defined previously, it would be on the western side of the trace of the WCF.

Surprisingly in WF-2, almost 90% of the lithology was composed of interbedded black shale and laminated cherts of the Claremont Formation. Below a 108 ft (32.9 m) depth, bedding and lamination of Claremont chert and mudstone are horizontal to subhorizontal, changing to a 45–60 degree dip. At about 146 ft (44.5 m), the dip becomes steeper and more irregular. At a 245 ft (74.67 m) depth, blocks of sandstone become incorporated into shale/cherts. Fine-grained gray sandstone is found, possibly as dikes (i.e., injected in shale/chert bedding) and/or mixed and folded with shale/chert.

Bleached and lithified siliceous breccias, white and massive, are found associated with zones rich in shale/chert. Most of them do not preserve lamination and are cut and sealed by a network of quartz veins.

A localized oil smell was noticed in two locations, at 78 ft (23.7 m) and 210 ft (64 m) depths, suggesting the possible presence of confined hydrocarbons.

WF3—WF-3 is located near the entrance of LBNL Building 85. Drilling of WF-3, a vertical borehole, started at 270.2 m above sea level. The total length of the core is 512 ft (156 m), encountering 8.38 m of colluviums along its length. Approximately 33% of the core is of Claremont Formation, found in between the Orinda on the top 100 m and the bottom 5 m of the borehole. The Claremont chert is dark red, laminated, and interbedded with dark mudstone. Bedding angles varies from 30 to 60 degrees. Sandstone is locally found at 466 ft (142 m) depth, extending for only 1 m.

WF-4—WF-4, an inclined borehole (30 degrees from vertical) located in the parking lot in front of LBNL Building 86, has a total length of 693.7 ft (211.44 m). Drilling for this borehole started at 265.1 m above sea level. The site was chosen to line up with previous boreholes, which were oriented at N53E, but WF-4 is off by 6–7 degrees with N60E orientation. (In this report, depth of core refers to the logged depth (linear length) and has not been converted to vertical depth.) The core log encountered 10.5 ft (3.2 m) of colluviums. Approximately 93% of the 211.44-meter-long core log is essentially Claremont Formation. Because it is an inclined borehole, the bedding of laminated cherts shows apparent attitudes. Sandstone is observed as a minor component in the interbedded shale and chert of the Claremont. The sandstone is cored as massive and macroscopically does not show any sedimentary texture, such as sorting or grading. The grains are fine and angular to subangular. Structures observed in the sandstone with the naked eye are several-millimetric dark seams, localized brecciation, and irregular contact with black shale and chert.

WF-5—WF-5, another inclined borehole, is located 120 m northwest from WF-1. Oriented at N46E, it is designed to extend to the fault zone found in the bottom of WF-4—since drilling further than 693.7 ft (211.4 m) in WF-4 was obstructed by wall collapses caused by crumbling fault material. The total length is 678 ft (206.65 m). As in WF-4, the depth of the core log described in this report refers to the logged depth and not vertical depth. The top 20 ft (6 m) is made up of colluviums, and over the entire length of 678 ft (206.6 m), 69% is Claremont Formation. In general, the Claremont chert is not as dark red as described in other core logs, but rather brown to light brown, laminated to massive, and interbedded with layers of dark mudstone. It almost seems that the chert has been lightly bleached. Lamination and bedding dip varies from 20–30 degrees, to 60 degrees, to subvertical.

4.5.3 General Petrography of Claremont chert and mudstone

The laminated chert interbedded with mudstone and sandstone, was microscopically analyzed to better define the mineral content. Detailed description of individual samples can be found in Karasaki et al. (2010).

Under the microscope, very fine layers of light brown to dark brown clay rich material characterize the laminated chert. Tiny grains of quartz and plagioclase can be identified, along with microfossils, mostly foraminifera (Figure 4-16). The microfossils are widespread in the Claremont chert and mudstone. These microfossils are also defining the lamination/layering.

The abundance of microfossils, which have not been described before in any previous studies, has been observed in almost all samples from this project. About 100 samples were collected from all core logs (one sample every 10 m) and given to a USGS micropaleontologist, Kristen McDougall, for analysis. (The analysis is under way but has not been completed at the time of this report.) The importance of having the microfossils characterized in the study area is that they will provide a better understanding of the lithology depositional age, depositional environment, and tectonic implications for the basin.

The mineralogy of the cherts and mudstone is not identifiable, owing to the grain size and the substantial amounts of clay minerals. For that reason, bulk XRD was conducted, in general indicating the presence of quartz, calcite and/or dolomite, plagioclase, pyrite, and clay minerals. No further analysis of clay minerals was conducted in these samples. Kiho et al. (2012) has performed XRD for clay minerals in gouges, but no conclusive results were found.

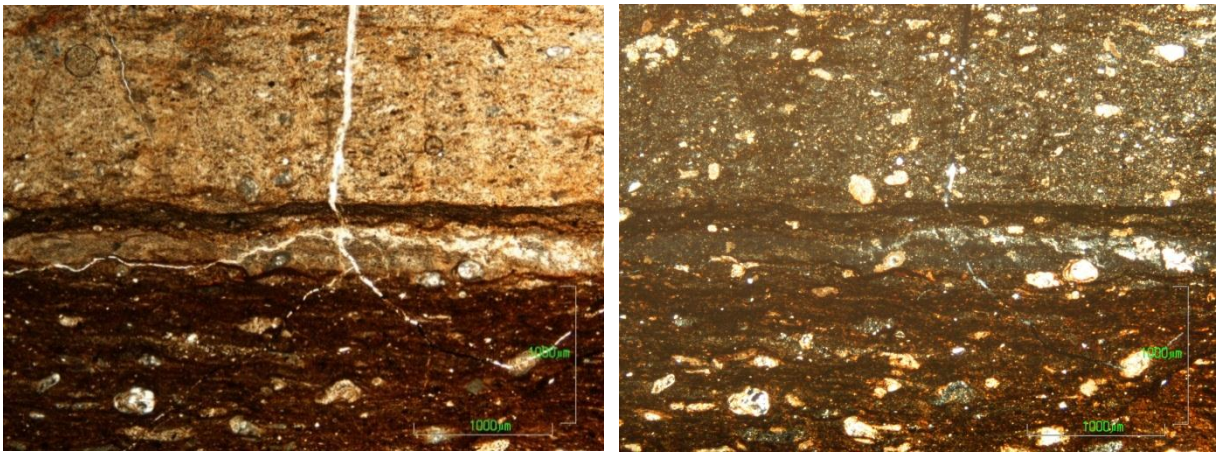

Figure 4-16. WF-1 at 130 ft (39.6 m)—Foram rich laminated chert (left—cross nicols; right—open nicols)

The siliceous layer is rich in microcrystalline quartz, as shown in Figure 4-17. The layers can be undulatory and generally defines the lamination.

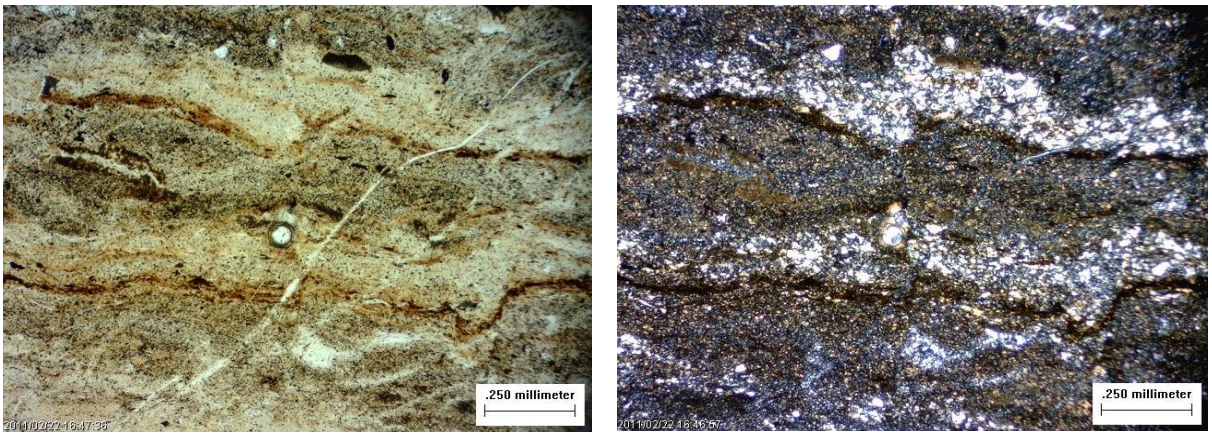

Figure 4-17. WF-2 at 297 ft (90.5 m)—Quartz and mud rich layers (left—cross nicols; right—open nicols)

4.5.4 X-ray Diffraction of Claremont chert and mudstone

Qualitative bulk x-ray diffractometry was performed in samples of Claremont chert. The result is shown in Table 4-1.

Table 4-1. Results from qualitative bulk XRD for Claremont chert and mudstone
(◎ denotes positive response)

Sample Depth (ft)	Quartz	Plagioclase	Calcite	Dolomite	Pyrite	Clay Minerals
WF-1_437	◎	◎	◎	◎	◎	◎
WF-1_321.6	◎	◎	◎	◎	–	◎
WF-3_391	◎	◎	◎	◎	◎	◎
WF-4_268	◎	◎	◎	–	◎	◎
WF-4_368	◎	◎	–	◎	–	–

4.5.5 Claremont Formation Sandstone

Sandstone is observed and described in all trenches and core logs. The amount of sandstone depends on location, but in any case it is well represented in the core logs of WF-1. As described previously, in the trenches they are found as dikes (TR-3 and TR-5) but in the core logs they are massive, light gray, fine-grained sandstone, as shown in Figure 4-18. No textural variations (grain size, gradation) are observed in this lithology; they seem very homogenous.

Figure 4-18. Massive sandstone from WF1

According to Levin (1987), there are four major types of sandstone (Figure 4-19):

- *Quartz sandstone* (also called quartz arenite)— dominated by quartz grains.
- *Arkose*—contains 25% or more feldspar with quartz.
- Graywacke—contains about 30% of dark fine-grained matrix (clay, silt, chlorite, micas) along with quartz, feldspar, and rock fragments.
- Lithic sandstone (or subgraywacke)—dominated by quartz, muscovite, chert, and rock fragments with matrix less than 15%. Feldspars are scarce.

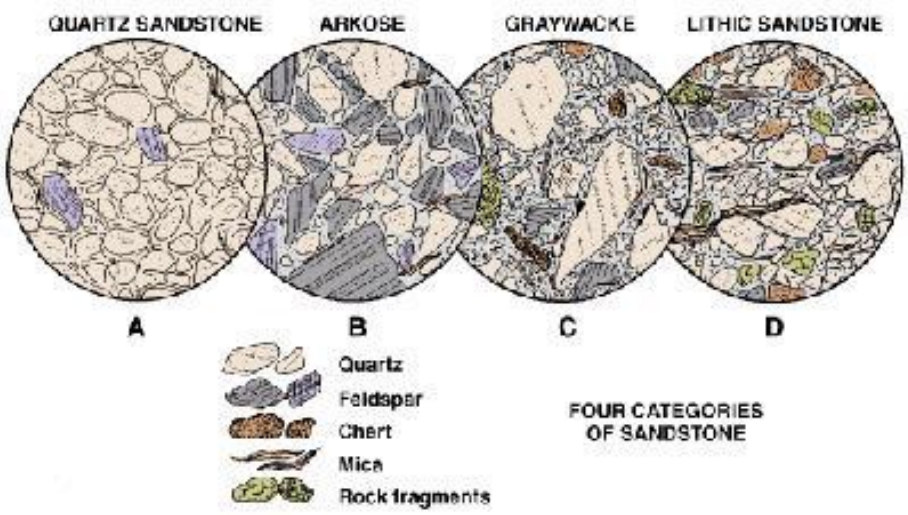

Figure 4-19. Types of sandstone

Macroscopically the sandstone of the Claremont Formation would fit in the arkose classification. However, microscopic evaluation shows a very immature type of sandstone (angular to subangular shapes), poor to moderately sorted, composed mainly by quartz, feldspars

(plagioclase, K-feldspar), opaque, lithic fragments (volcanic rocks, mudstone), white mica, zircon, and cryptocrystalline quartz. Grains of glauconite and zircon vary in amount throughout the core. Cement is usually made of very fine grains of quartz and clay minerals and/or carbonate. They are massive with no visible texture. The large amounts of feldspars and lithic or rock fragments suggest that sandstones in the Claremont Formation are indeed lithic subarkose (≥75% of quartz, ≥25% of feldspar, ≥10% of lithic materials) according to the classification of sandstone by Price (2010) (after McBride, 1963). (See Figure 4-20.)

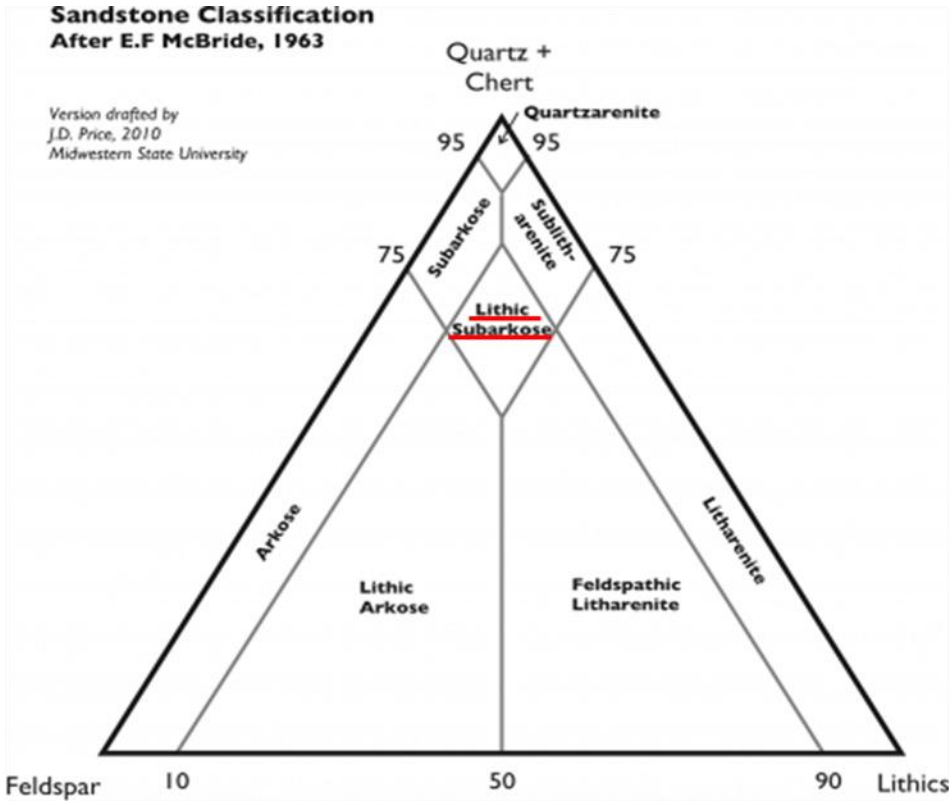

Figure 4-20. Diagram showing sandstone classification

Presenfce of glauconite indicate shallow marine environment. It is a green grain of a hydrous potassium iron alumino-silicate mineral, which forms exclusively in marine environments, usually in fairly shallow waters (Adams et al., 1984). Glauconite is found in Claremont Fm., Orinda Fm. and San Pablo Gr. samples. According to Mackenzie (2005) present-day glauconite are found in low depositional rate environment such as in the shallow water of a continental shelf at depths between 50 and 1000m (Selley, 2000). Glauconites are commonly found in the presence of phosphates (Fountain and McClellan, 2000 in Mackenzie, 2005).

4.5.6 X-Ray Diffraction of Claremont Sandstone

Examples of sandstone with glauconite are shown in

Figure 4-21; lithic fragments in Figure 4-22. Table 4-2 shows the main composition for

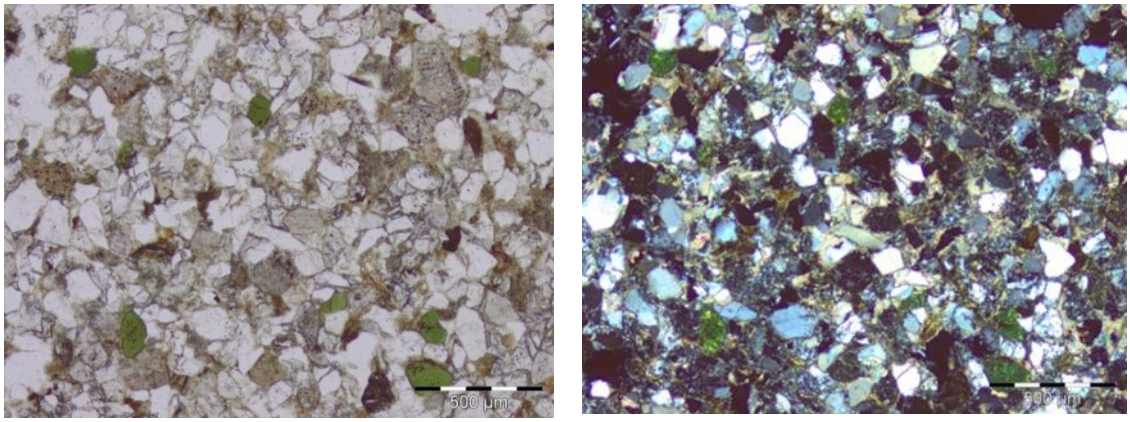

sandstone under XRD.

Figure 4-21 Example of sandstone from WF-1 at 504.7 ft (154 m). Green grains are glauconite (open and cross nicols)

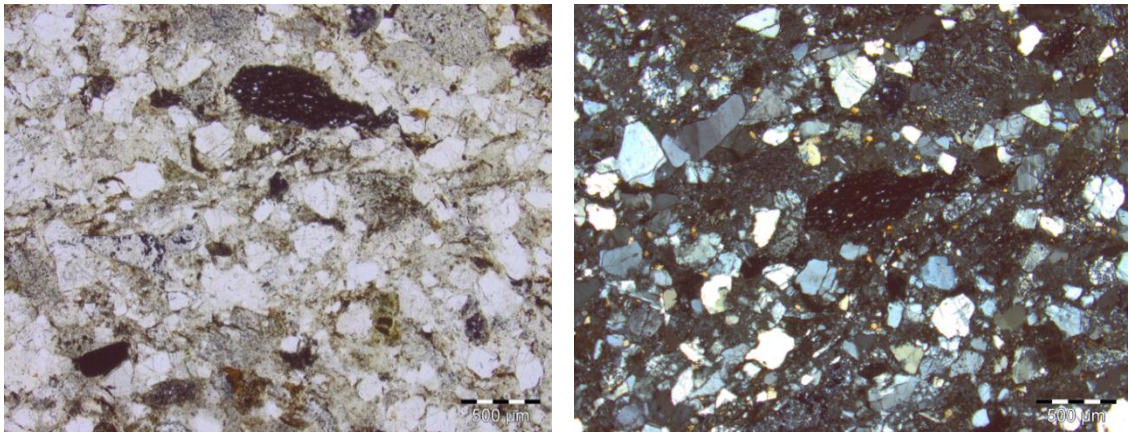

Figure 4-22 Thin section of WF-4 at 298 ft (90.8 m) showing lithic fragments in sandstone (open and cross nicols)

Table 4-2. Qualitative bulk XRD for sandstone in Claremont Fm. (◎ denotes positive)

Sample Depth (ft)	Quartz	Plagioclase	Calcite	Dolomite	Glauconite	Diopside	Clay Minerals	Mica
WF1_353	◎	◎	–	–	◎	◎	nacrite	◎
WF4_390	◎	◎	–	–	–	–	smectite	–
N4 160 Tc	◎	◎		◎				

4.5.7 Claremont bleached, brecciated, and lithified siliceous carbonate

A curious type of rock is found interbedded with the Claremont chert, mudstone, and sandstone. It is found in all five boreholes, but the thickness and number of locations are variable. Macroscopically, it is a bleached laminated chert, intensely brecciated but lithified, and cut by a network of carbonate veins. It is very hard (siliceous) and its thickness is variable. The thickest section of this material, 5 and 20 ft (1.5–6.1 m) is found in WF1 at 415–420 ft (126.5–128 m) and 491–511 ft (150–156 m) depth.

Usually the top and bottom contacts with dark laminated chert are irregular with pieces of this material floating in the dark chert or accompanied by a zone of brecciation, as observed in WF1 (Figure 4-23), or near a major fault zone, or in contact with volcanic tuff in WF-2 at 221 ft (67 m). According to Yousif Kharaka (verbal communication, 2011) a change in pH is capable of bleaching the chert. The nature and importance of this material in the Claremont Formation is secondary; as a consequence, no further studies were made on this material.

Figure 4-23. Example of bleached material from WF1 at 498 ft.

When viewed microscopically, the rock is found to be made of two types of carbonate, one fine grained and laminated, the other more granular. They are both cut by a network of well-crystallized quartz veins (Figure 4-24) and have substantial amounts of microfossils (Figure 4-25).

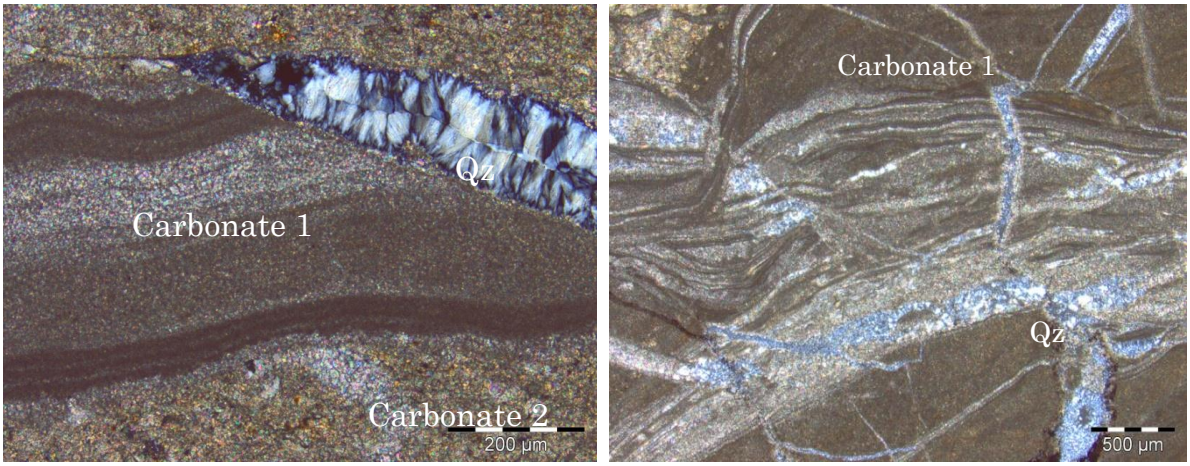

Figure 4-24. View under microscope shows two types of carbonate cut by quartz veins. (both cross nicols)

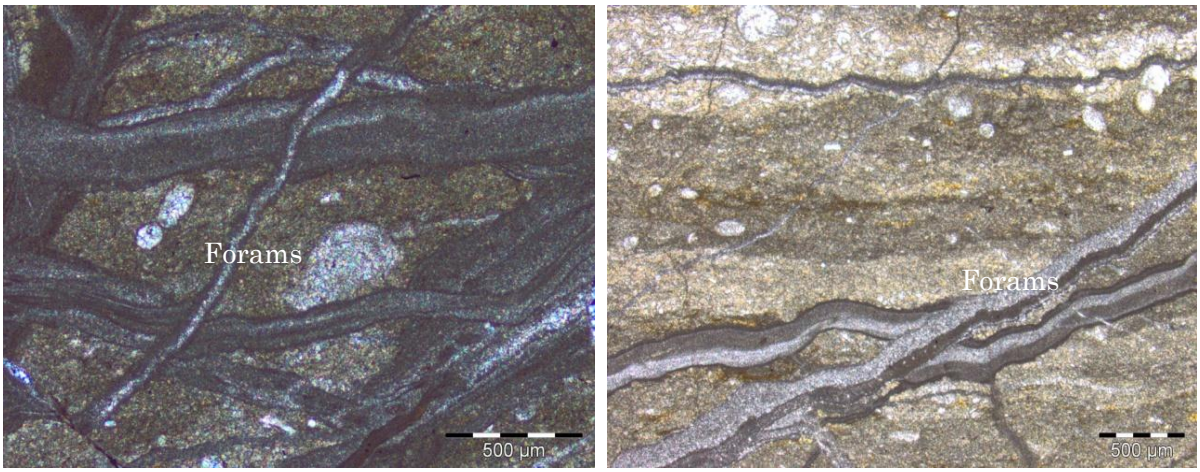

Figure 4-25. Presence of forams in the bleached material (both cross nicols)

4.5.8 XRD patterns in the Claremont Formation

Diatoms, radioloaria, and other siliceous organisms precipitate silica from seawater as amorphous opal (opal-A). After deposition, silica progress from opal-A towards quartz, the stable phase, through an intermediate phase, opal-CT. Empirical evidence suggests sthat each transition occurs through dissolution and reprecipitation (Murata and Randall, 1975, Pisciotto,

1981, Rimstidt and Barners, 1980) in Chaika, 1998. This type of silica progress is typical in the Monterey Group due to progression of lithologic and mineralogic changes related to burial diagenesis and thermal alteration as shown in Figure 4-26.

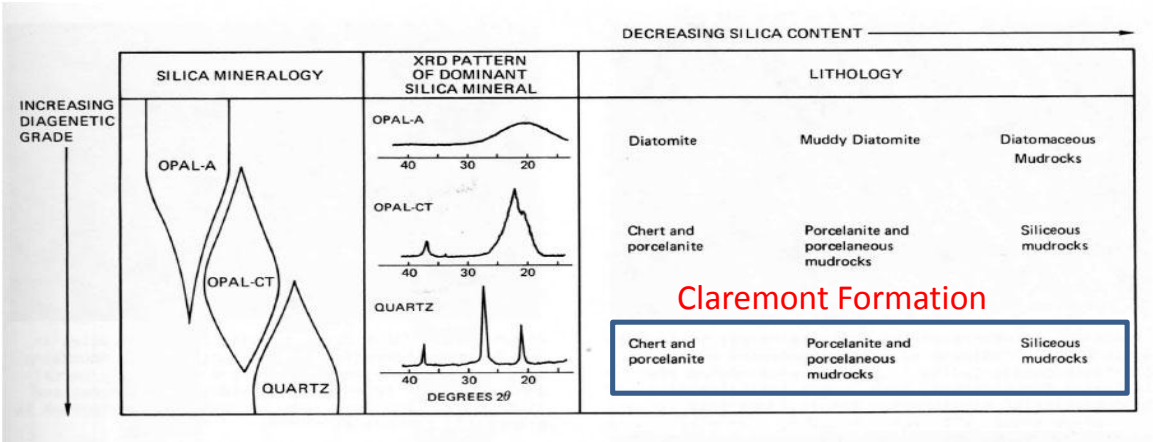

Figure 4-26. XRD patterns for the Monterey Group by Pisciotto and Garisson, 1981.

Although Claremont Formation is part of the Monterey Group, the age of sediment and basin formation differs from the other Monterey Group basins found in the southern and central coast of California. One main difference is in the XRD patterns for the siliceous rocks. As shown in Figure 4-27, Figure 4-28, Figure 4-29, Figure 4-30, and Figure 4-31 all the silica from the XRD pattern is composed of quartz, not preserving the other early diagenetic features, such as opal-A or opal-Ct.

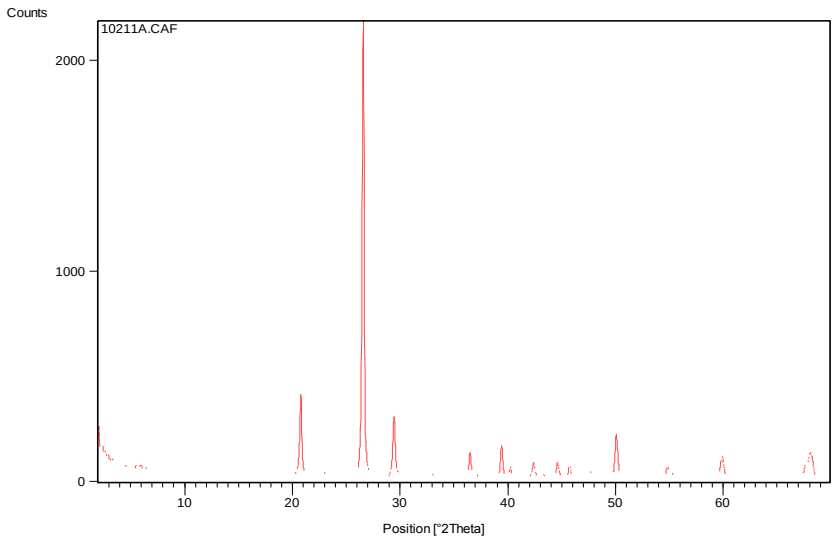

Figure 4-27. XRD pattern for WF-1 at 437 ft (133.2 m) depth

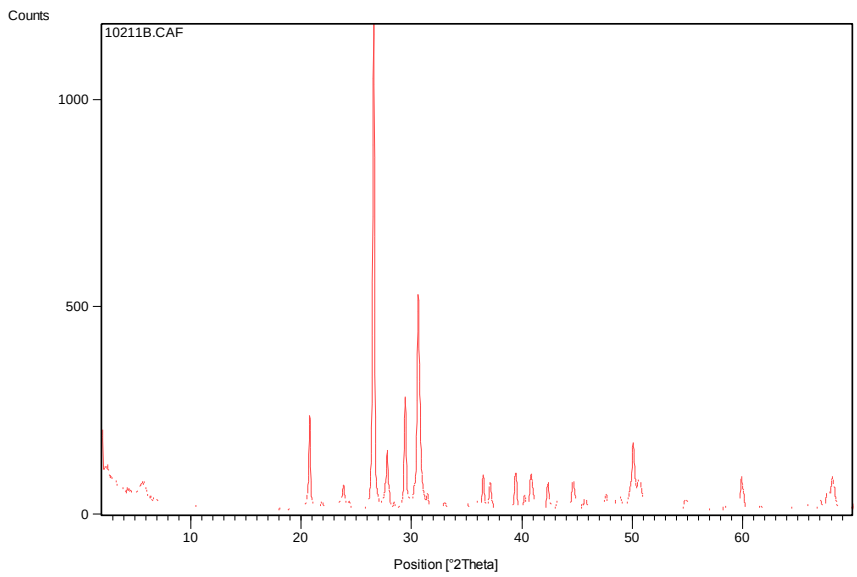

Figure 4-28. XRD pattern for WF-1 at 321.6 ft (98 m) depth

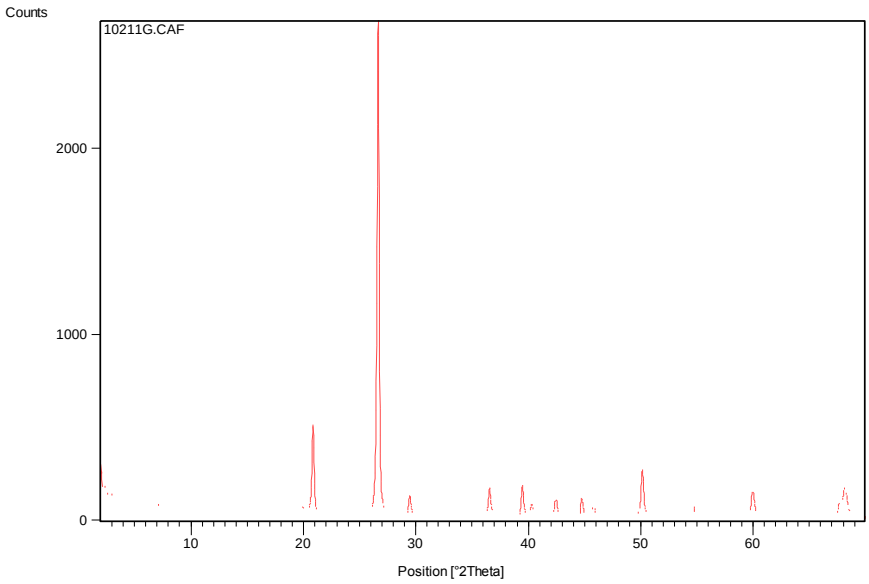

Figure 4-29. XRD pattern for WF-3 at 391 ft (119 m)

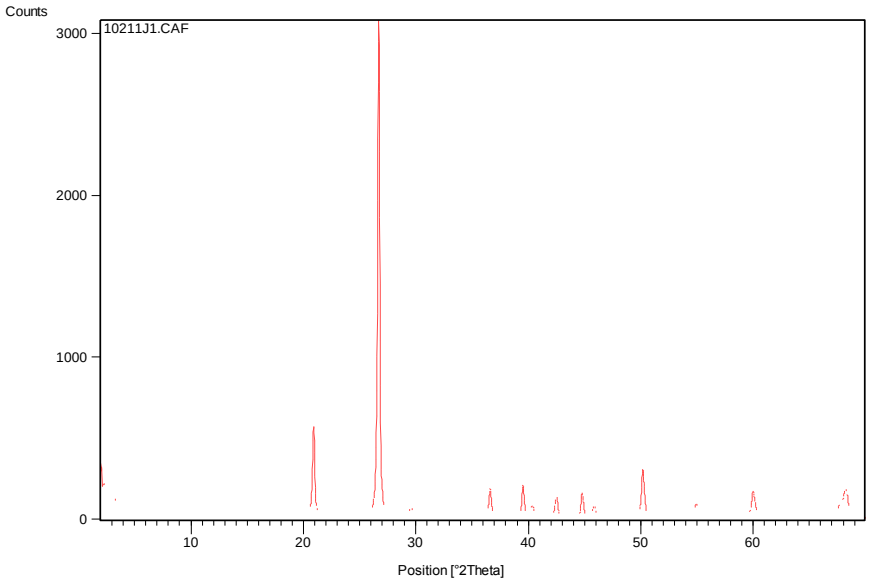

Figure 4-30. XRD pattern for WF-4 at 268 ft (82 m) depth

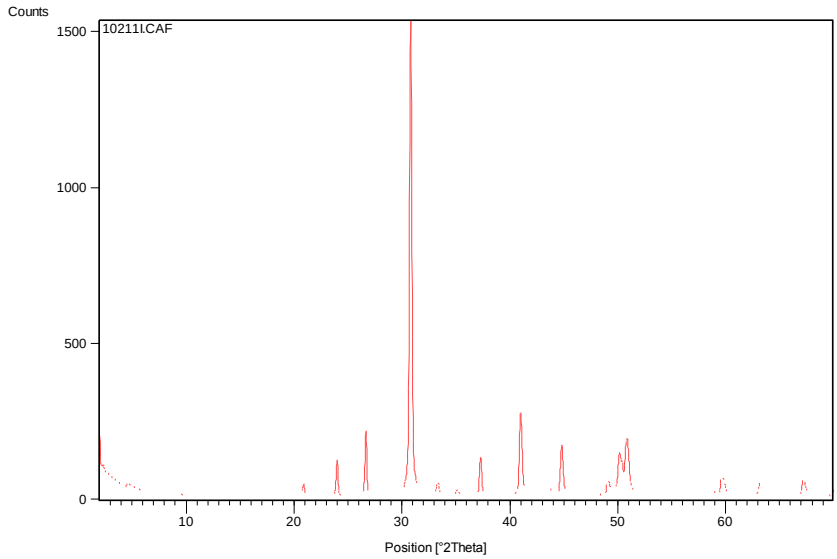

Figure 4-31. XRD pattern for WF-4 at 368 ft (112 m) depth

4.6 Orinda Formation in the Berkeley Hills

According to Graymer et al. (2000), the Orinda Formation consists of distinctly to indistinctly bedded nonmarine, pebble to boulder conglomerate, conglomeratic sandstone, coarse- to medium-grained lithic sandstone, and green and red siltstone and mudstone. Conglomerate clasts are subangular to well rounded and contain a high percentage of detritus derived from the Franciscan complex (Figure 4-32).

The Orinda Formation within LBNL is described as mudstone, siltstone and fine- to medium-grained sandstones, ranging in color from blue to greenish-gray to reddish-brown, and intensely-to-mildly fractured, friable, and little-to-moderately weathered (LBNL and Parsons, 2000), as shown in Figure 4-33.

Doell (1930) describes the Orinda Formation in the Berkeley Hills as composed of fine to coarse well-rounded conglomerate, sand, and sandy clay. All those units vary greatly in color and degree of sorting. The Orinda Formation, as indicated by borehole data from geotechnical reports and previous trenches in the LBNL property, includes:

- Mottled brown claystone to mottled yellow/orange brown and light gray-brown silty and pebbly sandstone (Subsurface Consultants, 1994);

- Yellowish-brown to gray shale, gray-green sandy siltstone, red-brown claystone to siltstone, gray-green siltstone, mottled yellow-brown sandstone, mottled red-brown and green claystone, gray fine sandstone to blue-gray silty sandstone (HLA, 1977, 1980);
- Gray to green-gray fine grained siltsone, red-brown to purple-brown siltstone, gray sandstone interbedded with siltstone and shale, red-brown silty clay, purple-gray siltstone-claystone (Converse Consultants, 1983);
- Dark gray to light gray-brown siltstone, mottled light blue and gray clay-sand-gravel, gray-brown clayey sandy gravel, green silty sandstone (Kleinfelder, 2001),
- Blue-gray sandstone, gray-brown siltstone to sandy siltstone (Geo/Resources Consultants, 1994).
- Massive with fine-grained sand and stringers of clay and silt (AKA, 2008 in WLA, 2008)
- Mottled grayish green to dark reddish brown, fine grained silty sand (WLA, 2008)

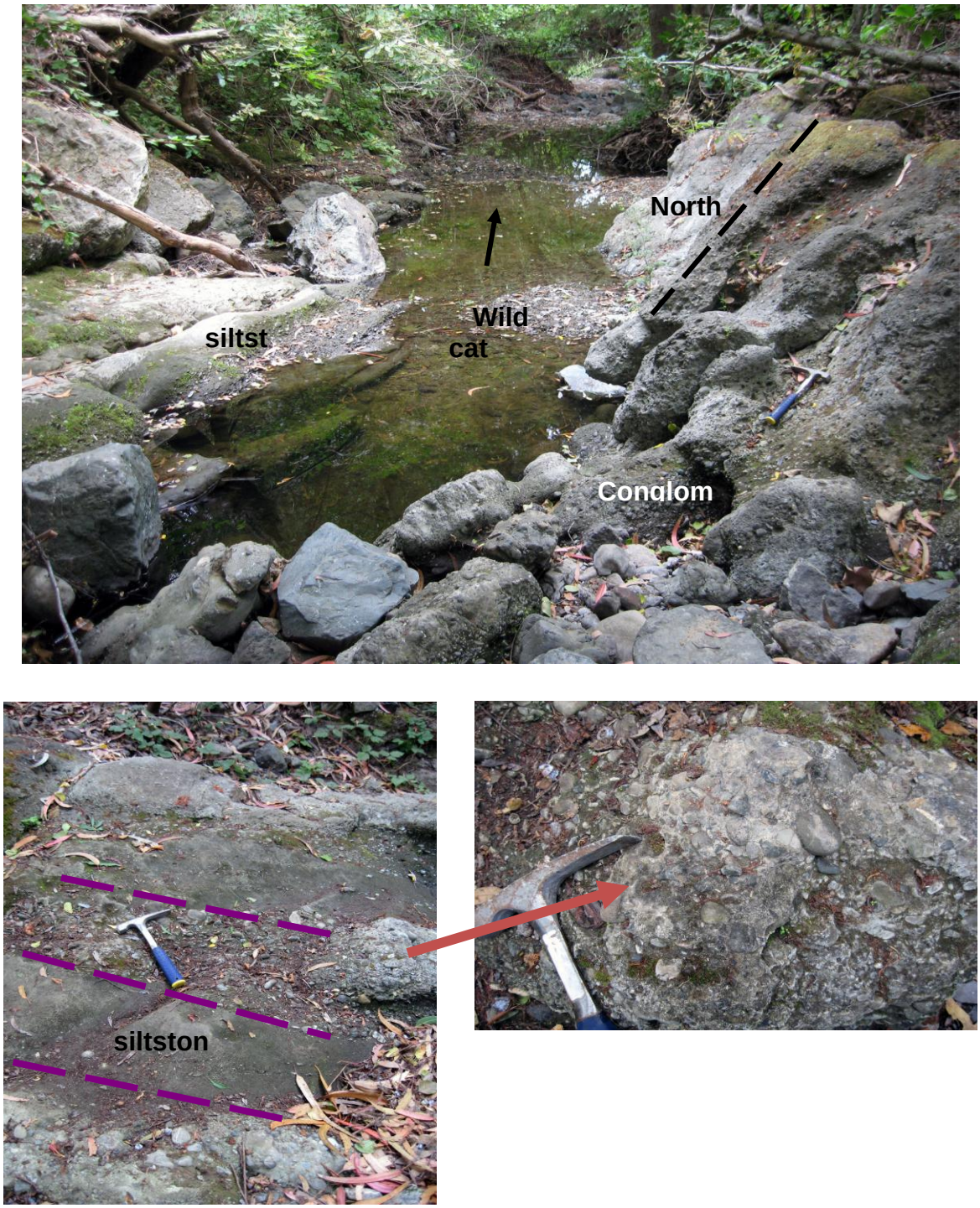

Figure 4-32. Outcrop of interbedded conglomerate and siltstone next to the cross road between the Fire Trail and Rifle Range road north of Jewel Lake in Tilden Regional Park. There was no evidence of the fault in the creek.

Figure 4-33. Intercalation of greenish fine sandstone and reddish clay-rich sediments—Orinda Formation in the Fire Trail.

4.6.1 Orinda Formation – Trenches

The mottled fine-grained sandstone, siltstone, and dark red mudstone of the Orinda Formation are found in TR2, TR3, TR4 and TR5. It was well defined in the TR2, where most of the trench encountered the Orinda Formation as shown in Figure 4-34. In TR3, siltstone and mudstone is found in the western side of the fault. They are weathered, and only small portion of the trench encountered the mottled dark mudstone with siltstone. Orinda Formation evidence as found within TR4 and TR5 is described in Kiho et al. (2010).

Figure 4-34. The typical mottled green sandy to siltstone and dark mudstone in TR2

4.6.2 Orinda Formation – Core logs

WF-1—No rocks of Orinda Fm and/or San Pablo Group are found in the WF1 core log.

WF-2—The greenish-gray fine-grained sandstone to siltstone in WF-2 appears below the colluvium at 25 ft (7.62 m). It is approximately 8 m long and the bedding is near horizontal. It shows evidence of bioturbation and has fragments of fossils in the bedding planes.

WF-3—Approximately 60% of the core is of sedimentary rocks from the Orinda Formation and San Pablo Group The rocks are mainly fine to coarse sandstone locally rich in fragments of marine fossils and interbedded with zone of mottled siltstone and mudstone (Figure 4-35). Zones of coarse sandstone to conglomerate are found at 53–68 ft (16–21 m), 133–150 ft (40.5–46 m), 155–160 ft (47–49 m), 171 ft (52 m), 172 ft (52.4 m) and 210–213 ft (64–65 m). The conglomerate rich in marine shells of the San Pablo Group are specifically found at 242–266 ft (74–81 m) and 321–322 ft (97.8–98.1 m).

Figure 4-35. Typical greenish-gray silty to sandstone mottled with dark red mudstone—WF-3 at 182 ft (55.5 m)

WF-4—The Orinda Formation appears in WF-4 only within the top 50 ft (15.2 m) and below 10.5 ft (3.2 m) of colluvium. It is a greenish gray fine-grained sandstone to siltstone occasionally mottled with dark red mudstone.

WF-5—About 30% of WF-5 is made of the Orinda Formation. It is distributed in the top 220 ft (67 m) and consists of about five zones of mottled red mudstone and bluish-green siltstone transitioning to a clean silt-sandstone and at some locations to conglomerate. This may suggest episodes of sedimentation, with fine-grained material being deposited in the bottom of the basin followed by silt, sand, and conglomerate.

4.6.3 Petrography of Orinda Formation

Sandstone from the Orinda Formation at macroscale is less cohesive than the sandstone from the Claremont Formation. It has finer grain size, has a silty component, and is green in color. The greenish color likely results from green minerals such as chlorite and glauconite. According to Graymer (2011) (via e-mail) the sandstone is commonly lithic, with Franciscan detritus being common and mica absent. Under the microscope, the sample from WF-3 at 497 ft (151 m) depth (Figure 4-36, Figure 4-37) shows very similar composition to the Claremont Formation. It is fine grained and composed of poorly sorted angular to subangular grains of quartz, feldspars, lithic fragments, mica, biotite, pyrite, clay minerals, glauconite (Figure 4-38) and possible serpentine (as part of the Franciscan Group). There are also abundant microfossils in the Orinda Formation rocks, as shown in Figure 4-39 and Figure 4-40. The bulk XRD analysis in Table 4-3 of this sample also indicates the presence of quartz, albite, lizardite, and ankerite.

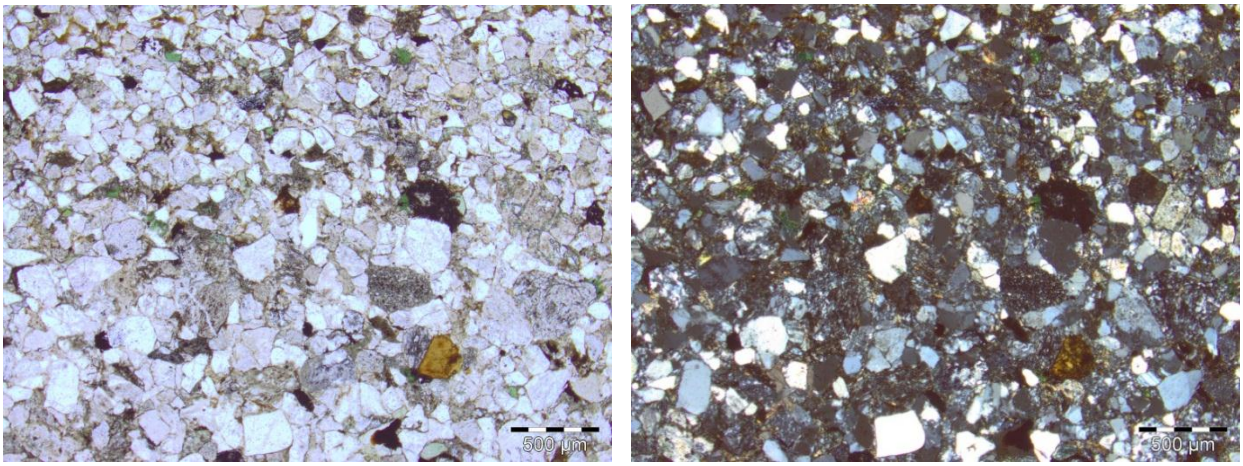

Figure 4-36. Contact of fine and medium coarse sandstone. WF-3 at 497 ft (151 m) depth, open and cross nicols.

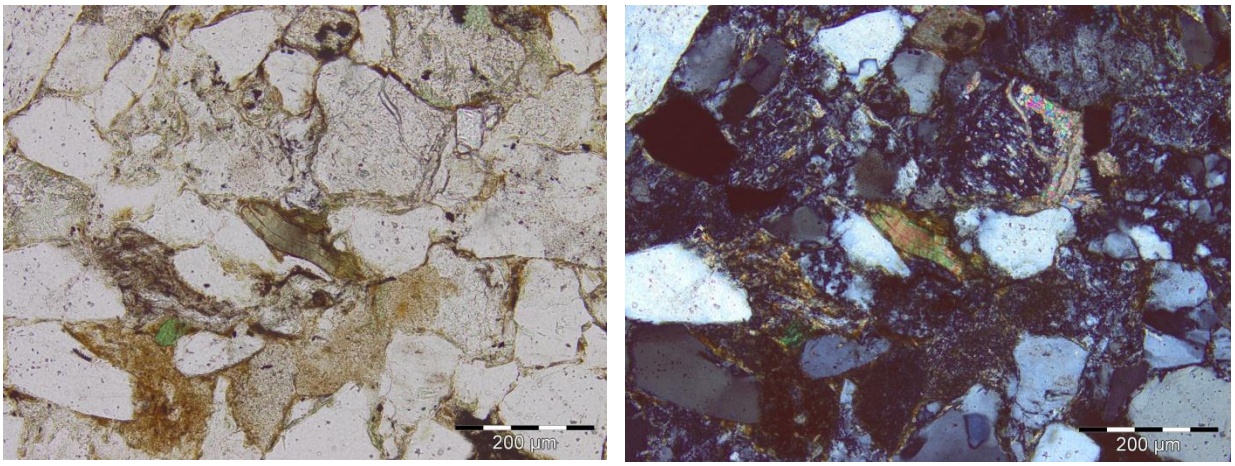

Figure 4-37. Presence of white mica (muscovite) WF-3 at 497 ft (151 m) depth, open and cross nicols.

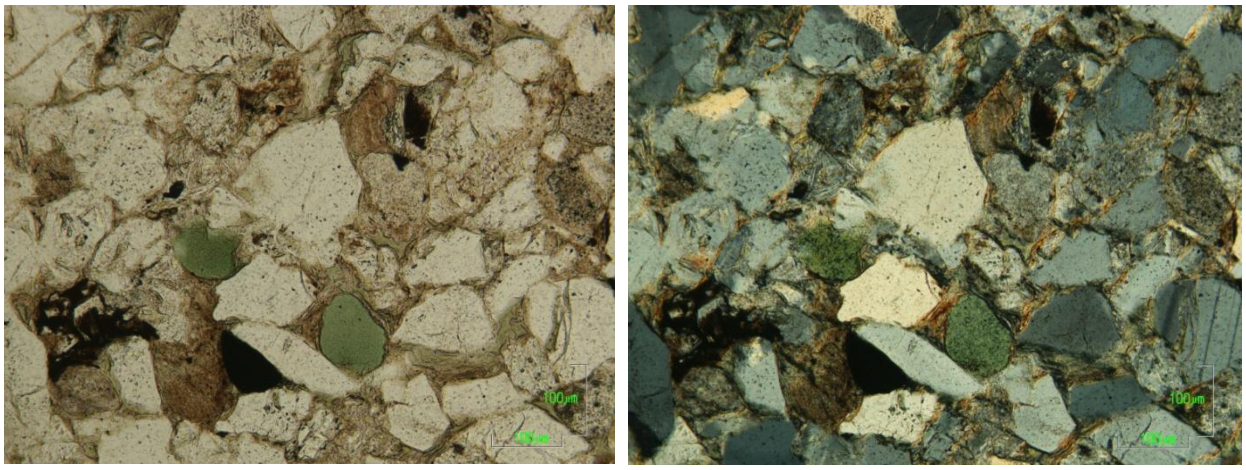

Figure 4-38. Presence of glauconite in WF-3 at 506 ft (154 m) depth, open and cross nicols

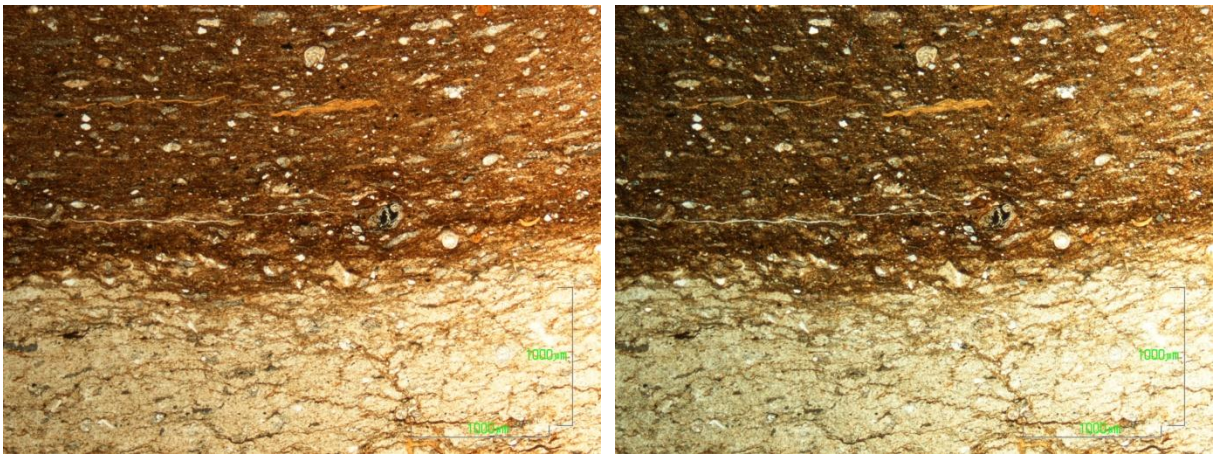

Figure 4-39. Orinda mudstone WF-3 at 216 ft (66 m) depth, open and cross nicols

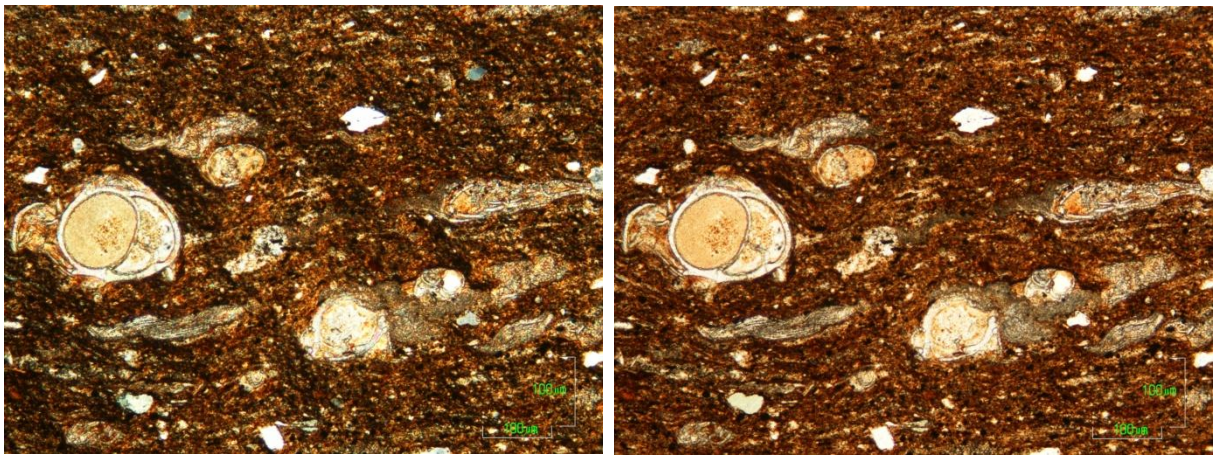

Figure 4-40. Microfossils are abundant in the Orinda Formation (open and cross nicols)

4.6.4 X-Ray Diffraction of Orinda Formation

Table 4-3. Mineral composition of Orinda Formation. ◎ indicates positive.

Sample Depth (ft)	Quartz	Plagio-clase	Calcite	Dolomite	Pyrite	Serpentine	Ankerite	Clay Minerals	Mica
WF3_497	◎	◎	–	–	–	Lizardite ?	◎	–	–

4.7 San Pablo Group in the Berkeley Hills

The presence of the San Pablo Group at LBNL is not well documented, and it seems that there is not a consensus among geologists about its classification. Fossiliferous marine sandstone, which contains bivalve and plant fossils, was discovered in the eastern portion of LBNL near Building 85 (Geo/Resources Consultant, 1994), and was thought by D.L. Jones to be part of the San Pablo Group (LBNL and Parsons, 2000). However, there is still uncertainty in defining the extent of this Group within the study area. A queried San Pablo Group is used by WLA (2008) trench studies near Building 74, but J. Baldwin (personal communication, 2008) agreed that the lack of fossils makes it difficult to differentiate the sediments of the San Pablo Group from the Orinda Formation.

The findings from WF-3 indicate that within the study area, the San Pablo Group contains several fragments of shells, including intact imprint of mollusks. Paleontologist, Dr.

Charles Powell from USGS conducted a quick visual analysis of the fossils and concluded that the big shell imprint is from the Mactridae Family, while the small imprint is possibly a member of the Brachiopod Phylum (

Figure 4-41 and Figure 4-42). Dr. Powell believes that they are from a shallow marine environment. According to the literature, the age for these fossils ranges from Oligo-Miocene to Pleistocene. The only fossil report (a one-page report) for the LBNL property (by USGS. scientists Earl Brabb and Charles Powell) is from 1993. The only sample was collected from a sandstone bed just east of Building 84. The sample is described as Mollusca Bivalvia (Middle Miocene to Holocene) and Gastropoda (Early to Late Miocene).

Figure 4-41. Samples from core log showing the presence of large shells preserved in the San Pablo Group

Figure 4-42. Typical San Pablo Group core log from WF-3

Under the microscope, the coarse, immature sandstone shows large fragments of shell fossils. The fragments are mainly composed by angular to subangular grains of quartz and feldspars, lithic fragments and carbonate in matrix (Figure 4-43).

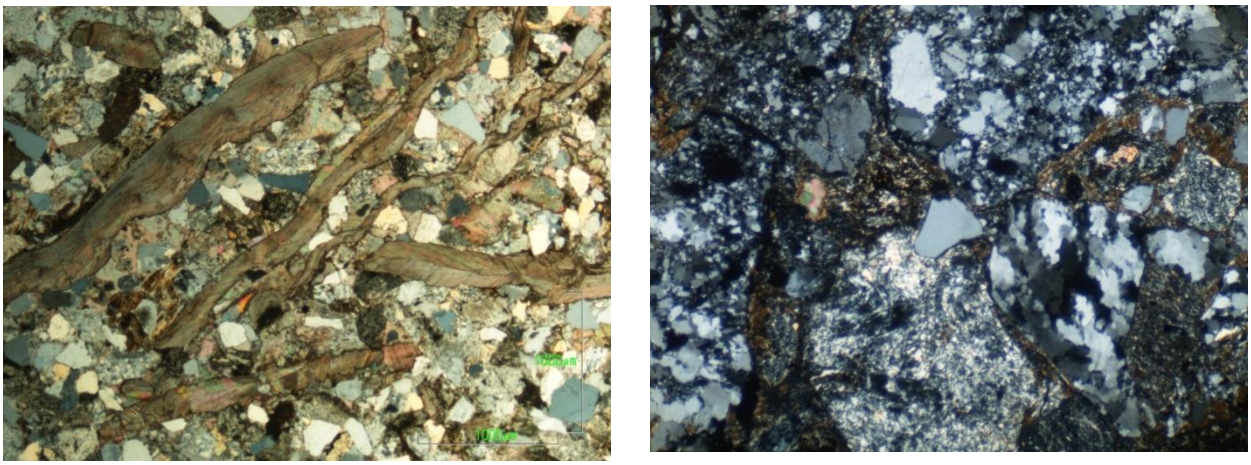

Figure 4-43. WF-3 at 262 ft (80 m) depth—Fragments of shell in coarse sandstone (both cross nicols)

4.8 Wildcat Fault (WCF) in the Berkeley Hills

Several geotechnical reports have been compiled since the middle 1970s to evaluate the geologic conditions of LBNL. The reports focus on potential geological hazards such as earthquake and landslides for construction of roads and buildings. In these geotechnical reports, the WCF has been assessed for its activity; however, no evidence of Holocene (last 11,000 years) deposit displacement in the area has been found. The study of the WCF in the LBNL is summarized below:

- Field notes by Korbay (1975), discussed in Gilpin (1994), documents a fault exposure in bedrock bench cut east of Building 84. The fault trend is N15W and dip 70NE.

- Korbay and Lewis, in HLA (1980), evaluated the WCF and cross faults north of the LBNL property line and Building 74. In Trench A, located in the northern part of LBNL property, the fault is described as consisting of several thin shears separating the green-red highly mottled clay of the Orinda sediments from sandstone of either the Sobrante or Claremont unit. It is described as two and one-half inches wide, with fine vertical striations on a plane striking N6W/vertical. Trench B normal to the cross fault was located SW of Building 74. After trenching up to 13 ft (4 m), Korbay and Lewis did not

encounter the bedrock, but rather a dark gray to black silty clay, as well as light-colored volcanic on the bottom of the trench. The investigators did not found any conclusive evidence of the cross fault in the trench.

- According to Curtis (1989), the Moraga Formation has been displaced ~6 km northwest, from a position adjacent to the volcanic center at Round Top along the WCF.

- Jones and Curtis (1991) interpret the WCF as a thrust fault associated with a fold and thrust belt attributed to left stepping on the Calaveras-Hayward fault system.

- Gilpin (1994) conducted a review of previous geotechnical investigations of the WCF and provided an independent assessment of whether the fault is active. Galpin argued that ductile deformation observed in the Orinda at the Hazardous Waste Handling Facility excavation is part of a landslide, but the review by Korbay found that the vertical fault observed during HLA trench excavation was not the result of landslide.

- Jordan (1997) observed that the excavation of Building 84 exposed the WCF. The fault separates the sandstone of the Miocene San Pablo Group from chert and shales of the Miocene Claremont Formation. The fault gouge is ~14 cm to 1.5 m. According to Jordan (personal communication), a very thin (<1 cm) dark vitreous material was observed in the fault near Building 74.

- Jones (personal communication, 2010) in LBNL and Parsons (2000) stated that the San Pablo Group exposed adjacent to the fault at LBNL may have been displaced from similar San Pablo Group rock, on the opposite side of the WCF system near Lake Chabot, 14 km to the south.

- Graymer (2000), in the regional geologic map of the East Bay, includes several traces of a fault cutting through the LBNL property. To the north, the fault traces merged near Grizzly Peak, while to the south, the faults are cut and displaced by two EW-oriented faults. According to Graymer (personal communication 2009), the main trace of the WCF is considered to be the contact between the Claremont Formation in the east and the Orinda Formation in the west. The fault eventually merges with the Hayward Fault south of LBNL, near Oakland.

- In 2008, William Lettis and Associates (WLA) (2008) logged three trenches, T1, T2 and T3, about 2 m south of the parking lot of Building 74. The trenches intersected the previously mapped locations of the WCF. In these trenches, cherts of the Claremont Formation were exposed in the eastern part, and siltstone and sandstones of the San Pablo Group were exposed in the western part. The dip of bedded chert varies from east to west, possibly due to a downslope creep process. Relict folding, S-type and chevron type, is described as affecting the bed dip. The WCF mapped in trenches T2 and T3 is described as a contact between the weathered chert and sandstone with silt and clay, grayish green to dark-reddish brown, described as belonging to the San Pablo Group. In T2, the fault strikes N50E/20E. The fault zone contains mottled clay that supports the chert-rich matrix (WLA, 2008). The same fault is observed in T3. The fault strikes N17 to N40 and dips 40–42E and is about a meter wide.

- Previous studies (i.e., HLA, 1974, 1980; WLA, 2008) indicated that the fault is not active. The site is not located within the California Special Earthquake Fault Studies Zone (formerly referred to as the Alquist-Priolo Special Studies Zone) by the California Division of Mines and Geology (1992) in Kleinfelder (2001).

- Graymer (personal communication, 2009) argued that it is possible that the WCF could have previously been a trace of the Hayward Fault and could possibly be one of the branches (having a flower structure) of the existing trace of the Hayward Fault.

4.8.1 Faults related to the WCF Zone—Trenches

TR1—Several small faults are observed near the bottom of TR1. Although it is a deep trench, most of the material is colluvium. A fault trending N64W and dipping 40E is observed near the middle of the 20 m long trench. The fault is defined as a thin layer of gouge between highly fractured and weathered cherts in the east and a zone of mixed layers of thin sandstone and siltstone in the west (Figure 4-44).

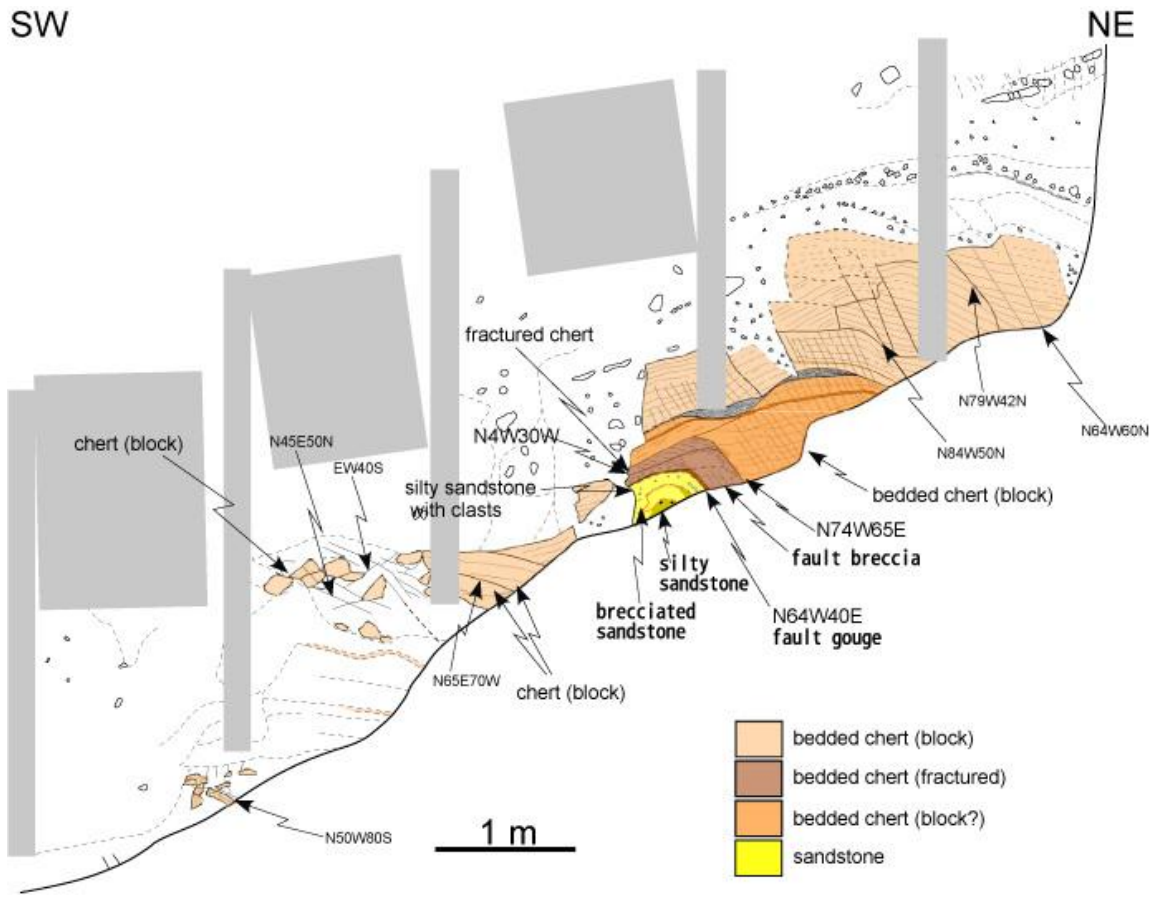

Figure 4-44. Trench log of TR1 by Kiho et al. (2009)

TR2—Two main faults are observed during trench logging (Figure 4-45). A major contact fault is mapped between light-brown medium-to-fine grained, moderately consolidated sandstone, and a mixture of dark red mudstone and gray-to-light green siltstone of the Orinda Formation. The fault is located in the eastern end of the trench, and the orientation is N19–20W dipping 37–39NE. The deformation is concentrated in the lower siltstone to mudstone of the Orinda Formation, in the plastic dark-red mudstone. The kinematic indicator includes shear bands (R and P), S-C fabric, and asymmetric features in the gray siltstone. All these indicate a right-lateral sense of shear (Figure 4-46 and Figure 4-47). The second major fault was observed in the middle of the 14 m long trench. It is oriented N19W dipping 25NE (Figure 4-48). The fault contacts the mottled dark red mudstone, bleached oxidized siltstone, and medium-grained green to gray sandstone of the Orinda Formation (Figure 4-49). A thin seam of clay gouge (about 1 cm thick) separates portions of the deformed Orinda Formation.

Figure 4-45. View to the west of trench NUMOTR2 near the north gate to the Fire Trail.

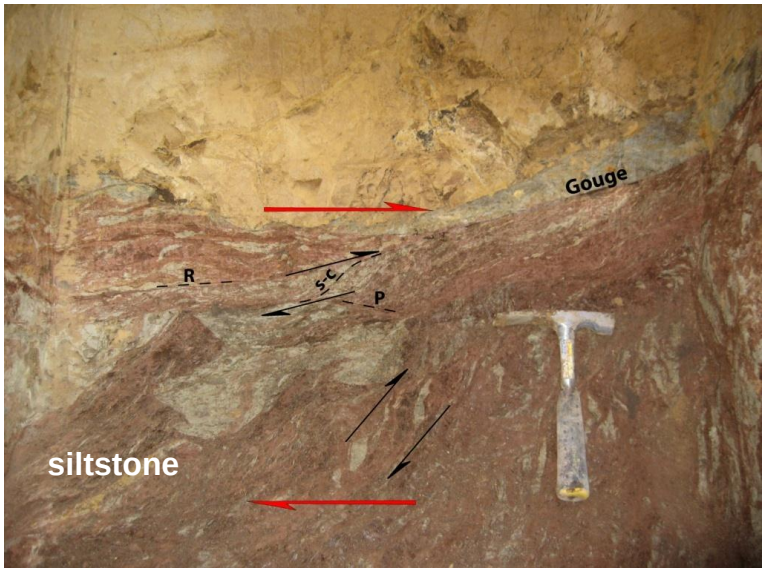

Figure 4-46. Main fault in TR2 showing main deformation concentrated in the Orinda Formation.

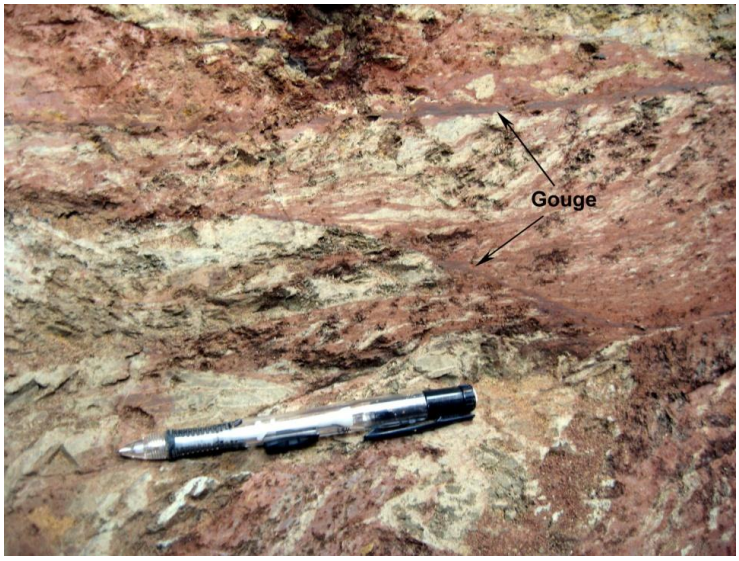

Figure 4-47. Clay gouges in the faulted Orinda Formation

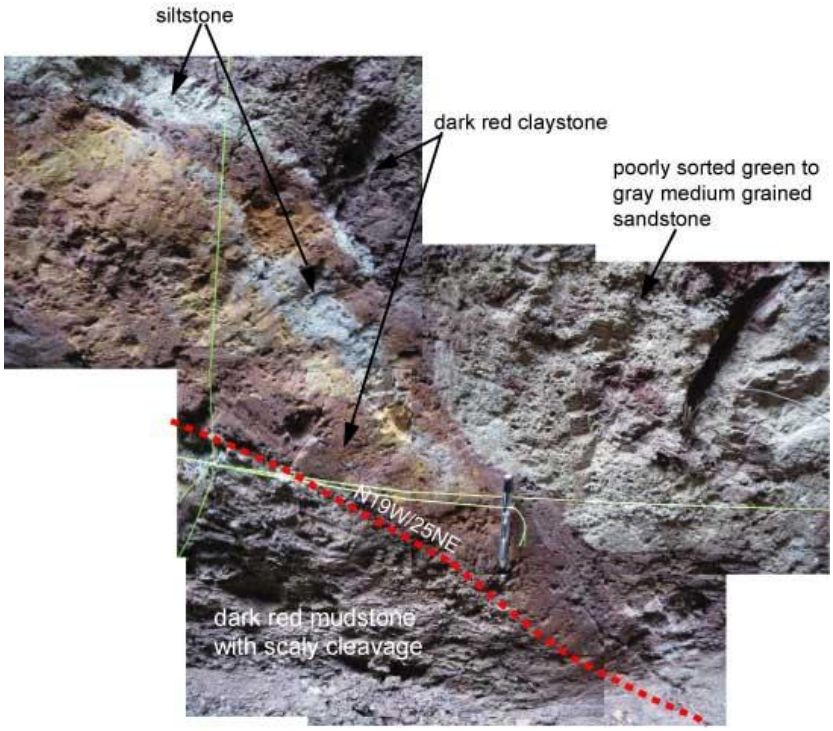

Figure 4-48. Mosaic of second fault observed in the middle of TR2.

East West

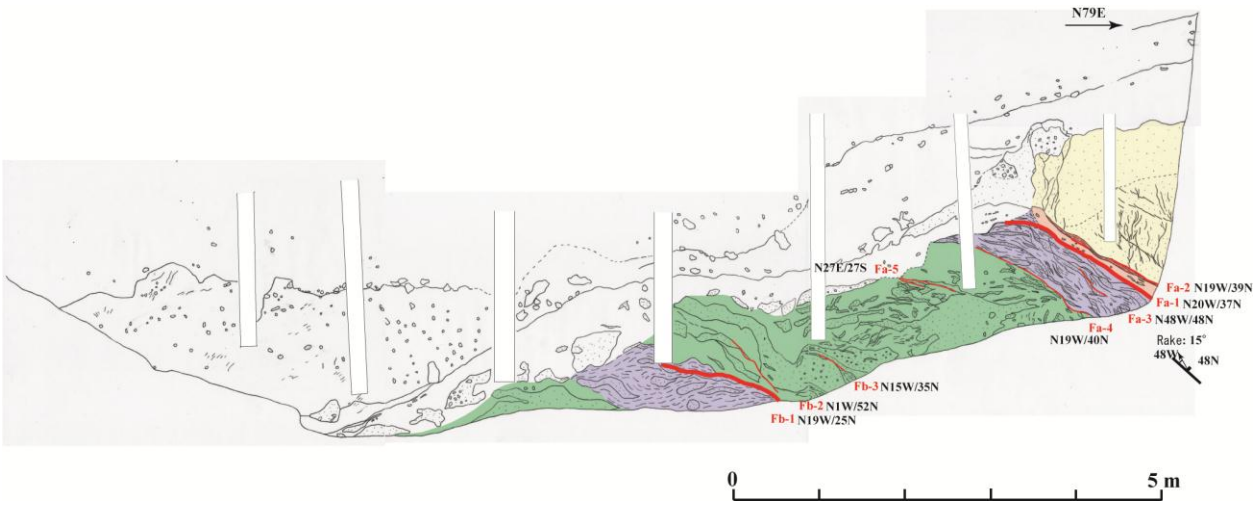

Figure 4-49. Sketch of TR2 by Kiho et al. (2009)

TR3—The fault zone is a sharp contact between light-green siltstone of the Orinda Formation in the west and cherts of the Claremont Formation in the east. At the fault contact, a 2 cm thick gouge is observed (Figure 4-50, Figure 4-51). In the gouge, angular fragments of siltstone and cherts are aligned parallel to the fault. The fault orientation is N25W and dip sub-vertically to the SW. The cherts near the fault are highly fractured. A sketch of the trench is shown in

Figure 4-52.

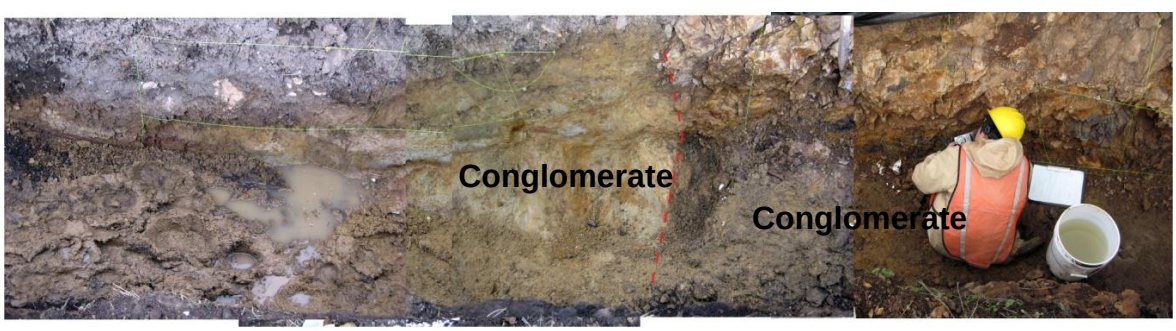

Figure 4-50. Fault contact between Orinda and Claremont formations.

Figure 4-51. Sample of fault contact by Kiho et al. (2009)

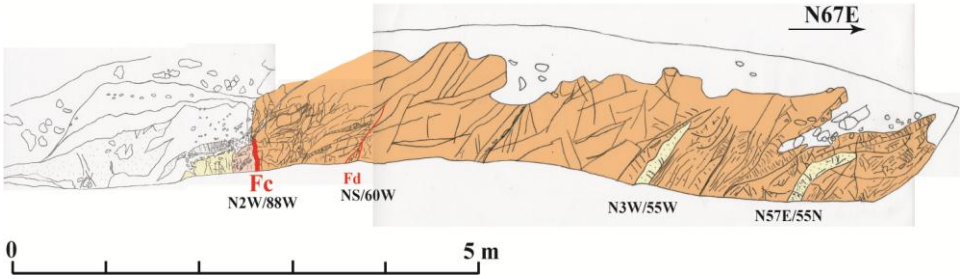

Figure 4-52. Sketch of trench TR3 by Kiho et al. (2009)

TR4—Kiho et al. (2009) conducted a field survey at TR-4 (Figure 4-53). This trench, about 60 m long and 4.5 m deep (Figure 4-54) and located along the fault contact mapped by Untermann (1935), indicates a Claremont-Claremont contact fault at this location. The top layer includes gravel debris suggesting an old landslide. An unconformity is observed with weathered Claremont Fm. Several faults were observed and described in this trench. The main contact, Orinda Formation with Claremont Formation, is described as a strike-slip fault with reverse component, 1 cm thick gouge, and fault plane oriented N45W/77SW (Kiho et al., 2009). The deformation is high in the hanging wall where fracture and joints are widespread. Several zones of sandsone are also observed in contact with the Claremont cherts.

Figure 4-53. View of TR-4 **[TR4?]** along Panoramic Road

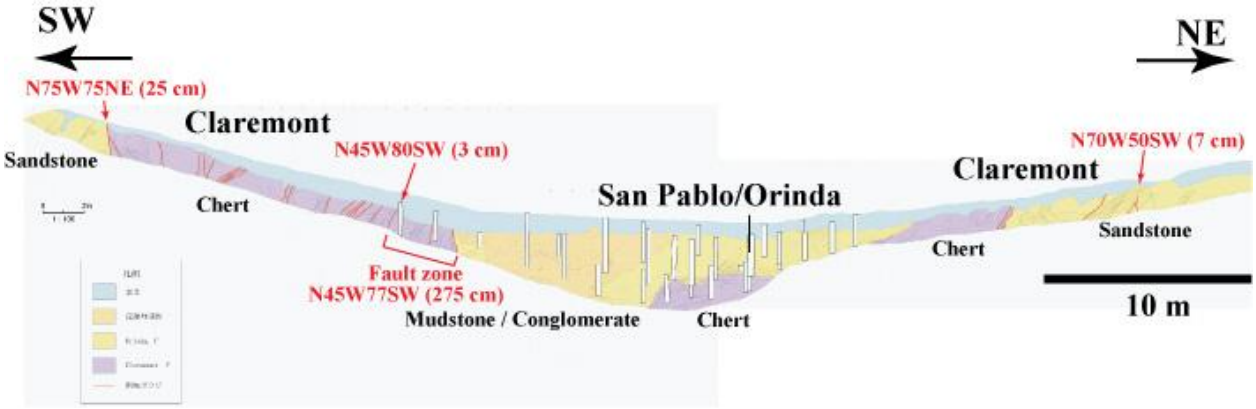

Figure 4-54. Sketch of TR-4 by Kiho et al. (2010)

TR5—Kiho et al. (2009) also conducted a field survey at TR5, west of TR4 along Panoramic Road in the Berkeley Hills (Figure 4-55). The trench is 55 m long, 1 m wide and 0.5 m deep and oriented N75E (Figure 4-56). During the survey, zones of mixture between cherts, sandstone and siltstone were observed and described. According to Karasaki (2009 personal communication), these zones would align with the orientation of the main trace of the Wildcat.

Consequently, this trench was excavated to confirm the existence of the fault. Indeed, several faults are identified as shown in Figure 4-56.

Figure 4-55. View of the shallow trench TR5

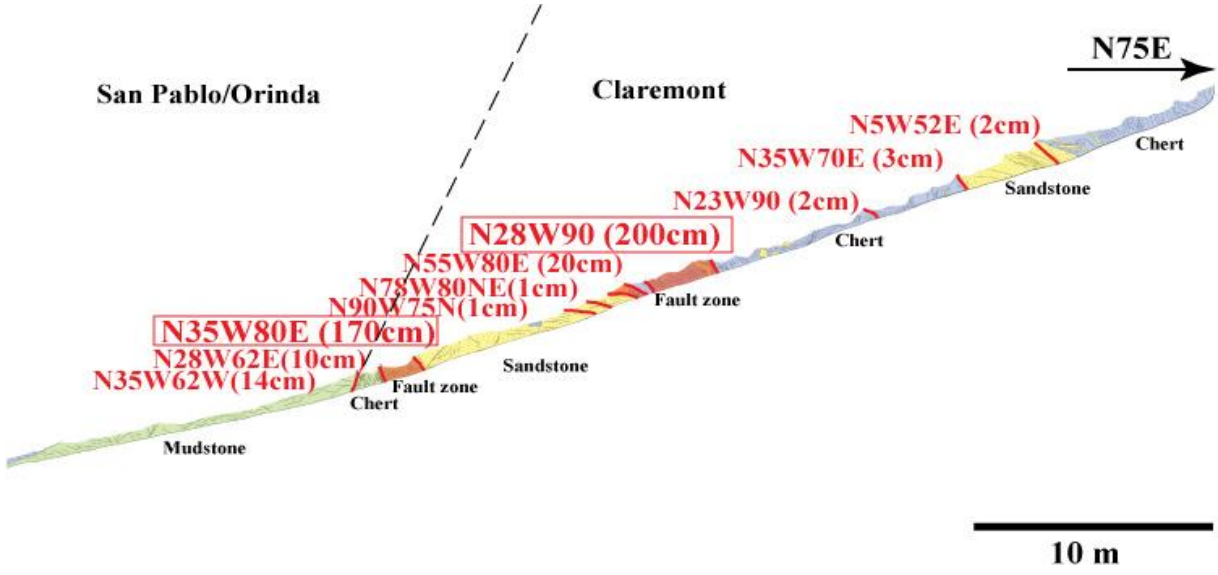

Figure 4-56. Schematic drawing of TR5

4.8.2 Faults related to the Wildcat Fault Zone – Core logs

4.8.2.1 Contact Orinda Fm/San Pablo Gr. – Claremont Fm.

WF-2—A sharp contact Orinda/San Pablo-Claremont chert is observed at 55 ft (16.76 m) depth. The Orinda/San Pablo is composed of fine-grained siltstone with some thin lamination, suggesting a sedimentary structure. It is juxtaposed to a layer of about 30 cm of dense material that resembles a coarse homogeneous conglomerate or a lithified gouge (Figure 4-57).

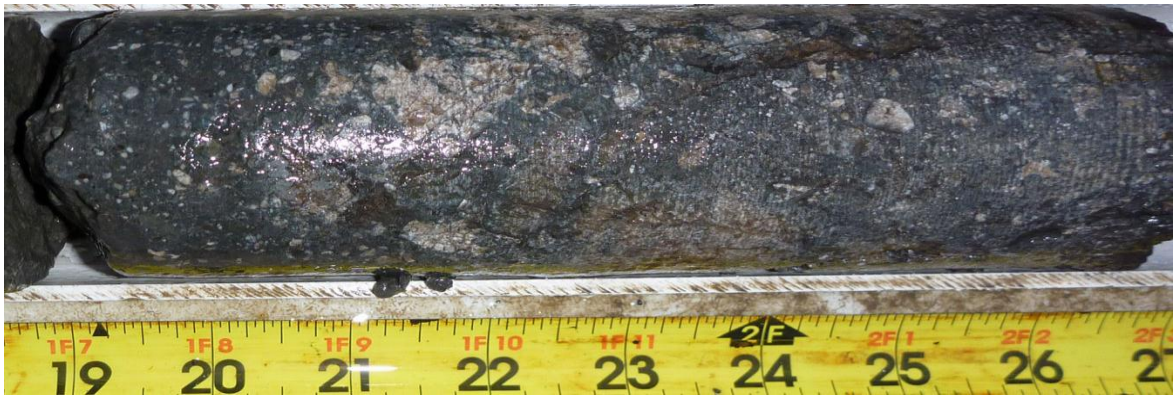

Figure 4-57. Dense material found in the contact between Orinda/San Pablo and Claremont.

Under the microscope, the contact is a brecciated conglomerate

Figure 4-58), mainly composed of round clasts of laminated chert and mudstone, both rich in microfossils. Locally, the clasts are brecciated (Figure 4-59). The cement is carbonatic, very fine, and locally lamellar. Some clasts have been previously brecciated and filled with carbonate veins. Grains of quartz, plagioclase, K-feldspar, glauconite, lithic fragments, opaque are found within the matrix. The combined features of this sample suggest that this contact is a fault or unconformity.

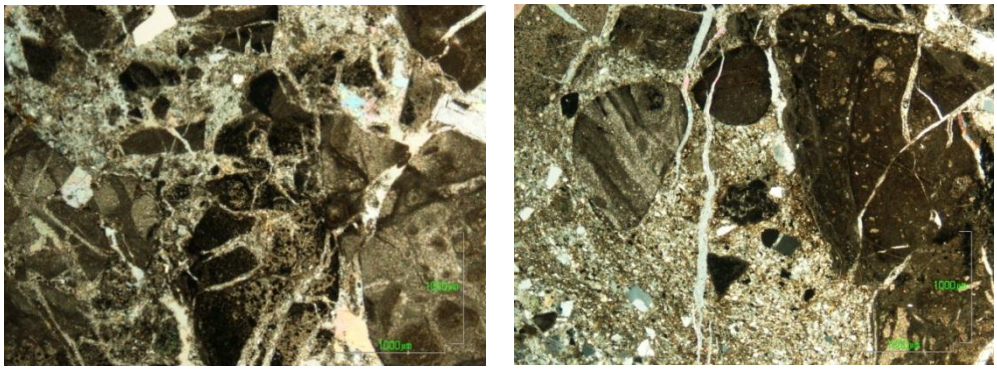

Figure 4-58. Under the microscope the clasts and matrix are intensely cut by carbonate veins (both cross nicols)

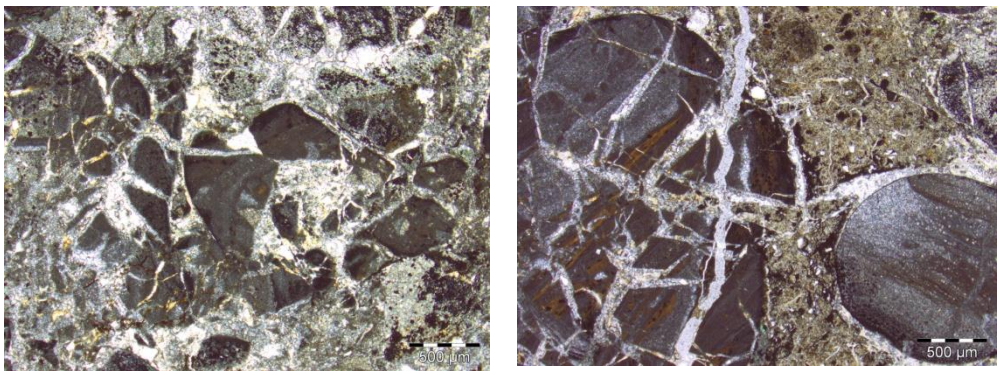

Figure 4-59. Brecciated clasts of laminated chert cut by carbonate veins (open and cross nicols)

WF-3—At 321.9 ft (98 m), a sharp contact between overlying Orinda Formation and San Pablo Group is observed in the core (Figure 4-60). Macroscopically, it is a conglomerate with clasts of laminated chert, mudstone, siltstone, carbonate material in a matrix of mudstone rich in carbonate.

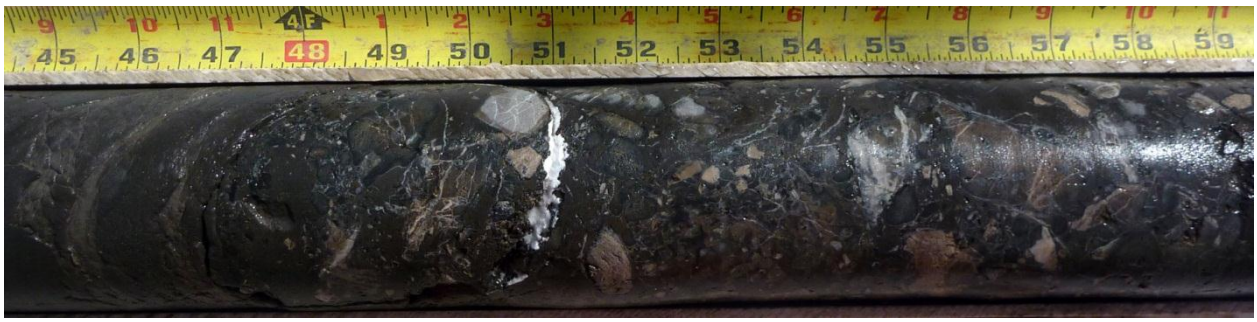

Figure 4-60. Conglomerate found in the contact between Orinda/San Pablo and Claremont.

Under the microscope, the rock resembles the sample from WF-2 where the borehole encounters Orinda Formation–Claremont Formation contact at 55 ft (16.76 m) depth. Clasts of various sizes, composed mainly by laminated chert, mudstone, lithic fragments and quartz, are cemented by a fine carbonate material. Microfossils are observed in the clasts as well a network of veins, suggesting a previous stage of fracturing. Within the cement, large fragments of oyster shells are observed (Figure 4-61), possibly suggesting a channel filling material along the fault/unconformity.

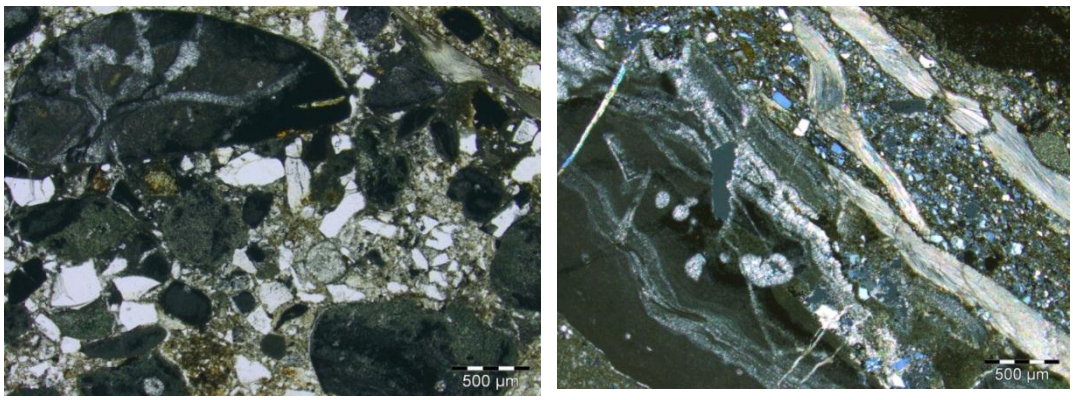

Figure 4-61. Similar clasts and matrix as described in WF2. Note the presence of fragments of shells.

WF-3—Another fault contact is observed and described at 486.5–492.2 ft (143–150 m) (Figure 4-62). Cherts of the Claremont Formation transition to mixed zone, including fragments of possibly volcanic material or siltstone, below which is gouge and a high strain zone.

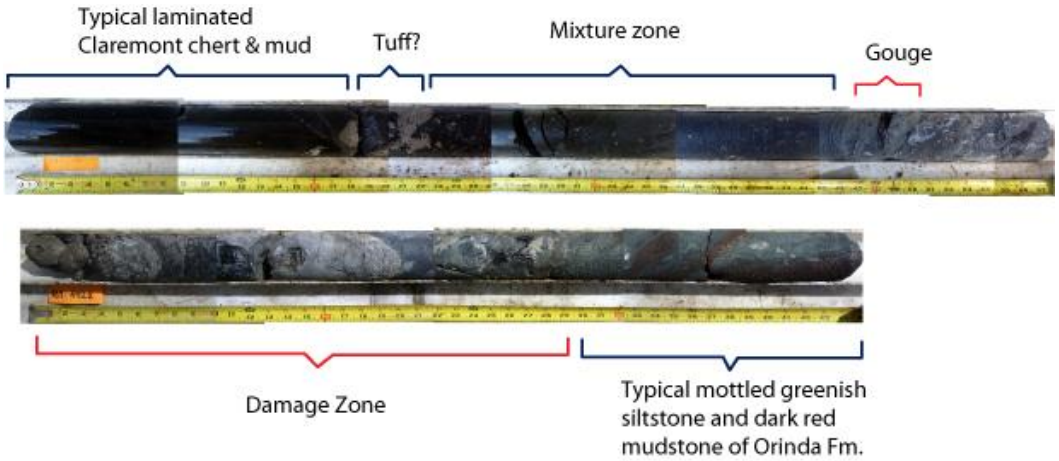

Figure 4-62. Fault zone in WF-3 showing contact between Claremont Formation and Orinda Fm.

WF-4—In WF-4, the contact between the Orinda Formation and San Pablo Group is characterized by a core loss of about 3 ft (1 m) at 60.5 ft (18.4 m) depth. Besides the lack of core, geophysical logging does not show significant anomalies, which could be compared with the same contact in WF-2 or WF-3. It is possible that the contact is the result of a fault zone.

WF-5—Similar to WF-3 at 486.5–492 ft (143–150 m) depth, this fault zone is the one encountered in WF-5 at 220–242 ft (67–74 m) depth. The main fault zone is concentrated in less than 2 ft (0.6 m), but a wide zone of deformation is followed by a zone of mixture, until it clearly transitions to cherts and mudstone of the Claremont Formation. Kinematic indicators in the main deformation zone suggest a reverse sense of shear, as shown in Figure 4-63.

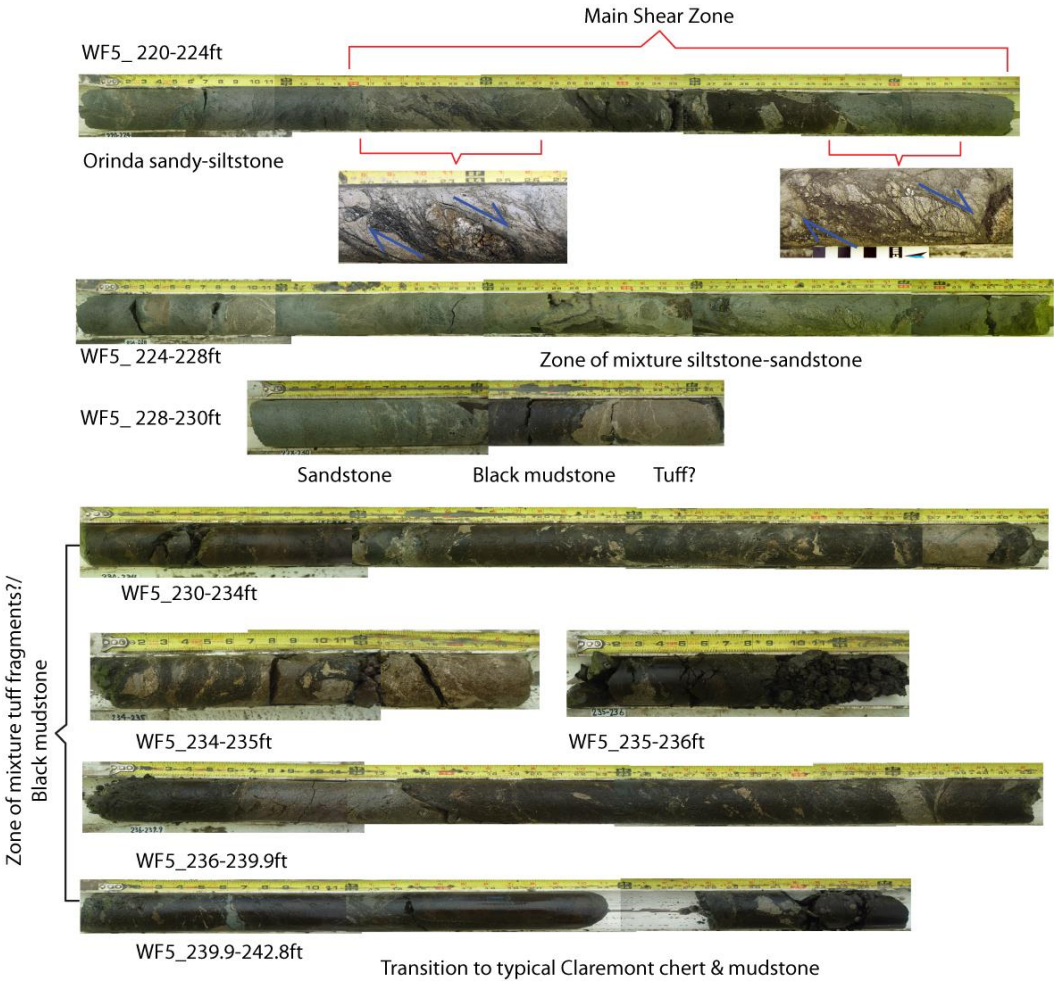

Figure 4-63. Fault contact between Orinda and Claremont formations in WF-5

4.8.3 Faults in the Orinda Formation

WF-2—Zone of brecciation and flow is observed at 224.5 ft (68.42 m) through 240.6 ft (73.33 m) depth interval in WF-2. The deformation is focused in fine-grained sandstone to siltstone, with a planar fabric showing a preferential orientation of indurated sandstone clasts in a fine-grained sandstone matrix (Figure 4-64). Some of the clasts show possible disaggregation features, suggesting possible hydrofracturing. In some locations, the clasts seem floating in the fine siltstone to sandy matrix, suggesting they were deformed in ductile regime. The clasts vary in size but are mostly round to sub-round in shape. Pebbly sandstone to conglomerate is observed near the end of this interval, suggesting channel-fill material. The bottom contact is not clearly marked by a defining fault surface.

Figure 4-64. Clasts in sheared matrix of fine-grained sandstone to siltstone

Under the microscope, the deformation is characterized by a foliation defined by phylossilicates (mica) surrounding intraclasts of dark brown, very-fine-grained material (Figure 4-65). This material also engulfs grains of quartz and siltstone. Locally, they are partially disrupted by the deformation. The deformation is anastomosed and the matrix includes quartz, lithic fragments, *opaque* plagioclase, K-feldspar, quartz aggregates, glauconite, and zircon (Figure 4-66). Bulk XRD indicates the presence of quartz, dolomite, pyrite, plagioclase, and clay minerals.

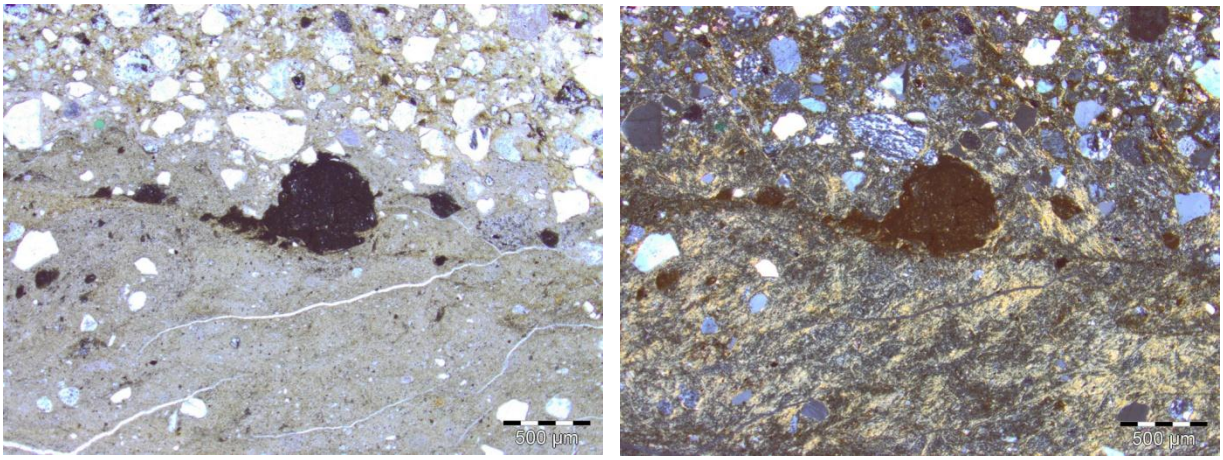

Figure 4-65. Intraclasts of dark material near the contact of granular and fine-grained material (open andcross nicols)

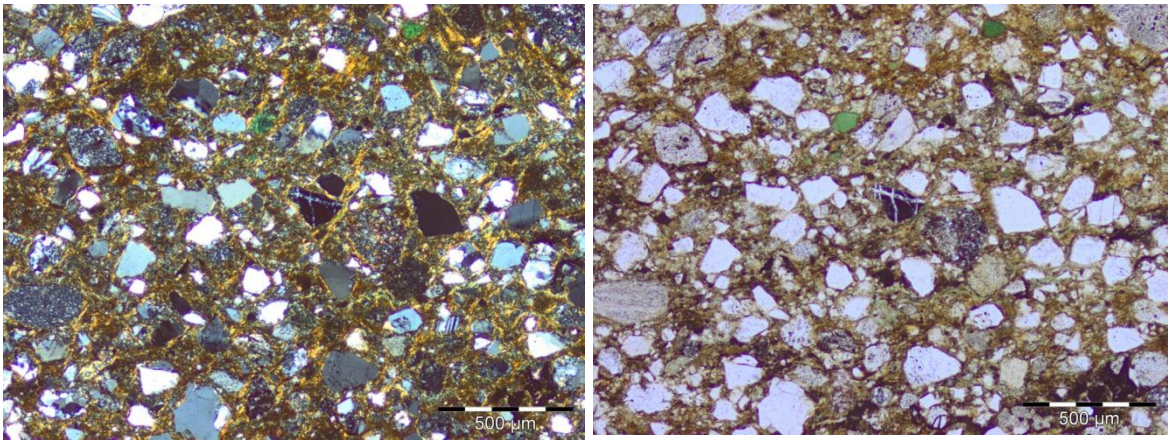

Figure 4-66. Immature sandstone with fine mica and glauconite (green mineral), open and cross nicols.

WF-3—Zones of possible shearing are observed in WF-3 at 53–59 ft (16–18 m), 88–98 ft (27–30 m), and 131–136 ft (40–41.4 m). The deformation seems to be focused in the greenish gray siltstone and is characterized by a network of fine (hairline) carbonate veins, which separate domains of siltstone (Figure 4-67). Minor faults with gouges in the sandy siltstone found at 69–74 ft (21–22.2 m) are described by Kiho et al. (2010).

Figure 4-67. Deformation in the Orinda Formation in WF-3

WF-5—Zones of deformation similar to WF-3 are found in WF-5, although it is not clear how wide this zone is. It is defined by web-like shear bands, which separate into domains of various sizes, showing a rough texture**.** One example is shown in Figure 4-68. A kinematic indicator is not clearly identified in the hand specimen.

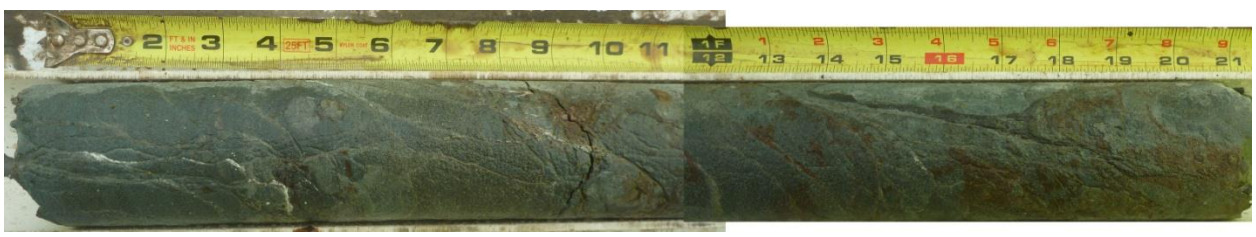

Figure 4-68. Zone of deformation in the Orinda Formation in WF-5 at 148–150 ft (45–46 m)

According to Kiho et al. (2012), the deformation observed in the Orinda Formation in WF-3 and WF-5 are connected with a fault called Fa, and the deformation in WF-2 with a fault called Fc. Fault Fa is related to the East Canyon fault by LBNL and Parsons (2000).

4.8.3.1 Foliated cataclasite

WF-2—A zone of high strain is observed at a 301 ft (91.74 m) to 303 ft (92.35 m) depth interval, followed by a zone of less sheared but mixed and brecciated fragments down to 310 ft (94.48 m) depth. The more elevated interval consists of two zones of cohesive foliated cataclasite (each one about 20 cm thick and separated by 15 cm of thick black shale(?) (Figure 4-69). The two foliated cataclasites consist of cohesive highly sheared material with asymmetric fragments, defined by preferred orientation of rock fragments of light yellow, soft-to-hard siltstone (possibly tuffaceous material) and light gray sandstone embedded in a matrix of sheared black shale. No

visible chert fragments are observed in the shear zone, although chert appears 30 cm above the shear zone. This zone is followed by 2 m thick brecciated interval of intermixed centimetric fragments of sandstone, black shale, and gray siltstone. They are roughly broken, and the contact between fragments is very irregular. Some fragments with rounded edges and folding suggest deformation under ductile conditions.

Figure 4-69. Foliated cataclasite at 91.74 m depth

Petrographic analysis clearly suggests domains of concentrated deformation along zones of high strain, as shown in Figure 4-70 and Figure 4-71. Sheared grains of fine quartz and lithic fragments are engulfed in a zone of high strain rich in clay minerals. Bulk XRD analysis for the cataclastic zone indicates the presence of quartz, plagioclase, dolomite, pyrite, and clay minerals.

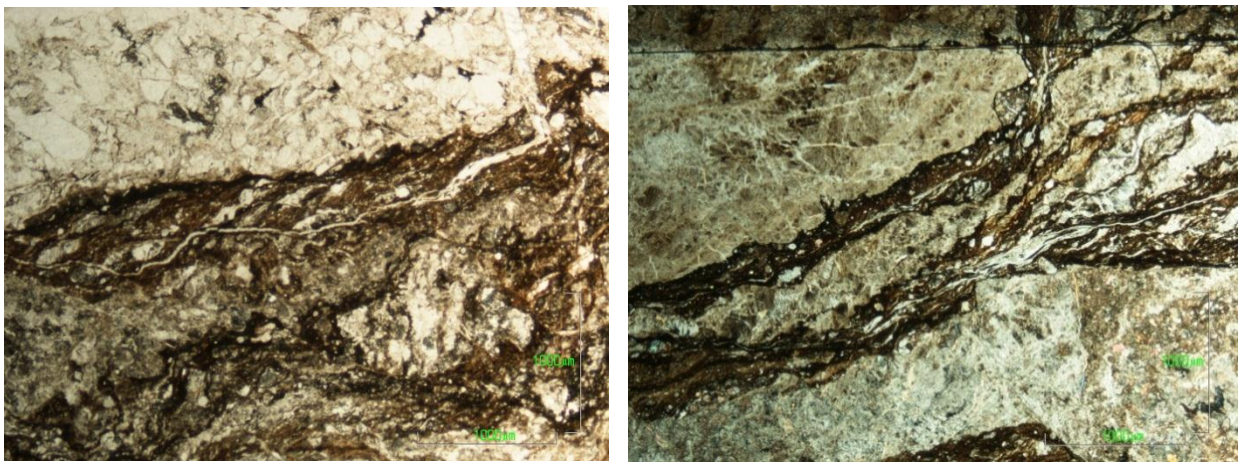

Figure 4-70. Features of typical cataclasite is observed under the microscope (both open nicols)

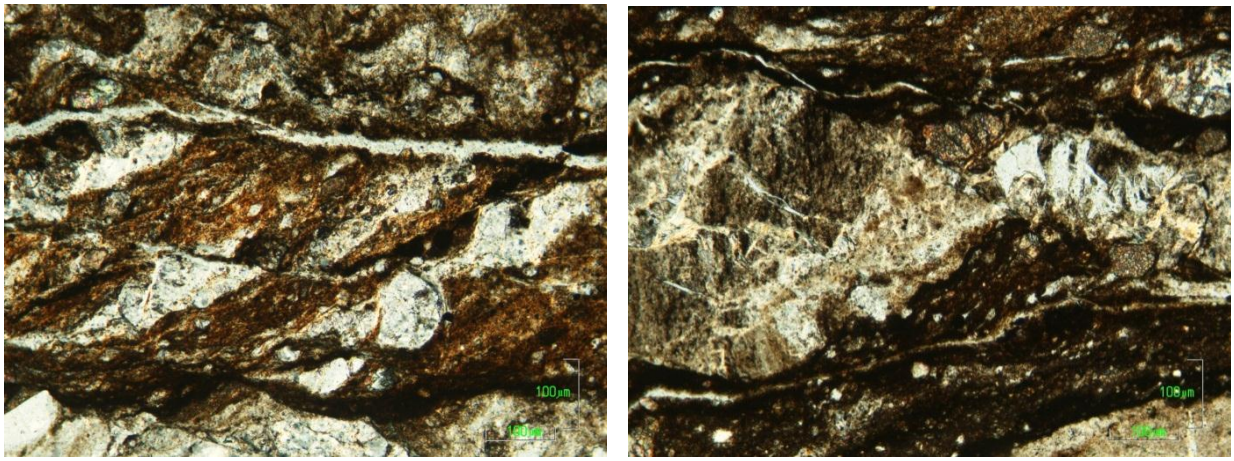

Figure 4-71. Shear bands and dark bands are typical features of cataclastic deformation (both open nicols)

4.8.3.2 Late stage fault

WF-4—Although there were several localized zones of deformation in WF-4, the major active fault seems to be located from 600 to 670 ft (183 to 204 m). The evidence for this is not only the large amounts of core loss, but also the increase in progressive deformation towards the end of the core as well as substantial water loss. Several thin sections that were analyzed by carbon isotope techniques showed an increase in deformation and density of carbonate veins towards the end of the core.

The 500–600 ft (152–183 m) interval seems to be an extensively damaged zone (Figure 4-72). A thick gouge zone is observed at 504 ft (154 m), and although carbonate veins are widespread, they are not as thick or dominant as in zones below 600 ft (183 m)(

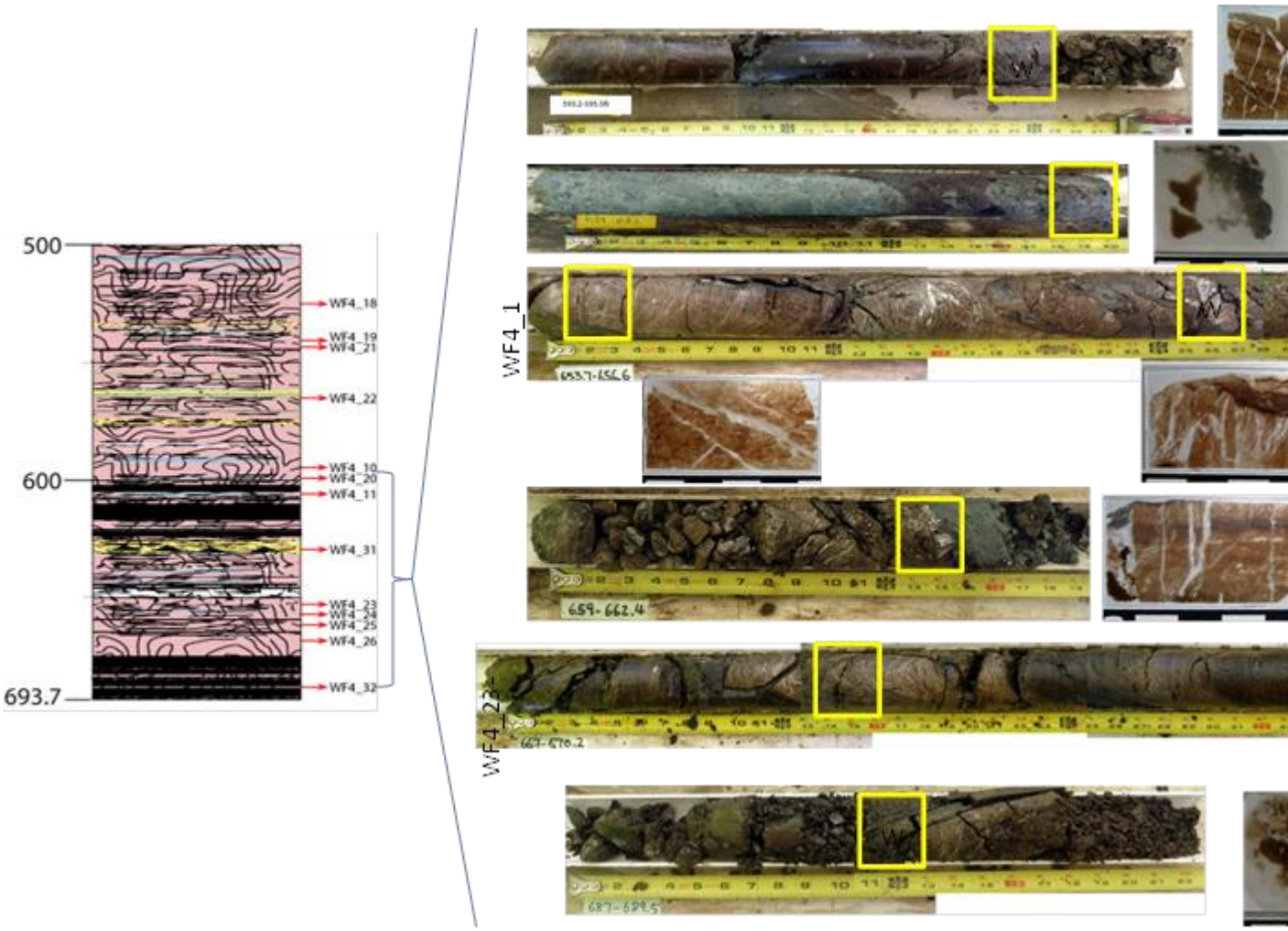

Figure 4-73). Carbonate veins were collected for petrographical, geochemical, and XRD analysis.

The samples analyzed with microscopy are mostly from the laminated to nonlaminated Claremont chert, bedded with mudstone to locally fine-grained sandstone and rich in microfossils. The carbonate veins range from calcite to dolomite and have various thicknesses sometimes showing web-like features.

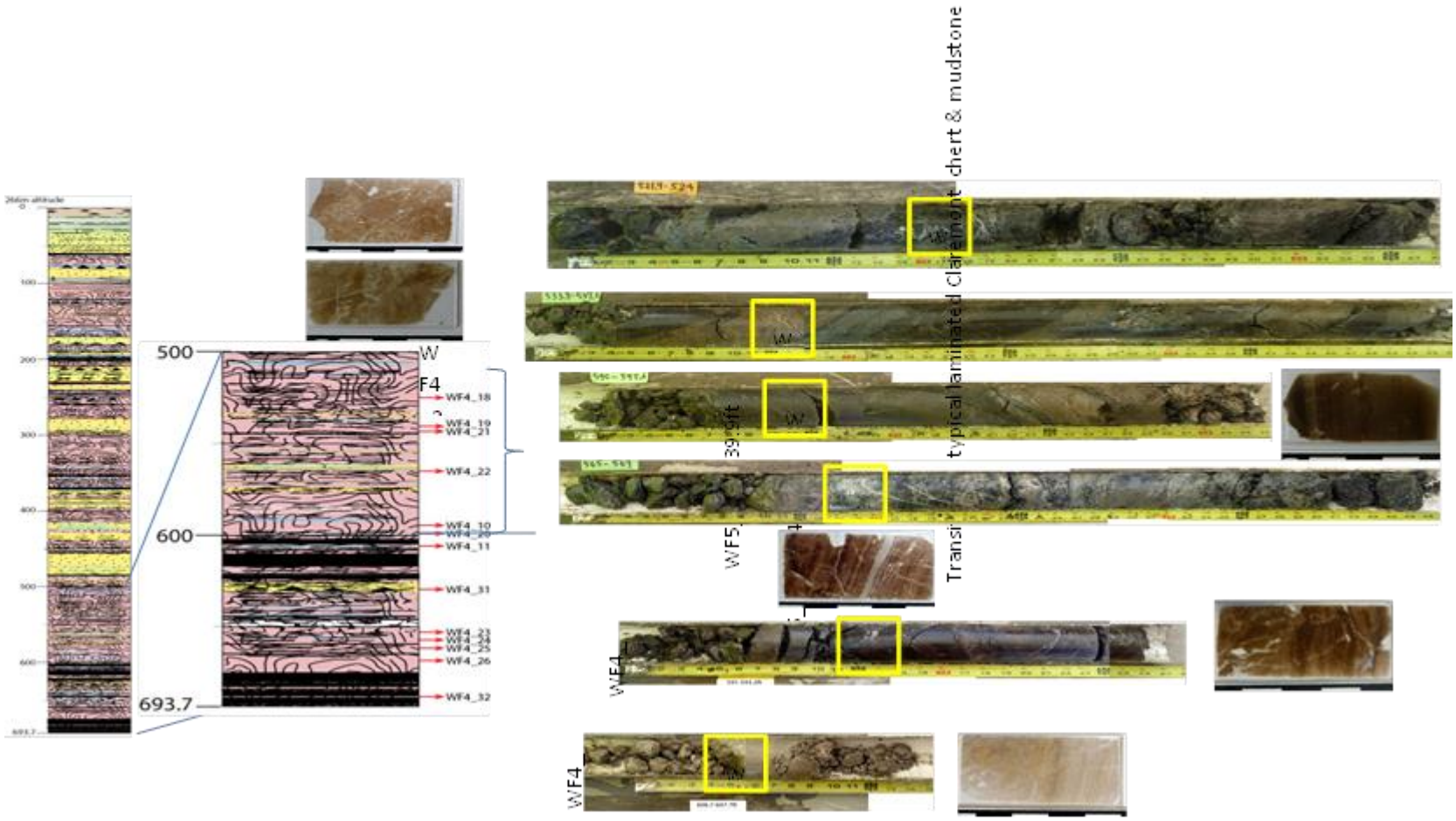

Figure 4-72. Deformation observed from 500 to 600 ft depths. Location of thin section matches with location of carbonate istope sampling

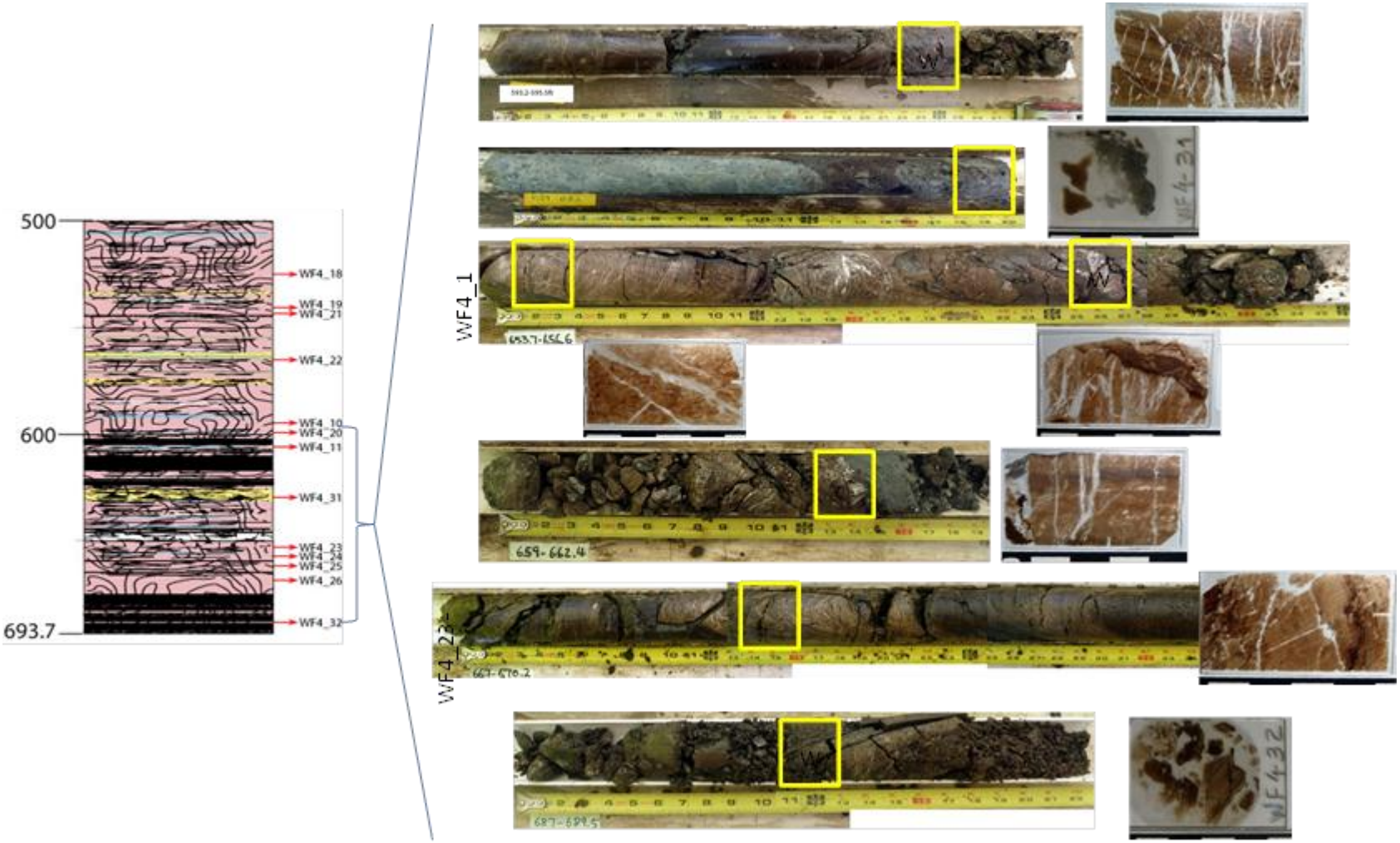

Figure 4-73. The main zone of deformation occurs below 600 ft (183 m). Note the increase in the number of carbonate veins.

From thin section analysis, sample WF-4_20 (595.5 ft or 181.5 m) shows laminated dark brown clay-rich and light brown quartz-rich rock containing an abundance of microfossils. The entire sample is cut by thick carbonate veins that displace the lamination (Figure 4-74). XRD analysis indicates the presence of quartz, calcite, plagioclase, pyrite, dolomite, and clay minerals.

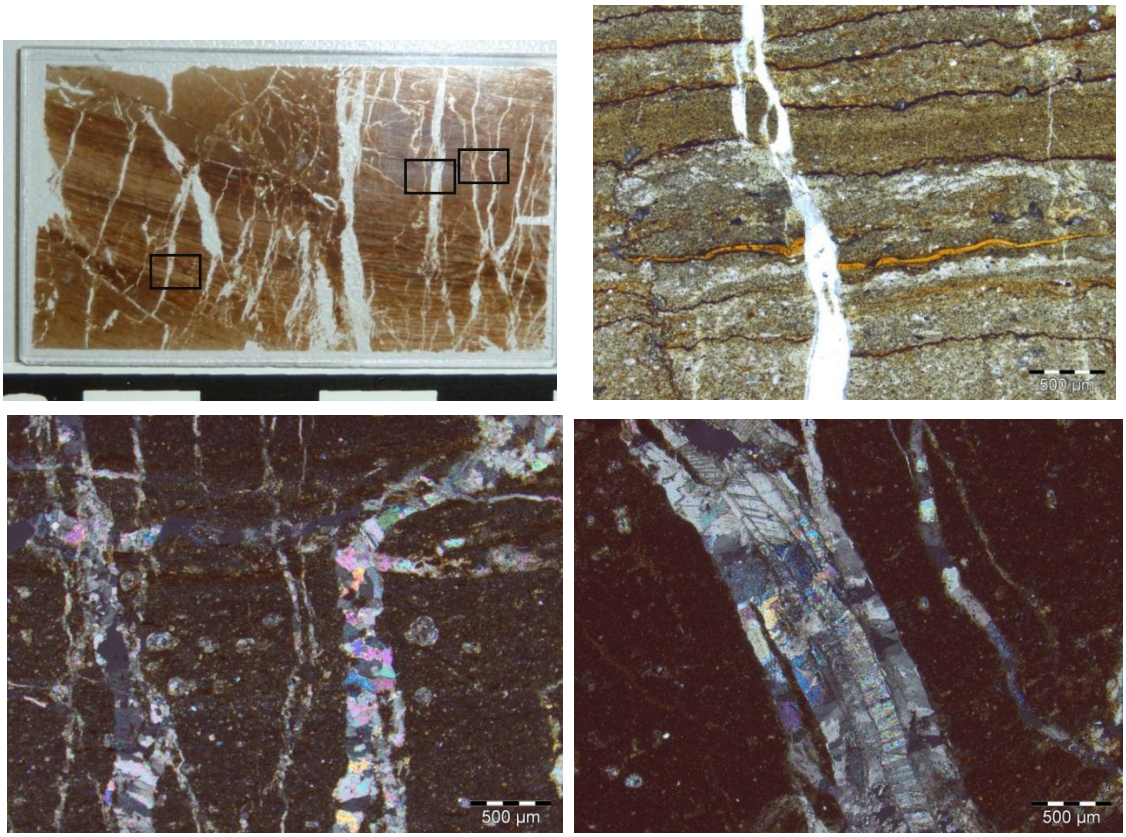

Figure 4-74. Lamination and carbonate veins in cross-polarized views

Another example of deformation is shown in a thin section from WF4_24 at 655.8 ft (200 m) (Figure 4-75). It shows that deformation is focused in the dark brown clay-rich material where cataclastic deformation is observed. Shearing, S-C structure, and fine white mica are found in the deformation band. This deformation seems to postdate the stage of carbonate veins, suggesting more than one stage of deformation.

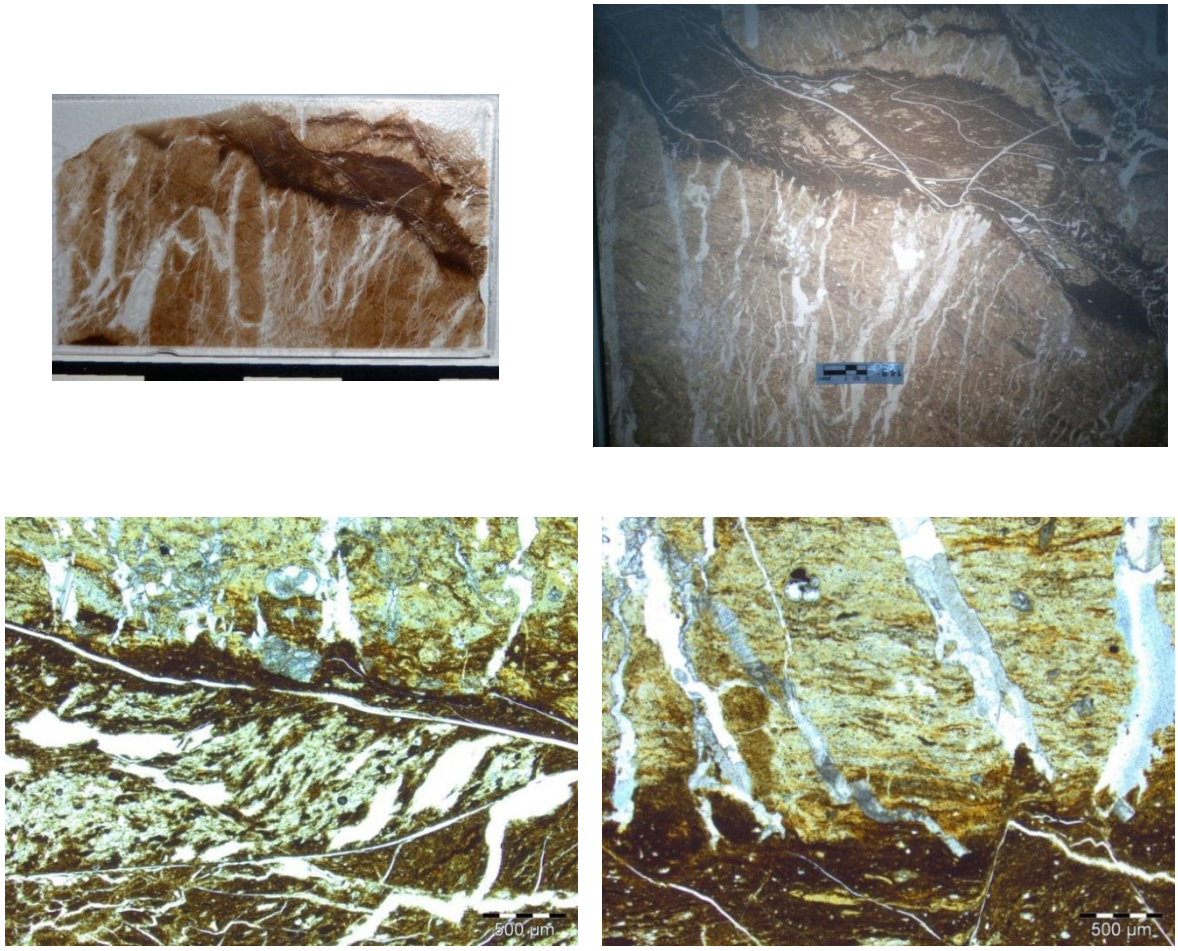

Figure 4-75. Cataclastic flow along the dark brown zone and distribution of carbonate veins and S-C structure. All open nicols.

WF-5—Although WF-5 was intended to examine the eastern side of the fault found in the last 100 ft (30.5 m) of WF-4, the core log did not encounter the same type of deformation as in WF-4. The deformation in the Claremont chert and mudstone is weak compared to WF-4. One zone of brecciation in the slightly bleached Claremont chert (light brown instead of dark brown) starting at 379 ft (115.5 m) is followed by a 5 ft (1.5 m) core loss at 410 ft (125 m). The zone of core loss also has a strong hydrological signature. It is possible that the core loss represents the fault zone. Surprisingly there is no increase in carbonate veins or core-loss regions as observed in WF-4.

Table 4-4 summarizes the XRD analysis for samples from the same location analyzed for carbonate isotopes (see Chapter 6). Whole XRD analyses of samples from the fault zone mainly indicate the presence of quartz, pyrite, calcite and/or dolomite, plagioclase, and clay minerals.

These analyses show a wide variety of minerals encountered near the fault material, but they do not give a conclusive picture of characteristic minerals that could help to identify different stage of faulting. Kiho et al. (2012) analyzed clay minerals among the gouge and fault material, but did not find any link that could correlate the faults.

Carbonate isotope analysis was conducted in the same sample collected for thin sectioning in WF-4, as shown in Figure 4-72 and

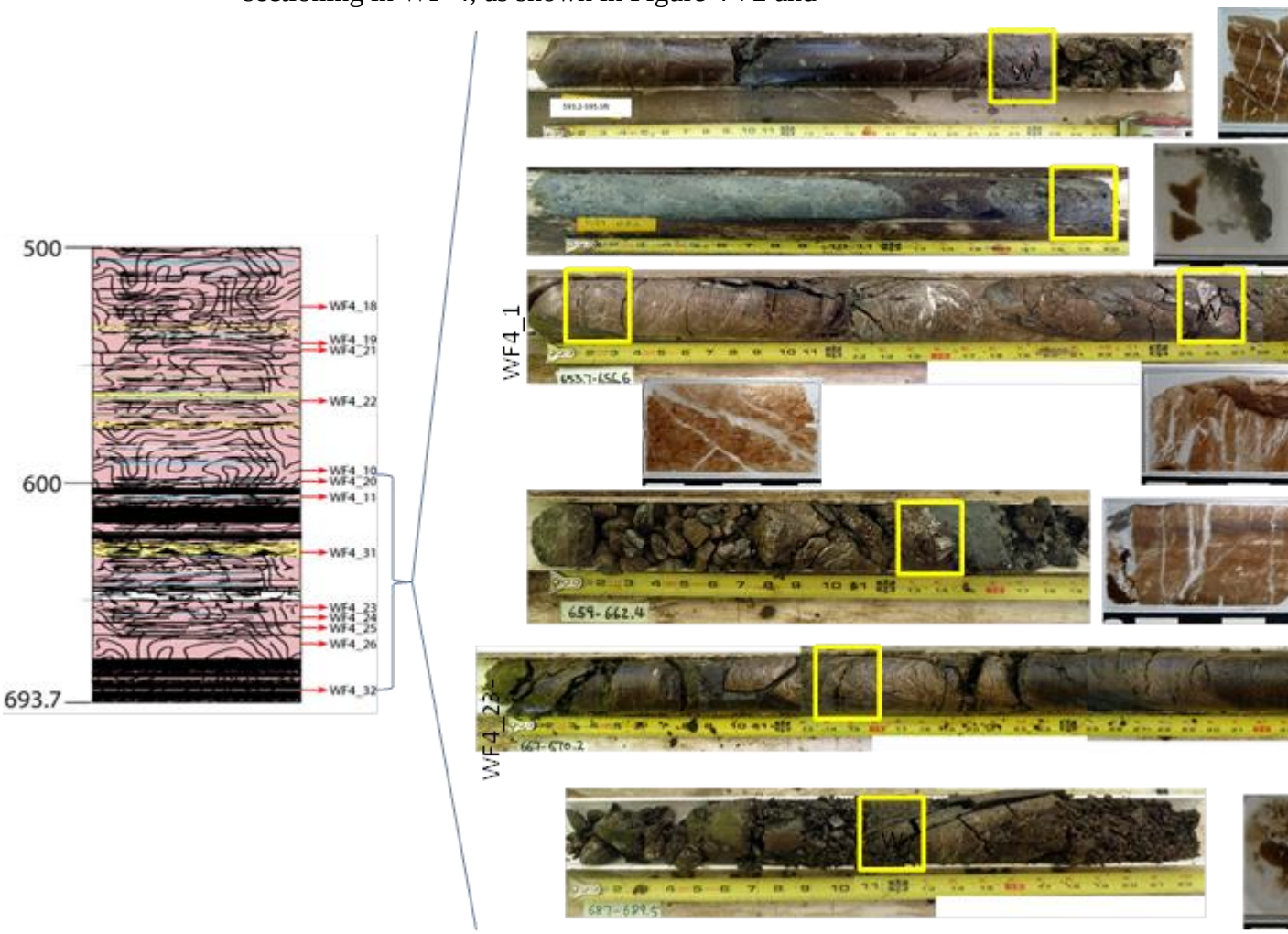

Figure 4-73. Based on the isotope compositions the several carbonate samples from 500 to 678 ft in WF-4 suggests modern-day groundwater compared to carbonates from other parts of the Claremont chert.

Table 4-4. Summary of XRD analysis for fault rocks

(◎ indicates positive)

Sample Depth (ft)	Quartz	Plagioclase	Calcite	Dolomite	Pyrite	Piroxene	Gypsum	Siderite	Hematite	Ankerite	Clay Minerals	Mica
WF1_130	◎	◎	–	–	◎	–	◎	–	–	–	◎	Muscovite
WF2_221.5	–	◎	◎	–	–	–	–	◎	◎	–	◎	–
WF2_224.5	◎	◎	–	◎	◎	–	–	–	–	–	◎	–
WF2_300.5	◎	◎	–	◎	◎	–	–	–	–	–	◎	–
WF3_321.9	◎	◎	◎	◎	–	–	–	–	–	–	◎	–
WF4_81.4	◎	◎	–	–	–	◎	–	–	–	–	◎	–
WF4_541	◎	◎	◎	◎	◎	–	–	–	–	–	◎	–
WF4_595.5	◎	–	◎	–	–	–	–	–	–	◎	◎	◎
WF4_653.7	◎	–	◎	◎	–	–	–	–	–	–	–	–
WF4_660.2	◎	◎	◎	◎	–	–	–	◎	–	–	◎	–
WF4_687	◎	◎	–	◎	◎	–	–	–	–		◎	–

4.8.3.3 Minor faults

Zones of minor faults including breccias and gouge are usually better preserved in the brittle Claremont chert and mudstone than in the more plastic siltstone of the Orinda Formation. As a consequence, this section applies exclusively to Claremont Formation rock.

WF-1—Brittle deformation is characterized by brecciation and crushing with thin layers of clay gouge. Those zones are found at 125 ft (36 m), 135 ft (41 m), 140 ft (42.6 m), 320 ft (97.5 m) and 405 ft (123 m) depths. Intervals with bleached, brecciated and lithified chert are found between 415 and 420 ft (126 and 128 m) and between 490 and 510 ft (149 and 155 m). They are extremely hard and cut by a network of quartz veins.

WF-2—Several minor faults indicated by localized gouge are observed during core logging. They include the presence of 1–3 cm thick gouge zones in interbedded black shale and chert at 91 ft (23 m), 125.8 ft (38 m), 131 ft (40 m), 135 ft (41.1 m), 145.8 ft (44.4 m), 171.8 ft

(52.3 m), 216.3 ft (65.92 m), 217.3 ft (66.2 m), and 256.6 ft (78.2 m) depths. A brecciated zone is observed at 145.6 ft (44 m) depth.

WF-3—As described in Section 4.6.2, 60% of the core log is of Orinda Formation/San Pablo Group. Given their lithological characteristics, the deformation in the sediments of the Orinda Fm. is broad; no gouges are observed. In contrast, minor faults observed in the Claremont chert are characterized by brecciation observed at 368–375 ft (112–114 m), 380 ft (116 m), 438–465 ft (133–142 m) and a thin gouge at 415 ft (126 m).

WF-4—Among the core logs, WF-4 is the most damaged, with 93% of the core log corresponding to the Claremont chert and mudstone as described in Section 4.5.2. From the beginning of the core, the rock is fractured and broken, with fractures starting along the bedding contact in the laminated chert and mudstone. Localized brecciation and incohesive crushed rock, especially in the chert, are observed at 124 ft (38 m), 137 ft (42 m), 180 ft (55 m), 256 ft (78 m), 261 ft, (80 m), 279 ft (85 m), 295 ft, (90 m) 311–315 ft (95–96 m), 322 ft (98 m), 324 ft (99 m), 329–333 ft (100–101 m), 336 ft (102 m), 356 ft (108 m), 363 ft (111 m), 398–403 ft (121–123 m), 442 ft (135 m), and 497 ft (151 m). Below 500 ft (152.4 m) depth is considered a fault zone extends to the end of the core. Gauge was found at 505 ft (154 m), 522 ft (159 m), 554 ft (169 m), and 627 ft (191 m).

Sandstone in general is fractured to locally brecciated, and in only one location did we find a sandstone protocataclasite at 629 ft (191.7 m). As shown in Appendix 5, fractures, brecciation, and gouge are often observed. A zone of protocataclasite is observed in the sandstone in the main fault zone.

WF-5—Localized brecciation is observed at 107 ft (33 m) in the Orinda Fm and at 273 ft (83 m), 339 ft (103 m), 382 ft (116 m), 435 ft (133 m), 446 ft (136 m), and 471 ft (143.5 m). Gouge is observed at 419 ft (127.7 m), 420 ft (128 m), 517 ft (158 m), 581 ft (177 m), 617 ft (188 m), and 676 ft (206 m).

The red dots in Figure 4-76 indicate the location of all gouges from all core logs. Using Earth Vision, and comparing the gouges from each core log, we attempted to correlate gouges was made; however, from the existing data points, no distinguishable correlation could be determined —the gouges seem to be randomly distributed.

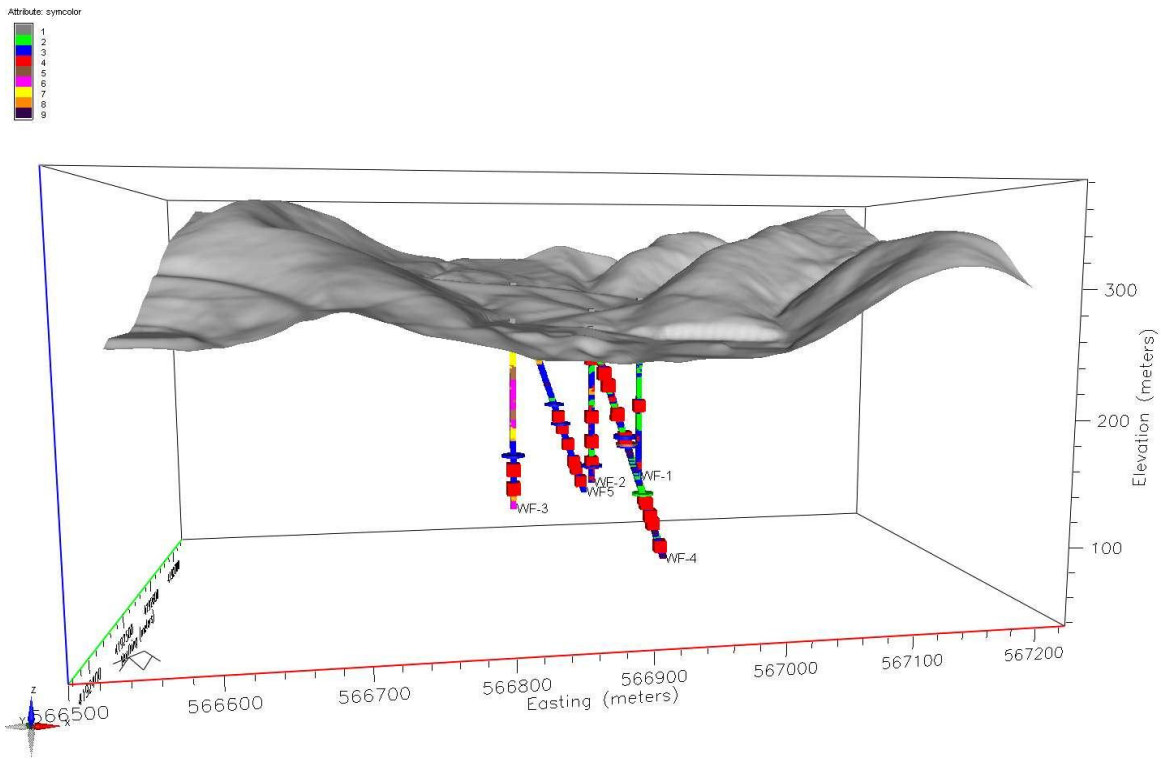

Figure 4-76. 3D view of locations where gouge (red dots) were identified.

One plausible explanation for the random distribution of the gouge is the presence of a fault network. As shown in the model by Flodin and Aydin (2004) (Figure 4-77), each core log might cross through a network of faults, each one represented by gouge.

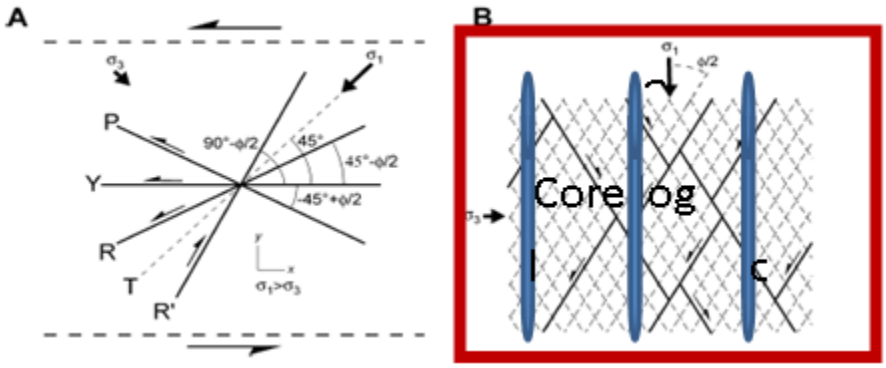

Figure 4-77. Possible model for the fault network indicated by the gouge distribution in core logs (after Flodin and Aydin, 2004)

4.9 3D geological Model

A 3D structural model was constructed using Earth Vision software. Two models, a regional and a local area model, were constructed. Input for these geologic models is based on data from previous geologic mapping by Graymer (2000), geologic survey trenching studies, BTV combined with field survey, cores from deep drilling, and additional borehole data from a previous geotechnical study conducted at LBNL. Fault data are based on projections of surface data from core logs (WF-1, WF-2, WF-3 WF-4 and WF-5), trenching (Karasaki et al., 2010; WLA, 2008), and a previous geologic map (HLA, 2004; Graymer, 2000).

To construct the regional and local-well geologic model, we imported a 10 m resolution digital elevation model (DEM) and an ARC/INFO digital coverage [program?] into Earth Vision. Earth Vision calculates a data grid based on 3D data points. The 2D grid for the regional area ranges from 4194000 to 4190500 NS and 566400 to 569000 EW. It provides an area of ~3.5 by 2.6 km., including the hills on the east, north and south with the Contact Fault (Figure 4-78). Earth Vision also allows slicing the model along any of the three axes. Figure 4-79 illustrates a slice of the model up to the location of the boreholes. The 2D grid for the local borehole area ranges from 4192340 to 4192745 NS and 566490 to 567224 EW, with a grid size of 302.165. It covers only the location of the wells around Calvin Road (Figure 4-80).

Within Earth Vision, the geologic contact and fault data obtained from boreholes and surface data points are interpolated using a 2-D minimum tension gridding technique. In the case of one data point, vector gridding is used based on strike and dip. Once the gridding is completed, the faults are imported to the model and a fault tree is built manually, based on the fault hierarchy (i.e. crosscutting relationships). The stratigraphy is also relevant to the model, since the faults are locally considered as lithological contacts.

Earth Vision uses faults to subdivide the study volume area into fault blocks. Faults in the geologic model include: (1) the low angle contact fault between the Great Valley Sequence and Orinda Formation to the west of the main study area; (2) the contact fault between the Claremont and Orinda Formations based on WF-2, WF-3, WF-4 and WF-5; (3) a possible sliver of the Orinda Formation that connects the end part of WF-3 and a zone of the Orinda Formation in the

middle of WF-2; (4) the most recent fault, which connects the end part of WF-4, the 5 ft core loss in WF-5, and the fault contact in TR-3; (5) the contact between the Claremont and Orinda Formations in the east, based on Graymer (2000); and (6) the contact between the Orinda Formation and Moraga volcanic to the east, based on Graymer (2000).

The resulting local borehole area model consisted of five main fault blocks; the resulting regional area model consisted of ten. Each fault block in the regional area model is further subdivided into stratigraphic units with depositional surfaces. The only depositional contact is the intersection between **[?]** the Orinda Formation, San Pablo Group, and Moraga volcanic; all other contacts are modeled as faults and/or unconformities. Faults are the only structure used in this model; although the area has been folded, no fold information has been used.

Modeling results show the distribution of the main lithologies: the Great Valley Sequence, Claremont Formation, Orinda Formation, and Moraga Volcanics. The geologic block model shows nine faults separating ten major blocks.

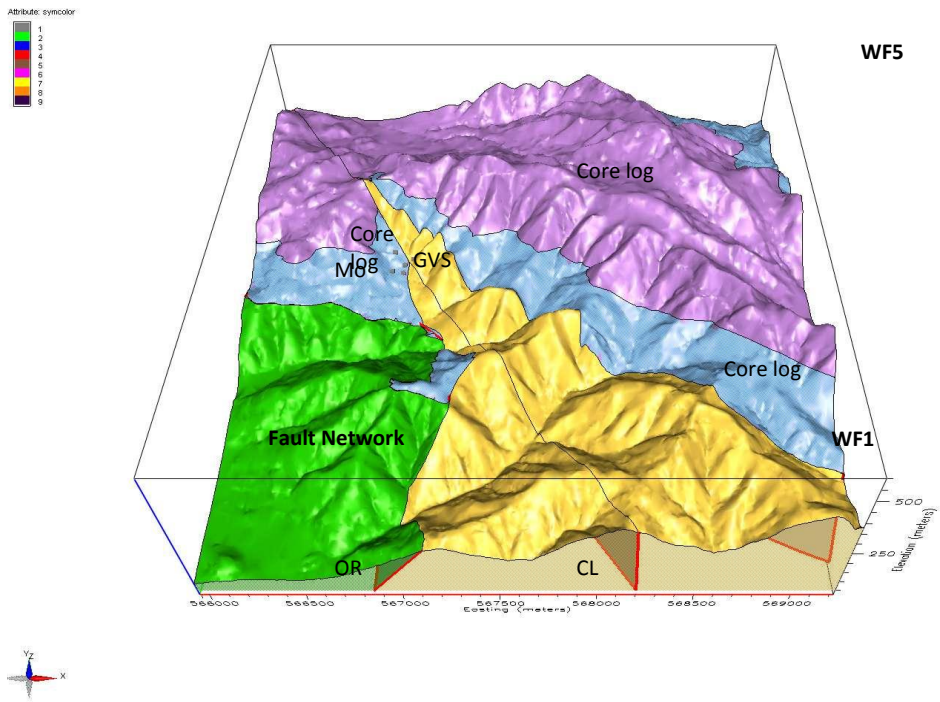

Figure 4-78. 3D regional geologic model for the study area.

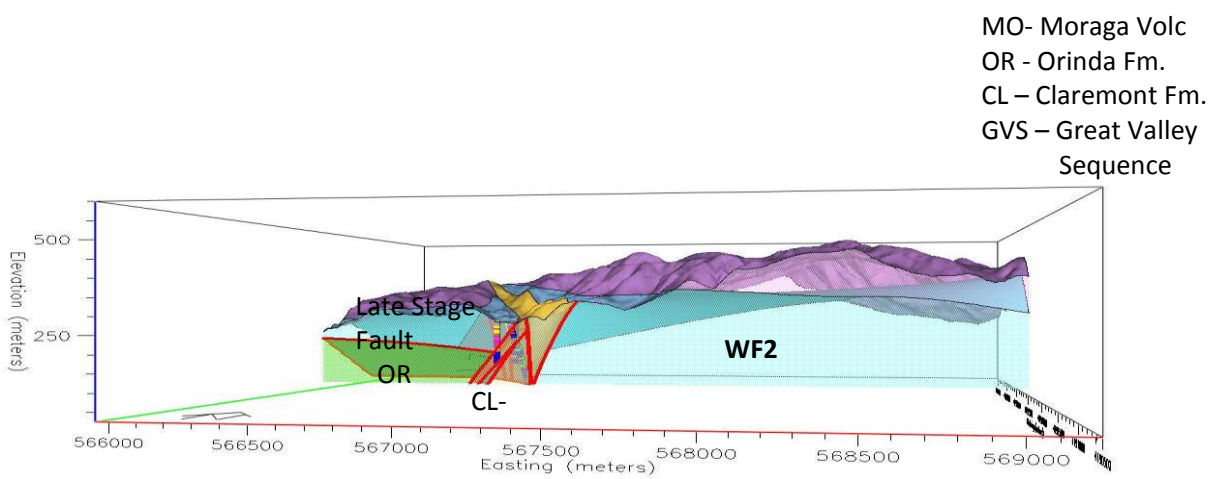

Figure 4-79. Sliced view of the regional model showing the borehole logs .

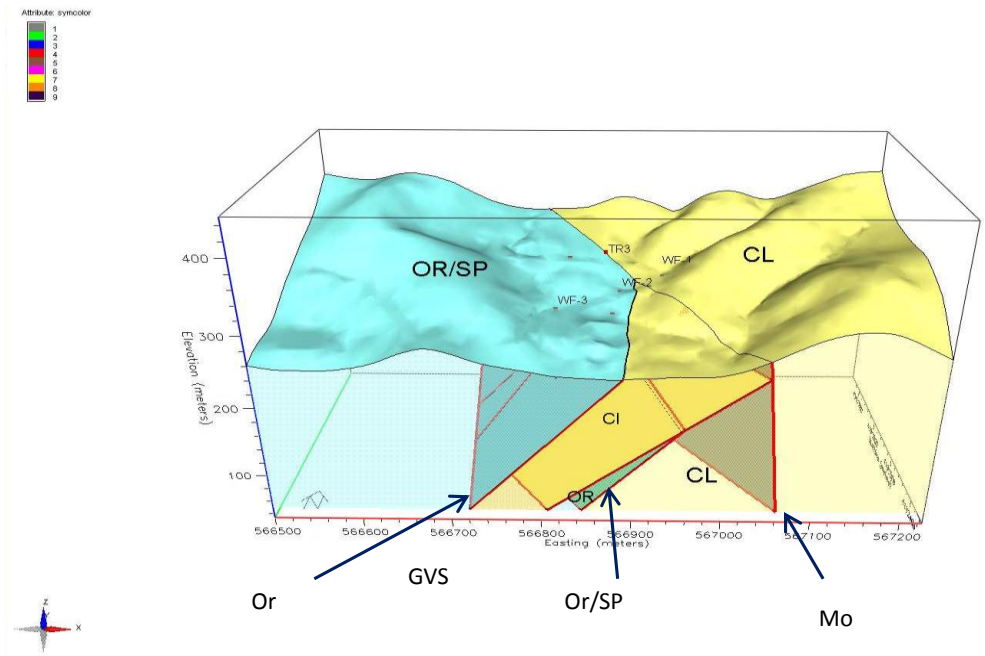

Figure 4-80. Local borehole model illustrating the main faults in the study area.

In general, the WCF Zone can be divided into three main stages of deformation:

I. **Early Stage**—Faults in this stage are deformed in a zone of high strain, with a well-developed foliation defined by preferred orientation of rock fragments. Chester et al. (1985) and Noda and Shimamoto (2005) demonstrated in laboratory experiments that foliated cataclasite can develop in shallow crustal depths. In the study area, this fault is encountered in WF-2 at 300 ft (91.4 m) and described in Section 4.8.3.1. It fits the literature description of foliated cataclasite. The intense shearing resulting in tectonic reduction of grain size and alignments of clay minerals may suggest that this zone has deformed at an early stage and may act as barrier to fluid flow. Because it is one of the early-stage faults, it might have been disrupted by the intermediate and later-stage faults.

II. **Intermediate Stage**—The intermediate stage can be subdivided into three substages (the chronological sequence for these stages may not follow the order in which they are described here):

- *Substage contact fault*—The fault contact between the Orinda Formation, San Pablo Group, and Claremont Formation is clearly observed in four of the five boreholes, as follows: (1) Fault contacts in WF-2 at 55 ft (16.76 m) and in WF-3 at 321.9 ft (98 m) show similar features, such as carbonate conglomerate rich in microfossils, locally broken and suggesting possibly a fault or unconformity; (2) WF-4 core loss at contact at 60.5 ft (18.4 m) and (3) WF-5 cataclasite and wide zone of deformation along the contact at 220 ft (67 m).
- *Substage fault sliver*—The presence of the Orinda Formation in fault contact with the Claremont Formation in WF-3, ~468 ft (143 m), and the presence of faulted Orinda Formation in WF-2, ~224 ft (~68 m), may suggest that a sliver of the Orinda Formation has been dragged along the fault and trapped within the Claremont Formation rocks.
- *Substage fault network*—As described in Section 4.8.3.3 above, a number of gouges were identified during core logs. The plots of these gouges within the 3D geologic model results in a very chaotic distribution, with the correlation among them undetermined at the time of this writing. Conceptually, they suggest a web of local faults, i.e., a fault network. Flood and Aydin (2004) describe this concept in the literature.

III. **Late Stage—**The late-stage faults comprise the deformation observed in the last 200 ft (61 m) in WF-4 and the 5 ft (1.5 m) core loss in WF-5 at 410 ft (125 m). Deformation patterns from WF-4 at 500–600 ft (152–183 m) suggest a zone of damage, which increases with depth. The increase in core loss, the increase in carbonate veins, and the modern groundwater (from carbonate isotope studies) suggest that this zone is the most active among the faults mapped.

Kiho et al. (2012) take a different approach to explain the geometry of the faults in the study area, classifying the faults as follows: (1) **Fa** is the fault that cuts through the Orinda Formation-San Pablo Group in WF-3 and branches to WF-5; (2) **Fb** is the contact fault between Orinda Formation and the Claremont Formation observed in WF-2, WF-3, WF-4 and WF-5; (3) **Fc** comprises the foliated cataclasite described by Kiho et al. (2012) in WF-2, WF-3, WF-4 and WF-5; (4) **Fd** is the wide zone of deformation observed in WF-3, WF-1, and WF-5. According to Kiho et al. (2012), the fault splits in two branches at the surface, one merging with fault Fa, the

other one connecting with the contact of Claremont Formation and Orinda Formation to the east, near the Fire Trail. See Kiho et al. (2012) for details.

4.10 Summary and Recommendations

1. Surface geologic and trench studies are valuable for understanding the distribution of geological units and faults observed in the trenches. The WCF is not a simple fault plane separating the Claremont Formation to the east and the Orinda Formation/San Pablo Group to the west, as described previously—it is a more complex structure. The geometry of the fault is also complex, suggesting that it is indeed a fault zone with a wide zone of deformation. Although the fault zone can be as wide as 500 m (based on the trenches TR4 and TR5 in the south), it is not clear if this zone of deformation has similar width throughout its length, i.e., in the north. This is partially because the Pliocene Moraga volcanic overlies the Orinda Formation north of the study area. If the age of the fault is older than the deposition of the volcanic rocks, then the fault plane cannot be characterized.
2. Drilling and core logs provide a better understanding of the stratigraphy and distribution of the faults in the subsurface. Based on core logs, it is clear that the complexity is greater than suggested from the surface studies. Although the drilling boreholes are located less than 100 m apart from each other, no stratigraphic correlation is possible.
3. Deformation in the Orinda Formation is less evident because of the characteristics of the rock. Siltstone and mudstone are plastic and seal after deformation, without leaving any clear evidence of deformation. Overall, there are several locations (from the core logs) where it seems that the Orinda Formation encountered some kind of deformation—as shown in WF-3 and WF-5 and described in Section 4.6.2. Deformation in the Claremont Formation is evident from the brittle nature of the rock, especially in the laminated Claremont cherts. Such deformation is characterized by brecciation, crushing (pulverization), gouge, cataclasite, protocataclasite, and foliated cataclasite.
4. The WCF zone is divided into three main stages:
    a. Early Stage—dominated by older deformation and characterized by foliated cataclasite.

b. Intermediate Stage— subdivided into three substages: (1) fault contact, (2) fault sliver, and (3) fault network.
c. Late Stage—characterized by broad brittle deformation and fluid flow.

5. There are two surface fault contacts between Orinda and Claremont Formations as shown by Graymer (2000). Although this project has focused on the fault located in the west, Kiho et al. (2012) suggested that the main active fault from WF-4 links to the fault mapped in the east by Graymer (2000).
6. XRD analysis does not give a conclusive result in terms of identifying major changes in fault-zone mineralogy as described by Kiho et al. (2012); however, the results from the cherts suggests that the silica is unanimously composed of pure quartz, confirming the siliceous characteristics of the Claremont Formation.
7. The WCF zone project has provided valuable lessons to all the disciplines involved:
    a. Faults in sedimentary rocks are not a simple structure, as previously thought. It may be that the WCF is unusually complex due the proximity of a major active fault – the Hayward Fault—with an overlap of fault structures occurring in the study area.
    b. In general, faults are unique. Each one has to be studied carefully to make meaningful comparisons.
    c. Because of the interdisciplinary aspect of the project, different opinions have emerged, resulting in several models rather than a single unified model. We believe that all models have their merit. The project should adapt to the different options and solutions instead of believing that there must be only one solution for the problem.
    d. Planning for site characterization should not strictly follow the steps already set in the documentation. Things change in the course of characterization and must be re-evaluated. For example, the new seismic survey along the orientation of the drilling boreholes may help to understand the distribution and orientation of the complex fault zone.
    e. The schedule and budget for site characterization should be flexible enough to accommodate changes that occur during the progress of the work. Unknown issues may arise during drilling and hydrologic testing—just as in this project.

f. The WCF project highlights the need for a better understanding of fault geometry. Fault complexity might result from the proximity of other major active faults in the area, but it could also be that most of the pertinent models are oversimplified at present.

g. The WCF project is a challenging project, but an essential one, because faults are everywhere—and they are one of the key parameters for nuclear waste disposal program site characterization. Above all, we still do not have a full understanding of fault geometry, how to characterize gouge, or how to relate these issues to faulting events.

4.11 References

Adams, A.E, MacKenzie, W.S., and Guilford, C., 1984, Atlas of sedimentary rocks under the microscope. Prentice Hall, 104p.

Aydin, A., 1982, The East Bay hills, a compressional domain resulting from interaction between the Calaveras and Hayward-Rodgers Creek fault, in Hart, E.W. Hirschfeld, S.E., and Schulz, S.S., eds., Proceedings conference on earthquake hazards in the easternn San Francisco Bay Area: California Division of Mines and Geology Special Publication 62, p.11-22.

Barron, J.A., 1986, Paleoceanography and tectonic controls on deposition of the Monterey Formation and related siliceous rocks *in* California: Paleogeography, Paleoclimatology, Paleoecololgy, v.53, p.27-45.

Bishop , C.C., Knox R.D., chapman R.H. Rodgers D.A., and Chase G.B., 1973, Geological and Geophysical Investigations for TriCities Seismic Safety and Environmental Resources Study. California Division of Mines and Geology Preliminary

Chaika, C.J., 1998, Physical properties and silica diagenesis , PhD dissertation: Stanford University, Stanford, California, 117p

Chester F.M., Friedman, M. and Logan, J.M.-1985 – Foliated cataclasites. Tectonophysics 111:139-146

Curtis, G.H., 1989, Late Cenozoic volcanic rocks of the central Coast Range, in Wahrhaftig, C., and Sloan, D., Geology of San Francisco and vicinity, Field trip guidebook T 105: Washington, D.C., American Geophysical Union, p. 33-35

Dames & Moore, 1962, Soil Investigation, First increment, Proposed Animal Bioradiological Laboratory, Lawrence Berkeley Laboratory Berkeley, California. Report # 236_00001Doell, E.C., 1930 – Correlation of the Campus and Orinda Formations in the Berkeley Hills, California, MS Thesis, University of California Berkeley, p.78

Doell, E.C., 1930 – Correlation of the Campus and Orinda Formations in the Berkeley Hills, California, MS Thesis, University of California Berkeley, p.78

Dynamic Graphics Inc., Earth Vision 8, Work Flow Manager and Geologic Structural Building http://www.dgi.com/earthvision/evmain.html

Flodin, E.A. and Aydin, A. 2004, Evolution of a strike-slip fault network, Valley of Fire State Park, Southern Nevada. GSA Bulletin, 116:1/2,42-59

Geo/Resource Consultants, Inc., 1994, Geotechnical Investigation. Replacement Hazardous Waste Handling Facility. Lawrence-Berkeley Laboratory, Building 85, Berkeley, California. GRC job number 1393-000. Report # 339_085. pp.133

Gilpin, L., 1994, Geologic Evaluation, Wildcat Fault, Human Genome Laboratory, Laboratory, Lawrence Berkeley Laboratory Berkeley, California. Report # 396_00001

Graymer, R.W., 2000, Geologic map and map database of the Oakland metropolitan area, Alameda, Contra Costa and San Francisco Counties, California. USGS Miscellaneous Field Studies MF3242g. Version 1.0

Graham, S. A., McCloy, C., Hitzman, M.,Ward, R., and Turner, R., 1984, Basin evolution during change from convergent to transform continental margin in central California: American Association of Petroleum Geologists Bulletin, v. 68, p. 233–249.

Harding Lawson Associates (HLA), 1974, Geologic investigation – Building 74 addition, Lawrence Berkeley Laboratory Berkeley, California. Report # 238_00001

Harding Lawson Associates (HLA), 1977, Foundation investigation - Cell Culture Facility, Lawrence Berkeley Laboratory Berkeley, California. Report # 183_00063

Harding Lawson Associates (HLA), 1980, Wildcat Fault Study Bio Medical Laboratory II Project Lawrence Berkeley Laboratory Berkeley, California. Report # 041-0020

Harding Lawson Associates (HLA), 1982, Geology of Lawrence Berkeley Laboratory. HLA Job no. 2000,135.01. Report # 042_00

Harding Lawson Associates (HLA), 1985, letter provides our evaluation of the proposed library site located along the southwest edge of the existing paved parking lot west of Building 74. Report # 164-0001

Ingle, J.C. Jr., 1981, Origin of Neogene diatomites around the north Pacific rim*in* Garrison, R.E., Douglas, R.G., Prisciotto, K.A., Isaacs, C.M., and Ingle, J.C.Jr, eds.The Monterey Formation and related siliceous rocks of California: Pacific Section, Society of Economic Paleontologists and Minearlogist, Speical Publication, p. 159-180.

Isaacs, C.M., 1983, Compositional variation and sequence in the Miocene Monterey Formation, Santa Barbara coastal

Isaacs, C.M., 1984, Hemipelagic deposits in a Miocene basin, California: Toward a model of lithologic variation and sequence, *in* Stow, D.A., and Piper, D.J.M., eds., Fine grained sediments: deep water processes and environments: Geological Society of London Special Publication 15, p. 481-496.

Jones, D.L. and Curtis, G., 1991, Guide to the geology of the Berkeley Hills, Central Coast Ranges, California in Geologic Excursions in Northern California: San Francisco to the Sierra Nevada, California Departmanent of Conservation, Division of Mines and Geology. Special Publication 109, pp 63-73.

Jordan, P.,1997, Wildcat Fault Observations at Building 84 excavation. Letter to LBNL Facilities #359-084.

Karasaki, K., Onishi, C.T. and Zimmer, V., 2010, Development of Hydrologic Characterization on Technology of Fault Zones – Phase II Interim Report-, NUMO-LBNL-CRIEPI Collaboration Research Project.

Kleinfelder, 2001, Geothechnical Investigation – Proposed road and water tank Lawerence-Berkeley National Laboratory, Berkeley California. Report #384_00002.

Kiho, K., Ueta, K., Miyakawa, T., Hasegawa, T., Tanaka, S., Ito, H., Hamada, M., Tsukuda, K, 2010, CRIEPI Technical Report, Survey and Analysis related to Development of Hydrologic Characterization Technology of Fault Zones

Kiho, K., Ueta, K., Miyakawa, T., Hasegawa, T., Tanaka, S., Ito, H., Hamada, M., Tsukuda, K, 2011, CRIEPI Technical Report, Survey and Analysis related to Development of

Hydrologic Characterization Technology of Fault Zones

Kiho, K., Ueta, K., Miyakawa, T., Hasegawa, T., Tanaka, S., Ito, H., Hamada, M., Tsukuda, K, 2012, CRIEPI Technical Report, Survey and Analysis related to Development of Hydrologic Characterization Technology of Fault Zones

Kleinfelder, 2001, Geothechnical Investigation – Proposed road and water tank Lawerence-Berkeley National Laboratory, Berkeley California. Report #384_00002.

Lawerence-Berkeley National Laboratory (LBNL) and Parsons Engineering Science, 2000, RCRA Facility Investigation Report for the Lawrence-Berkeley National Laboratory Environmental Restoration Program. 190p.

Lawson, A.C. and Palache, L., 1900, Geological Map of Portion of the Berkeley Hills

Lawson, A.C., 1914, Description of the San Francisco District; Tamalpais, San Francisco, Concord, San Mateo, and Hayward quadrangles: U. S. Geological Survey Geological Atlas Folio 193, 24 p., scale 1:65,500.Levin, H.L., 1987 – The Earth Through Time. Saunders College Publishings

MacBride, E.F., 1963 - A classifiation of commons sandstones: Journal of Sedimentary Petrology, V.54, p. 65-87.

Mackenzie, F.T., 2007 – Sediments, diagenesis, and sedimentary rocks, Treatise on Geochemistry, Elselvier

Noda, H. and Shimamoto, T. - 2005 – Thermal pressurization and slip weakening distance of a fault: an example of the Hanore fault, Southwest Japan. Bull. Seism.. Soc. Am. 95:1224-1233.

Page, B.M., 1950, Geology of the Broadway Tunnel, Berkeley Hills, California. Economic Geology, v.45, pp.142-166.

Pisciotto, K.A. and Garrison, R.E., 1981, Lithofacies and depositional environments of the Monterey Formation, California, *in* Garrison, R.E., Douglas, R.G., Pisciotto, K.A., Isaacs, C.M., and Ingle, J.C. Jr., eds. The Monterey Formation and related siliceous rock of California: Pacific Section, Society of Economic Paleontologists and Mineralogists, Special Publication, p. 97-122.

Radbruch, D.H., 1969, Areal and engineering geology of the Oakland East quadrangle, California: U.S. Geological Survey Miscellaneous Geologic Quadrangle Map GQ-769, 15p, 1 sheet, scale 1:24,000

Radbruch, D.H., 1964, Log for field trip through Caldecott Tunnel, Berkeley Hills, California: U.S. Geological Survey, Open File Report 756.

Selley, R.C., 2000, Applied Sedimentology,. Second edition, Academic Press.

Sloan, D., Karachewski, J., 2006, Geology of the San Francisco Bay Region (California Natural History Guides) no. 79. 337p.

Simpson, R.W., 2000, Watching the Hayward Fault, Science, 18 August 2000. pp. 1147-1148. http://www.sciencemag.org/cgi/content/full/289/5482/1147

Stereonet v.1.2.0. http://www.geo.cornell.edu/geology/faculty/RWA/programs/

Untermann, B.R., 1935, A study of the Wildcat fault in the Berkeley Hills, M.S. Thesis, University of California Berkeley

U.S. Geological Survey, 2008, Understanding Earthquake Hazards in the San Francisco Bay Region. The Hayward Fault – Is it due for a repeat of the powerful 1868 Earthquake? USGS Fact Sheet 2008-3019. http://pubs.usgs.gov/fs/2008/3019/fs2008-3019.pdf

William Lettis and Associates, Inc. (WLA), 2008, Surface-fault rupture hazard investigation of the Wildcat fault. roposed General Purpose Lab. Lawrence-Berkeley National Laboratory, Berkeley, California. 57

Woodruff, F., Savin, S.M., and Douglas, R.G., 1981, Miocene stable isotope record: a detailed deep Pacific Ocean study and its paleoclimatic implications: Science 8, v. 212, no. 4495, pp. 665-668.

5 Hydrologic Investigation

5.1 Introduction

Hydraulic tests are the only direct method by which to evaluate the hydrologic properties of rocks *in situ*. Various geophysical, geological, and geochemical tools have been proposed to correlate nonhydrologic parameters to hydrologic properties. However, except for layer-cake sedimentary formations, such efforts have yielded mixed results at best. Especially in fractured and faulted rocks, such tools have never been effective. For example, the surface geophysical surveys discussed in Chapter 2 did not yield definitive results for pinpointing the location of faults, and the borehole geophysical loggings conducted in the Wildcat Fault (WF) boreholes in our investigation of the Wildcat Fault did not correlate well with the flow zones, as discussed in Chapter 2. In this chapter, we discuss the results of the hydraulic tests and monitoring efforts conducted in the Project and draw some conclusions and recommendations for similar efforts in the future.

We conducted pump tests in WF boreholes where and when feasible. Long-term pump tests can stress a larger volume of formation than slug tests and other short-term tests. Thus, the results of long-term tests are more representative of the subsurface hydraulic parameters at a larger scale. In general, it is better to conduct a pump test as long as possible. However, we had some limitations on when we could conduct pump tests: We could not discharge into a sanitary sewer 24 hours before, during, and until 24 hours after a rain event, because the groundwater from WF boreholes contained trace amounts of hydrocarbons during that time (Karasaki et al., 2011). Thus, the longest pump test we ended up conducting lasted approximately three weeks.

Where permeability was very low, we conducted slug tests. In WF-3, this was the case for the entire hole. We also conducted slug tests in WF-1 through WF-3 overnight after a day's drilling operation. For slug injection tests, we used water from a nearby fire hydrant, which may not have been a good idea. We now suspect that this fresh water from the hydrant may have made the Orinda siltstone swell, and thereby alter the permeability and/or enhance the likelihood of hole collapse in WF-3 and WF-4. We used fresh water in to conduct FFEC logging (Chapter 2) in all WF boreholes, which also may have caused the difficulties in the holes that drilled through the Orinda siltstone (WF-3, -4 and -5).

In this chapter, we first discuss the results of hydraulic tests conducted in WF-4 and WF-5 in FY2011. We then summarize the results of the long-term monitoring in WF and SSL boreholes. Detailed results from previous tests are contained in Karasaki et al. (2009, 2010 and 2011). (The locations of the WF and SSL boreholes are shown in Figure 5-1.) A summary of hydraulic test results are shown in Table 5-1.

5.2 Hydraulic Tests in WF-4

WF-4 penetrated a major fault zone, and we sought to hydraulically test this fault zone itself and the zones above and below it, using packers to isolate intervals. However, it turned out that isolating intervals was very difficult. As discussed in Chapter 2, WF-4 was drilled 60° from horizontal, which made it prone to collapse. We could not recover cores from many borehole sections because the rocks were too pulverized. It was also very difficult to determine the exact location of the main fault plane. Furthermore, the borehole wall was very rough and enlarged at various locations, and consequently we could not choose the packer locations at will. We will discuss this problem and propose a solution later in this chapter. In this section, we describe the results of the hydraulic tests conducted in WF-4 that were not covered in Karasaki et al (2011).

5.2.1 WF-4#3 Pump Test

We conducted two pump tests in the #3 interval (the bottom most interval) in WF-4 with three packed off intervals isolated by two sets of double packers. Double packers were used to ensure that the packed off sections are isolated from each other. The bottom set of double packers (8 ft long) were first placed at 535–543 ft depth. When the #3 interval was pumped, the pressure in the #2 interval decreased (Karasaki et al., 2011). Believing that the packers were perhaps not placed at the right location to prevent communication between the intervals and we moved the bottom set of packers 40 ft down, so that the bottom of the bottom set of packers was at 583 ft, very close to the suspected fault at 591 ft.

Figure 5-3 shows the pressure transients at selected monitoring intervals in response to the pumping in WF-4#3. The test was conducted from 4/2/2011 to 4/22/2011, including the recovery period. Pumping interval #3 extended from 583 to 693.7 ft (177.7 to 211.4 m). Note that the WF-1#5 interval responds quickly and draws down ~5 m, while the drawdown in the pumping interval is ~16 m, indicating a good hydraulic communication. We believe that WF-4 intersects a high permeability zone associated with the Wildcat, which runs very close to WF-1. (We discuss

this further below.) Also note that WF-4#2 interval draws down ~3 m. This might result from the packers not sealing well, which is still possible with a double packer system. Another possibility is that the intervals above and below the packers are naturally hydraulically connected through fractures.

We had assumed that the fault zone had a low permeability core that hydraulically separates the zones above and below it, and that there was a distinct high permeability zone associated with the Wildcat. We had wanted to test these zones by isolating each by packers. However, because we did not know exactly where those zones were, and because we could not choose packer locations at will due to rough walls, we feared that the packers were not effectively hydraulically isolating the zones.

Figure 5-4 shows the Horner plot of the recovery data of the WF-4#3 pumping test. As can be seen from the figure, the slope of the asymptotic line is flatter at the large time compared to that of the middle time, indicating that there is a higher permeability region encountered at distance. Based on the Horner analysis, the transmissivity at the later period is 5.2×10^{-5} m^2/s. This permeability could be calculated by dividing it by the interval length of 60 m. However, we were not very comfortable doing this, because we believed that the permeability was not equally distributed along the entire interval length. It is more likely that one or two isolated features were responsible for most of the transmissivity.

5.2.2 WF-4#2 Pump Tests

After conducting pump tests in the #3 interval in WF-4, which contained the main fault zone, we changed the packer string configuration so that we could pump from the middle interval, #2. The top set of the double packers was placed from 223 to 231 ft, and the bottom was set at 486–494 ft— thus, the pumping interval was from 221 to 486 ft. It was assumed that this interval is above and west of the Wildcat. Figure 5-5 shows the pressure transients during and after the pumping. Note that part of the WF-1 and WF-2 data was lost due to a software bug. WF-4#1 shows only a slight response, indicating that the top set of packers are sealing effectively. None of the WF-3 intervals responded noticeably. Only the pressure in WF-3#5 is shown in the figure. The WF-2#5 interval showed the greatest response, with a maximum drawdown of 4.5 m when that of the pumping interval was ~18 m. This hydraulic connection was observed previously

during the drilling of WF-4. The pressure in WF-2#3, #4 and #5 spiked when the drilling depth reached ~250 ft (Karasaki et al., 2011).

Figure 5-6 show the Horner plot of the recovery period data. The asymptotic slope of the curve at late time again shows flattening, indicating a higher permeability at a distance. Note that in Figure 5-5, the WF-4#3 interval draws down about 3 m, which in turn caused a drawdown response in WF-1#5. Again it was not immediately clear if the pressure transmittal was caused by borehole short-circuiting or by natural fractures. We decided to move the bottom packers to a higher position, assuming that the main fault zone is wider than the initial interval between the sets of double packers based on the fault-zone structural model of Kiho et al. (2011). Figure 5-20 shows their most recent interpretation (Figure 2.4-2 in Kiho et al, 2012).

In the 2nd pump test configuration, the pumping interval was set from 229 to 376 ft. The pumping continued—Figure 5-7 shows drawdown responses at various observation intervals. As can be seen in the figure, almost all intervals responded to varying degrees. Three intervals in WF-2 (#3, #4 and #5) drew down the most: ~5 m with ~22 m drawdown in the pumping interval, the ratio similar to the previous test. The drawdown in WF-4#3, the interval below the pumping interval, was ~2 m, less than the previous test, indicating that less communication exists between the WF-4#2 and WF-4#3 intervals. Still, the drawdown in #3 nonetheless caused WF-1#5 to respond; in fact, all the intervals in WF-3 except for the #1 interval appeared to respond, with the magnitude of the response greatest in #5 and least in #2. From this we can hypothesize that WF-3#5 is connected to WF-2 through the Fc feature, and that the drawdown propagated vertically upward in WF-3. Below, we will discuss another piece of evidence indicating that the bottom interval of WF-3 is connected to the middle section of WF-2.

Figure 5-8 shows the semi-log lot of the drawdown in the pumping zone. Assuming a radial flow and using the slope of the best-fit straight line, we calculate a transmissivity of 1.4×10^{-5} m^2/s. Although the flow geometry is probably not of a radial flow, there appears to be a straight line whose slope matches with the first slope of the Hornor plot shown in Figure 5-9.

Figure 5-9 shows the Horner plot for the recovery period of the 2nd pump test. As can be seen in the figure, the slope of the asymptotic straight line becomes roughly three times steeper at late time, indicating that a low permeability region is encountered at a distance. This can be interpreted as the region near the pumped interval having a transmissivity of 1.4×10^{-5} m^2/s, but

farther away, the overall transmissivity is roughly 1/3 of the region near the borehole. This behavior is the opposite of the previous test findings, implying that the bottom set of packers are now set above the postulated low permeability zone, separating the high permeability zone below it and the #2 interval. In the previous test, the pumping interval included [?] the permeable zone associated with the main fault zone. As can be seen from Figure 5-6, the slope of the Horner curve flattens.

It must be pointed out that Horner analysis is an empirical method. For a confined radial flow, one can analytically show that it yields the theoretical transmissivity value. In our case, the flow geometry is most likely not that of radial flow. Thus, the values should be treated as relative, but the analysis of the late-time behavior should be qualitatively valid.

5.3 Pump tests in WF-5

WF-5 is also an inclined borehole, like WF-4. As discussed in Chapters 2 and 3, we had a difficult time drilling and logging the hole, and installing packers for pump tests. As was the case with WF-4, we divided WF-5 into three intervals but this time using only two single packers. The double packer configuration was not employed because the cost-versus-benefit ratio had been rather unclear in WF-4. In none of the four pump tests we conducted in WF-4 were we able to hydraulically isolate nonpumping intervals from the pumping interval. It is nearly impossible to tell whether the hydraulic connection between intervals in the same borehole results from packers not sealing well or from natural fractures. Double packers theoretically decrease the chance of intraborehole connection; it may not be worth the extra cost and effort involved. Furthermore, we learned that the more complex the system is, the more prone for something to go wrong (Murphy's Law).

5.3.1 WF-5#2

As discussed in Chapter 3, the FFEC log in WF-5 indicated that there was an inflow point at ~350 ft, a wide inflow zone from 450 to 550 ft, and an inflow point at ~630 ft. Based on this information, the WF-5 borehole was sectioned into three intervals: #1 from GL to 365 ft, #2 from 369 to 579.8 ft, and #3 from 585 to 678 ft. We conducted pump tests in the middle interval first.

Figure 5-10 shows the head transients in selected intervals in WF boreholes during the first pump test, which was terminated prematurely due to a pump failure. The pumping period was slightly more than 2 days at the rate of 2 GPM. As was the case with the pump tests in WF-4,

the pumping rate could not be kept steady, as can be seen in the figure, but we did not expect that to affect the overall results. As can be seen from the figure, the intervals in WF-1 responded noticeably, while no response was observed in WF-2 or WF-3. The heads in WF-1#5 and WF-4#3 are plotted against the left vertical scale, which is magnified. Although small, the two intervals responded. (Note that monitoring continued after the pumping stopped.) Figure 5-11 shows the Horner plot of the recovery period data. As can be seen in the figure, the slope of the asymptotic straight line flattens at small Horner time, indicating the existence of a higher permeability feature. The monitoring of the recovery data ends on 11/1/2011, when a second pump test was started.

The second pump test was initiated after observing the recovery data from the 1st pump test for one week. We would have liked to have waited a little longer, but went ahead with the test because we feared that the rainy season would start soon: rain can cause problems with power and influence observed pressure. Figure 5-12 shows the pressure transients during the 2nd pump test in selected intervals of WF-1, WF-2, and WF-4, as well as the intervals in the pumping borehole, WF-5. The drawdown in the pumping interval was ~27 m at the end of ~8 days of pumping at the rate of 2 GPM (7.6L/min). The interval below the pumping interval, WF-5#3, drewdown 2.6 m and the interval above, WF-5#1, less than 1 m, indicating a relatively good seal by both packers.

Figure 5-13 shows the head changes in various monitoring intervals since the start of the pumping test. Heads in WF-1 are shown in light blue lines, WF-2 in green, and WF-4 in purple. As can be seen in the figure, the intervals in WF-1 (light blue lines) and WF-4#3 (purple broken line) responded noticeably. Within WF-1, the #4 interval drew down most, by 3.2 m, followed by #3 (2.7 m), #2 (1 m) and then #5 (0.8 m). WF-4#3, which is more than 40 m further away, drew down almost the same amount as WF-1#5 did—another indication that the bottom of WF-4 and WF-1 are hydraulically very well connected. Note that as shown in Table 5-2, the 3D distances from the pumping interval to the four monitoring intervals in WF-1 are almost identical: ~90 m, where the 3-D distance is calculated as the closest distance between two line segments in 3-D space. The pumping interval in WF-5 is ~214 ft (64 m) long and oriented 54°E from true north and 30° off vertical, whereas WF-1 is vertical and the five monitoring intervals in it have varying lengths (Figure 5-16). In a homogeneous isotropic continuum, the responses should be identical

when the 3-D distance is the same. One possible explanation for intervals with nearly identical 3-D distance having varying magnitude of responses is that the permeability of the fault zone is anisotropic, with high horizontal permeability and low vertical permeability. Figure 5-16 shows the geometric relationship between WF-5, WF-1, and the Wildcat.

Figure 5-14 shows the head transients in WF-2#2~#5 intervals compared to those in WF-1#5 and WF-4#3. Because the absolute heads are different, they are plotted against two different axes with the same scale. As can be seen in the figure, WF-1#5 and WF-4#3 intervals clearly respond to the pumping, whereas no responses are apparent for the intervals in WF-2.

Figure 5-15 shows the Horner plot of the recovery period of the 2nd pump test in WF-5#2. As can be seen from the figure, the slope of the asymptotic straight line to the late time data (small Horner time) is nearly one-quarter that of the straight line (green) fitted to the data of the Horner time between 10 and 100. This indicates that the pumped interval is connected to a larger permeability feature at some distance, whose transmissivity is estimated to be ~1.1×10^{-5} m^2/s. As mentioned previously, the transmissivity values should be treated as relative.

5.3.2 Permeability Anisotropy of Fault Zone

One of our theories assumes that the intervals WF-4#3 and WF-5#2 straddle the main fault plane of the Wildcat Fault zone. The pressure disturbance created by the pumping tests in those intervals can be thought to have propagated mainly within the fault plane. In analyzing the drawdowns in WF-1 intervals, we noted that the magnitudes of drawdown correlate with the distance in the vertical direction as shown in Table 5-3, where the drawdowns at the end of each pumping are listed. The WF-1#1 interval was considered as nonresponding to either pumping test. It is straightforward to compare the drawdowns in WF-1 during WF-5 pumping, because the 3-D distance is almost the same for all four intervals (#2, #3, #4 and #5), as can be seen in Table 5-2. However, the 3-D distances from the Fd feature in WF-4 to WF-1 intervals vary. Thus, the drawdowns cannot be directly compared as they are—there is a way to compare the drawdowns after some arithmetic manipulations as shown below.

Assuming a developed radial flow, when the Cooper and Jacob (1946) equation can be applied, the drawdown in an isotropic medium can be written as:

$$\Delta h = \frac{2.3Q}{4\pi T} log \frac{2.25Tt}{r^2 S} \quad (1)$$

where Δh, Q, T, S, r and t are the drawdown, flow rate, transmissivity, storativity, radius, and time, respectively. In the x-z coordinate system, $x = r \cdot cos\theta$ and $z = r \cdot cos\theta$, where θ is the angle to the positive x direction. If the medium is anisotropic and the axis of anisotropy is rotated by α from the coordinate axis, the transformation is:

$$\begin{pmatrix} x' \\ z' \end{pmatrix} = \begin{pmatrix} \cos\alpha & -\sin\alpha \\ \sin\alpha & \cos\alpha \end{pmatrix} \begin{pmatrix} x \\ z \end{pmatrix} \tag{2}$$

If the anisotropy ratio of principal direction to minor direction is T_1/T_2, the coordinate system x′ and z′ can be replaced with x″ and z″ where x″ = x′ and z″ $= z'\sqrt{T_1/T_2}$.

Thus in the transformed x″–z″ coordinate system, Eq. (1) is still valid. The dimensionless drawdown can be expressed as

$$\Delta h = \frac{2.3Q}{4\pi\sqrt{T_1T_2}} log \frac{2.25\sqrt{T_1T_2}t}{r^2S} \tag{3}$$

The dimensionless drawdown h_{D1} at radius r_1 can be expressed as:

$$h_{D1} = \frac{\Delta h_1}{\left(\frac{2.3Q}{4\pi T}\right)} = log \frac{2.25Tt_1}{{r_1}^2S} \tag{4}$$

Then the difference of the diemsionless drawdowns at r_1 at t_1 and r_2 at t_2 can be written:

$$h_{D1} - h_{D2} = log \frac{2.25Tt_1}{{r_1}^2S} - log \frac{2.25Tt_2}{{r_2}^2S} = \log\left({t_2r_1^2}/{t_1r_2^2}\right) \tag{5}$$

If the drawdown is measured at the same time, Eq. (3) further reduces to

$$h_{D1} = h_{D2} + 2\log\left({r_1}/{r_2}\right) \tag{6}$$

Thus, the dimensionless drawdown at r_1 can be expressed in terms of the dimensionless drawdown at r_2. Eq. (3) was used to adjust the dimensionless drawdowns at WF-1 intervals during each pump test, using a reference radius. For the WF-4#3 pump test, we chose the distance to WF-1#5, 48.4 m, as the reference distance and used Eq. (4). The adjusted dimensionless drawdown can be seen in the third column from right in Table 5-3. In order to compare the drawdowns in WF-1 during the pumping in WF-5#2 to those during the pumping in WF-4#3, the drawdowns should be adjusted using Eq. (3). This is because we chose to use the

drawdowns at the end of each pumping test with different durations. Alternatively we could use the drawdown value at 7×10^5 seconds for WF-4#3 test as well.

We used Eq. (3) to adjust the drawdowns at WF-1 during the WF-5 pump test so that the drawdowns are at the same t/r^2 value, as shown in Table 5-4. Now, the values in the two right-most columns can be plotted together, as shown in Figure 5-17. In this plot, if the medium is isotropic, all drawdowns at $t_D=16$ would plot on a circle of radius $log_{10}16$ = 1.2. Note that this value is large enough for Copper and Jacob's logarithmic approximation. As can be seen in the figure, the variation in the drawdowns in WF-1 intervals can be explained if the fault zone is a planar feature with 10-to-1 horizontal-to-vertical permeability anisotropy, with the principal axis coinciding with the horizontal axis. One may get a slightly better match with 5° rotation and 12:1 ratio as shown, which for all practical purposes, is not significant. That the fault has anisotropic permeability is consistent with the fact that the Wildcat is a right lateral strike slip fault. Most of the many slickensides we observed in the cores from WF boreholes were indeed horizontal. One would expect enhanced permeability in the direction of fault movement.

Although the fit of ellipse to the drawdowns is relatively good, it appears that the permeability between WF-1 and WF-4#3 is larger than that between WF-1 and WF-5#2. It is possible that the fault that intersects WF-5 may be a splay, and that the higher permeability main fault runs on the east side of WF-1 through WF-4, as Kiho et al. (2012) postulate. It is also possible that the fault is heterogeneous and the permeability is locally lower at WF-5.

5.3.3 WF-5#3

After the pump tests in the #2 interval, we pulled packers to re-configure the plumbing, so that we could pump from the #3 interval. The first trial failed when a packer inflation line became disconnected upon inflation. In the second trail, the bottom packer was punctured by a suspected rock fragment when it was inflated in the hole. Only in the third trial were we finally able to set the packers in place. This is a further illustration of the many problems encountered with this inclined hole.

The pumping interval was set from 178 m to 207 m (585 to 678 ft), the bottom of the hole. As can be seen from the high core recovery rate shown in Figure 3-6 and the core pictures shown in the Appendix, the rock is relatively intact in this interval. As can be seen in Figure 3-19, there

is a distinct inflow point at 192 m. We expect that any permeability in the interval would be associated with this feature.

Figure 5-18 shows the head changes in the pumping interval from 12/10//2012 to 12/28/2012. As can be seen from the figure, the interval drew down very quickly and recovered slowly. The pump was at ~80 m from the surface, but it went dry very quickly. We repeated the pumping many times, hoping to develop the zone. However, as can be seen from the figure, the permeability of the zone did not improve. We ended up pumping/purging the zone 13 times. We used the recovery data from several pumpings for Horner analysis. Figure 5-19 shows the Horner plot of four different tests. The asymptotic straight line to the recovery curves at the late time gives an estimated transmissivity of 5×10^{-8} m^2/s. This value is more than two orders of magnitude smaller than that of the main fault zone. The permeability would be 1.8×10^{-9} m/s when we divided by the zone length, which is still 2 to 4 orders of magnitude larger than that obtained from cores reported by Kiho et al. (2012). Thus, it is probably safe to conclude that the transmissivity from this zone still comes from the fractures.

5.4 Pressure Monitoring

Pump tests are a direct way to estimate the permeability of the subsurface. However, they have limitations. To obtain the permeability values, the flow geometry must be known. Permeability is only pertinent to the radius of influence, which is generally less than 200 m. In order to properly analyze pump tests, the baseline trend of pressure has to be known. Pressure monitoring is not only important to obtain such baseline pressure data for analyzing such pump test, but long-term pressure monitoring can provide useful information regarding hydraulic connectivity between boreholes. It can also provide useful information for estimating the large-scale permeability, which we will discuss in Chapter 7, the hydrologic modeling chapter. In this section, we will focus on the pressure behaviors we observed in WF and SSL boreholes.

5.4.1 WF Boreholes

Figure 5-22, Figure 5-23, and Figure 5-24 show the head transients observed in WF-1, WF-2 and WF-3, respectively, since January 2011. The earlier period of data can be found in Karasaki et al (2011). Also shown in the right axis of the figures is the daily rainfall amount in millimeters. Analysis of these figures leads to several interesting observations:

The effects of the rainfall intensity and amount of rainfall on the observed pressures vary hole by hole. The pressure in WF-2#2 appears to increase and diminish sharply in response to large rain events but not to minor rain events, whereas the magnitude of the seasonal changes is greatest in WF-1 and least in WF-3. This is probably because the total recharge on the east side of the Wildcat is greater than the west side. These facts point to the possibility that WF-1, WF-2, and WF-3 are by and large hydraulically disconnected. This could happen if there exits one (or more) continuous fault core, which is low permeability. However, the longest monitoring data are only two years long. Considering that the rainfall amount varies by more than 50% year to year, longer-duration monitoring data and analysis are necessary to make more definitive conclusions.

The rate of decline of heads in WF-1 during a dry season is roughly 3–4 m/year. These data can be used to calibrate or verify a hydrologic model. This issue will be discussed further in Chapter 7.

The head of the topmost interval in all of the holes is higher than the rest of the intervals in the same hole. The WF-2#1 and WF-3#1 interval do not respond to the rainfall events as much as WF-1#1. In particular, the head in WF-3#1 increases steadily without much regard to the rainfalls or pump tests. There may be a perched zone in WF-2 and WF-3, where the lithology near the surface is Orinda Formation., which is predominantly low permeability siltstone.

The drilling of WF-4 affected pressures in WF-1 and WF-2. When the depth was near 250 ft, the #3, #4 and #5 monitoring intervals in WF-2 responded. These were upticks in the pressure, probably due to the high circulation pressure in WF-4, which is believed to have propagated through the Fc feature, as shown in Figure 5-20. More notable are the responses observed in the WF-1 intervals, particularly in #5, when the drilling depth passed 183 m (600 ft) on Sept. 14th, 2010 (see Karasaki et al., 2011). The pressure disturbance is believed to have traveled through the Fd feature shown in Figure 5-20. The drilling of WF-4 did not affect WF-3.

The pressure in WF-1#2 dropped quite markedly three times: on 9/21/2010, 4/27/2011, and 1/16/2012, as can be seen in Figure 5-22. We initially suspected that the sensor became defective. But the pressure tracked the trend of the adjacent interval, which a defective sensor could not do. One possible explanation is that the steeply east dipping Claremont Formation has hydraulically semi-compartmentalized layers, as shown in Figure 5-25. The WF-4#3 interval is open to all the

layers with different heads that decrease in the westward direction, and it serves as an intermittent short-circuit path for the #2 interval. The #2 interval originally had the 2nd highest head among the five intervals, but owing to the three time head drops, it is now at about the same head as the #4 interval. If this theory is correct, the head in #2 should never become lower than that of WF-4#3, which remains to be seen. Another explanation may be that the pressure drops are due to the partially and intermittently leaky casing joints in WF-1. However, intermittency is more likely to happen in the open WF-4#3 interval than in WF-1, which is sand packed.

The pumping in WF-4#3 and other pressure-disturbing activities, including packer installations and plug failures, affect the pressure in the WF-1 zones, with the magnitude of response in decreasing order from #5 to #2. The 3-D distances from the WF-4#3 to these zones do not vary much, as can be seen in Table 5-2. However, the vertical distances vary from 19 m to 84 m. These phenomena can be successfully explained by the model shown in Figure 5-21.

As can be seen in Figure 5-23, the pressure response in WF-2#2 to rainfall events is sharp and large, although the interval above, WF-2#1 is practically unresponsive. This could mean that WF-2 is in the landslide zone, that the bottom of the landslide plane may be quite permeable and is connected to WF-2#2, and that the #1 interval is either in a low permeability landslide material or grouted in by mistake.

WF-3's only marked transients come from the pumping in WF-4. The disturbance likely propagated through the Fc feature. As can be seen in Figure 5-24, the magnitude of response is greatest in #5, where the Fc feature intersects, and the magnitude decreases with the decrease in the interval number (higher elevation).

On November 30, 2011, the packer configuration was changed in WF-4. Starting on this date, the pressures began changing in WF-2 and WF-3. It is suspected that the work in WF-4 changed the plumbing of the Fc feature.

5.5 All WF Boreholes

Figure 5-26 shows the head changes of selected intervals in WF boreholes since August 1st, 2011. As opposed to the plots in Figure 5-22, Figure 5-23, Figure 5-24 and
Figure 5-27, where the actual head values are plotted, it is easier in this figure to compare the magnitude of changes between intervals. As can be seen from the figure, WF-1 appears to be

most responsive to the rainfall (and to the lack thereof). During the dry months, the head decreased more rapidly than the other WF holes, and increased more than those other holes after rain events except for WF-2#2, which sharply responded to the rainfall events in late January 2012. The head of the intervals in WF-1 declined by ~2 m over a half-year period, as indicated by the green ellipse, whereas the intervals in WF-2 and 3 remained relatively flat (red ellipse). This indicates that WF-1 may be in a separate hydrologic system from that of WF-2 and WF-3, p due to the low permeability core(s) of the Wildcat Fault zone.

5.5.1 SSL Boreholes

A pump installed in SSL-1, which is historically called the Shively well (Convers Consultants, 1984), to mitigate landslides has been pumping at 38 liter/min (10 GPM) over 35 years. We installed flow and pressure sensors in these boreholes for our project, as described in Karasaki et al. (2010).

Figure 5-27 shows the pressure transients in SSL-1 and SSL-2 since the installation of sensors and the daily precipitation measured at LBNL. Installation of a sensor in SSL-2 (10/21/2009) predates that of SSL-1 (2/1/2010). (The location of the SSL holes can be found in Figure 5-1.) Spikes on the SSL-1 pressure curve in 2010 result from an accidental shutdown of the pump due to unknown causes. As can be seen from the figure, the pressure has been declining ever since the monitoring started. The effects of precipitation can be seen from the slowdown of the pressure decline since the beginning of this year. The pumping rate and the water-level data are used to constrain the hydrologic model described in the next section.

While it was not meant to be a pump test, and the initial conditions and other borehole parameters (such as the screen length and locations) are not known, the pumping in SSL-1 was effectively a pump test. The pressure drawdown is plotted against a time log in Figure 5-28, using the time of the restart of pumping as time zero. As can be seen from the figure, two straight lines can be fit to the drawdown curve. Using the Jacob's method, we obtain a transmissivity of 3.0×10^{-5} m^2/s from the first slope and $8.3\times10^{-6} m^2/s$ from the second slope. Because the screen length is not known, it is difficult to calculate permeability. The maximum zone length would be 100 m, which is the approximate length of the borehole, and the minimum would be the current water level above the pump, ~30 m. We use this number to arrive at the high and low permeability listed in Table 5-1. That there are two straight-line portions in the drawdown curve, and that the latter slope is ~1/4 of the former, indicate that the aquifer is limited in extent, perhaps by a fault or faults.

Figure 5-27 shows a couple of humps (increases and decreases in pressure), first in mid-February 2010 and the second in late April 2010. The first hump was initially thought to be the response to the pump shut-off in SS-1 for the sensor installation reaching the peak 20 days after

the restart of the pump in SSL-1. However, the second hump was observed in late April without any activities in SSL-1 to cause such an increase. This hump is most likely caused by the infiltration of the rain, as can be seen from the precipitation rate during those months. At this time we are not sure if the first hump was an actual interference signal from SSL-1. Lennert (1979) reported that there is the "University Fault" between the two wells, and that the wells are hydraulically separated by it, although the findings of the Converse Consultants (1984) refute the existence of such a fault.

On August 18, 2011, we switched off the pump and observed pressure recovery in SSL-1 and SSL-2 for two months until October 18, when we turned the pump on again. We chose the timing so that it would not have a negative impact on slope stability mitigation, which is why the borehole is there in the first place. Summer time is usually the driest season in the Bay Area, although it did rain some in July and August 2011. Although we wanted to have a longer shut-off period, we could not wait too much longer because the rainy season typically starts in November. During this shut-in test, we began drilling WF-5, which in retrospect was not a very good idea: We would not know if any changes in pressure in the intervals of WF boreholes were caused by the drilling or the shut-in test. In November, we replaced packers in WF-4, which created disturbances in WF-2 and WF-3 intervals, which could overlap with the signal from the shut-in. It took ~17 days for the disturbance of shut in to propagate from SSL-1 to SSl-2, which are ~135 m apart. Assuming a radial flow in a homogeneous medium, it would take 10 times longer or 170 days for the signal to reach WF-3, which is 443 m away from SSL-1.

The Horner time is defined as the ratio of the time since the start of pumping to the shut-in duration. Thus, the time of the start of pumping has to be known. To calculate transmissivity, the average pumping rate has to be known. However, there is not much record left regarding the SSL-1 borehole. The pump itself was replaced several times, which required stopping it for some time. Most recently, the pump was stopped and pulled to replace it with a new one and to install sensors from January 12th to February 1st, 2010. Figure 5-29 shows the Horner plot of the shut-in period. It shows two sets of data: one assuming that the pump was started on April 15, 1975, soon after the drilling; and the other on February 1st, 2010, when the current pump was installed. As can be seen from the figure, the asymptotic straight line of both curves has nearly identical

slope, which yields the transmissivity of T = 1.7 × 10^{-5} m^2/s. It shows the robustness of the Horner analysis. This value is comparable to that of the drawdown analysis shown in Figure 5-28.

For both curves, the Horner time is larger than ideal for straight-line analysis—the curves could develop an inflection at late time. Thus, it would have been better to have allowed for a longer recovery period. An average flow rate of 10 GPM was used to arrive at the transmissivity, which is the rate that has been actually observed since February 1, 2010. Prior to that, there was no flow meter, and hand recordings reported by Converse (1984) between 1979 and 1983 were anywhere from 12–84 GPM, including several periods with no pump operation. Thus, the average rate over the 30-year period can only be guessed. For example, if the average rare is 20 GPM, the transmissivity would be twice, i.e., 3.4 × 10^{-5} m^2/s.

The difference between the two curves is the Y-intercept, which indicates the initial head. The Y-intercept of the line for April 15, 1975, would show 347 m as the initial head, whereas the intercept of the line for February 1, 2010 shows 337 m. On December 7, 1983, the head was reported to be 333 m (200 ft below GL of 393 m), when a pump was replaced. Thus, the initial head of 347 m may be a good estimate.

Note in Figure 5-27 that the head increased from the mid-March to the beginning of August 2011 despite the pumping. Apparently, heavier-than-usual rainfall caused this rise. In the previous year, there was a very small increase in SSL-2, almost indistinguishable because the pump in SSL-1 had been stopped until January 30th, which also caused the level rise in SSL-2. As can be seen from the figure, it can be estimated that the rise in water level due to rainfall is ~8 m. Although rather crude, one can estimate the porosity of the Moraga Formation into which SSL-1 is drilled if the recharge rate is known (assuming it is uniform), or vice versa. For example, if the recharge rate is 120 mm, 10% of the rainfall amount of 1200 mm for the time duration, the porosity would be *120÷8000 = 0.015*. We will use this information in Chapter 8 when we model the recharge events.

5.5.2 Hydraugers

As part of landslide mitigation efforts, there have been many hydraugers drilled into the hills of the LBNL site, in order to drain water off the hills. Many of them were drilled some 30 years ago, and not much of a record has been kept on them. Some were destroyed by new road and building construction, and some collapsed naturally. Some locatable outfalls of hydraugers have

no flow, but we have identified three hydraugers that have significant flow (Figure 5-30). Lennert-1 is the longest, over 1200 ft in length, which produced >2000 GPM initially. It was drilled in the direction of Well 789-1, which we now call SSL-2. The flow meter we installed at the outfall in 2011 measures only 7–8 liters/min throughout the year (Figure 5-31). It may very well be broken somewhere in the middle—the flow rate does not seem to correlate to the rainfall. Another hydrauger that produces an even more significant amount of water is Quarry-1, with 23–61 liters/min. This hydrauger was installed to drain the artesian well dug by a farmer who used to have a ranch nearby before LBNL was built. These outflow data are taken into account in the hydrogeologic model discussed in Chapter 7, Hydrologic Modeling.

5.6 Conclusions

In this chapter, we discussed the analysis results of the hydraulic tests and monitoring of pressure/temperature over a two-year period in and around the Wildcat Fault zone. Below are summary observations and conclusions.

- A near-vertical high-permeability planar feature associated with the Wildcat or the main fault plane itself is penetrated by WF-4 at ~600 ft and by WF-5 at ~450 ft. This feature runs very close to WF-1.
- The transmissivity of the Wildcat Fault zone is at a minimum 1×10^{-5} m^2/s, which is 2~3 orders of magnitude larger than that of the protolith Claremont Formation.
- The transmissivity near WF-5 is less than that near WF-1 and WF-4 bottom. One explanation is that the main Wildcat extends to the east of WF-5—a theory promoted by Kiho et al. (2012). Another possible explanation is that the permeable zone is heterogeneous and that the degree of damage is a function of depth. The elevation difference between the permeable zone in WF-5 and WF-4 is approximately 60 m.
- The permeability of the fault zone is anisotropic, with 10 times higher horizontal permeability.
- Fractures and faults are responsible for all the transmissivity values.
- WF-1 and WF-2 may be separated by a low permeability feature. This is evidenced by (1) a ~10 m head separation between WF-1 and WF-2, as shown in Figure 5-33, (2) Response to WF-5 pumping is seen in WF-1 but not in WF-2; (3) WF-1 and WF-2

have different seasonal head fluctuations; and (4) a distinct difference in buildup behavior between the two boreholes, as shown in Figure 5-32.

- When WF-4#3 was pumped, WF-1 responded markedly, while WF-2 responded slightly; when WF-4#2 was pumped, WF-1 responded slightly. Although we do not know for certain whether the hydrologic connection is natural or an artificial short-circuit through the borehole, we suspect the latter.
- The common practice is to use a few packers to isolate intervals in boreholes to conduct pump tests or monitor responses. However, if the hole is long, open intervals become very long, which can cause artificial short-circuits. We propose that long, continuously sealing packers be developed and used (more on this in Chapter 8).
- Based on our experience, it is probably better to use vertical boreholes on opposite sides of a fault to test the hydraulic connection across a fault, rather than an inclined hole.
- The head profiles in WF-1–WF-3 holes indicate that there is a downward gradient, which suggests that the entire site is in a recharge zone.
- Long-term passive pressure monitoring may be useful in discriminating hydrologic systems at a larger scale than borehole hydraulic tests.
- Calculating permeability from transmissivity is not trivial in fractured rock. Straight averaging by the zone thickness can be misleading.

5.7 References

Converse Consultants, 1984, Hill Area Dewatering and Stabilization Studies, Report No. 037.

Cooper, H.H., J.D. Bredehoeft, and I.S. Papadopoulos, 1967, Response of a finite-diameter well to an instantaneous charge of water, Water Resources Research, 3, pp. 263-269.

Cooper, H.H. and C.E. Jacob, 1946,A generalized graphical method for evaluating formation constants and summarizing well field history, *Tans. Amer. Geophys. Union,* 27, pp. 526-534.

Karasaki, K., Onishi, C.T., Doughty, C., Gasperikova, E., Peterson, P., Conrad, M., and Cook, P., 2011, Development of Hydrologic Characterization on Technology of Fault Zones – Phase II 2nd Report–, NUMO-LBNL-CRIEPI Collaboration Research Project.

Karasaki, K., Onishi, C.T. and Zimmer, V., 2010, Development of Hydrologic Characterization on Technology of Fault Zones – Phase II Interim Report-, NUMO-LBNL-CRIEPI Collaboration Research Project.

Karasaki, K., C.T. Onishi, and Y.S. Wu, 2009, Development of Characterization Technology for Fault Zones, LBNL-1635E, pp 157.

Karasaki, K., J.C.S. Long, P.A. Witherspoon, 1988, Analytical Model of Slug Tests, Water Resources Research, 24(1), 115-126.

Kiho, K., Ueta, K., Miyakawa, T., Hasegawa, T., Ito, H., Hamada, M., Nakada, H., Tanaka, S., and Tsukuda, K, 2012, CRIEPI Technical Report, Survey and Analysis related to Development of Hydrologic Characterization Technology of Fault Zones IV.

Lennert and Associates, 1979, Hill Area Dewatering Program, Letter Report from Lennert to CP Russo, Job 789, November 26, 1979 includes map and plates.

Table 5-1 Calculated transmissivity and averaged permeability in WF and SSL boreholes.

	Geology	Zone Length(m)	Transmissivity (m^2/s)	K (m/s)
WF-1 bottom	Tc	117	9.5E-05	8.1E-07
WF-2 bottom	Tc	76	1.2E-06	1.6E-08
WF-3 bottom	Tsp/Tc	112	2.3E-07	2.1E-09
WF-4 middle	Tc	45	4.2E-6	9.3E-8
WF-4 bottom	Tc/Wildcat	33.7	5.2E-5	1.5e-6
WF-5 middle	Tc/Wildcat	64	1.1E-5	1.7E-7
WF-5 bottom	Tc	28	5E-8	1.8E-9
SSL-1	Moraga Volcanic	30	3.00E-05	1.0E-06

Table 5-2 Comparison of distances between the pumping zones to monitoring intervals in WF boreholes.

	Coordinates of Interval Top (UTM)			Coordinates of Interval Bottom (UTM)			Distance								
	x1	y1	z1	x2	y2	z2									
WF-4#2	566908.9	4192509.4	204.8	566928.8	4192520.3	166.8	WF-4#2 Pumping			WF-4#3 Pumping			WF-5#2 Pumping		
WF-4 Fc	566918.8	4192514.8	185.9	566918.9	4192514.9	185.7									
WF-4#3	566929.9	4192520.9	164.7	566972.4	4192544.3	83.4	3-D distance from:		Vertical distance from Fc	3-D distance from:		Vertical distance from Fd	3-D distance from:		Vertical distance from Fd
WF-4 Fd	566960.8	4192537.9	105.6	566960.9	4192538.0	105.3									
WF-5#2	566871.0	4192638.9	203.1	566896.7	4192656.9	146.4	WF-4#2	WF-4 Fc		WF-4#3	WF-4 Fd		WF-5#2	WF-5 Fd	
WF-5 Fd	566890.4	4192652.5	160.3	566890.5	4192652.6	160.4									
WF-1#1	566936.7	4192575.2	273.4	566936.7	4192575.2	254.9	87.2	93.4	69.0	105.5	155.8	149.3	105.2	130.6	94.5
WF-1#2	566936.7	4192575.2	249.4	566936.7	4192575.2	189.7	60.0	63.0	3.7	60.2	95.1	84.1	90.3	94.8	29.3
WF-1#3	566936.7	4192575.2	185.1	566936.7	4192575.2	165.9	55.5	62.9	0.8	52.5	74.9	60.3	89.9	90.3	5.5
WF-1#4	566936.7	4192575.2	160.1	566936.7	4192575.2	148.8	55.9	67.9	25.8	48.4	62	43.3	90	90.1	-0.2
WF-1#5	566936.7	4192575.2	142.3	566936.7	4192575.2	124.8	60.6	76.4	43.7	44.9	48.4	19.2	91	91.9	-18.0
WF-2#1	566886.2	4192537.4	264.6	566886.2	4192537.4	245.4	54.3	71.5	59.4	93.2	158.5	139.8	111	143.2	85.0
WF-2#2	566886.2	4192537.4	240.8	566886.2	4192537.4	217.0	38.1	50.4	31.1	70.1	134.1	111.5	103.6	128.4	56.6
WF-2#3	566886.2	4192537.4	211.9	566886.2	4192537.4	192.4	36.0	40.2	6.4	54.3	114.5	86.8	102.6	119.6	32.0
WF-2#4	566886.2	4192537.4	186.9	566886.2	4192537.4	163.1	38.4	39.7	0.9	46.7	94.2	57.5	103.9	115.2	2.7
WF-2#5	566886.2	4192537.4	157.6	566886.2	4192537.4	124.1	46.3	48.6	28.3	47.2	76.9	18.5	110.9	115.2	-2.7
WF-3#1	566812.8	4192492.6	245.8	566812.8	4192492.6	218.4	98.5	113.1	32.4	131.9	191.5	112.8	158.2	187	58.0
WF-3#2	566812.8	4192492.6	215.3	566812.8	4192492.6	191.5	97.6	108.4	5.6	123.4	177	86.0	157.5	180.5	31.1
WF-3#3	566812.8	4192492.6	188.2	566812.8	4192492.6	142.5	99.0	108.3	2.2	120.5	159.1	36.9	158.2	177.7	0.0
WF-3#4	566812.8	4192492.6	188.2	566812.8	4192492.6	142.5	99.0	108.3	2.2	120.5	159.1	36.9	158.2	177.7	0.0
WF-3#5	566812.8	4192492.6	139.4	566812.8	4192492.6	115.9	117.1	46.5	46.5	123.1	155.1	10.4	169.8	179	-20.9
WF-4#1	566886.2	4192492.1	265.0	566907.8	4192508.8	206.9							135.3	152.1	46.5
WF-4#2	566908.9	4192509.4	204.8	566928.8	4192520.3	166.8							134	137.8	6.4
WF-4#3	566929.9	4192520.9	164.7	566972.4	4192544.3	83.4							135.2	136.2	0.0
WF-4fd	566890.4	4192652.5	160.3	566960.8	4192537.9	105.6							141.2	145.2	54.7
WF-5#1	566826.5	4192607.7	301.0	566870.6	4192638.6	203.9	133	134	17.9	137.5	167.2	98.3			
WF-5#2	566871.0	4192638.9	203.1	566896.7	4192656.9	146.4	134	134.1	0.0	135.2	141.2	40.8			
WF-5#3	566897.2	4192657.3	145.3	566908.6	4192665.2	120.3	142.2	149.6	-40.3	137	138.3	14.7			

Table 5-3. Adjusted dimensionless drawdowns in WF-1 intervals in response to the pumping in WF-4#3 and WF-5#2.

	Monitoring Interval	3D Distance	Elevation difference	Dx (m)	Arctan	Drawdown Δh (m)	Dimensionless drawdown h_D	Distance adjusted h_D	Δh_{DX}	Δh_{DZ}
WF-4#3	WF-1#2	95.1	84.1	44.4	1.09	0.18	0.05	0.64	0.30	0.56
	WF-1#3	74.9	60.3	44.4	0.94	1.00	0.29	0.67	0.40	0.54
	WF-1#4	62.0	43.3	44.4	0.77	2.40	0.69	0.91	0.65	0.63
	WF-1#5	48.4	19.2	44.4	0.41	5.70	1.65	1.65	1.51	0.65
WF-5#2	WF-1#2	94.8	29.4	-90.1	2.83	1.00	0.43	1.40	-1.33	0.43
	WF-1#3	90.3	5.6	-90.1	3.08	2.70	1.17	2.10	-2.09	0.13
	WF-1#4	90.1	-0.2	-90.1	3.14	3.10	1.34	2.27	-2.27	0.00
	WF-1#5	91.9	-18.0	-90.1	3.34	0.80	0.35	1.29	-1.26	-0.25

Table 5-4. Parameters used to non-dimensionalize, adjust distance and fit an ellipse shown in Figure 5-17.

Pumping Zone	Q		T (m^2/s)	S	Time (S)	Reference radius (m)	t/r2	t_D	Log(t_D)
	GPM	L/min							
WF-4#3	3	1.89e-4	1.0E-05	1.0E-03	1.70E+6	48.4	7.26E+02	16.3	1.2
WF-5#2	2	1.26e-4			7.0E+5	31			

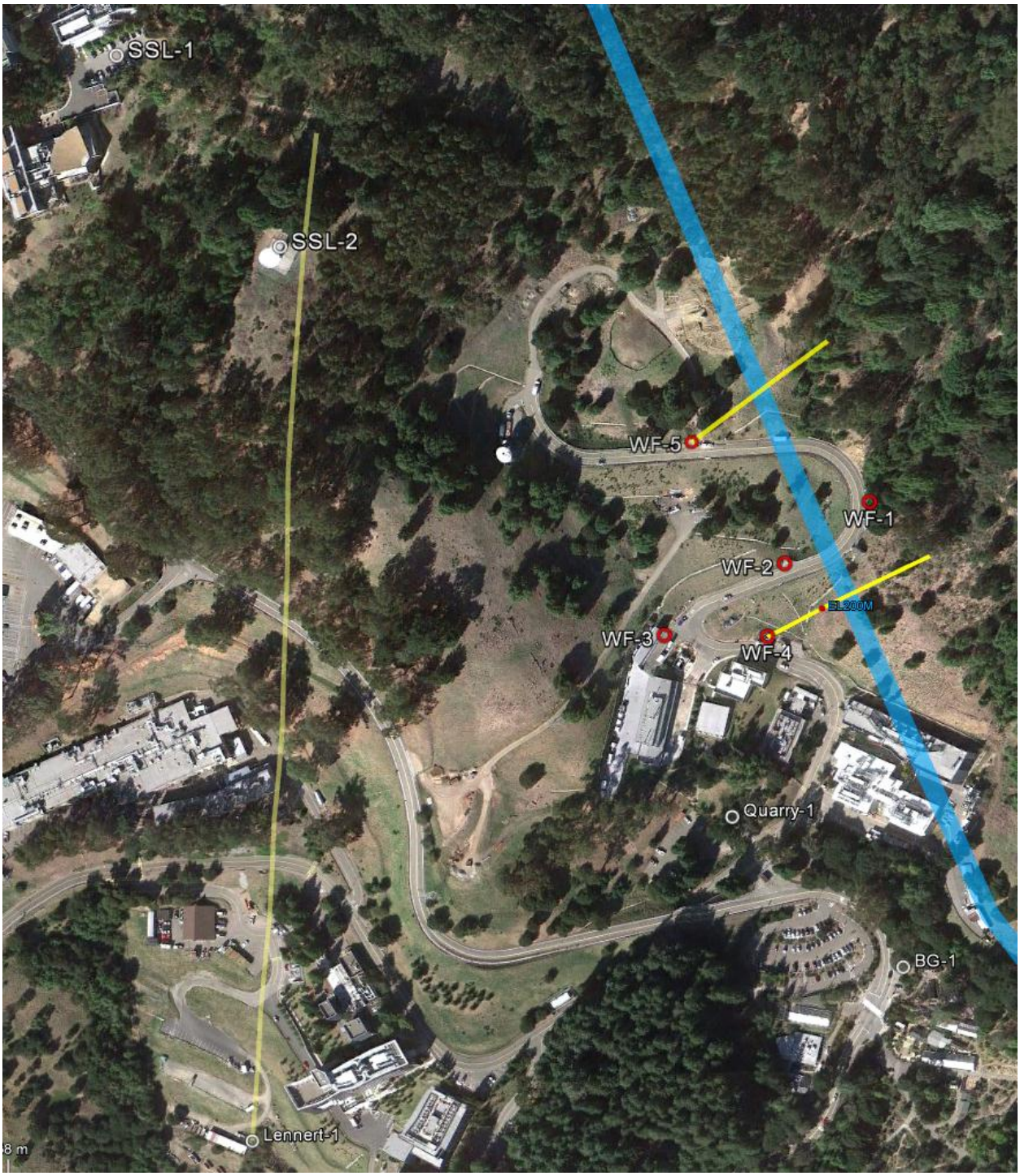

Figure 5-1. Aerial map of the boreholes in the study area incluindg WF-1~5 and SSL-1~2. Also shown are hydraugers, Lennert-1, Quarry-1 and BG-1.

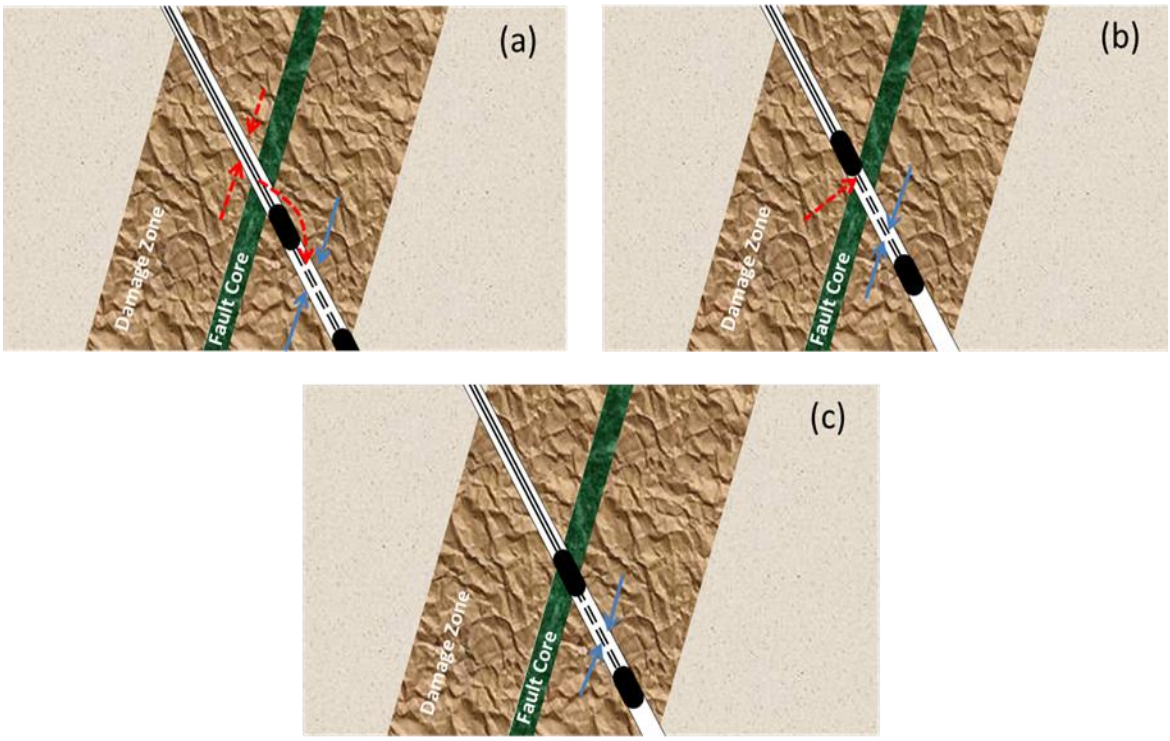

Figure 5-2. Packer locations in relation to fault core with red arrows indicating short-cut paths. Packer is located either (a) below or (b) above the fault core to allow for leakage through borehole. (c) Packer is placed just right at the fault core.

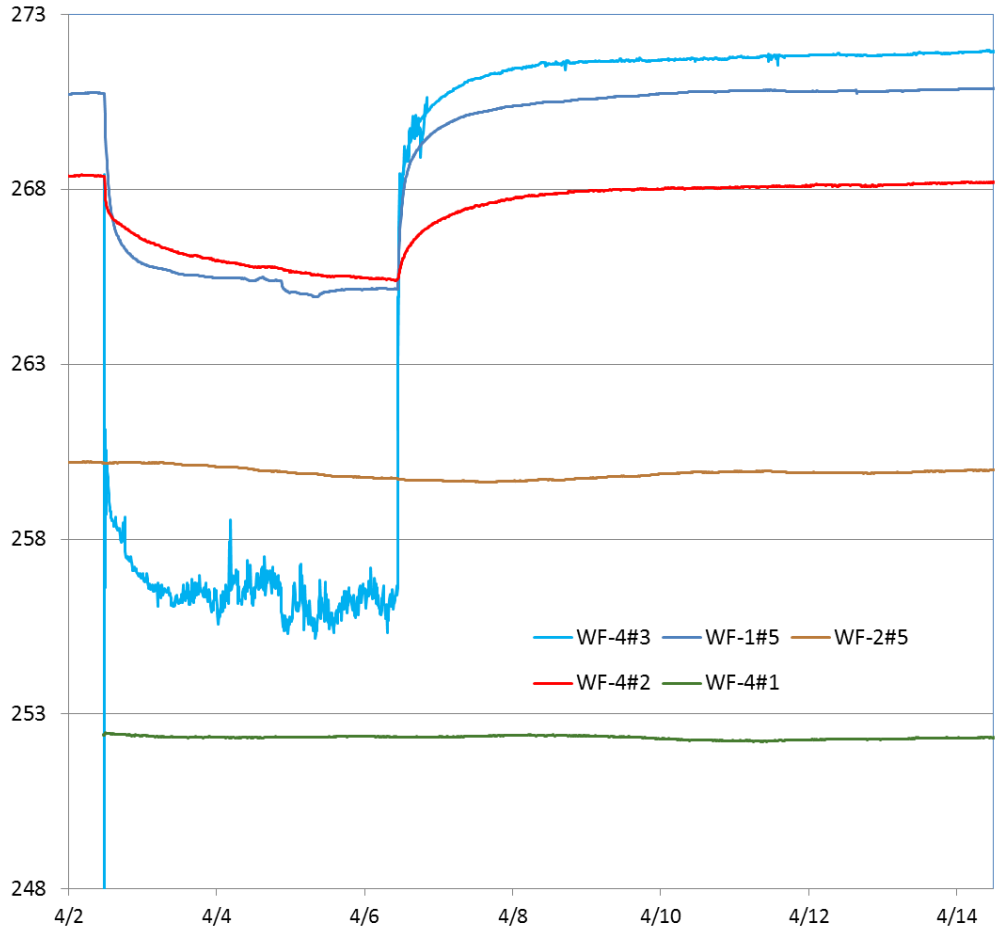

Figure 5-3. The pressure transients of the pump test in WF-4#3. Note the quick response in WF-1#5. WF-4#2 also responds. The pressure sensor readings in the pumping zone became very noisy duruing the pumping. It failed and was replaced during the recovery period.

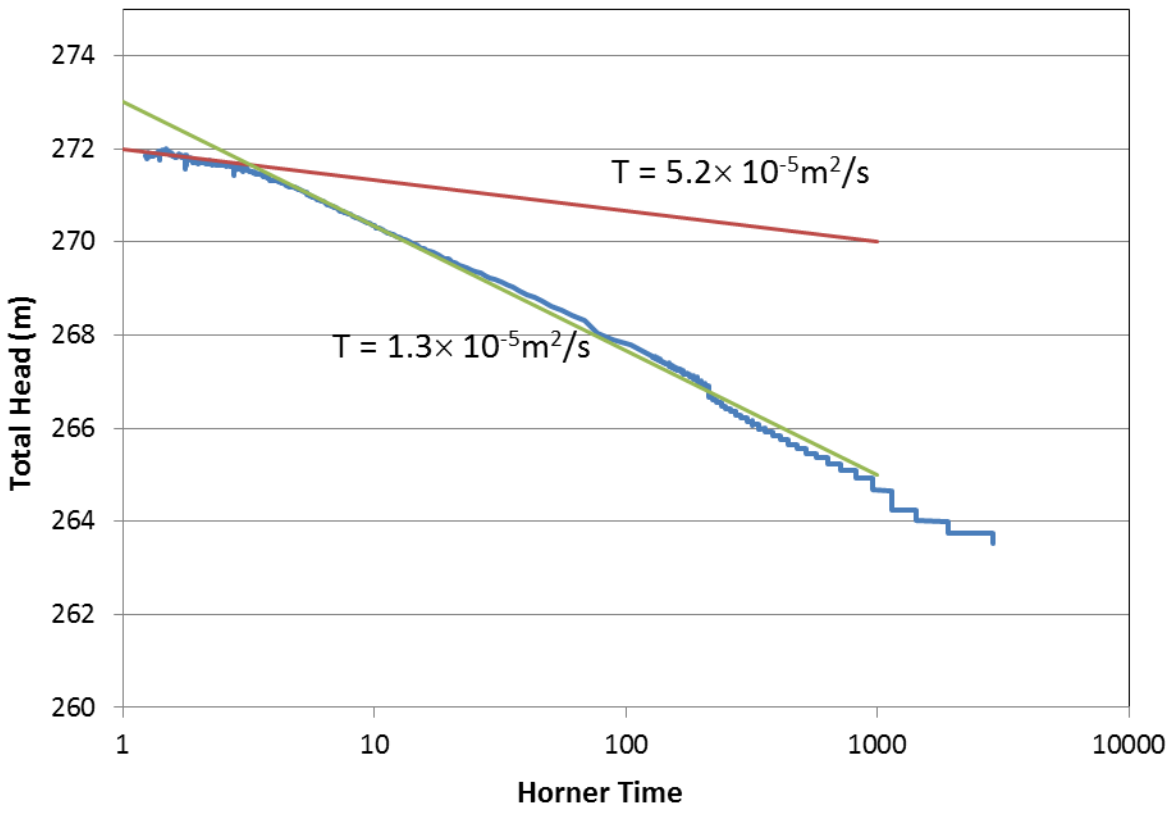

Figure 5-4. Horner plot of the recovery data of the 2nd WF-4#3 pumping test. Note that the slope flattens to nearly half at large time (near unity in Horner time).

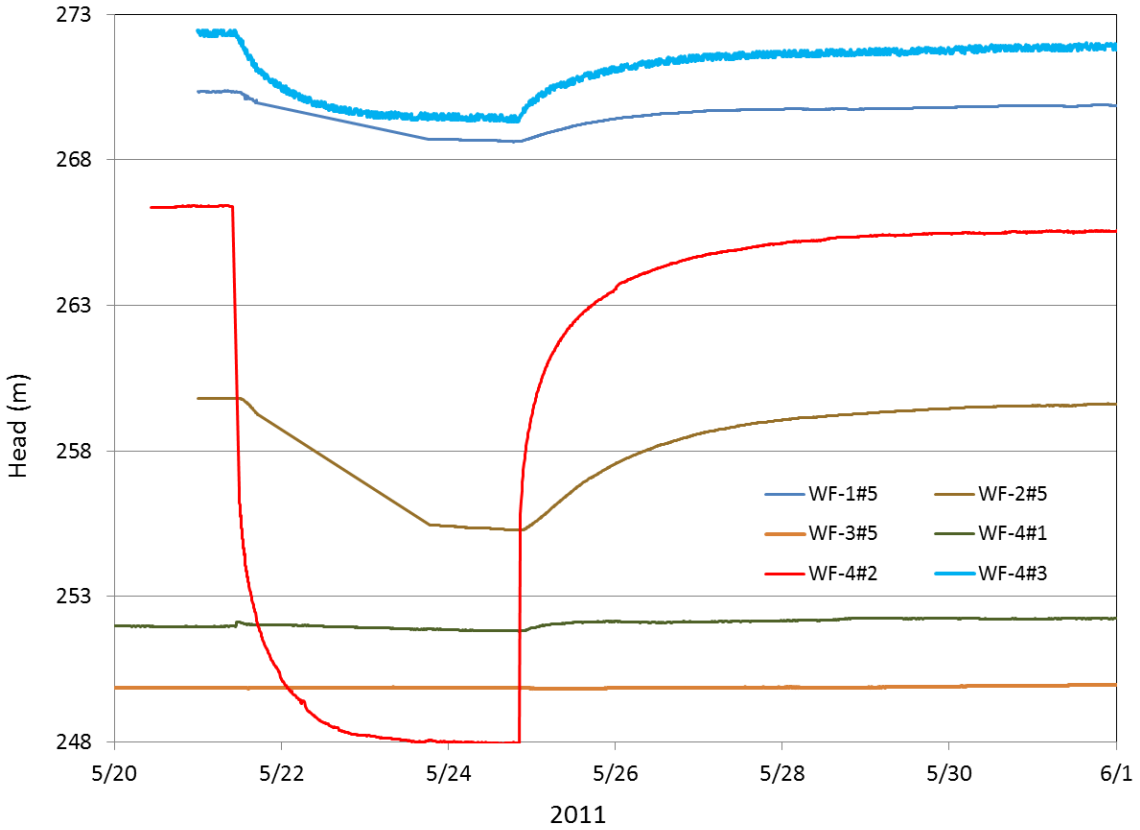

Figure 5-5. Pressure transients during a pump test in WF-4#2 (231–486 ft) started on 5/21/2011. WF-2#5 responded most. The response in WF-1#5 is believed to be due to the drawndown in WF-4#3.

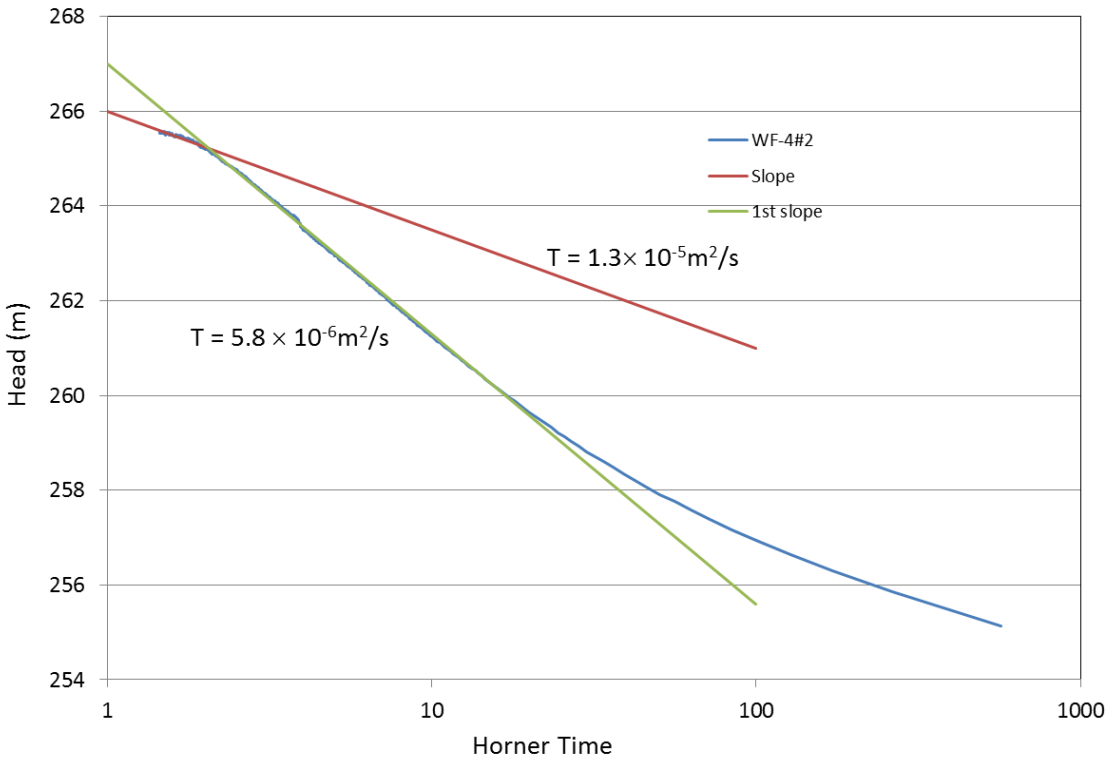

Figure 5-6. Horner plot of the recovery data of WF-4#2 (231–486 ft) pumping test. Note that the slope halves at large time (near unity in Horner time).

.

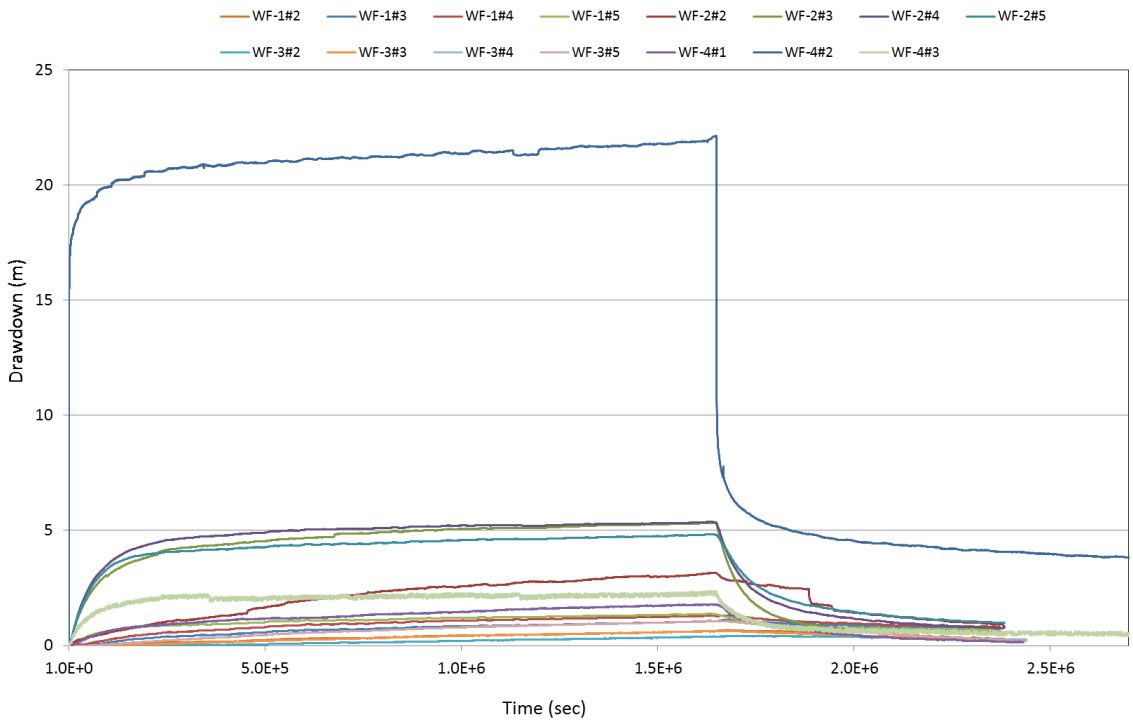

Figure 5-7. Drawdown responses in WF-1#2~5, WF-2#2~#5, WF-3#2~5 as well as WF4#1,during the pumping in WF-4#2. Note that the pressure in the pumping interval did not recover fully to the pre-test level. The zones in WF-2 responded much stronger than those in WF-1 and -3.

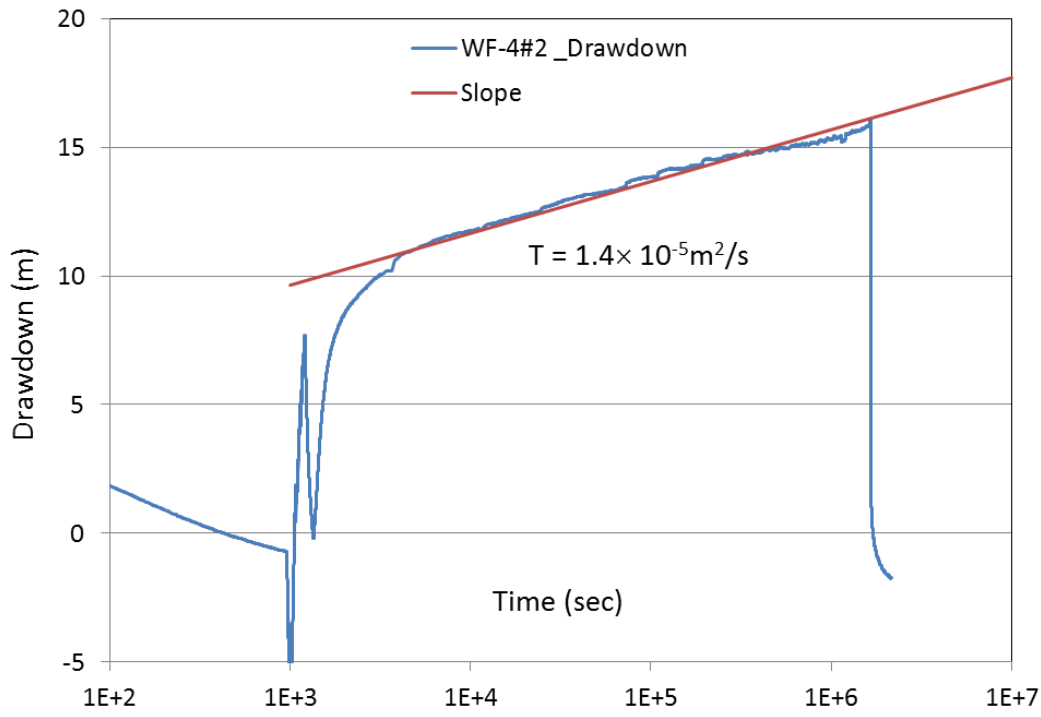

Figure 5-8. Semi-log plot of the drawdown in the pumping zone during the WF-4#2 pumping test and the straight line analysis.

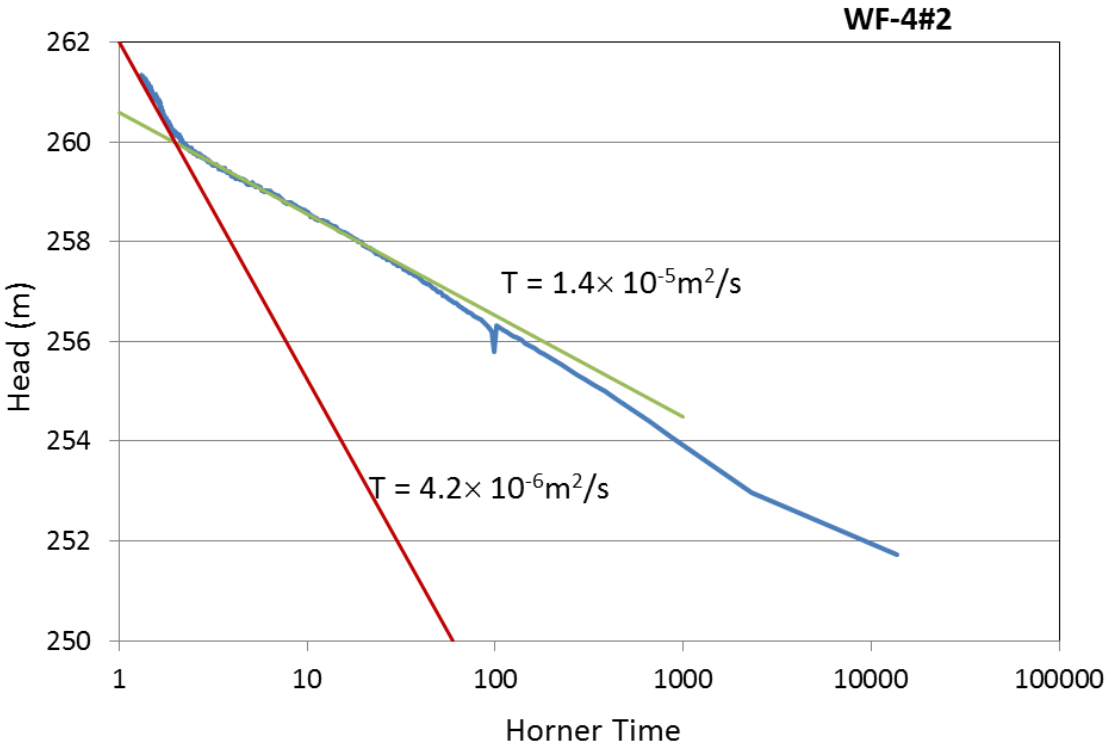

Figure 5-9. Horner plot of the recovery data of the 2nd pump test in WF-4#2.

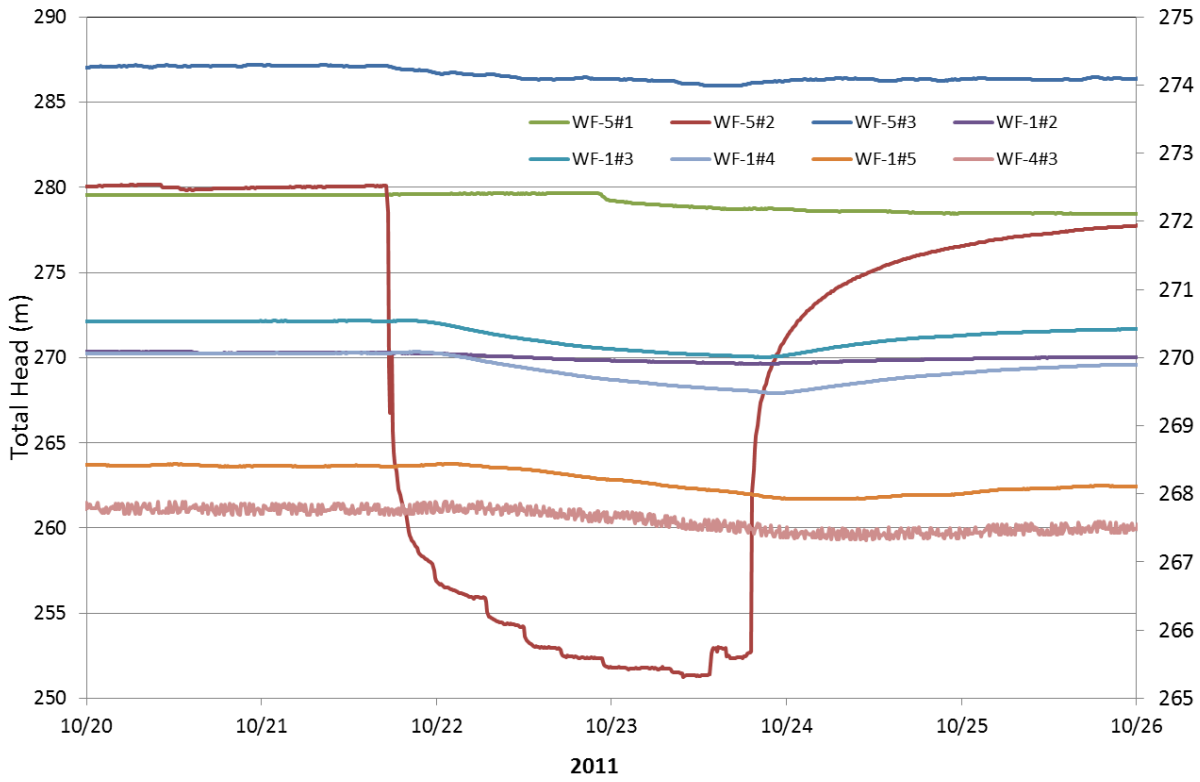

Figure 5-10. Head transients in selected intervals of WF-1, WF-2 and WF-4 during the first pump test in WF-5#2. WF-1#3,4,5 and WF-4#3 responded. The head in WF-1#5 and WF-4#3 are plotted against the right axis for maginifcation. No responses in WF-2 zones are detected.

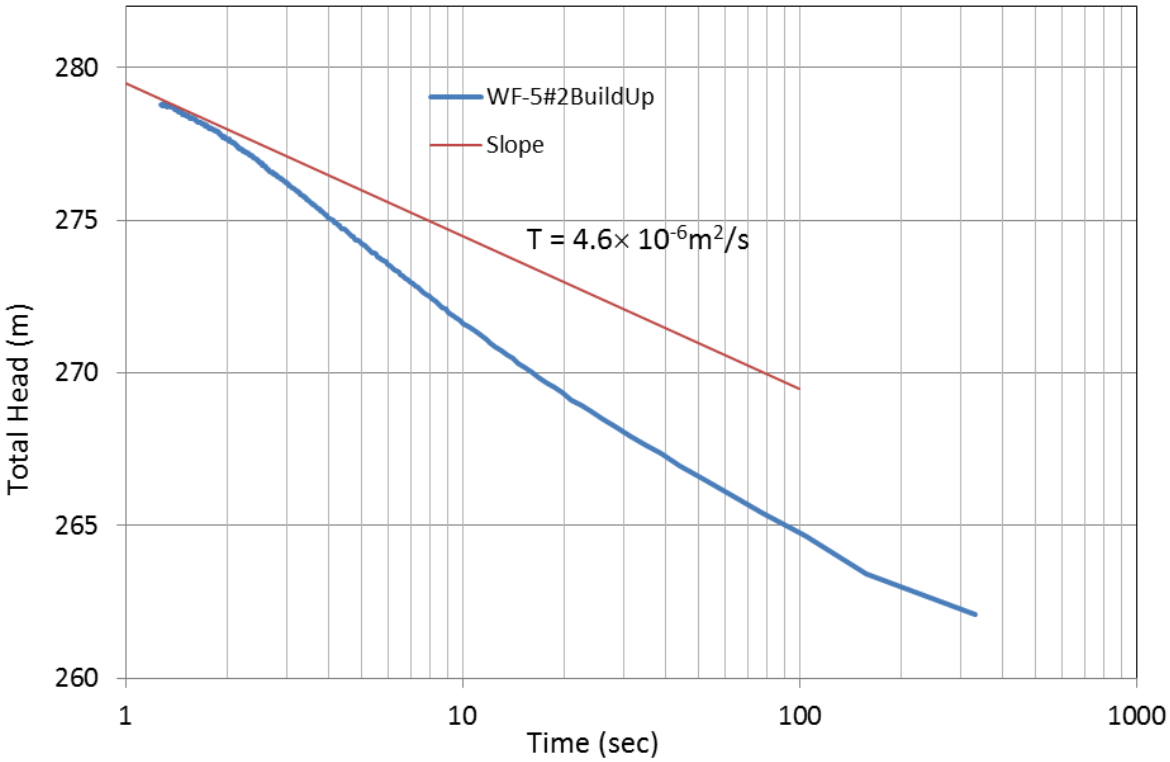

Figure 5-11. Horner plot of the recovery period of the 1st pump test in WF-5#2.

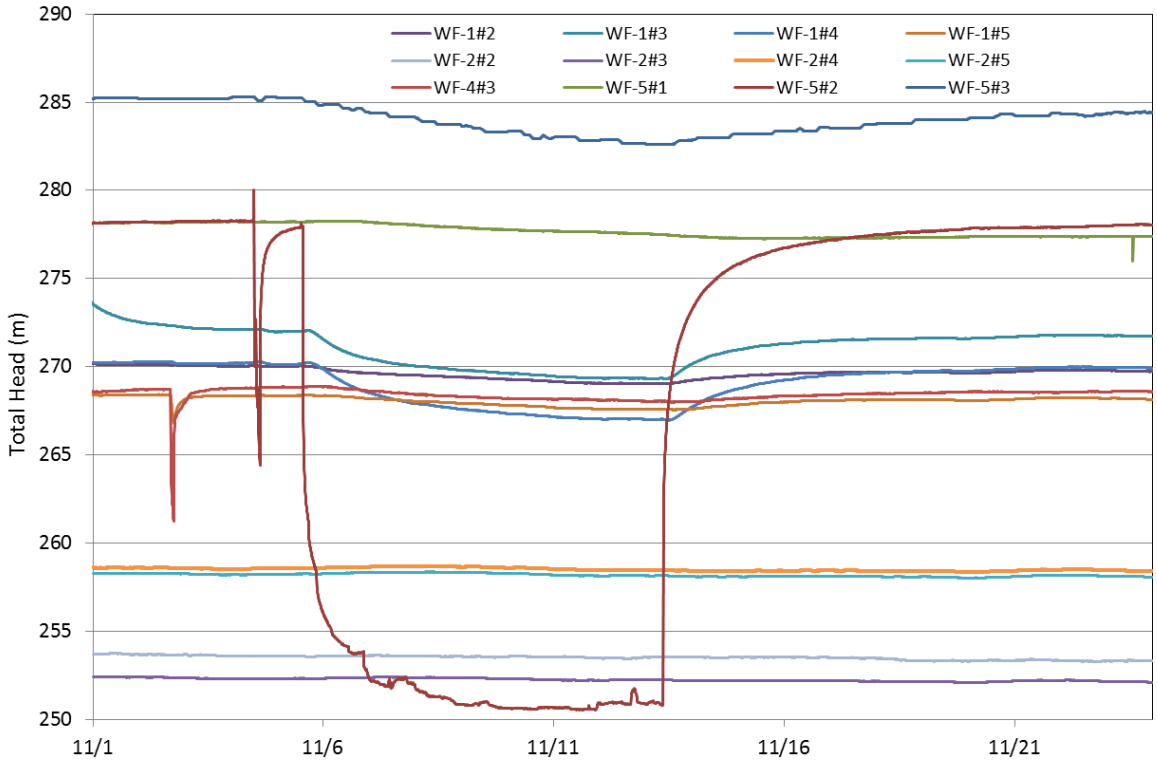

Figure 5-12. Pressure response in WF-1, WF-2 and WF-4 invervals to the 2nd pumping in WF-5#2. Zones in WF-1 and WF-4#3 respond clearly. No responses in WF-2 zones are detected.

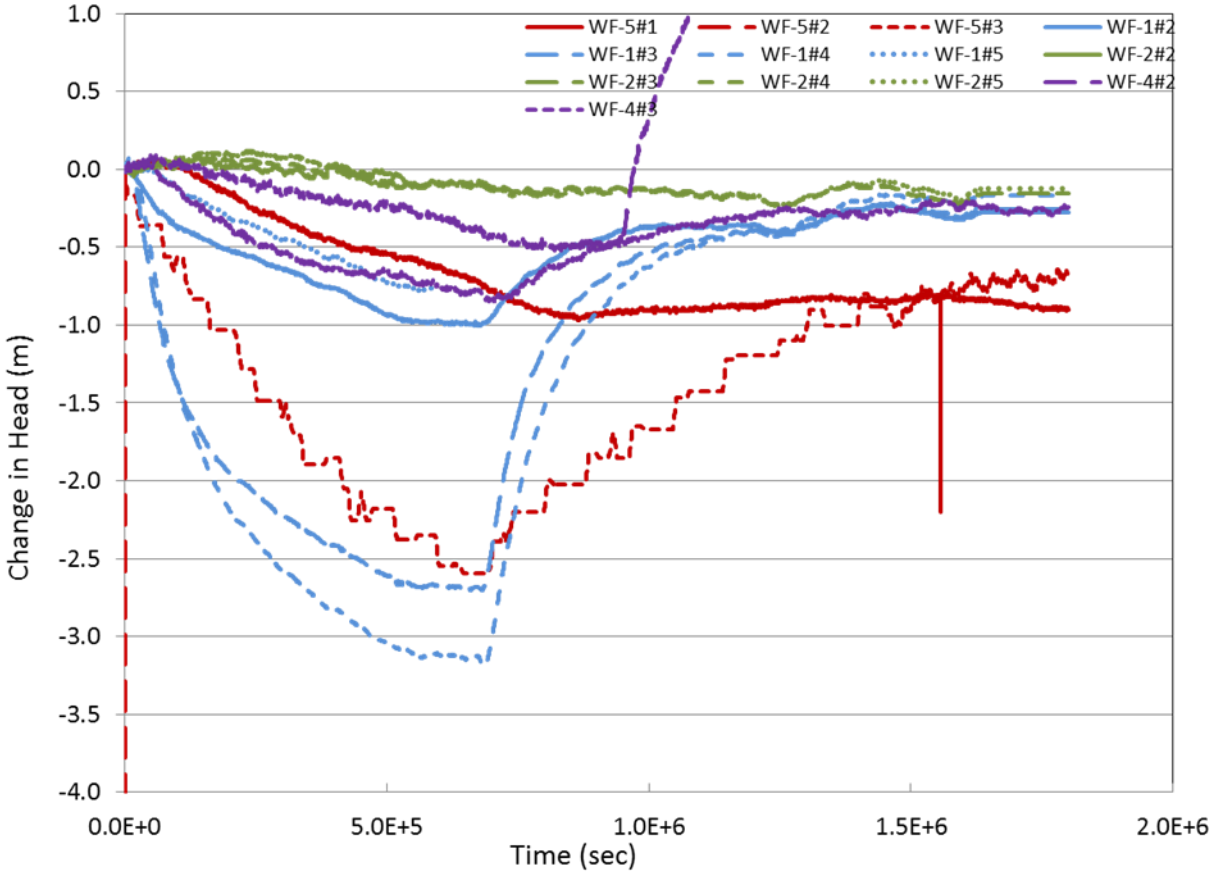

Figure 5-13. Head changes in the monitoring zones in WF-1, 2, 4 and 5. Blue lines are for WF-1, green for WF-2, purple for WF-4 and red for WF-5. The sensor of WF-4#2 failed after 1×10^6 seconds.

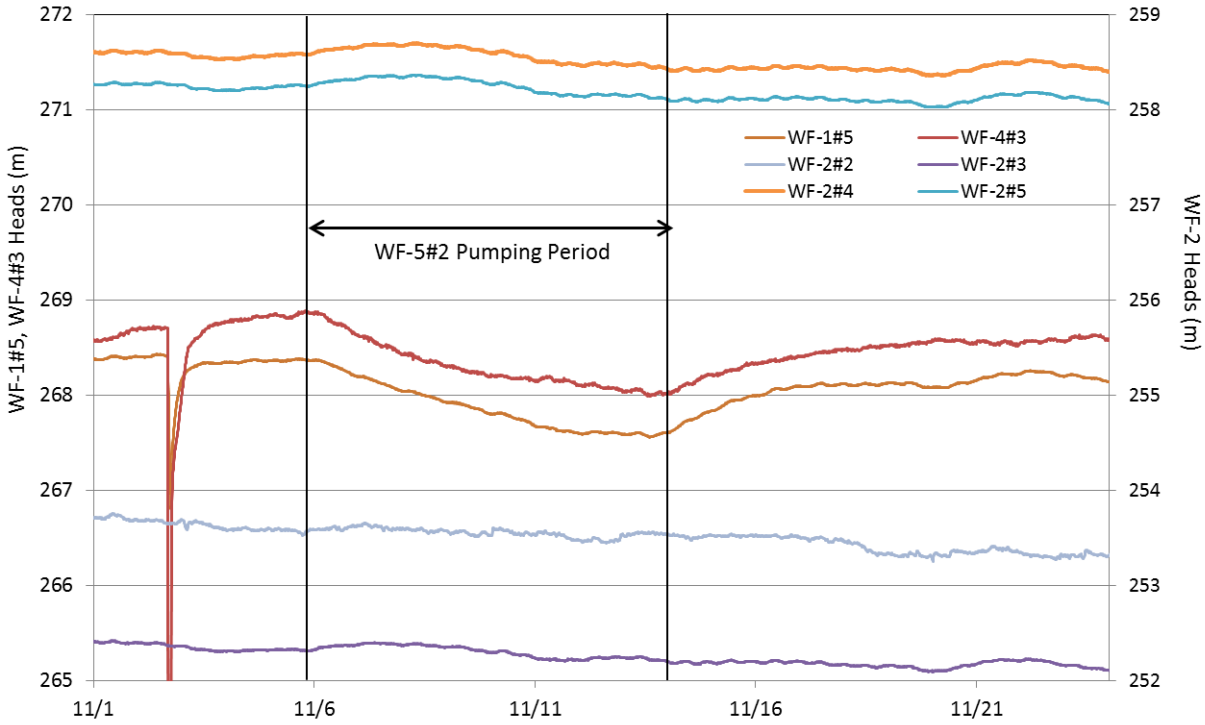

Figure 5-14. Comparison of pressure responses of WF-2 intervals (right vertical axis) to WF-1#5 and WF-4#3 (left axis) during the pumping in WF-5#2. WF-1#5 and WF-4#3 respond clearly. No responses in WF-2 intervals are detected although they are closer to the pumping zone than WF-4#3. Note the scale of both axes is the same.

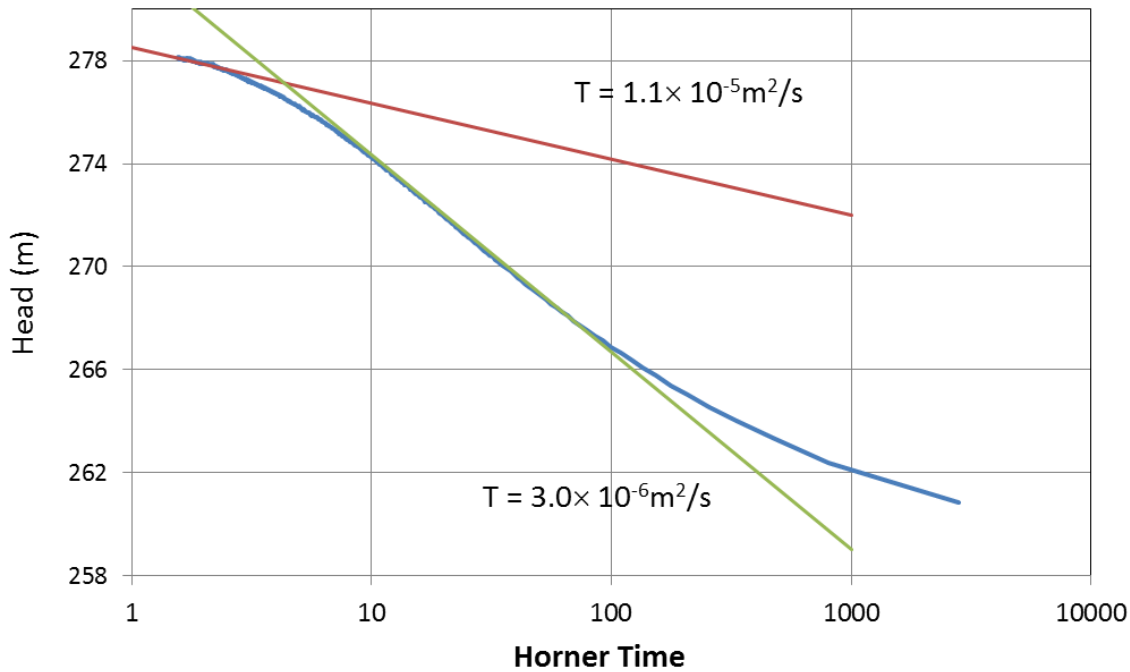

Figure 5-15. Horner plot of the recovery period of WF-5#2 pump test. Note that the slope of the curve flattens toward late time (smaller Horner time).

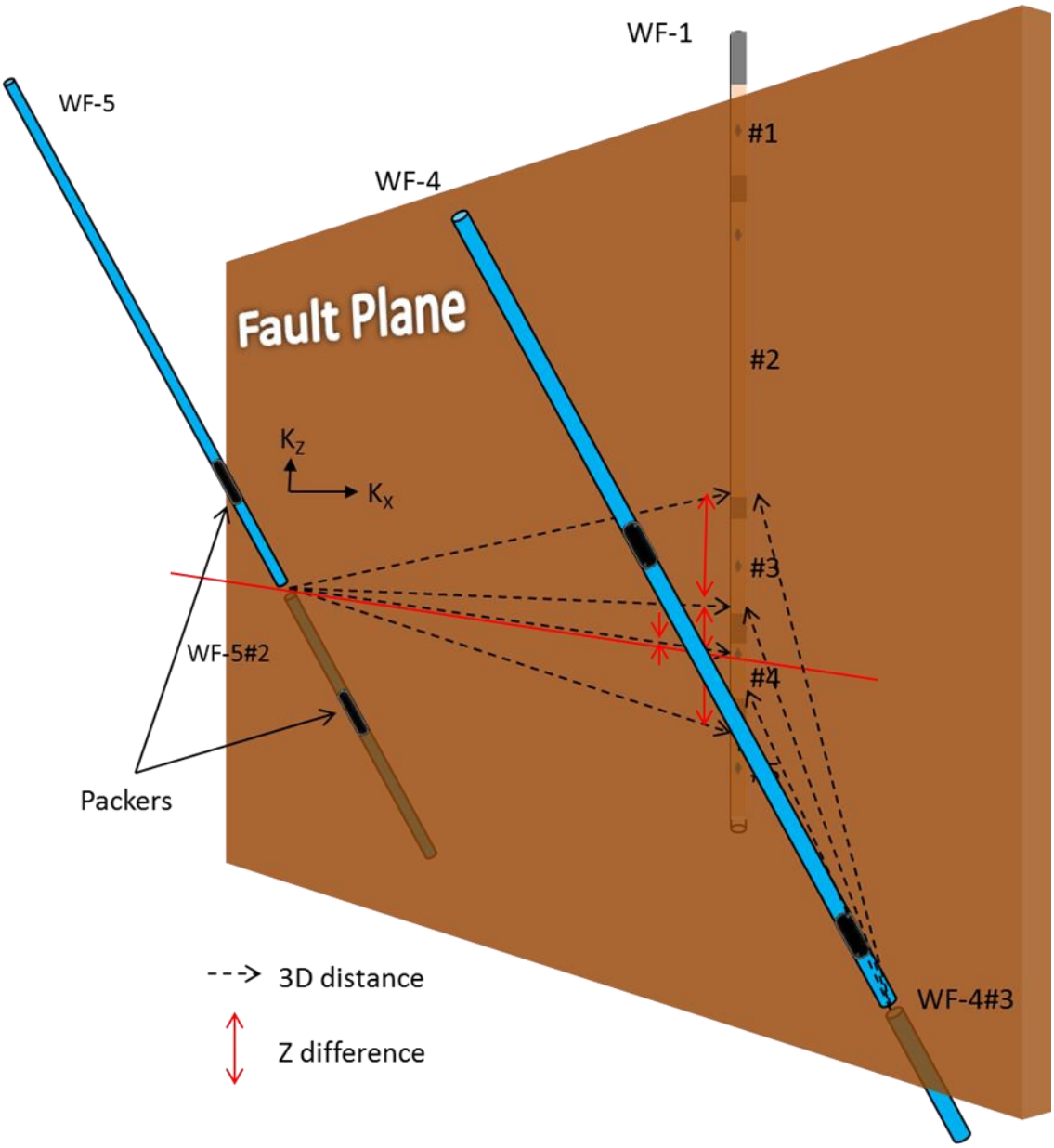

Figure 5-16. Possible explanation of the variation of responses in WF-1despite nearly identical 3D distances from the pumping location in WF-5. See Table 5-2 for comparison. WF-1 is assumed to be very near the fault.

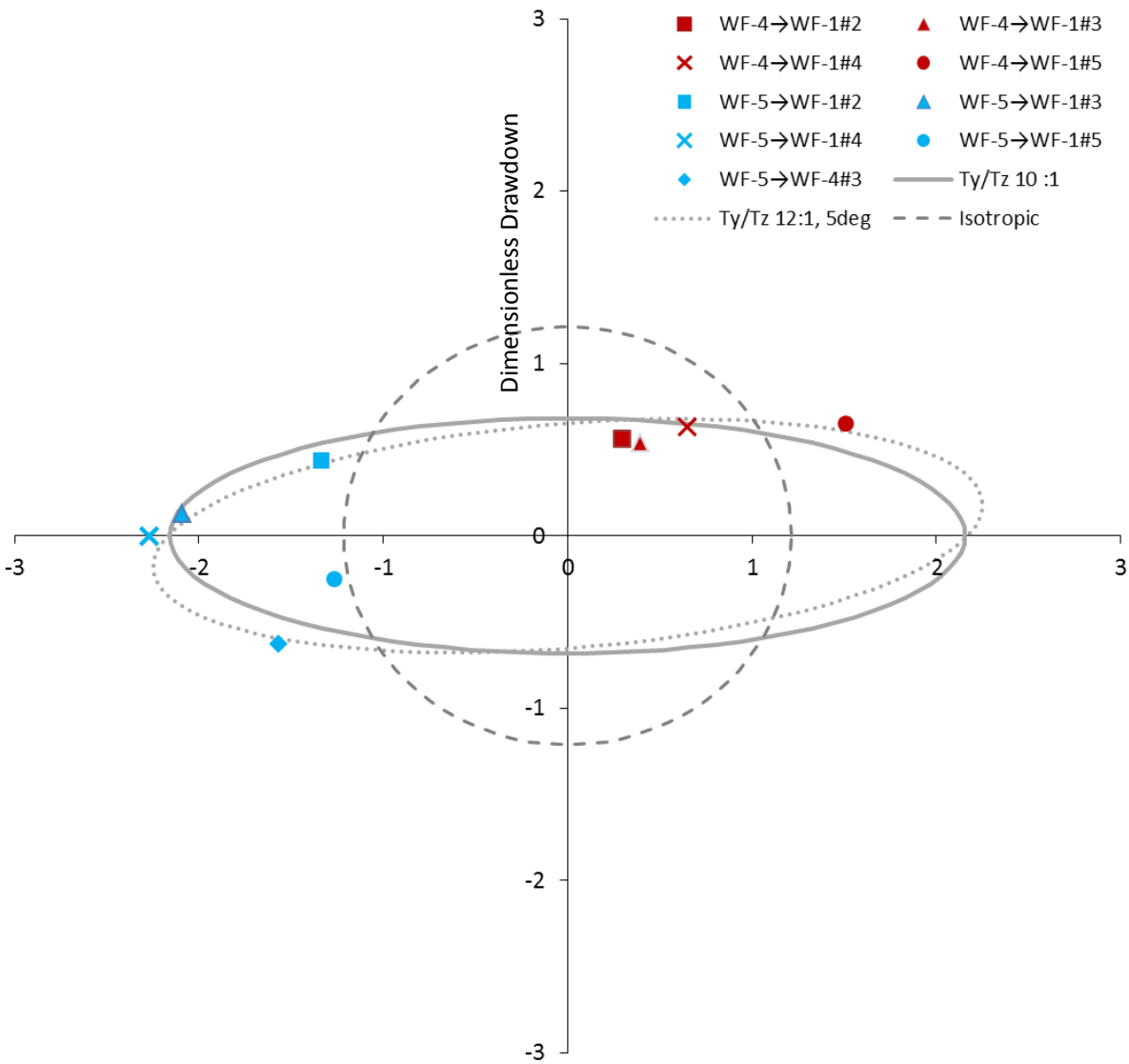

Figure 5-17. Permeability ellipse (K_X/K_Z=10) fitted to the dimensionless drawdowns in WF-1#2~5 and WF-4#3 intervals during WF-4#3 and WF-5#2 pump tests at dimensionless time t_D=16. Broken circle indicates the drawdown for an isotropic system. Dotted ellipse is a better fit with 12:1 anisotropy ratio and rotated 5° from the x-axis.

t_D=16

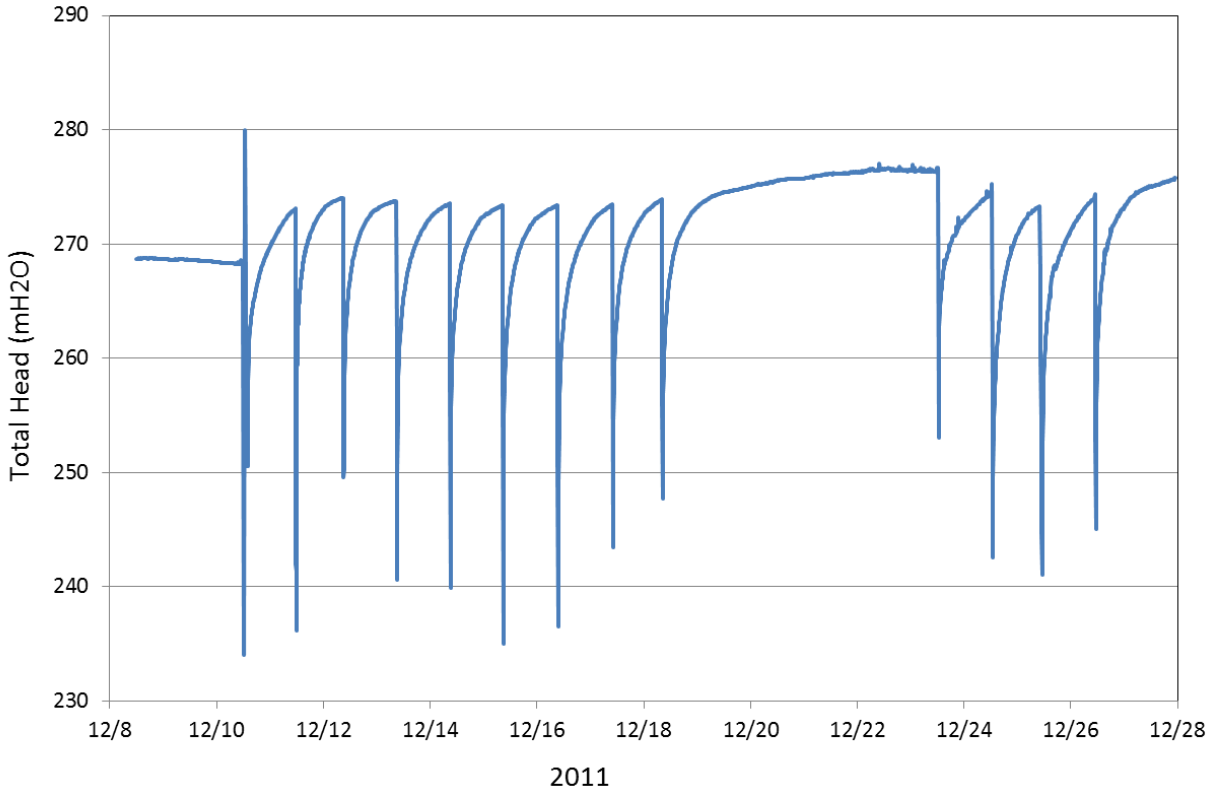

Figure 5-18. Head changes in WF-5#3 during purging to develop the zone. Some of them are analyzed as pump/recovery tests.

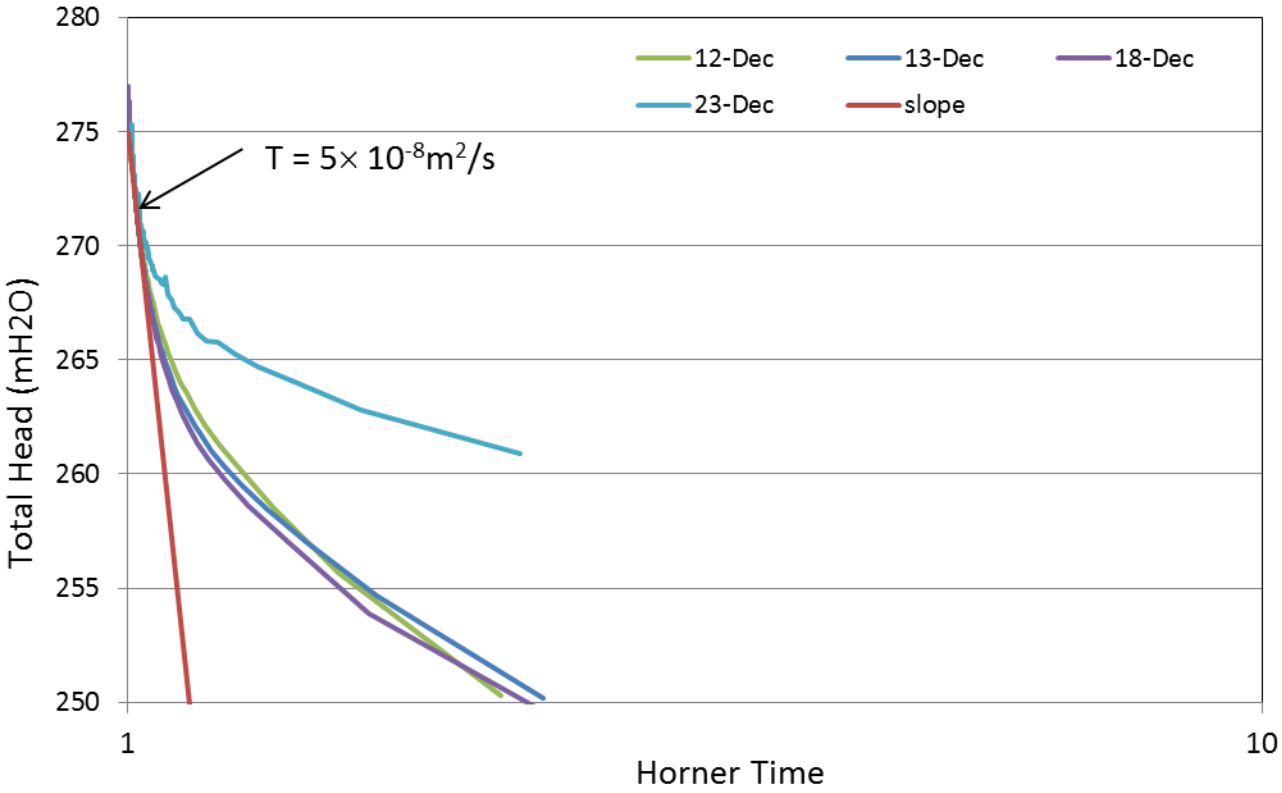

Figure 5-19. Horner plot of the recovery period of four different WF-5#3 pump tests. All four curves converge at late time (Horner time near 1).

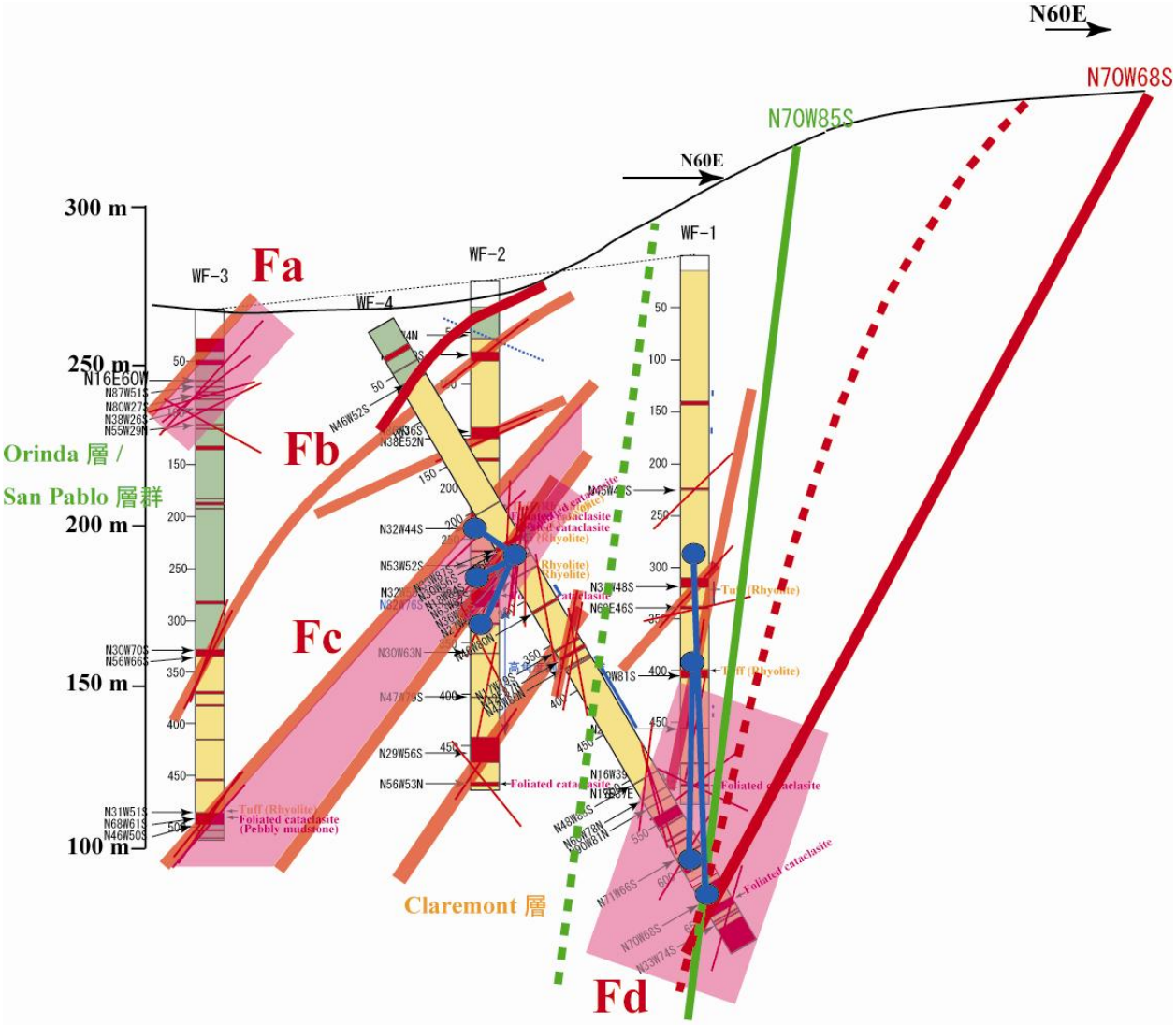

Figure 5-20. The Wildcat Fault zone structure intersecting WF holes (Figure 2.4-2 in Kiho et al., 2012).

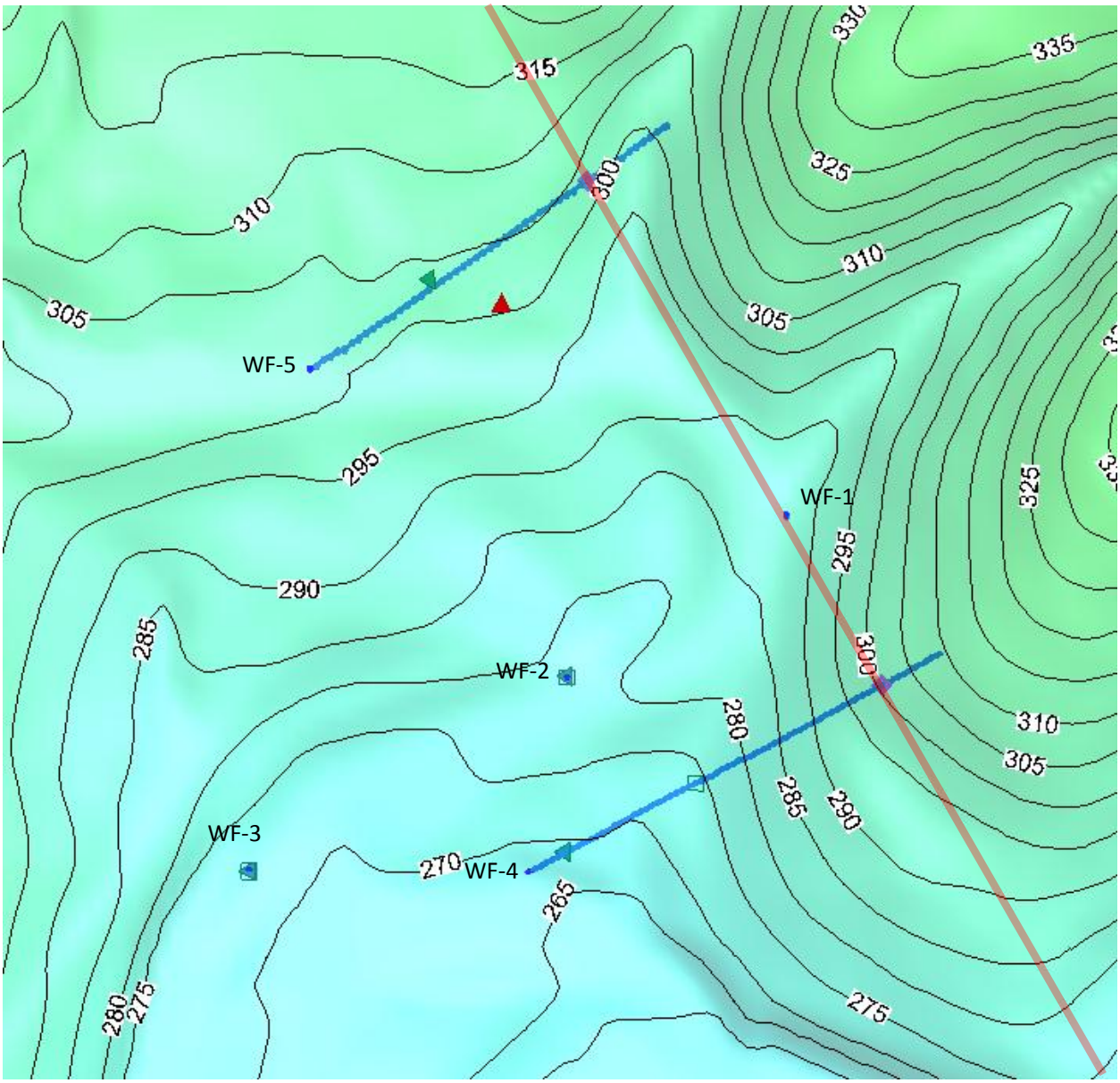

Figure 5-21. LBNL interpretation of the Wildcat Fault zone structure intersecting **[?]**

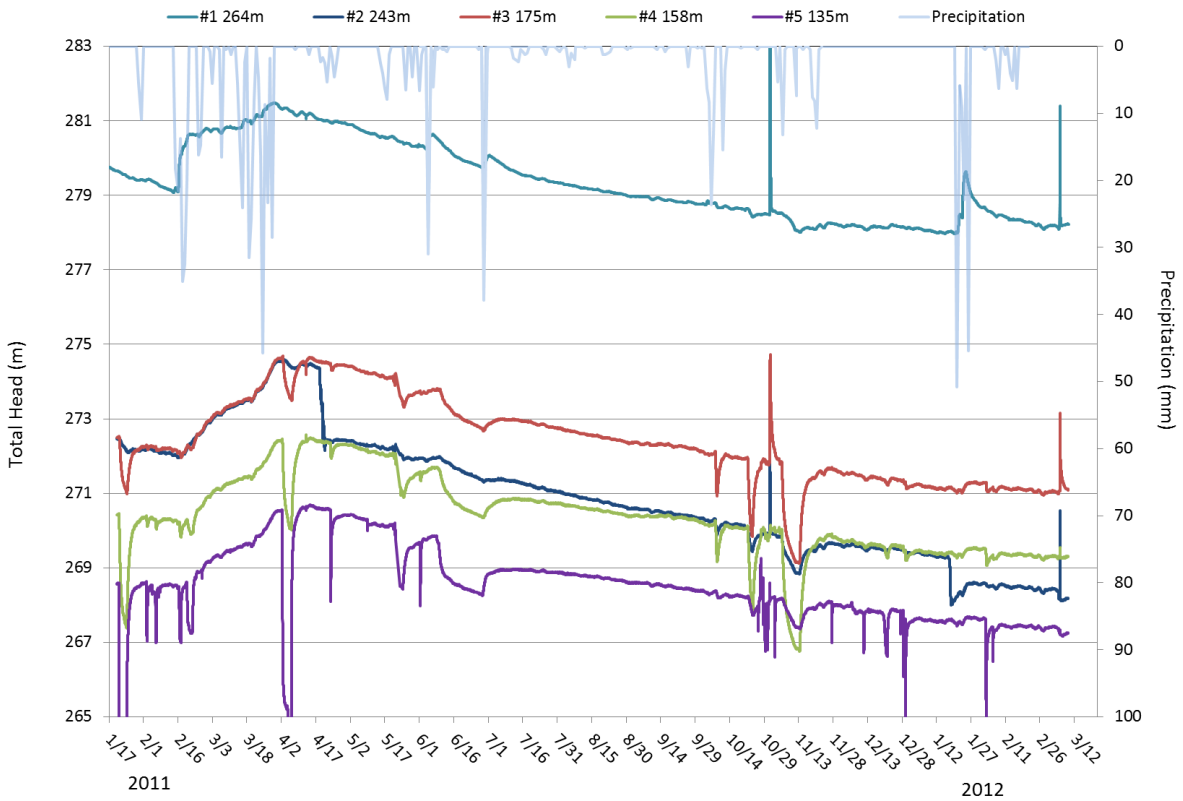

Figure 5-22. Head transients in WF-1 since January 2011. The #2 sensor's readings dropped fast three different times. Two such drops can be seen in April 2011 and January 2012.

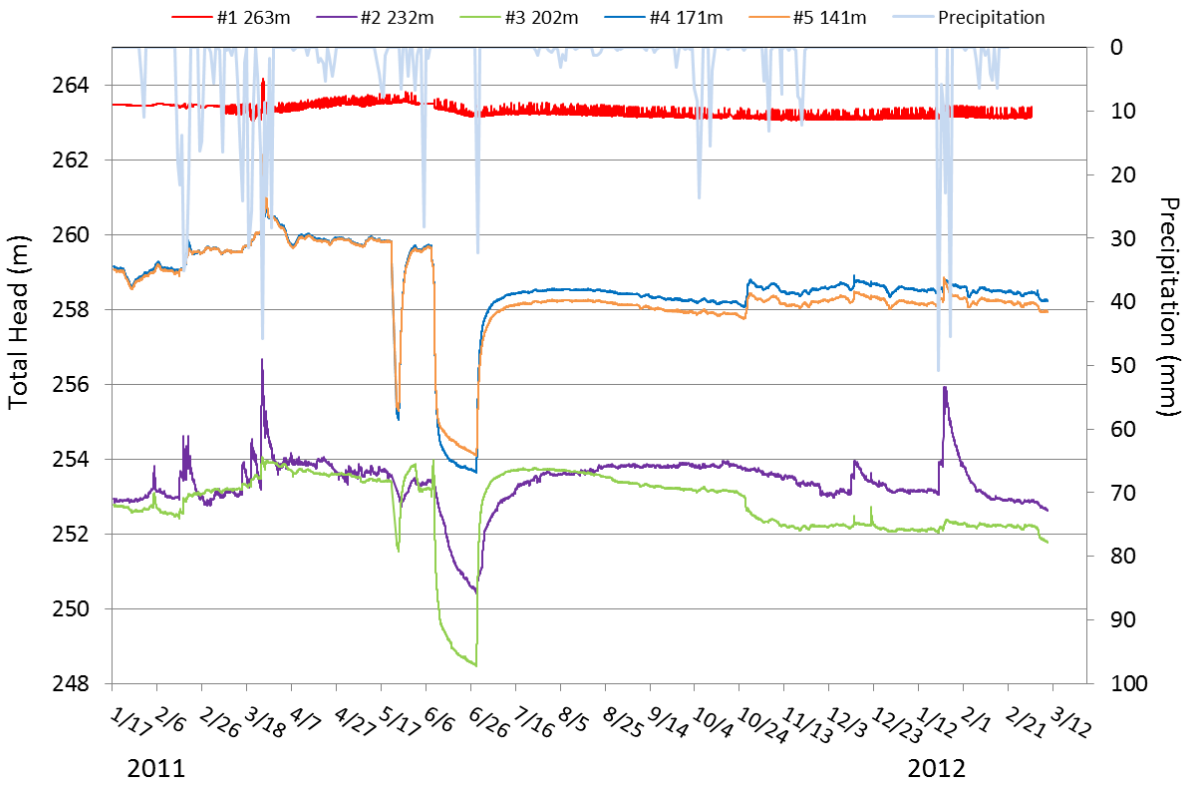

Figure 5-23. Head transients in WF-2 since January 2011.

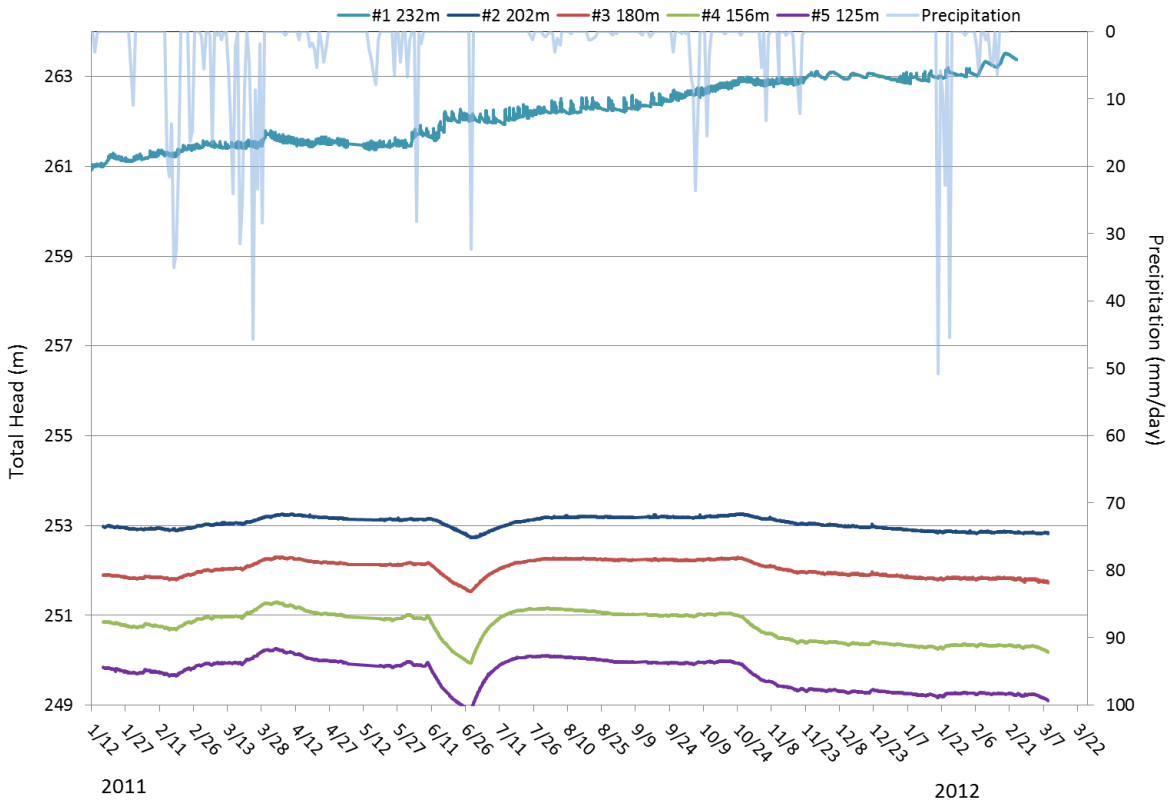

Figure 5-24. Head transients in WF-3 since January 2011.

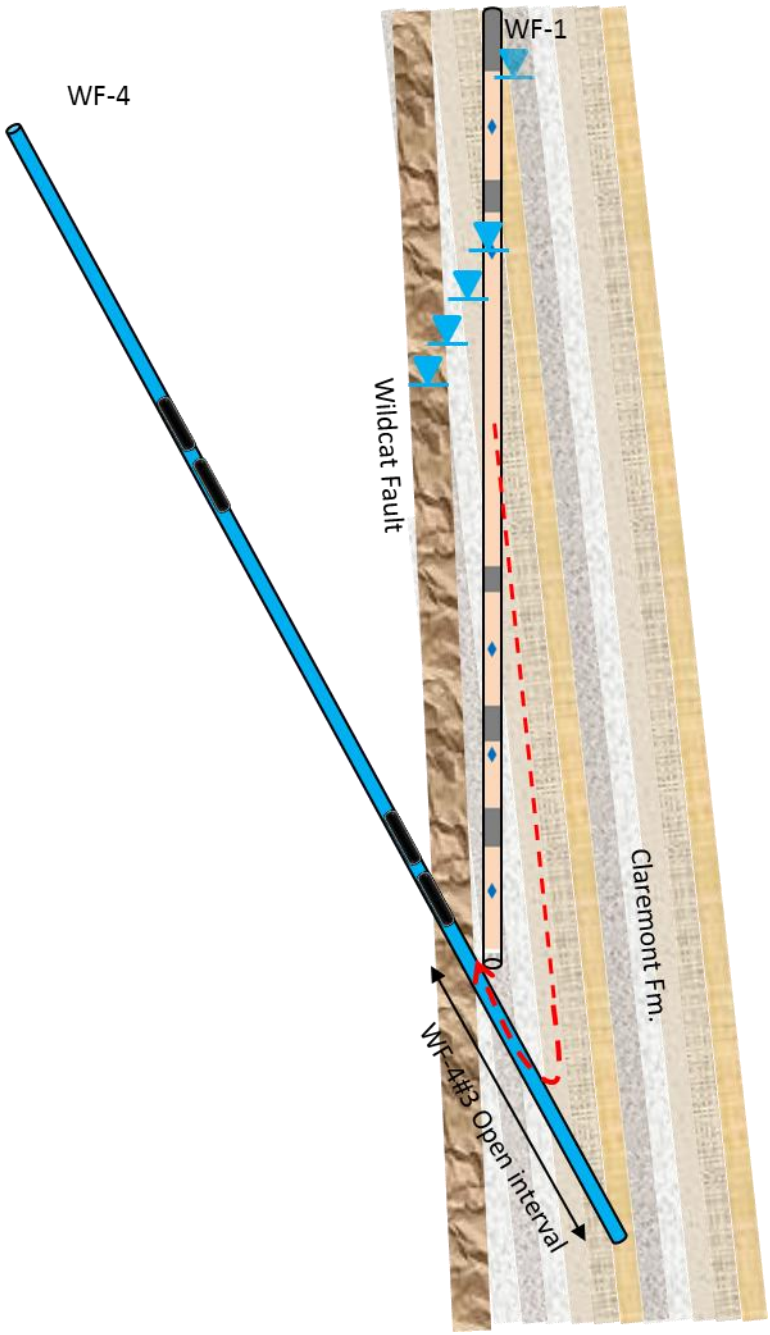

Figure 5-25. Possible explanation of the strange behavior of the sensor in WF-1#2. The WF-1 sensors. The heads decrease in the order from #1 to #5 due to compartmentalization of the steeply east dipping layer. WF-4#3 zone short cuircuits the pressure in WF-1#2 but not the others.

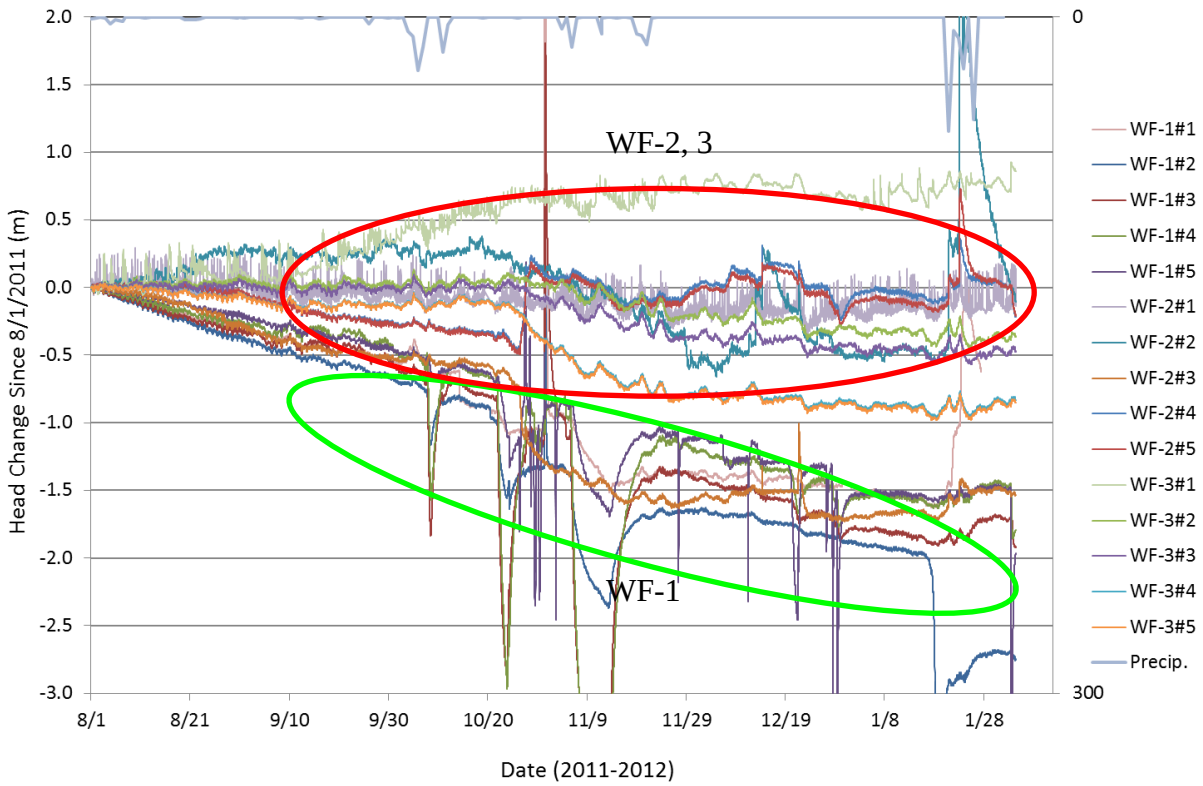

Figure 5-26. Head changes since August 1st, 2011 in WF-1~3 boreholes. The head of the intervals in WF-1 declined at a rate of 4 m/year, whereas the intervals in WF-2 and 3 remained relatively flat. The heads in WF-3 was almost constant until the end of October, when the packer configuration was changed in WF-4.

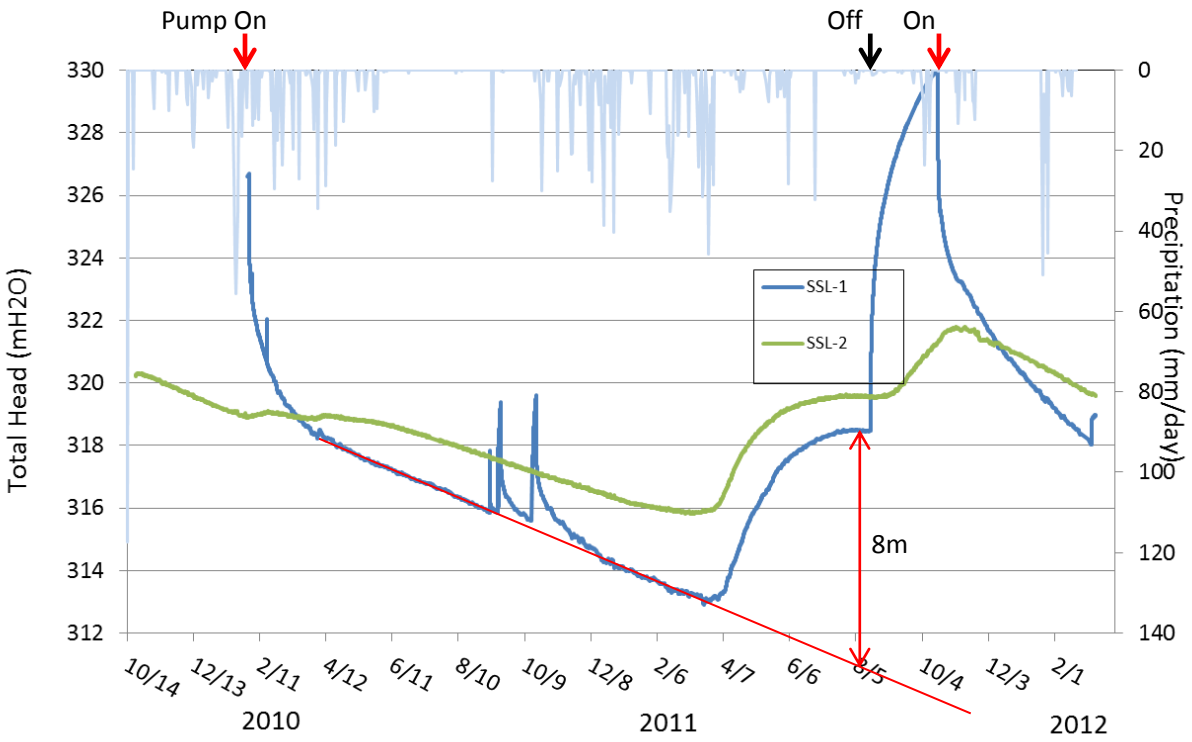

Figure 5-27. Head transients in SSL-1 and SSL-2. Daily precipitation is on the right axis.

$T = 3 \times 10^{-5}$ m²/s

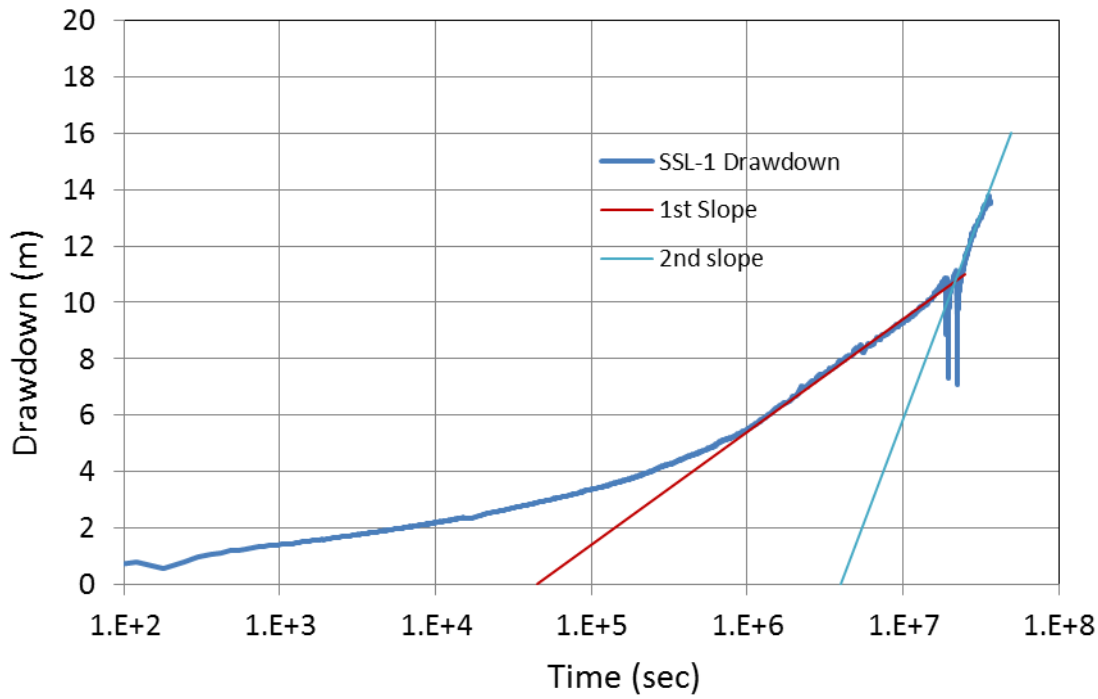

Figure 5-28. Semi-log plot of the observed drawdown at SSL-1.

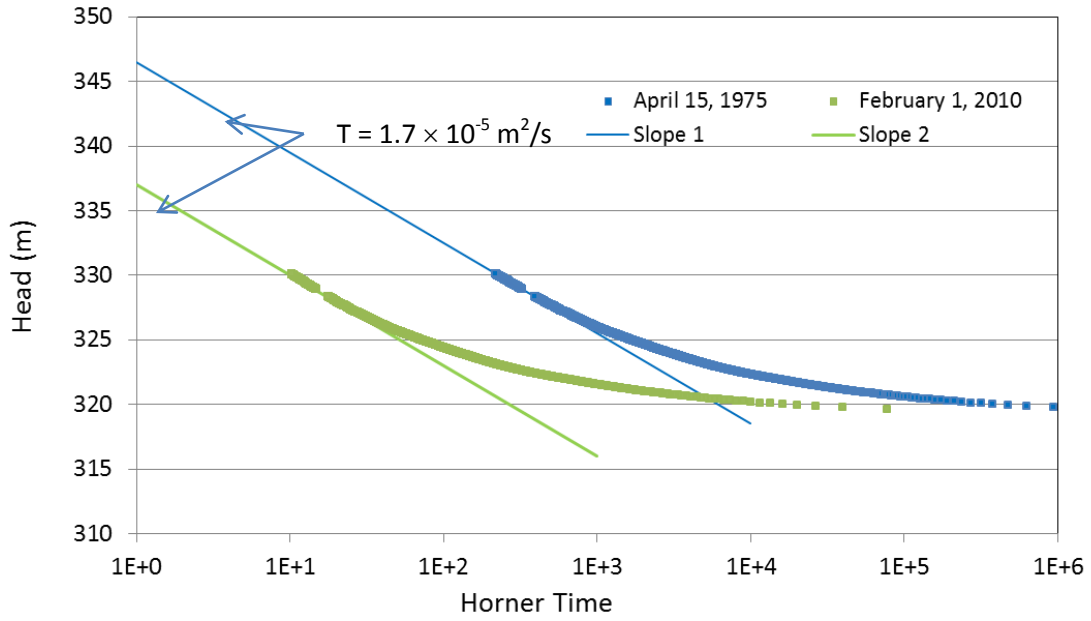

Figure 5-29. The Horner plot of the recovery data from SSL-1 after Aug 16, 2011, shut-in. Two drastically different pumping start time still yield similar transmissivity.

Figure 5-30. Locations of hydraugers and the average flow rate in the East Canyon area of LBNL.

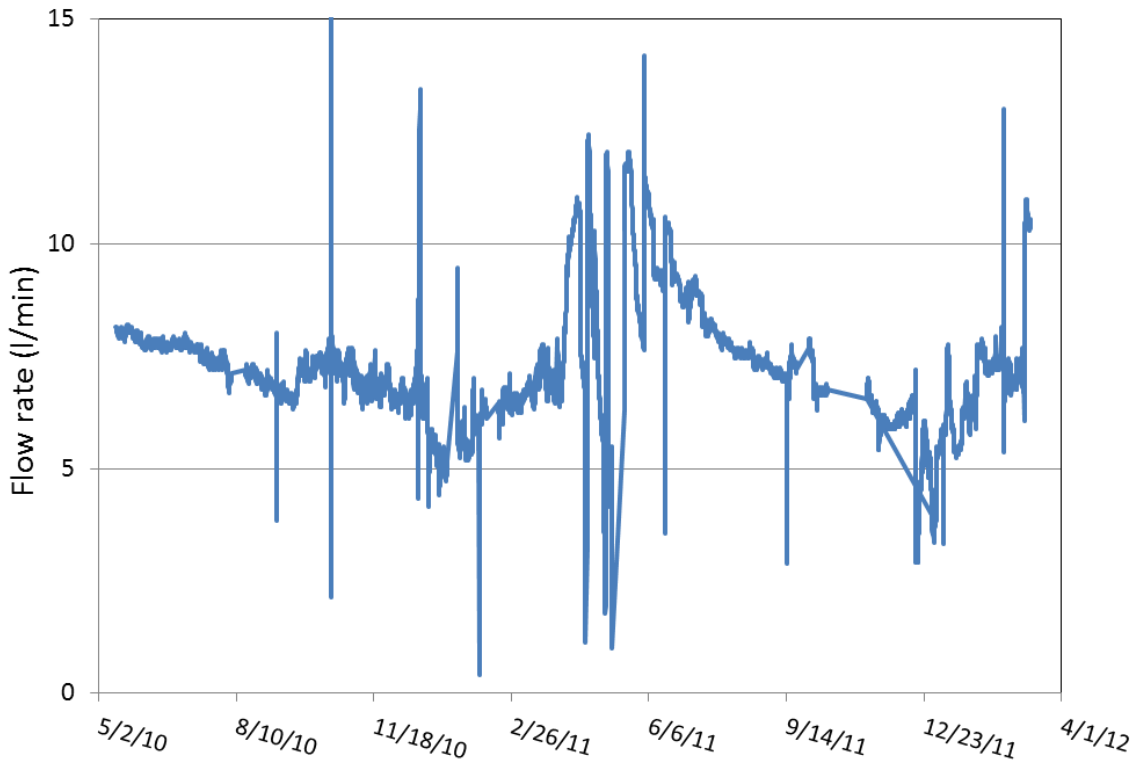

Figure 5-31. Flow-rate fluctuations at the outfalls of the Lennert-1. It averaged 7.5 L/min over the period with some seasonal fluctuations.

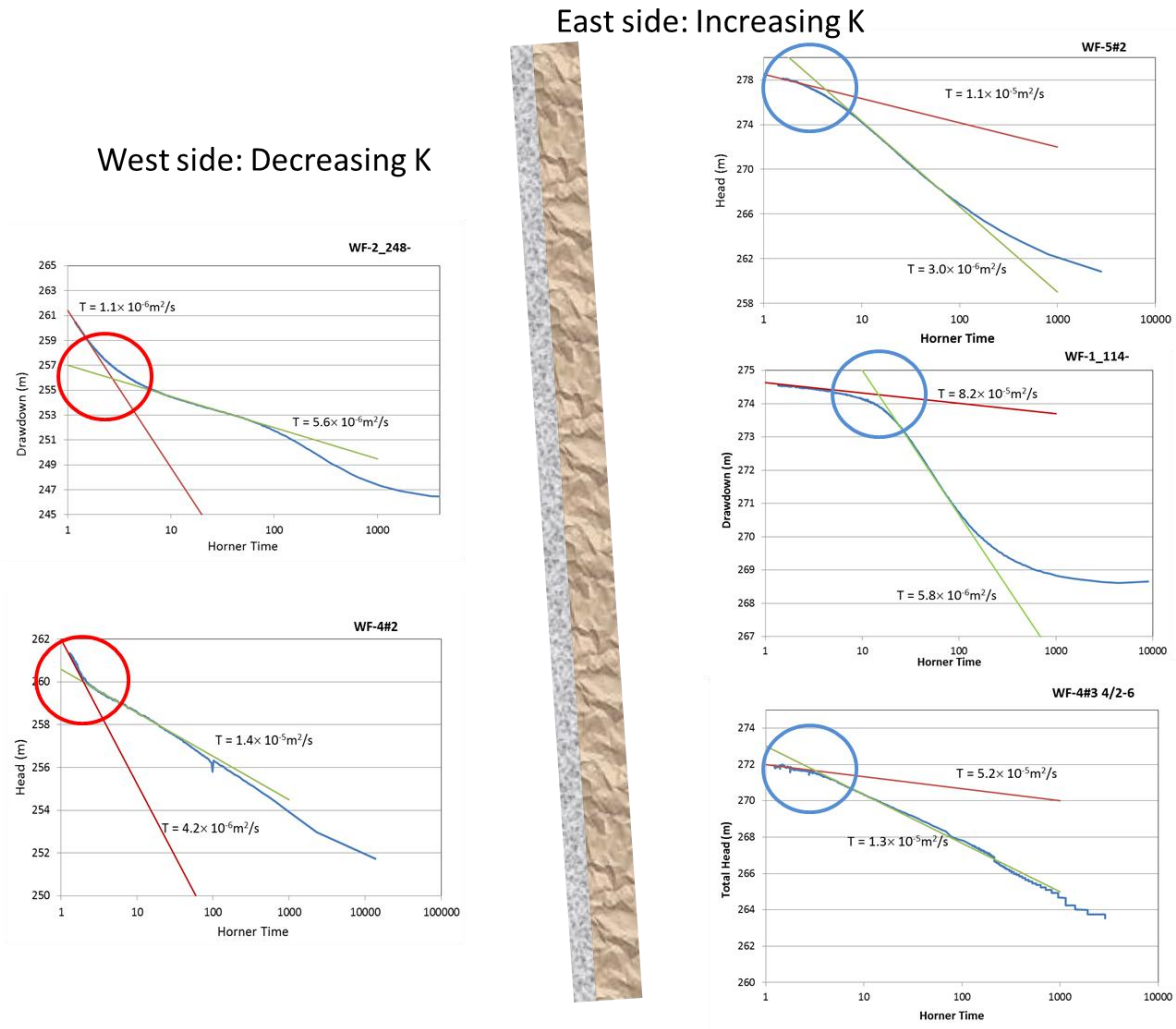

Figure 5-32. Difference in buildup behavior on opposite sides of the fault. The late time behavior of the recovery test data on the east side all indicate the existence of higher permeability feature whereas those on the west side show inflection toward lower permeability.

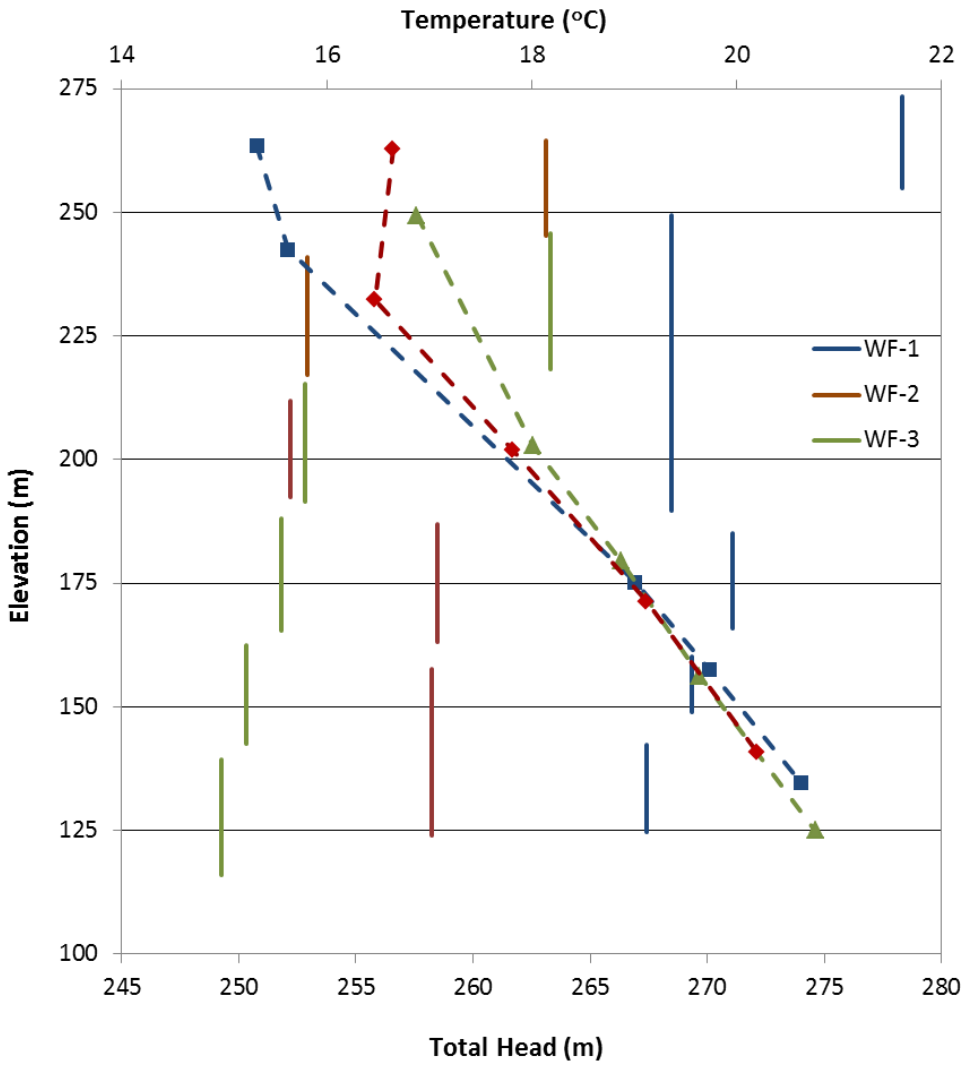

Figure 5-33. Head and temperature profile along WF-1, 2 and 3 observed in March 2012. Solid vertical lines indicate the head in each interval and the broken lines are the temperature at the sensor location. The sensors are numbered from the top. The general trend is that the head decreases as a function of depth except the 2nd zone in WF-1 and the 2nd and 3rd zone in WF-2.

6 Geochemical Investigation

6.1 Introduction

Our main goal in this project is to develop an effective characterization methodology for fault-zone hydrology that can be applied at a potential candidate site for geologic disposal of nuclear wastes. As is often the case with any characterization effort, available hydrological data were limited both spatially and temporally. We thus needed to utilize all available and relevant data and integrate them to develop a reliable predictive model, based on the correct conceptual model of the Wildcat fault-zone hydrology. We examined the geomorphology of the area and conducted geologic mapping and geophysical surveys. We drilled five boreholes (WF-1–WF-5) and carefully examined the cores. In these boreholes, we conducted hydraulic tests to estimate transmissivity. We also gathered pressure, temperature, and flow data from SSL-1 and pressure and temperature data from SSL-2. We also measured the outflow rate from the outfall of historic hydraugers. The data gathered from these sources of information are not yet enough to characterize the hydrology of the Wildcat Fault definitively. At this juncture, we are still debating if or where the main fault plane of the Wildcat is.

We are determined to use any other information available that may help us understand the hydrology of the fault zone. In this section, we describe the geochemical analysis of water and rock, which may help in estimating the hydrologic properties of the Wildcat. Geochemical studies in the previous years can be found in Karasaki et al. (2010 and 2011) and Kiho et al. (2011). A preliminary study of the isotopic compositions of water samples and carbonate fracture fillings in the boreholes has been conducted to determine the relationship between secondary minerals and groundwater flow in the fault zone. The findings of this work thus far are summarized below.

6.2 Stable isotope (δD, $\delta^{18}O$) of Fault Zone Waters

Following completion and pumping of the first two boreholes, WF-1 and WF-2, a single sample of water was collected for water isotope analyses. From WF-4, a series of 6 samples were collected over a two-week period following completion of the well. One sample from WF-5 has also been analyzed (additional samples are being collected on a quarterly schedule to check for seasonal changes in the isotopic composition of the groundwater). For comparison, two samples

of groundwater from the Space Sciences Lab well (SSL), collected a year and a half apart, were also analyzed.

The isotopic compositions of the samples collected from the different wells varied slightly. The δD values of the different samples ranged from -40 to -43‰, and the $\delta^{18}O$ values ranged from -6.4 to -6.6‰. This differed slightly from the compositions from the SSL well, which averaged -44‰ for δD and -7.1‰ for $\delta^{18}O$. While these are small differences, they might represent slightly different sources of recharge. The average isotopic compositions of precipitation in Berkeley vary, with lower values at higher elevations.

6.3 Carbon isotope compositions ($\delta^{13}C$) of Groundwater Dissolved Inorganic Carbon (DIC)

The $\delta^{13}C$ of DIC in the groundwater samples from WF-1 and WF-2 had an average value of -6.5‰. By comparison, the first SSL sample had a much lower value of -12‰. Typically, groundwater recharged through organic-rich surface soils will be in the range of -10 to -20‰. However, a number of factors can influence this, especially interaction with carbonate minerals with higher $\delta^{13}C$ values, such as marine carbonates, which are common in the rocks in the vicinity of the boreholes in the Wildcat Fault zone (WCFZ). Isotope compositions ($\delta^{13}C$, $\delta^{18}O$) of Carbonate Fracture Fillings

Fracture systems in the WCFZ have abundant fractures containing secondary carbonate minerals, but the relationship between these carbonate minerals and fault activity is not clear. The isotopic compositions of 75 samples of these carbonates were analyzed to further examine this relationship.

The $\delta^{18}O$ values of secondary vein carbonate samples collected from Borehole WF-4 are plotted in Figure 6-1. Sample images of the carbonates that were analyzed are shown in Figure 6-2. The $\delta^{18}O$ values range from -7.5‰ to -0.3‰. The lowest values are concentrated in zones of highly fractured rock. Calcite precipitated in oxygen isotopic equilibrium with water with a $\delta^{18}O$ value of -6.5‰ (the average value measured for water from the fault zone) at 15°C will have a $\delta^{18}O$ value of -7.1‰ (VPDB). Similar patterns of oxygen isotopic compositions were observed in the other boreholes. The apparent oxygen isotopic equilibrium between the present-day groundwater and the secondary carbonates in these fractures is evidence that these zones are active flow paths for groundwater.

The $\delta^{13}C$ values of the carbonate minerals range from normal marine values (-4 to +4‰) to very high (more than +20‰) values for either marine or freshwater carbonates. The origin of the high $\delta^{13}C$ values of the carbonate is not clear. High $\delta^{13}C$ values have been observed in other fault zones and have been attributed to precipitation under highly reducing conditions, accompanied by biological methanogenesis resulting from CO_2 reduction. However, these highly reducing conditions are generally observed only in shallow systems with very high concentrations of organic matter that don't exist in this area. Another possible explanation involves sudden pressure release (e.g., accompanying faulting) leading to de-gassing of CO_2 from the groundwater. To achieve the high values observed in some of the borehole samples would require 80-90% loss of dissolved inorganic carbon under equilibrium conditions, but there could also be a kinetic isotope effect associated with the sudden degassing from pressure release during faulting. We plan to test this theory.

6.4 $^{87}Sr/^{86}Sr$ of Groundwater Strontium

The strontium isotope ratios of groundwater are strongly affected by the isotopic compositions of the aquifer rocks. Johnson and DePaolo (1997) measured the $^{87}Sr/^{86}Sr$ of groundwater along presumed flow paths and found significant variations, which they interpreted to be caused by slow groundwater flow velocities (<0.2 m/yr). The waters collected from WF-1 and WF-2 had relatively high strontium isotope ratios of 0.7080 and 0.7086, respectively, which are higher than any ratios measured by Johnson and DePaolo (1997) except for samples collected much lower in the stratigraphic section. We suspect that these samples were collected before the drilling fluids used for the boreholes were adequately flushed from the system. The $^{87}Sr/^{86}Sr$ of groundwater from the other wells (WF-4, WF-5 and SSL) that were all flushed much longer before the samples were collected were lower, ranging from 0.7060 to 0.7069. These values are similar to values reported by Johnson and DePaolo (1997) for samples collected from a similar stratigraphic level.

6.5 $^{87}Sr/^{86}Sr$ of secondary carbonates

The isotope ratios of strontium in 15 samples of secondary carbonate from the boreholes were analyzed as part of this study. The $^{87}Sr/^{86}Sr$ of those samples ranged from 0.7065 to 0.7086, which is higher than the values measured for the groundwater samples (especially if the values measured for WF-1 and WF-2 are determined to be contaminated by drilling fluids).

Those values are similar to whole rock $^{87}Sr/^{86}Sr$ measured by Johnson and DePaolo (1997) for samples of the Orinda Formation and the Great Valley Sequence (0.7062 to 0.7126), indicating Sr isotopic exchange between the precipitating fluids and the host rock.

6.6 Groundwater Ages

Kiho et al. (2012) concluded that the groundwater is likely evolving, Ca-HCO_3 → Na-HCO_3, from shallow to deeper depths (from upstream to downstream) (Figure 6-5). This is consistent with the head distributions observed in boreholes, as well as with the geography, and reflects the overall hydrologic flow. No significant concentrations of ^{3}H were observed in the samples that come from WF boreholes (Figure 6-3), which means that the transit time of the recharged water is longer than 60 years, and which indicates that the water is not moving very fast even in the fault zone. After $\delta^{13}C$ calibration allowing for the dissolution of marine carbonates, the ^{14}C age dating yielded 4,000–6,000 for shallow and 7,000–8,000 for deeper waters. Many ^{4}He samples (Figure 6-4) were suspected to be contaminated by air and were estimated to be less than 10,000 years old. Some samples yielded in the order of 100,000 years.

6.7 Conclusions

Based on the studies conducted thus far, the following conclusions can be made:

- Oxygen isotope compositions of carbonates in fracture zones appear to be a good indicator of active (or recent) hydrologic zones.
- Some carbonates in fractures have anomalously high $\delta^{13}C$ values (5‰ to >20‰). Possible causes for this are:
  - Methanogenic biological activity
  - Low-temperature diagenesis
  - Fault zone processes
- Strontium isotope compositions of carbonates are complicated, but seem to indicate fast paths and/or very high water/rock ratios in active flow zones.
- The groundwater is evolving, Ca-HCO_3 →Na-HCO_3, from higher to lower elevations at the site.
- The ages are estimated to be ~4,000 years at shallow and ~7,000 years at deeper levels.

6.8 References

Karasaki, K., Onishi, C.T. and Zimmer, V., 2010, Development of Hydrologic Characterization on Technology of Fault Zones – Phase II Interim Report-, NUMO-LBNL-CRIEPI Collaboration Research Project.

Karasaki, K., C.T. Onishi, C. Doughty, E. Gasperikova, J. Peterson, M. Conrad and P. Cook, 2011, Development of a Hydrologic Characterization Technology for Fault Zones—Phase II 2nd Report —.

Kiho, K., Ueta, K., Miyakawa, T., Hasegawa, T., Tanaka, S., Ito, H., Hamada, M., Tsukuda, K, 2011, CRIEPI Technical Report, Survey and Analysis related to Development of Hydrologic Characterization Technology of Fault Zones.

Kiho, K., Ueta, K., Miyakawa, T., Hasegawa, T., Ito, H., Hamada, M., Nakada, H., Tanaka, S., and Tsukuda, K, 2012, CRIEPI Technical Report, Survey and Analysis related to Development of Hydrologic Characterization Technology of Fault Zones IV.

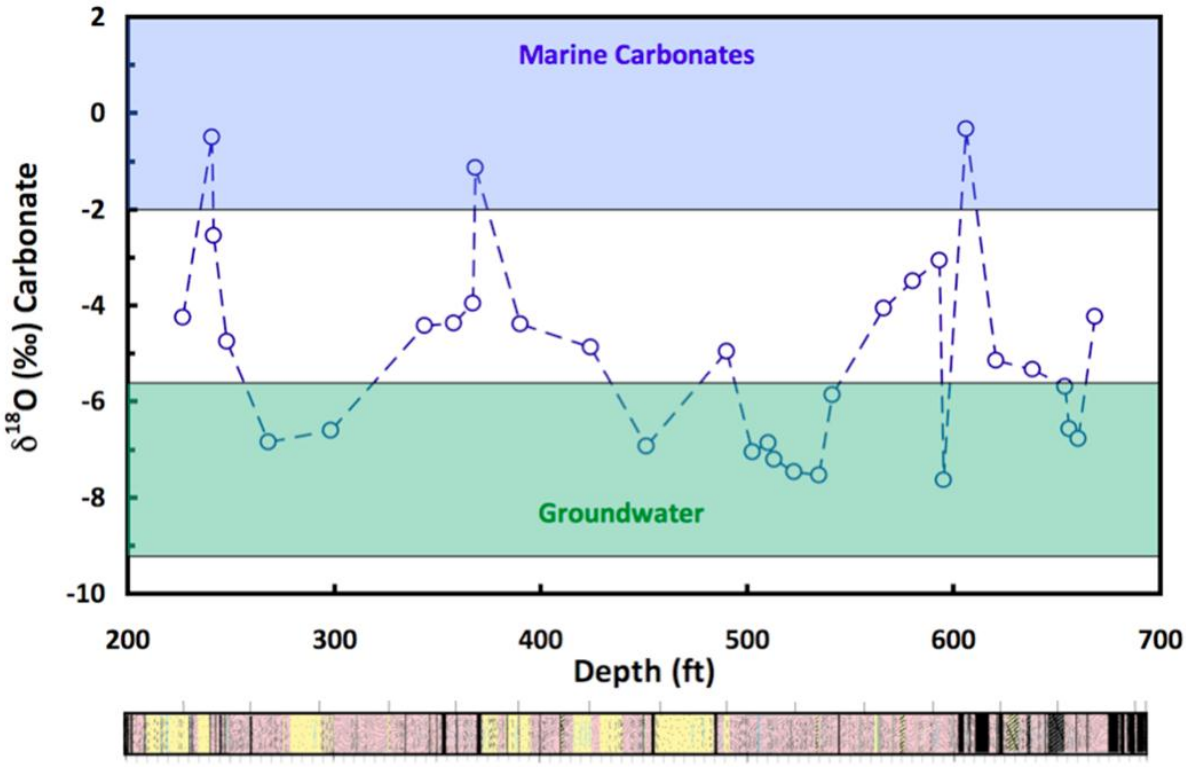

Figure 6-1. Oxygen isotope compositions of secondary carbonate minerals in fractures in Borehole WF-4. Also shown are the approximate range of $\delta^{18}O$ values for marine carbonates and for calcite in equilibrium with measured values of present-day groundwater (average $\delta^{18}O$ = -6.5‰).

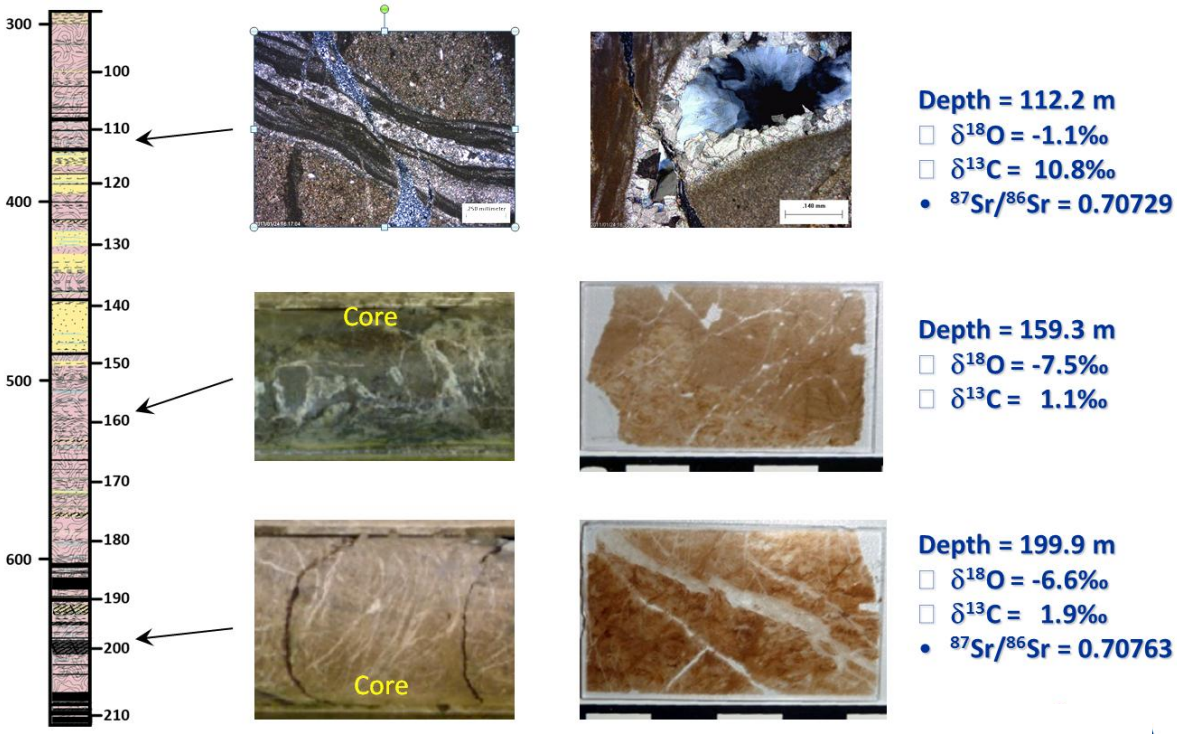

Figure 6-2. Examples of the carbonates analyzed. Note that the upper one has high $\delta^{18}O$ values and has open cavities with minimal signs of shearing (from the preserved cross cutting features). The bottom two have low $\delta^{18}O$ values and have many veins in sheared chert.

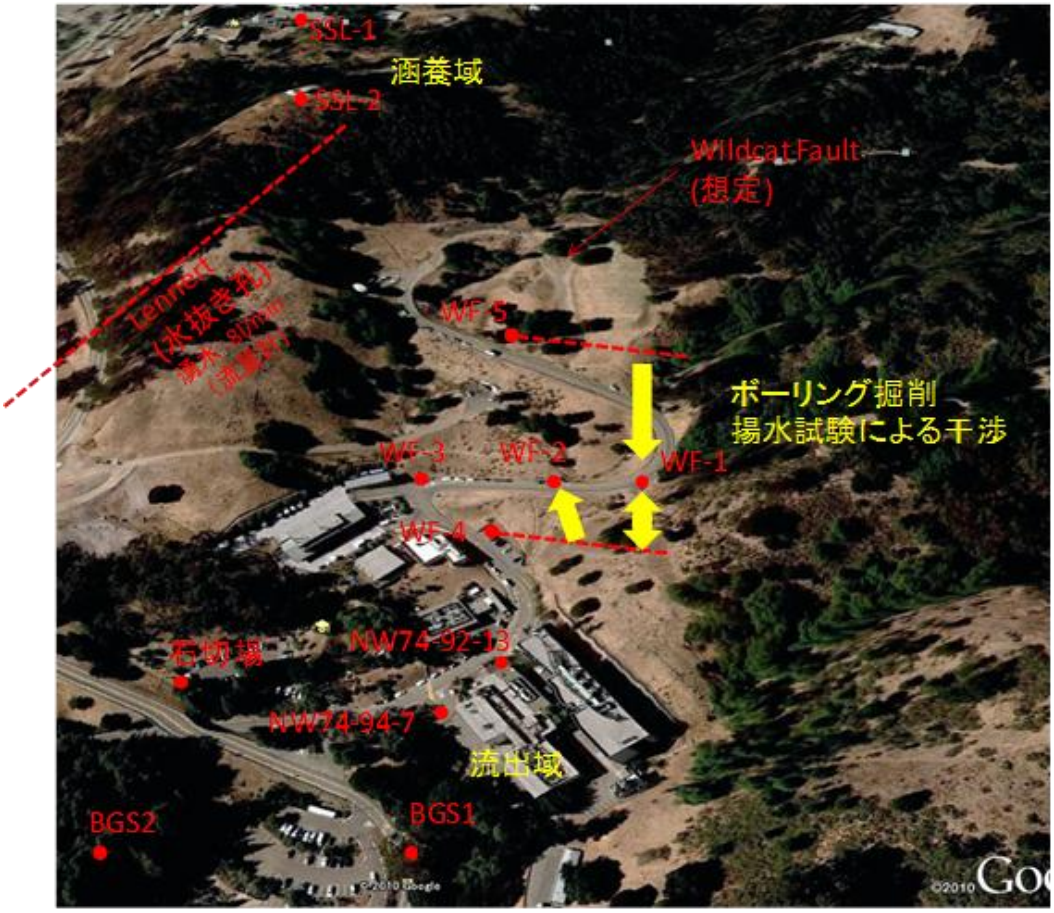

Figure 6-3. Bird's eye view of the study area showing the boreholes where water samples were collected (Kiho et al., 2012).

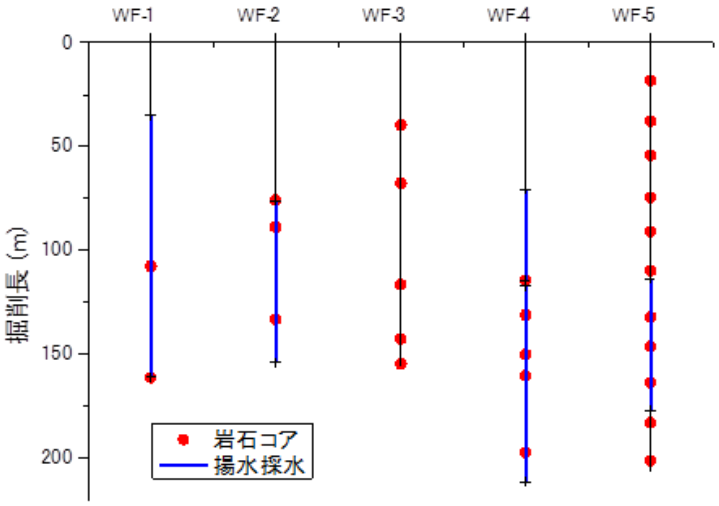

Figure 6-4. Locations where water samples and ^{3}He core samples were collected (Kiho et al, 2012).

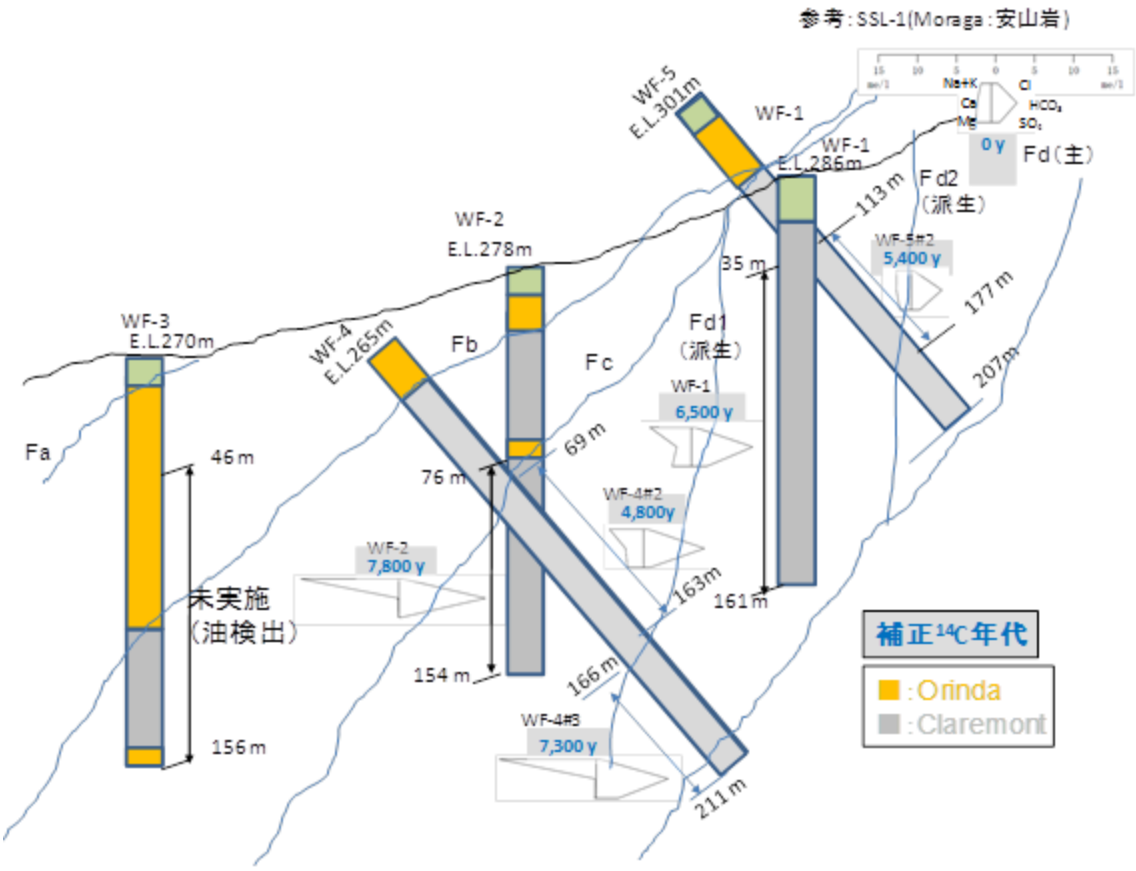

Figure 6-5. Conceptualization of groundwater flow direction and ages in the WF borehole area (Kiho et al., 2012).

7 Hydrologic Modeling

7.1 Introduction

The primary objective of the Fault Zone Hydrology Project is to develop an effective and reliable methodology for fault zone characterization. To this end, we have conducted field investigations of the Wildcat Fault (WF) starting with a literature survey, an aero photo based geomorphological study, geologic mapping, geophysical surveys, trenching, borehole drilling, and hydraulic testing in the LBNL area. According to the systematized investigation flow proposed in Karasaki et al. (2009 and 2010) and Kiho et al. (2012), a geologic model would be constructed as information and data gathered by the field investigation start to come in. Then the geologic model would become the basis of a hydrologic model that honors hydraulic data obtained by passive and active hydrologic tests. The hydrologic model would then be used to make predictions of the outcome of the next stage of investigations, and to identify data holes if any. Thus the field investigation, geologic model, and hydrologic model would make a circular feedback loop.

In this section, we outline the effort of constructing the geohydrologic model of Strawberry Canyon (Berkeley, California), the basin within which our current study area is concentrated. We also created a smaller subregion model of the East Canyon. One of our goals is to understand the role of the Wildcat Fault in controlling natural-state groundwater flow, and one means to assist in developing this understanding is to develop a numerical model of groundwater flow in the basin containing the fault. The strategy for flow modeling is to calculate the natural-state flow field and also to investigate the transient inter-well response to drilling, well tests, long-term pumping, and precipitation.

7.2 Data available

A great deal of site characterization data is available from which to construct the model, including

- Geologic map (Graymer, 2000; Karasaki et al., 2009, 2010, and 2011, Kiho, et al., 2012)
- Digital elevation model (up to 3 m resolution)
- Surface fault location in trenches (TR-1~5)

- Three vertical wells with geophysical log information and permanent pressure and temperature sensors at 5 depths (WF-1–WF-3)
- Two diagonal wells crossing the fault (WF-4 and WF-5)
- Two deep wells with water-level and pumping rate data (SSL-1 and 2)
- Flow rates for three existing wells/hydraugers (Lennert, BG-1, Quarry)
- Many shallow wells with water-level data and permeability estimates (often from slug tests) from the Site Environmental Remediation Project
- Precipitation record
- Air temperature record

7.3 Numerical Simulator

The TOUGH2 code, a general purpose numerical simulator for fluid flow and heat transport in geological media (Pruess et al., 1999), is used for the numerical simulations. TOUGH2 preliminary simulations use the equation of state module EOS9, which considers single-phase liquid water or a two-phase water/air system in which air is a passive spectator (a common soil-physics approximation) and temperature does not change. Results of TOUGH2/EOS9 simulations include steady-state and transient hydraulic head distributions, infiltration rates, and flow rates from various outlets in the model (creeks, springs, hydraugers). We also use equation of state module EOS3, which generally considers fully-coupled multiphase flow of water, air, and heat, but we use it in isothermal mode for the Strawberry Canyon model. That is, we specify an initial temperature distribution in which the temperature increases linearly with depth (surface temperature is 12.8^{o}C, gradient is 0.03^{o}C/m), but that temperature cannot change during the simulation. We use the fully coupled nonisothermal EOS3 module for the East Canyon submodel. Temperature profiles in boreholes can provide up-flow or down-flow signatures of groundwater.

7.4 Model Domain

Figure 7-1 shows a 3 m resolution digital elevation map (DEM) of the Berkeley Hills area. The map is shaded to show the topographic relief, so that basins are easily identified. Note that our study area is in a well-defined basin, the Strawberry Canyon. We chose the model area to coincide with the basin (Figure 7-2), which covers the Strawberry Creek watershed east of the Hayward Fault. The model is roughly diamond-shaped, with diagonal lengths 3 km in the E-W direction and 2.4 km in the N-S direction. Boundaries to the northwest, northeast, and southeast were determined by following ridgelines on the DEM, as shown in Figure 7-3. The surface trace

of the Hayward Fault forms the southwest boundary of the model. It follows a strong break in slope between the hilly terrain of the model and the much gentler slope that extends to San Francisco Bay. The elevation along this boundary is gently undulating, with several creeks running NE-SW crossing the fault. The rectangular area in Figure 7-1 with no streets shown is the University of California, Berkeley Campus. Note that there are several creeks running EW, which are the continuation of Strawberry Creek displaced by the Hayward Fault.

In the vertical direction, the model extends from the ground surface, which ranges from about 120 masl to 540 masl, to an elevation of -400 masl. No wells extend any deeper than 0 masl, but the large vertical extent is provided so that the model horizontal-to-vertical aspect ratio is near one, in order to not artificially constrain natural groundwater flow lines.

7.5 Boundary Conditions and Sources and Sinks

The boundary conditions for the preliminary version of the model are as follows.

- Ridgelines: closed (symmetry lines between watersheds)
- Hayward Fault: closed, except at surface, which provides outflow from model
- Bottom: closed
- Top: constant pressure at $P=P_{atm}$ (allows gas flow in or out of the model and liquid flow out of the model)

Conditions at the bottom boundary are unknown, but the boundary is purposefully placed far below the depths of the boreholes, so as not to unduly influence groundwater flow. Our initial conceptualization for major faults such as the Hayward Fault is that at depth they provide barriers to flow across the fault. This hypothesis will be tested by trying different flow conditions at this boundary.

The top boundary essentially represents the ground surface. Each element in the model layer below this boundary contains a mass source to represent a user-specified fraction of precipitation that has the potential to infiltrate into the subsurface. Source strength is adjusted between gridblocks such that a uniform flux (mass flow rate per unit area) is assigned. If the permeability in the vicinity of the mass source is too low to accept the specified flow, then pressure increases and liquid flows upward into the constant-pressure boundary and is lost from the model. This lost flow could represent surface water flow, eventually ending up in storm drains or creeks, or it could represent evapotranspiration.

7.6 Geologic Model

A plan view of the geologic model is shown in

Figure 7-4, based on available geologic maps (Graymer, 2000; Karasaki et al., 2010). Because the available geologic maps are two-dimensional, some assumptions have to be made regarding the subsurface geologic structure. Kiho et al. (2012) refined the geologic map proposed by Graymer (2000) through conducting additional field geologic mapping along the Wildcat and building upon Karasaki et al. (2009, 2010, and 2011) in addition to the new information obtained from the cores from WF-4 and WF-5. They proposed the geologic cross sections shown in

Figure 7-5. At the scale of the WF borehole cluster, we again refer to the structural model proposed by Kiho et al. (2012) as shown in

Figure 7-6. In fact, Kiho et al.'s fault structure model (Figure 7-7) and the structural model discussed in Chapter 4 have much in common. The current geologic model used in the hydrologic simulation can be seen in Figure 7-8 and Figure 7-9. It essentially incorporates Fb, Fc and Fd structures proposed by Kiho et al. (2012), except our model assumes that Kihoet al's Fd-branch is the main Wildcat.

Currently, Fb is modeled as the geologic boundary between the Orinda Formation/San Pablo Group and Claremont Formation, without any thickness or independent permeability. Fc is modeled as a permeable structure, while Fd is modeled as a dual structure, with low permeability perpendicular to the fault and high permeability parallel to the fault. All the features are treated as a plane.

We assume that hydrologically there are two types of Orinda Formation and Claremont Formation The Orinda Formation observed in WF-2, WF-3, and WF-4 appears to be subhorizontal, whereas the same formation on the east of the Wildcat Fault is reported to be subvertical, as is the Claremont Formation on the east side of the Wildcat (Geomatrix, 2008). In general a sedimentary layer is anisotropic, with a lower vertical permeability than horizontal when it is in the original depositional state. Therefore, we expect a lower permeability in the vertical direction of the Orinda Formation in the west and vice versa on the east. As for the

Claremont Formation, we only assumed that the Claremont on the west is of a different material than on the east of the fault.

7.7 Grid

The preliminary numerical grid is constructed of 23 layers, each with the same lateral discretization. Lateral discretization is done with Voronoi tessellation and is variable, with finest resolution near the wells and Wildcat Fault, and a gradually coarsening grid beyond that (Figure 7-10). Each layer has 4295 gridblocks, and the total number of active gridblocks for the model is 101,024 (the top layer, representing the constant atmospheric boundary, is inactive). Three features are present in the numerical model that are not shown in the original geologic model: the Hayward Fault, the Strawberry Creek Fault, and the Moraga landslide.

The top of the model is defined by the DEM, and layer thickness gradually adjusts to conform to it (Figure 7-11). Note that the top three layers are thinner, to better represent surface changes in topography. Figure 7-12 indicates that the lateral resolution is fine enough to resolve all the features present in the geological model. The resolution of the grid can be further checked by extracting just the elements that represent the wells, as shown in Figure 7-13. Note that the arrangement of different materials is consistent with interpretations of logging and coring for all the WF wells (see Figure 2-4). Permeabilities for all the materials are given in Table 7-1, taken from last year's modeling (Karasaki et al., 2011).

Kiho et al. (2012) took a different approach. They uniformly discretized the structural model of a much larger area (shown in Figure 7-7) to produce a numerical mesh as shown in Figure 7-14. They assumed uniform properties for all the faults identified in the structural model.

Simulation Results for Natural-state Head Distribution

Figure 7-15 shows a perspective view of the natural state head distribution for the base-case simulation. Figure 7-16 shows head iso-surfaces of the same; Figure 7-17 shows the cross-sectional views of the hydraulic head distribution. The impact of the Wildcat Fault is apparent as a small jump in pressure. Figure 7-18 shows the same view of the gas saturation distribution. A vadose zone develops where permeability is larger than needed to accommodate the specified infiltration flux. Figure 7-19 further illustrates the surface boundary by showing the flux of liquid out of the model. Where flux out is zero, infiltration is occurring. Where flux out is small (e.g.,

over most of the Orinda Formation), this generally means that the local permeability is too small to accommodate the specified infiltration rate. Where flux out is large (e.g., along Strawberry Creek and at the downhill edge of the Moraga), it suggests that changes in topography are creating a groundwater-to-surface-water transition—a spring. The large flux along the Hayward Fault occurs because this is the lowest elevation in the model, and therefore, must provide an outflow boundary.

Several simulations were run with varying amounts of infiltration, including 50%–100% of the average annual precipitation rate of 1,000 mm/yr. Figure 7-20 compares hydraulic head values observed at the WF and SSL **[define?]** wells with model values for the simulation, with the best match between the two denoted as the base case. Here, infiltration is specified as 67% of precipitation. If precipitation is too low, well SSL-1 cannot sustain the observed pumping rate. Although the modeled heads are somewhat too large for all the wells, the separation between wells WF-1 and WF-2 observed in the field is captured by the model.

Figure 7-21 through Figure 7-23 illustrate the results of simulations that vary the properties of the WF. In Figure 7-21, the fault does not have a low-permeability core. Although the match for Well WF-1 is improved, the model does not give enough separation between this well and WF-2 and WF-3. In Figure 7-22, the fault does not have a high-permeability damage zone. Now all the modeled head profiles decrease too rapidly with depth. In Figure 7-23, the fault does not exist at all (that is, the area where the fault is located just has the properties of the adjacent Claremont Formation). In this figure, the model head profiles do not show the WF-1 separation and also decrease too rapidly with depth.

7.8 East Canyon Sub-Model

The Strawberry Canyon model we have discussed thus far is based on a topography that clearly defines a closed basin, as shown in Figure 7-1. Using the hydraulic test results and pressure monitoring data, we estimated the permeability structure of the fault and the surrounding rocks. However, the parameters we obtained are, strictly speaking, only valid within the extent of the tests. We did find that long-term monitoring of seasonal changes in pressure may be useful in estimating the parameters of a larger volume outside of the well field. In particular, we found that the rate of decline of pressure during a dry season may be used to further calibrate or to verify the model. We used a Voronoi tessellation for the Strawberry

Canyon model to keep the number of elements to a manageable size and still have fine discretization near a borehole. But for the purpose of matching the static pressure and temperature profiles in boreholes and seasonal fluctuations due to rainfalls, no discretization is necessary in the vicinity of boreholes. Rather, a regular-sized **[?]** grid with the finest affordable resolution is better for accuracy and manageability. For these reasons, we created a submodel, which we call the East Canyon Submodel, with regular discretization, whose boundary is shown with the red broken line in Figure 7-1. As can be seen from the figure, the submodel captures a smaller but less well-defined basin. Figure 7-24 shows the numerical mesh of the East Canyon submodel.

In the Strawberry Canyon model, we represented the duality of the Wildcat, i.e., high permeability along the fault and low permeability across it, by using asymmetric material connections. This is done by assigning high permeability between the cells with same material but low permeability between different materials, specifically between the fault material and Orinda or Claremont Formations. In the East Canyon model, we represented the Wildcat with two side-by-side planar features,—one representing the high permeability damaged zone and the other the low permeability core, as can be seen in Figure 7-24.

We assigned a 10-to-1 ratio of anisotropy to the fault damage zone, based on the findings discussed in Chapter 5. A recharge rate of 2.2×10^{-6} kg/m^2/s was assigned as the top boundary condition, which is approximately 7% of the yearly average rainfall of 1,000 mm in this area. The temperature profile data from WF boreholes indicate that the geothermal gradient is ~4°C/100m, which is relatively high. This is the result of the balance between cold rain recharging form the surface and the heat flux from a deeper subsurface. The bottom heat flux boundary condition was set at a constant rate of 85 mW/m^2. Karasaki et al. (2011b) used a similar approach by utilizing the temperature profile from boreholes to reduce the uncertainties of a geohydrologic model.

Figure 7-25 shows the comparison between the observed head data in WF-1–WF-3 boreholes to one of the best simulation results. Note that the simulation reproduces the decreasing head distribution along the depth of the boreholes, the separation of heads between WF-1 and WF-2, and the low head anomaly in WF-2, which is likely caused by the permeable Fc feature that drains water to lower elevation. Figure 7-26 shows the data and simulation

comparison for WF-4 and WF-5. As can be seen in the figure, the model does not reproduce the higher head toward the bottom of the boreholes. Recall that both boreholes are inclined and drilled into the hill, which can explain the higher head. We suspect this is partly a mesh-resolution problem. It is possible to obtain a better match in WF-5 by locally introducing a low permeability zone. Figure 7-27 shows the simulated and observed temperature distributions along the WF boreholes. The solid and broken lines denote the observed and simulation results, respectively. As can be seen from the figure, the simulation reproduces the temperature profiles relatively well. The observed head data are represented by vertical line segments and the temperature data are continuous lines, because the head within an observation interval is assumed constant along the entire length as it is packed with coarse sand—whereas the temperature is thought to be linearly varying within an interval. This raises the question of the soundness of the traditional approach, in which observation intervals are very long and isolated by short packers. (In our case, grout was used in place of packers.) We thus developed a continuous sealing system with short open intervals and long sealing rubber elements. (This will be discussed further in Chapter 8.)

Figure 7-28 shows the flow vectors above a 200 m elevation as well as the pressure distribution at that elevation. As can be seen in the figure, the flow vectors converge to the Wildcat Fault and flow along it. There is outflow at Quarry-1, an artesian well, which is actually diverted to a storm drain. Also, flow along the Strawberry Creek is noticeable.

Figure 7-29 shows the liquid saturation distribution. Near-surface areas at high elevations in the East Canyon are in two-phase flow. Lower elevations to the south of the WF boreholes are saturated. In reality, there is a network of storm drains throughout the canyon that directly diverts near surface water to Strawberry Creek.

7.9 Model Verification

Now we have an East Canyon submodel that reasonably reproduces the key aspects of head and temperature distribution observed in WF holes. In fact, several combinations of permeability produce similar goodness of fit. The next question is, how good are these models in predicting phenomena that were not used in the model calibration. Recall in Chapter 5 that we discussed the rate of decline of heads in WF-1 being ~2 meters per half year during a dry period.

We now try to see if the models predict a similar rate of decline by imposing a boundary condition simulating a wet and dry season.

In developing the East Canyon model, we imposed a constant mass-flow-rate boundary condition (2.2×10^{-6} kg/m^{2}s, equivalent to 7% of the annual average rainfall) on the surface and ran the simulation until steady state was reached, which is typically over 100,000 years in simulation time. We then use the steady-state condition produced by models that match the borehole head profiles as the initial condition to simulate rainfall during a rainy season, followed by a dry season, for one year. Although we could use the actual daily rainfall data from the previous year as the boundary condition, we simplified the recharge event to a constant flux at 1×10^{-5} kg/m^{2}s for 80 days for the rainy period and zero rainfall thereafter for one year.

Figure 7-30 shows the head transients at WF-1#3 from January 2011 through the end of February 2012, compared to the simulation results. The negative spikes in the observed data are due to pumping tests, which were not simulated. Both red and green lines have the same permeability structure that produce the match shown in Figure 7-26 and Figure 7-27. Specifically, they have the 10:1 anisotropy ratio in the fault zone. The only difference between the two curves is the porosity: the red line represents the case in which the rock has 10% porosity and the green, 5%. As can be expected, the larger porosity value has less rise in head during the rainy period and slower decrease in head during the dry period. Also shown is the pink curve (10% porosity) predicted by the model, which matched the head profiles just as well but with an isotropic Fd feature. During the dry period from June and thereafter, the green curve declines in parallel with that of the observed data. The red line is too slow, while the pink declines too fast.

It is possible that having a constant recharge for 80 days represent the rainy period is too much of a simplification. The rate of decline during the dry period is controlled by the overall through-flow permeability from the area around the boreholes and to the discharge location, as well as by the porosity. Out of the three models, the 5% porosity model with 10:1 anisotropy ratio may be the best model thus far. Note that porosity was not directly used in the calibration when we tried to match the head profiles along WF boreholes. Consequenty, choosing the 5% porosity over 10% is actually a secondary calibration.

It should be noted that the crude porosity estimate of 1.5% in the Moraga Formation, based on the level observation in SSL-1, is not reflected in the model. Although both numbers are at

least in the ball park, and the porosity variation in the Moraga Formation is expected to have little impact on the borehole area because it is rather far away, the model run with the 1.5% porosity should be examined.

7.10 Conclusions

We developed a hydrologeologic model of the Strawberry Canyon basin that incorporates most of the geologic features and faults identified. We performed both manual and automated inversion analysis and produced reasonable matches between the observed head data and model predictions. The use of a constant-pressure surface boundary eliminates the need to specify a variable recharge rate depending on the surface rock type—the model accomplishes this automatically. We do have to vary the specified infiltration rate for the high-permeability regions where a vadose zone develops, and for these regions, specifying infiltration as 67% of precipitation produced the best match to observed head data. This 67% rate is rather high and may result from an artifact of the way we handled recharge; actual recharge into the model may be much less. By varying the structure of the WF, we find that the base-case representation, which includes a high permeability damage zone and a low permeability fault core, best matches the observed head data.

It is possible to obtain better matches to the observed heads with a mesh refinement and local adjustments of parameter values. However, our objective here is to develop a methodology by which to understand the role of faults at a bigger scale though numerical modeling. If a better match is obtained by local refinements, it is probably not very important at a larger scale, unless the refinement itself is some culmination of a larger scale property.

We constructed a submodel with uniform horizontal gridding and carried out a two-phase nonisothermal simulation utilizing the pressure and temperature data from the boreholes. We also used information obtained from conducting the hydrologic investigation discussed in Chapter 5, such as the anisotropic permeability in the fault zone. After parameter searches, we were able to match the head and temperature profiles along boreholes relatively well. We then used the best matching models to predict the rate of head decline during a dry period, and found that an anisotropic fault zone with 5% porosity predicts the rate of decline reasonably well. Further optimization may be possible by using more realistic boundary conditions.

In theory, the larger the degree of freedom in the model, the easier it is to match the observed data. However, the goal here is not to simply match the observed data. Typically, data are limited in numbers and areal extent. We would like to build a model that is valid for a scale larger than the observation area. There is the potential that the rate of decline may be used to estimate the permeability downstream of the borehole complex, although more study is necessary to verify this claim.

It should be noted that the gridding used in the model, in a strict sense, violates the conditions for the finite model approximation, where the line that connects adjacent element centers should be perpendicular to the element boundary. Although we don't expect a significant error, it should be examined.

7.11 References

Finsterle, S., iTOUGH2 User's Guide, Report LBNL-40040, Lawrence Berkeley National Laboratory, Berkeley, Calif., 1999.

Geomatrix, Preliminary Geologic Section Along Proposed Fourth Bore Alignment , Caldecott Tunnel Improvement Project,Alameda and Contra Costa Counties, California, 2008.

Graymer, R.W., 2000, Geologic map and map database of the Oakland metropolitan area, Alameda, Contra Costa and San Francisco Counties, California. USGS Miscellaneous Field Studies MF3242g Version 1.0.

Karasaki, K., Onishi, C.T., Doughty, C., Gasperikova, E., Peterson, P., Conrad, M., and Cook, P., 2011, Development of Hydrologic Characterization on Technology of Fault Zones – Phase II 2nd Report–, NUMO-LBNL-CRIEPI Collaboration Research Project.

Karasaki, K., Onishi, C.T. and Zimmer, V., 2010, Development of Hydrologic Characterization on Technology of Fault Zones – Phase II Interim Report-, NUMO-LBNL-CRIEPI Collaboration Research Project.

Karasaki, K., C.T. Onishi, and Y.S. Wu, 2009, Development of Characterization Technology for Fault Zones, LBNL-1635E, pp 157.

Karasaki, K., K. Ito, Y.S. Wu, M. Shimo, A. Sawada, K. Maekawa, K. Hatanaka, 2011b, Uncertainty reduction of hydrologic models using data from surface-based investigation, doi: 10.1016/j.jhydrol.2011.03.039, Journal of Hydrology, 403 (1-2), pp49-57.

Kiho, K., Ueta, K., Miyakawa, T., Hasegawa, T., Ito, H., Hamada, M., Nakada, H., Tanaka, S., and Tsukuda, K, 2012, CRIEPI Technical Report, Survey and Analysis related to Development of Hydrologic Characterization Technology of Fault Zones IV.

Pruess, K., Oldenburg, C., and Moridis, G., TOUGH2 User's Guide, Version 2.0, Rep. LBNL-43134, Lawrence Berkeley National Laboratory, Berkeley, CA, 1999.

Table 7-1. Permeability values used for the Strawberry Canyon model. The Wildcat Fault (Fd) has both a core and damage zone, whereas Fc, the Hayward Fault, and the Strawberry Creek Fault just have damage zones. Within the Moraga landslide, the permeability is the same as the permeability in the Moraga, but between the Moraga landslide and any adjacent material, permeability is three times lower.

	Orinda		Claremont		Moraga	Great Valley	Fault Core	Fault Damage
	To_H	To_V	Tc_H	Tc_V				
Kx	8.0×10^{-16}	4.0×10^{-16}	1.0×10^{-14}	1.0×10^{-15}	7.0×10^{-15}	7.0×10^{-15}	2.6e-16	1.3×10^{-13}
Ky	8.0×10^{-16}	4.0×10^{-16}						
Kz	1.0×10^{-16}	8.0×10^{-16}						

Table 7-2. Permeability values used for the East Canyon submodel. The anisotropic values for the fault reflect the pumping test results. The rest of the values are optimized values to match the observation data.

	Orinda		Claremont		Moraga	Great Valley	Landslide Material	Surface deposits	Fc	Fault Core	Fault Damage
	To_H	To_V	Tc_H	Tc_V							
Kx	1.0×10^{-17}	1.0×10^{-17}	1.0×10^{-16}	5.0×10^{-17}	3×10^{-15}	1.5×10^{-16}	5×10^{-16}	2×10^{-11}	1×10^{-13}	1×10^{-17}	1×10^{-13}
Ky	1.0×10^{-17}	1.0×10^{-17}	1.0×10^{-16}	5.0×10^{-17}				2×10^{-11}		1×10^{-17}	1×10^{-13}
Kz	1.0×10^{-17}	1.0×10^{-17}	5.0×10^{-17}	1.0×10^{-16}				5×10^{-12}		5×10^{-18}	1×10^{-14}

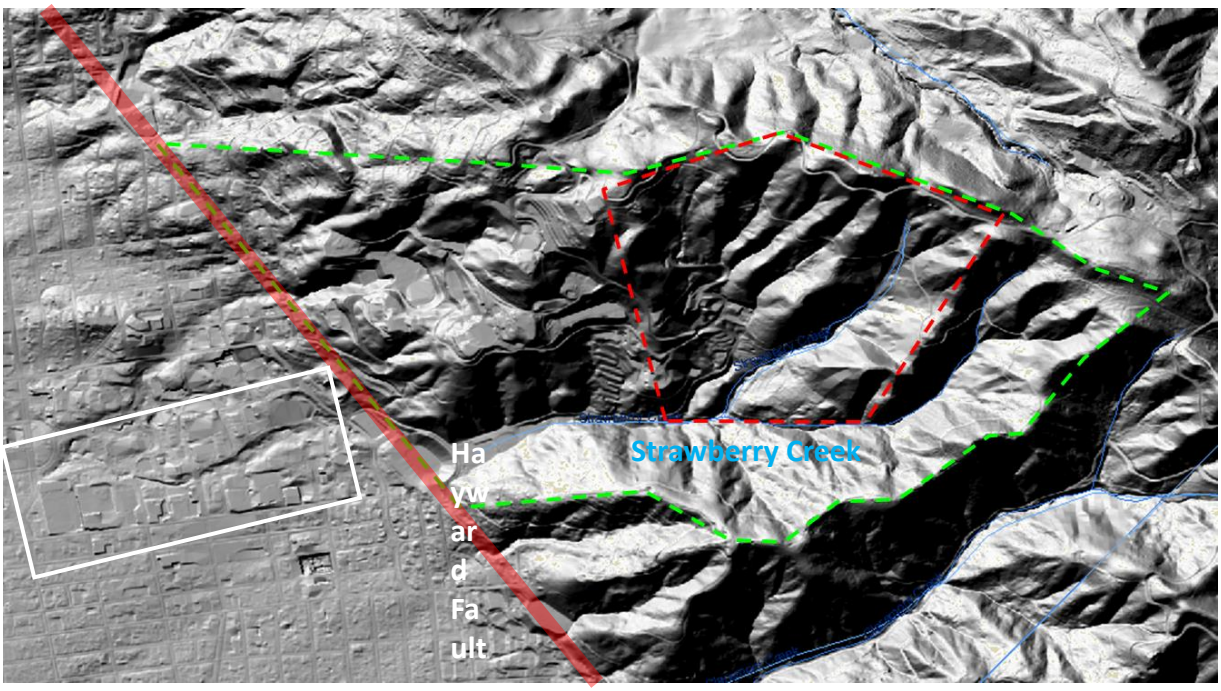

Figure 7-1. Shaded DEM map of the Berkeley Hills. The study area is outlined in green. The red line is the East Canyon Submodel area.

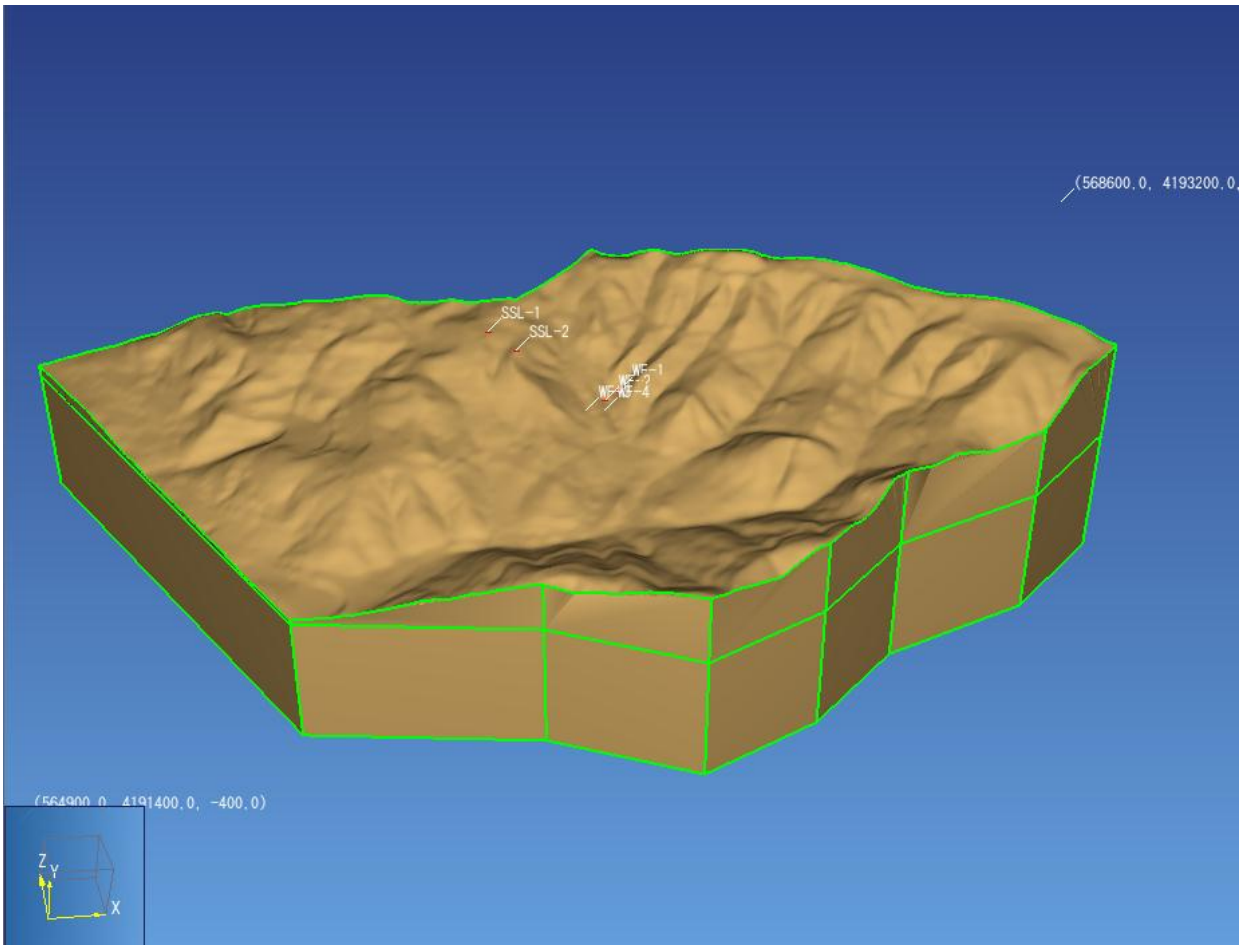

Figure 7-2. The domain of the model showing the surface relief and some of the boreholes.

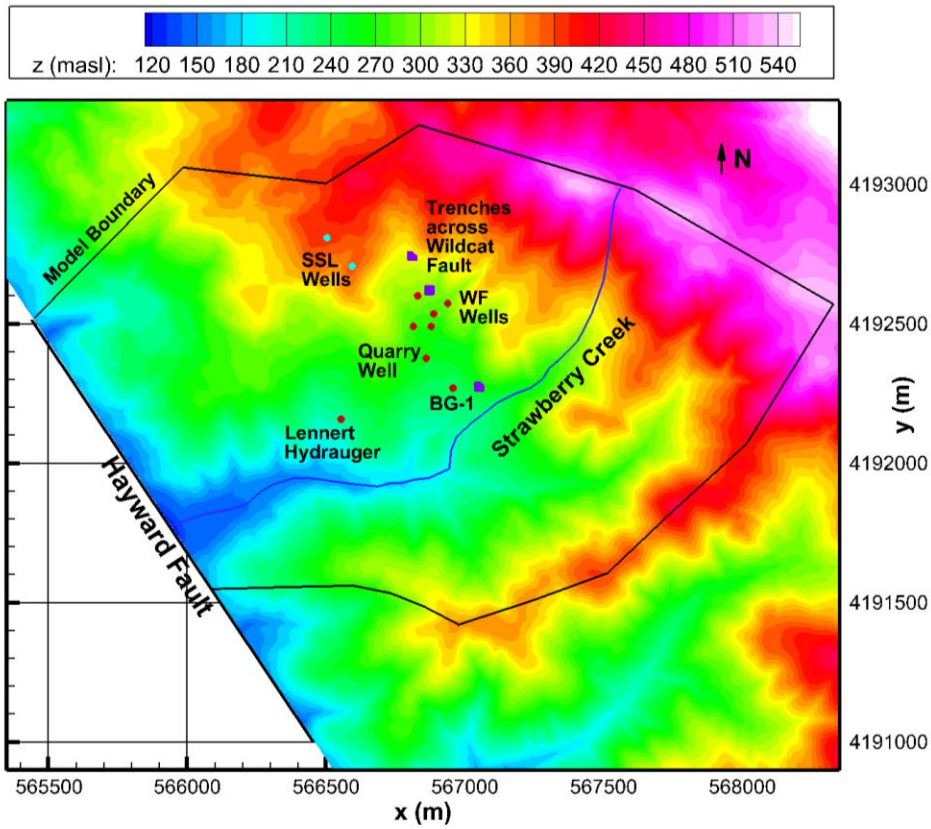

Figure 7-3. DEM with model boundary and various features shown: purple squares= trenches across the WF; red or cyan circles =wells.

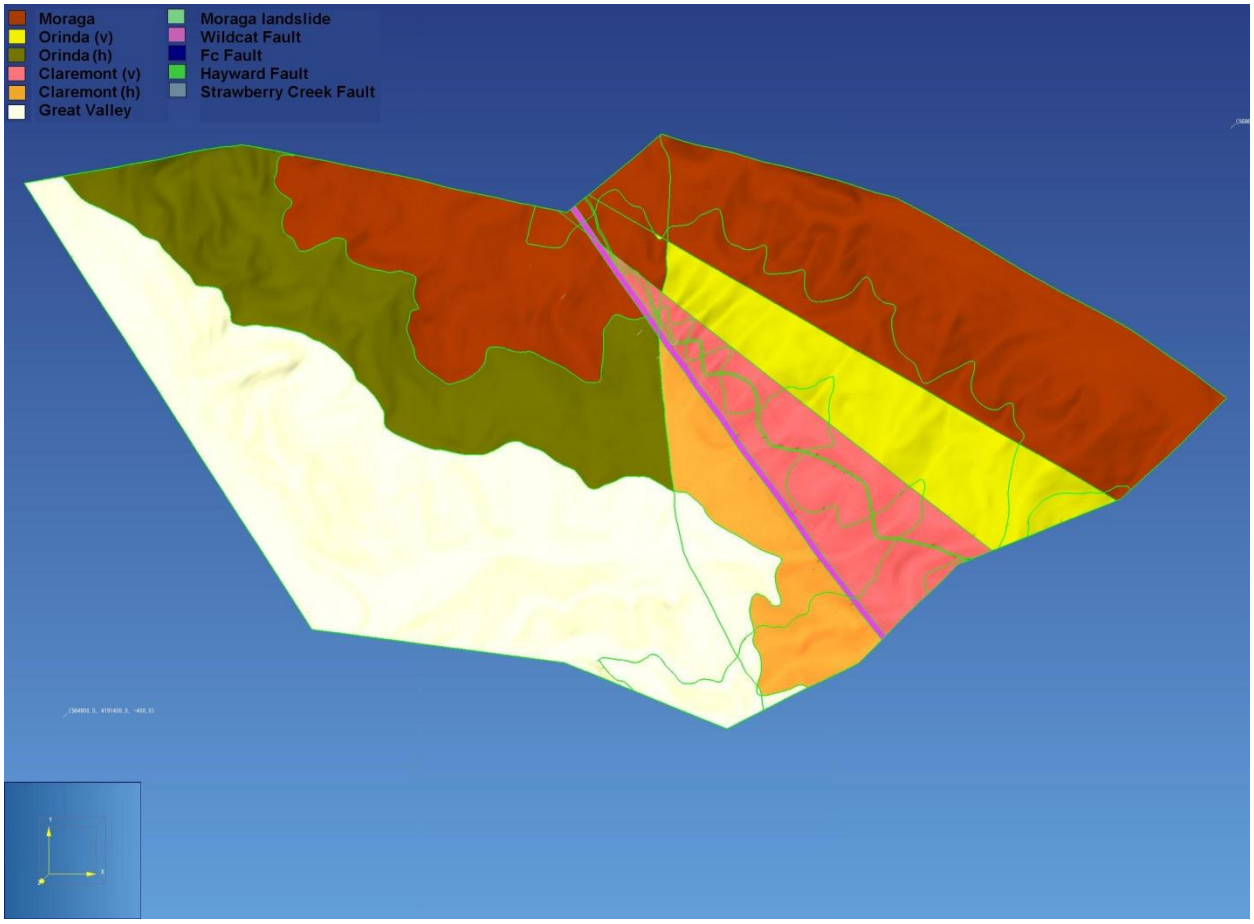

Figure 7-4. Plan view of the geologic model.

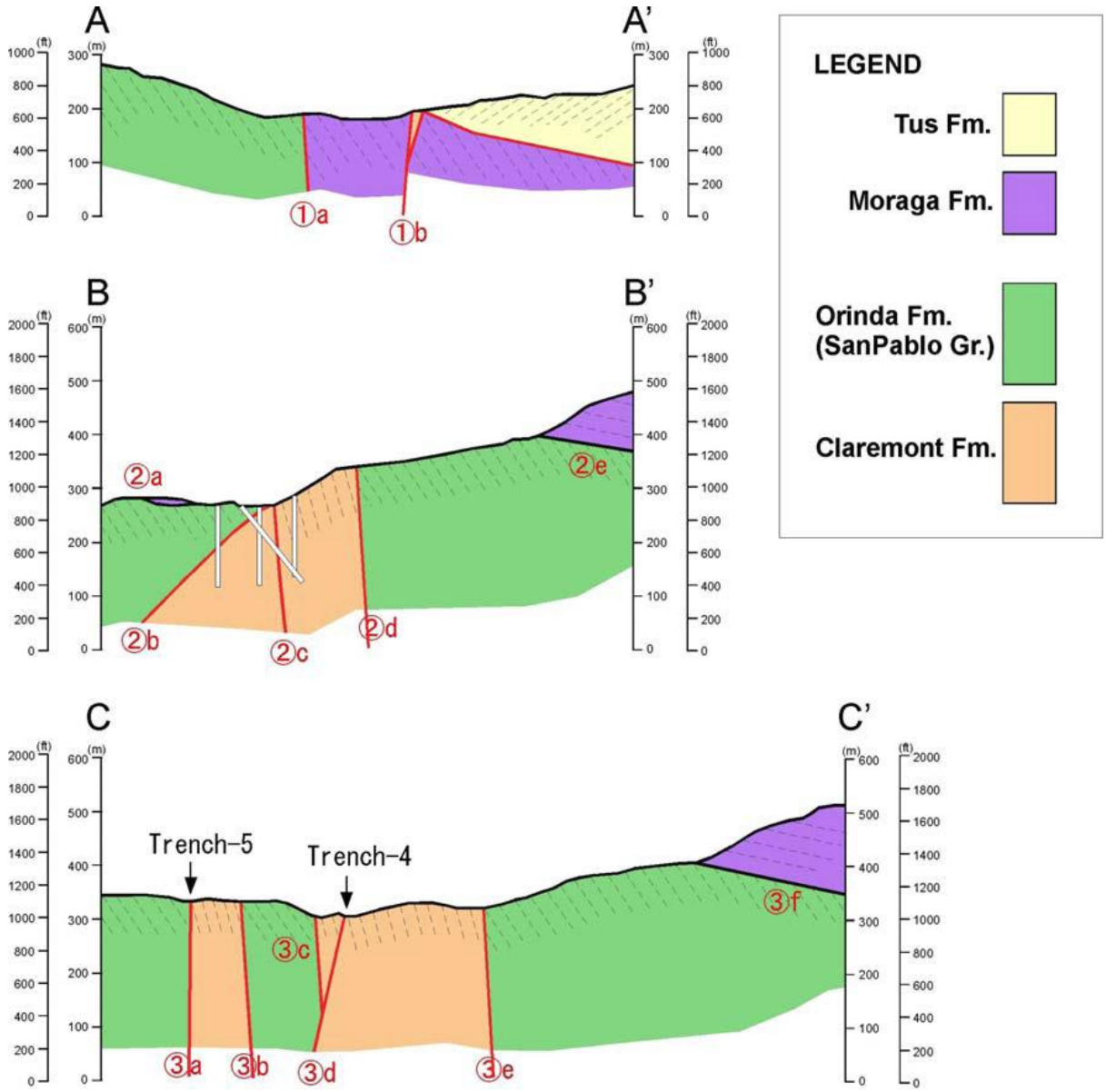

Figure 7-5. The cross sections of the geology along the WF (Kiho et al., 2011).

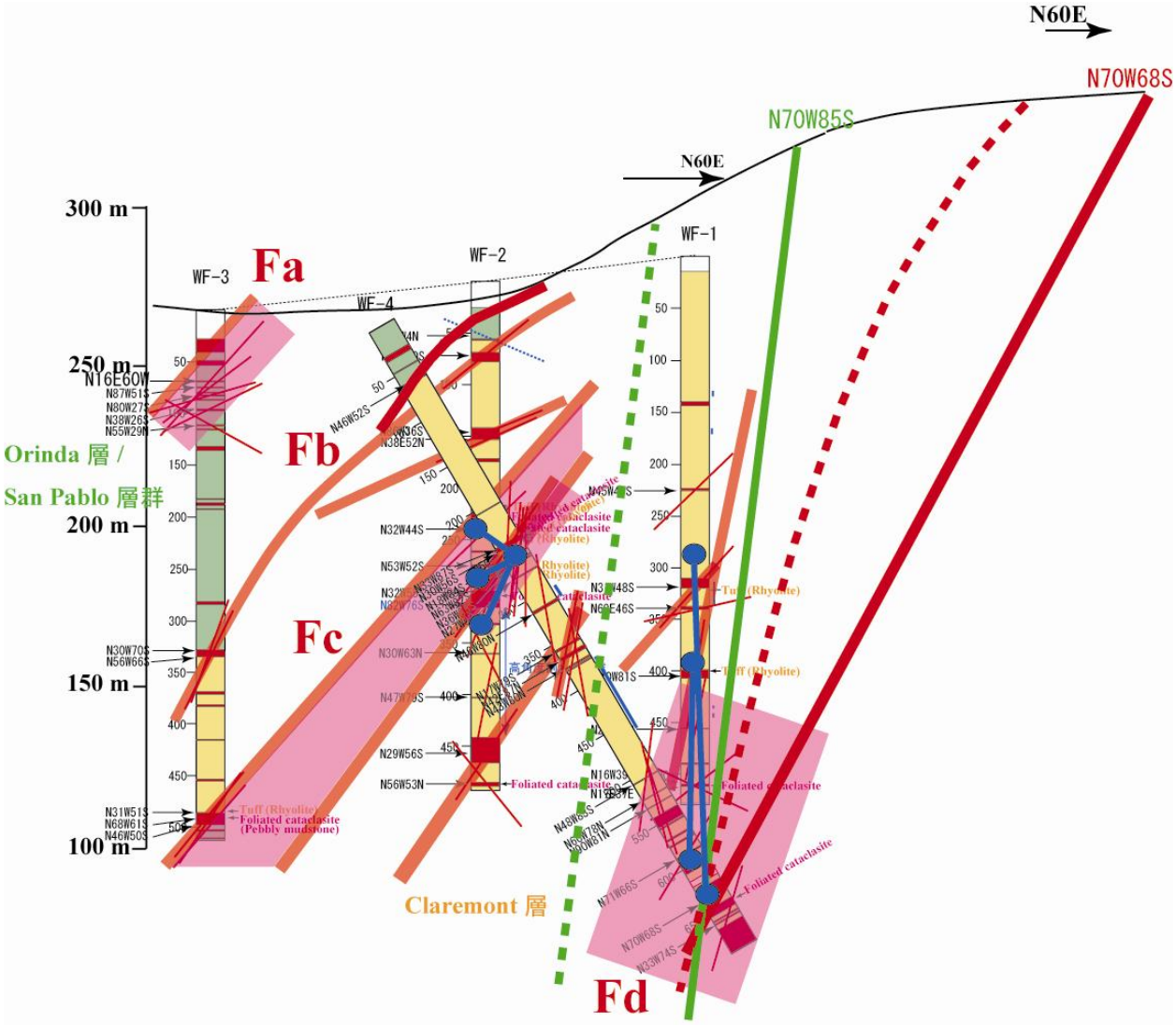

Figure 7-6. Fault structure model near WF boreholes proposed by Kiho et al. (2011).

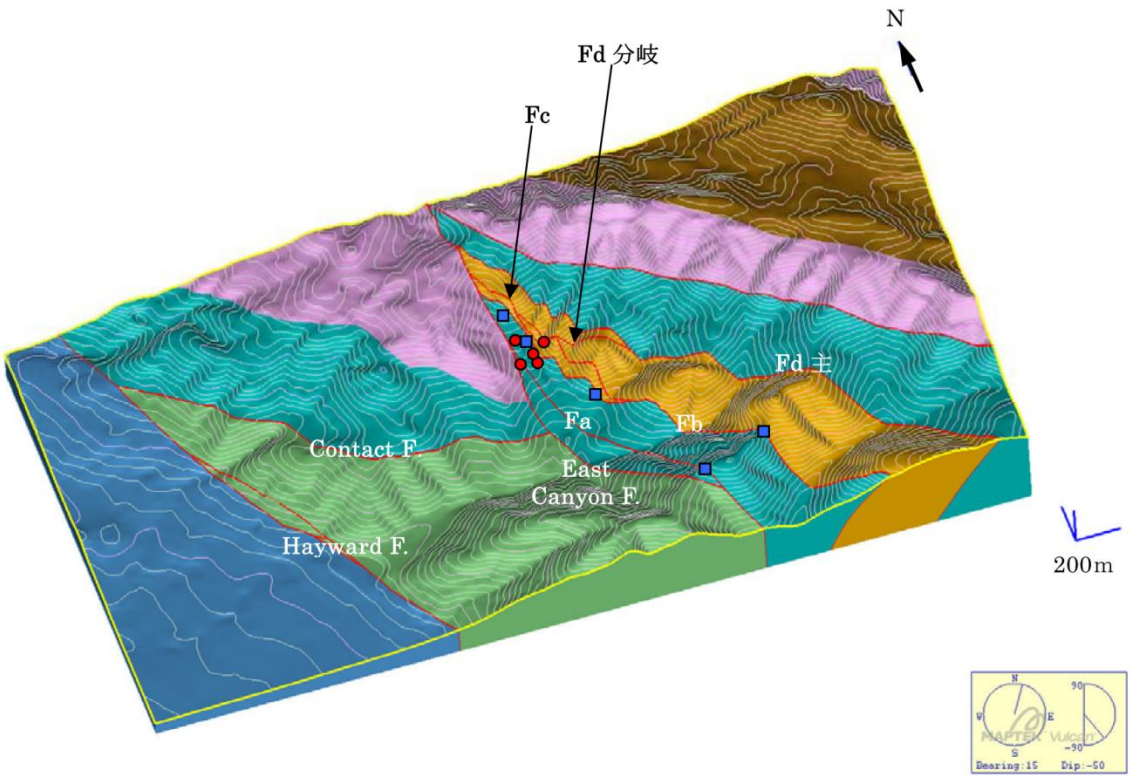

Figure 7-7. Geologic structure model (Model #1) of 3.9 km × 2.1 km area that includes the study area proposed by Kiho et al. (2012).

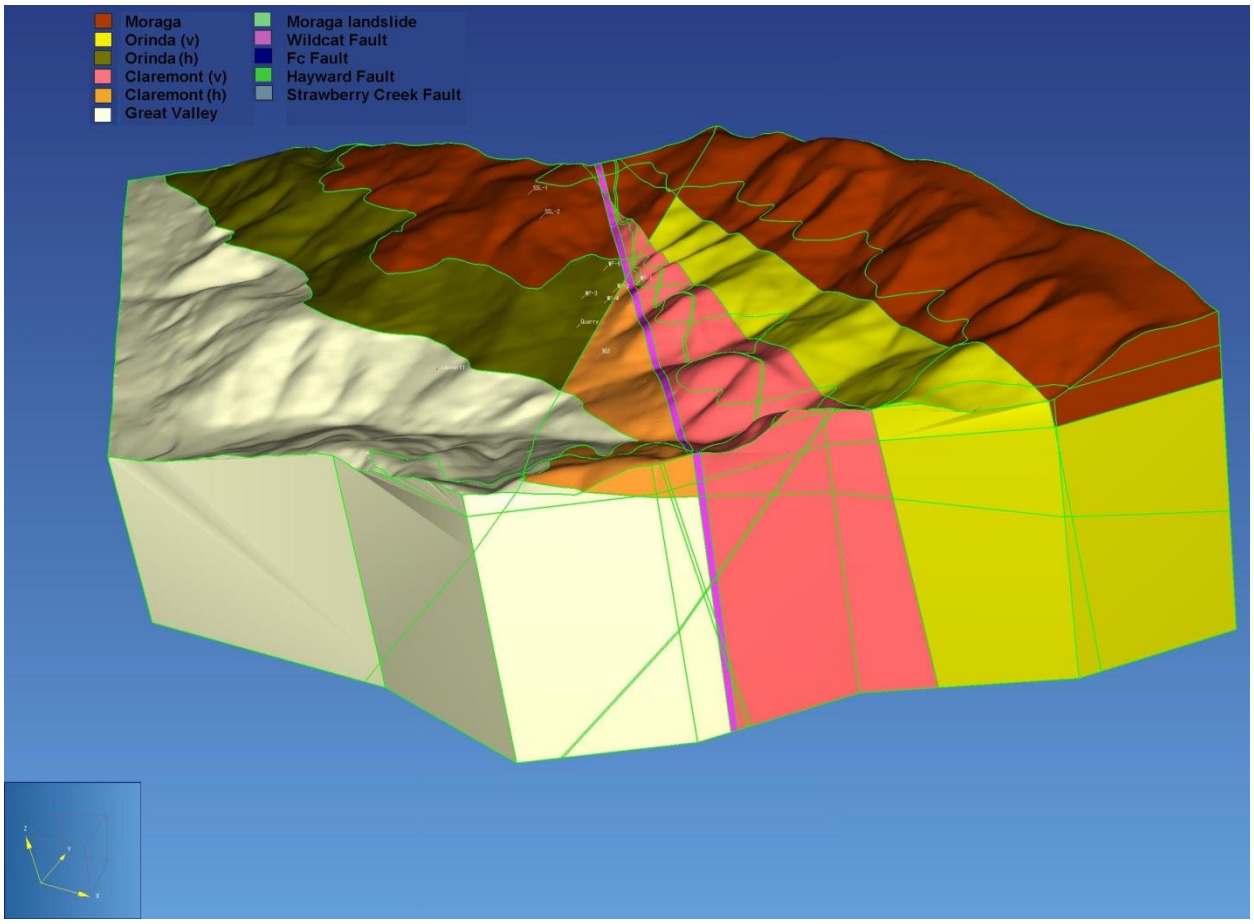

Figure 7-8. Perspective view of the geologic model.

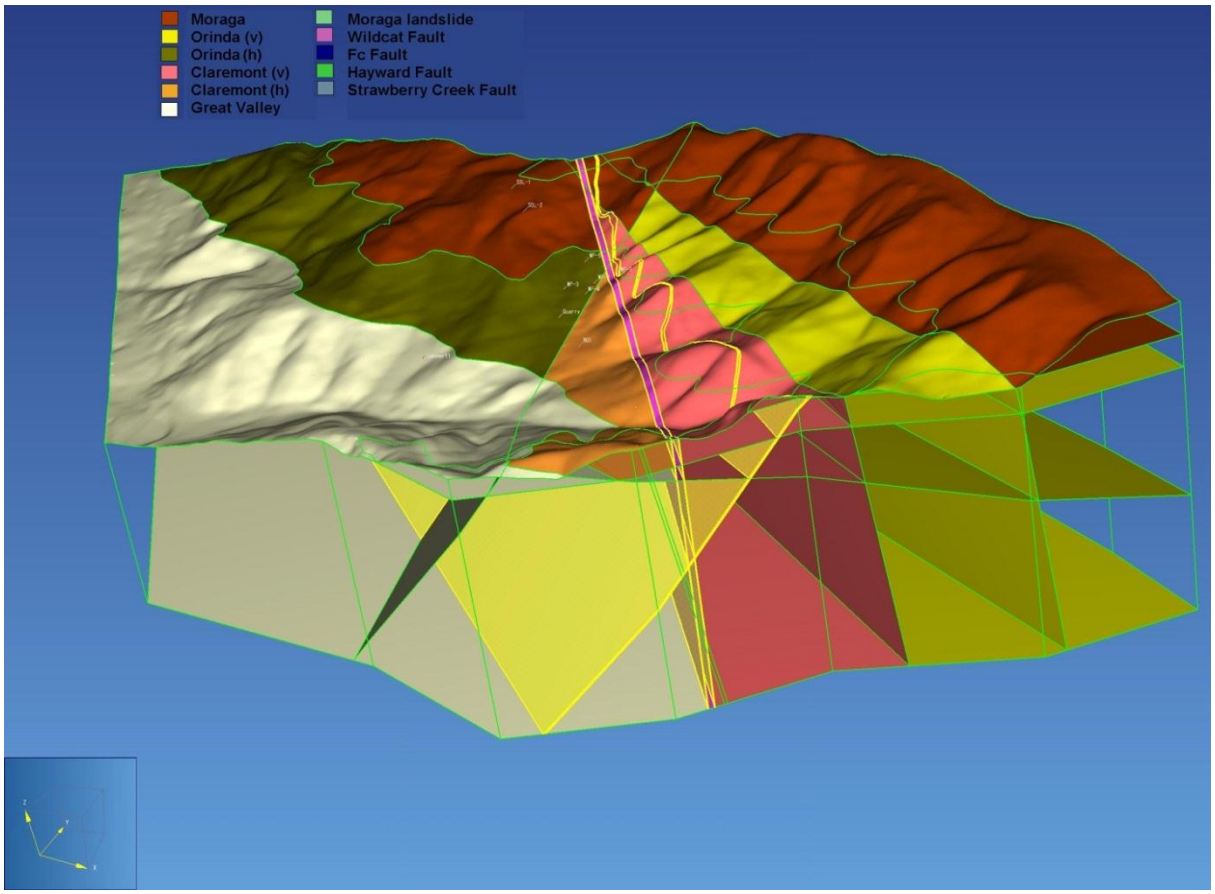

Figure 7-9. Perspective view of the geologic model showing faults and contacts between formations. Two faults are highlighted: the vertical Wildcat Fault (Fd) and the sloping Fc structure that is thought to provide good pressure communication between wells WF-2 and WF-3.

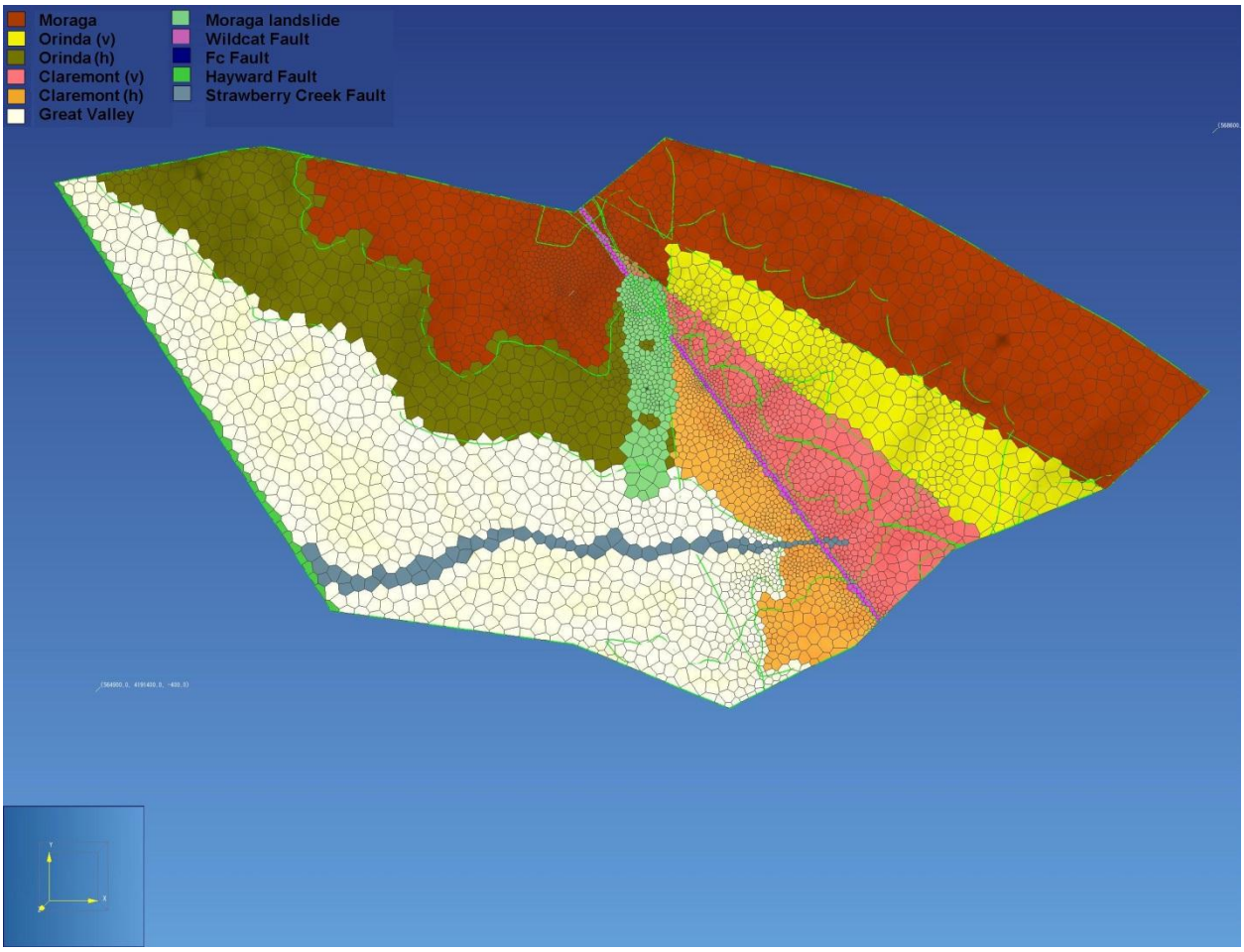

Figure 7-10. Plan view of the computational grid.

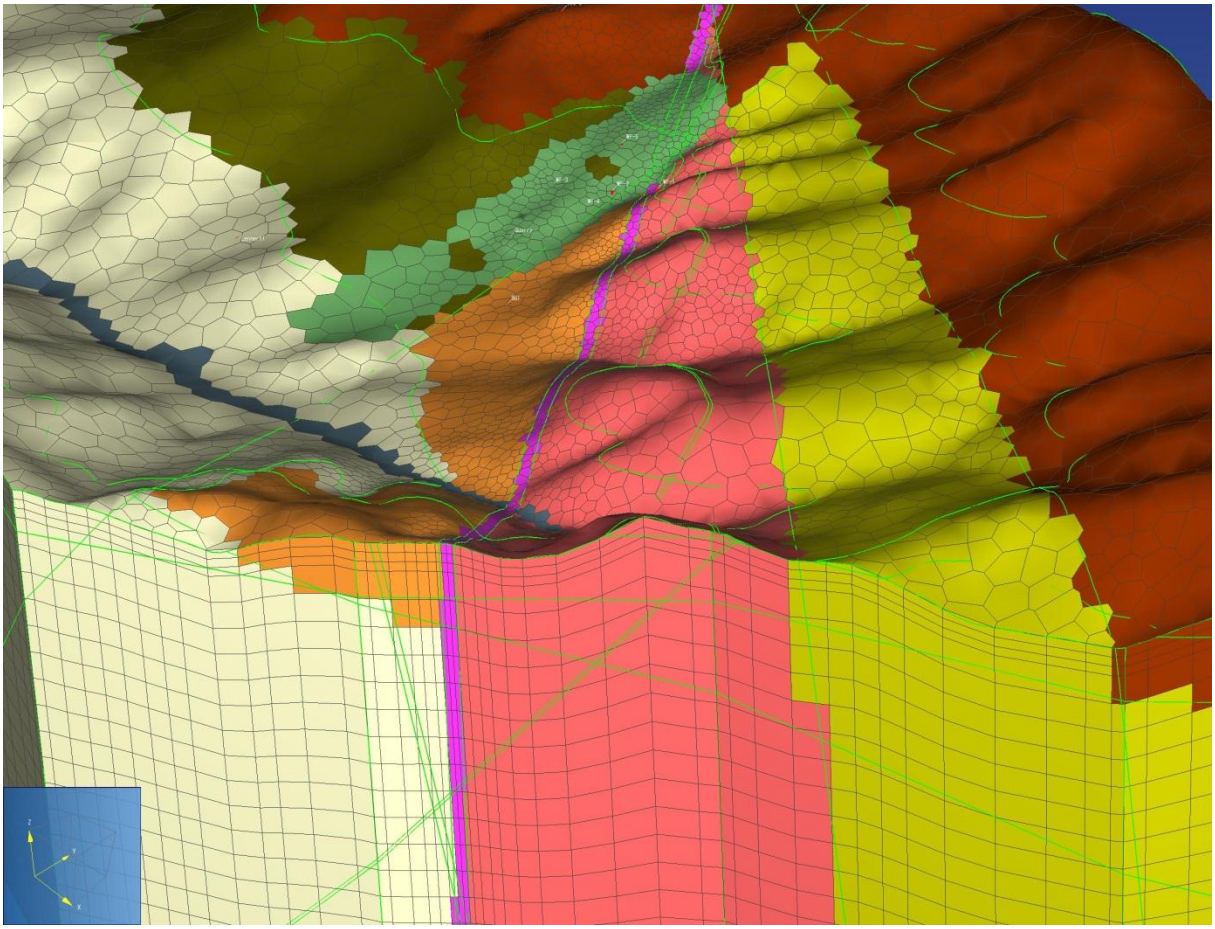

Figure 7-11. Perspective view of the central portion of the computational grid. The surface layer of inactive gridblocks is not shown.

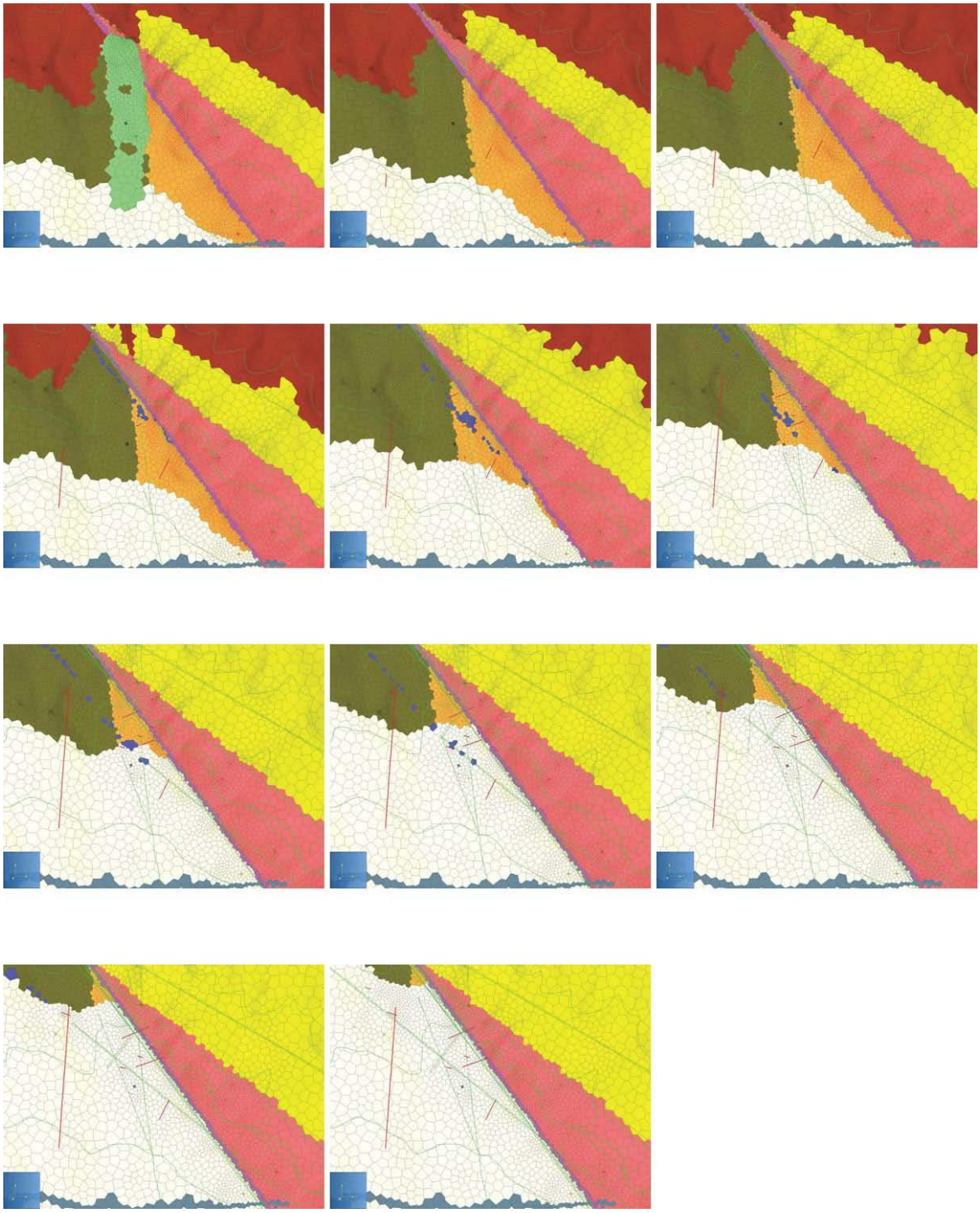

Figure 7-12. Plan views of the central part of the grid for the top 11 layers in the numbered order, which illustrates some of the 3D features of the model including the Fc Fault. It also demonstrates that the model resolution is adequate to represent various features. The light green material in the top layer shows the landslide material.

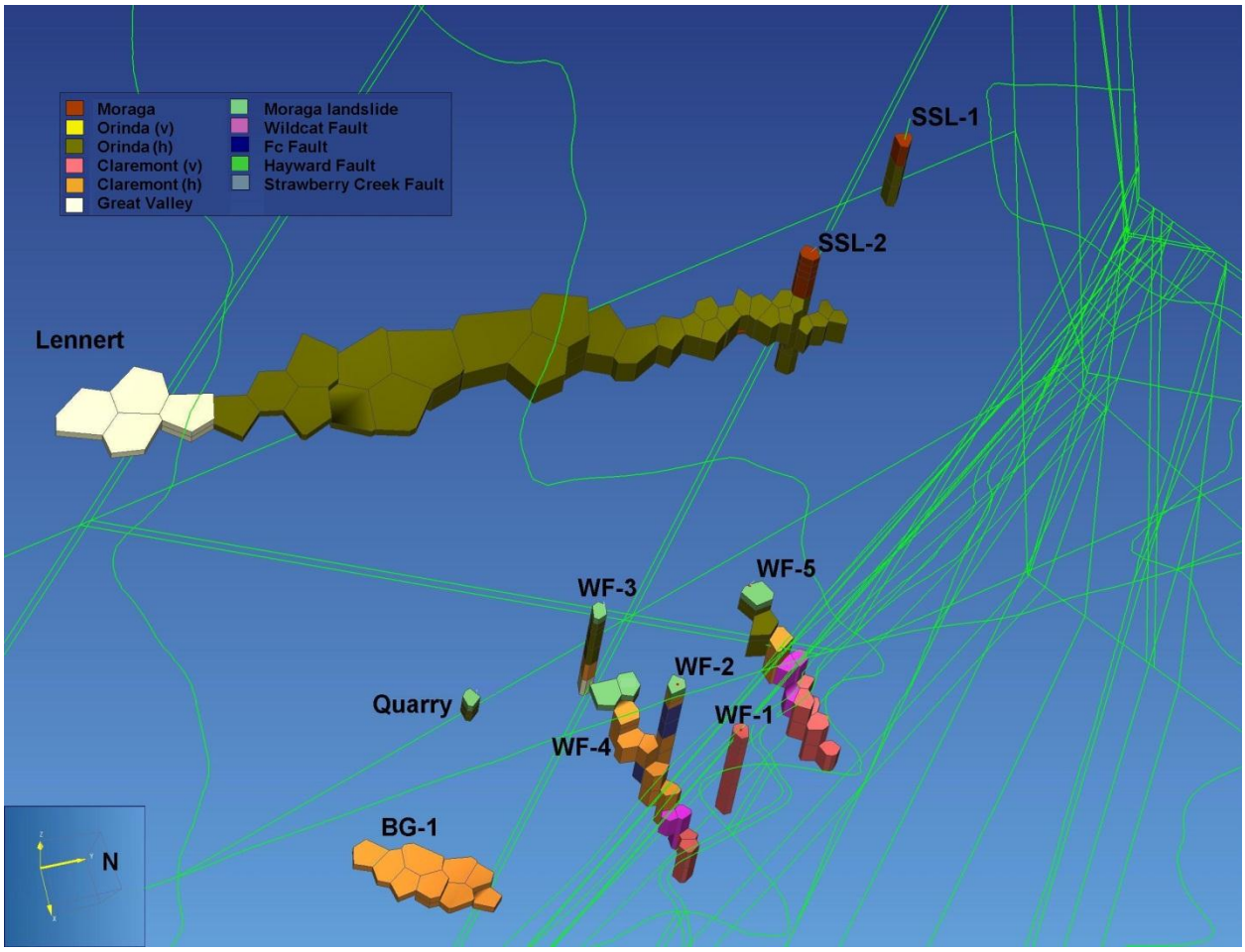

Figure 7-13. The gridblocks representing wells extracted from the computational grid.

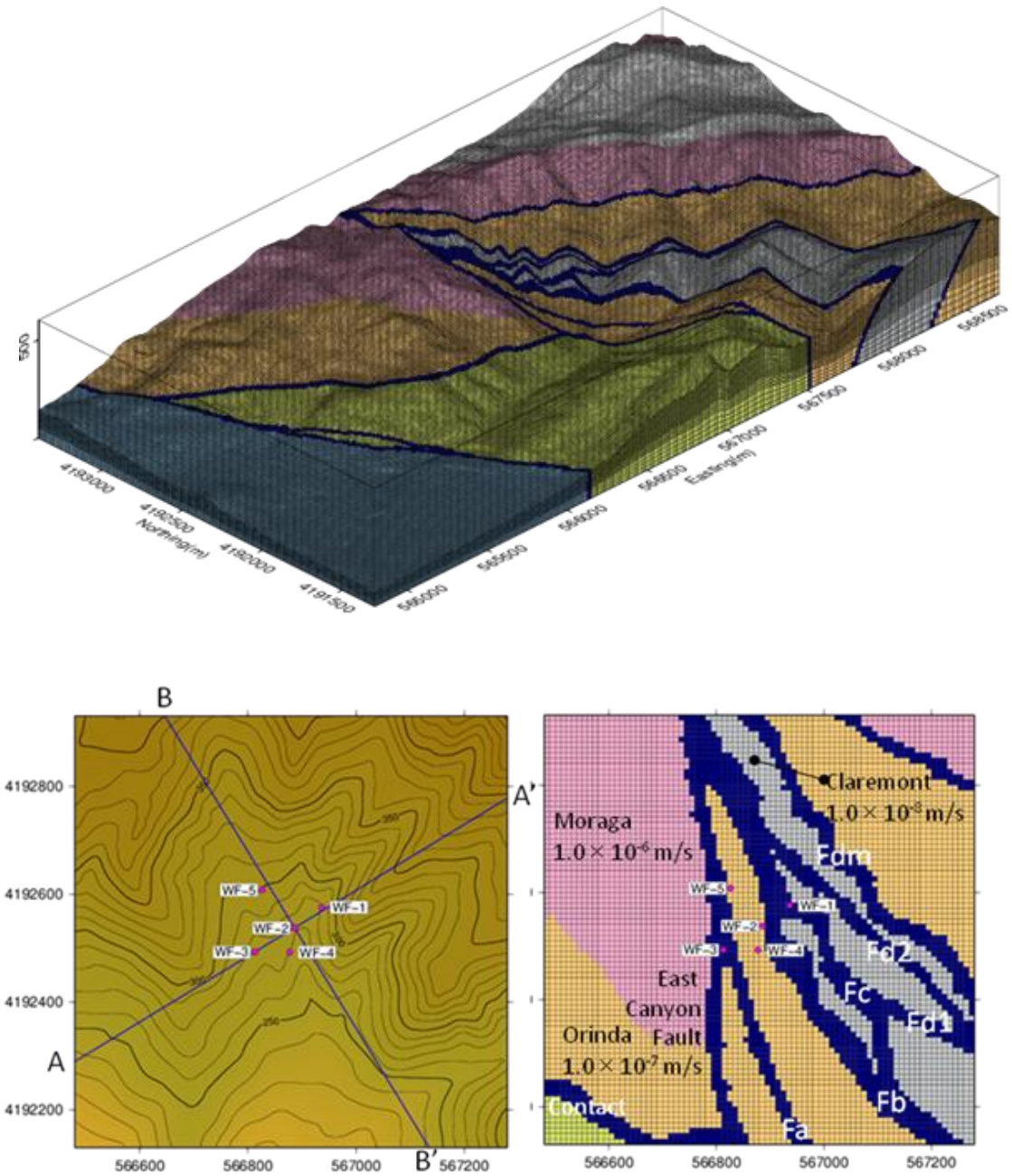

Figure 7-14. Numerical model used by Kiho et al. (2012). The bottom picture is an enlarged view of the borehole area.

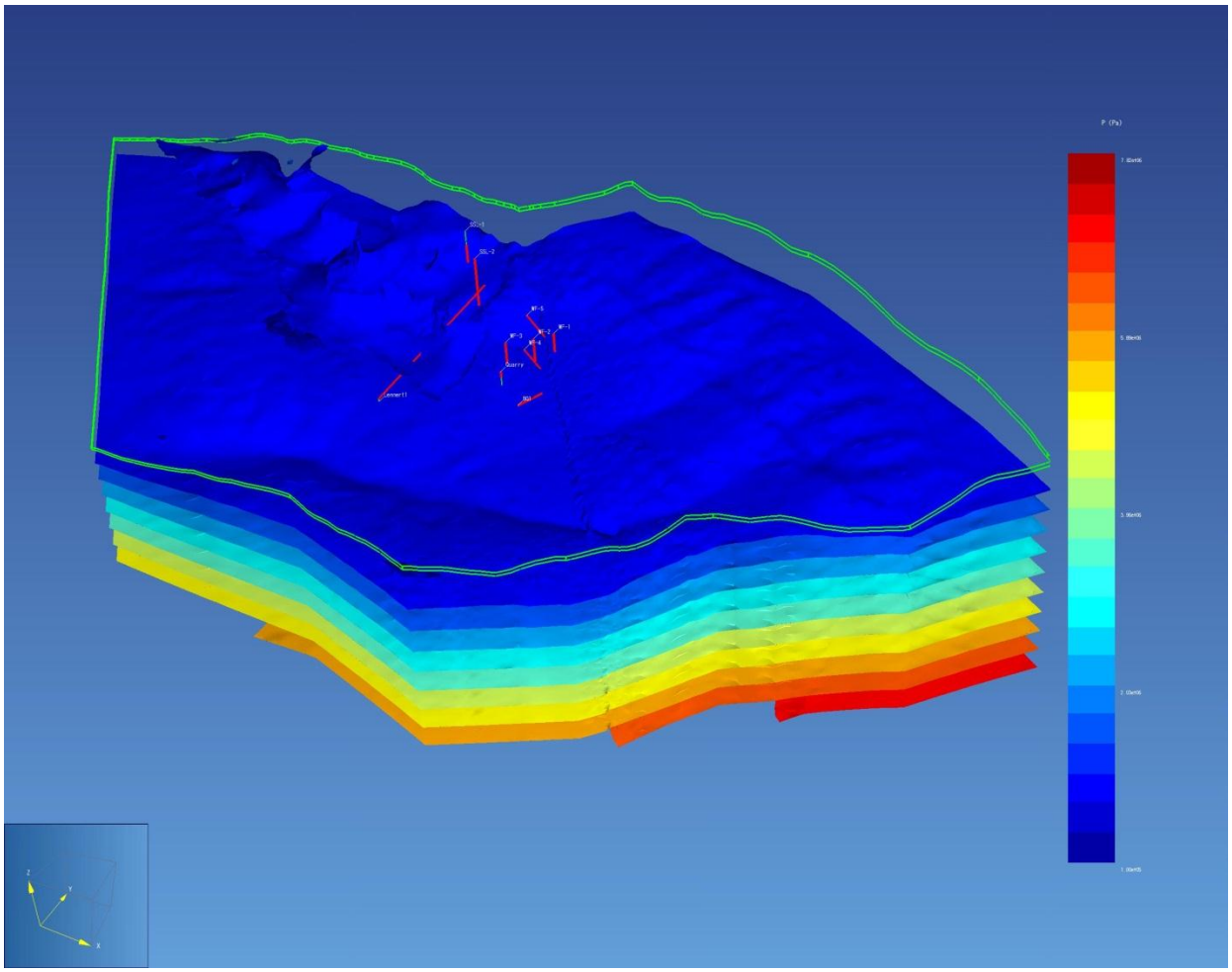

Figure 7-15. Perspective view of the hydraulic pressure distribution for the base case, showing pressure isosurfaces. Topographic features such as the Strawberry Creek canyon are visible, as is the small pressure drop across the Wildcat Fault.

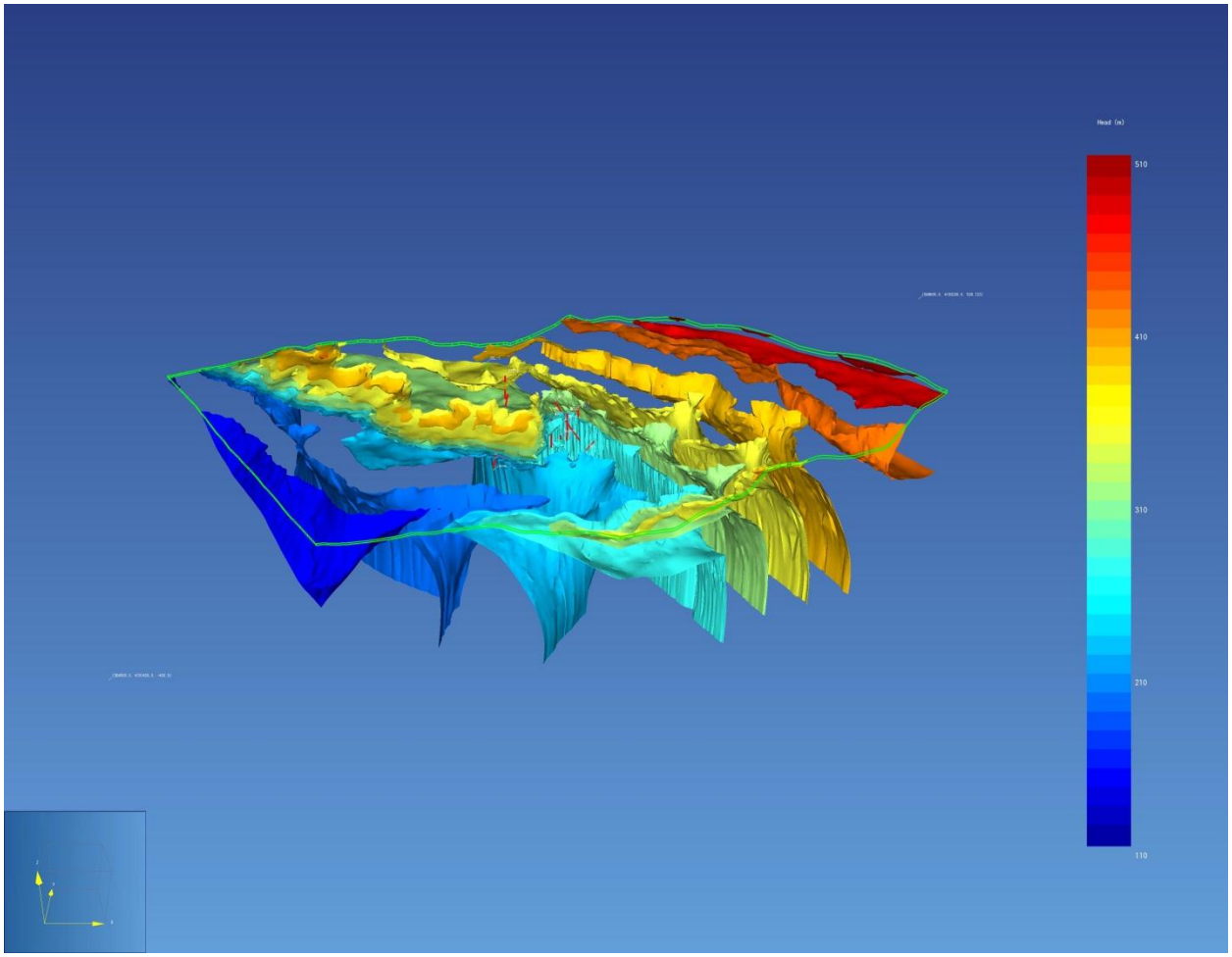

Figure 7-16. Perspective view of the hydraulic head distribution for the base case, showing head isosurfaces. Flow vectors are perpendicular to the head isosurfaces.

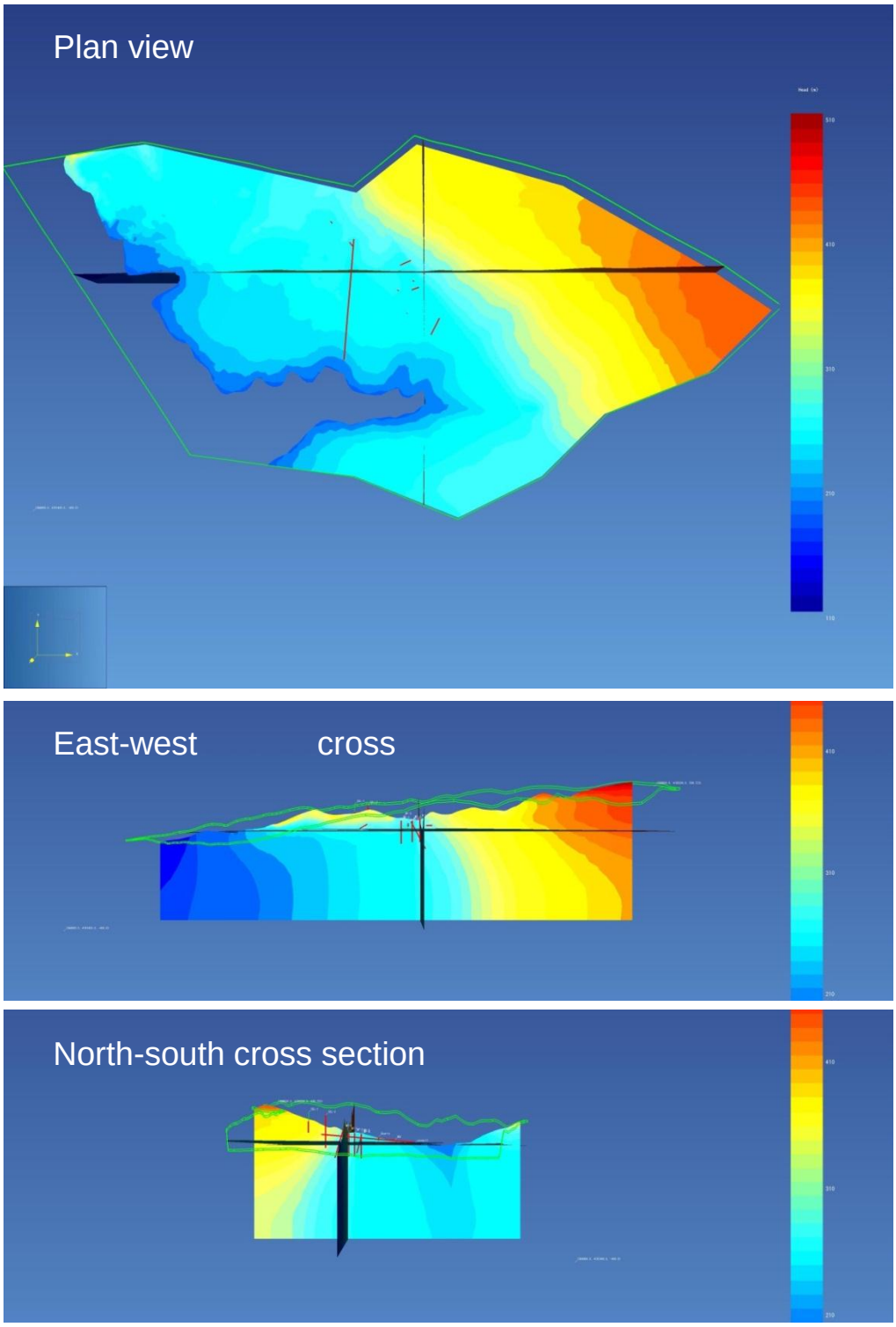

Figure 7-17. Cross-sectional views of the hydraulic head distribution for the base cases. Topographic features such as the Strawberry Creek canyon are visible, as is the small pressure drop across the Wildcat Fault.

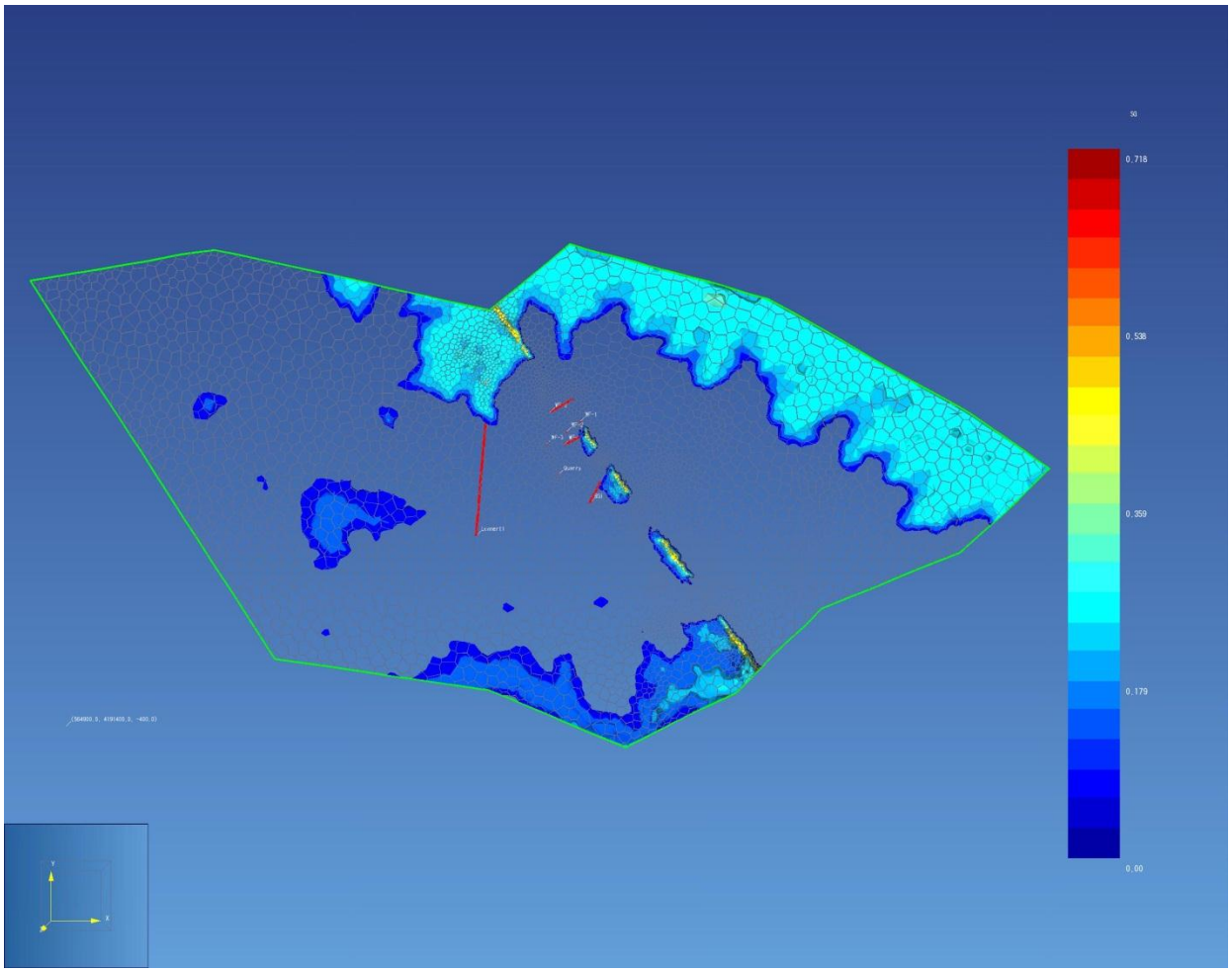

Figure 7-18. Perspective view of the gas saturation distribution for the base case, indicating the development of a vadose zone at high elevations and at places along the high-permeability structure of the Wildcat Fault.

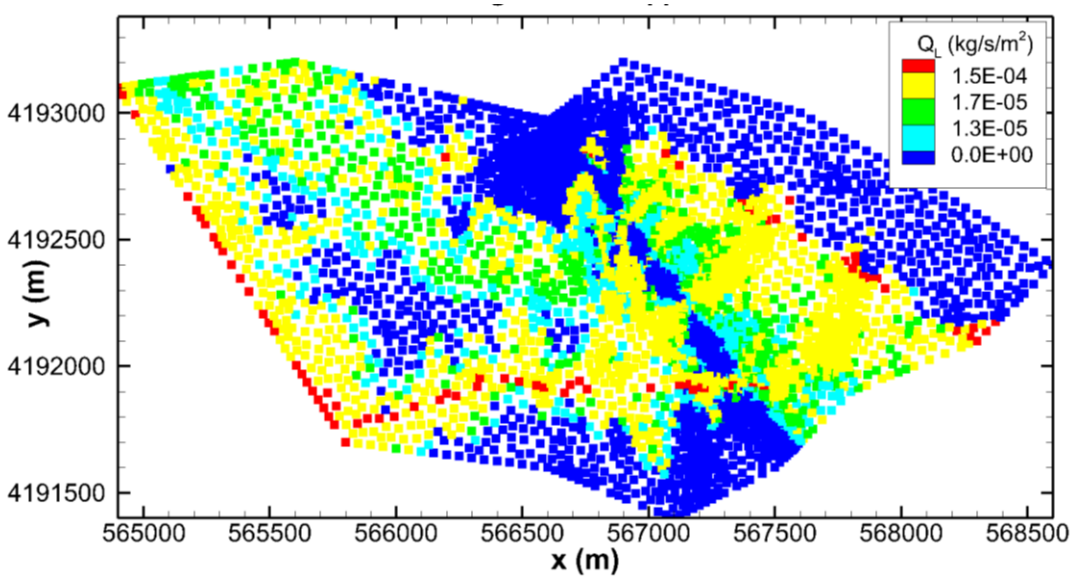

Figure 7-19. Distribution of liquid flux out of the top surface of the model for the base case.

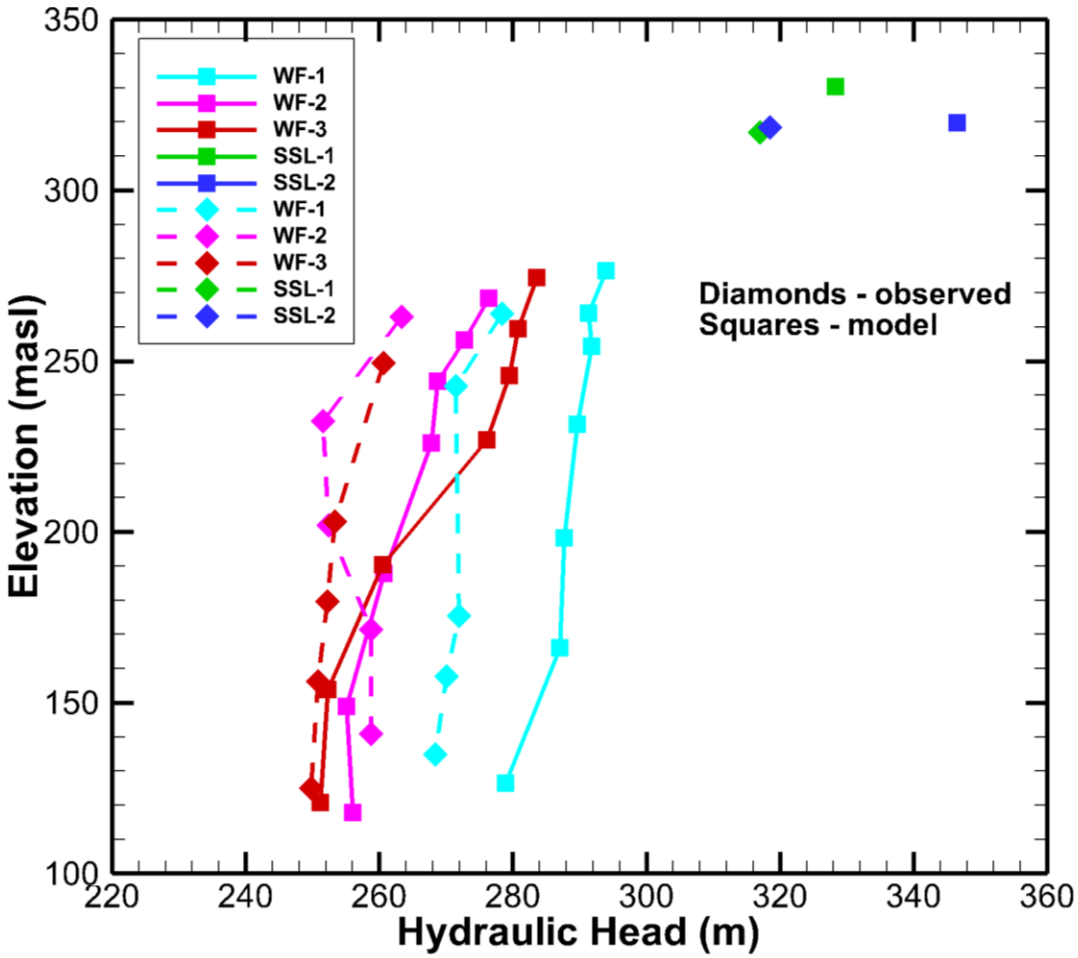

Figure 7-20. Comparison of modeled and observed hydraulic head measurements for the base case.

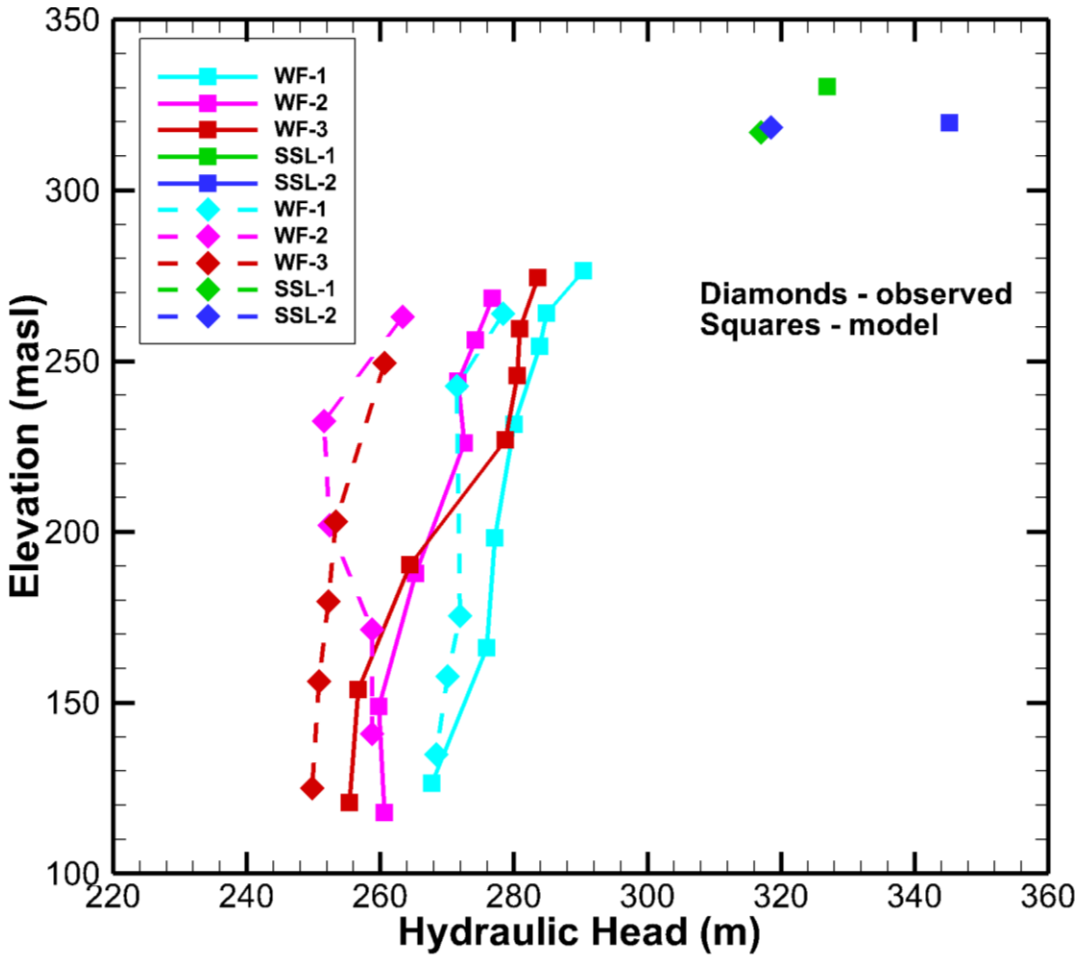

Figure 7-21. Hydraulic head profiles for a Wildcat Fault with no low-permeability fault core.

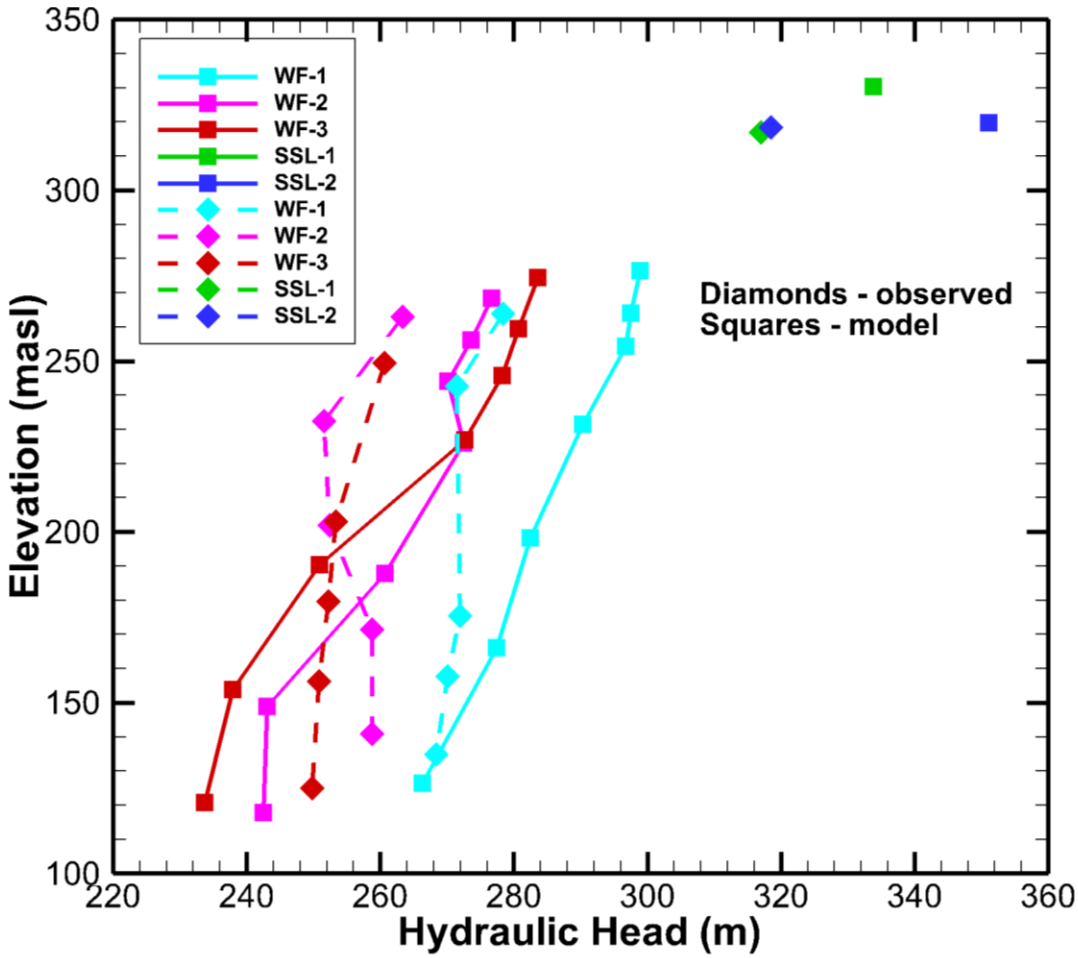

Figure 7-22. Hydraulic head profiles for a Wildcat Fault with no damage zone.

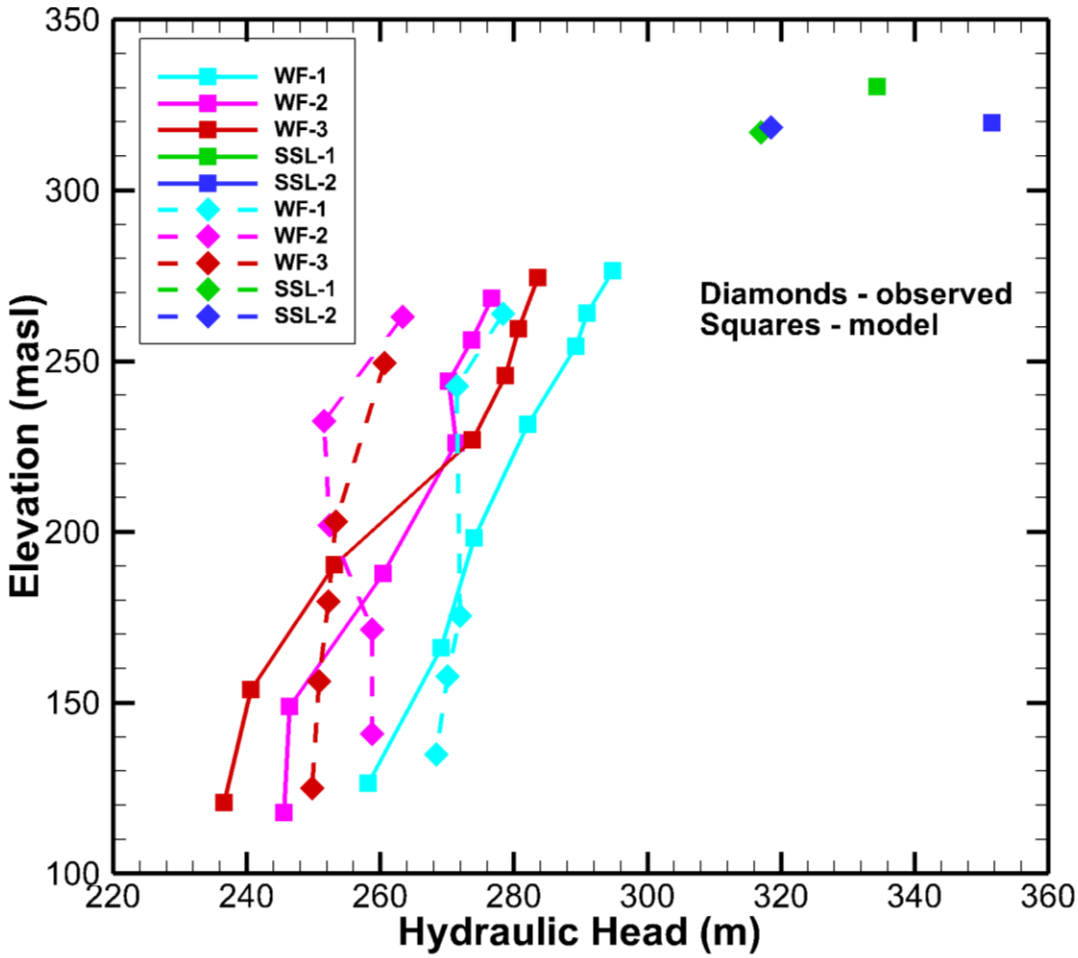

Figure 7-23. Hydraulic head profiles for the case with no Wildcat Fault.

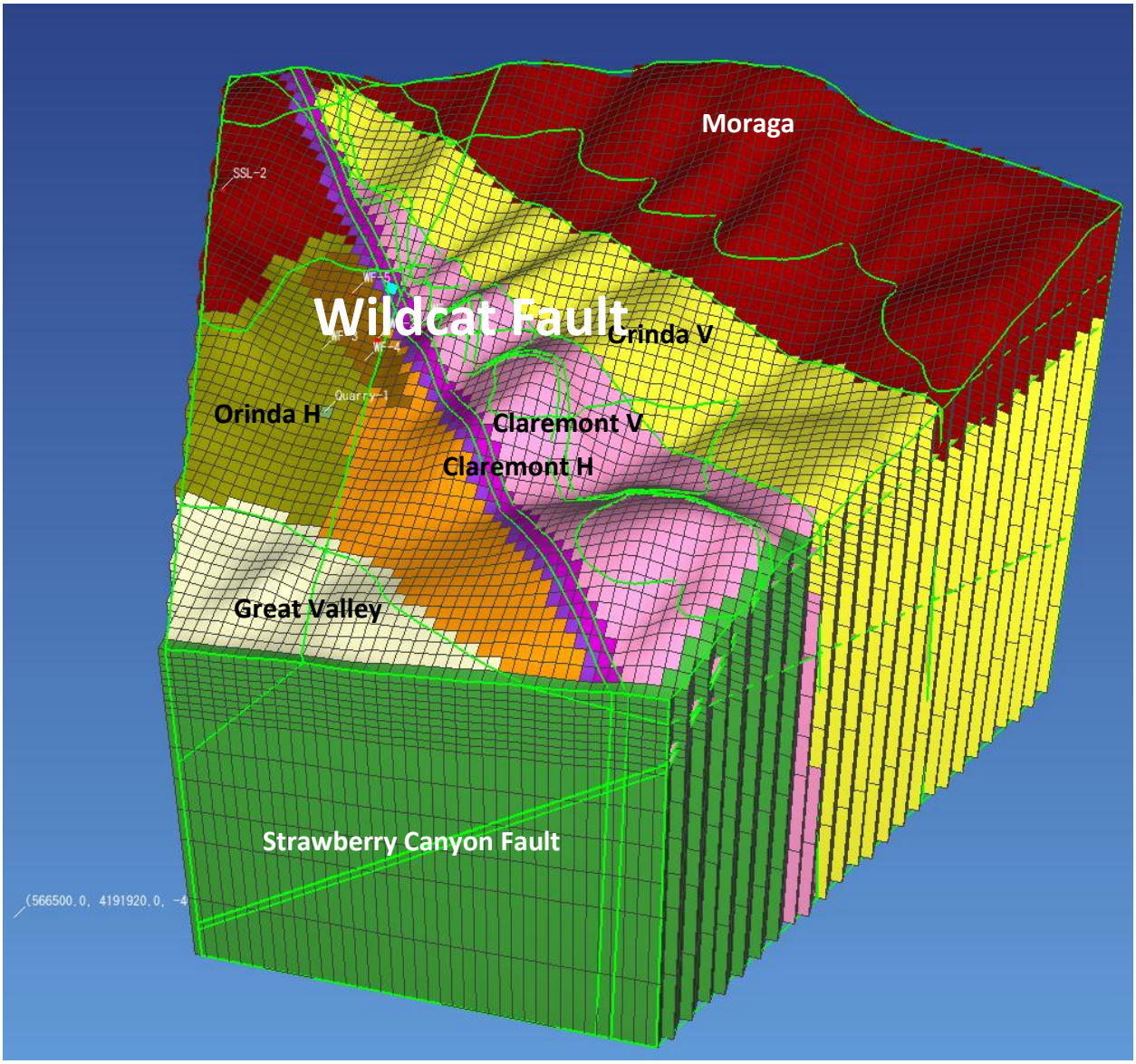

Figure 7-24. The numerical mesh of the East Canyon submodel. The Wildcat is modeled by two planes of low (purple) and high permeability (dark pink). The brown colored cells are the landslide material.

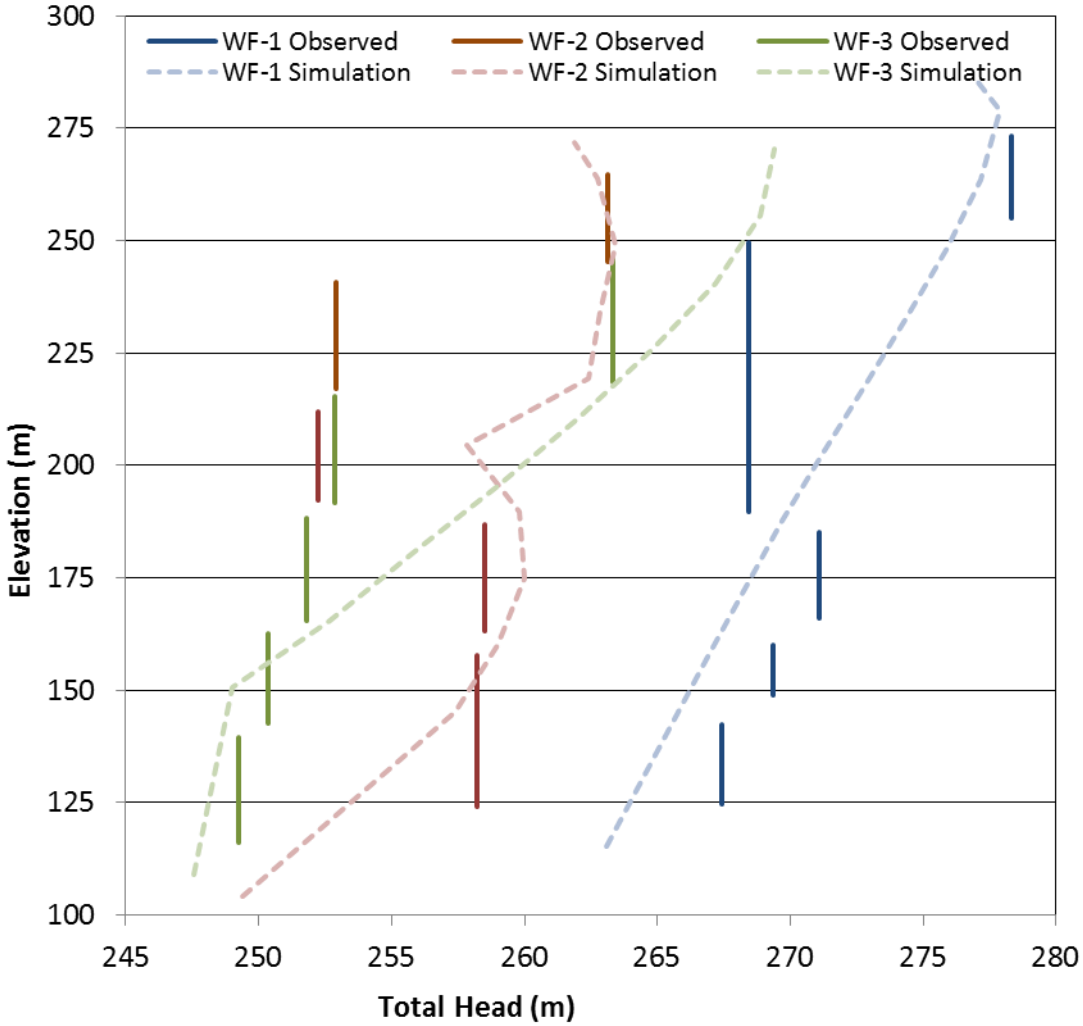

Figure 7-25. Comparison of simulation results with the observed head data of WF-1–WF-3. Note that the model reproduces the deceasing head with depth very well, as well as the low head anomaly in WF-1 possibly caused by the Fc fault.

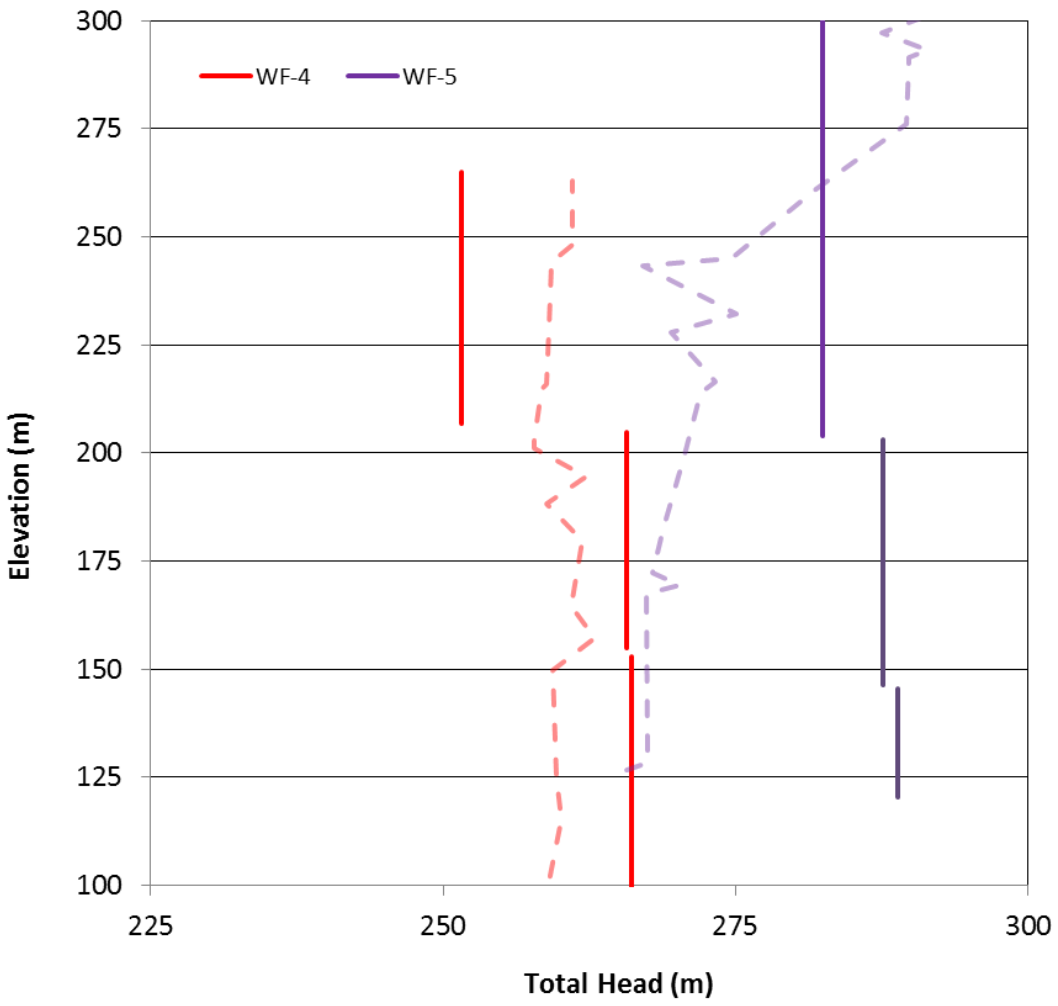

Figure 7-26. Comparison of simulation results with the observed head data for WF-4 and WF-5. Solid vertical lines are observed and broken lines are simulated. The simulation underpredicts the head toward the bottom of WF-5.

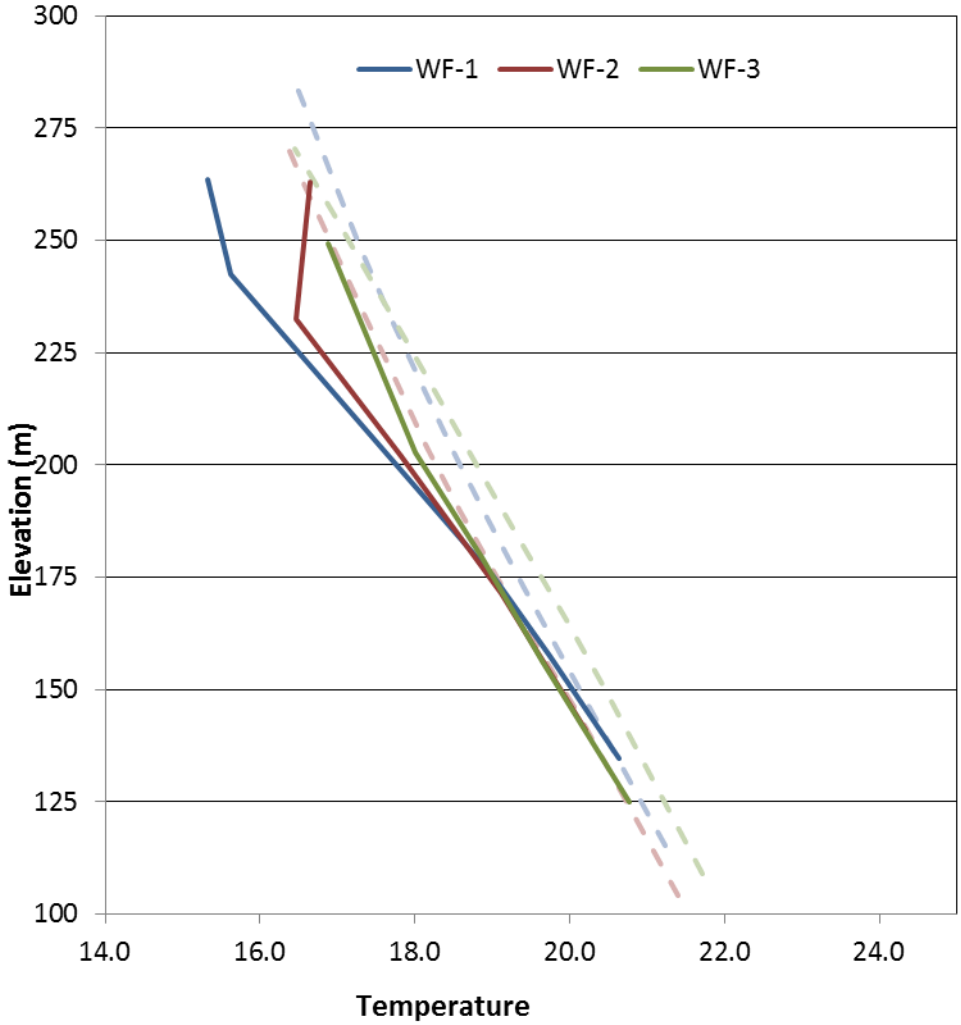

Figure 7-27. Comparison of simulation results with the observed temperature data from WF-1– WF-3. The data are solid lines; simulation results are broken lines. The model captures the geothermal gradient well, although they are offset by a few degrees.

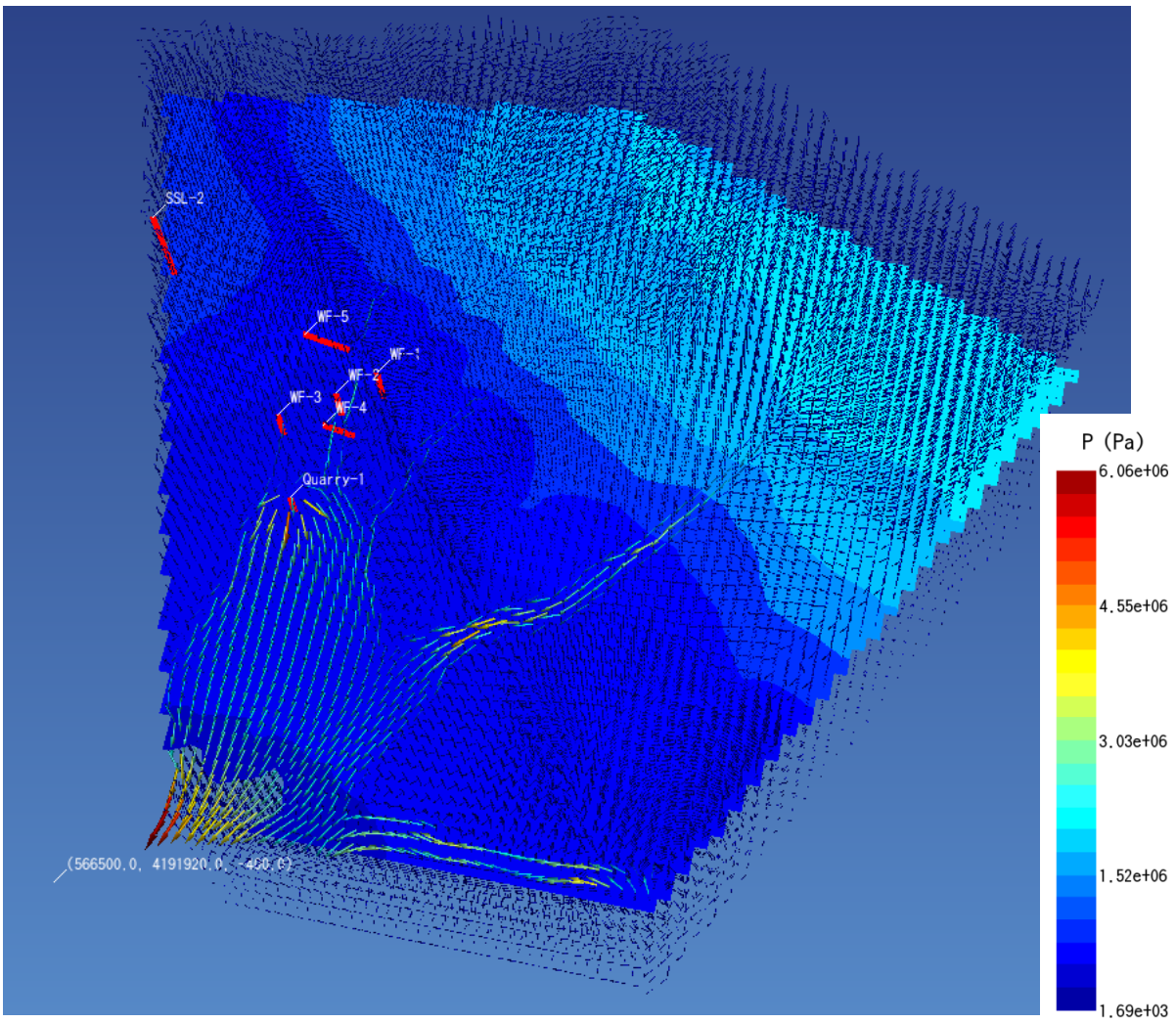

Figure 7-28. Flow vectors in the East Canyon submodel and the pressure distribution at 200 m elevation. Note the flow vectors converge along the Wildcat Fault. Flow out of the Quarry-1 well also noticeable.

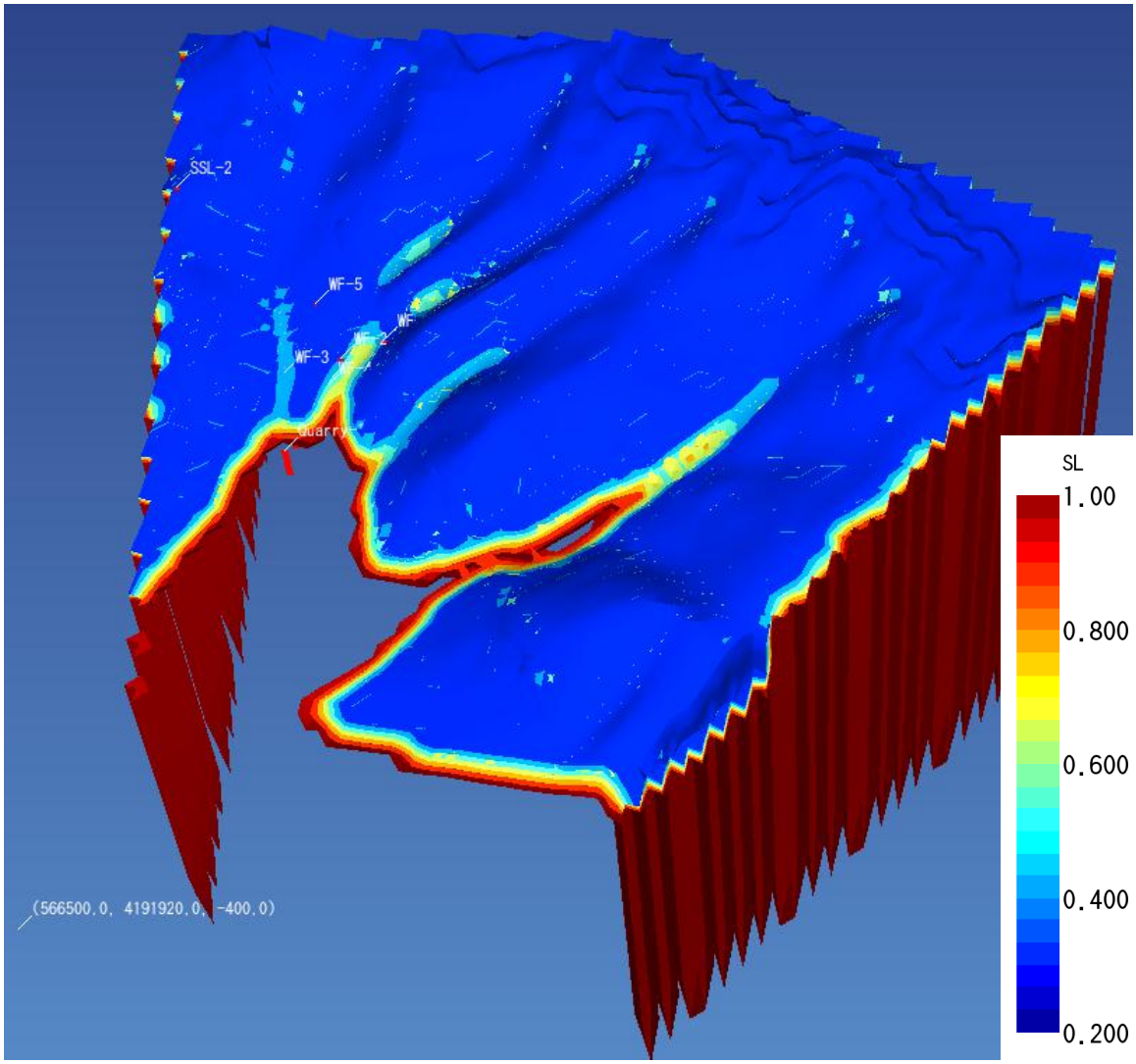

Figure 7-29. Saturation distribution of the East Canyon submodel. The area south of the WF boreholes are all saturated. In reality, the water is drained off through storm drains.

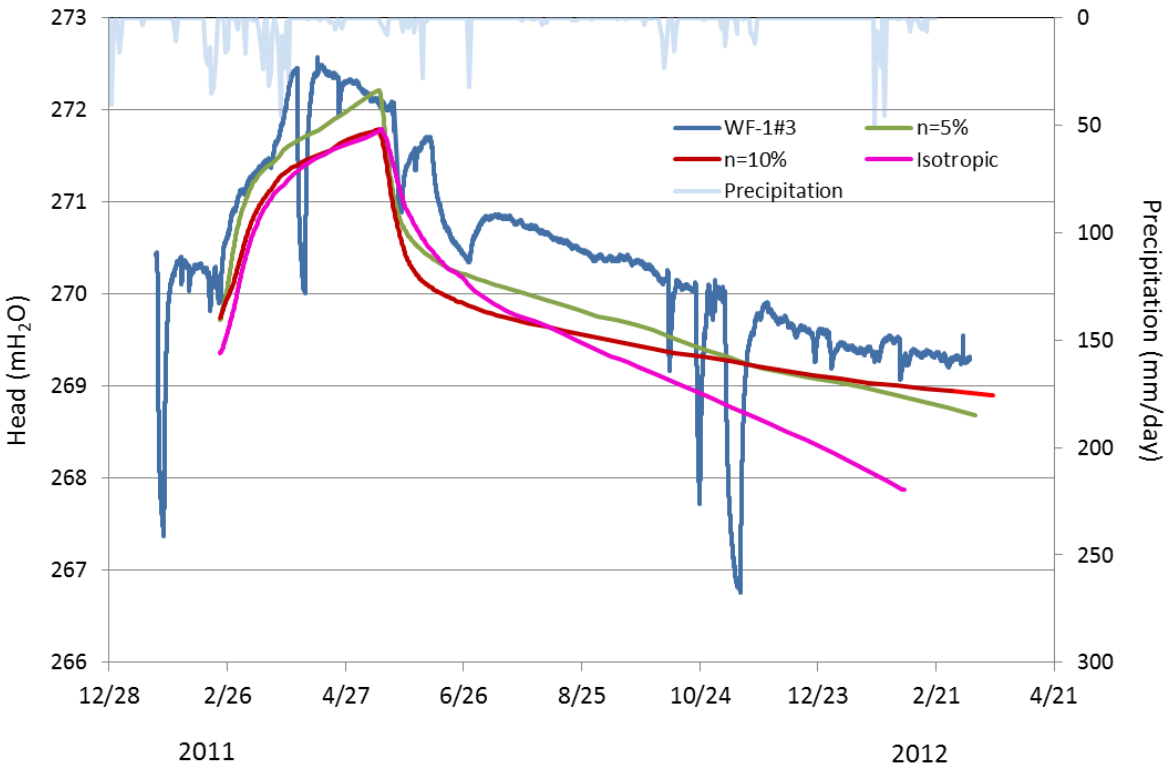

Figure 7-30. Compartion of simulation and observed head transients at WF-1#3 (blue) in response to seasonal rainfall using the best East Canyon submodel with 10% (red) and 5% (green) porosity, and isotropic Fd zone The daily precipitation (light blue) is plotted against the right axis. Negative spikes in head in data are caused by pump tests, which were not modeled. Note that the head decline rate during the dry period is reproduced better assuming 5% average porosity.

8 Lessons Learned, Conclusions, and Recommendations

8.1 Lessons Learned

The lessons learned through carrying out the field investigations for the present project are listed below. These are extremely valuable pieces of information that can be readily applied to any field projects to be conducted in the future. Overall, the project has been a great success. However, there have been numerous unanticipated incidents that negatively affected the schedule, budget, and the quality of data. It should never be assumed that field work will proceed as smoothly as planned before the start of the work.

8.1.1 Murphy's Law

Admittedly, it is a cliché, but it is still worth emphasizing, that Murphy's Law holds true universally for field work. Of course, all should be done to prevent mishaps, but inevitably something *will* go wrong. All pieces of equipment eventually fail. As a result, fallback plans are a must. Below is a brief list of such happenings in the course of our field work.

a. *Drilling:* Of all the site characterization activities, drilling is the work in which Murphy is by far most prevalent. We drilled five boreholes in total. Problems upon problems occurred in drilling these boreholes, and the cost and schedule ballooned far past our original budget. During the drilling of the first hole, WF-1, the drill pipe got stuck in a deep gouge zone and could not be rotated or pulled. We used various methods for recovery, including a reverse jack hammer, to no avail. It had to be over-cored, which delayed the schedule by one month. During WF-3 drilling, a drill string was accidentally dropped, which had to be fished out of the borehole, causing delays. In the same hole, PCV tremie pipes broke off in the middle and had to be left in the hole while delivering bentonite pellets for completion of the hole.

   We drilled the last two boreholes, WF-4 and WF-5, inclined 30 degrees from vertical. Inclined boreholes are a nightmare for drillers: The holes kept collapsing, and each hole had to be re-drilled several times. Re-drilling causes permeable zones to plug up, which is quite problematic for pump tests. Every time the hole is re-drilled, we had to re-develop the hole.

The Claremont chert formation was extremely difficult to drill except, for the sandstone portion. Several types of drill bits were used, but no single type was suitable throughout. Carbonado embedded drill bits performed best in shaley mudstone, while carbide was good in sandstone. An exposed diamond bit worked better than other bits in hard laminated chert—the problem is that you cannot predict a priori which kind of rock will show up next. Changing drill bits is a time-consuming operation, especially when the hole is deep, because there are many pipes to pull out and push in. Thus, it is an optimization problem with a big unknown: You want to change bits when drilling slows down, but at the same time, changing bits is time consuming. We had several occasions where as soon as we changed bits to match the formation, the rock type changed back against our bit.

b. *Sensor malfunction:* Sensors *will* sooner or later malfunction. They either stop transmitting signals completely or even worse, start drifting—and sensor drifts sometimes can be mistaken for reality. Figure 8-1 shows examples of pressure data from failing sensors. Figure 8-1(a) shows a sensor that became extremely noisy during a buildup test. Bubbling gas can also cause noisy pressure data. The bottom locus of the pressure still seemed more or less good until 4/14, when it started to go out of range. This failure mode is similar to the failed temperature sensor installed in the first reactor at Fukushima Daiichi in 2011. Figure 8-1(b) shows sensor readings drifting upward. Initially, this was thought to be a real signal. Eventually the pressure increase became too large to be credible. Figure 8-1(c) shows downward drifting sensor data, which is unusual. This declining pressure was thought to be real as well, until it was pulled out and tested. Figure 8-1(d) shows an even more unusual mode of failure, in which the pressure first went down and then increased, much like the response to a pump test and recovery, although no pump test was being conducted during the period. In this case, we had a redundant sensor, which stayed steady—we had installed redundant sensors wherever possible, learning from the previous years' lessons.

We have been using sensors from various manufacturers, namely Diver® by Schlumberger Water Services, VW Piezometer by DGSI (Durham Geo Slope Indicator), Level TROLL® by In-Situ, and AccuLevel® by Keller. The Diver's

sensor is based on a Wheatstone bridge with a ceramic diaphragm, VW Piezometer uses a vibrating wire, TROLL® and AccuLevel® are based on a piezo-resistive sensor. Approximately half of Schlumberger sensors failed, as well as half of the cable connectors for the optical interface. One DGSI vibrating wire sensor failed, and another is performing suspiciously.

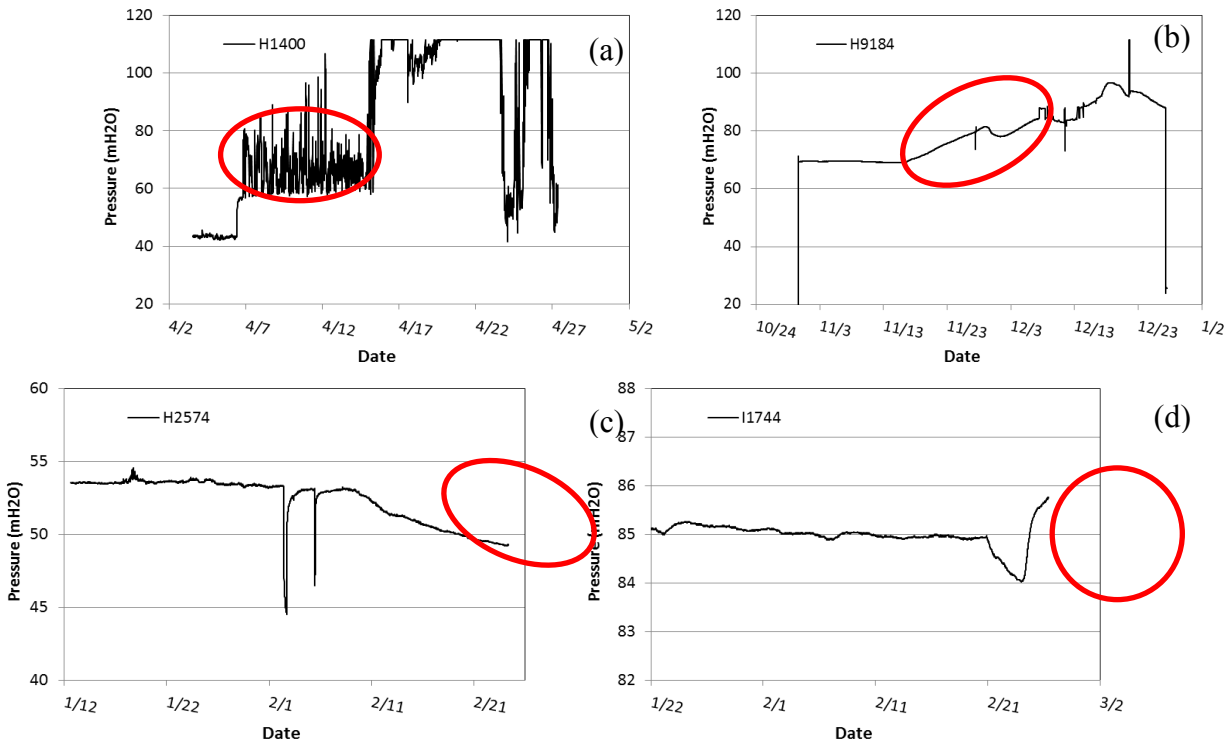

Figure 8-1. Example readings of failing sensors. a) Noisy signal. Similar to the pressure behavior when de-gassing is present. b) Upward drift. c) Downward drift . (d) First downward and then upward drift.

c. *Pump failure:* We used Grundfos-2®, frequency controlled pumps that fit inside 2 inch pipes. We "consumed" as many as five Grundfos® pumps in the course of conducting numerous pump tests. A primary cause for a pump failure is the abrasive particles suspended in the groundwater that cause the impellers of a pump to wear out very quickly. The particles are believed to come from the gouge material in the fault zone. Rainfalls caused a pump to halt a few times by triggering a GFCI (Ground Fault Circuit Interrupt). Pump failures can cause cascading schedule problems. Ideally, tests should not be resumed immediately after the stall until the pressure recovers to the pre-pump test state, unless the halt is very short.

d. *Cave-ins:* Boreholes caved in many times, particularly in the inclined boreholes. Cave-ins also occurred in some sections of vertical holes along the Orinda Formation, a soft silty formation. Logging an inclined borehole is a risky operation—logging probes are very expensive, and retrieving a stuck probe is time-consuming at best. Luckily, we never lost a probe, but we had several incidents where the hole became impassable during a logging operation. We then had to reposition, re-drill, and redevelop the hole. For each inclined hole, we had to have the logger come back three to four times to compete the logging. We could not even log a portion of WF-4 and WF-5 due to cave-ins, and had to install a casing.

e. To pump from different sections of a borehole, we needed to pull out and reinsert a packer string. Almost every time we did that, the hole caved in. One time, we experienced some resistance re-inserting a packer string, but we forced it in and the packer got damaged, as seen in Figure 8-2. It was a costly mistak,e because we had to pull everything out and replace the packer.

Figure 8-2. Damaged packer (below) and normal packer (above).

f. *Packer leaks:* We used pneumatic inflatable packers with a sliding sleeve to isolate zones in the boreholes. There are a number of things that can go wrong with a packer system other than physical damage during installation. Inflation tubings and pressure fittings can be sources of leaks, as can the packers themselves. When a packer is inflated at high pressure, the rubber gland gets pushed hard against the borehole wall. If a small piece of rock like a fragment of chert gets caught between the rubber and the wall, it can pierce through the rubber. We had a leaky packer in which we suspected exactly *that* happening—particularly frustrating because it happened during a third attempt at installing a packer string correctly.

g. *Weather:* Several times we planned to conduct pump tests, but then had to postpone them due to rain. One time we had to stop a test because of unanticipated precipitation. This was because the discharge permit to the sanitary sewer we had at the time had stipulated that no discharge was allowed 12 hours before, during, or within 12 hours after rain. At another time, rain caused a GFCI (ground fault circuit interrupt), which shut down electricity and stopped the pump.

8.1.2 Quality Assurance

Quality assurance is an important key to and an integral part of a successful characterization project. Although an unnecessarily inflexible QA program is a hindrance to progress and new ideas, good science and good recordkeeping can go hand in hand and should be adhered to. A QA program is not just a written procedure enforced top down that everybody needs to follow; there has to be a bottom-up culture in the course of doing science. Below are examples where a good QA helps in everyday field work.

There were several incidents when the depth of the hole was uncertain during the drilling. The most certain way is to count the number of pipes before the drilling and count the pipes remaining on the surface. It is not rocket science, but sometimes miscounts can happen. When the count is uncertain, the pipes need to be pulled and counted.

Sensors usually come calibrated by manufacturers. However, it is a good practice to test and calibrate them in the laboratory yourself before they are used in the field. It is more expensive to replace a sensor found to be off-calibration after they are put in a borehole. Also as noted above, sensors often drift. Data should always be examined to ensure that quality is maintained.

To conduct hydraulic tests in the deeper and more fractured zones, new sets of double packer systems were purchased. However, these packers leaked and caused major problems. Although packers were new and assumed to be of good quality, rigorous surface tests should have been conducted. Such tests translate to time and money, and when the resource is limited, it can be very difficult. However, it is much less costly than pulling up the packers after they are installed. Testing packers aboveground may mean less time to conduct tests, but it is far better to conduct one good test than many marginal or bad tests.

The quality of numerical simulations should be checked. In fact, there are so many switches and knobs to tweak in complex simulations, it is easy for a modeler to overlook a wrong set of input. Interpolating pressures to obtain velocity vectors can be very tricky and may result in erroneous travel time and paths. Beautiful 3-D graphics may be misleading.

8.1.3 Cost cutting

While it is virtuous as well as economical to try to reduce consumption in general, reusing used parts and materials such as packers, inflation tubing, fittings, or sensor cables may sometimes become sources of trouble later and should be exercised with great caution. Overlooked damage from previous use may cause leaks or shorts in the line. When that happens, a rig has to be called back on site, and the entire packer string has to be pulled and reinstalled, which would (after all) cost much more than buying and using new supplies every time.

We always tried to find less-expensive alternatives to everything we purchased for the project. But sometimes expensive tools and sensors are expensive for a reason, and using them ultimately cost less than inexpensive ones. Being consistently cost-effective is another optimization concern that must be attended to when engaging in a field project. Blindly buying the most expensive tools and sensors is not, of course, economical. Good all-round knowledge of testing, equipment and budgeting requirements is needed to make wise purchasing decisions—decisions that will ultimately save cost.

8.1.4 Pros and cons of inclined holes

We drilled two inclined boreholes, WF-4 and WF-5. We have mixed opinions regarding drilling inclined boreholes, which come with advantages and disadvantages. The advantages include:

- *Horizontal coverage:* Inclined boreholes cover some horizontal length, enabling us to sample horizontally varying geology. In both WF-4 and 5, we were able to locate the contact between the Orinda and Claremont formation.
- *Vertical features:* They intersect vertical features such as faults and fractures that would be missed by vertical holes. In WF-4 and 5, we intersected many vertical fractures and several high angle faults, which helped to formulate the conceptual model of the fault zone structure.

However, there are several disadvantages as well:

- *Costs:* They generally cost much more because they are harder to drill and keep open.

WF-4 and 5 cost us approximately three times more than the other vertical holes drilled to about the same total depth. The increased cost was not just for drilling. Inclination surveys have to be done periodically to ensure that the hole stays on course. Borehole logging is difficult and risky as well. In fact we had to have a logging company come back several times because of cave-ins during the logging. Instrumenting the holes and putting in packers are also very difficult.

- *Short circuits:* They can short-circuit otherwise disconnected aquifers and can mix waters, unless they are correctly isolated by packers immediately after the drilling. This may greatly impact geochemical analysis of groundwater. In WF-4, it was very difficult to find the right location to place packers, partly because the exact location of the main fault was unknown, and partly because the hole was very rough for packers to correctly seal.
- *Cave-ins:* As noted previously, inclined boreholes are more likely to cave-in, which necessitates re-drilling, which adds to the cost.
- *Analysis:* Hydrologic tests conducted in inclined boreholes are harder to analyze and model. Analytical models are limited, and gridding is a challenge for numerical analysis.

One needs to weigh the advantages and disadvantages of drilling inclined boreholes. In weak rocks, boreholes need to be cased and grouted, ideally with uniform perforation throughout. See recommendations below.

8.1.5 Fault Gouges

In WF-1, we encountered an ~30 cm thick clay gouge zone that froze the drill bit and prolonged the drilling by one month before we could release it by overcoring. Thus, in drilling WF-4, we expected to encounter a thick gouge zone. As it happens, no clay gouges thicker than 5 cm were recovered, but there were many intervals where core-loss occurred. There can be two interpretations for this. One interpretation is that there indeed was a main clay gouge zone, but it was washed away while drilling. Another is that we had missed the main fault to the east. A more plausible interpretation would be that there was no clay gouge to begin with in the fault core. It is unlikely for a thick gouge zone to get washed away by drilling. Our driller was confident that he would never lose clay cores. Thus, more plausible scenarios are that the main Wildcat Fault is too young, or some necessary geochemical/hydrothermal conditions had been missing to form clay in the fault core. The core filling material may have remained as pulverized, incoherent (loose), extremely fine-grained rock. It may be misleading to assume that every fault has clay gouge in the core.

8.1.6 Main Fault Plane

In the beginning of the project, largely based on the available literature, we had assumed that the Wildcat Fault is one fault plane. As it turned out, each of the five boreholes intersected multiple faults. Based on the cores from WF-4 and 5, there appears to be multiple fault planes between WF-1 and WF-2. We now believe that the Wildcat Fault is actually a fault zone consisting of multiple fault planes that developed in multiple stages. Just because there is a single solid or dashed line drawn on an existing geologic map does not necessarily mean that the fault consists of only a single plane. In fact, it is more likely that a fault consists of multiple planes and forms a zone.

8.1.7 Environmental Protection

Even when drilling in a pristine location, groundwater or rock may naturally contain some levels of hydrocarbons or minerals that are higher than environmentally permissible to be discharged or disposed of in a landfill. This was the case with the high fluorine and boron concentration in the pumped water from Mizunami URL. In our project, during the drilling of WF-3, a strong smell of some volatile hydrocarbon was noticed coming from the cores. Anthropogenic diesel contamination was initially suspected, but a subsequent analysis revealed that the hydrocarbons were of natural origin. Either anthropogenic or natural, proper disposal of drill spoils and water had to be carried out. We could not discharge water directly onto the hillside or to a storm drain. Instead, it had to be collected and treated. The drill cuttings that were initially thrown in a pit had to be dug up and collected for proper disposal. The pumped water from WF-4 had a low-enough concentration to be discharged into a sanitary sewer after obtaining a permit from EBMUD (East Bay Municipal Utility District), for a fee per gallon.

In the beginning of the project, we had not budgeted for the cost of environmental protection measures. We have since learned that it is necessary to anticipate and plan for such costs (and their schedule) ahead of time.

8.1.8 Core Recovery

It is relatively easy to determine where a fault plane is if 100% of cores are recovered. However, 100% recovery is extremely difficult when drilling through a relatively young fault zone with inclined drilling. Cores of naturally damaged rock do not enter the core tube properly. The tube inside the core barrel tends to rotate in an inclined hole, which can grind and further

damage the core. It is expensive to achieve good core recovery in such a situation. When the advancement of the drill bit slows down, it is advisable to pull up the core barrel, so that whatever the length of core already captured in the core barrel does not get ground and washed away. But pulling up every half foot or less significantly slows down the drilling, which we had to do at times, despite of which we could not achieve a good recovery rate **[?]** going through a fault zone.

When the drilling speed slows down, a new bit may be required. Using a worn bit negatively impacts core recovery as well. In order to determine whether the bit is worn, the pipes need to be pulled. The wear rate of the bit depends on many variables, but mainly on the rock properties. The mudstone/chert of Claremont Formation was particularly difficult to core. Diamond bits can handle hard rocks with some ease, but hard mudstone is an exception. Mudstone coats the diamonds with mud paste and makes it extremely had to cut. We found that exposed carbonado (black diamond) bits performed the best in the mudstone, but the drilling speed was still very slow.

If the budget allows, it would be constructive to make frequent wire-line trips to bring up cores and keep replacing bits. In our case, it was a difficult balancing act, because of budget limitations: spending more money in drilling cut into the funds left for conducting tests in the borehole.

8.1.9 Faults and fault zones

We excavated a total of five trenches and drilled five deep holes. In every single one of them, we encountered at least one fault. Based on the literature, we chose the location of the trenches to intersect the Wildcat, assuming it is a straight line except for TR-4. We know that the surface trace of a fault is not always a straight line, and even if it were, we did not surgical precision in locating them. WF-1, WF-2, and WF-3 boreholes are vertical, but still we encountered a fault or faults in every one of them. This leads to the conclusion that the Wildcat is better described as a fault zone instead of a fault with a single plane.

The same may be true for faults in Japan. Even if the literature gives a name and a solid line is drawn for a known fault, it could be a fault zone with a width and multiple slip planes.

8.1.10 Packer Zone

Packers need to be seated at relatively smooth, round walled sections of the hole to provide a good seal. But oftentimes, the zones that we want to test are fault-damaged zones where the walls are rough. Thus, we typically chose the closest locations to the zone of interest, where the wall is smooth, to set packers, based on caliper logs and BTVs. This, of course, has to be balanced with the need to test at particular depths or lithologies.

However, even if packers are seated well, there is a chance that zones communicate through natural fractures. In such a case, packers are almost meaningless. In the case of a fault with low permeability core and associated high permeability damaged zone(s), one would like to test the zones separately. However, it was almost impossible to do so, because we did not know precisely where the low permeability zone was. (At this point, we still don't know exactly where it is.) We do suspect that there is a low permeability fault core zone between WF-1 and WF-2, based on two lines of evidence: (1) None of the zones in WF-2 and WF-3 responded to the pumping from the WF-5#2 zone, whereas there was a clear response in the zones in WF-1 and WF-4#3; (2) The ambient hydraulic heads in WF-1 are much higher than those in WF-2 and WF-3. In our simulation, the numerical model required a low permeability zone between WF-1 and WF-2 to reproduce the head difference. At a preliminary investigation stage, it is more important to know whether a low permeability zone exists and the overall effects of the fault on the surrounding hydrology, than it is to pinpoint the exact location.

Figure 8-3 illustrates why it is important to set a packer at the right location to test a specific zone. Assume that there is a permeable damaged zone on both sides of a fault separated by a low permeability fault core. When trying to pump from the zone below the fault core, as can be seen from the figure, the packer shown in (a) and (b) does not prevent a pressure short circuit between the zones through the borehole. It is very difficult to ensure/verify isolation of zones by packers. A new approach for isolating the entire length of a borehole is called for. In the next section, we will discuss such an approach.

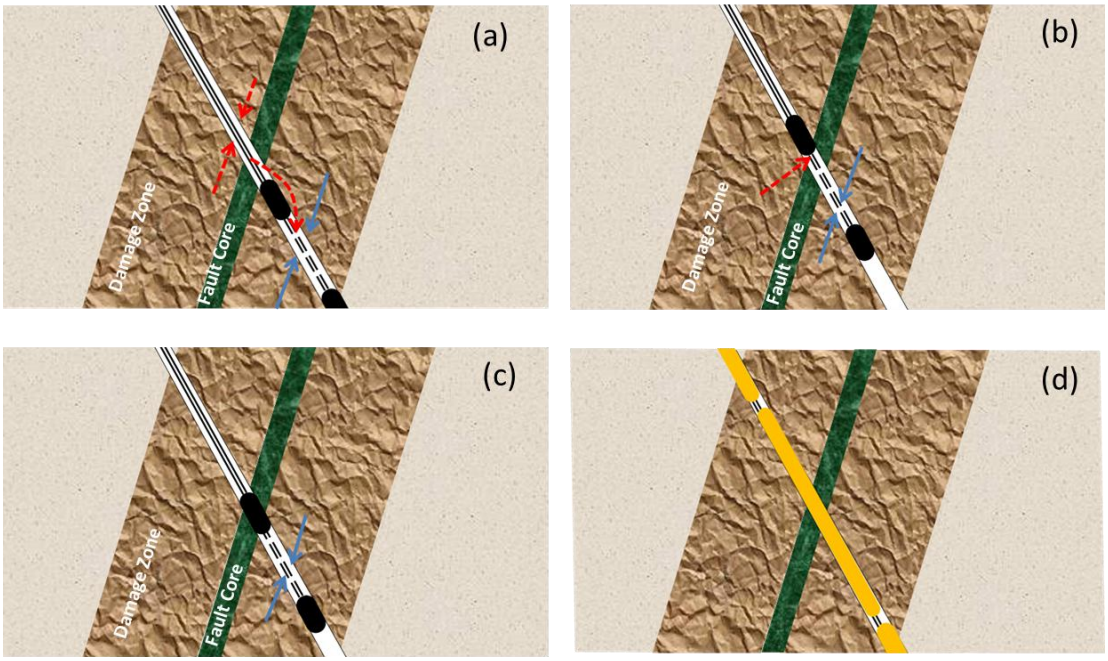

Figure 8-3. Packer locations in relation to fault core: Packer is located either (a) below or (b) above the fault core to allow for leakage through borehole. (c) Packer is placed just right at the fault core. (d) A newly proposed continously sealing packer system.

8.1.11 Continuous Borehole Sealing Packer

Because of the difficulties associated with properly sealing a borehole, we have developed a new packer-system concept that continuously seals a borehole. It is the opposite of the traditional packer system, in which short packers are used to isolate several long zones. Instead, our approach is to use very long packers, with short open intervals where sensors are located as shown in Figure 8-3(d). Multiple sensors are used that are bit-addressable and daisy-chained with only one cable. In this way, the borehole is continuously sealed with little chance of artificially short-circuiting the pressure through the borehole. We have fabricated a system that can be made neutrally buoyant with flush surfaces as shown in Figure 8-4. The system is yet to be permanently installed in one of the WF holes.

8.1.12 Take Time

Although one may not have a choice, ideally hydraulic tests should be conducted when the background is quiet or has monotonic trend. Thus, it is important to at least collect the background or baseline (trend) data before conducting hydraulic tests. Rainfall has a big impact on the hydraulic heads observed in boreholes, as can be seen in WF and SSL boreholes. One

year's worth of data may not be enough to develop an understanding of the natural state. Year to year, rainfall amounts amount can vary over 100%.

In addition, as was discussed in the previous sections, one must allow for breakdowns and other unexpected occurrences. Field work should not be conducted in a hurry. In particular, a good hydraulic test typically can take weeks, if not months. One should allow for at least double the pumping-period time to observe the recovery data. A characterization program should not be driven by a hasty schedule. It takes considerable time to characterize a site sufficiently, to build confidence in the engineering and science required. One should consider the repository characterization program as a 100-year project.

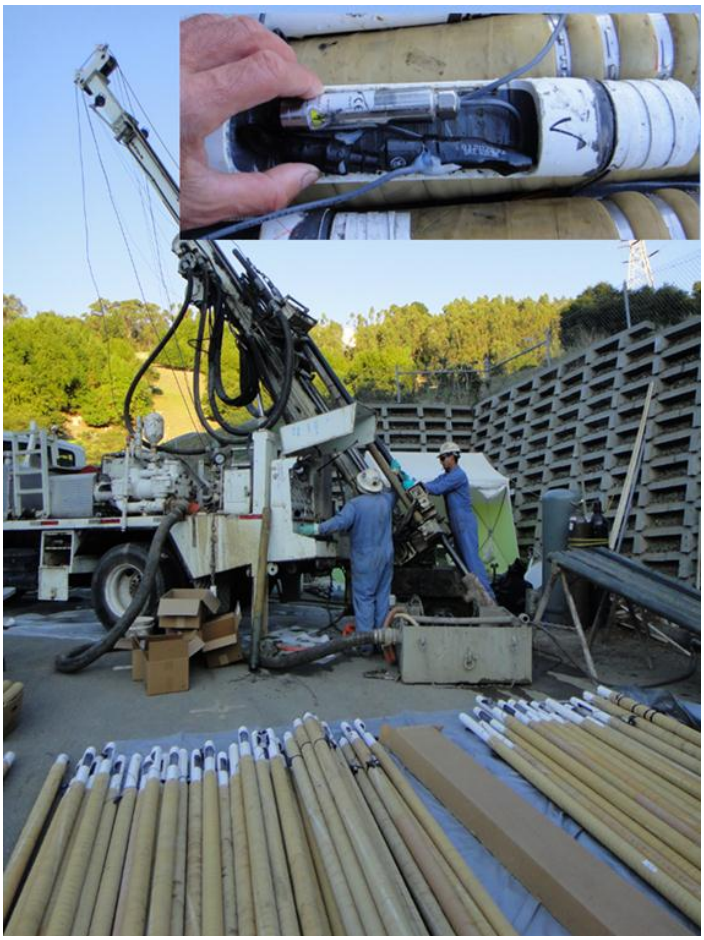

Figure 8-4. New concept packer system that continously seal the borehole to avoid artificial short-circutting of pressure through the borehole. Their surfaces are made flush and neutraly bouyant in water.

8.1.13 Geophysics

We conducted various geophysical surveys, including seismic reflection, seismic refraction (the results of which are still pending at this writing), electrical resistivity, and several kinds of borehole geophysical logs. It was hoped that such techniques would help us identify the location and the properties of the fault zone. However, the results were at best inconclusive. We learned that we cannot rely too heavily on the geophysical data. Geophysical techniques yield at best indirect information regarding the hydrologic properties of rocks. Geophysical surveys respond to such properties as the density, formation electrical resistivity, or porosity of the subsurface, depending on the technique used. These properties often do not directly correlate with hydrologic properties. On top of this, in a complex geologic setting like our study area, one may get very noisy data or inaccurate results.

As noted in Chapter 2, we probably should have had longer survey lines. The longer the lines, the wider the coverage and the deeper the signal penetration. Longer lines cost more and take longer time, but they are incremental compared to the total cost and time. Nonetheless, it is a difficult optimization problem when the budget is limited and the cost/benefit radio can only be calculated after the fact, if at all.

8.1.14 Heterogeneity of the fault zone

The results of the pump tests in the Wildcat fault zone showed that the fault zone is anisotropic and heterogeneous. The varying magnitude of drawdowns observed in the monitoring zones in WF-1 in response to the pumping in WF-5#2 indicated that the fault is anisotropic, with 10:1 horizontal-to-vertical permeability. This is actually expected for a strike-slip fault. In our numerical model, we assumed a uniform but anisotropic permeability for the Wildcat fault zone. The permeability of the fault observed near the bottom of WF-4 is higher than that observed in the middle of WF-5, indicating spatially varying permeability. We do not believe that this is unique to the Wildcat; rather, it is probably true with all faults.

It is impossible to test and evaluate the small-scale permeability of a fault as a function of spatial location; to do so would require too many boreholes and too much time. Even if we were able to collect many local parameters, we would not know how to put them together to result in a

large-scale parameter, which is more important. What we need is the large-scale permeability or through-flow permeability of a fault. A fault can be locally very permeable, but may not be as much at a larger scale. In characterizing a fault zone, the aim is to evaluate the overall permeability, such that we can predict its impact on the flow field surrounding the zone.

One direct way of estimating large-scale permeability is to conduct long-term pump tests. We were only partially successful in doing so. In one test, the electricity to the pump was cut off due to an unexpected rain event. Another time, a pump failed after a week. One "pump test" that continued over one year was the pumping at the SSL-1 borehole, where we conducted a shut-in test for two months. The tests (somewhat surprisingly) did not seem to have affected the pressures in WF boreholes roughly 500 m away. As a rule of thumb, 200 m is the maximum horizontal and radial distance a pump test can affect. This rule would probably not apply to a test in a fault zone, in which the flow would be constrained within a narrow fault plane. Another problem that may affect the success of a long-term test is rainfall. Heavy rainfall can mask the drawdown effect of a pump test, which was what happened in the SSL-1 pump test.

We found that an effective and reliable way to estimate large-scale permeability is to use the temperature and long-term seasonal-fluctuation pressure data. We were able to verify the permeability and porosity structure of the model that explains the pressure decline during the dry season, as well as the temperature distribution along boreholes that is a function of recharge rate.

8.2 Summary Conclusions

In this section we summarize the major conclusions of the five-year project. Also included are those by Kiho et al. (2012). These conclusions apply not only to the Wildcat Fault Zone but also to other faults of a similar type. Some of the conclusions are even more general and would apply to any fault types.

- The exact location of the main fault plane of the Wildcat Fault Zone is still at dispute among participating researchers, which highlights the fact that it is extremely difficult to uniquely characterize a fault zone.
- Information from the literature can be useful, but it should be used with caution.
- Fault zones greatly affect groundwater flow and transport.
- Long-term monitoring and analysis of groundwater pressure over several seasons is extremely important. Large-scale through-flow permeability, as well as the degree of hydrologic communication between boreholes, can be estimated by analyzing the

long-term pressure trend data.

- Temperature distribution along a borehole is useful in calibrating the permeability and recharge rate at large scales.
- A fault plane may not always be filled with coherent clay gouge and thus may be very permeable. The fault plane where the most recent movement is suspected may be too young to have clay gouges.
- Traditional approaches to isolating sections with ordinary packers may not be suitable for fault-zone characterization.
- It is best to complete holes penetrating a fault zone with grouted casing and uniform perforations. It is recommended that boreholes then be packed off systematically, using the newly proposed sealing system with multiple daisy-chained intelligent sensors.
- Inclined drilling is an effective tool for characterizing a vertical fault zone, but comes with some drawbacks.
- The Wildcat is not a single fault. It is a fault zone consisting of several fault planes which developed over several distinct stages. This could hold true for the faults at potential candidate sites in Japan with similar tectonic settings.
- No single geophysical survey technique captures everything. Electrical resistivity tomography (ERT) may be more effective than other methods in estimating subsurface structures in a complexly faulted, folded and fractured geologic setting. Refraction seismic surveys utilizing P- and S- wave sources are often better suited in highly faulted/fractured environment.
- Inversion analysis can be useful for calibrating hydrologic models.
- The hydrologic characteristics of the Wildcat Fault Zone indicate a dual-nature: high permeability along the direction of the fault zone, and low permeability across it. Our modeling study shows as much as three-orders-of-magnitude contrast. Within the fault zone, there is 10:1 horizontal-to-vertical permeability anisotropy.
- Isotopic analysis of carbonates (^{13}C, ^{18}O) from core samples may be used to estimate the location of present-day flow zones.
- Groundwater age analysis (^{4}He) may be used to infer the direction of groundwater flow and evolution.

9 Recommendations

Much knowledge has been gained from the Project thus far, but there still remain some important areas that were not completed or addressed. In this section, we list the recommendations for future work to further the understanding of and the characterization technology for fault-zone hydrology. Although much has been accomplished by the present project, there remains some room for improvement. Developing the methodology for evaluating the mass-transport properties of a fault zone is the next necessary step.

9.1 Verification study

Based on various geological, geophysical, hydrological, and hydrochemical investigations, we constructed a geohydrological model that best explains the observed data. In order to verify the soundness of the model and its prediction capability, a verification study should be performed. Verification of the model can be done by first making predictions using the model in conjunction with conducting field investigations that yield data different from those used to calibrate the model. The model predictions should be compared against the newly obtained data to verify the robustness of the model.

The locations and types of tests to be conducted should be based on a sensitivity analysis of the model to various parameters. To this end it is recommended that new boreholes be drilled on the east side of the Wildcat Fault Zone.

9.2 Transport studies

A primary way **[?]** of evaluating the safety of a repository is to conduct performance assessment modeling, in which transport analysis though the geosphere is a major part of the evaluation. For that purpose, the transport properties of the host rock must be known. In the Project, we focused exclusively on the methodology for characterizing the geologic structure and hydrologic properties of a fault zone. We did not specifically investigate transport properties. In order to assess the overall performance, transport properties, including the porosity, dispersivity (if applicable), and partition coefficient, K_d are needed. Now that we have arguably identified a fault plane, the Wildcat site is an ideal place to conduct transport studies in a fault zone. We have already amassed much knowledge and data on the hydraulic (flow) properties of the strike-slip fault. We can first use the hydrologic (flow) model to predict tracer transport in the fault, and then we should conduct tracer tests to verify/refute the prediction. The single most difficult and

important parameter for transport prediction is the porosity. In particular, the flowing (effective) porosity of fractured/faulted rock has eluded many researchers in the past.

Ijiri et al. (2009) and Sawada et al. (2005) found that travel-time predictions were spread over several orders of magnitude among modelers using the same hydraulic parameters from field data from the Tono Area in Gifu. The only crucial difference was the value of porosity that each modeler chose, since there were no direct field measurements. This highlights the importance of correctly estimating the porosity.

9.3 Safety and environmental protection

The safety of workers and protection of the environment have to be top priorities in conducting field work. Trenching, drilling, and borehole testing involve many potential hazards. Strict adherence to schedules and cost savings often compromise the safety and the environment. We are very fortunate that there were no injury accidents during the four years of field work—including the construction of five trenches, the installation of many geophysical survey lines, borehole drilling, and numerous packer tests—thanks to the safety culture of the drilling company (Pitcher Drilling) and the regulations enforced by the EH&S Division of LBNL.

We have also learned that protecting the environment is very important and can be achieved by planning ahead and setting aside additional costs. The quality of native groundwater may not be pristine. The groundwater from the Wildcat area contained natural hydrocarbons. Drill spoils and mud water had to be treated before disposal. Even natural water pumped out of the ground needed to be analyzed to ensure that concentrations of toxics were below environmental standards. Ignoring safety and environmental concerns for short-term gain will eventually come back to haunt a repository program.

9.4 Keep science in repository program

Science has to be an integral part of a repository program. There will be many unknowns and uncertainties in characterization and prediction of complex subsurface structures and processes. The program should not assume that everything is known and solvable though existing engineering means.

9.5 References

Ijiri, Y., Saegusa, H., Sawada, A., Ono, M., Watanabe, K., Karasaki, K., Doughty, C., Shimo M., and Fumimura K., 2009, Evaluation of uncertainties from different modeling approaches applied to analyze regional groundwater flow in the Tono area of Japan, Journal o/Contaminant Hydrology 103, 2009, 168-181.

Sawada, A., Saegusa H., , and Ijiri, Y, 2005, Uncertainty in Groundwater Flow Simulations Caused by Multiple Modeling Approaches, at the Mizunami Underground Research Laboratory, Japan, Geophysical Monograph Series, AGU, 2005.

Acknowledgements

This work was supported by Nuclear Waste Management Organization and performed under Contract No. DE-AC02-05CH11231.

WF1

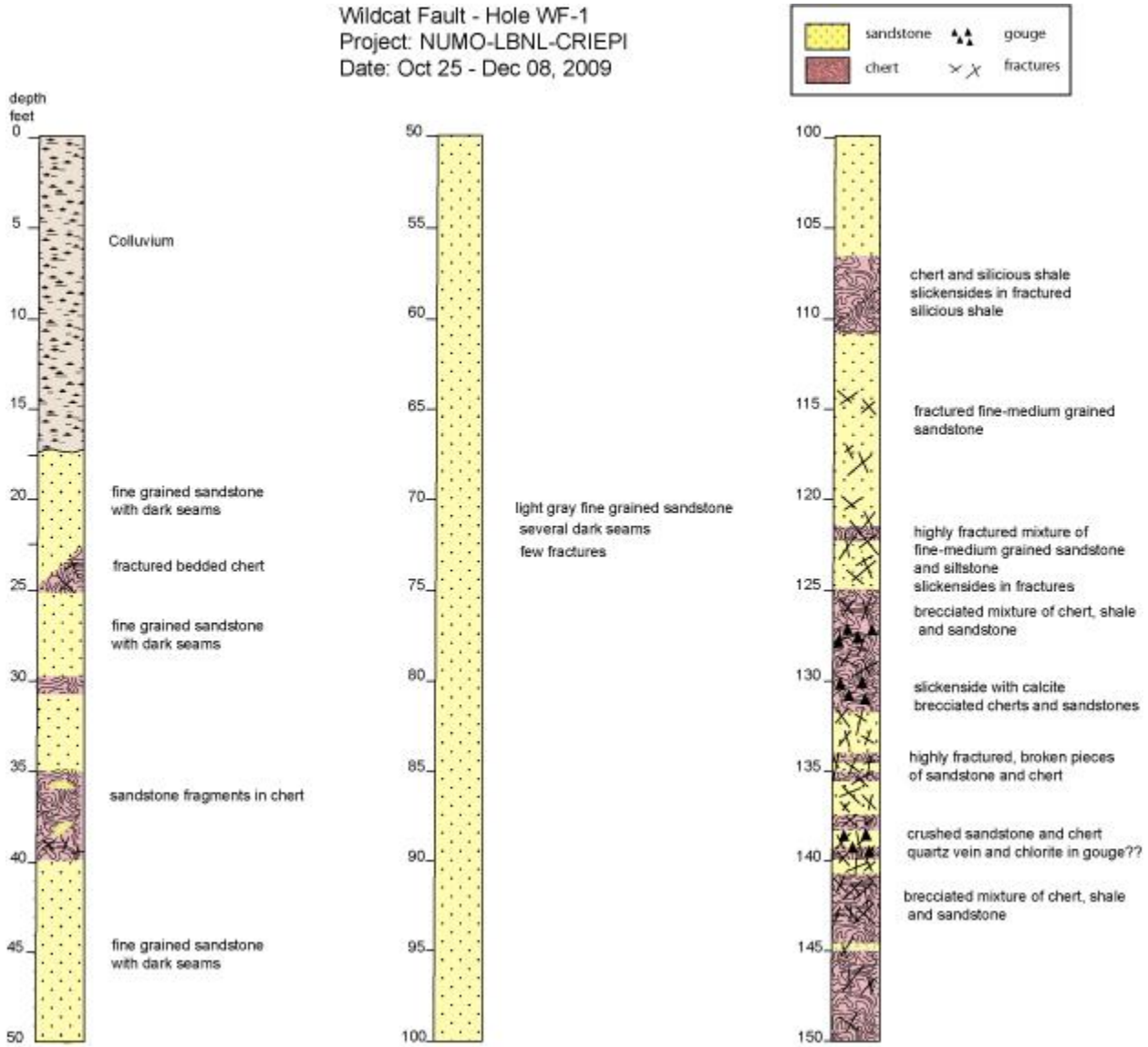
Wildcat Fault - Hole WF-1
Project: NUMO-LBNL-CRIEPI
Date: Oct 25 - Dec 08, 2009
sandstone
gouge
chert
fractures
depth
feet
0
5
10
15
20
25
30
35
40
45
50
Colluvium
fine grained sandstone
with dark seams
fractured bedded chert
fine grained sandstone
with dark seams
sandstone fragments in chert
fine grained sandstone
with dark seams
50
55
60
65
70
75
80
85
90
95
100
light gray fine grained sandstone
several dark seams
few fractures
100
105
110
115
120
125
130
135
140
145
150
chert and silicious shale
slickensides in fractured
silicious shale
fractured fine-medium grained
sandstone
highly fractured mixture of
fine-medium grained sandstone
and siltstone
slickensides in fractures
brecciated mixture of chert, shale
and sandstone
slickenside with calcite
brecciated cherts and sandstones
highly fractured, broken pieces
of sandstone and chert
crushed sandstone and chert
quartz vein and chlorite in gouge??
brecciated mixture of chert, shale
and sandstone

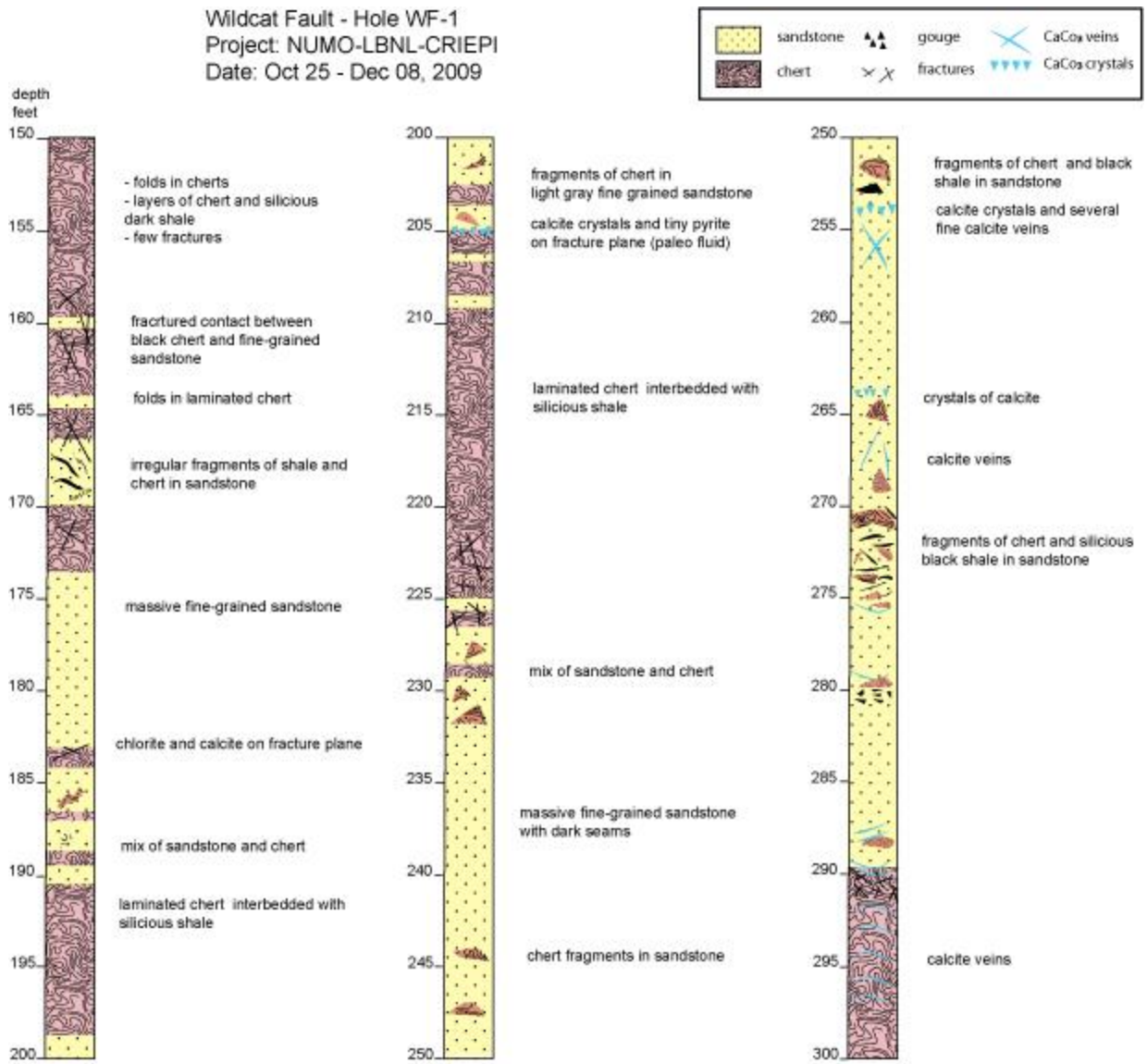
Wildcat Fault - Hole WF-1
Project: NUMO-LBNL-CRIEPI
Date: Oct 25 - Dec 08, 2009
sandstone
chert
gouge
fractures
CaCo3 veins
CaCo3 crystals
depth
feet
150
155
160
165
170
175
180
185
190
195
200
- folds in cherts
- layers of chert and silicious dark shale
- few fractures
fracrtured contact between black chert and fine-grained sandstone
folds in laminated chert
irregular fragments of shale and chert in sandstone
massive fine-grained sandstone
chlorite and calcite on fracture plane
mix of sandstone and chert
laminated chert interbedded with silicious shale
200
205
210
215
220
225
230
235
240
245
250
fragments of chert in light gray fine grained sandstone
calcite crystals and tiny pyrite on fracture plane (paleo fluid)
laminated chert interbedded with silicious shale
mix of sandstone and chert
massive fine-grained sandstone with dark seams
chert fragments in sandstone
250
255
260
265
270
275
280
285
290
295
300
fragments of chert and black shale in sandstone
calcite crystals and several fine calcite veins
crystals of calcite
calcite veins
fragments of chert and silicious black shale in sandstone
calcite veins

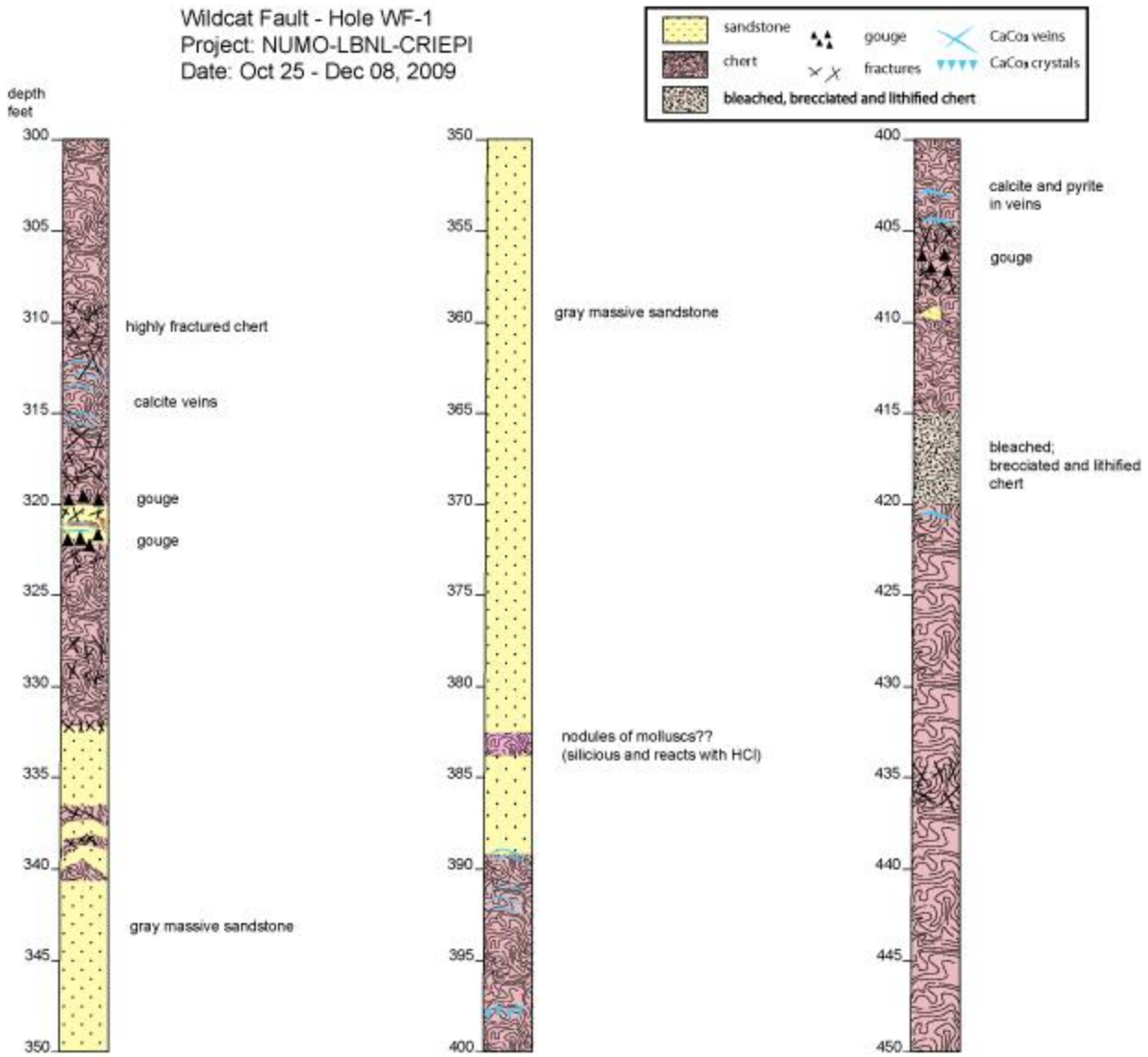
Wildcat Fault - Hole WF-1
Project: NUMO-LBNL-CRIEPI
Date: Oct 25 - Dec 08, 2009
sandstone
chert
bleached, brecciated and lithified chert
gouge
fractures
CaCo3 veins
CaCo3 crystals
depth
feet
300
305
310
315
320
325
330
335
340
345
350
highly fractured chert
calcite veins
gouge
gouge
gray massive sandstone
350
355
360
365
370
375
380
385
390
395
400
gray massive sandstone
nodules of molluscs??
(silicious and reacts with HCl)
400
405
410
415
420
425
430
435
440
445
450
calcite and pyrite
in veins
gouge
bleached;
brecciated and lithified
chert

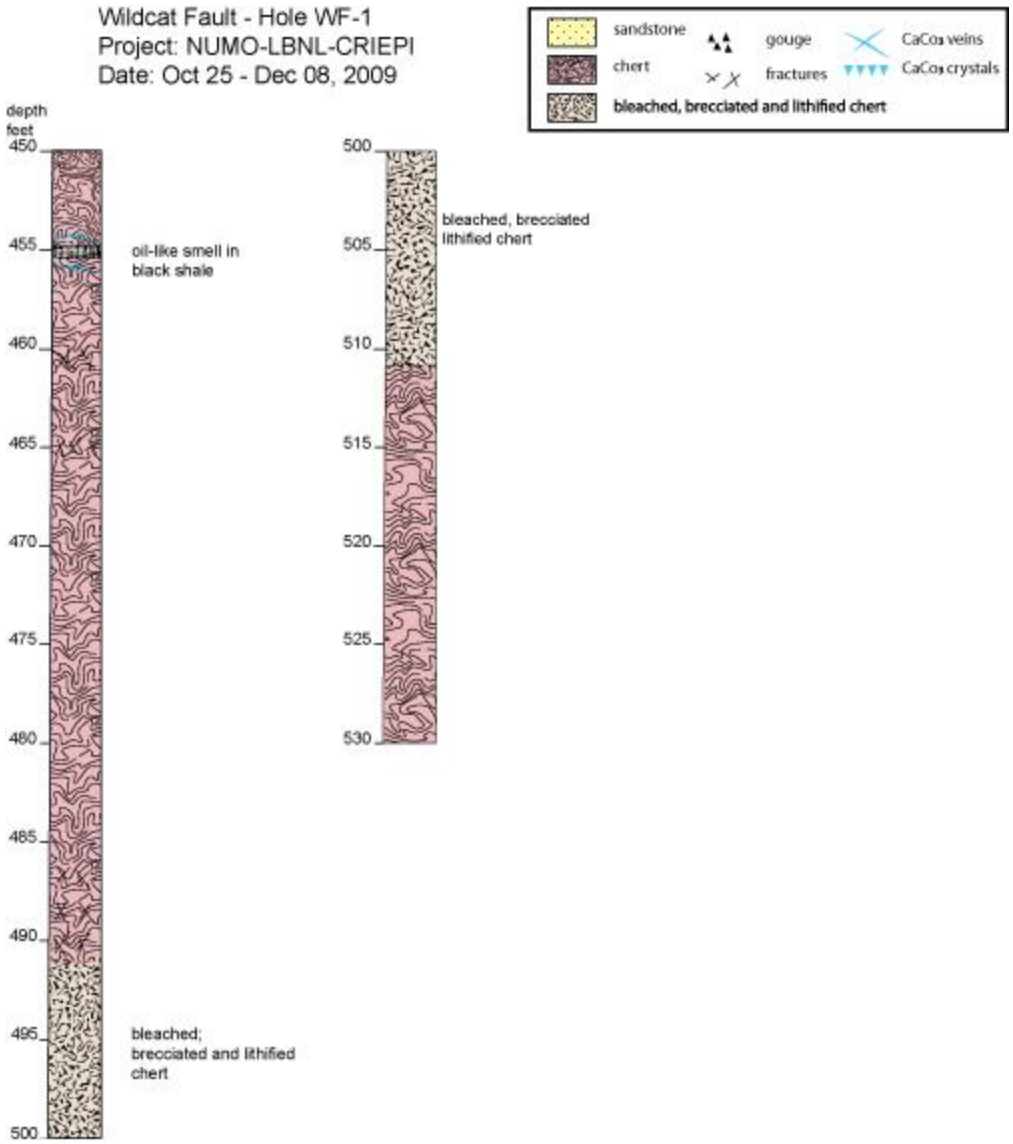
Wildcat Fault - Hole WF-1
Project: NUMO-LBNL-CRIEPI
Date: Oct 25 - Dec 08, 2009
sandstone
chert
gouge
fractures
CaCo3 veins
CaCo3 crystals
bleached, brecciated and lithified chert
depth
feet
450
455
460
465
470
475
480
485
490
495
500
oil-like smell in
black shale
bleached;
brecciated and lithified
chert
500
505
510
515
520
525
530
bleached, brecciated
lithified chert

WF2

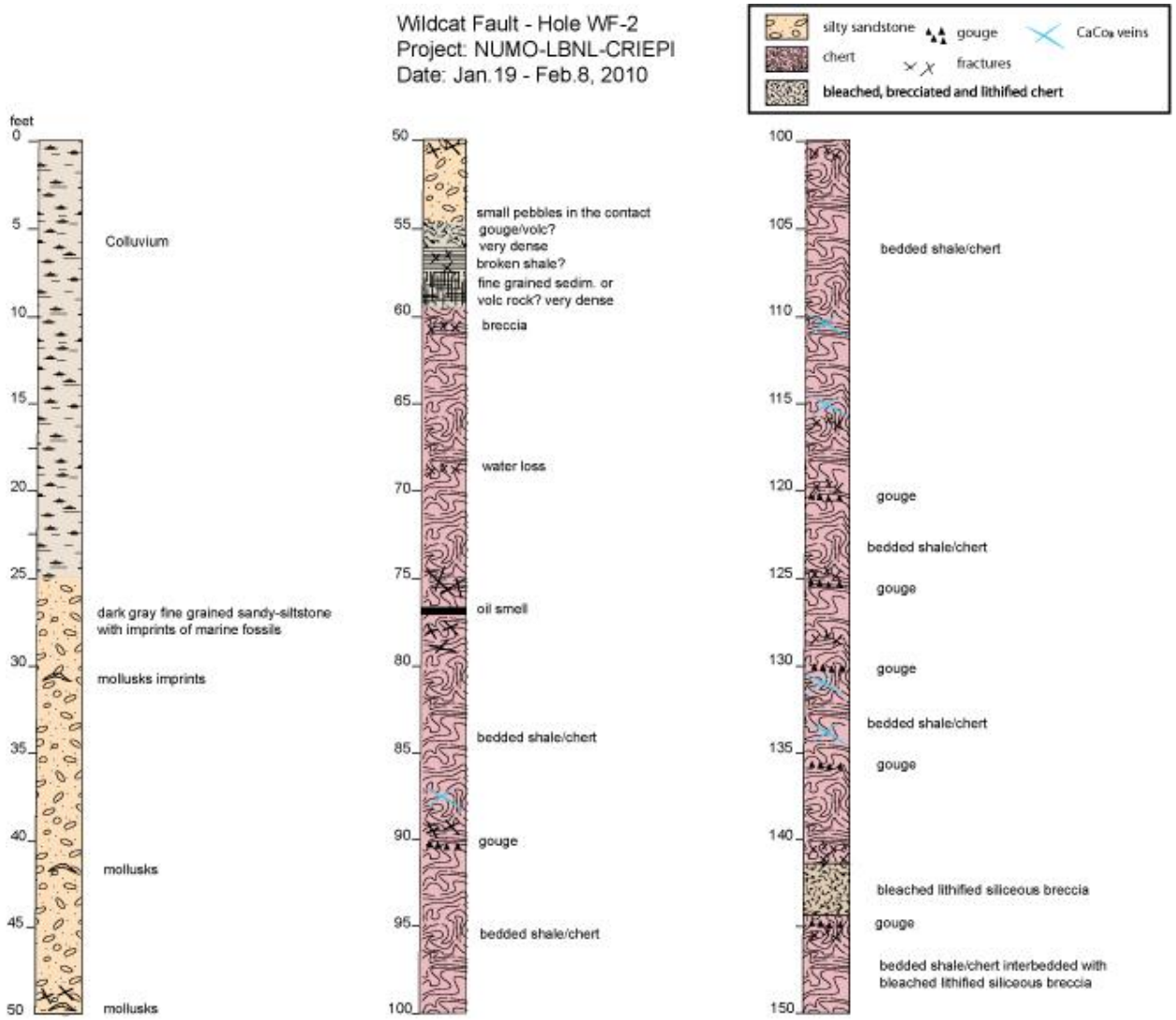
Wildcat Fault - Hole WF-2
Project: NUMO-LBNL-CRIEPI
Date: Jan.19 - Feb.8, 2010
silty sandstone
gouge
CaCo3 veins
chert
fractures
bleached, brecciated and lithified chert
feet
0
5
10
15
20
25
30
35
40
45
50
Colluvium
dark gray fine grained sandy-siltstone with imprints of marine fossils
mollusks imprints
mollusks
mollusks
50
55
60
65
70
75
80
85
90
95
100
small pebbles in the contact
gouge/volc?
very dense
broken shale?
fine grained sedim. or volc rock? very dense
breccia
water loss
oil smell
bedded shale/chert
gouge
bedded shale/chert
100
105
110
115
120
125
130
135
140
150
bedded shale/chert
gouge
bedded shale/chert
gouge
gouge
bedded shale/chert
gouge
bleached lithified siliceous breccia
gouge
bedded shale/chert interbedded with bleached lithified siliceous breccia

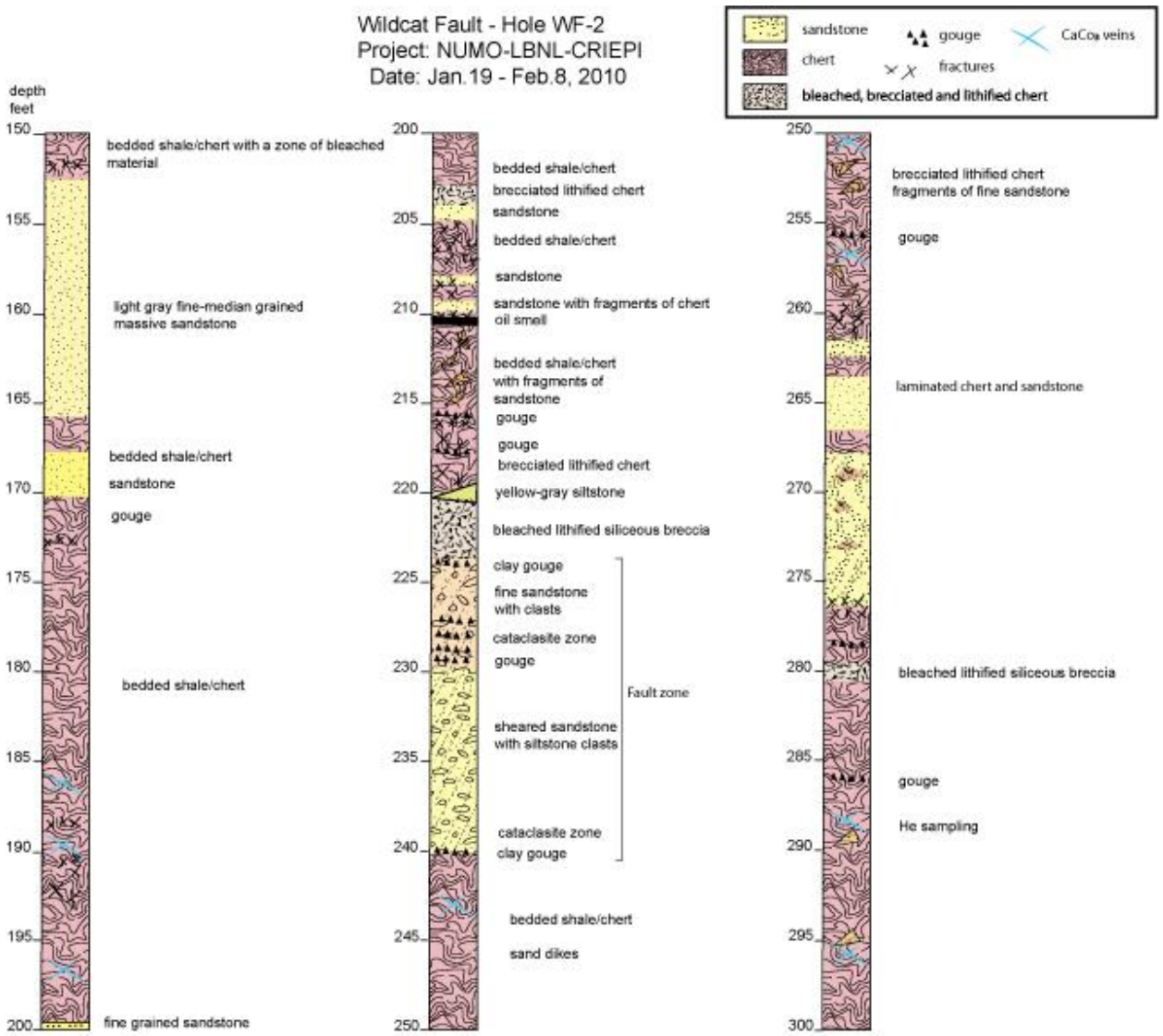
Wildcat Fault - Hole WF-2
Project: NUMO-LBNL-CRIEPI
Date: Jan.19 - Feb.8, 2010
sandstone
gouge
CaCO3 veins
chert
fractures
bleached, brecciated and lithified chert
depth
feet
150
155
160
165
170
175
180
185
190
195
200
bedded shale/chert with a zone of bleached material
light gray fine-median grained massive sandstone
bedded shale/chert
sandstone
gouge
bedded shale/chert
fine grained sandstone
200
205
210
215
220
225
230
235
240
245
250
bedded shale/chert
brecciated lithified chert
sandstone
bedded shale/chert
sandstone
sandstone with fragments of chert
oil smell
bedded shale/chert with fragments of sandstone
gouge
gouge
brecciated lithified chert
yellow-gray siltstone
bleached lithified siliceous breccia
clay gouge
fine sandstone with clasts
cataclasite zone
gouge
sheared sandstone with siltstone clasts
cataclasite zone
clay gouge
Fault zone
bedded shale/chert
sand dikes
250
255
260
265
270
275
280
285
290
295
300
brecciated lithified chert fragments of fine sandstone
gouge
laminated chert and sandstone
bleached lithified siliceous breccia
gouge
He sampling

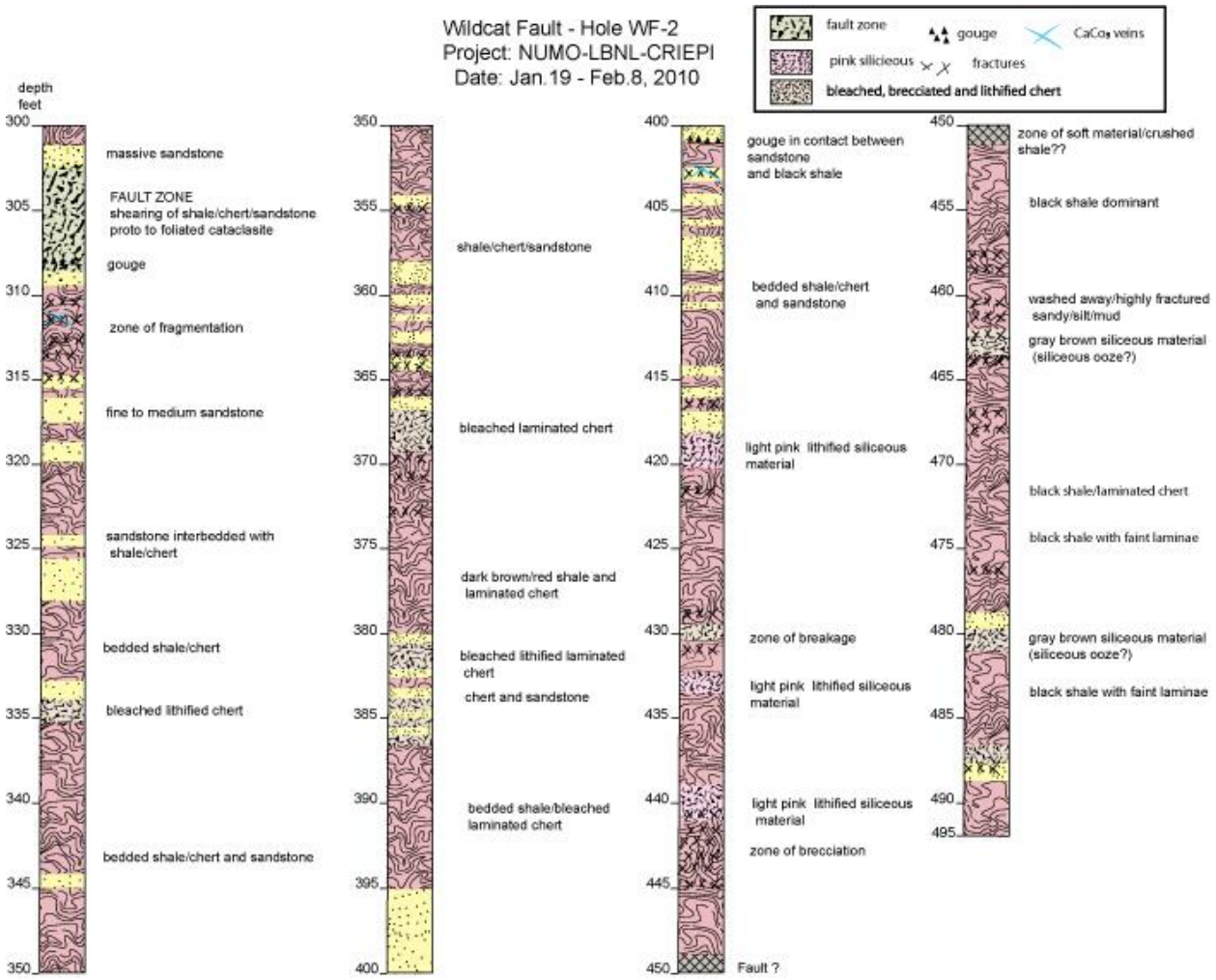
Wildcat Fault - Hole WF-2
Project: NUMO-LBNL-CRIEPI
Date: Jan.19 - Feb.8, 2010
fault zone
gouge
CaCo3 veins
pink silicieous
fractures
bleached, brecciated and lithified chert
depth feet
300
305
310
315
320
325
330
335
340
345
350
massive sandstone
FAULT ZONE
shearing of shale/chert/sandstone
proto to foliated cataclasite
gouge
zone of fragmentation
fine to medium sandstone
sandstone interbedded with shale/chert
bedded shale/chert
bleached lithified chert
bedded shale/chert and sandstone
350
355
360
365
370
375
380
385
390
395
400
shale/chert/sandstone
bleached laminated chert
dark brown/red shale and laminated chert
bleached lithified laminated chert
chert and sandstone
bedded shale/bleached laminated chert
400
405
410
415
420
425
430
435
440
445
450
gouge in contact between sandstone and black shale
bedded shale/chert and sandstone
light pink lithified siliceous material
zone of breakage
light pink lithified siliceous material
light pink lithified siliceous material
zone of brecciation
Fault ?
450
455
460
465
470
475
480
485
490
495
zone of soft material/crushed shale??
black shale dominant
washed away/highly fractured sandy/silt/mud
gray brown siliceous material (siliceous ooze?)
black shale/laminated chert
black shale with faint laminae
gray brown siliceous material (siliceous ooze?)
black shale with faint laminae

WF3

Wildcat Fault - Hole WF-3
Project: NUMO-LBNL-CRIEPI

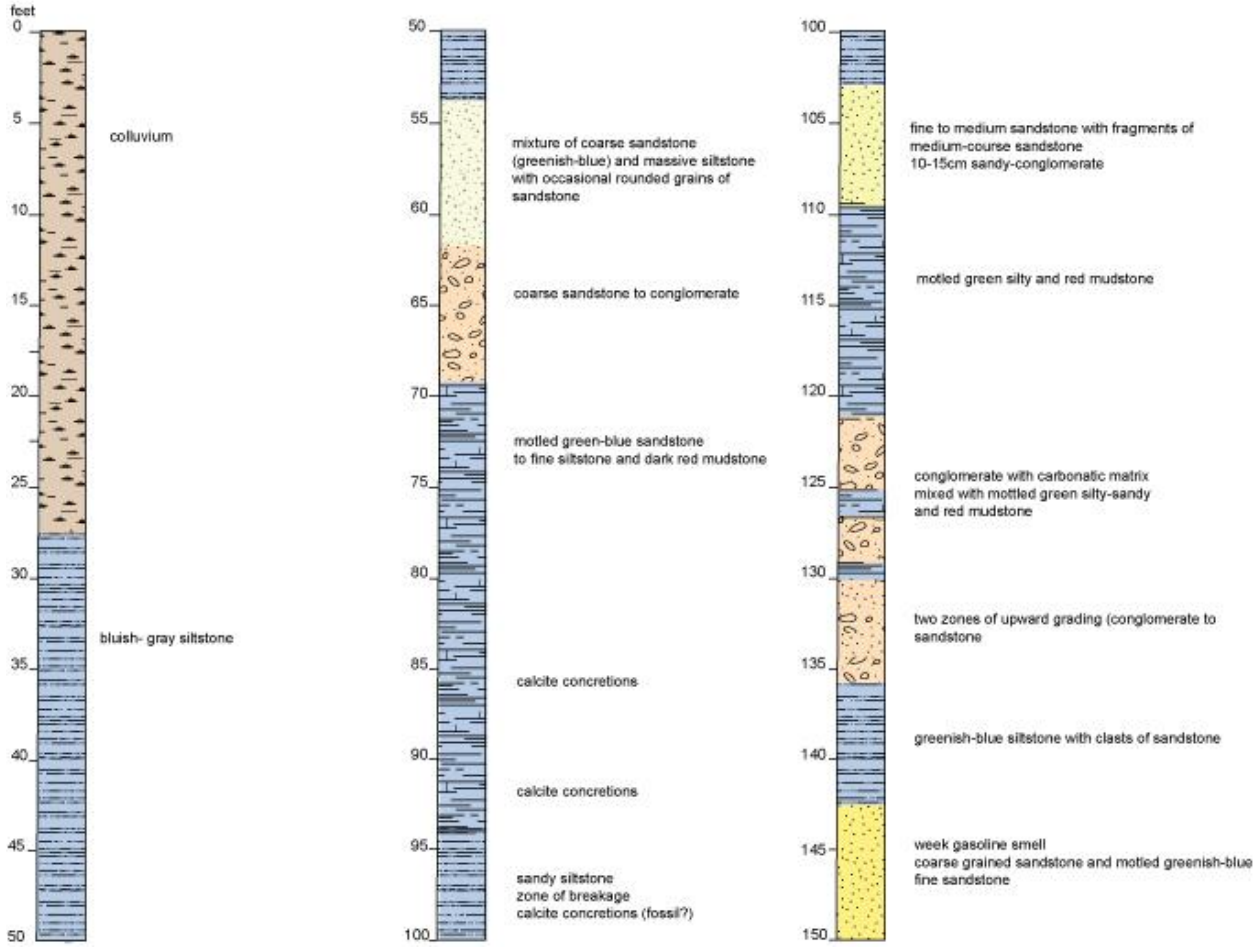

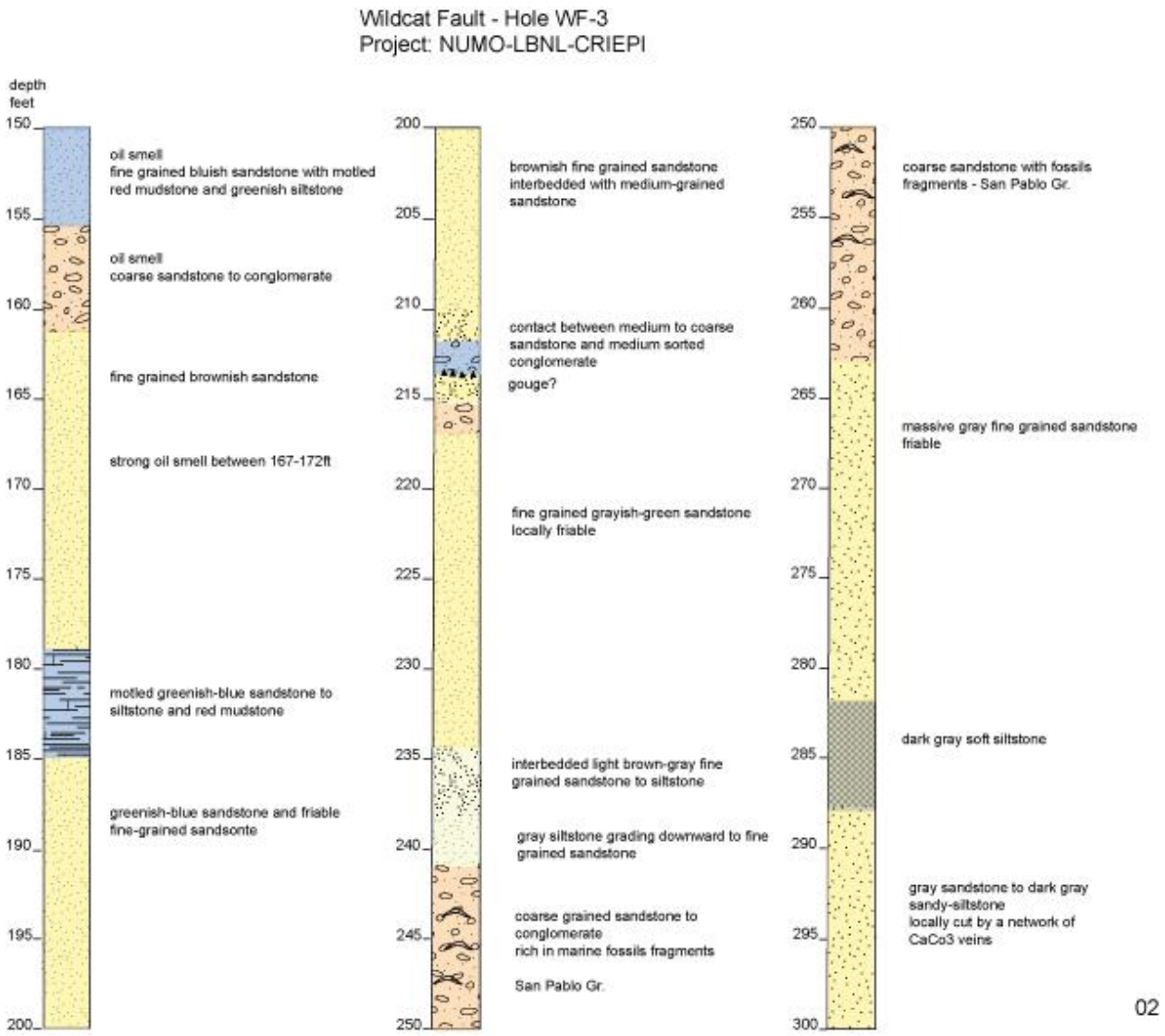
Wildcat Fault - Hole WF-3
Project: NUMO-LBNL-CRIEPI
depth
feet
150
155
160
165
170
175
180
185
190
195
200
oil smell
fine grained bluish sandstone with motled red mudstone and greenish siltstone
oil smell
coarse sandstone to conglomerate
fine grained brownish sandstone
strong oil smell between 167-172ft
motled greenish-blue sandstone to siltstone and red mudstone
greenish-blue sandstone and friable fine-grained sandsonte
200
205
210
215
220
225
230
235
240
245
250
brownish fine grained sandstone interbedded with medium-grained sandstone
contact between medium to coarse sandstone and medium sorted conglomerate
gouge?
fine grained grayish-green sandstone locally friable
interbedded light brown-gray fine grained sandstone to siltstone
gray siltstone grading downward to fine grained sandstone
coarse grained sandstone to conglomerate
rich in marine fossils fragments
San Pablo Gr.
250
255
260
265
270
275
280
285
290
295
300
coarse sandstone with fossils fragments - San Pablo Gr.
massive gray fine grained sandstone friable
dark gray soft siltstone
gray sandstone to dark gray sandy-siltstone
locally cut by a network of CaCo3 veins
02

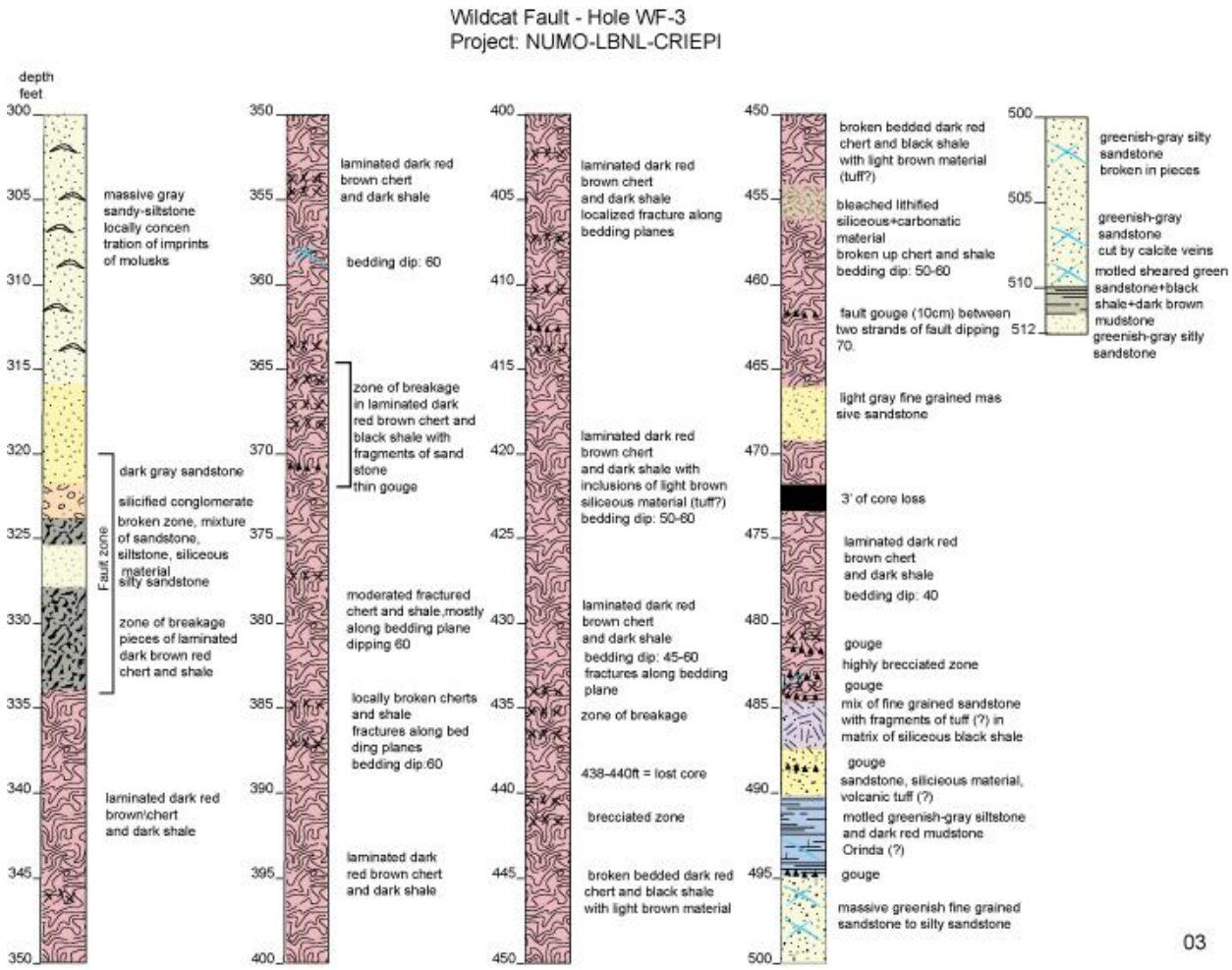
Wildcat Fault - Hole WF-3
Project: NUMO-LBNL-CRIEPI
depth
feet
300
305
310
315
320
325
330
335
340
345
350
massive gray
sandy-siltstone
locally concen
tration of imprints
of molusks
Fault zone
dark gray sandstone
silicified conglomerate
broken zone, mixture
of sandstone,
siltstone, siliceous
material
silty sandstone
zone of breakage
pieces of laminated
dark brown red
chert and shale
laminated dark red
brown\chert
and dark shale
350
355
360
365
370
375
380
385
390
395
400
laminated dark red
brown chert
and dark shale
bedding dip: 60
zone of breakage
in laminated dark
red brown chert and
black shale with
fragments of sand
stone
thin gouge
moderated fractured
chert and shale,mostly
along bedding plane
dipping 60
locally broken cherts
and shale
fractures along bed
ding planes
bedding dip:60
laminated dark
red brown chert
and dark shale
400
405
410
415
420
425
430
435
440
445
450
laminated dark red
brown chert
and dark shale
localized fracture along
bedding planes
laminated dark red
brown chert
and dark shale with
inclusions of light brown
siliceous material (tuff?)
bedding dip: 50-60
laminated dark red
brown chert
and dark shale
bedding dip: 45-60
fractures along bedding
plane
zone of breakage
438-440ft = lost core
brecciated zone
broken bedded dark red
chert and black shale
with light brown material
450
455
460
465
470
475
480
485
490
495
500
broken bedded dark red
chert and black shale
with light brown material
(tuff?)
bleached lithified
siliceous+carbonatic
material
broken up chert and shale
bedding dip: 50-60
fault gouge (10cm) between
two strands of fault dipping
70.
light gray fine grained mas
sive sandstone
3' of core loss
laminated dark red
brown chert
and dark shale
bedding dip: 40
gouge
highly brecciated zone
gouge
mix of fine grained sandstone
with fragments of tuff (?) in
matrix of siliceous black shale
gouge
sandstone, silicieous material,
volcanic tuff (?)
motled greenish-gray siltstone
and dark red mudstone
Orinda (?)
gouge
massive greenish fine grained
sandstone to silty sandstone
500
505
510
512
greenish-gray silty
sandstone
broken in pieces
greenish-gray
sandstone
cut by calcite veins
motled sheared green
sandstone+black
shale+dark brown
mudstone
greenish-gray sitly
sandstone
03

WF4

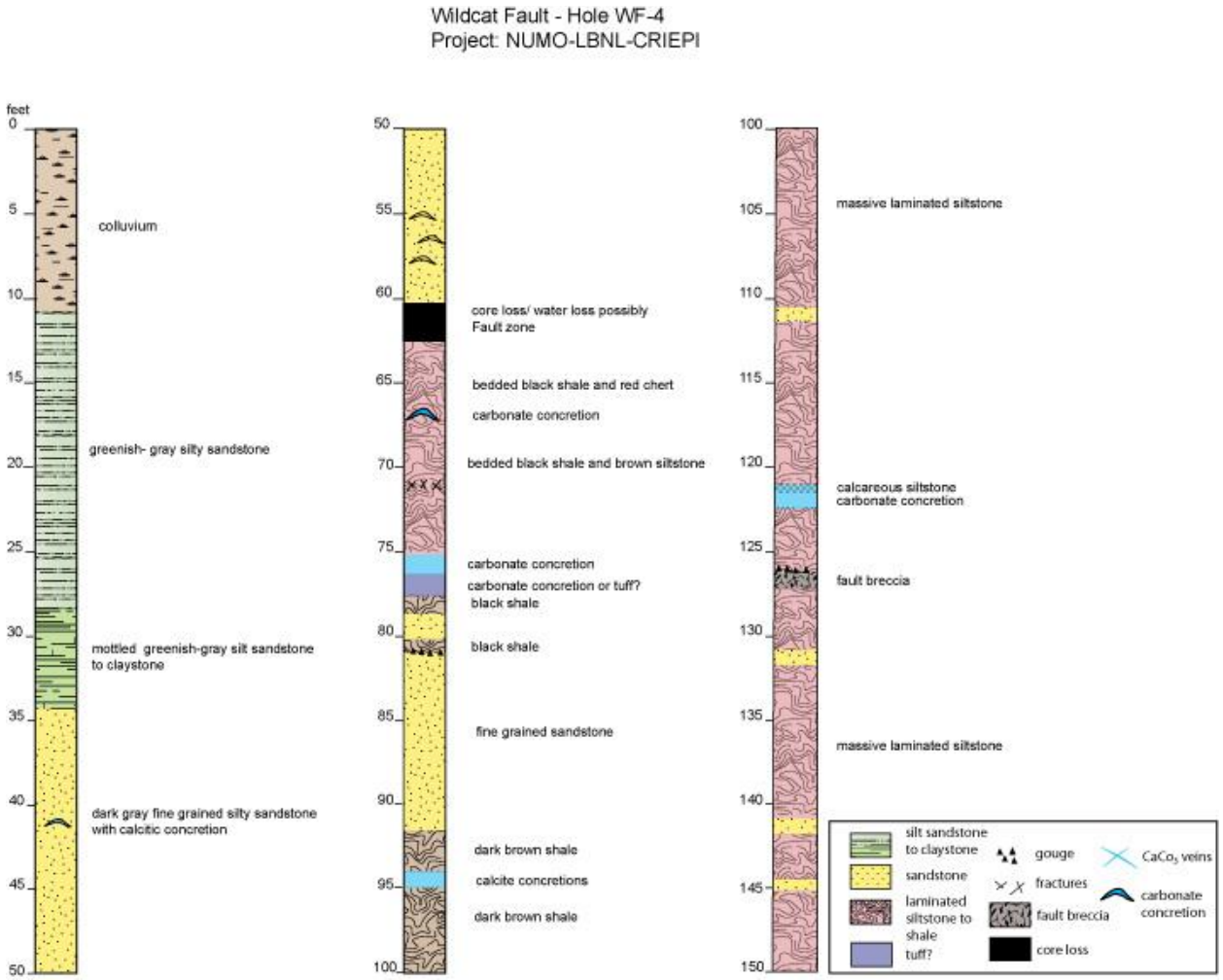
Wildcat Fault - Hole WF-4
Project: NUMO-LBNL-CRIEPI
feet
colluvium
greenish- gray silty sandstone
mottled greenish-gray silt sandstone to claystone
dark gray fine grained silty sandstone with calcitic concretion
core loss/ water loss possibly Fault zone
bedded black shale and red chert
carbonate concretion
bedded black shale and brown siltstone
carbonate concretion
carbonate concretion or tuff?
black shale
black shale
fine grained sandstone
dark brown shale
calcite concretions
dark brown shale
massive laminated siltstone
calcareous siltstone carbonate concretion
fault breccia
massive laminated siltstone
silt sandstone to claystone
sandstone
laminated siltstone to shale
tuff?
gouge
fractures
fault breccia
core loss
CaCo3 veins
carbonate concretion

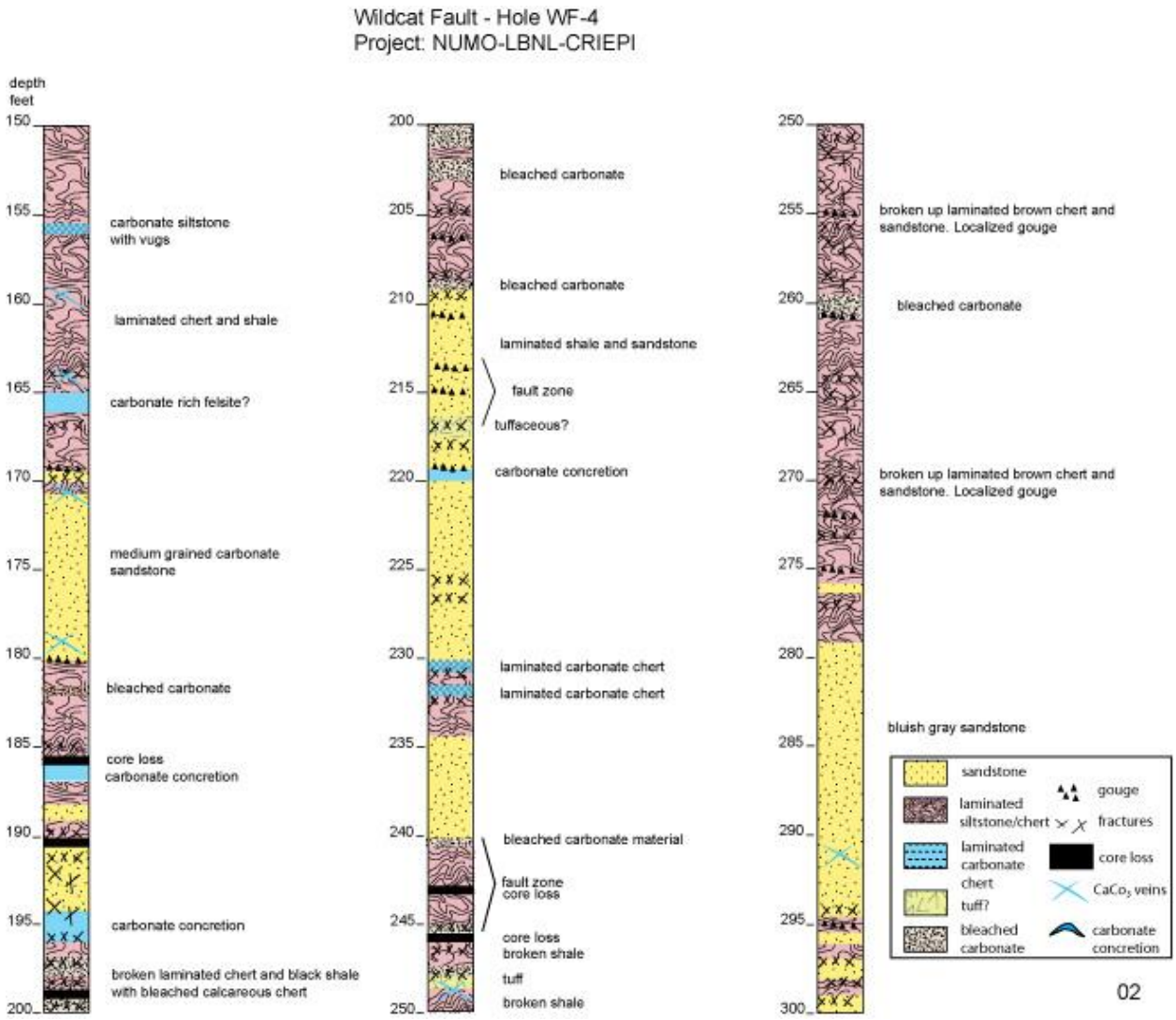
Wildcat Fault - Hole WF-4
Project: NUMO-LBNL-CRIEPI
depth
feet
150
155
160
165
170
175
180
185
190
195
200
carbonate siltstone
with vugs
laminated chert and shale
carbonate rich felsite?
medium grained carbonate
sandstone
bleached carbonate
core loss
carbonate concretion
carbonate concretion
broken laminated chert and black shale
with bleached calcareous chert
200
205
210
215
220
225
230
235
240
245
250
bleached carbonate
bleached carbonate
laminated shale and sandstone
fault zone
tuffaceous?
carbonate concretion
laminated carbonate chert
laminated carbonate chert
bleached carbonate material
fault zone
core loss
core loss
broken shale
tuff
broken shale
250
255
260
265
270
275
280
285
290
295
300
broken up laminated brown chert and
sandstone. Localized gouge
bleached carbonate
broken up laminated brown chert and
sandstone. Localized gouge
bluish gray sandstone
sandstone
laminated
siltstone/chert
laminated
carbonate
chert
tuff?
bleached
carbonate
gouge
fractures
core loss
CaCo3 veins
carbonate
concretion
02

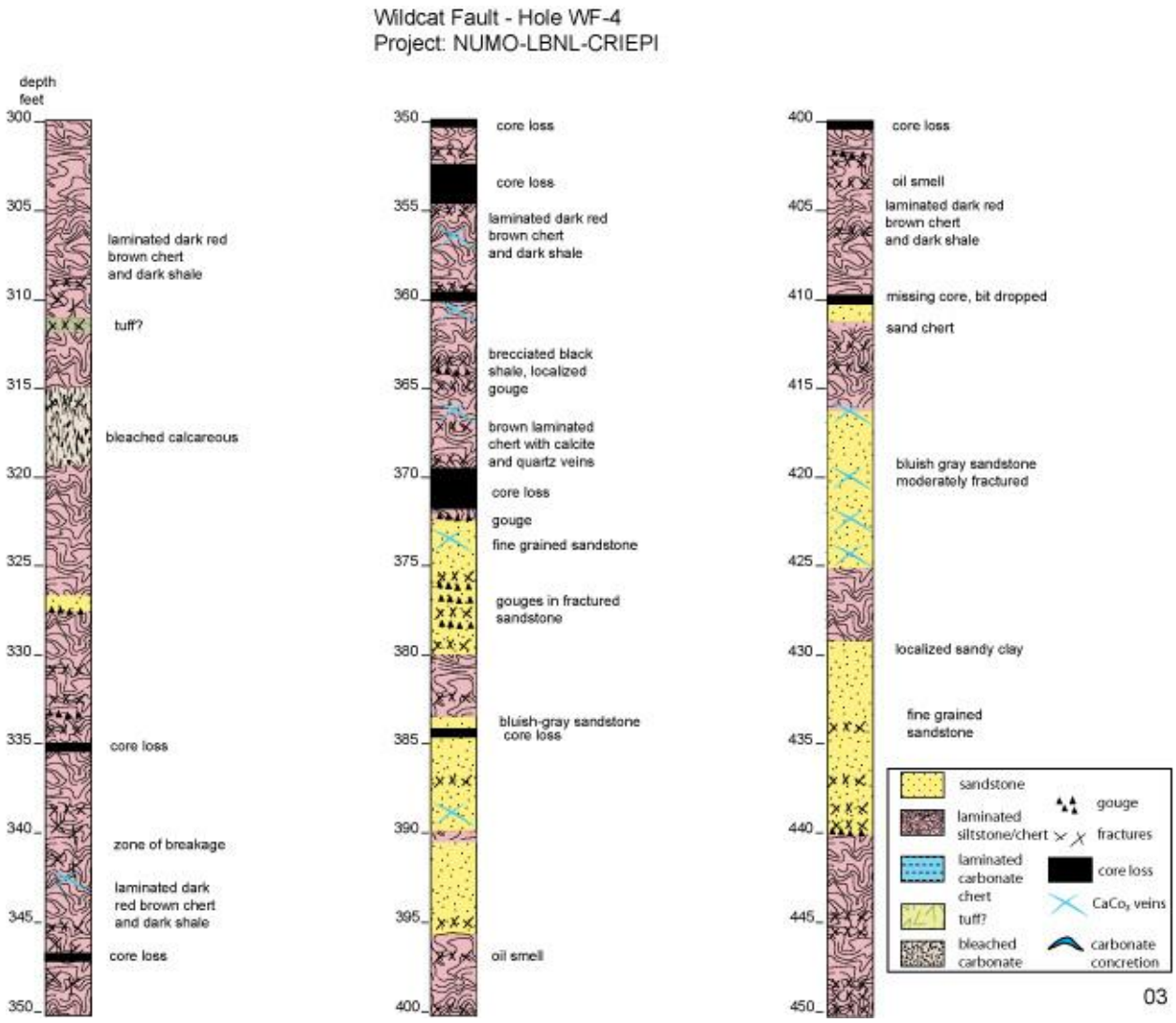
Wildcat Fault - Hole WF-4
Project: NUMO-LBNL-CRIEPI
depth feet
300
305
310
315
320
325
330
335
340
345
350
laminated dark red brown chert and dark shale
tuff?
bleached calcareous
core loss
zone of breakage
laminated dark red brown chert and dark shale
core loss
350
355
360
365
370
375
380
385
390
395
400
core loss
core loss
laminated dark red brown chert and dark shale
brecciated black shale, localized gouge
brown laminated chert with calcite and quartz veins
core loss
gouge
fine grained sandstone
gouges in fractured sandstone
bluish-gray sandstone core loss
oil smell
400
405
410
415
420
425
430
435
440
445
450
core loss
oil smell
laminated dark red brown chert and dark shale
missing core, bit dropped
sand chert
bluish gray sandstone moderately fractured
localized sandy clay
fine grained sandstone
sandstone
laminated siltstone/chert
laminated carbonate chert
tuff?
bleached carbonate
gouge
fractures
core loss
CaCo3 veins
carbonate concretion
03

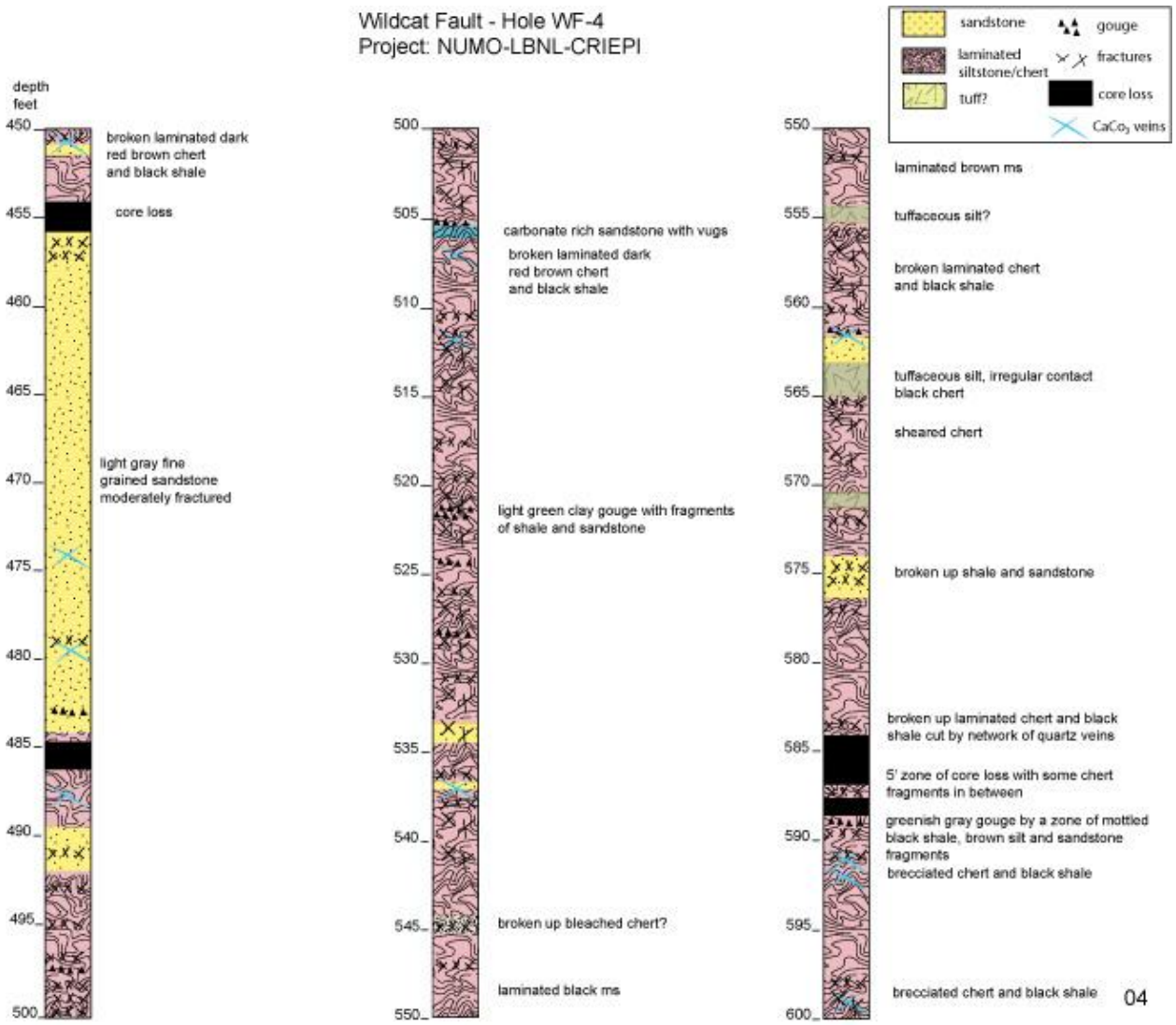
Wildcat Fault - Hole WF-4
Project: NUMO-LBNL-CRIEPI
sandstone
gouge
laminated siltstone/chert
fractures
tuff?
core loss
$CaCO_3$ veins
depth feet
450
455
460
465
470
475
480
485
490
495
500
broken laminated dark red brown chert and black shale
core loss
light gray fine grained sandstone moderately fractured
500
505
510
515
520
525
530
535
540
545
550
carbonate rich sandstone with vugs
broken laminated dark red brown chert and black shale
light green clay gouge with fragments of shale and sandstone
broken up bleached chert?
laminated black ms
550
555
560
565
570
575
580
585
590
595
600
laminated brown ms
tuffaceous silt?
broken laminated chert and black shale
tuffaceous silt, irregular contact black chert
sheared chert
broken up shale and sandstone
broken up laminated chert and black shale cut by network of quartz veins
5' zone of core loss with some chert fragments in between
greenish gray gouge by a zone of mottled black shale, brown silt and sandstone fragments
brecciated chert and black shale
brecciated chert and black shale
04

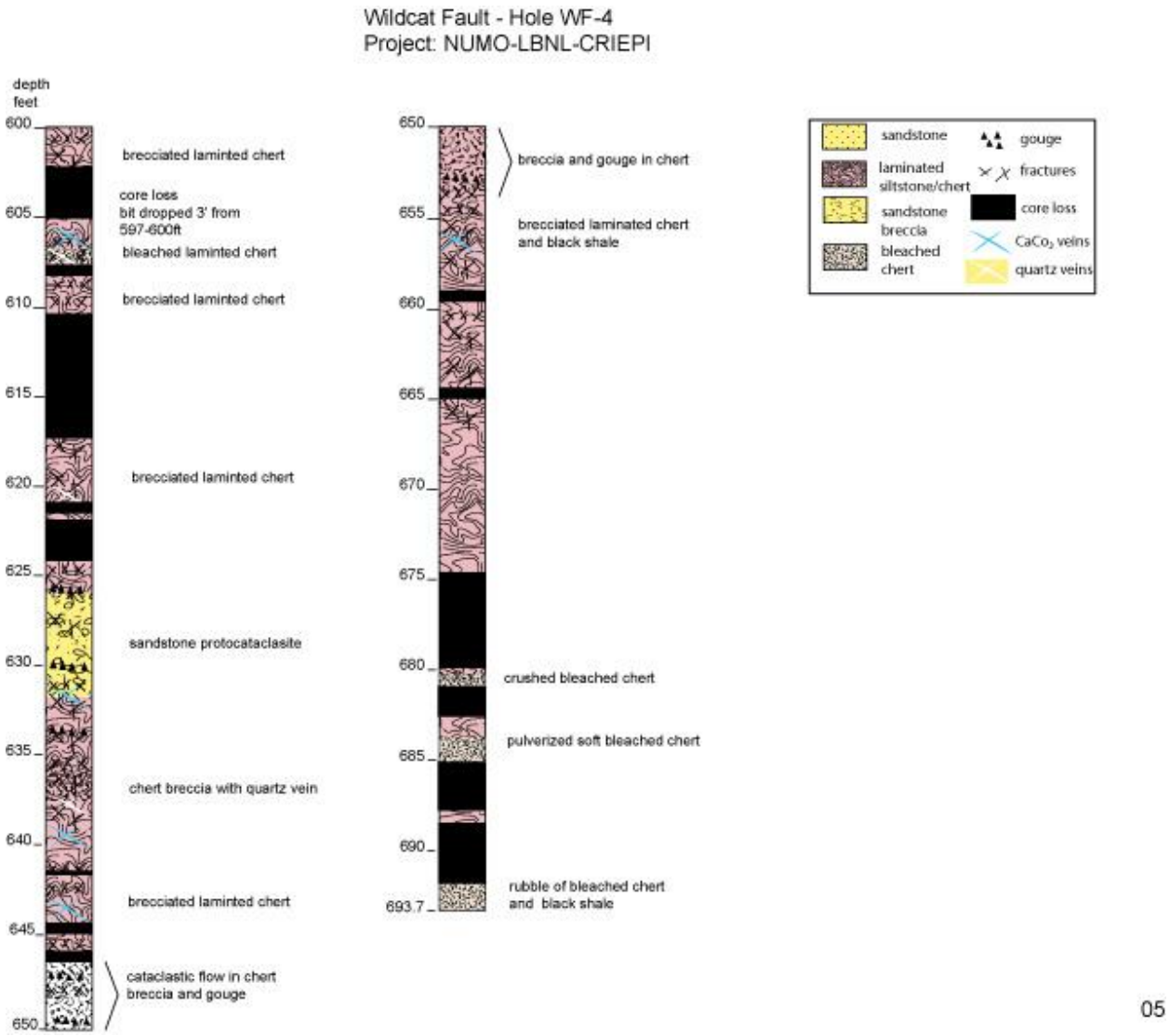
Wildcat Fault - Hole WF-4
Project: NUMO-LBNL-CRIEPI
depth
feet
600
605
610
615
620
625
630
635
640
645
650
brecciated laminted chert
core loss
bit dropped 3' from
597-600ft
bleached laminted chert
brecciated laminted chert
brecciated laminted chert
sandstone protocataclasite
chert breccia with quartz vein
brecciated laminted chert
cataclastic flow in chert
breccia and gouge
650
655
660
665
670
675
680
685
690
693.7
breccia and gouge in chert
brecciated laminated chert
and black shale
crushed bleached chert
pulverized soft bleached chert
rubble of bleached chert
and black shale
sandstone
laminated
siltstone/chert
sandstone
breccia
bleached
chert
gouge
fractures
core loss
CaCo3 veins
quartz veins
05

WF5

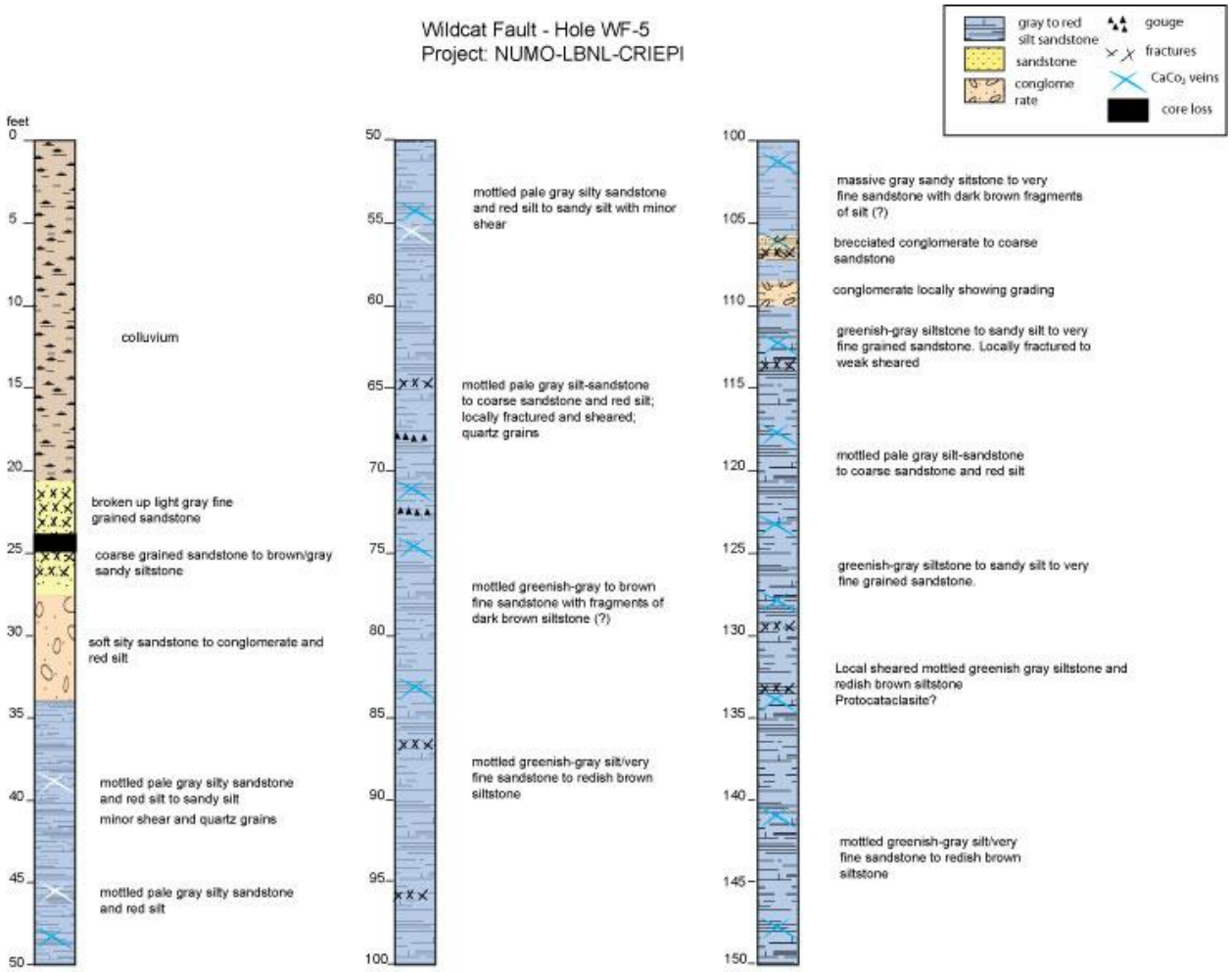
Wildcat Fault - Hole WF-5
Project: NUMO-LBNL-CRIEPI
gray to red silt sandstone
sandstone
conglomerate
gouge
fractures
CaCo3 veins
core loss
feet
colluvium
broken up light gray fine grained sandstone
coarse grained sandstone to brown/gray sandy siltstone
soft sity sandstone to conglomerate and red silt
mottled pale gray silty sandstone and red silt to sandy silt
minor shear and quartz grains
mottled pale gray silty sandstone and red silt
mottled pale gray silty sandstone and red silt to sandy silt with minor shear
mottled pale gray silt-sandstone to coarse sandstone and red silt; locally fractured and sheared; quartz grains
mottled greenish-gray to brown fine sandstone with fragments of dark brown siltstone (?)
mottled greenish-gray silt/very fine sandstone to redish brown siltstone
massive gray sandy sitstone to very fine sandstone with dark brown fragments of silt (?)
brecciated conglomerate to coarse sandstone
conglomerate locally showing grading
greenish-gray siltstone to sandy silt to very fine grained sandstone. Locally fractured to weak sheared
mottled pale gray silt-sandstone to coarse sandstone and red silt
greenish-gray siltstone to sandy silt to very fine grained sandstone.
Local sheared mottled greenish gray siltstone and redish brown siltstone
Protocataclasite?
mottled greenish-gray silt/very fine sandstone to redish brown siltstone

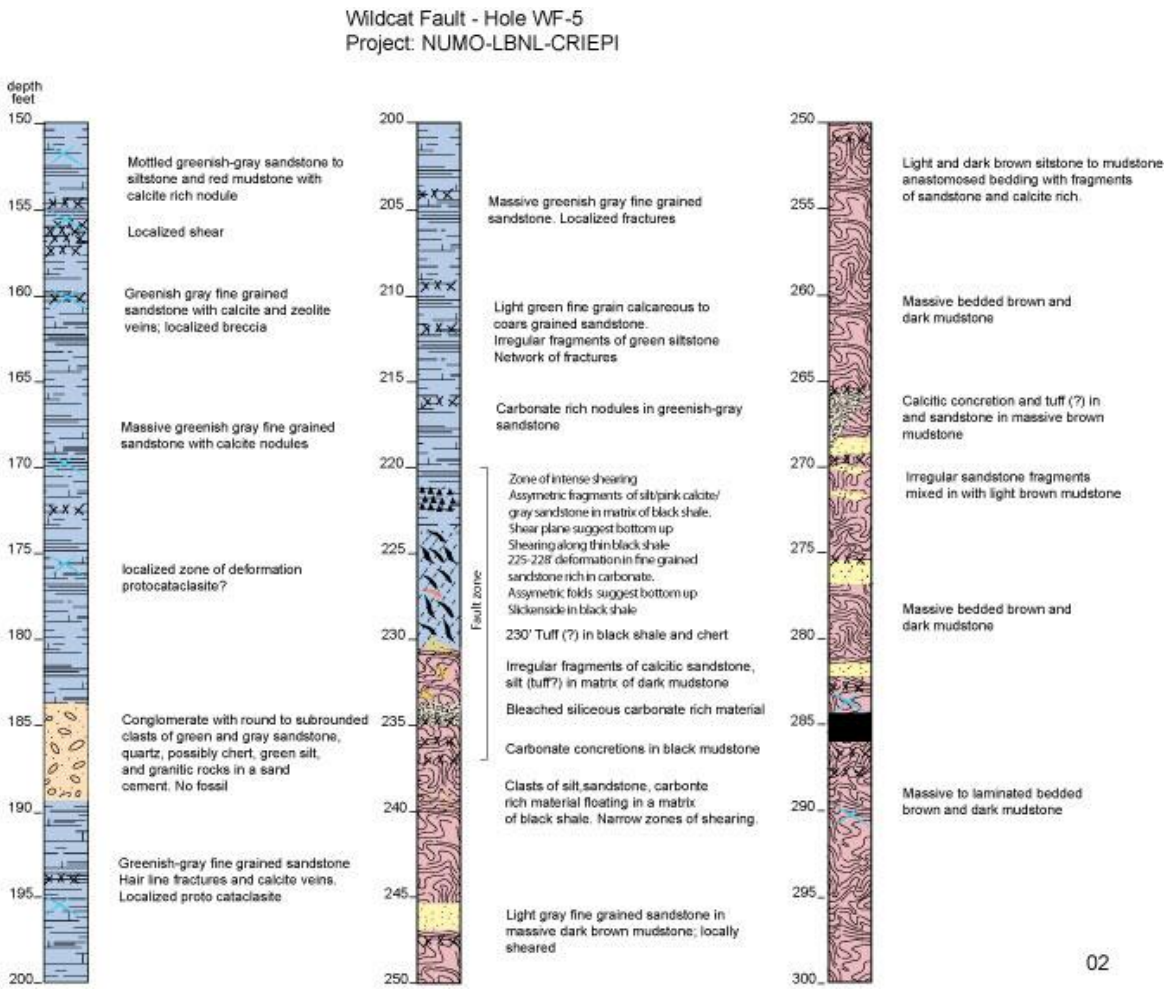
Wildcat Fault - Hole WF-5
Project: NUMO-LBNL-CRIEPI
depth feet
150
155
160
165
170
175
180
185
190
195
200
Mottled greenish-gray sandstone to siltstone and red mudstone with calcite rich nodule
Localized shear
Greenish gray fine grained sandstone with calcite and zeolite veins; localized breccia
Massive greenish gray fine grained sandstone with calcite nodules
localized zone of deformation protocataclasite?
Conglomerate with round to subrounded clasts of green and gray sandstone, quartz, possibly chert, green silt, and granitic rocks in a sand cement. No fossil
Greenish-gray fine grained sandstone Hair line fractures and calcite veins. Localized proto cataclasite
200
205
210
215
220
225
230
235
240
245
250
Massive greenish gray fine grained sandstone. Localized fractures
Light green fine grain calcareous to coars grained sandstone. Irregular fragments of green siltstone Network of fractures
Carbonate rich nodules in greenish-gray sandstone
Fault zone
Zone of intense shearing
Assymetric fragments of silt/pink calcite/ gray sandstone in matrix of black shale.
Shear plane suggest bottom up
Shearing along thin black shale
225-228' deformation in fine grained sandstone rich in carbonate.
Assymetric folds suggest bottom up
Slickenside in black shale
230' Tuff (?) in black shale and chert
Irregular fragments of calcitic sandstone, silt (tuff?) in matrix of dark mudstone
Bleached siliceous carbonate rich material
Carbonate concretions in black mudstone
Clasts of silt,sandstone, carbonte rich material floating in a matrix of black shale. Narrow zones of shearing.
Light gray fine grained sandstone in massive dark brown mudstone; locally sheared
250
255
260
265
270
275
280
285
290
295
300
Light and dark brown siltstone to mudstone anastomosed bedding with fragments of sandstone and calcite rich.
Massive bedded brown and dark mudstone
Calcitic concretion and tuff (?) in and sandstone in massive brown mudstone
Irregular sandstone fragments mixed in with light brown mudstone
Massive bedded brown and dark mudstone
Massive to laminated bedded brown and dark mudstone
02

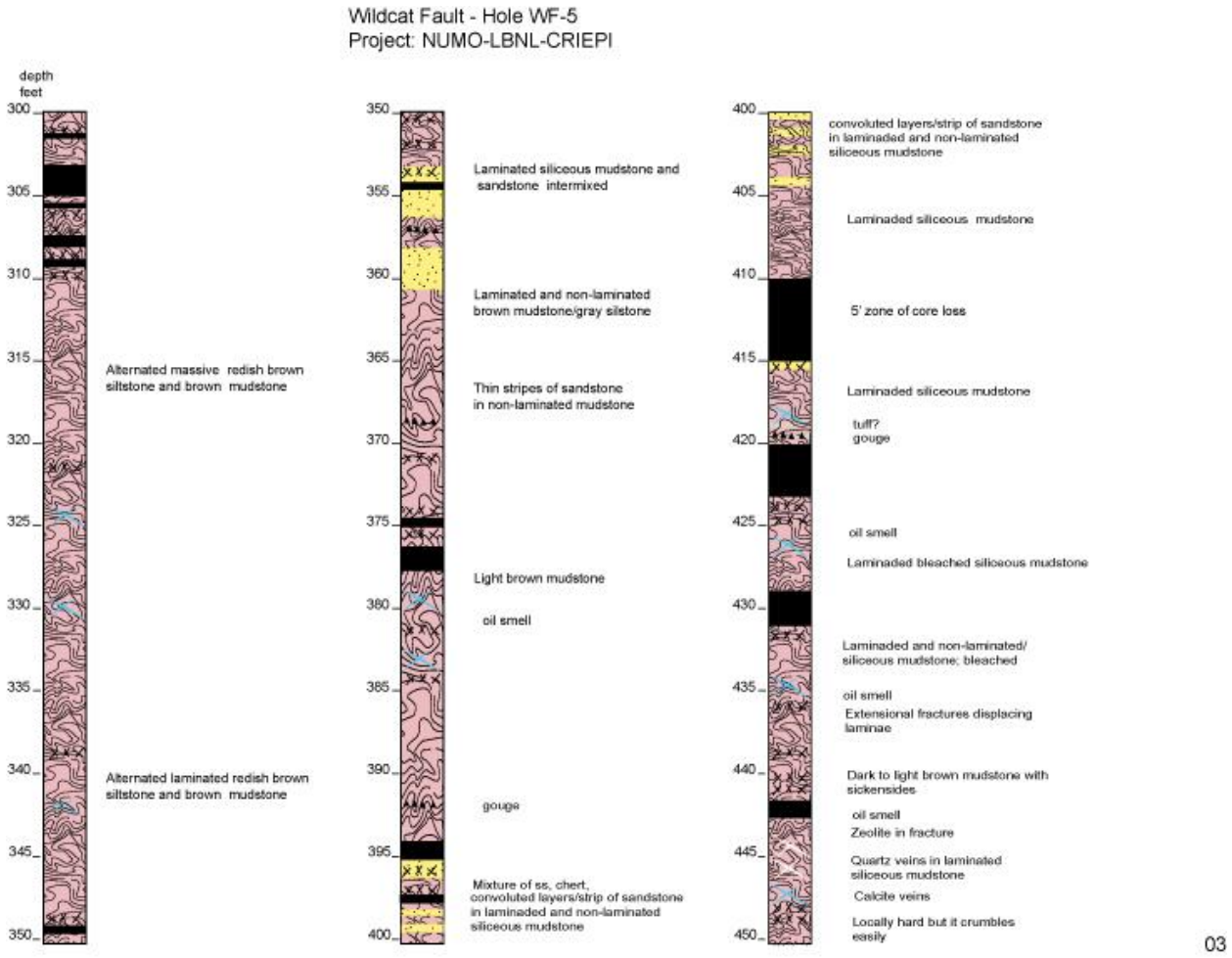
Wildcat Fault - Hole WF-5
Project: NUMO-LBNL-CRIEPI
depth
feet
300
305
310
315
320
325
330
335
340
345
350
Alternated massive redish brown siltstone and brown mudstone
Alternated laminated redish brown siltstone and brown mudstone
350
355
360
365
370
375
380
385
390
395
400
Laminated siliceous mudstone and sandstone intermixed
Laminated and non-laminated brown mudstone/gray siltstone
Thin stripes of sandstone in non-laminated mudstone
Light brown mudstone
oil smell
gouge
Mixture of ss, chert, convoluted layers/strip of sandstone in laminaded and non-laminated siliceous mudstone
400
405
410
415
420
425
430
435
440
445
450
convoluted layers/strip of sandstone in laminaded and non-laminated siliceous mudstone
Laminaded siliceous mudstone
5' zone of core loss
Laminaded siliceous mudstone
tuff?
gouge
oil smell
Laminaded bleached siliceous mudstone
Laminaded and non-laminated/ siliceous mudstone; bleached
oil smell
Extensional fractures displacing laminae
Dark to light brown mudstone with sickensides
oil smell
Zeolite in fracture
Quartz veins in laminated siliceous mudstone
Calcite veins
Locally hard but it crumbles easily
03

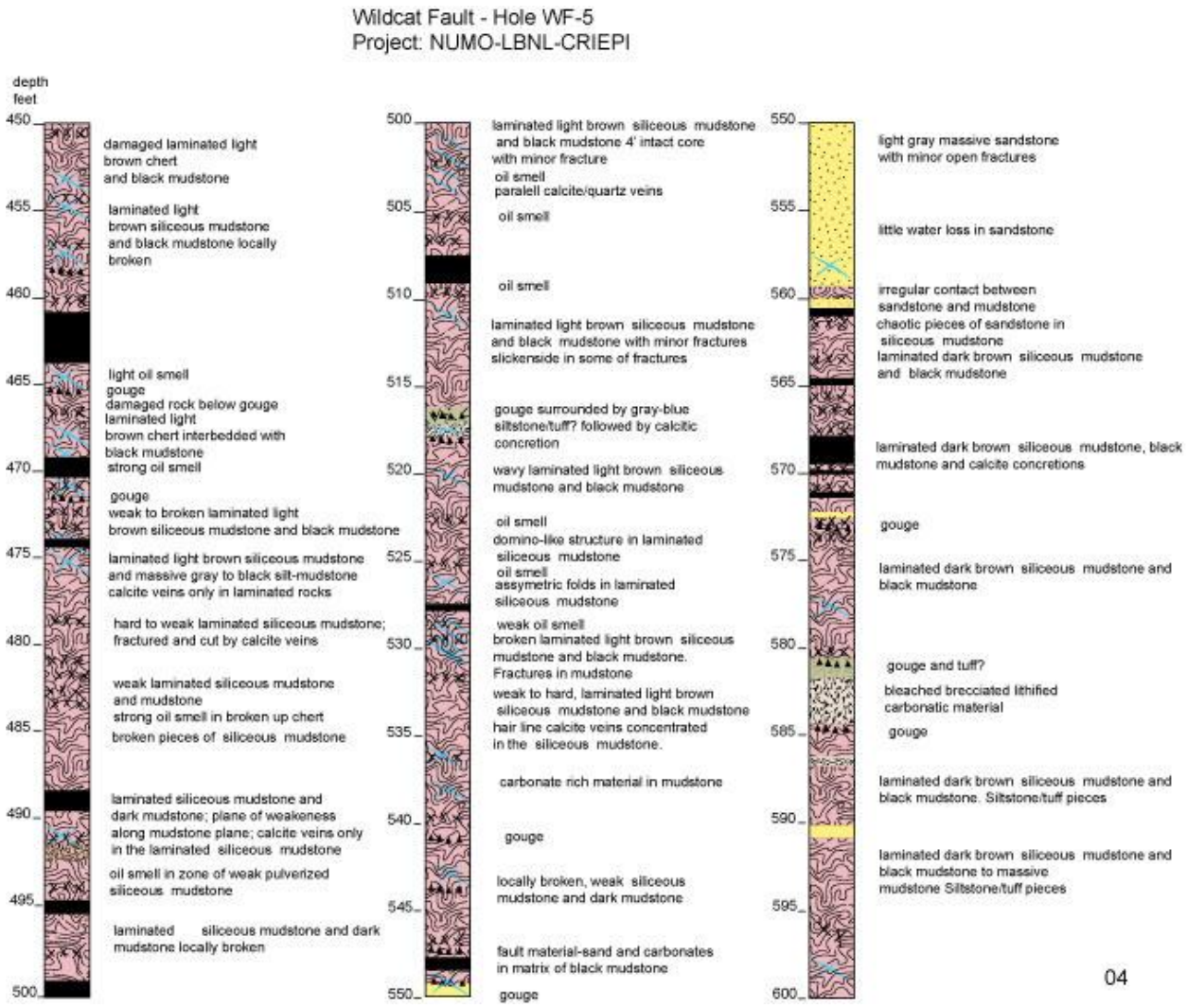
Wildcat Fault - Hole WF-5
Project: NUMO-LBNL-CRIEPI
depth
feet
450
damaged laminated light
brown chert
and black mudstone
455
laminated light
brown siliceous mudstone
and black mudstone locally
broken
460
465
light oil smell
gouge
damaged rock below gouge
laminated light
brown chert interbedded with
black mudstone
470
strong oil smell
gouge
weak to broken laminated light
brown siliceous mudstone and black mudstone
475
laminated light brown siliceous mudstone
and massive gray to black silt-mudstone
calcite veins only in laminated rocks
hard to weak laminated siliceous mudstone;
fractured and cut by calcite veins
480
weak laminated siliceous mudstone
and mudstone
strong oil smell in broken up chert
485
broken pieces of siliceous mudstone
laminated siliceous mudstone and
dark mudstone; plane of weakeness
490
along mudstone plane; calcite veins only
in the laminated siliceous mudstone
oil smell in zone of weak pulverized
siliceous mudstone
495
laminated siliceous mudstone and dark
mudstone locally broken
500
500
laminated light brown siliceous mudstone
and black mudstone 4' intact core
with minor fracture
oil smell
paralell calcite/quartz veins
505
oil smell
510
oil smell
laminated light brown siliceous mudstone
and black mudstone with minor fractures
slickenside in some of fractures
515
gouge surrounded by gray-blue
siltstone/tuff? followed by calcitic
concretion
520
wavy laminated light brown siliceous
mudstone and black mudstone
oil smell
domino-like structure in laminated
siliceous mudstone
525
oil smell
assymetric folds in laminated
siliceous mudstone
weak oil smell
530
broken laminated light brown siliceous
mudstone and black mudstone.
Fractures in mudstone
weak to hard, laminated light brown
siliceous mudstone and black mudstone
535
hair line calcite veins concentrated
in the siliceous mudstone.
carbonate rich material in mudstone
540
gouge
locally broken, weak siliceous
mudstone and dark mudstone
545
fault material-sand and carbonates
in matrix of black mudstone
550
gouge
550
light gray massive sandstone
with minor open fractures
555
little water loss in sandstone
560
irregular contact between
sandstone and mudstone
chaotic pieces of sandstone in
siliceous mudstone
laminated dark brown siliceous mudstone
and black mudstone
565
laminated dark brown siliceous mudstone, black
mudstone and calcite concretions
570
gouge
575
laminated dark brown siliceous mudstone and
black mudstone
580
gouge and tuff?
bleached brecciated lithified
carbonatic material
585
gouge
laminated dark brown siliceous mudstone and
black mudstone. Siltstone/tuff pieces
590
laminated dark brown siliceous mudstone and
black mudstone to massive
mudstone Siltstone/tuff pieces
595
600
04

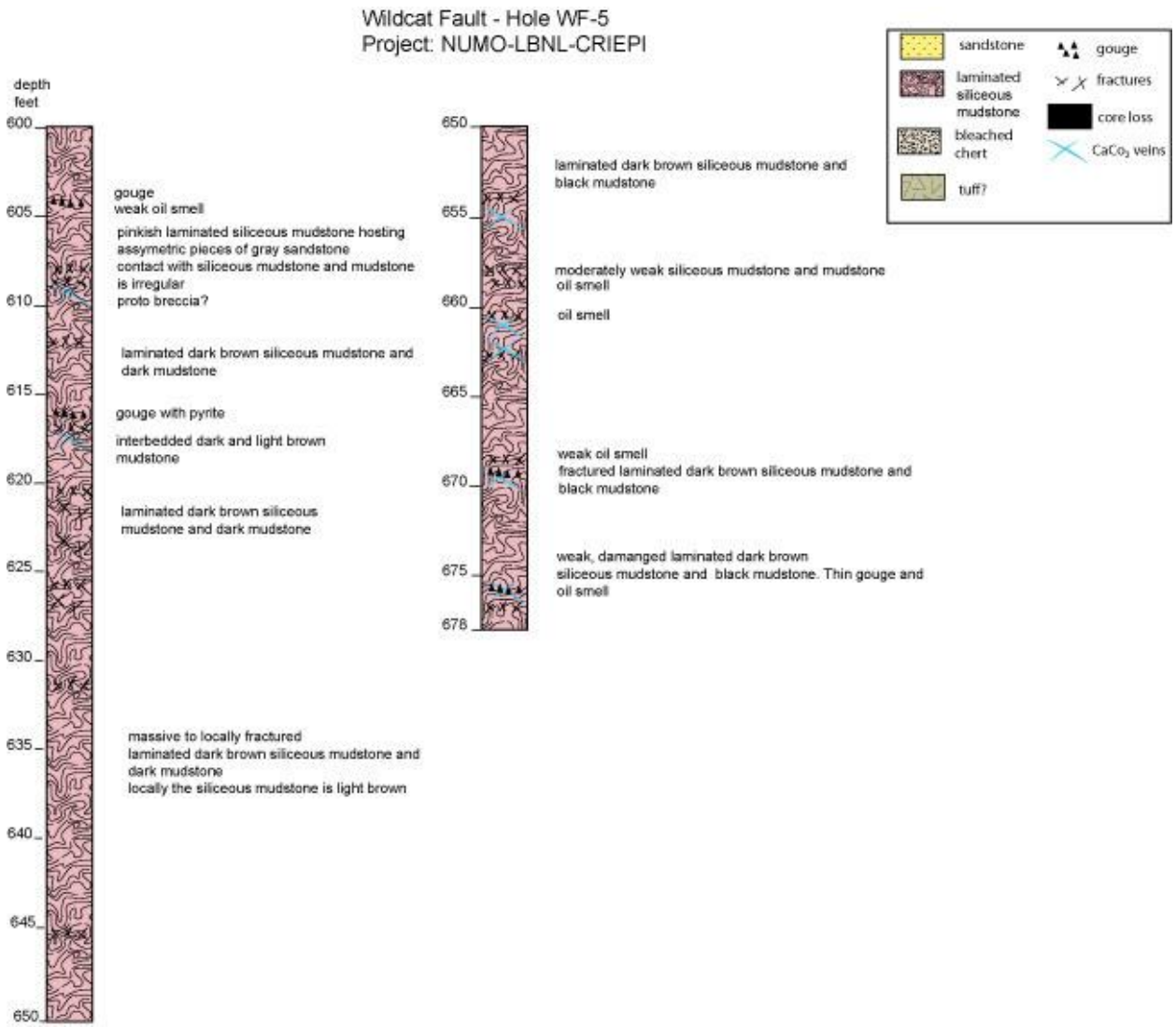
Wildcat Fault - Hole WF-5
Project: NUMO-LBNL-CRIEPI
depth
feet
600
605
610
615
620
625
630
635
640
645
650
gouge
weak oil smell
pinkish laminated siliceous mudstone hosting
assymetric pieces of gray sandstone
contact with siliceous mudstone and mudstone
is irregular
proto breccia?
laminated dark brown siliceous mudstone and
dark mudstone
gouge with pyrite
interbedded dark and light brown
mudstone
laminated dark brown siliceous
mudstone and dark mudstone
massive to locally fractured
laminated dark brown siliceous mudstone and
dark mudstone
locally the siliceous mudstone is light brown
650
655
660
665
670
675
678
laminated dark brown siliceous mudstone and
black mudstone
moderately weak siliceous mudstone and mudstone
oil smell
oil smell
weak oil smell
fractured laminated dark brown siliceous mudstone and
black mudstone
weak, damanged laminated dark brown
siliceous mudstone and black mudstone. Thin gouge and
oil smell
sandstone
gouge
laminated
siliceous
mudstone
fractures
core loss
bleached
chert
CaCo3 veins
tuff?

Appendix 2 - Core Images _WF1

Appendix 2 - Core Images _WF1

Appendix 2 - Core Images _WF1

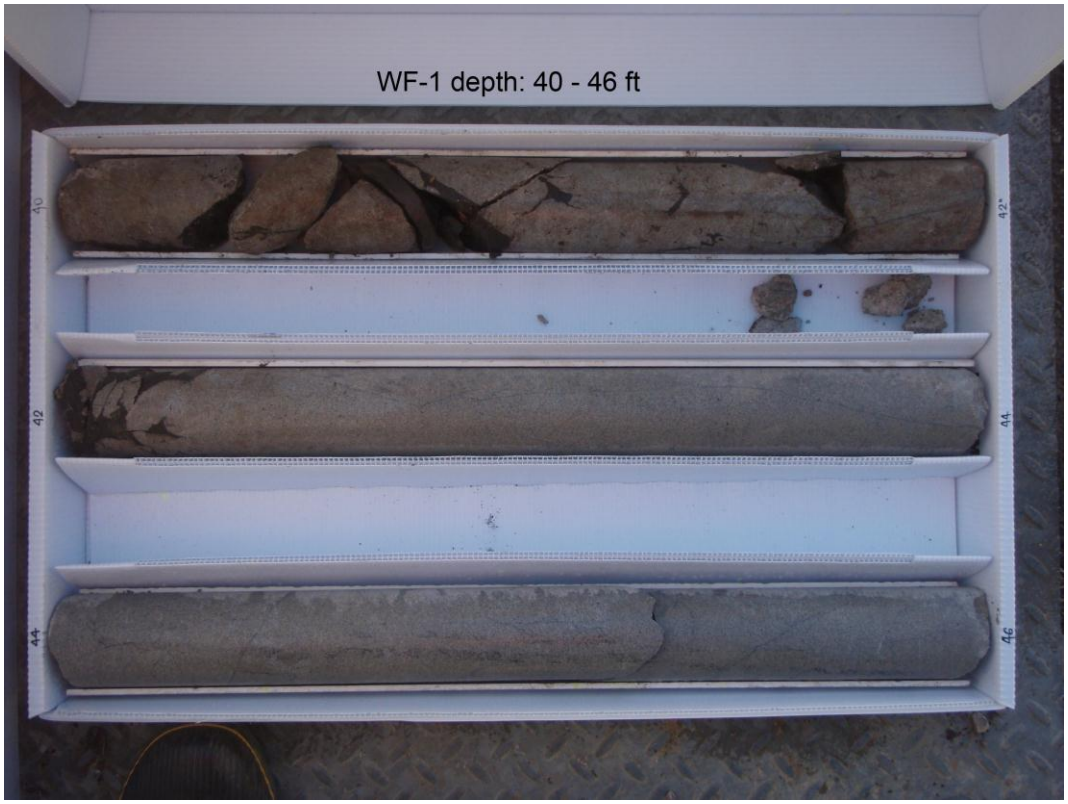

WF-1 depth: 50 ft 10 inch - 56 ft 9 inch

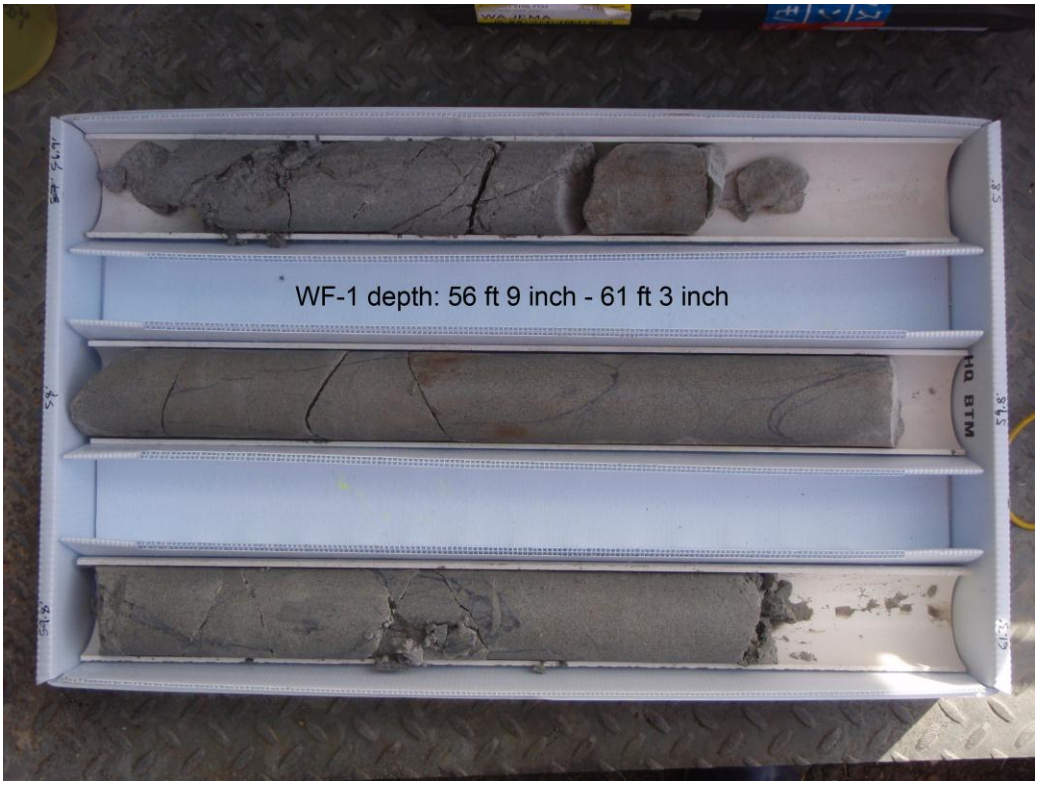
WF-1 depth: 56 ft 9 inch - 61 ft 3 inch

Appendix 2 - Core Images _WF1

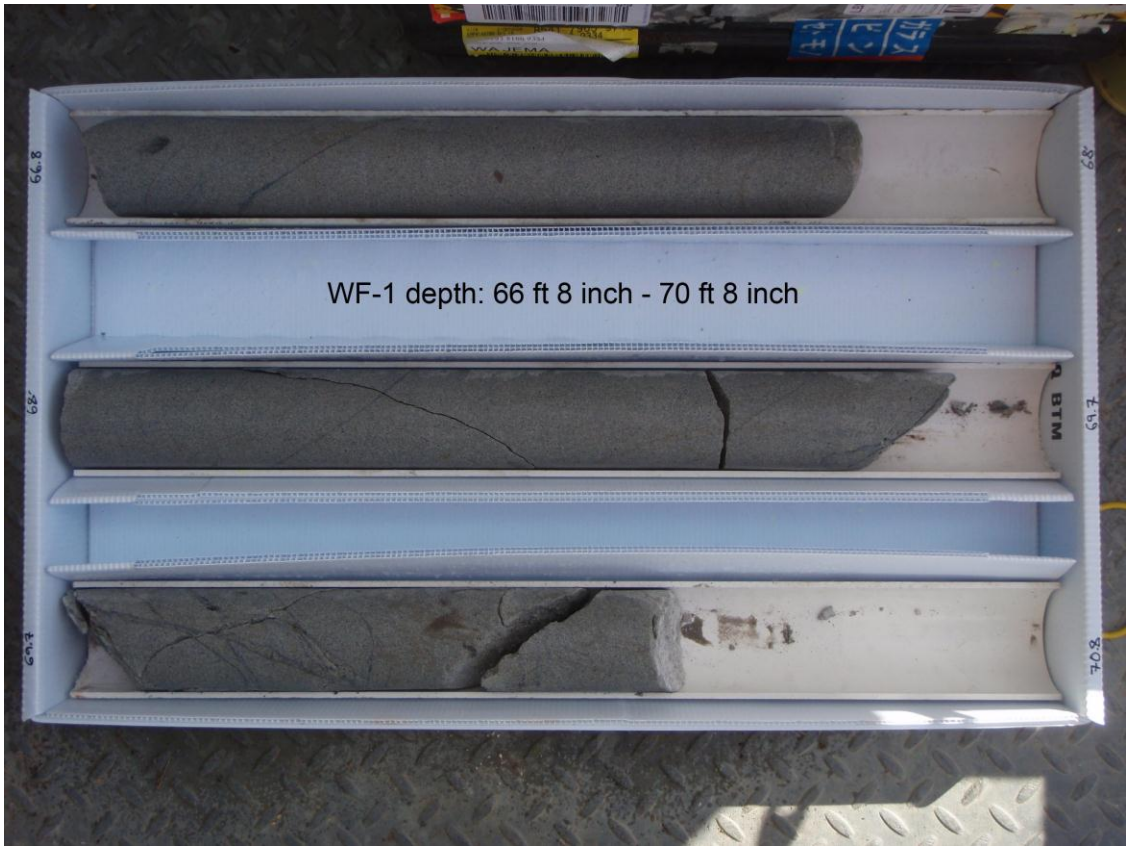

Appendix 2 - Core Images _WF1

Appendix 2 - Core Images _WF1

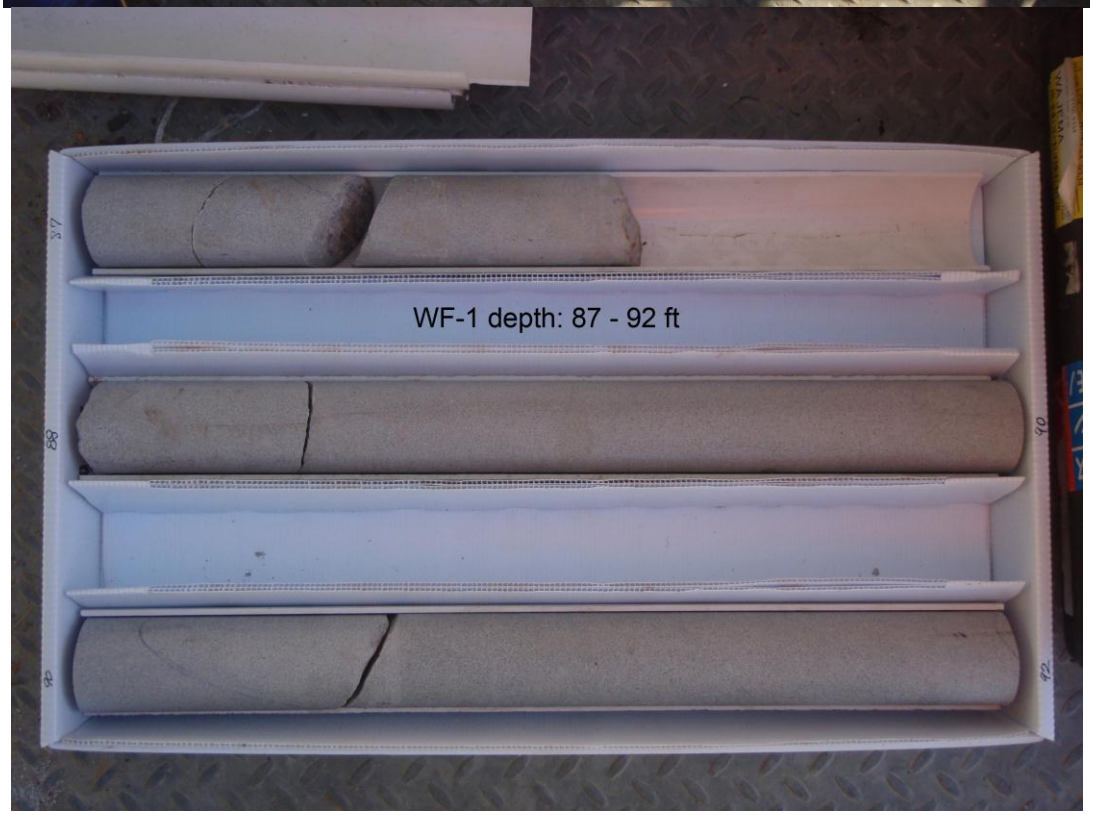

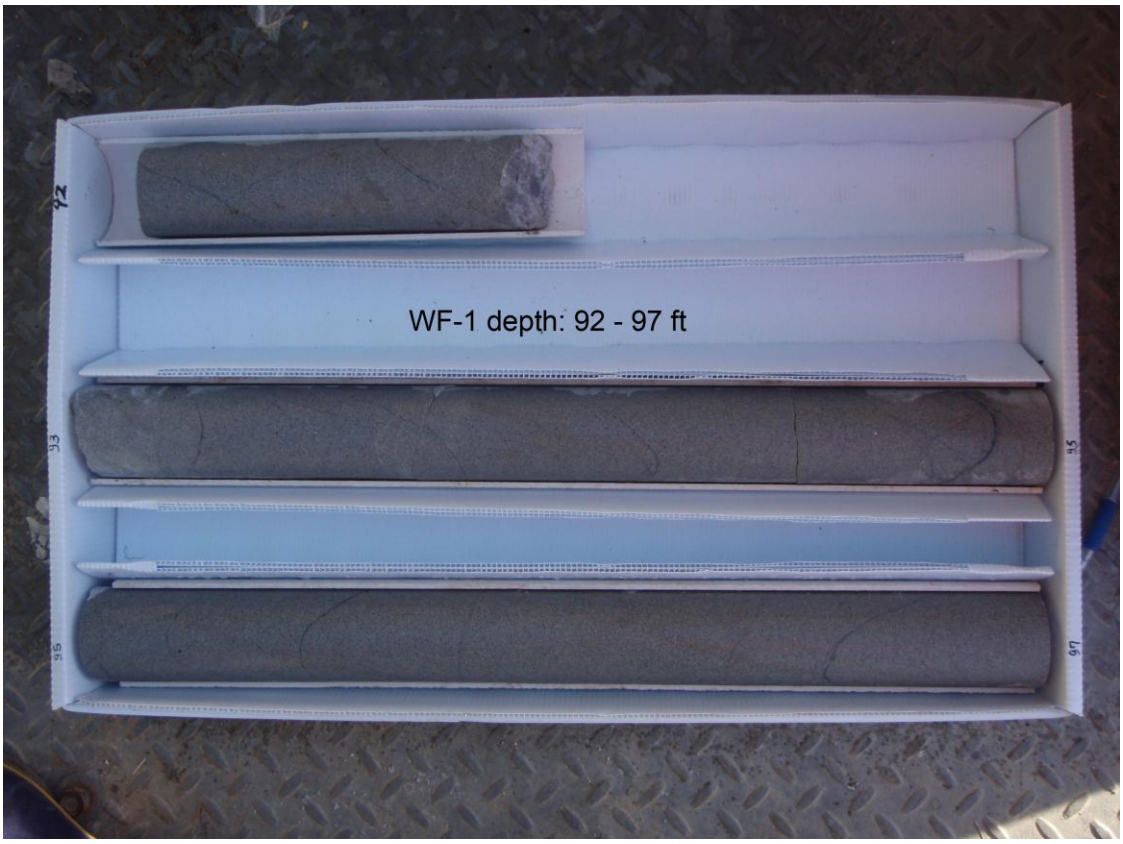
WF-1 depth: 92 - 97 ft
92
93
95
95
97

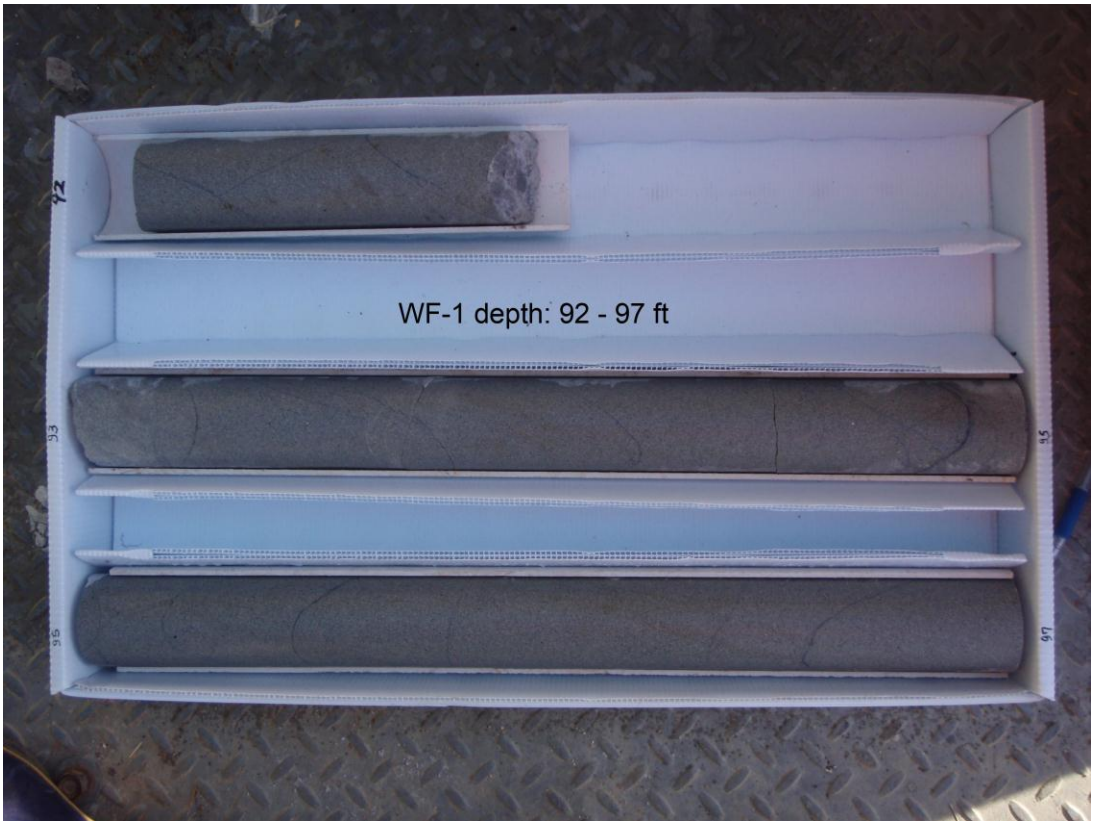
WF-1 depth: 92 - 97 ft
92
93
95
95
97

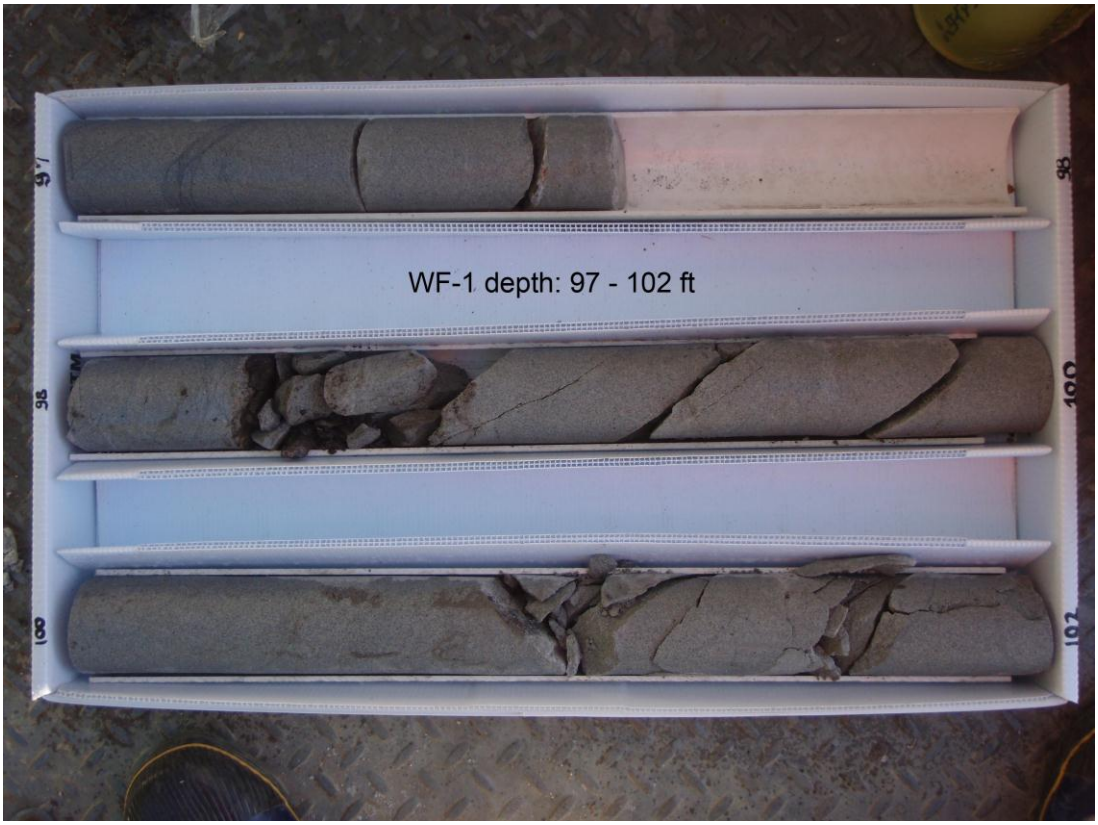
WF-1 depth: 97 - 102 ft

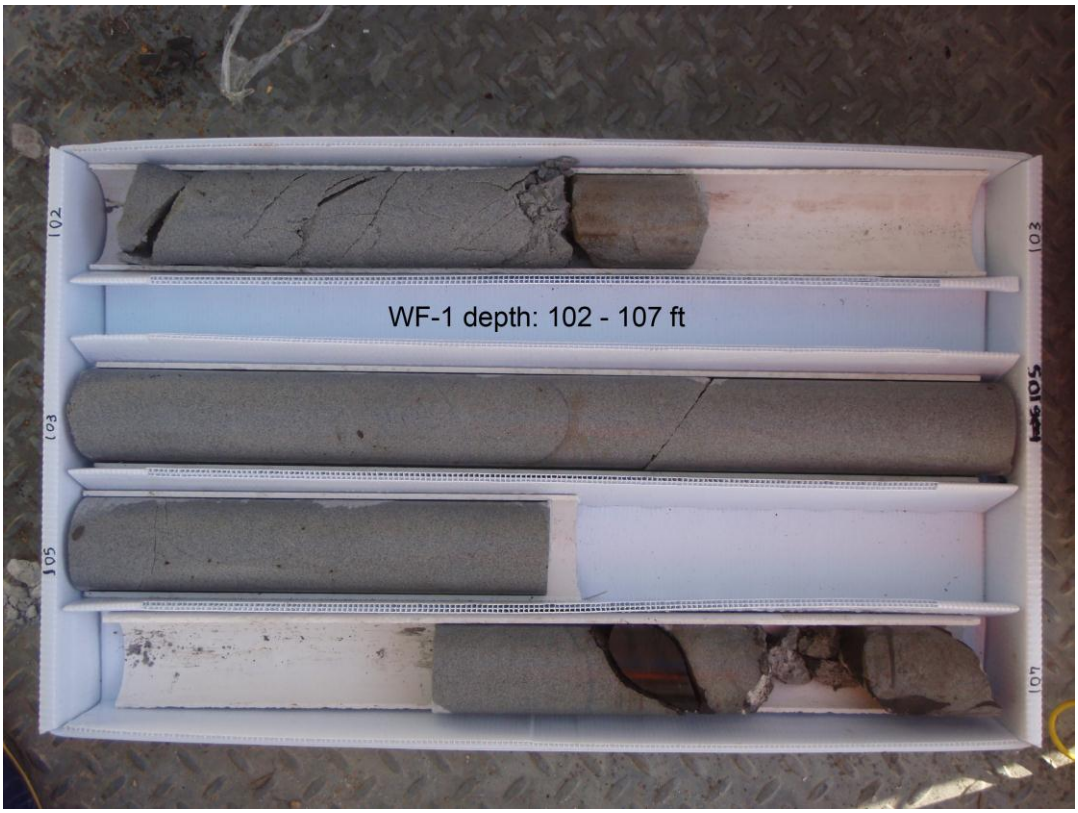
WF-1 depth: 102 - 107 ft

107
WF-1 depth: 107 - 112 ft
112

112
WF-1 depth: 112 - 117 ft
Q BTM
117

Appendix 2 - Core Images _WF1

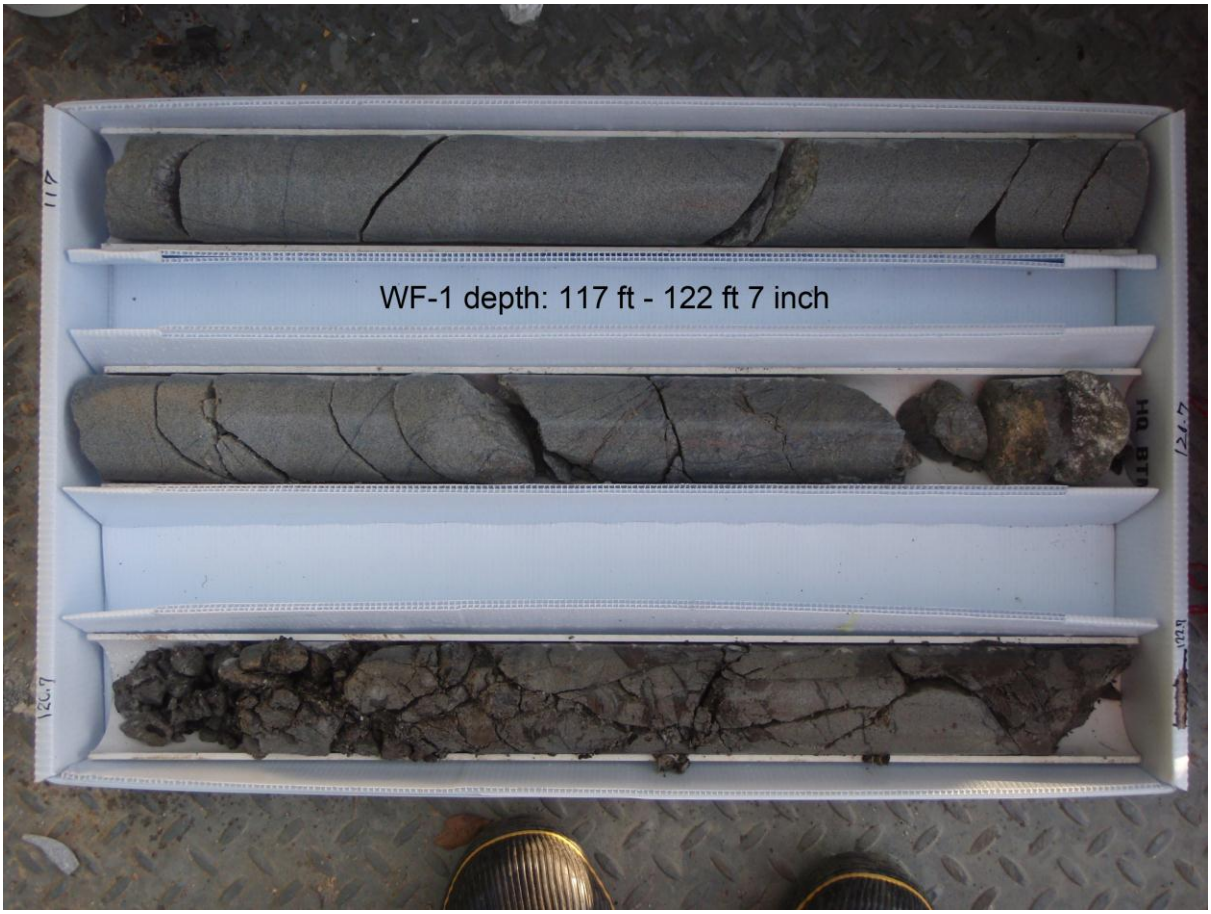

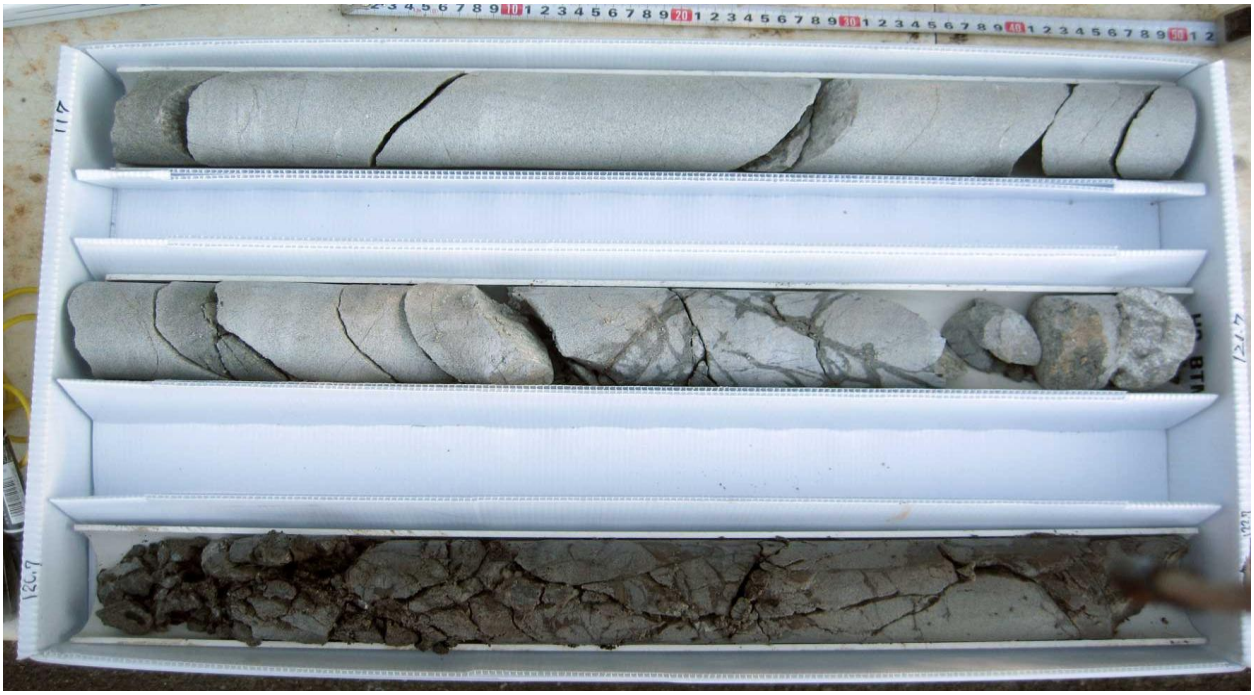

Appendix 2 - Core Images _WF1

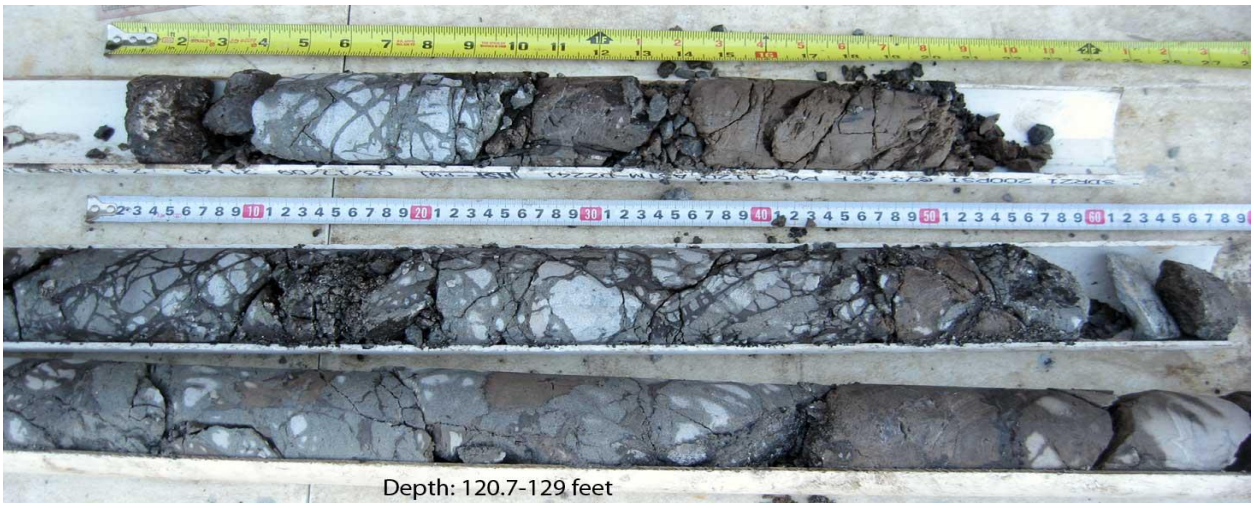

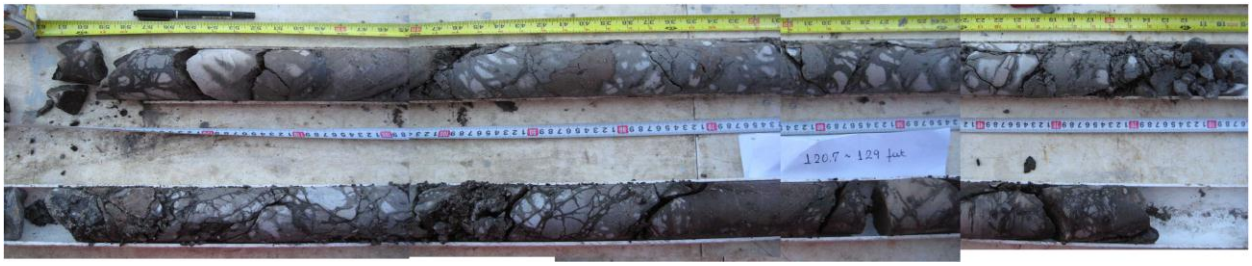

Appendix 2 - Core Images _WF1

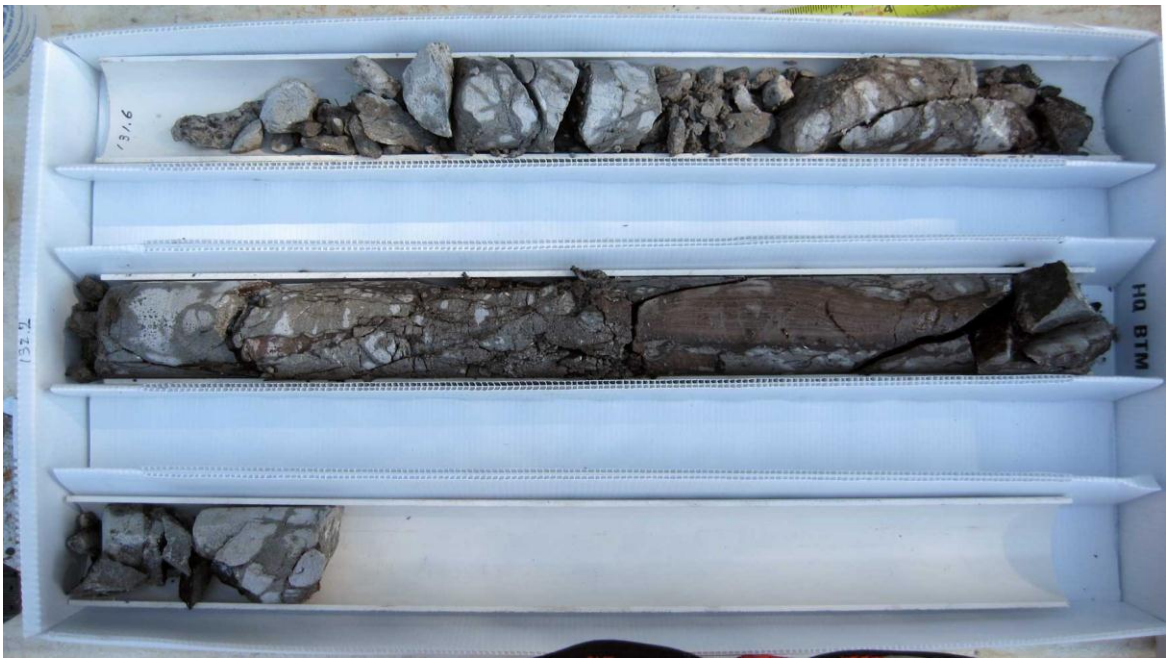

Appendix 2 - Core Images _WF1

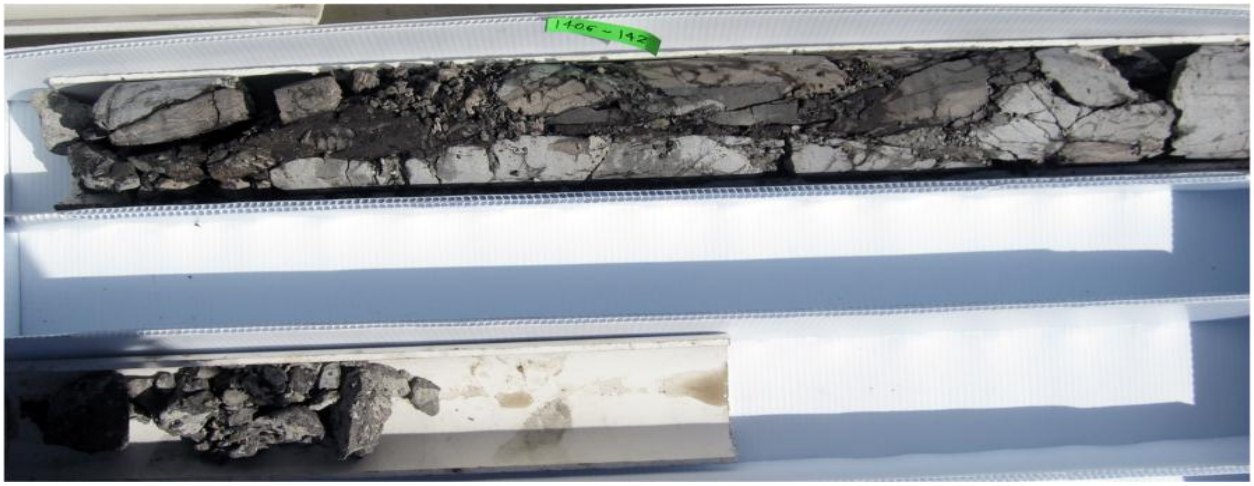

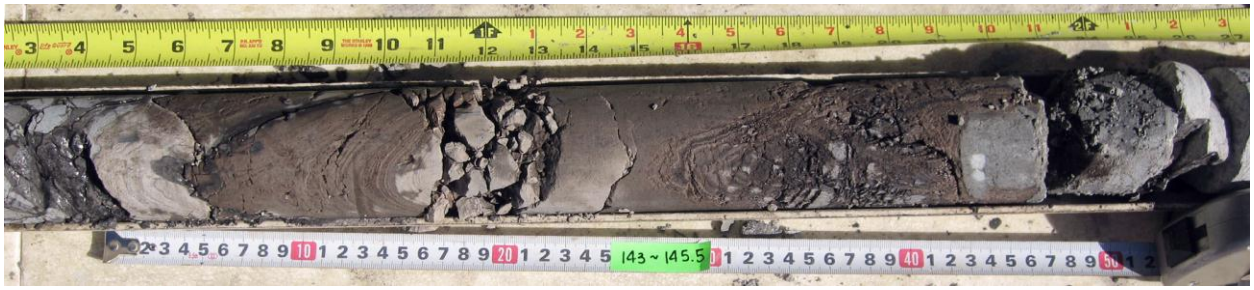

Appendix 2 - Core Images _WF1

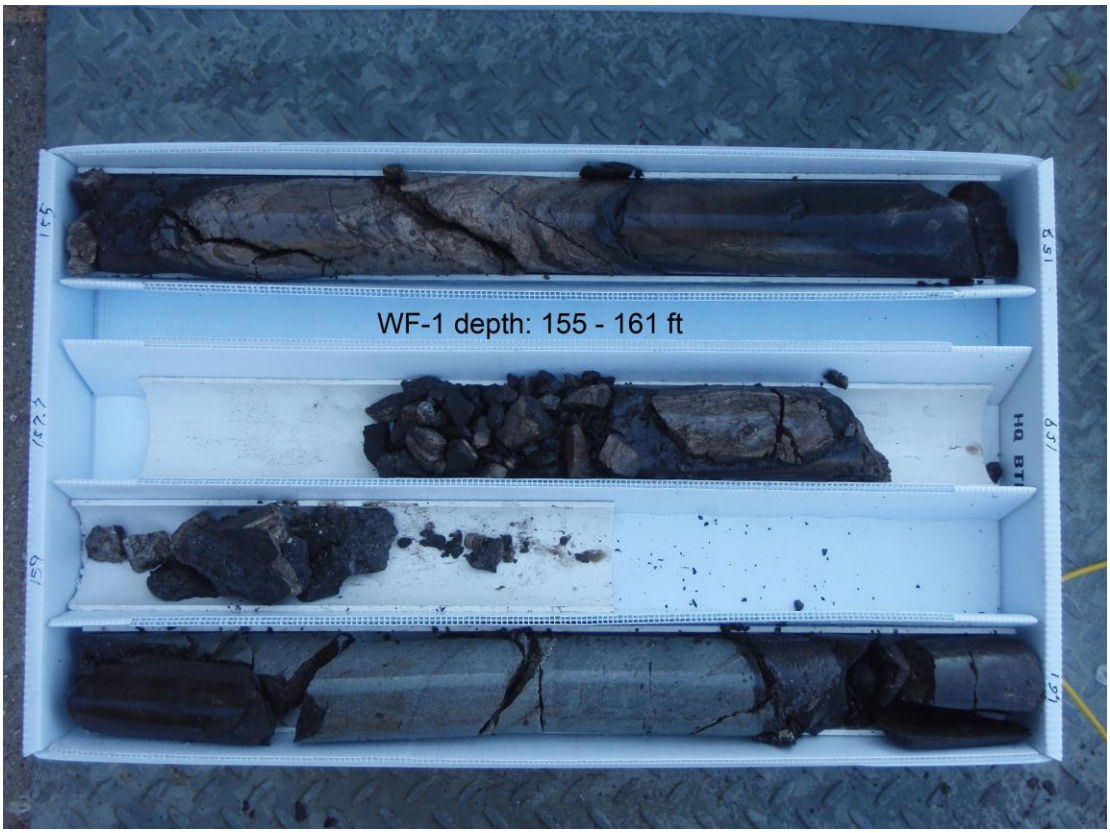
WF-1 depth: 155 - 161 ft

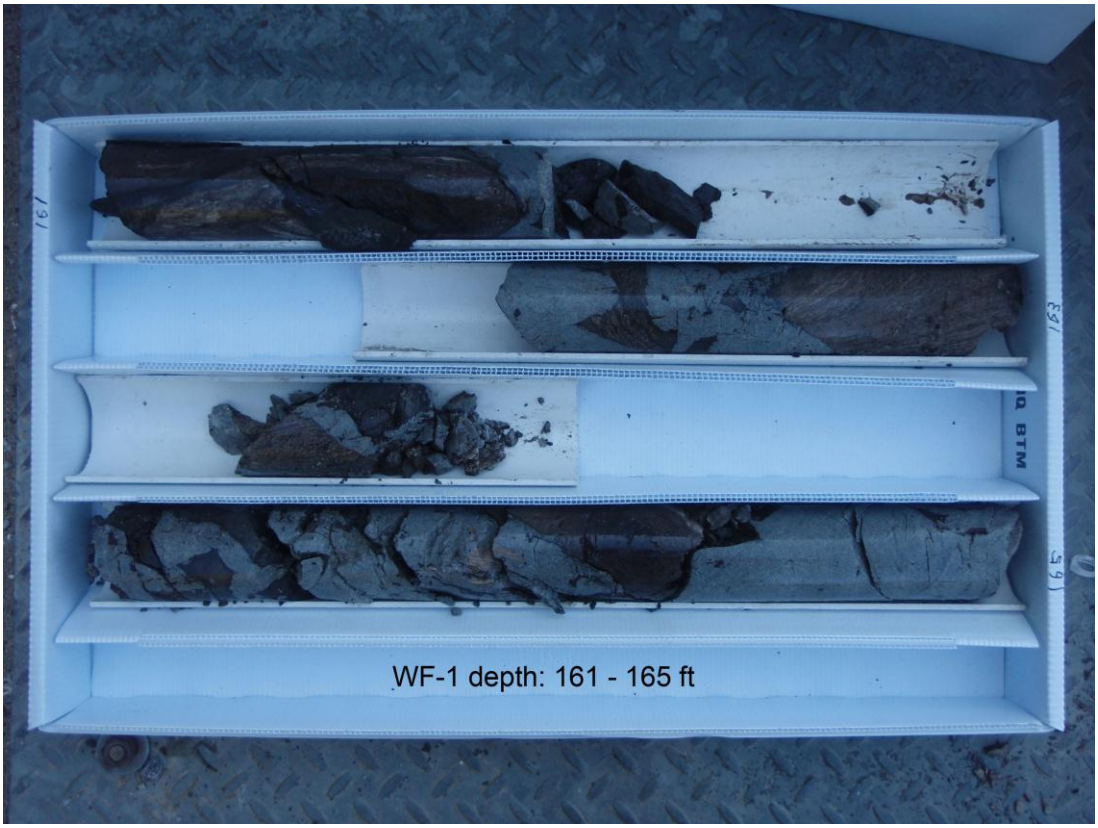
WF-1 depth: 161 - 165 ft

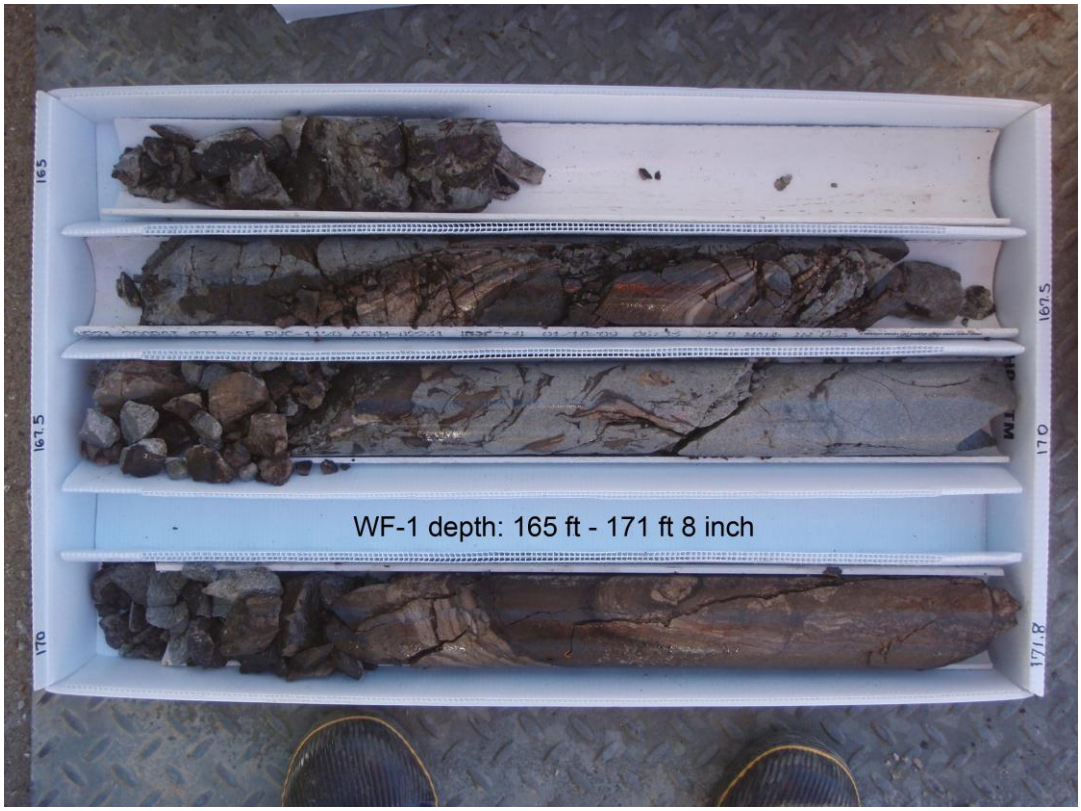
165
167.5
170
WF-1 depth: 165 ft - 171 ft 8 inch
167.5
170
171.8

176.9
178.3
180
WF-1 depth: 176 ft 9 inch - 182 ft
178.3
180
182

WF-1
depth: 187-192 feet

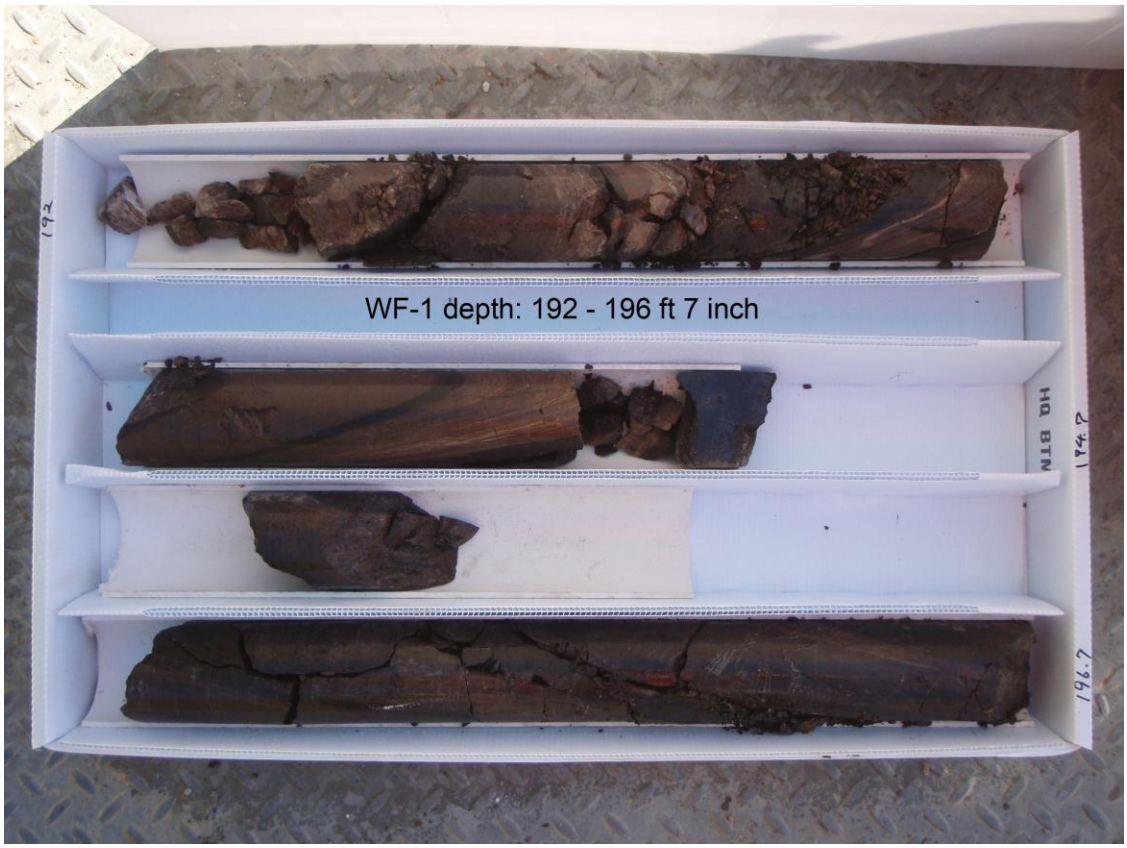
192
WF-1 depth: 192 - 196 ft 7 inch
HQ BTM
194.7
196.7

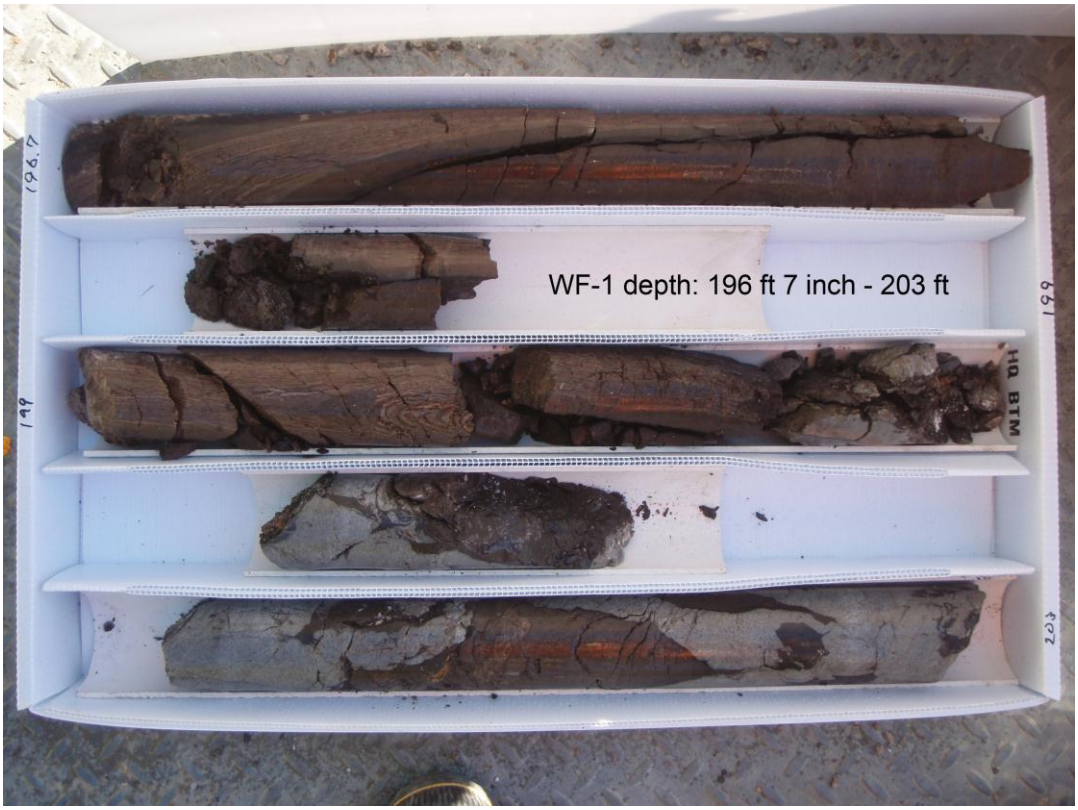
198.7
199
WF-1 depth: 196 ft 7 inch - 203 ft
HQ BTM
199
203

Appendix 2 - Core Images _WF1

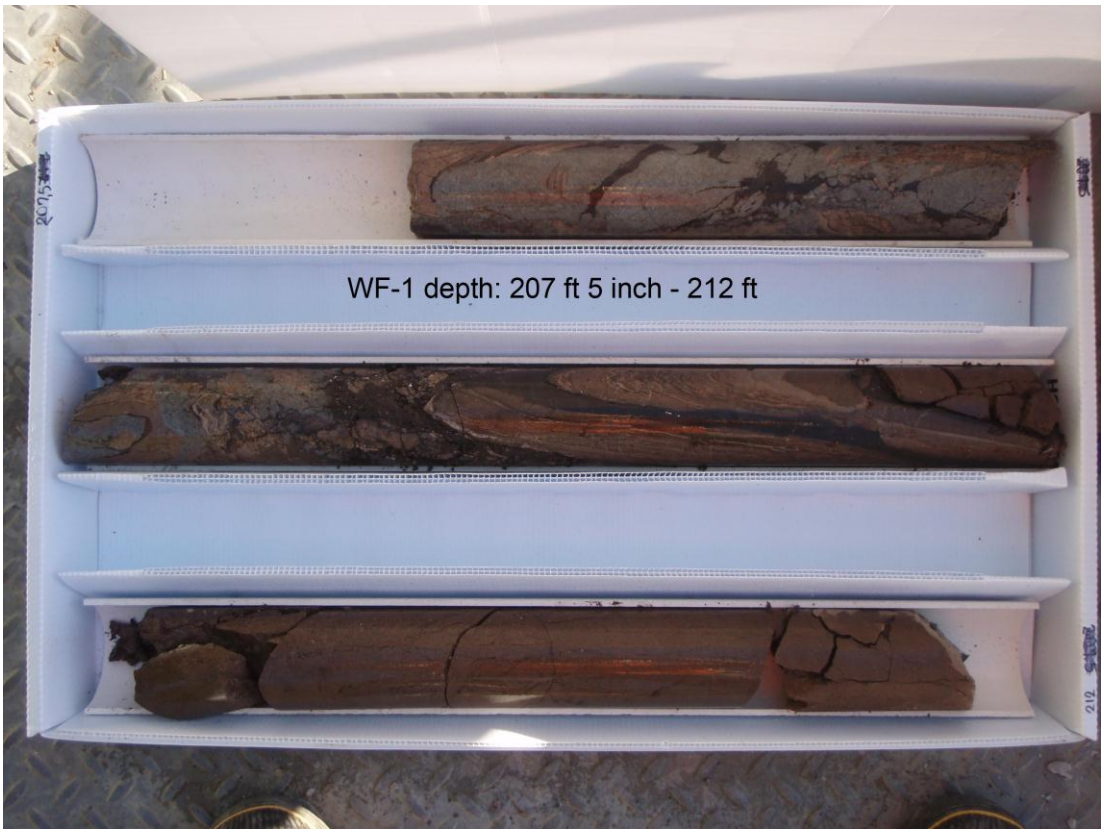

Appendix 2 - Core Images _WF1

Appendix 2 - Core Images _WF1

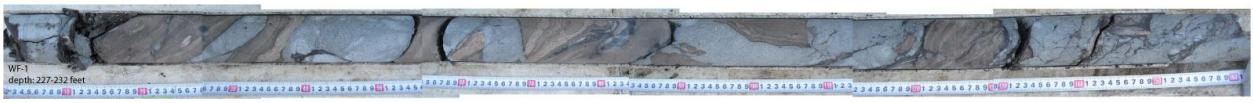

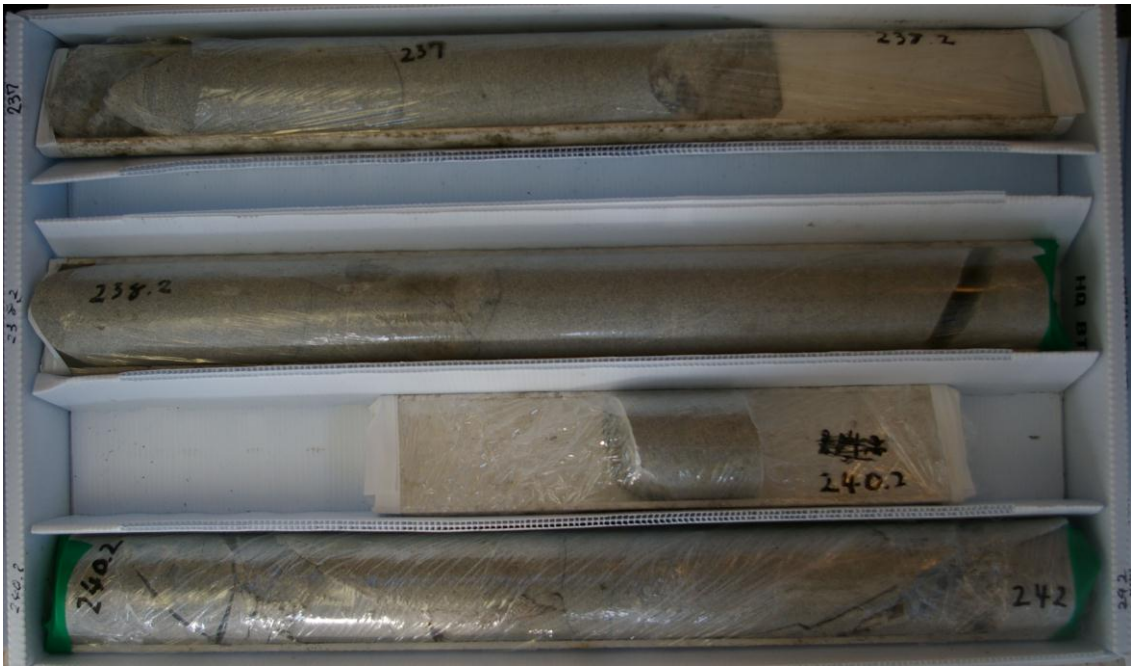
237
237.2
238.2
240.2
240.2
242

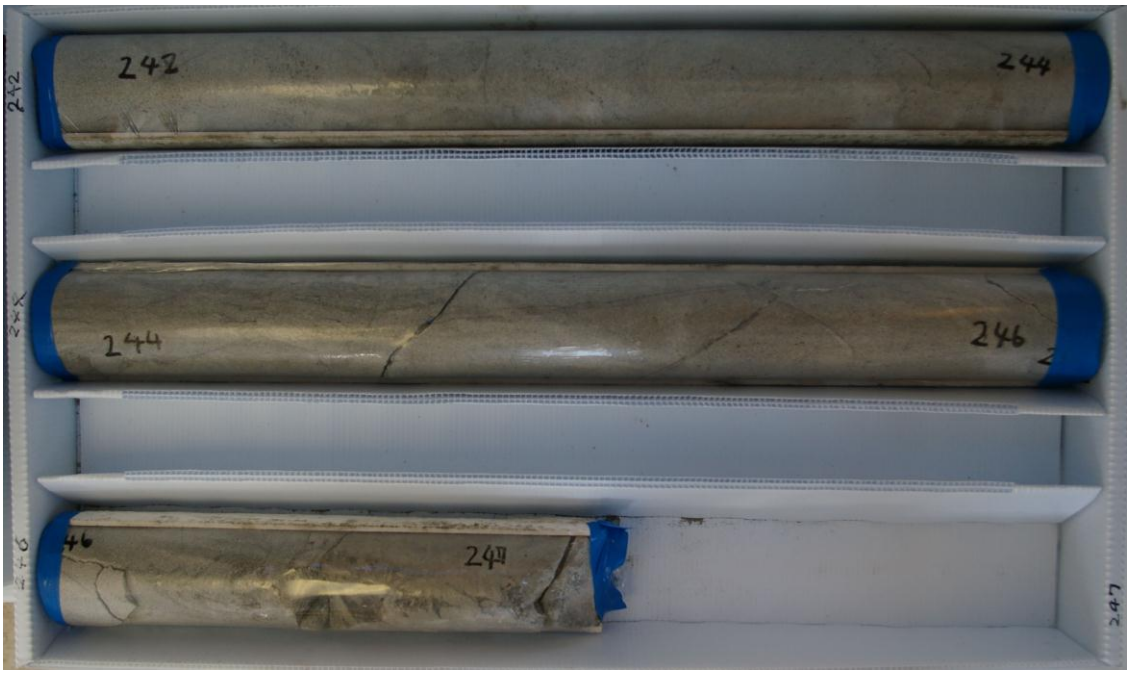
242
244
244
246
247

WF1- 247-252 feet

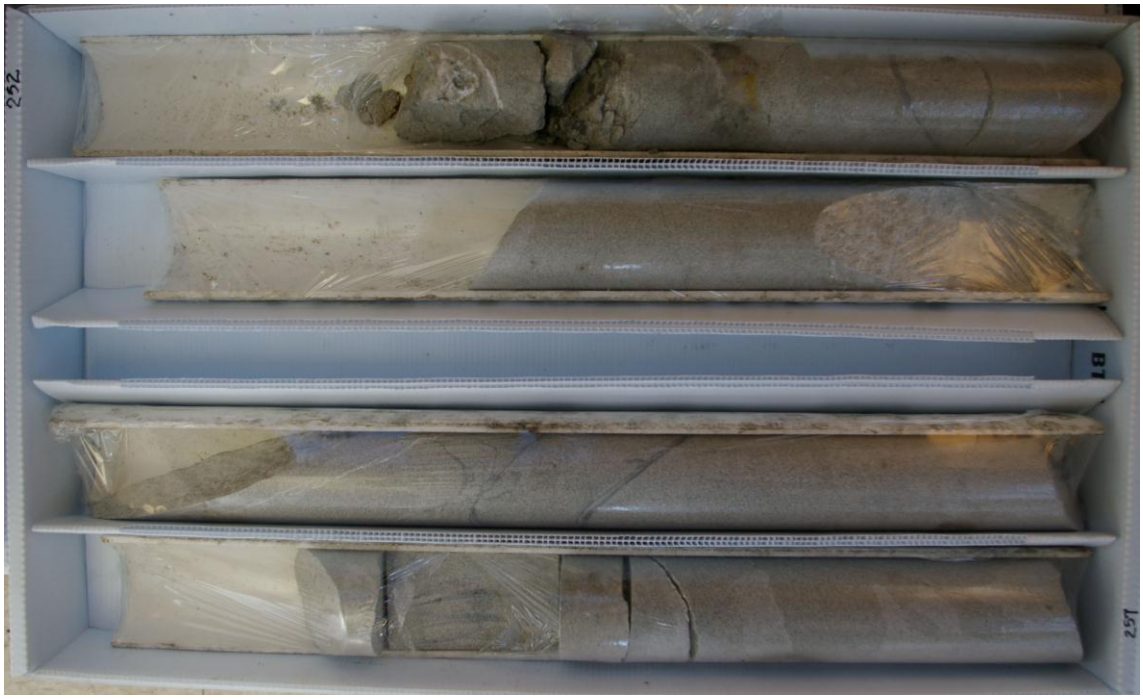
252
257

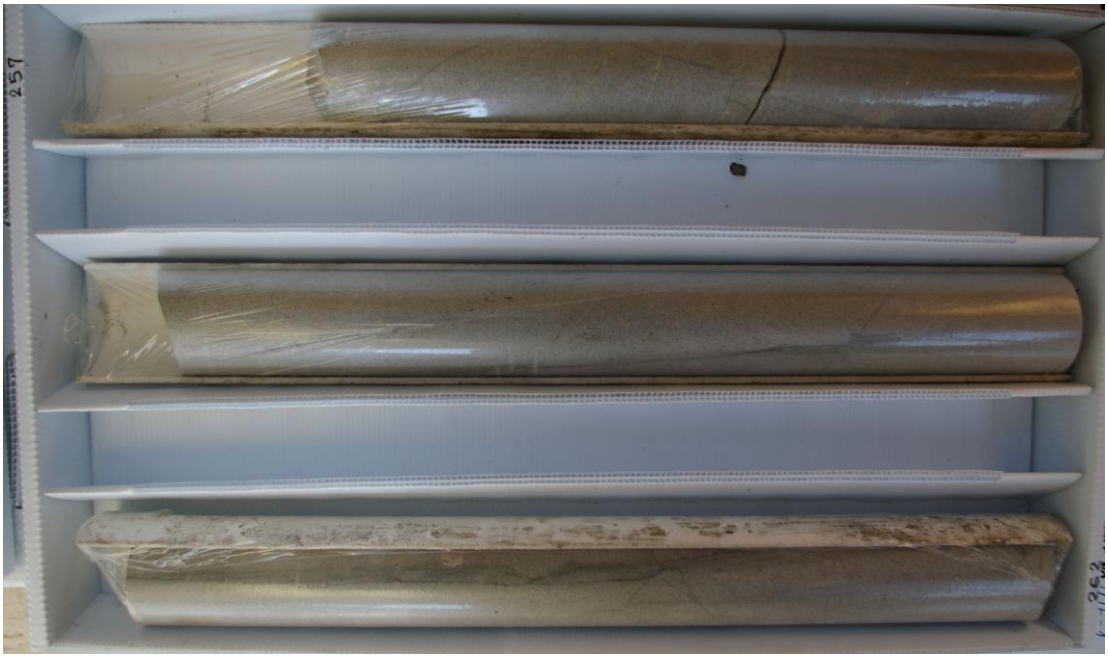
257

Appendix 2 - Core Images _WF1

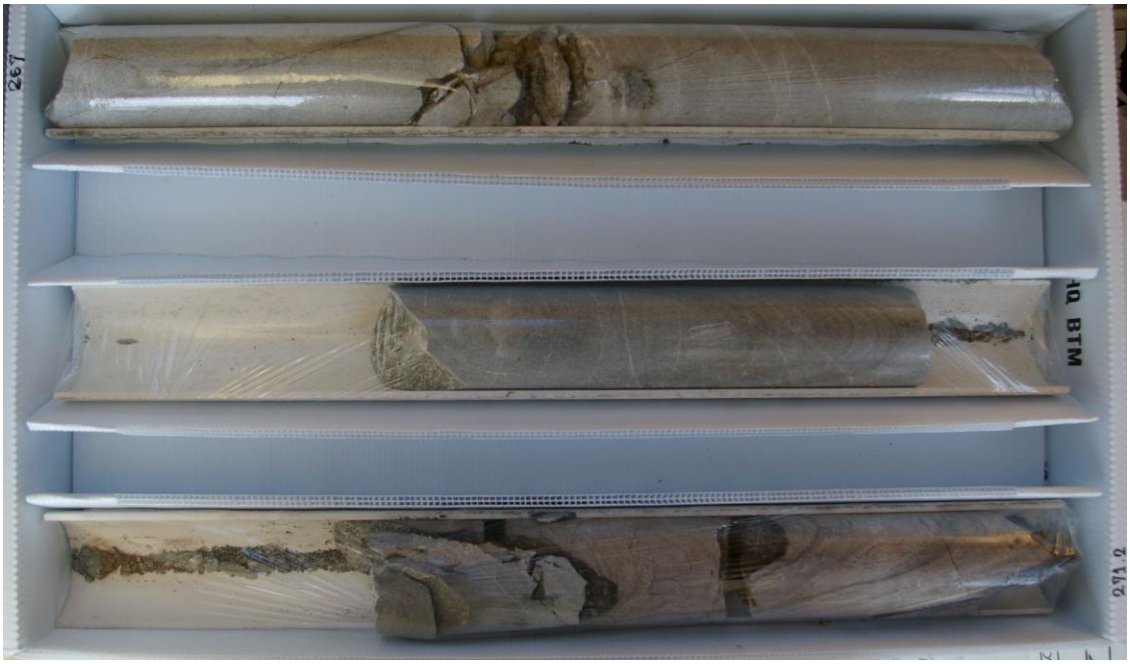

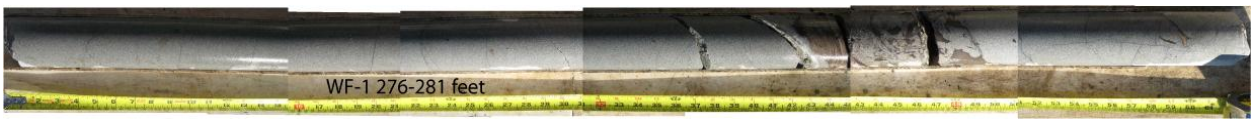

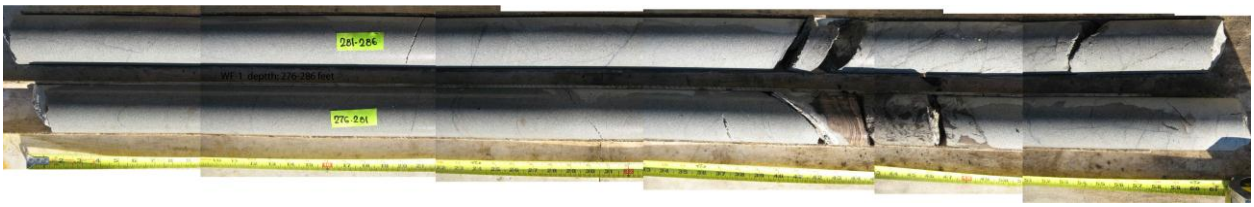

Appendix 2 - Core Images _WF1

Missing core image from 294.5-297.8ft

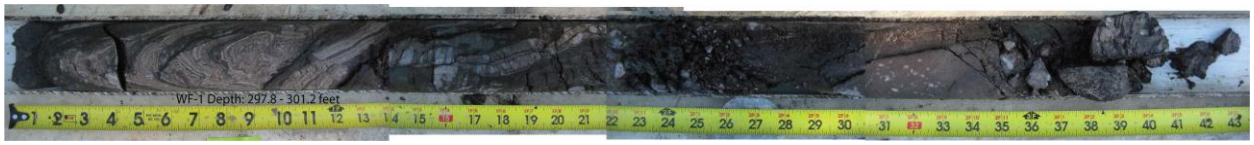

Appendix 2 - Core Images _WF1

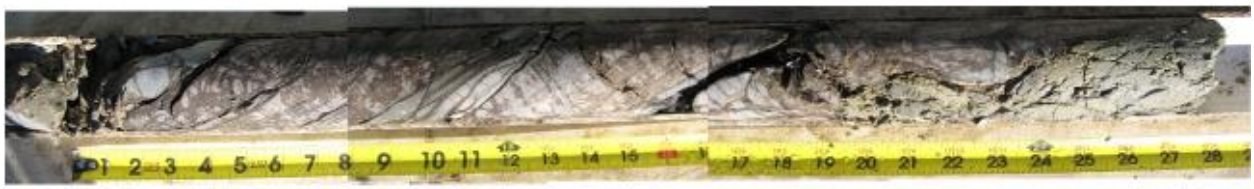

WF-1
Fault Gouge
320.2-322.4 feet

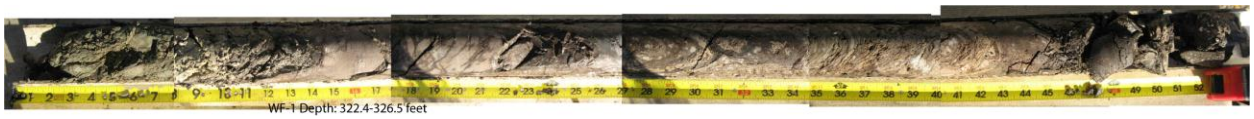

Appendix 2 - Core Images _WF1

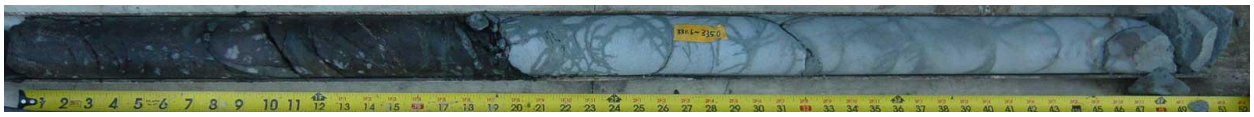

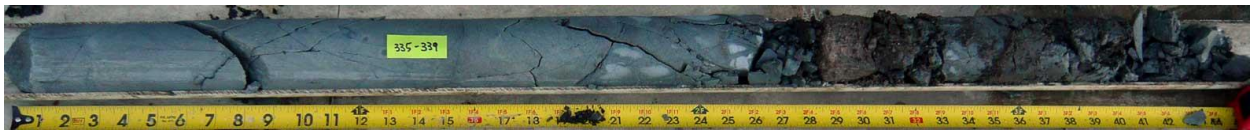

Missing core image: 343-346.2ft

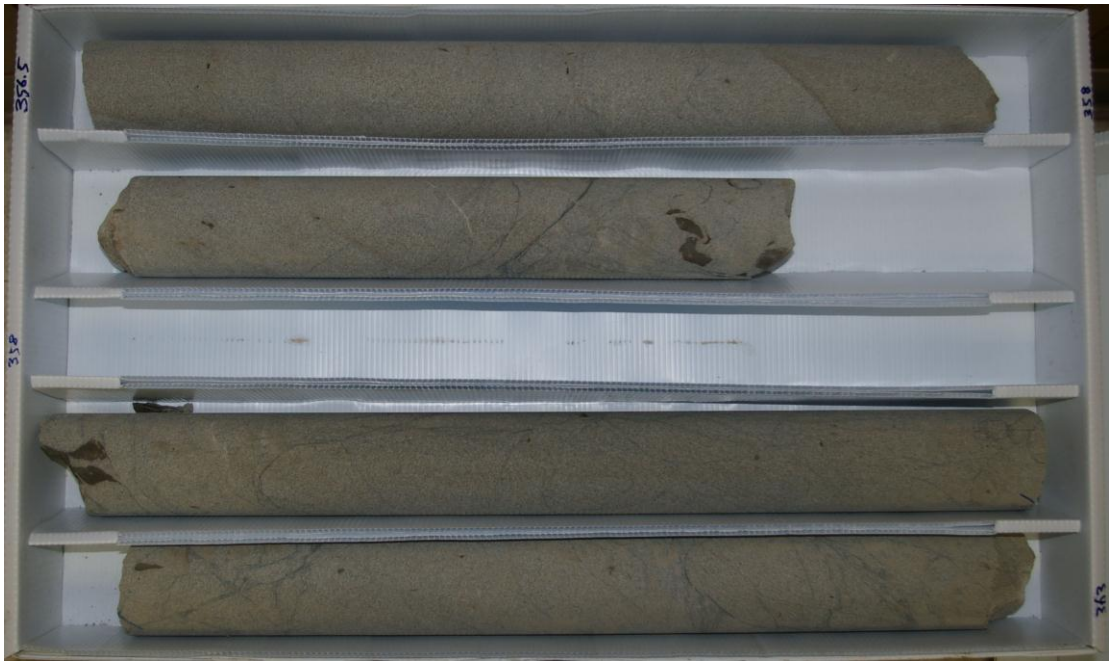

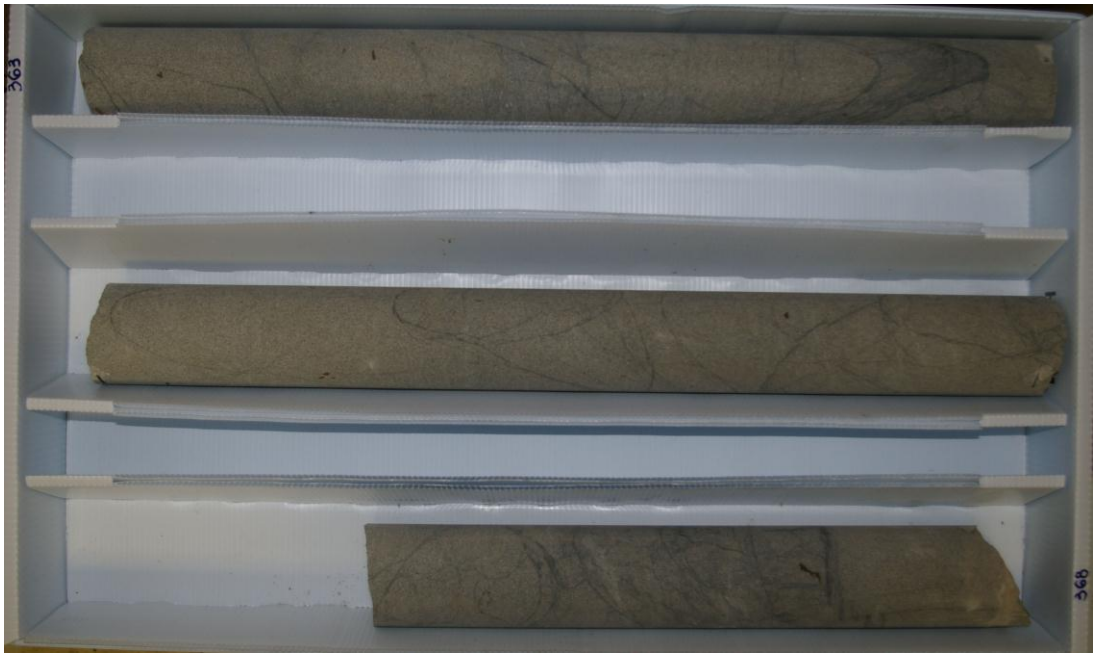
363
366

368
HO 81
373

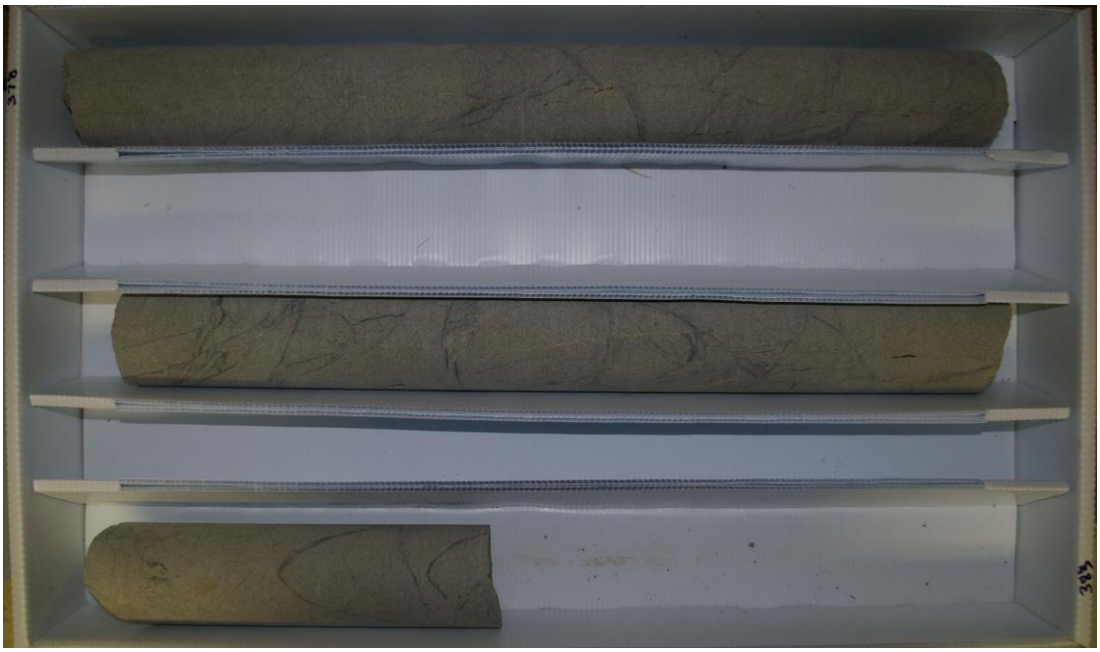

WF-1 388-393ft

Missing core image: 410.2-415ft

Missing core image: 423.4-428ft

Appendix 2 - Core Images _WF1

Appendix 2 - Core Images _WF1

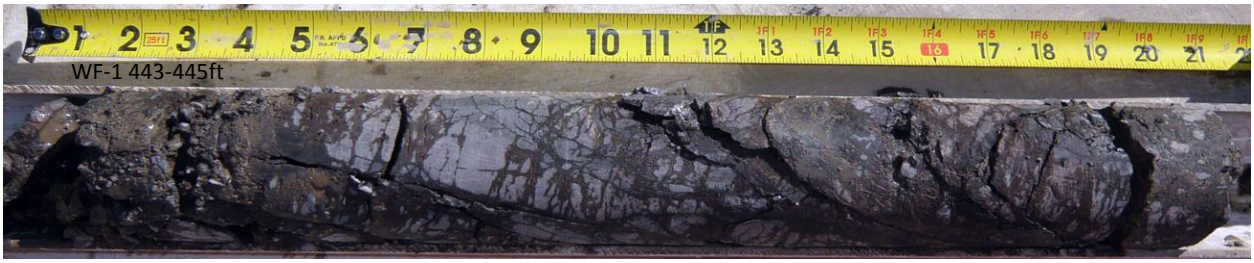

Appendix 2 - Core Images _WF1

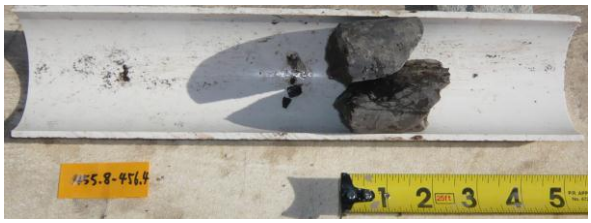

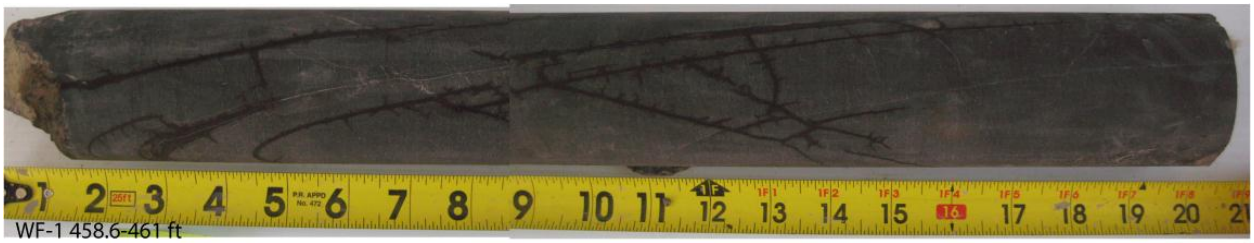

Appendix 2 - Core Images _WF1

Appendix 2 - Core Images _WF1

Missing core images: 474.6-487.6ft

WF-1 511-516ft

Missing core image: 525-530ft

Appendix 3 - Core Images _WF2

WF-2 (25-29ft)

WF-2 (29-32.2ft)

WF2-32.2-33ft

WF2_33-37ft

WF2_37-40.2ft

WF2_40.2-44ft

WF2_44-48ft

Appendix 3 - Core Images _WF2

WF2_48-50ft

WF2_50-53ft

WF2_ 53-55.3ft

WF2_55.3-58ft

WF2_58.3-61.5ft

WF2_63-67ft

Appendix 3 - Core Images _WF2

WF2_70-72.3ft

WF2_72.3-74ft

Appendix 3 - Core Images _WF2

WF2_74.1-76.7ft

WF2_76.7-79.2ft

WF2_79.2-81ft

WF2_82.2-84ft

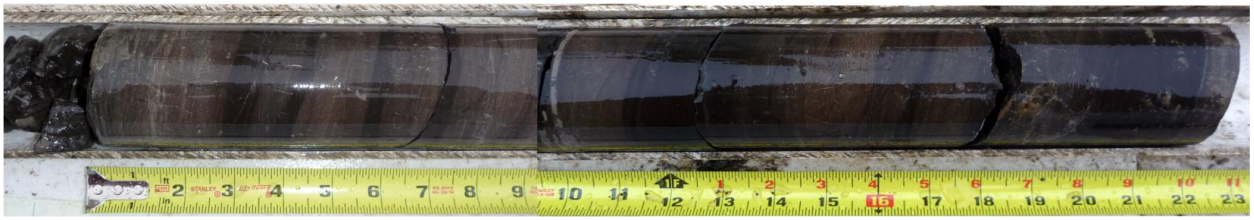

WF2_84-86ft

Appendix 3 - Core Images _WF2

WF2_86-90ft

Wf2_90-92ft

WF2_92-94ft

WF2_94-97ft

WF2_97-100ft

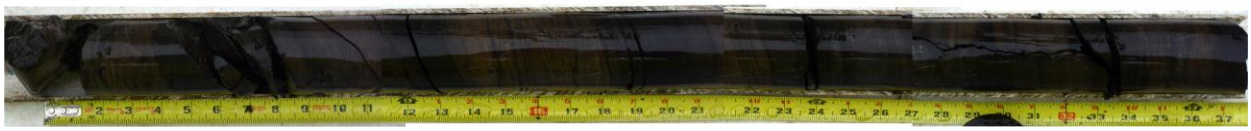

WF2_100-102ft

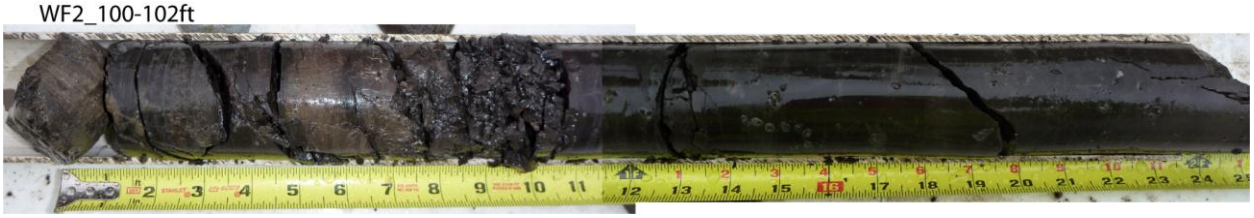

WF2_101.5-106ft

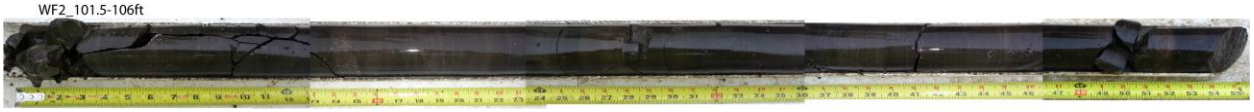

WF2_106.5-108ft

WF2_112-114ft

WF2_114-117ft

WF2_117-121.4ft

WF2_121.4-122.6ft

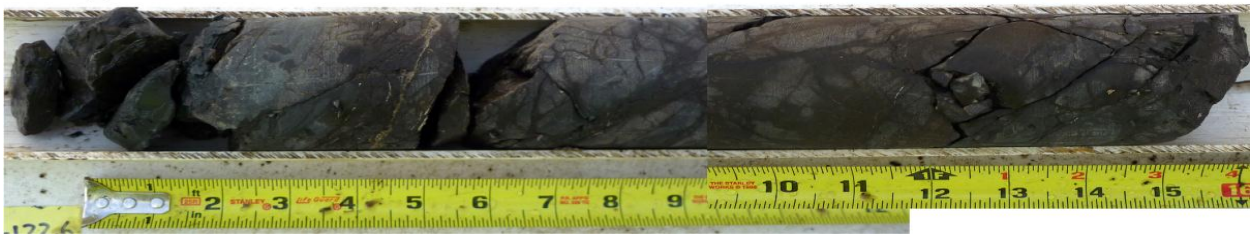

WF2_125-127ft

WF2_127-132ft

WF2_132-134.2ft

WF2_134.2-137ft

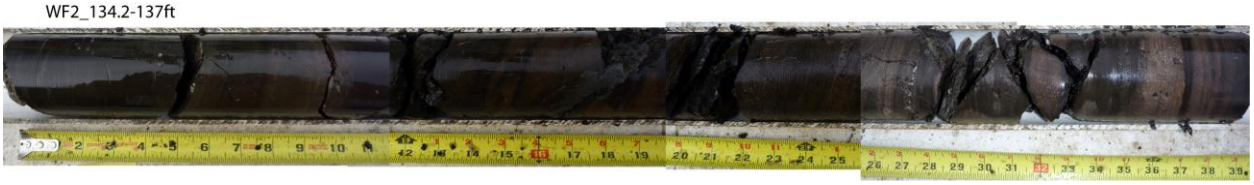

WF2_137-139ft

WF2_139-141.1ft

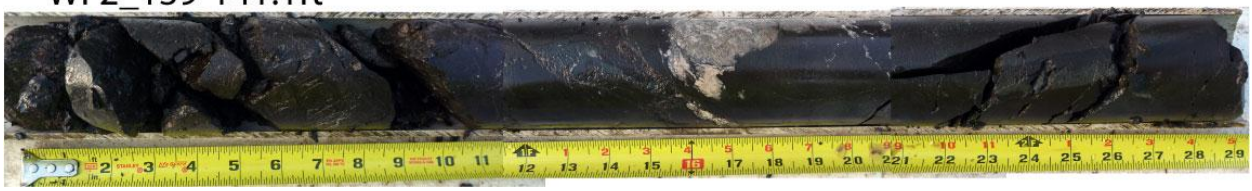

WF2_141.4-144.1ft

WF2_144.1-146.3ft

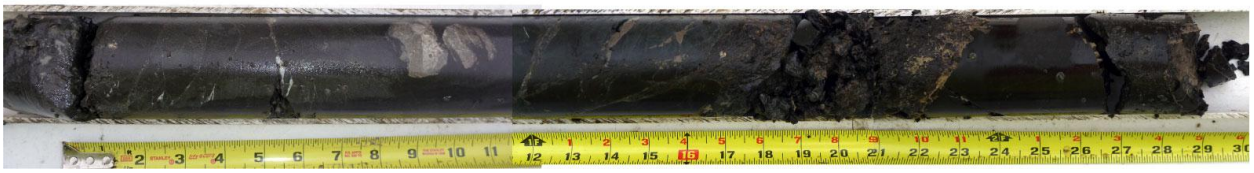

WF2_170.7-173ft

WF2_173.3-177ft

WF2_177-178.5ft

WF2_178.5-182ft

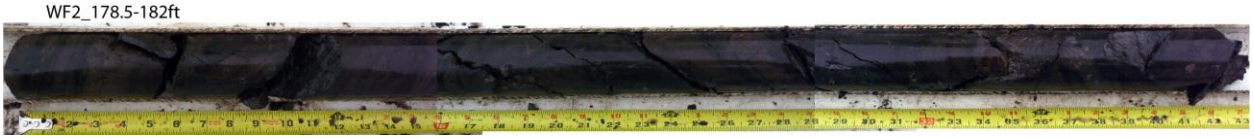

WF2_182-187ft

WF2_187-189ft

WF2_189-192ft

WF2_192-193.5ft

WF2_193.5-195ft

WF2_195-197ft

WF2_197-200.6ft

WF2__ 200.6-201ft

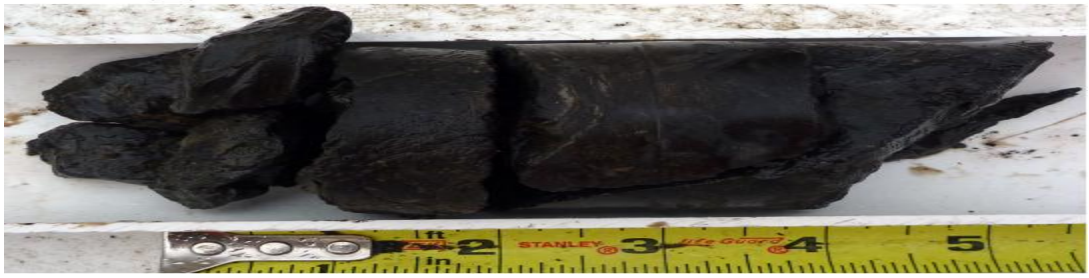

WF2_201-204ft

WF2_204-205ft

WF2_205-206ft

WF2_206-207ft

WF2_207-208.5ft

WF2_208.5-209.5ft

WF2_209.5-210.5ft

WF2_210.2-211.5ft

WF2_211.5-212.5ft

WF2_214-216.5ft

WF2_216.5-217.5ft

WF2_219.5-221.2ft

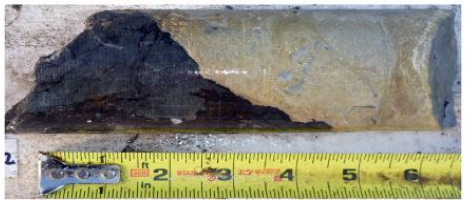

WF2_221.2-224.2ft

WF2_224-227ft

WF2_227-229.4ft

WF2_229.4-232ft

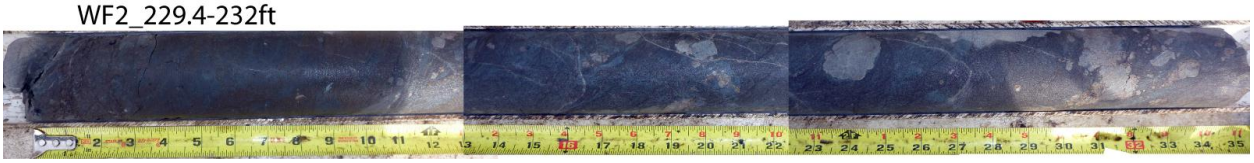

WF2_232-237ft

WF2_237-240.6ft

WF2_240.6-242.7ft

WF2_242.7-246.5ft

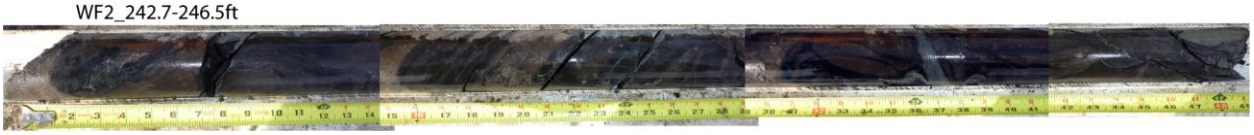

WF2_246.5-249.1ft

WF2_249.1-250ft

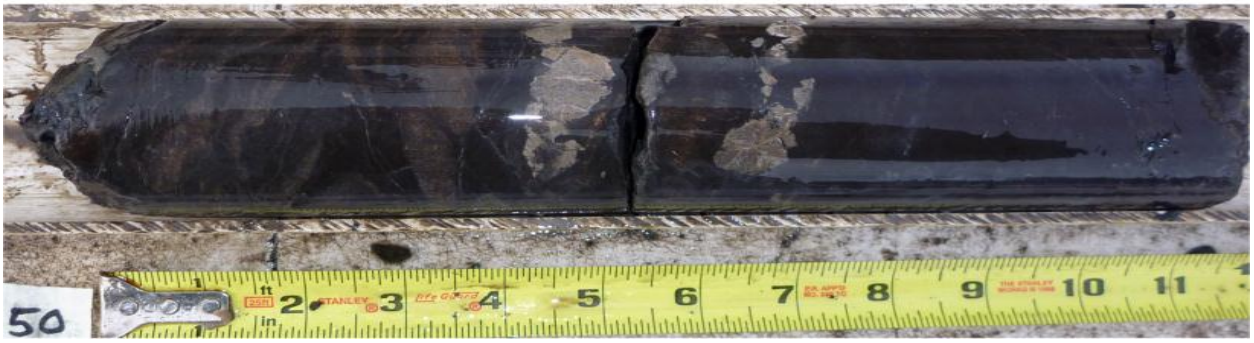

WF2_250-252ft

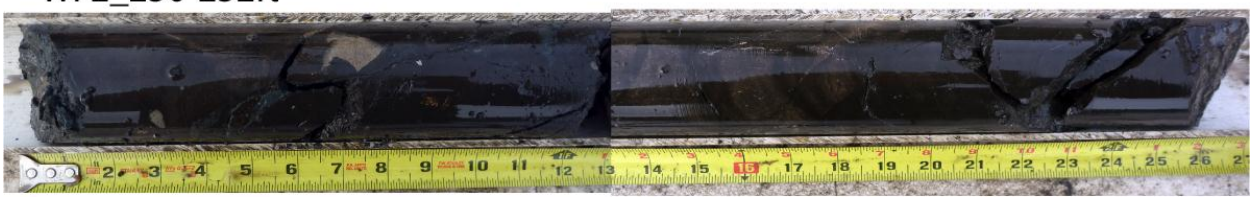

WF2_252-254.9ft

WF2_254.9-256.6ft

WF2_256.6-258ft

WF2_258-260ft

WF2_260.6-262ft

WF2_262.1-267ft

WF2_267-272ft

WF2_272-276.2ft

WF2_276.2-279.8ft

WF2_279.8-282ft

WF2_282-287ft

WF2_287-292ft

WF2_292-297ft

WF2_297-302ft

WF2_302-306ft

WF2_306-309ft

WF2_309-312ft

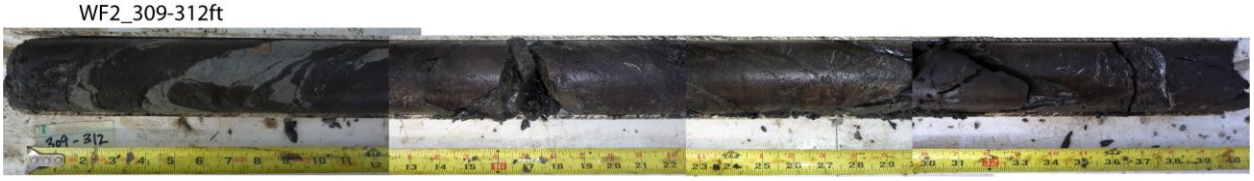

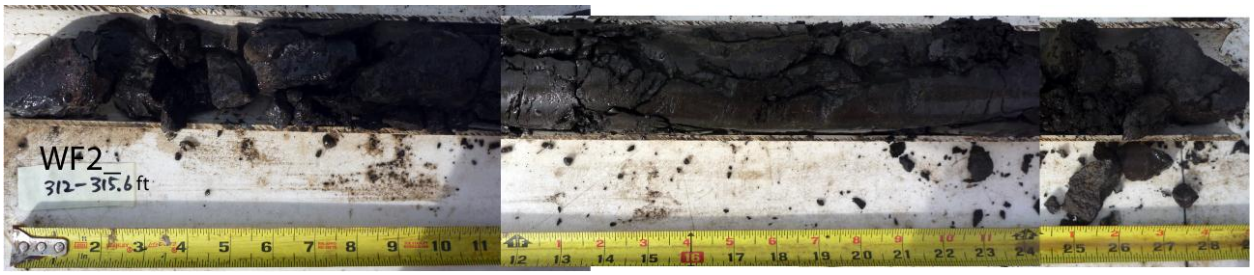

WF2_315-318.3ft

WF2_318-322ft

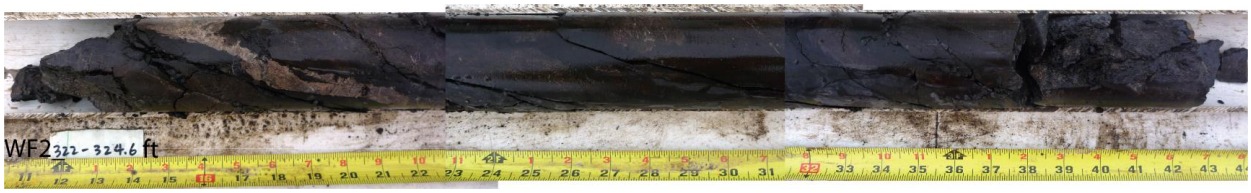

WF2_324.6-327ft

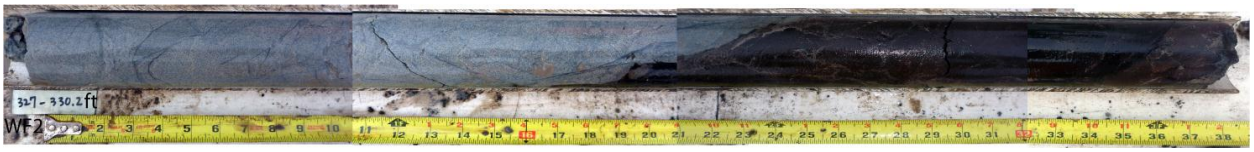

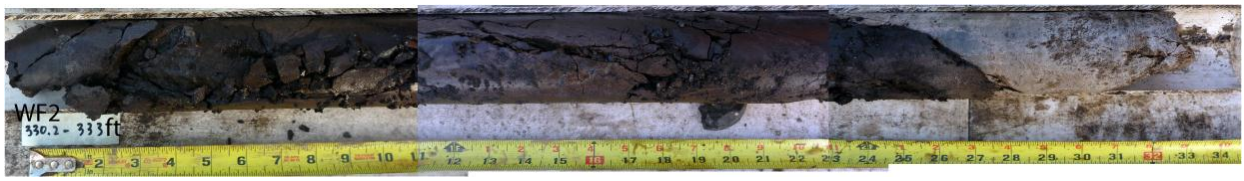

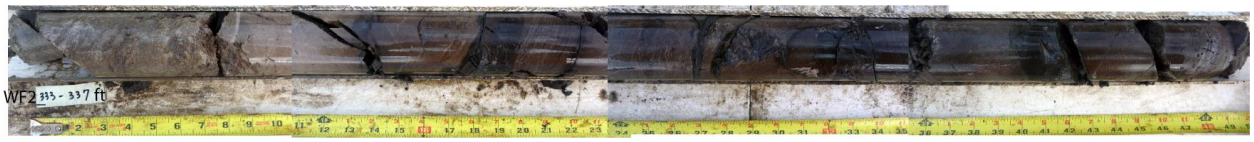

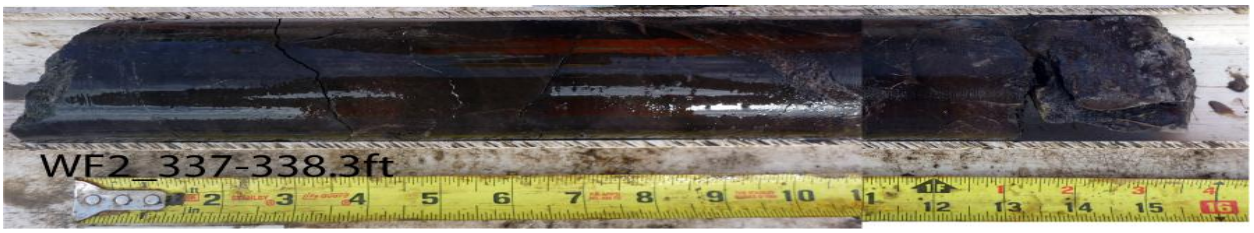

WF2_338.3-342ft

WF2_342-345.8ft

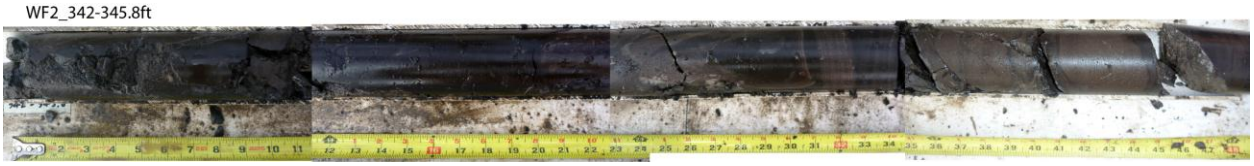

WF2_345.8-351ft

WF2_351-355ft

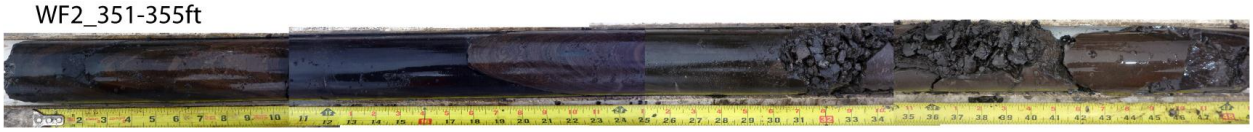

WF2_356.6-359ft

WF2_360.5-362ft

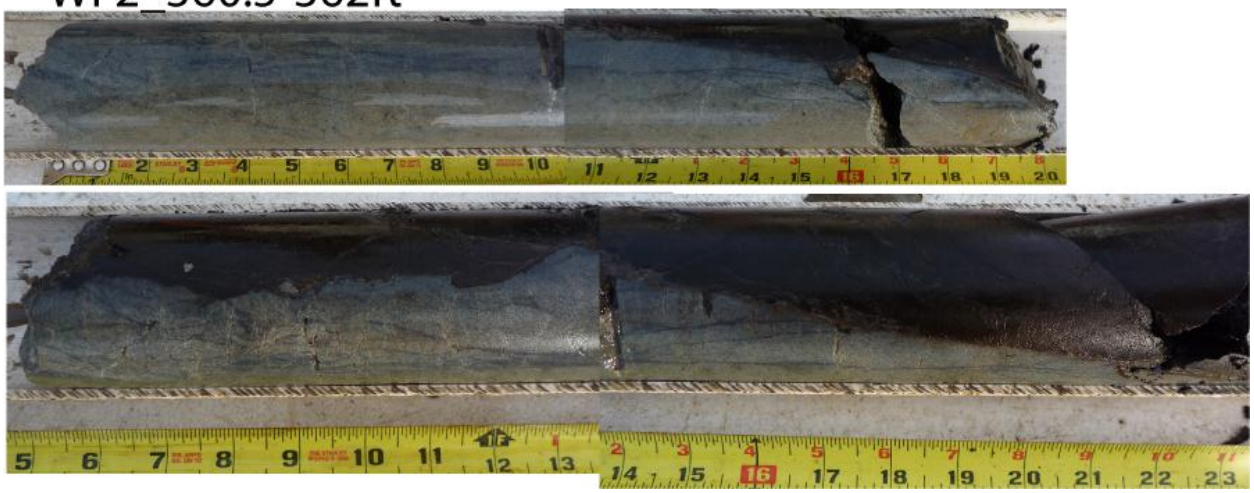

WF2_362-366ft

WF2_367-370ft

WF2_370-372ft

WF2_372-374.6ft

WF2_374.6-376.2ft

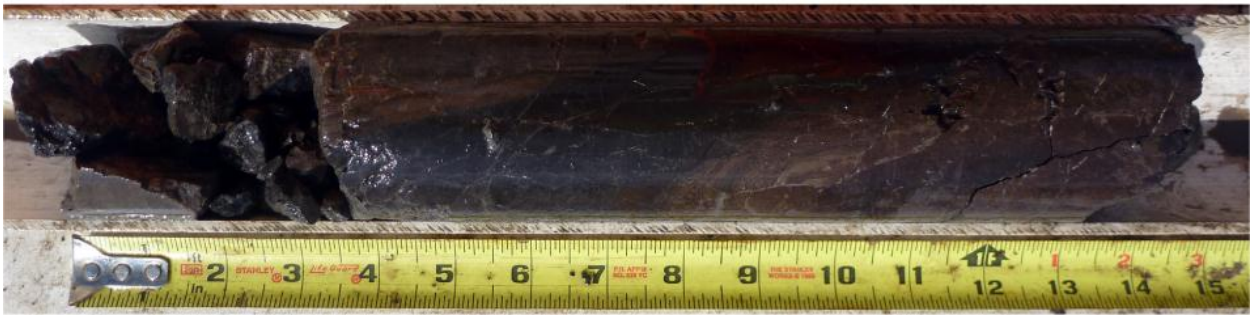

WF2_376.2-379.6ft

WF2_379.6-382ft

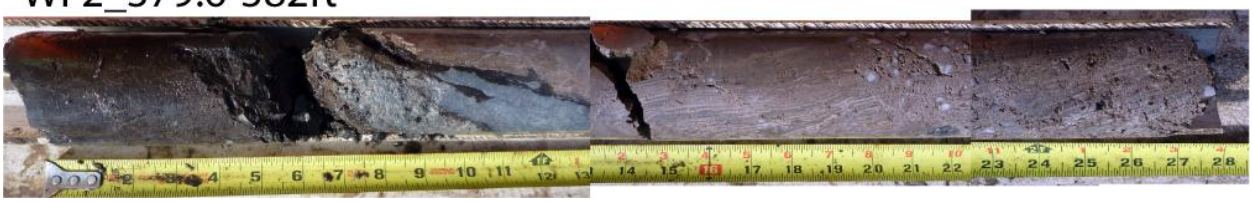

WF2_382-387ft

WF2_387-392ft

WF2_392-395.3ft

WF2_395.3-400ft

WF2_400-403.2ft

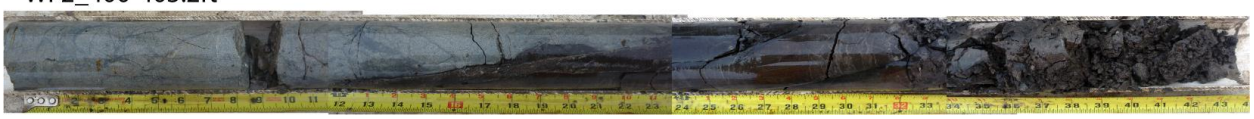

WF2_403.2-407ft

WF2_407-408ft

WF2_408-411.7ft

WF2_411.7-414.6ft

WF2_414.6-417ft

WF2_417-422ft

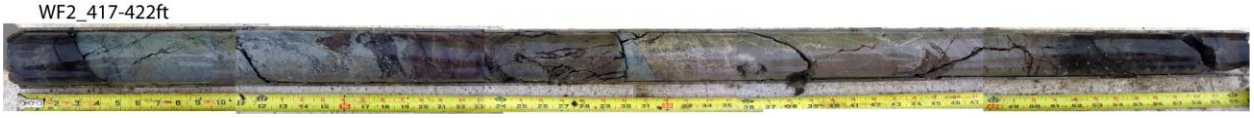

WF2 425.6-429ft

WF2_429-431ft

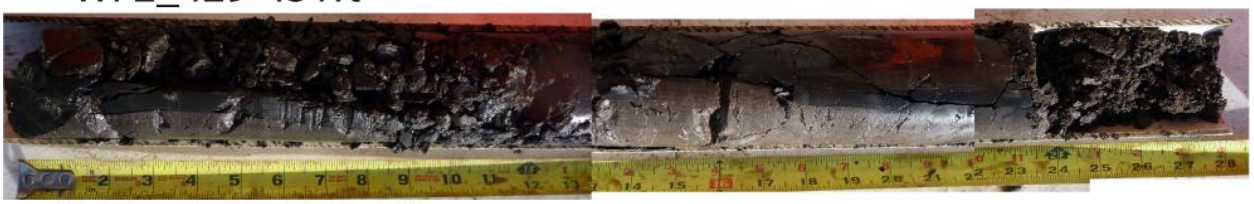

WF2_431-432.9ft

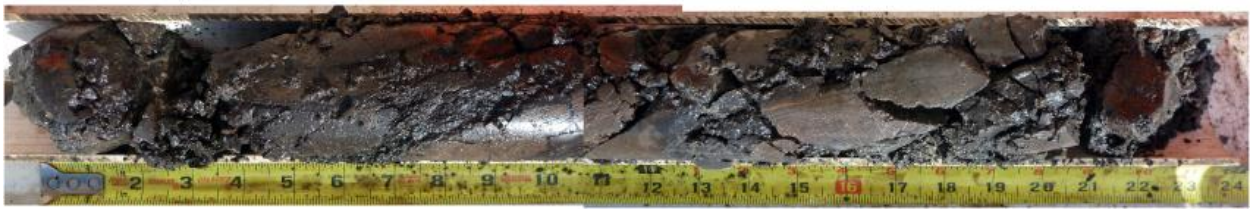

WF2_432.9-435.6ft

WF2_435.6-438.6ft

WF2_438.6-422ft

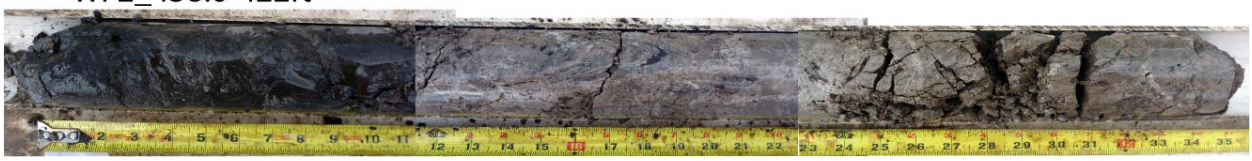

WF2_442-446.3ft

WF2_449.2-451.5ft

WF2_451.5-456ft

WF2_456-458.4ft

WF2_458.4-460.3ft

WF2 4693-4718 ft

WF2 4718-4765 ft

Appendix 4 - Core Images _WF3

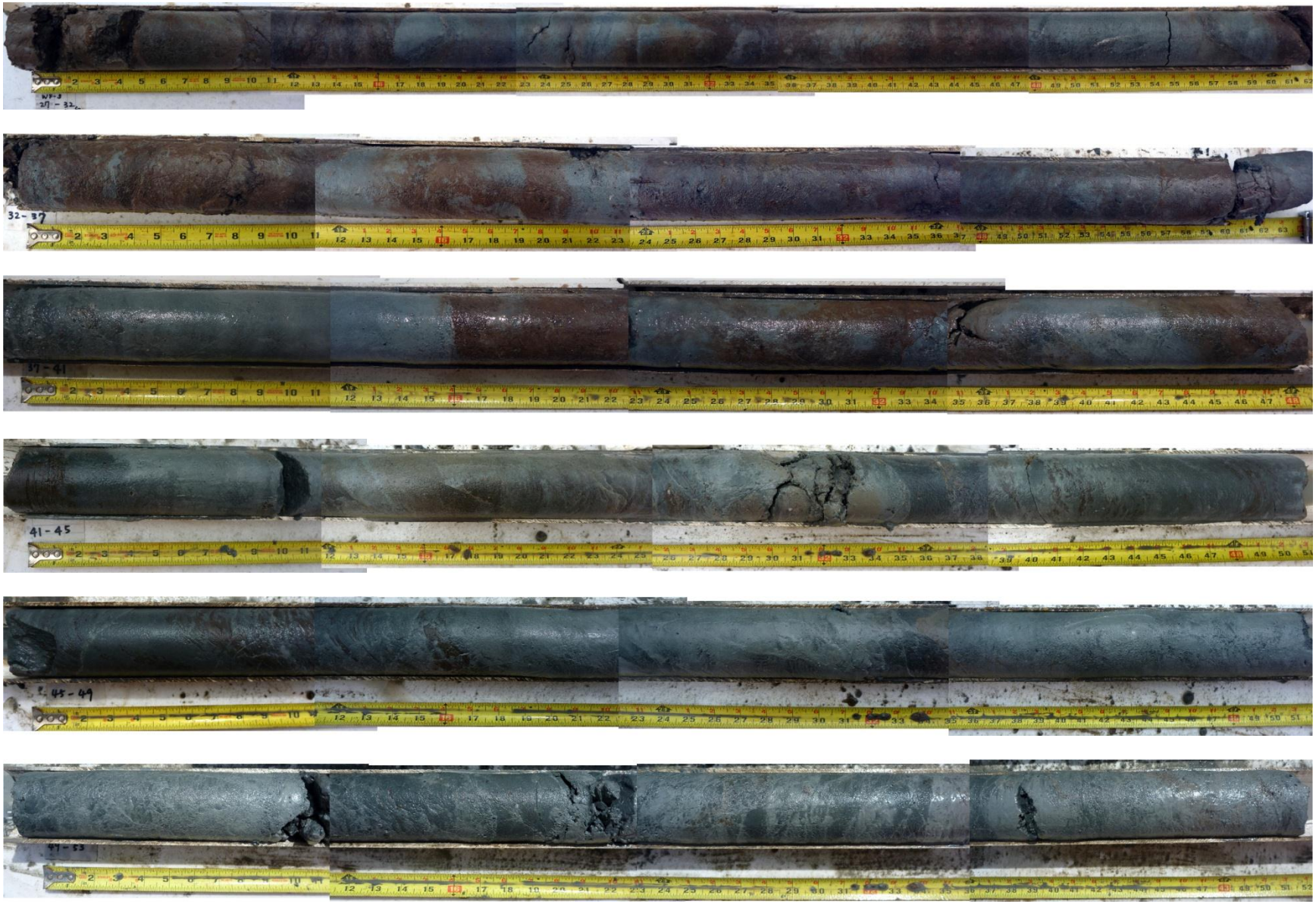

Appendix 4 - Core Images _WF3

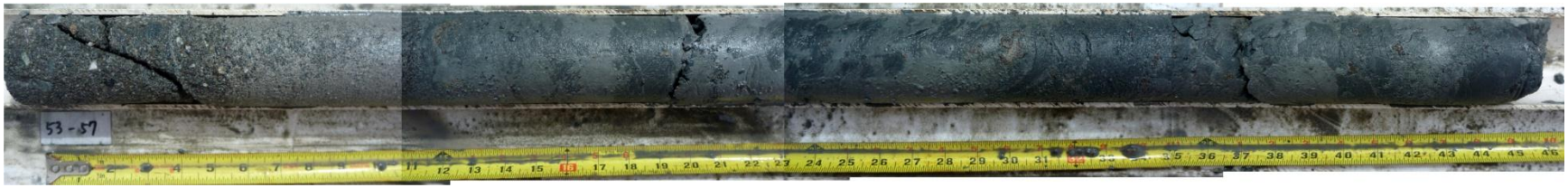

Appendix 4 - Core Images _WF3

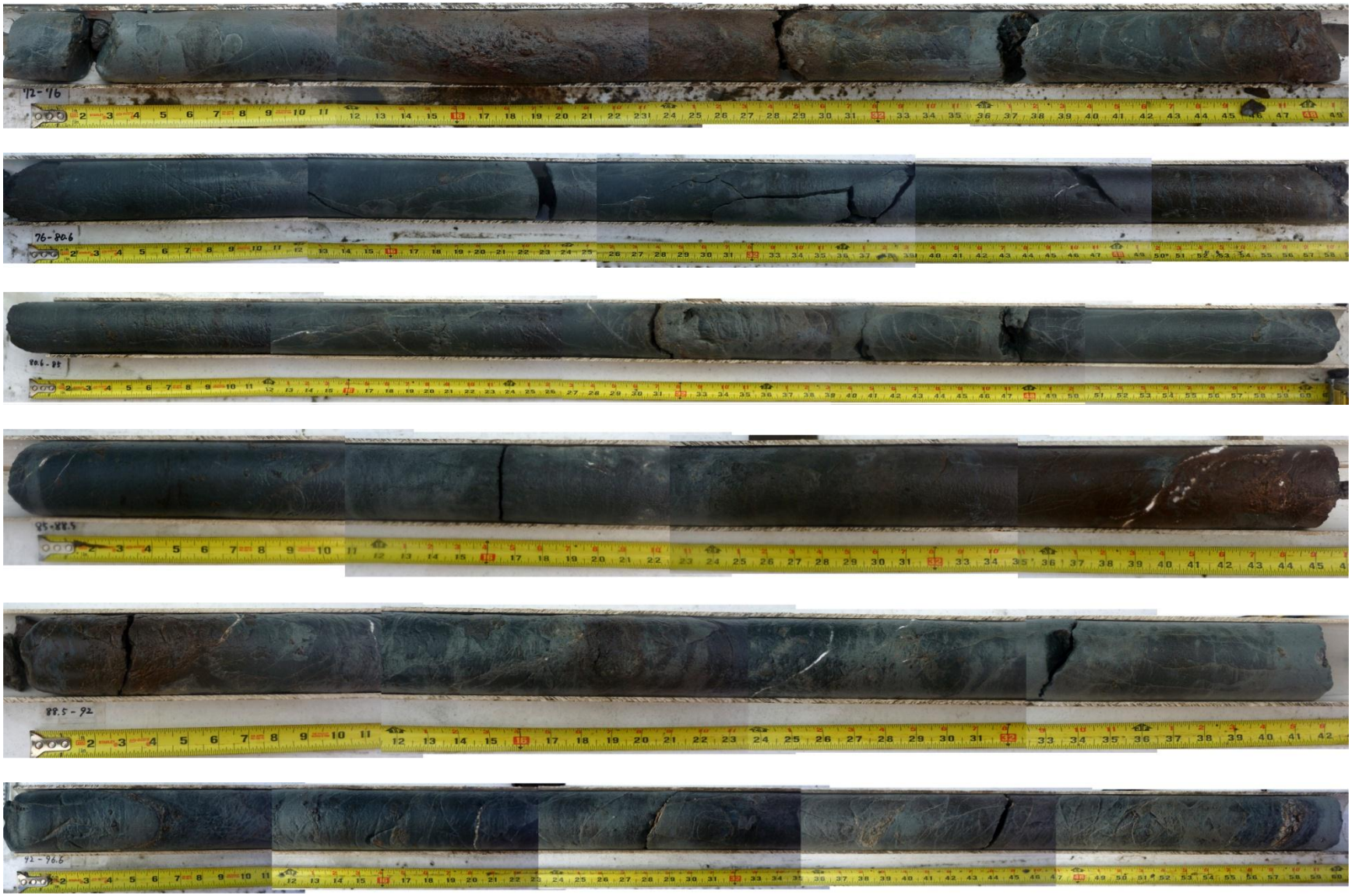

Appendix 4 - Core Images _WF3

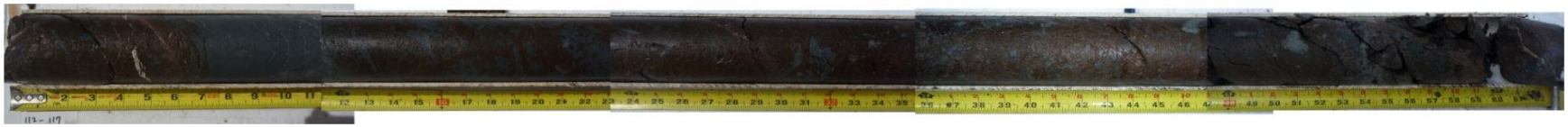

Appendix 4 - Core Images _WF3

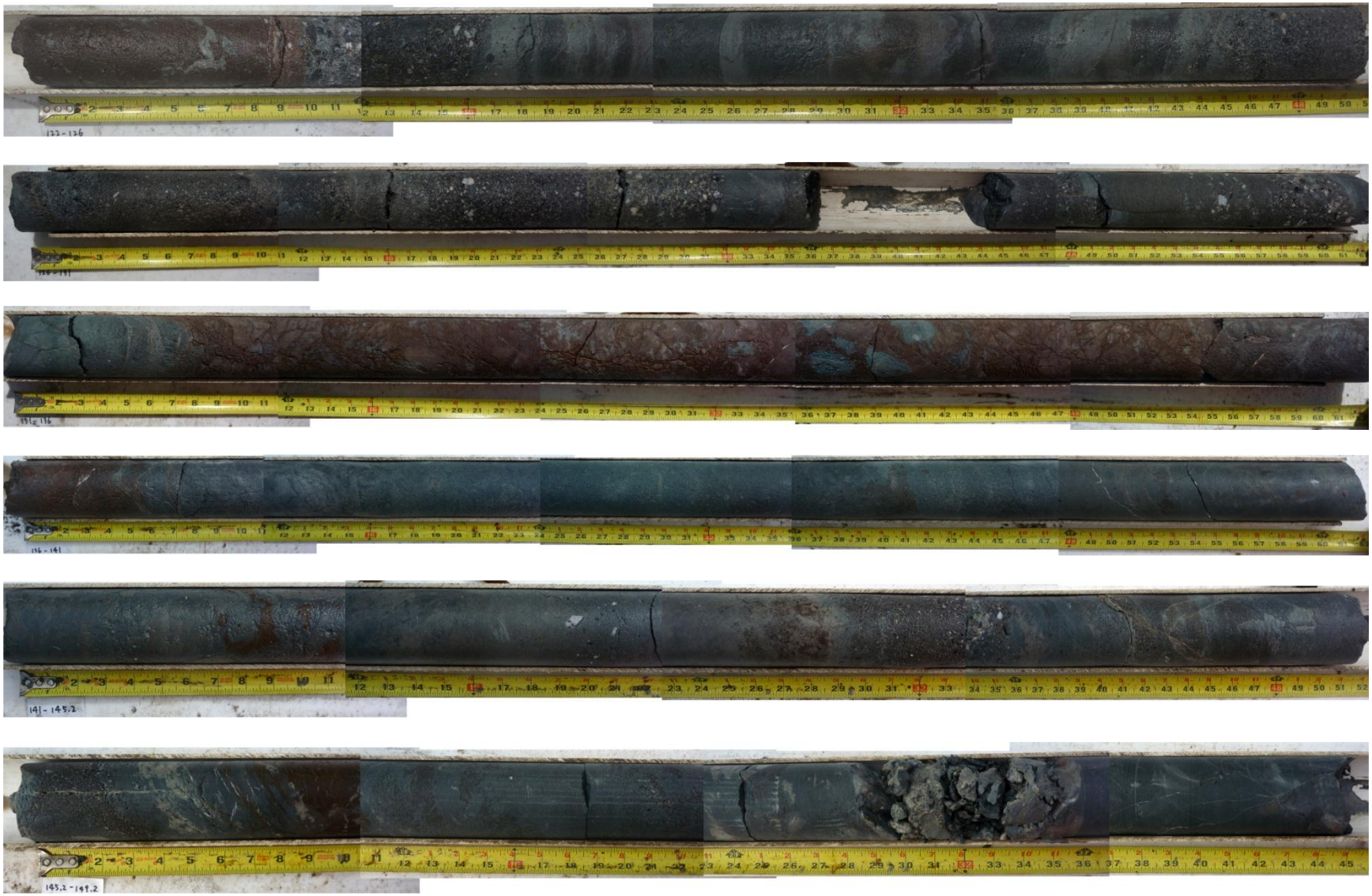

Appendix 4 - Core Images _WF3

Appendix 4 - Core Images _WF3

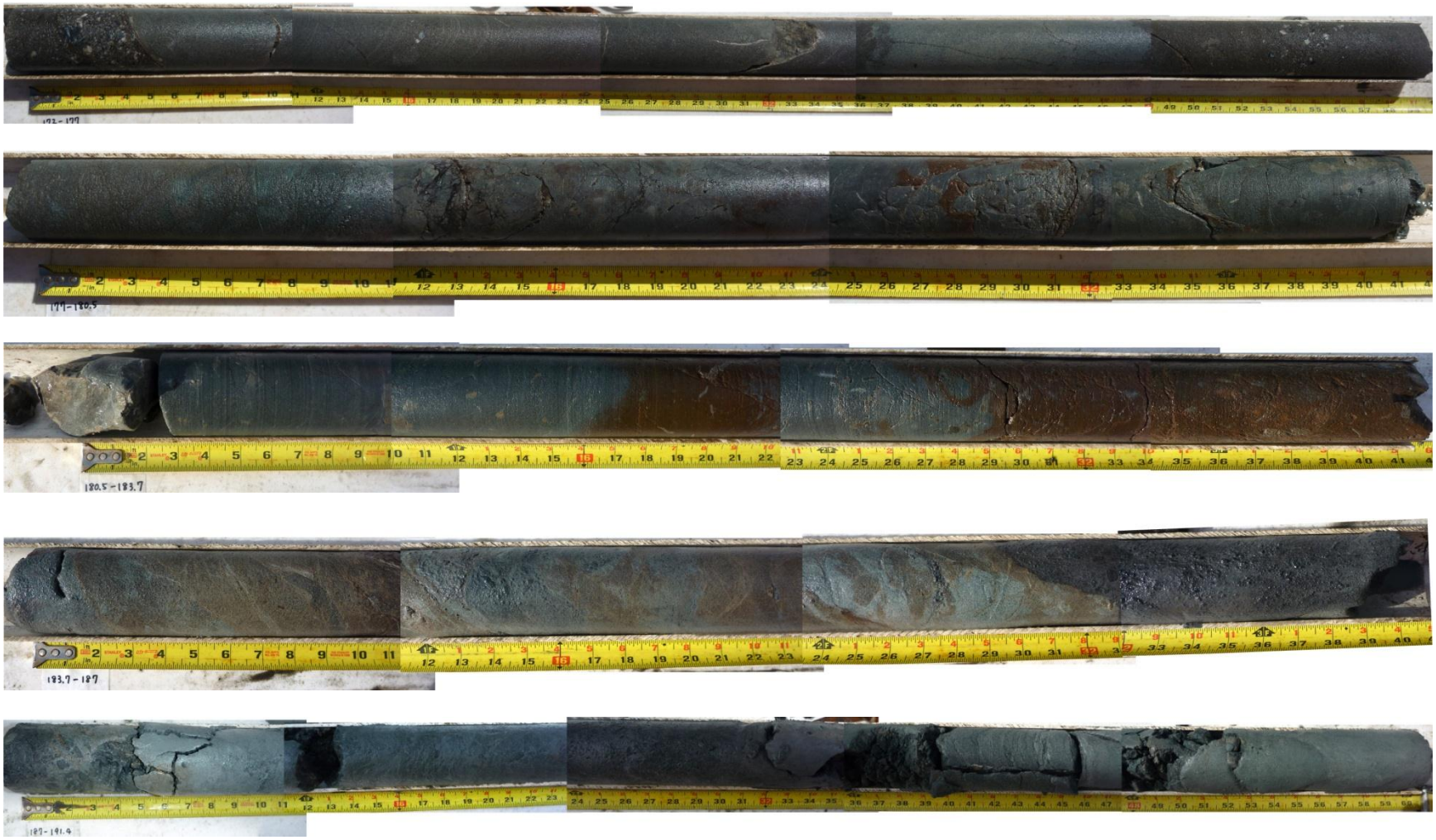

Appendix 4 - Core Images _WF3

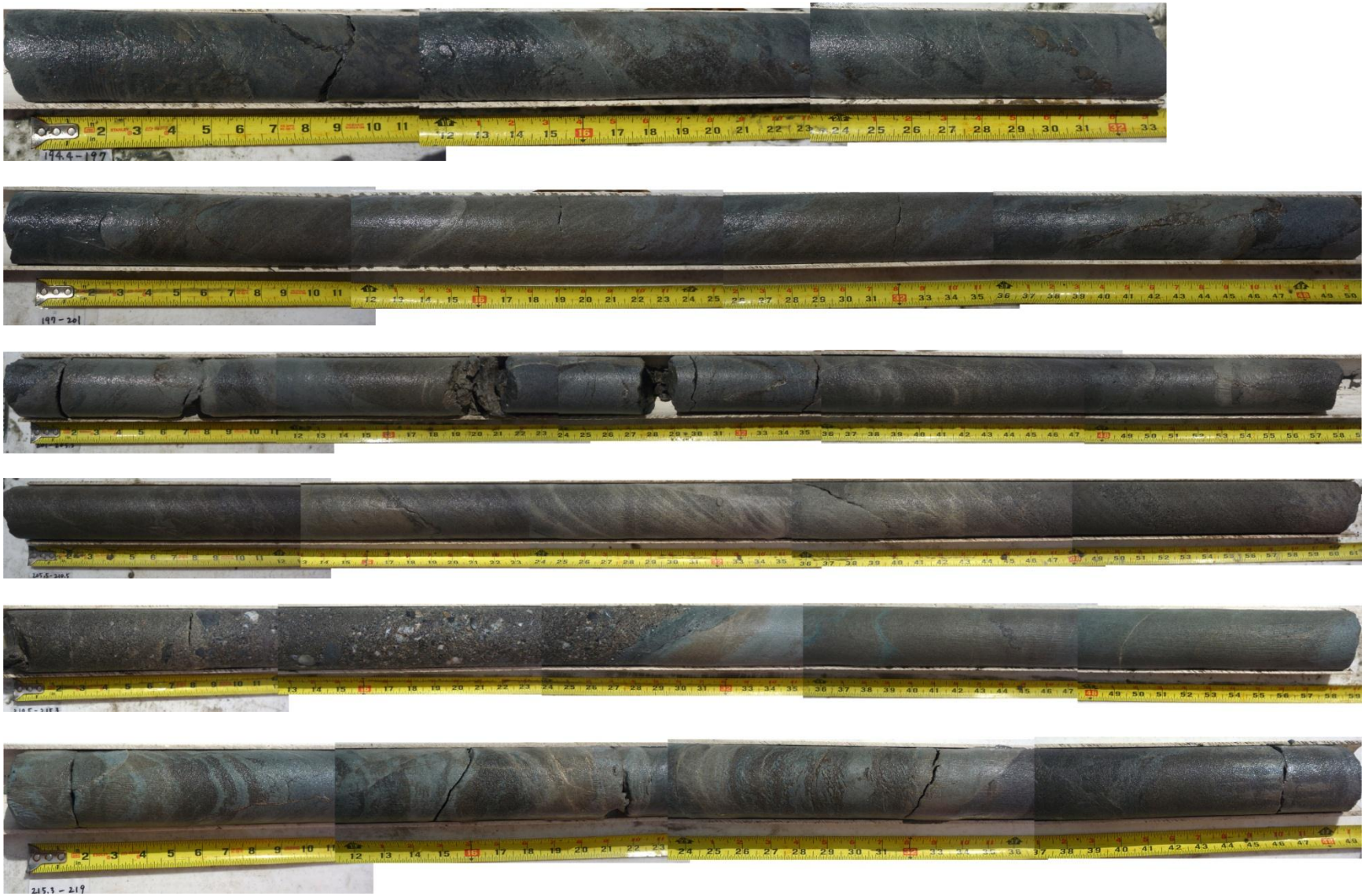

Appendix 4 - Core Images _WF3

Appendix 4 - Core Images _WF3

Appendix 4 - Core Images _WF3

Appendix 4 - Core Images _WF3

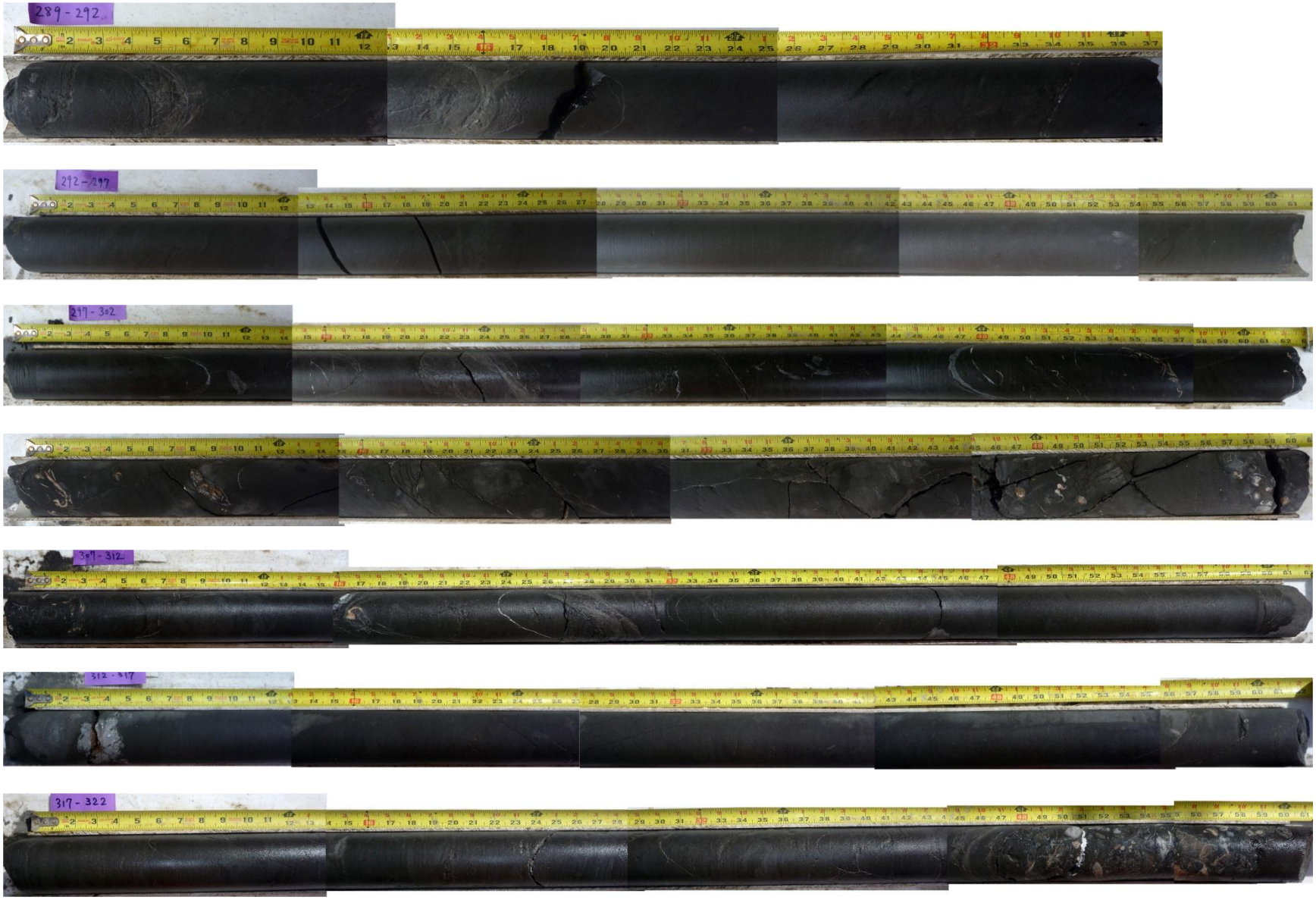

Appendix 4 - Core Images _WF3

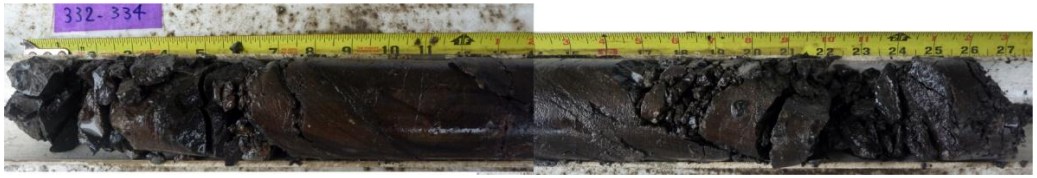

Appendix 4 - Core Images _WF3

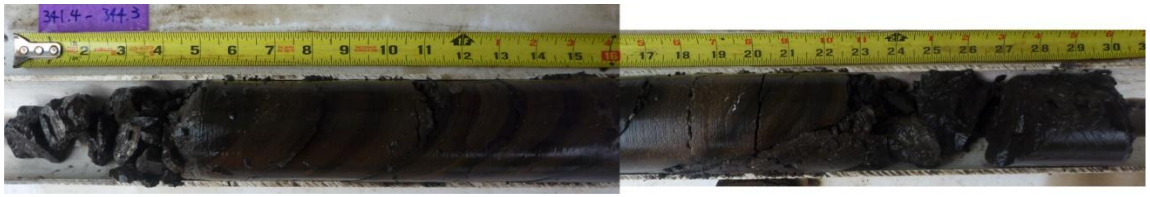

Appendix 4 - Core Images _WF3

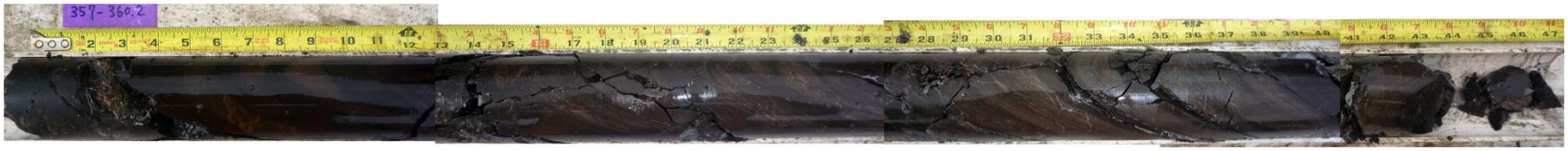

Appendix 4 - Core Images _WF3

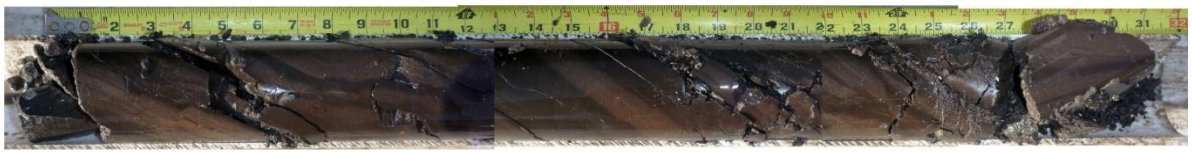

Appendix 4 - Core Images _WF3

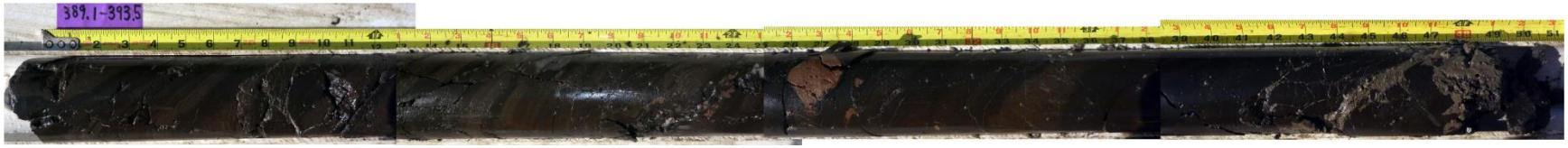

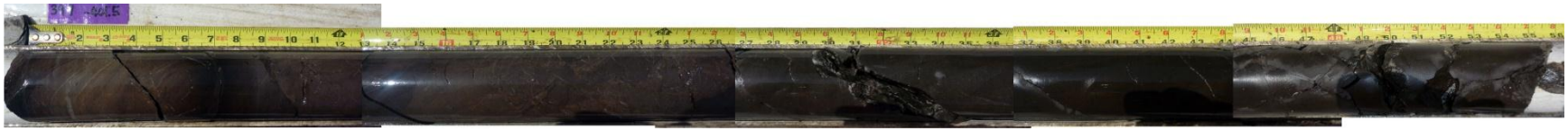

Appendix 4 - Core Images _WF3

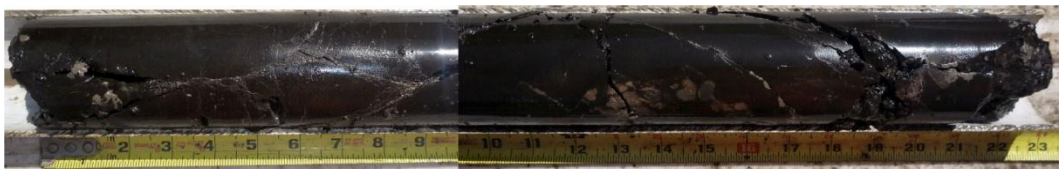

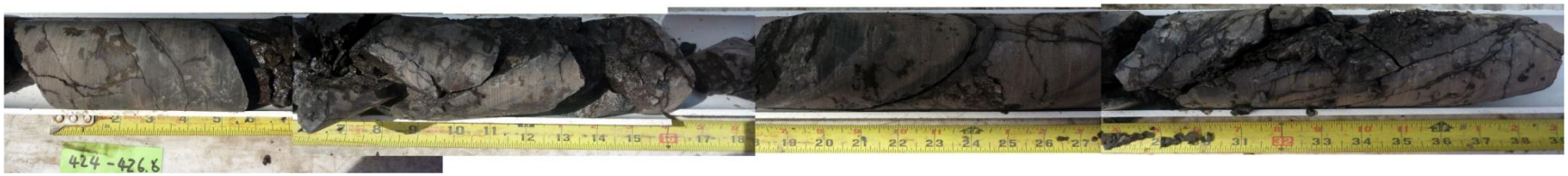

Appendix 4 - Core Images _WF3

Appendix 4 - Core Images _WF3

Appendix 4 - Core Images _WF3

Appendix 4 - Core Images _WF3

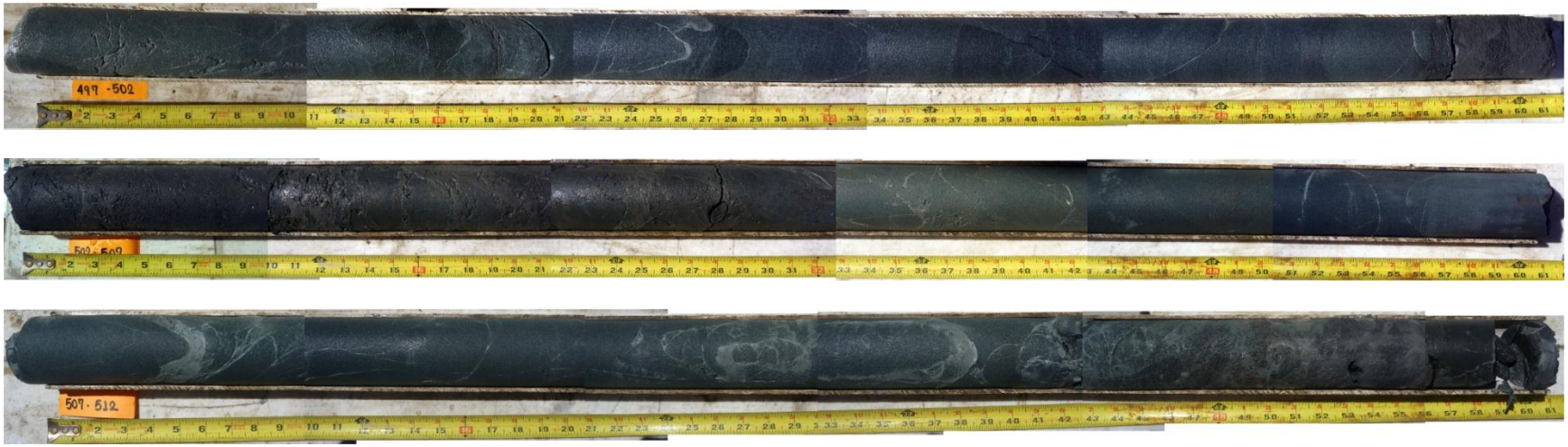

Appendix 5 – Core Images WF4

39-44

44-47.5

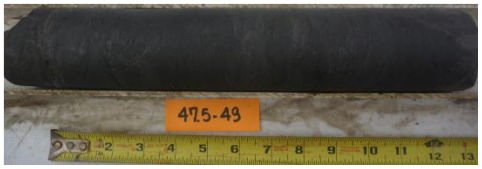
47.5-49

49-54

54-59

59-60.5

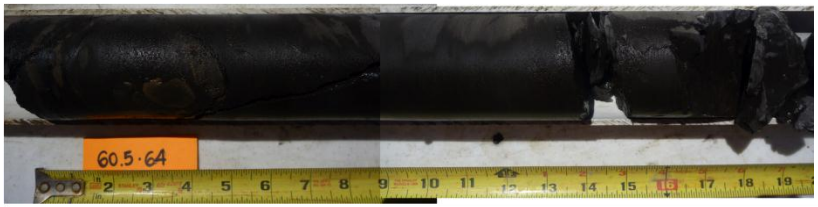
60.5-64

64-68

68-73

73-75

75-76

76-78.5

78.5-81.4

86-89

81.4-86

96-96.6

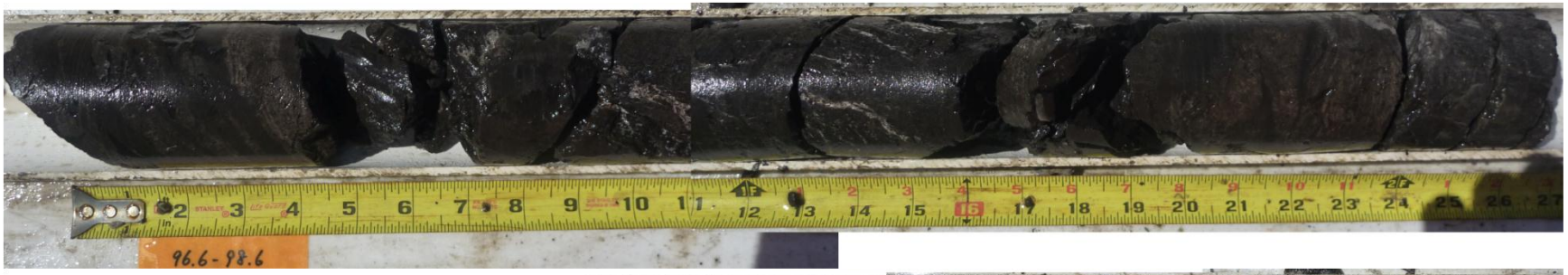
96.6-98.6

103.6-105.2

105.2-109

109-112.5

112.5-115

Appendix 5 – Core Images WF4

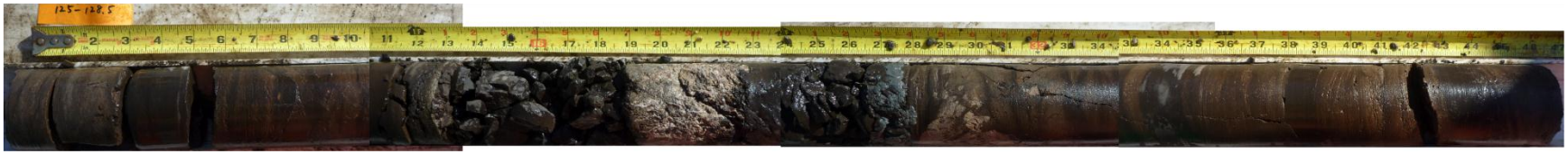

131.4-135

135-138.3

138.3-142

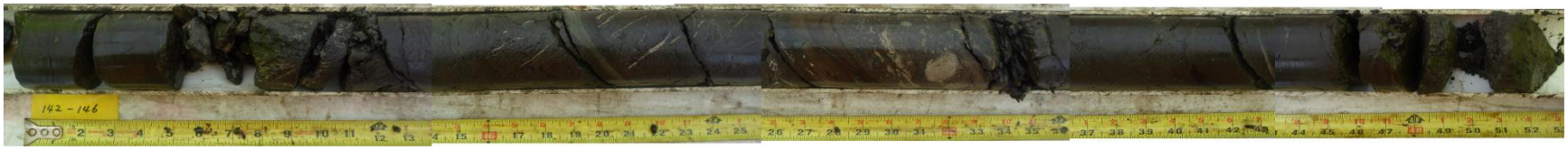
142-146

146-149

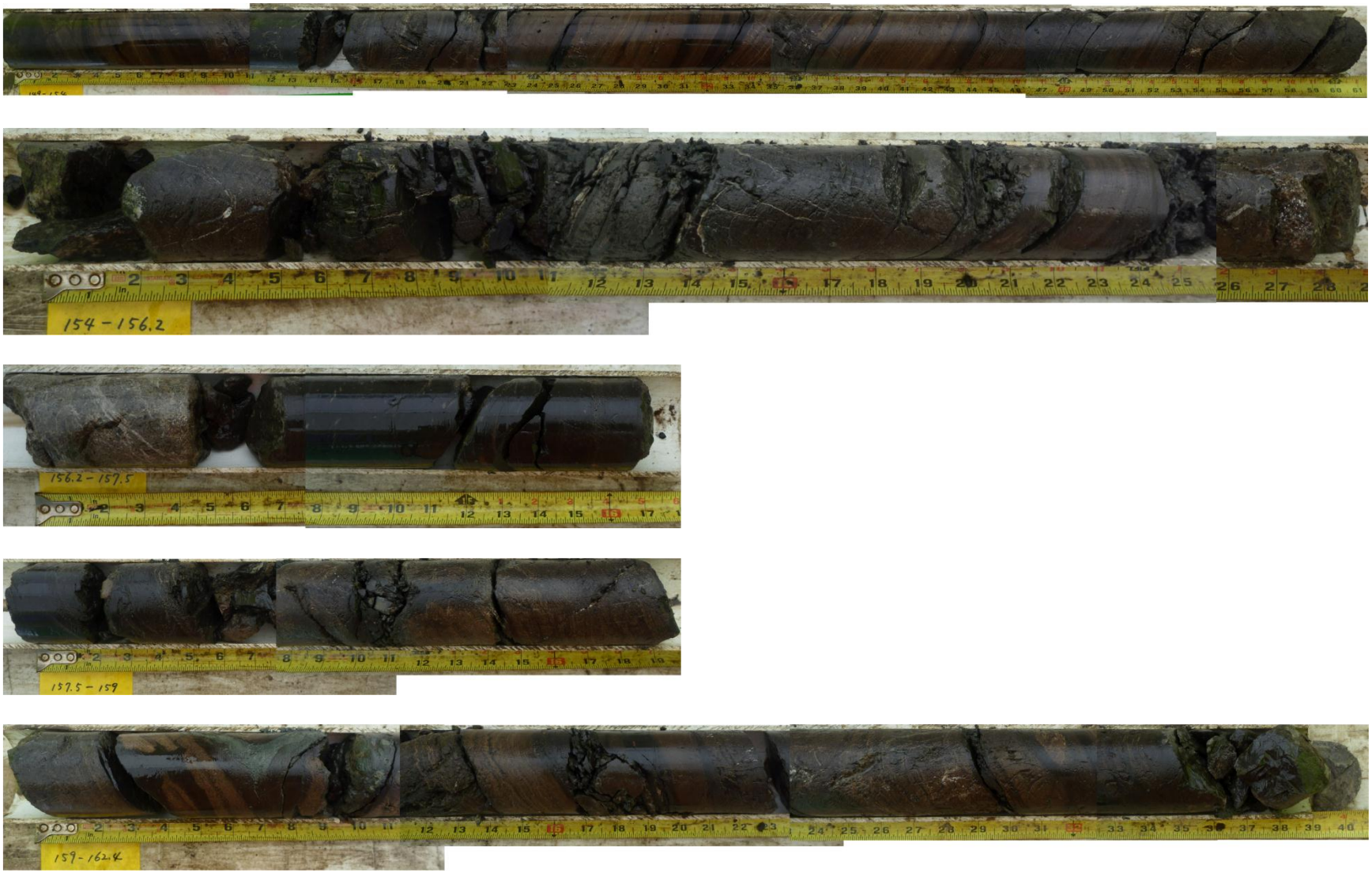
154 – 156.2
156.2 – 157.5
157.5 – 159
159 – 162.4

162.4 - 165

165 - 166.1

166.1 - 166.5

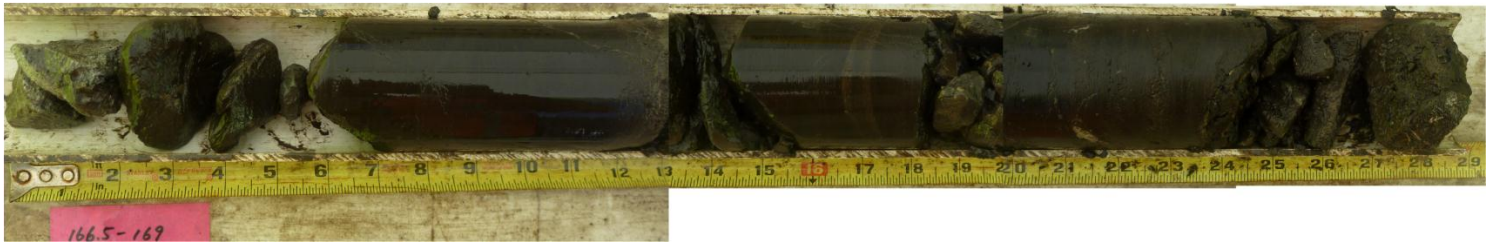
166.5-169

169-173.2

173.2-178

182.2-186

186-188

188-190.7

190.7-194.2

194.2-199

199-203

203-207.3

207.3-209

209 – 213

213 – 216.7

216.7 – 219

219 – 223

223 – 226

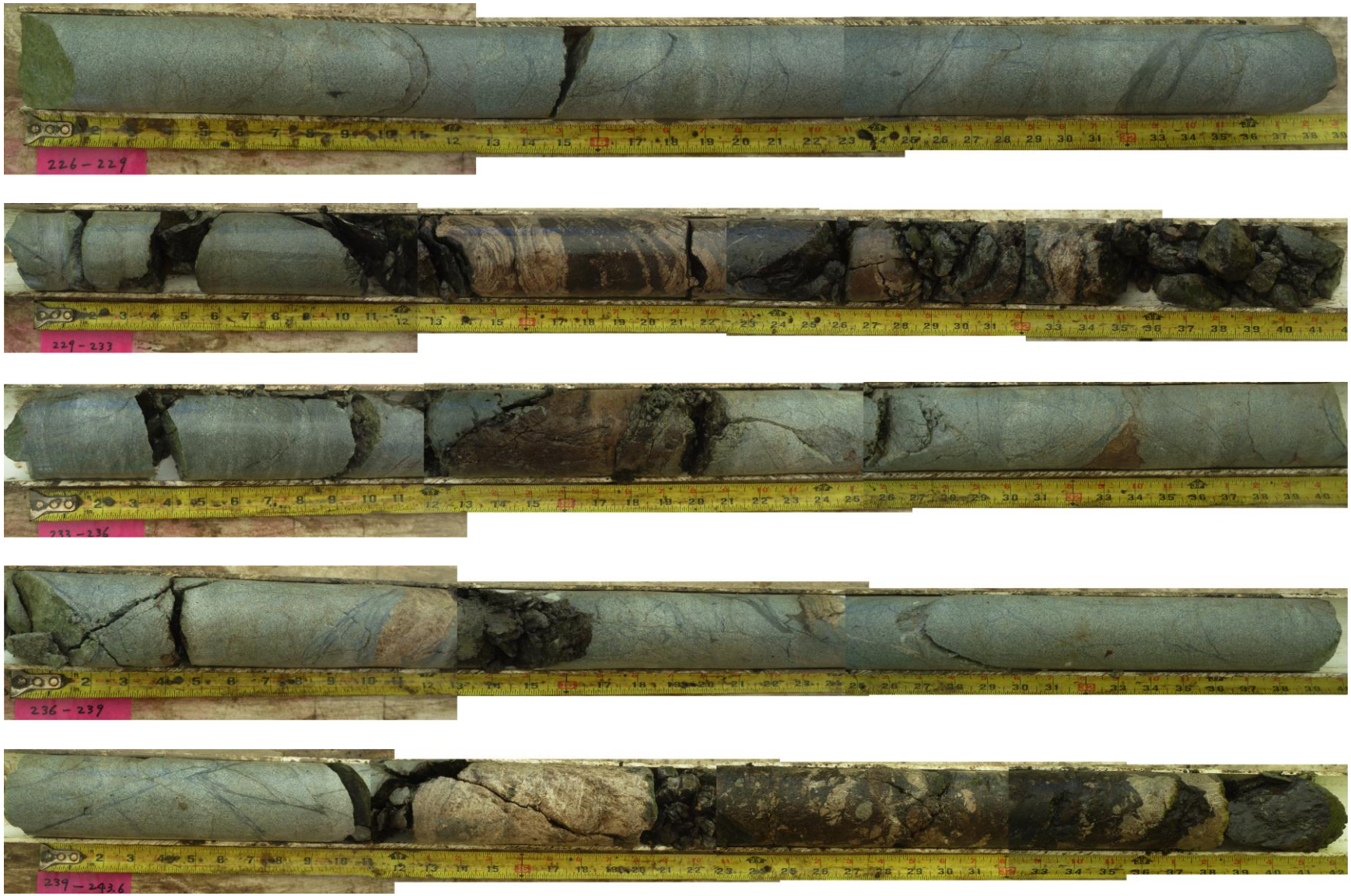
226 – 229
229 – 233
233 – 236
236 – 239
239 – 243.6

243.6-246.5

246.5 - 249

253 - 256.7

256.7-259.4

259.4-262.5

262.5-266.2

266.2-269

269 – 272.9

272.9 – 275.7

275.7 – 279

297-294

297-299

299 - 302.3

302.3 - 306

306 - 309

309 - 312.9

312.9 - 315.7

315.2-319

319-322.5

322.5-326

326-329

329 - 333

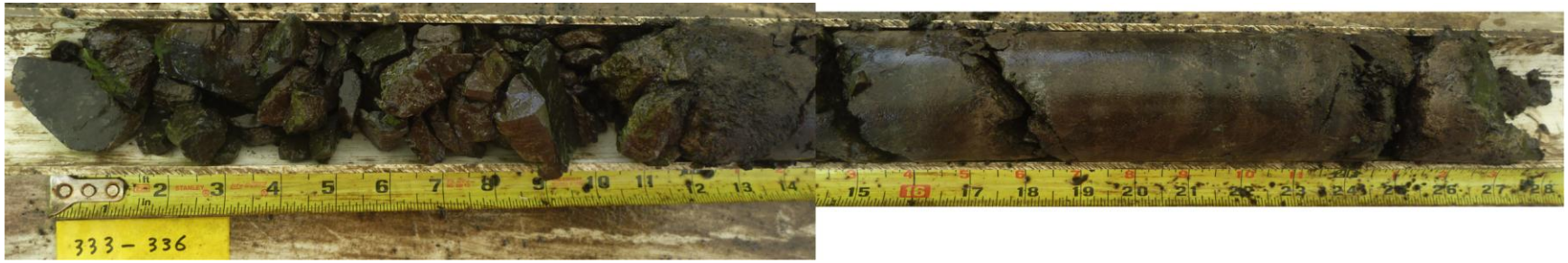
333 – 336

336 – 339

339 – 342.3

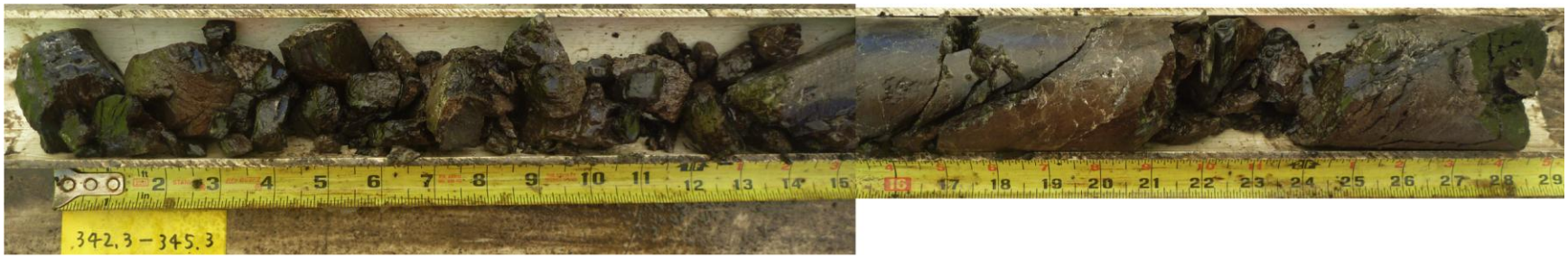
342.3 – 345.3

345.3-348.4

348.4 – 351.5

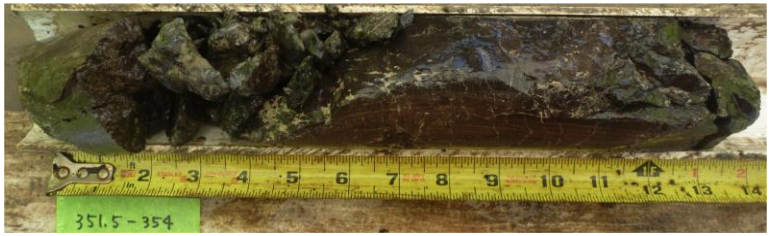
351.5 - 354

354 - 355.5

355.5-356.6

356.6 - 359

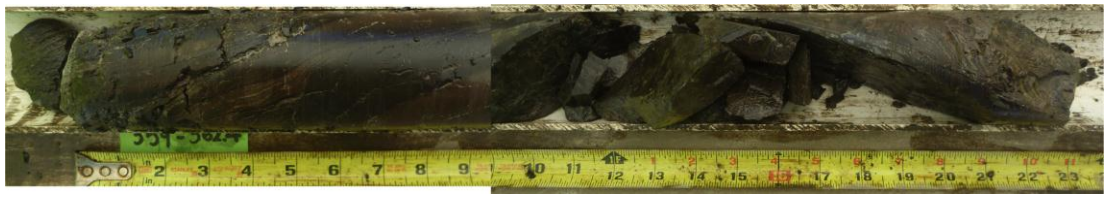

362.4 - 366

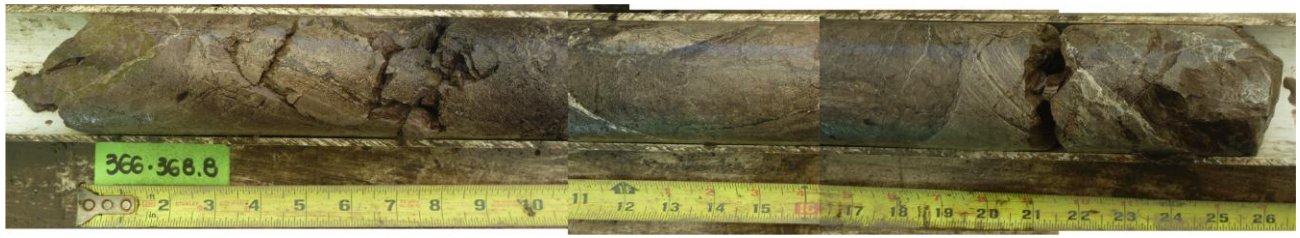
366 - 368.8

368.8 - 372.5

372.5-376
Hl Sample

376-379
379-381.4
381.4-384

384-386.5
386.5-389
389-393
398-401

401- 403.2

403.2 -406

406-409

MISSING FAST DRILL
409-412

412-415

393-398

415-418

418-423

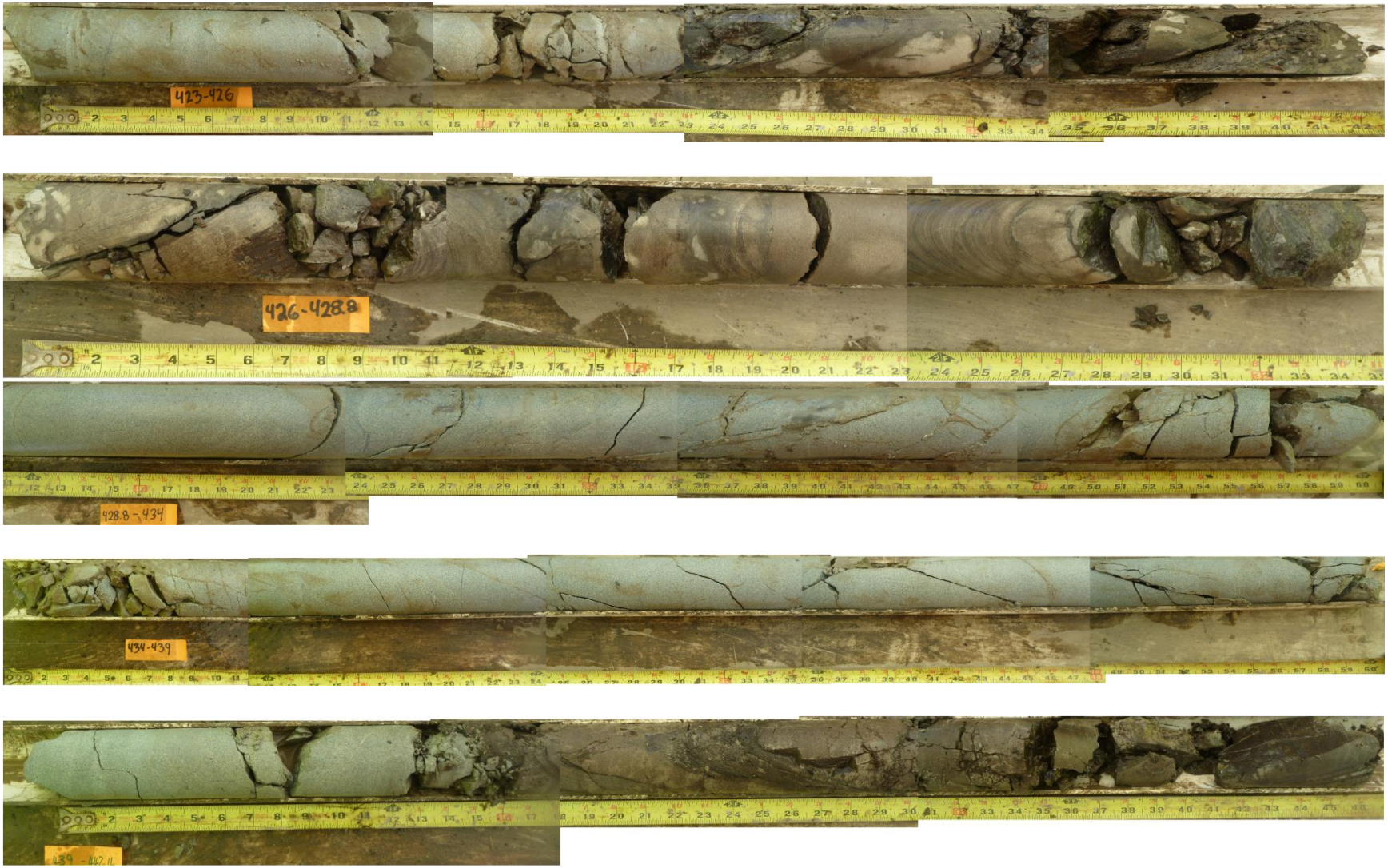
423-426
426-428.8
428.8-434
434-439

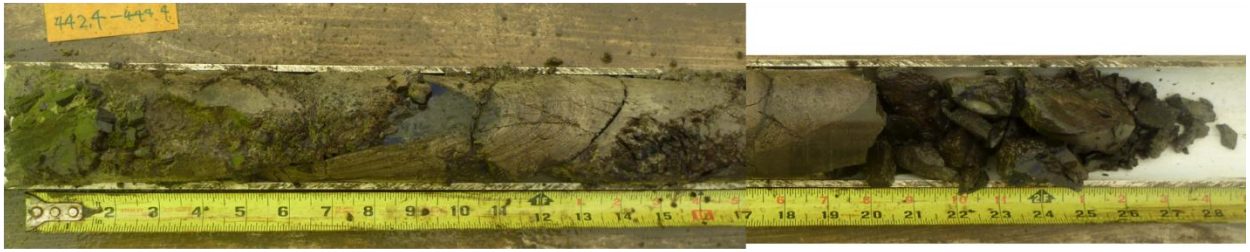

454-456.5 ft Core loss

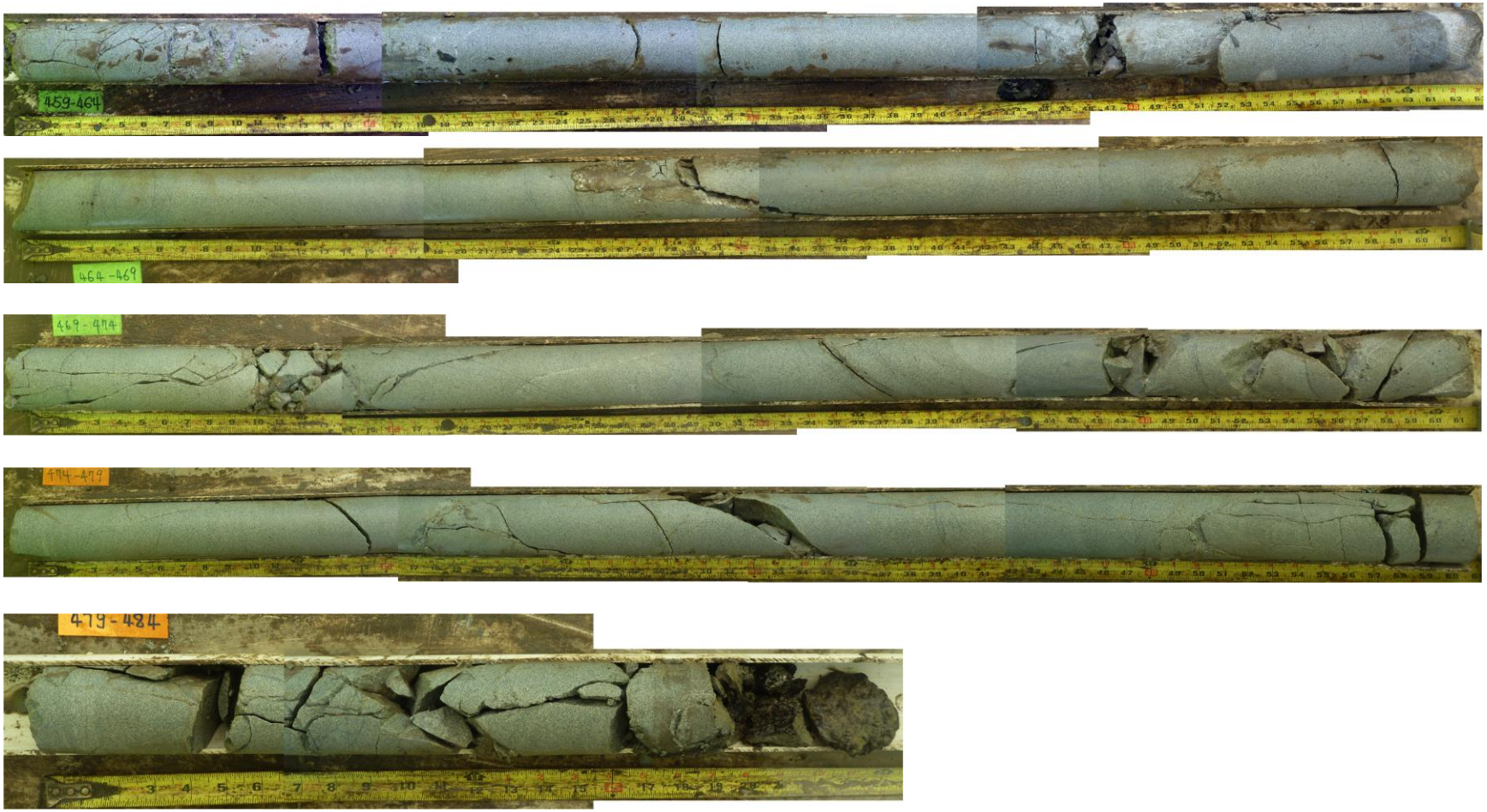
459-464
464-469
469-474
474-479
479-484

484 - 486.6

486.6-489.5

489.5-492

492.5-493

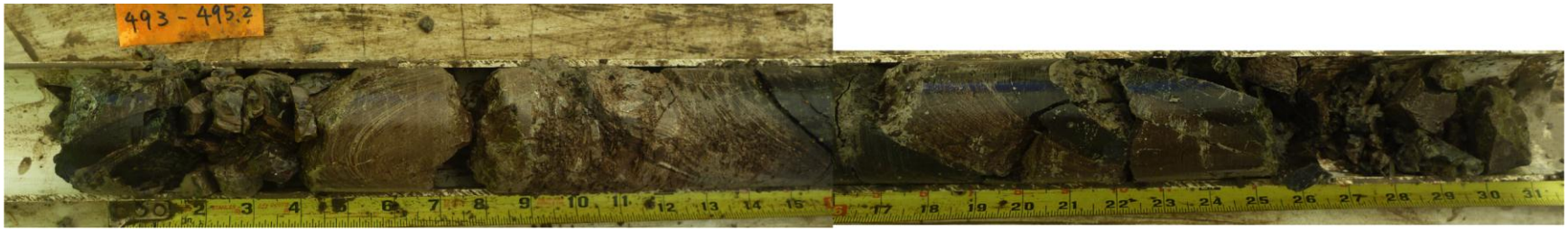
493 - 495.2

495.2-497.5

497.5 - 501

501 - 504

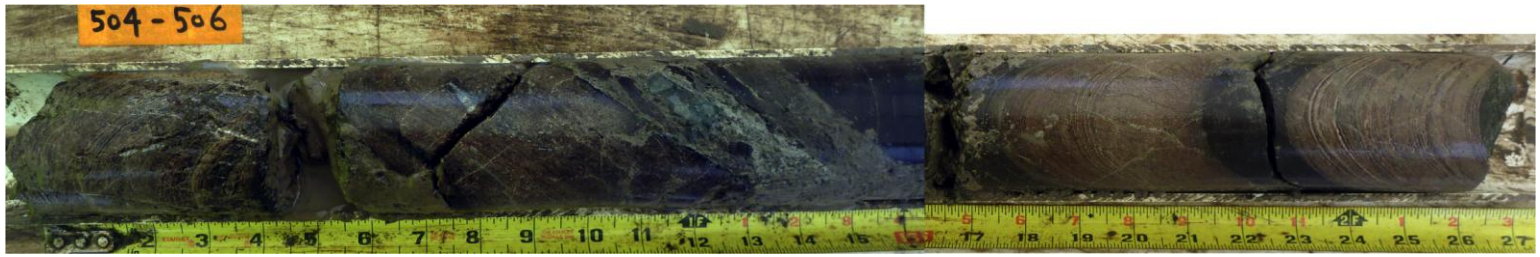
504 - 506

506 - 508.2

508.2 - 511

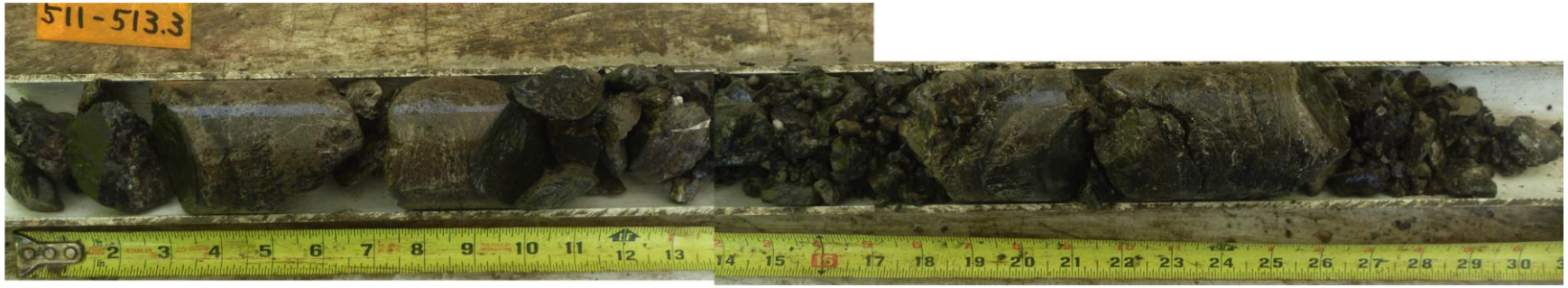
511-513.3

513.3-515.8

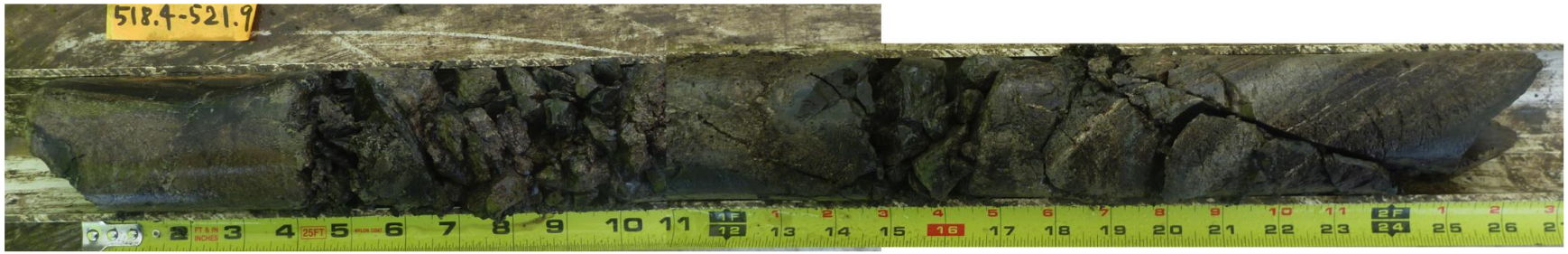
518.4-521.9

521.9-524

524-526.7

526.7-529

529-531

531-533.0

533.8-537.6

537.6-540

540-542.6

542.6-545
545-547.7
547.7-551.5
551.5-554.2

554.2-556.2

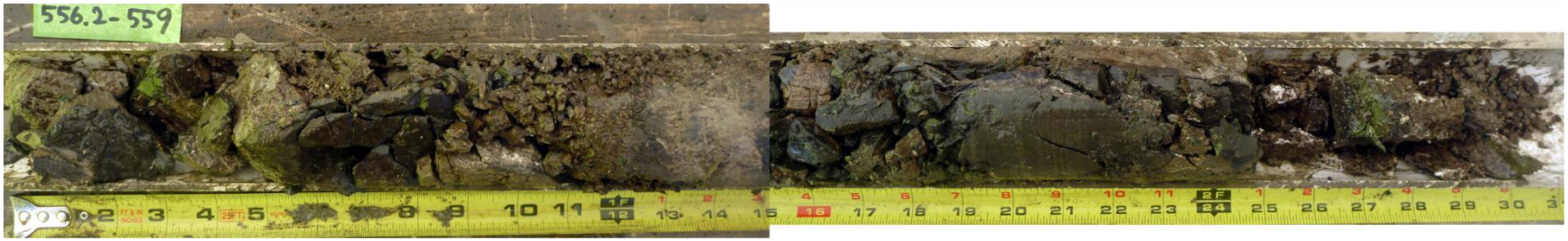
556.2-559

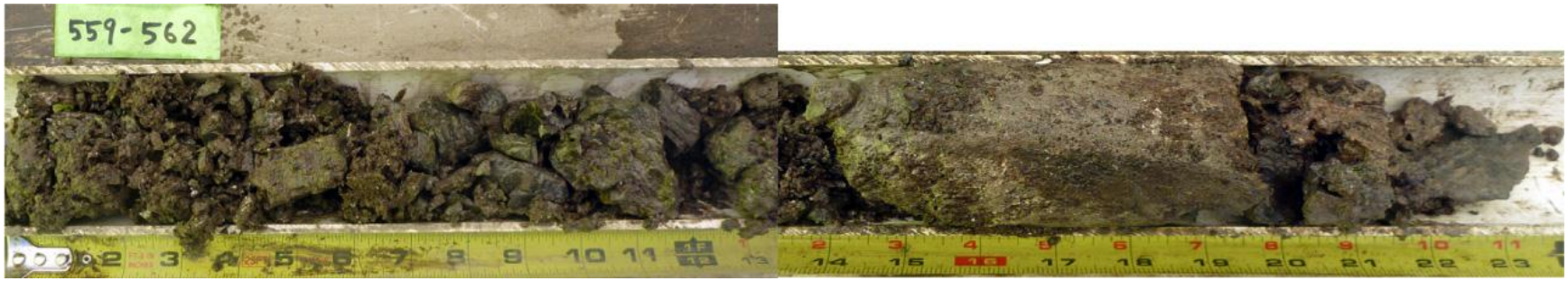
559-562

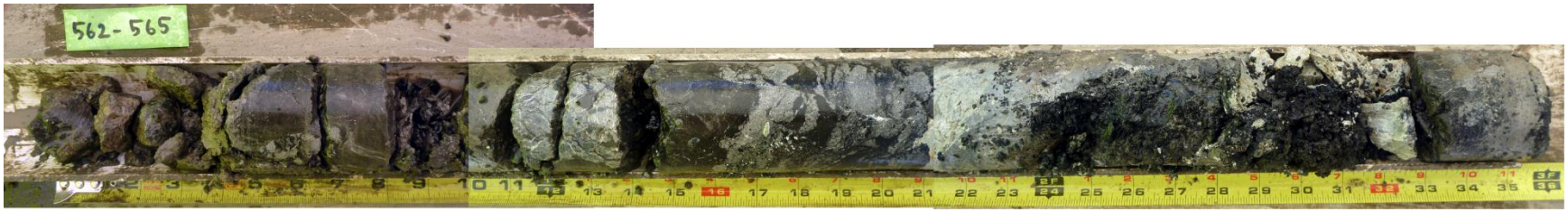
562-565

565-569

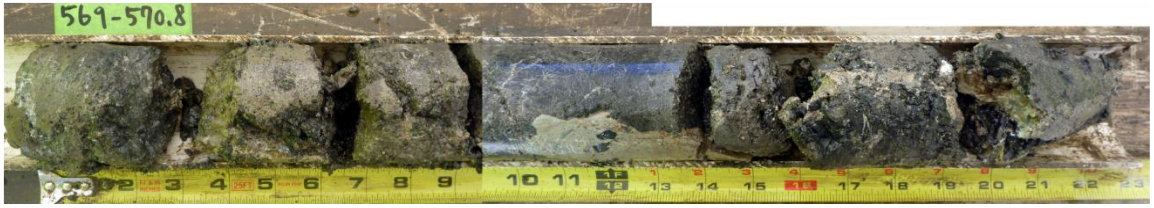
569-570.8

570.8-573.3

573.3-576

576-578.8

578.8-582

582 - 584

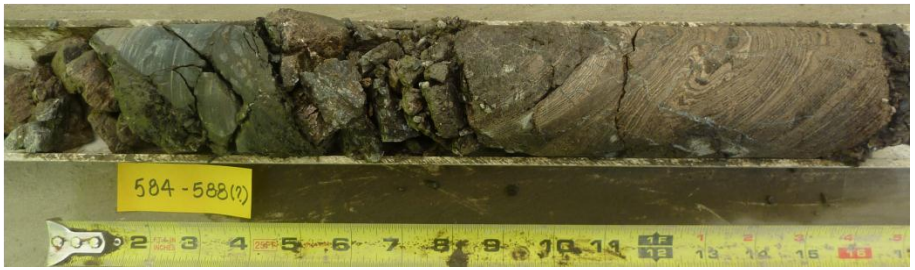
584 - 588(?)

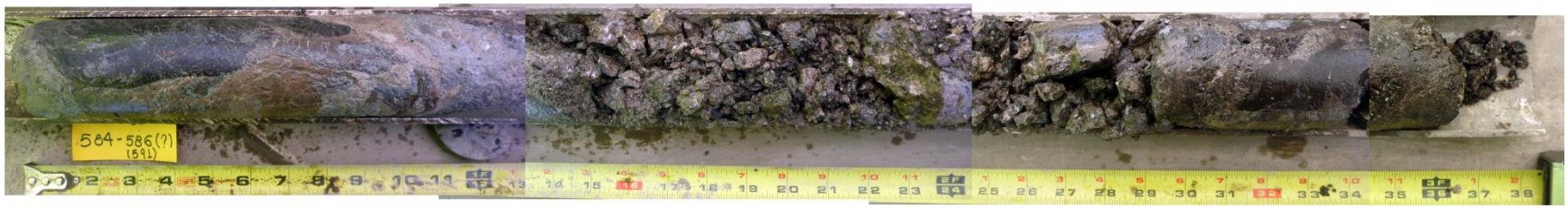
584-586(?)
(591)

591-593.2ft

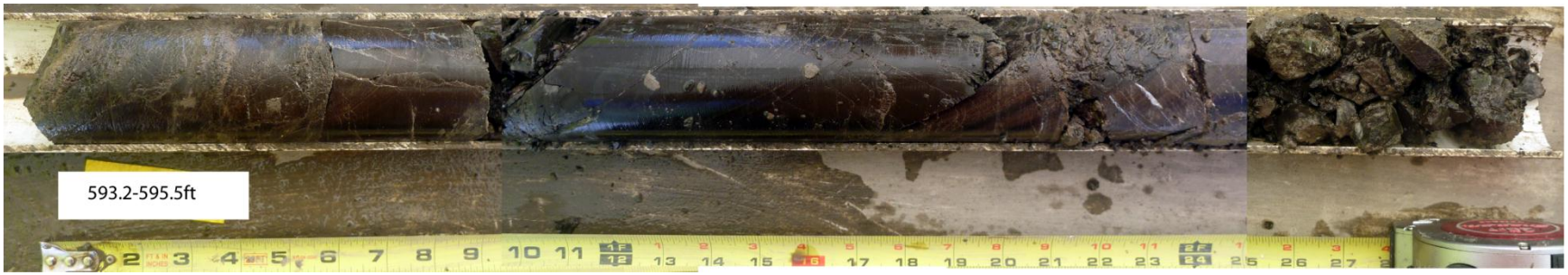
593.2-595.5ft

595.5-598ft

598.5-602ft

Core Loss 613.4-617ft

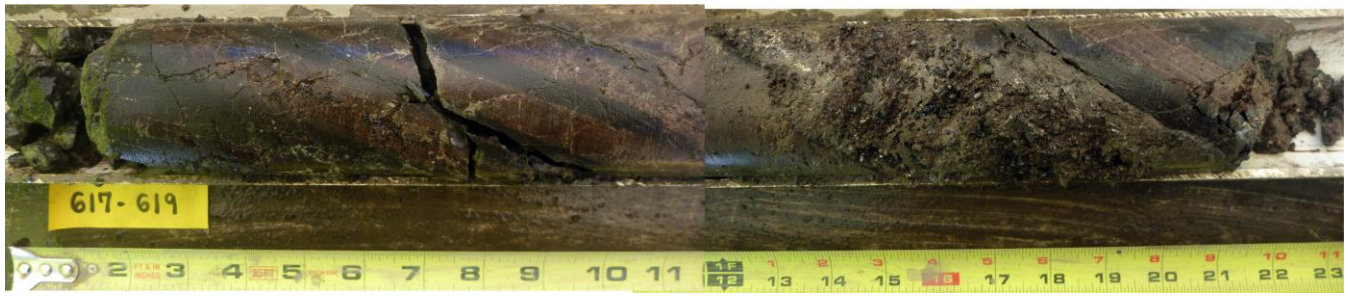

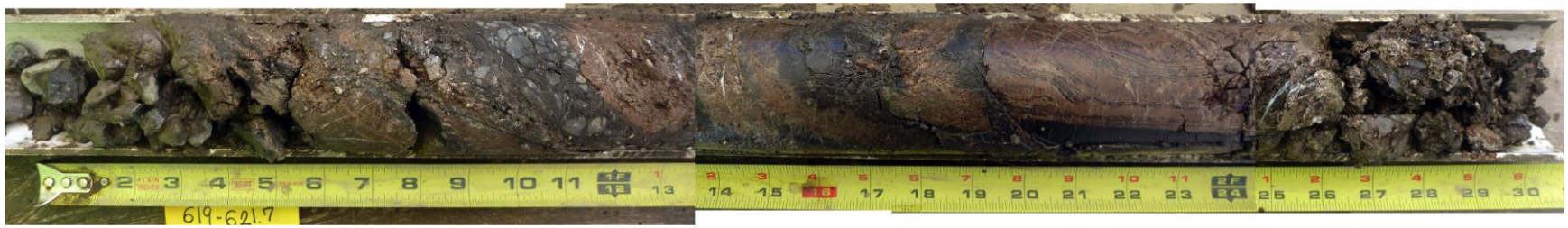

Core Loss 622.4-623.6ft

Core Loss 623.6-624.4ft

Instead of 631 is 632ft

634.4 - 636.4

636.4 - 637.6

637.6 - 639.5

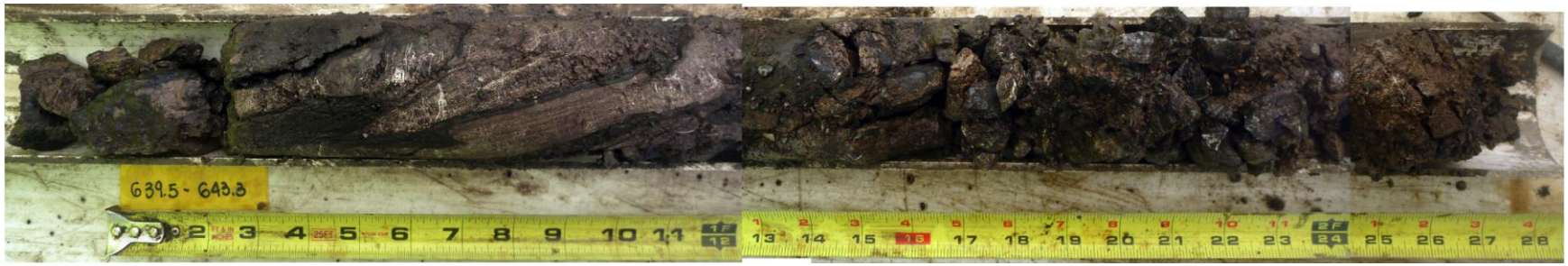
639.5 - 643.3

643.3 - 645.1

645.1 - 646.9

646.9 - 650

650-653.7

653.7-656.6

656.6-659

659-662.4

6624

664-667

667-670.2

670.2-672

672-674.2

674.2-677.2

680-681

Core Loss 681-681.7ft

Core Loss 689.5-691.2ft

Core Loss 691.2-692.3ft

Missing photo 692.1-693.7ft

Appendix 6 - Core Images _WF5

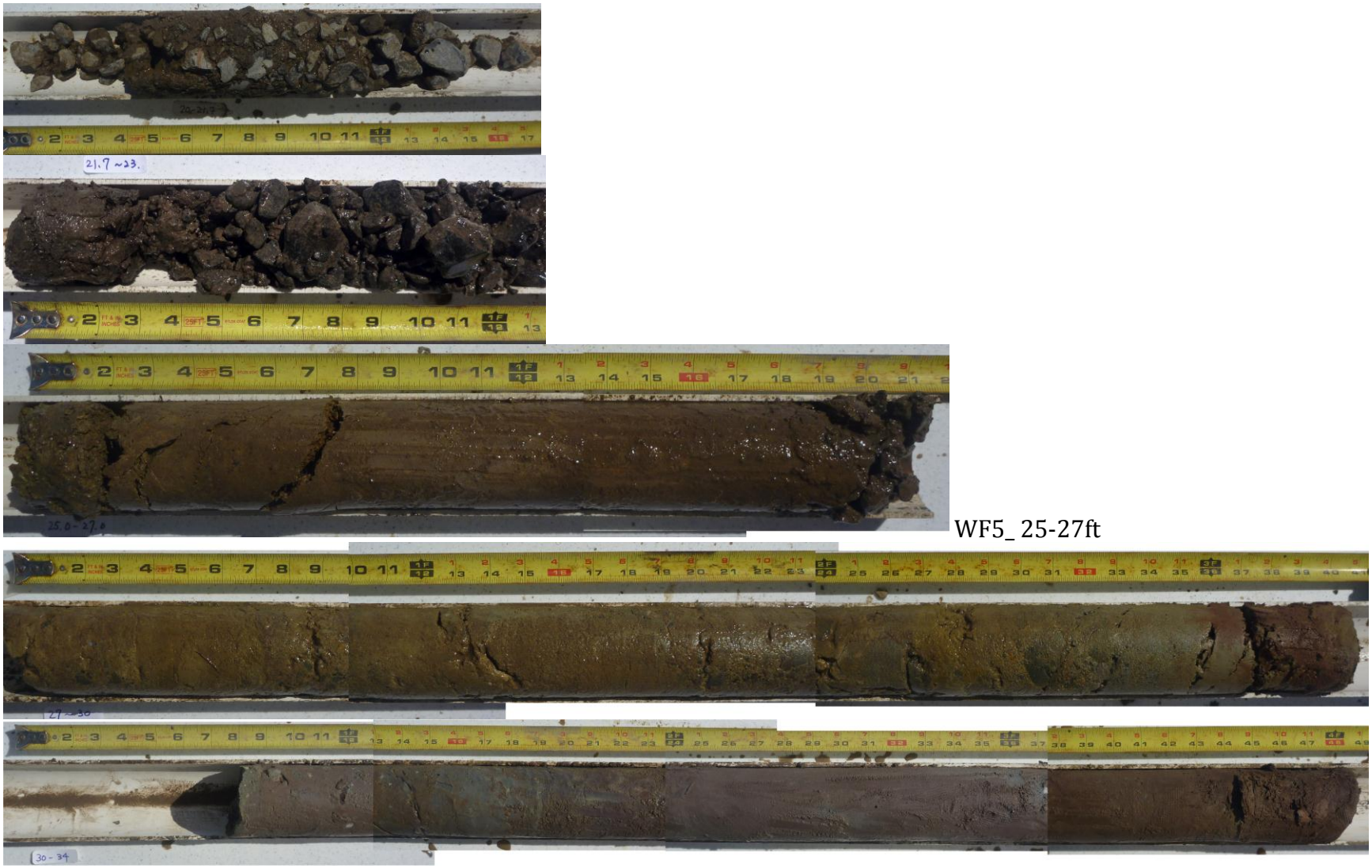

WF5_ 25-27ft

Appendix 6 - Core Images _WF5

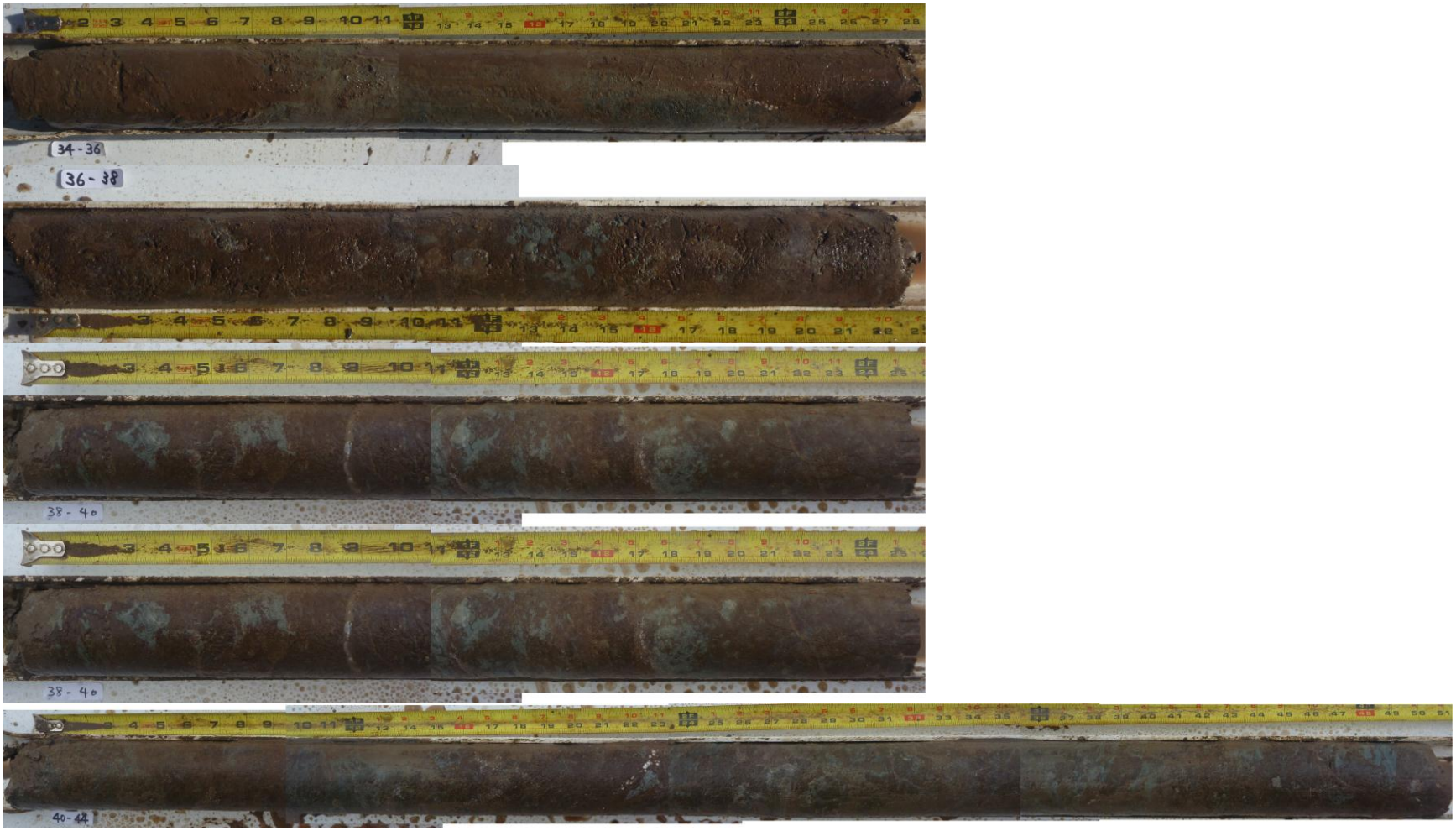

Missing 44-48ft

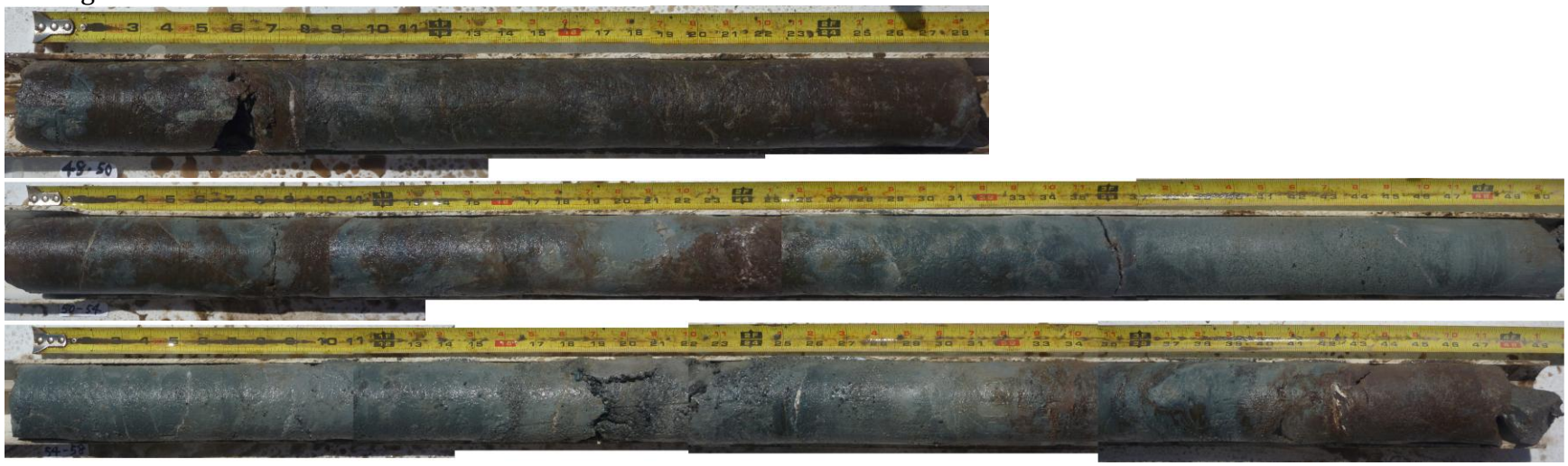

WF5_54-58ft

WF5_ 60-64ft

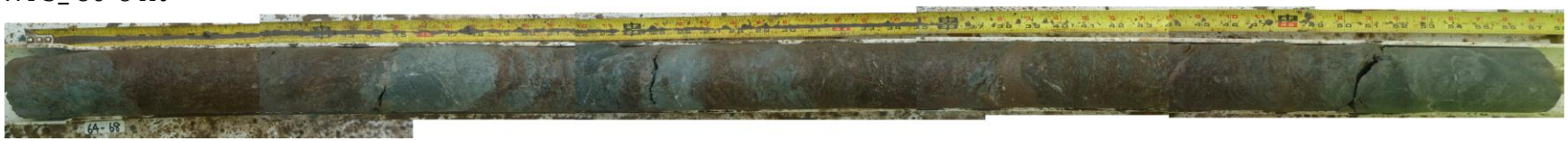

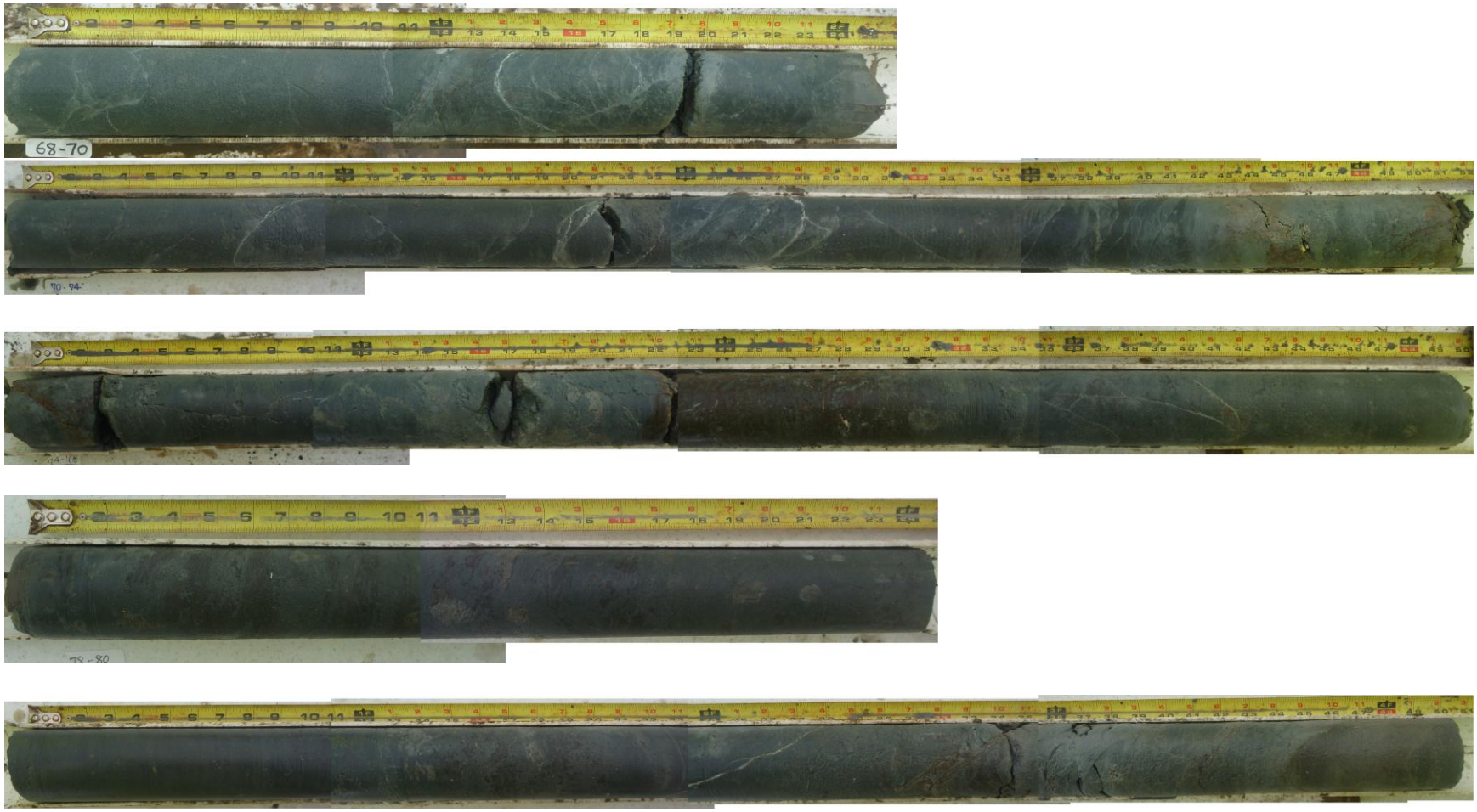

WF5_ 80-84ft

Appendix 6 - Core Images _WF5

WF5_ 84-88ft

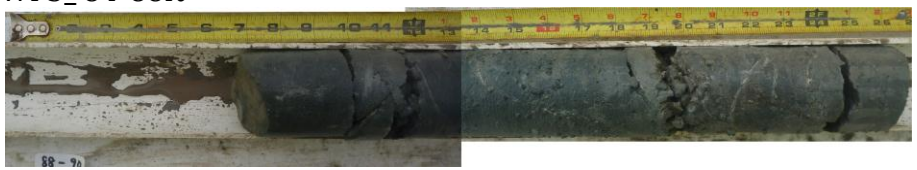

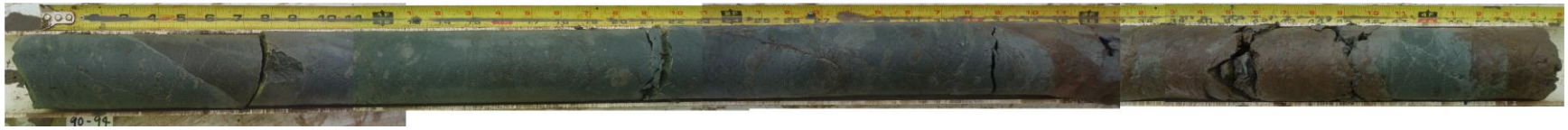

Appendix 6 - Core Images _WF5

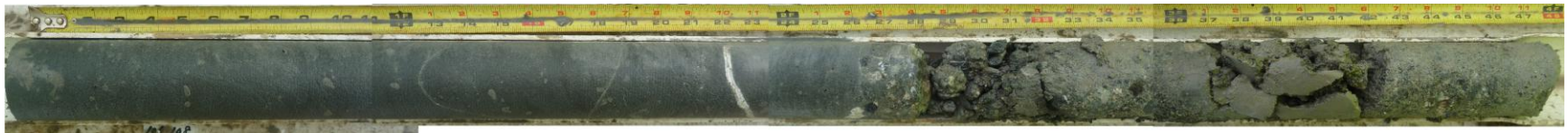

WF5_113.7-118ft

WF-120-124ft

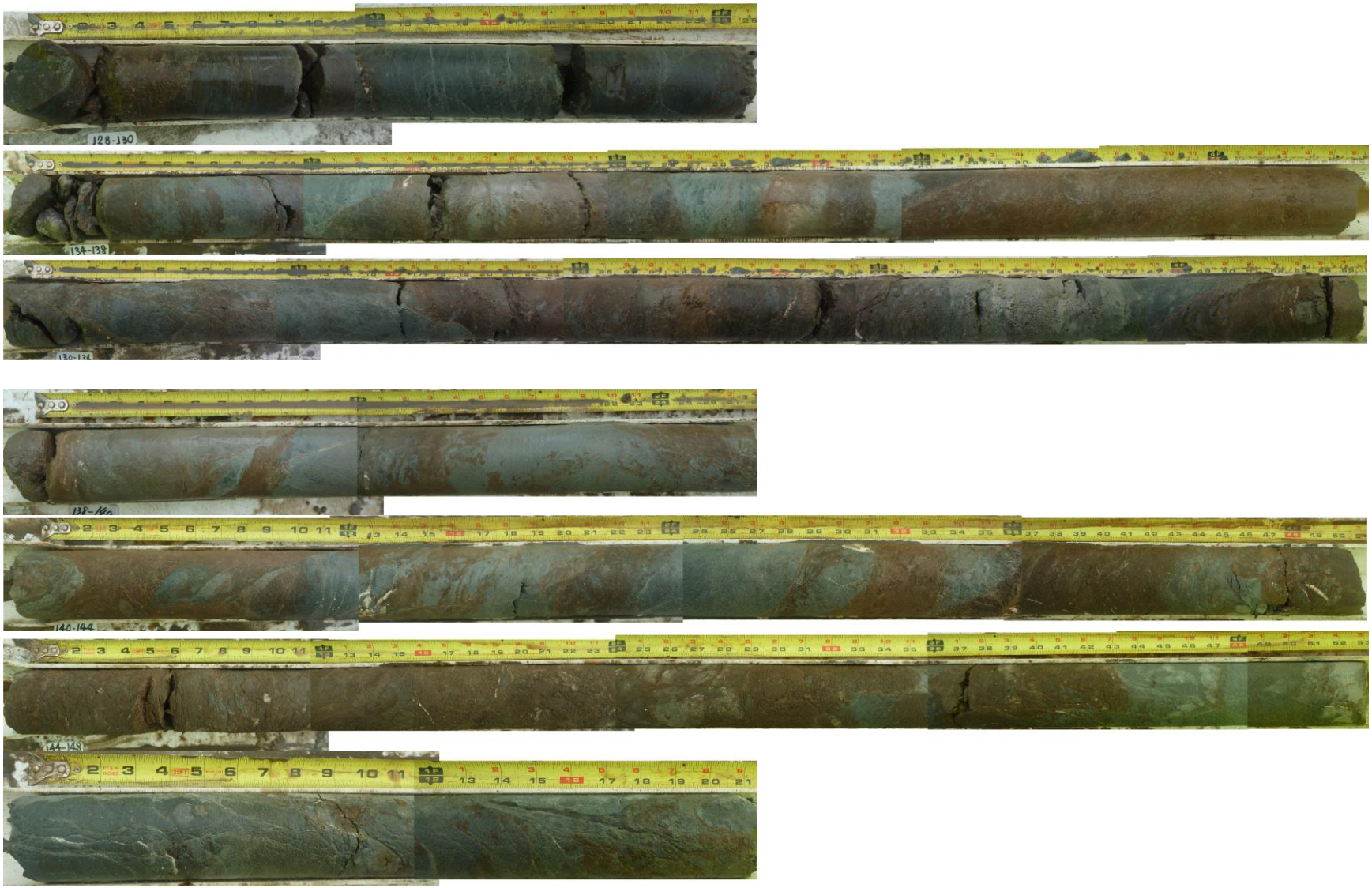
128-130
134-138
130-134
138-140
140-144
144-149

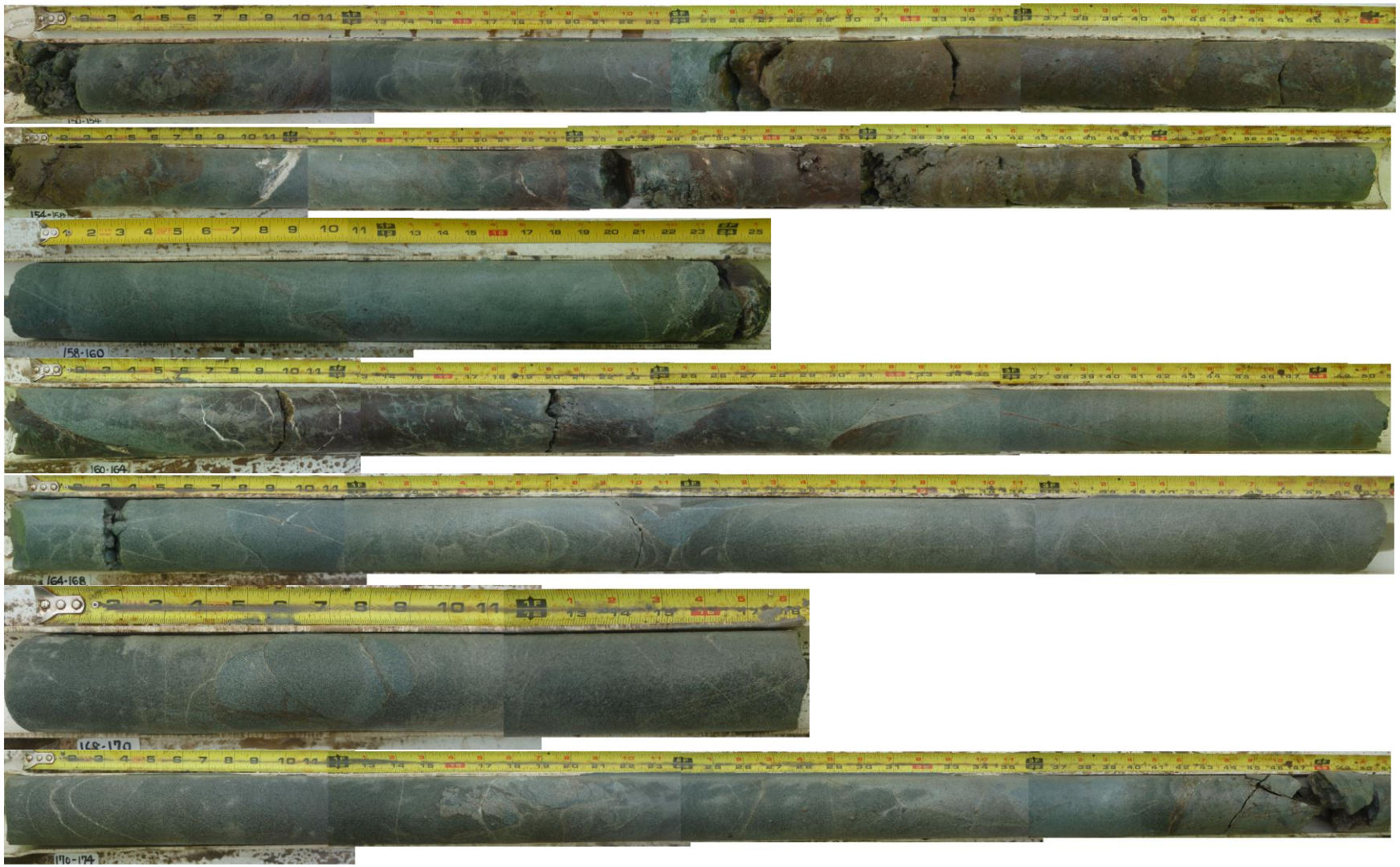
154-158
158-160
160-164
164-168
168-170
170-174

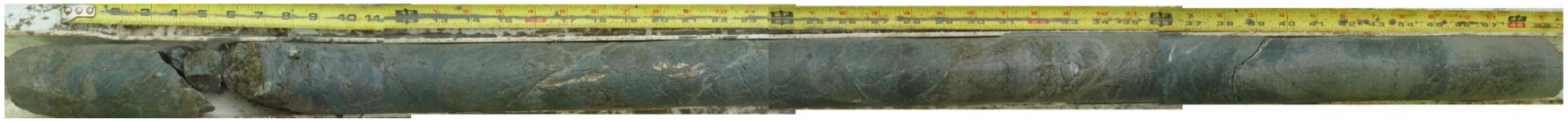

WF5_174-178ft

WF5_184-188

WF5_194-198ft

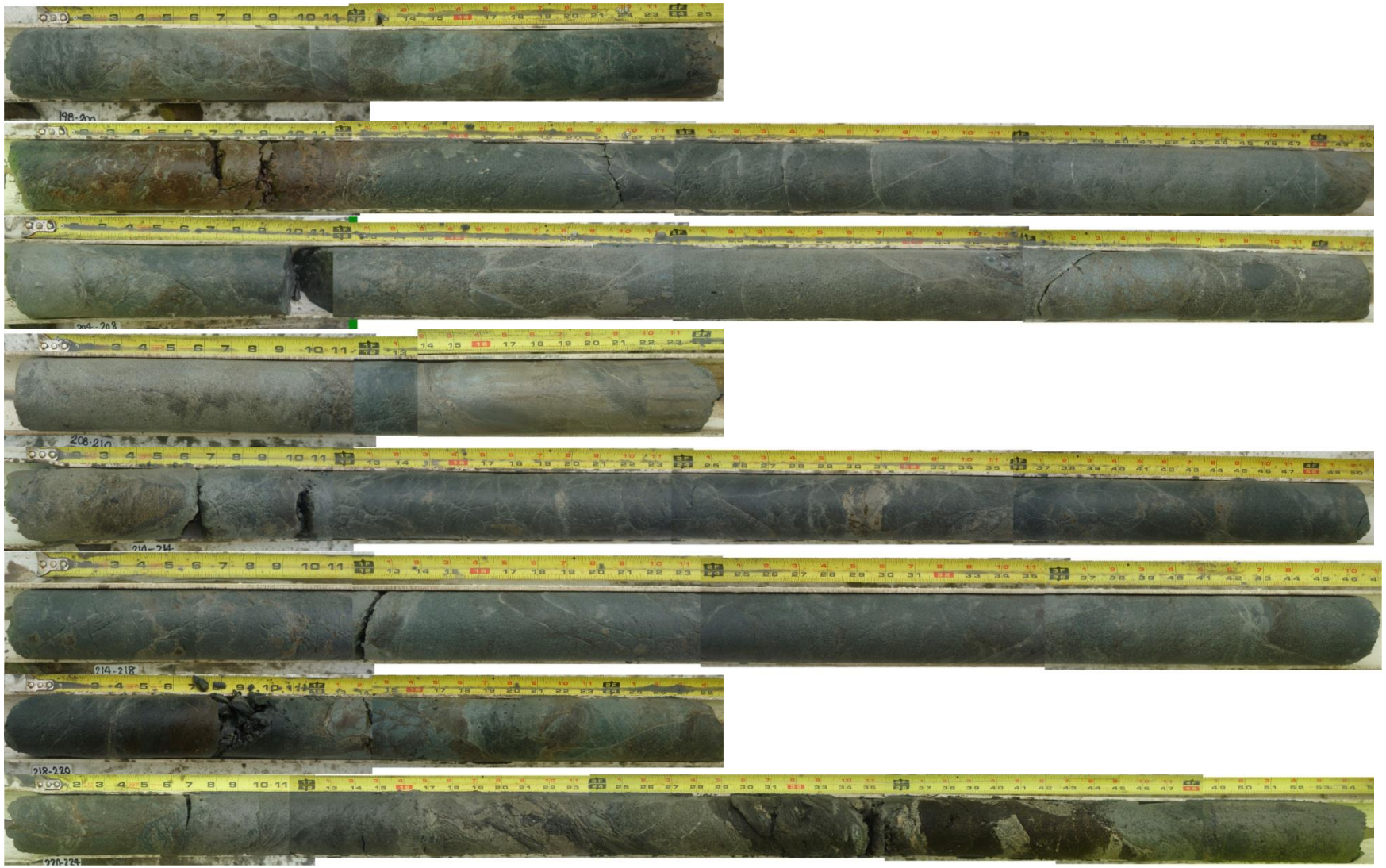

FAULT

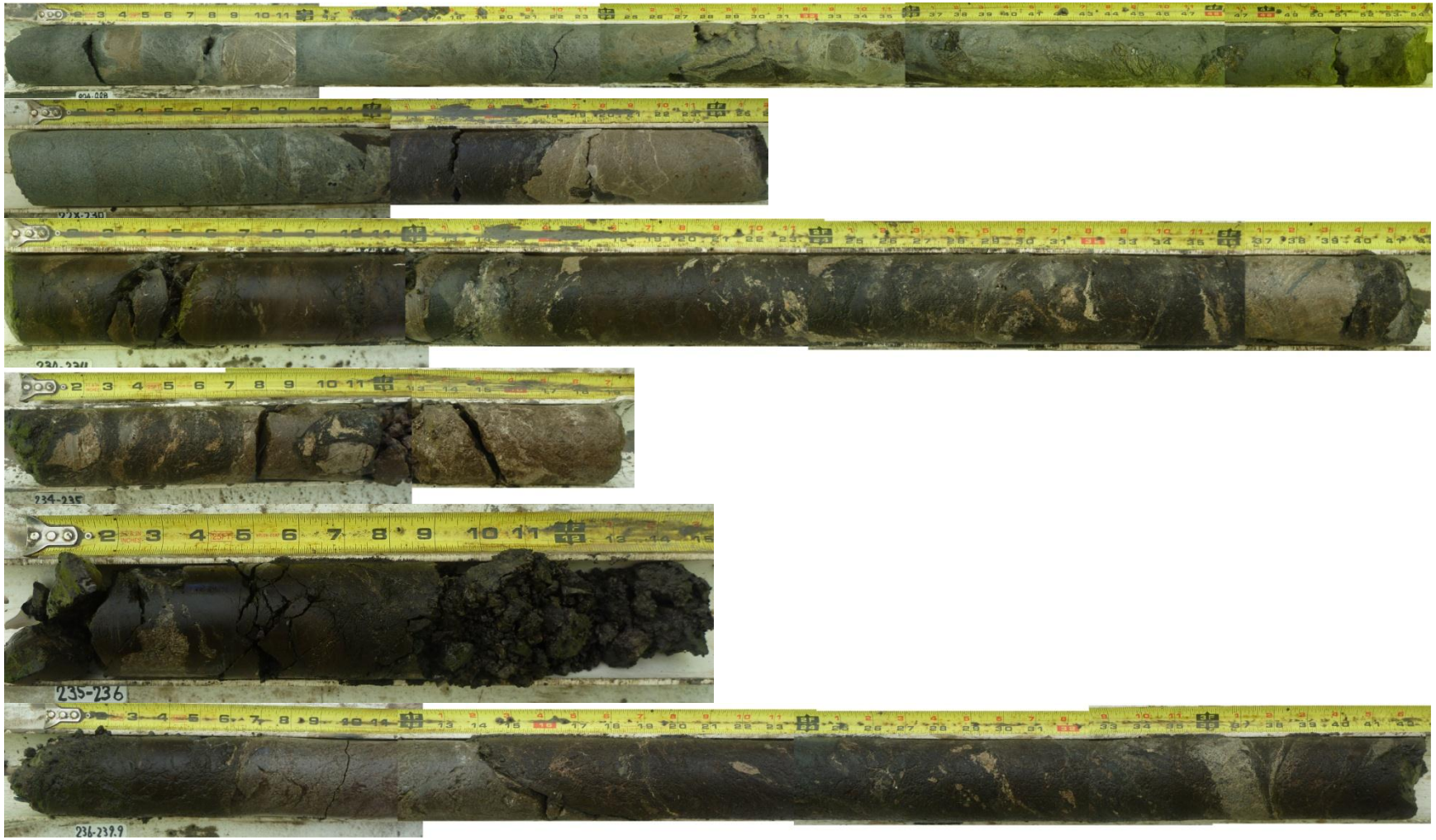
235-236
236-239.9

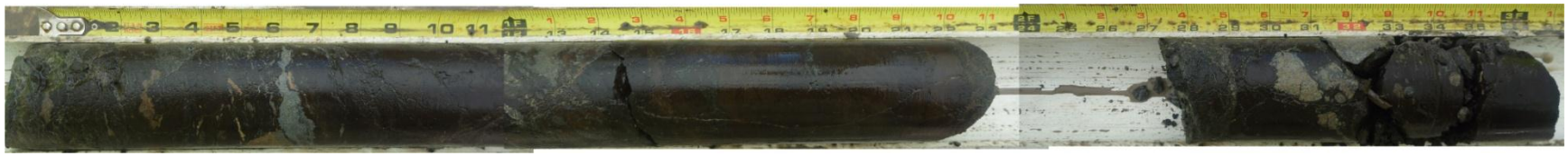

WF5_239.9-242.8ft

WF5_ 244.8-247ft

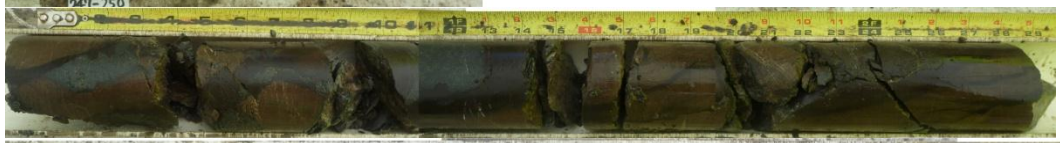

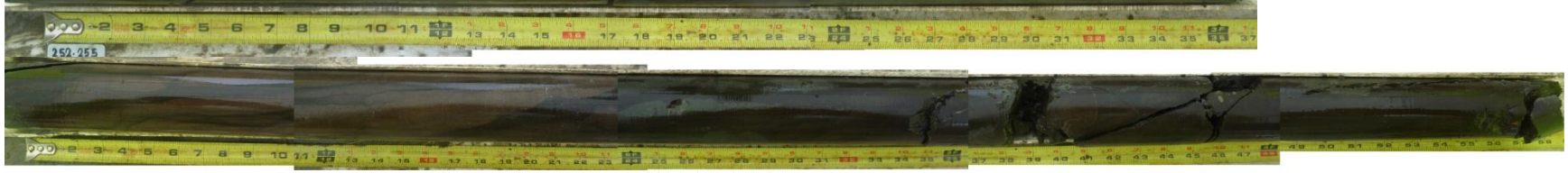

WF5-255-259.8ft

Appendix 6 - Core Images _WF5

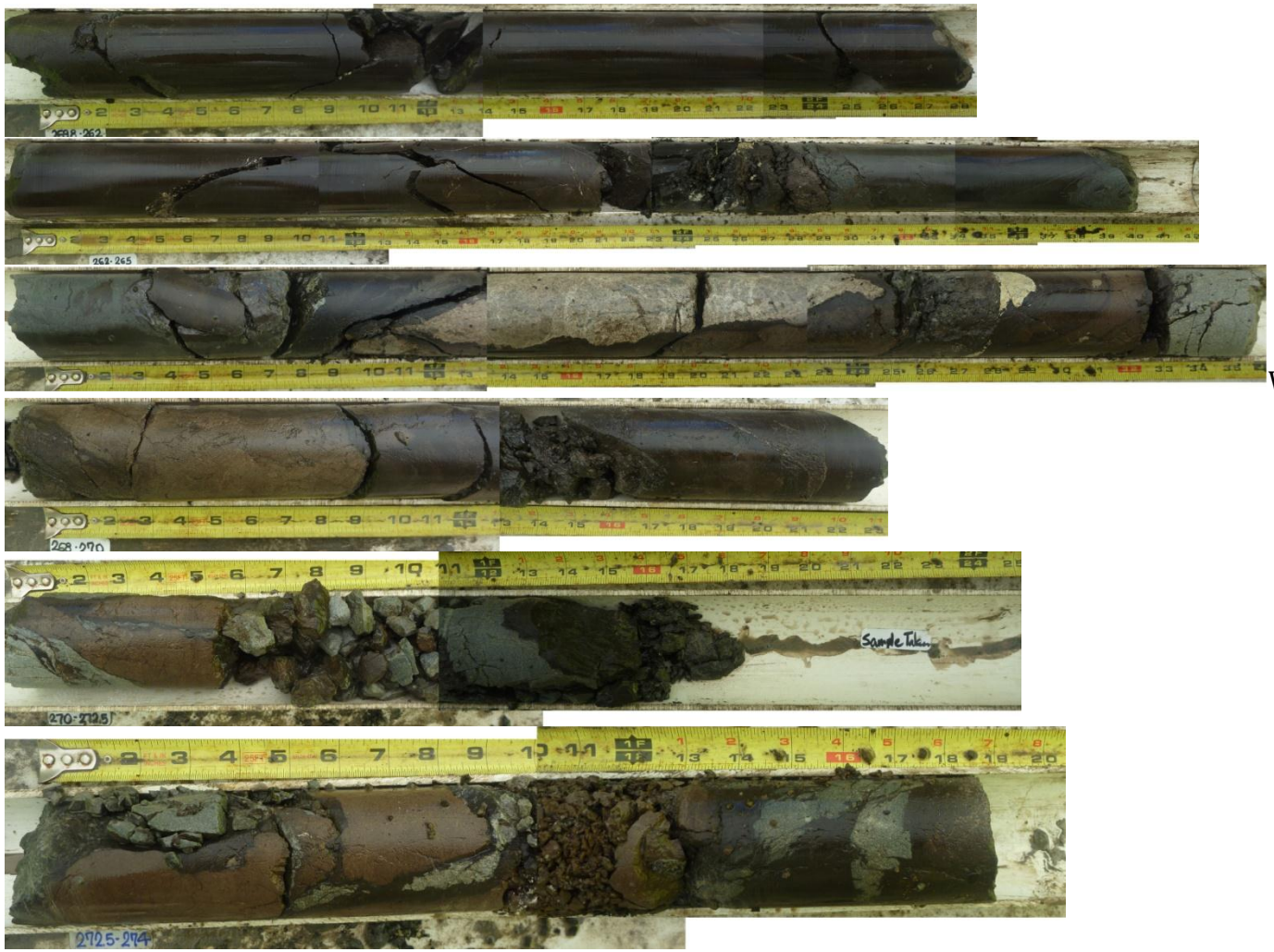

WF5_265-268ft

Missing 285-286ft

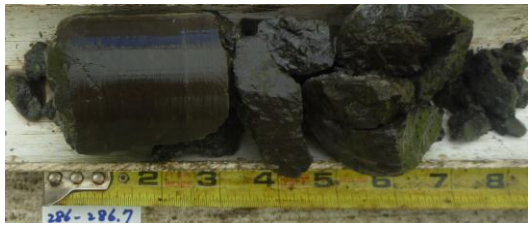

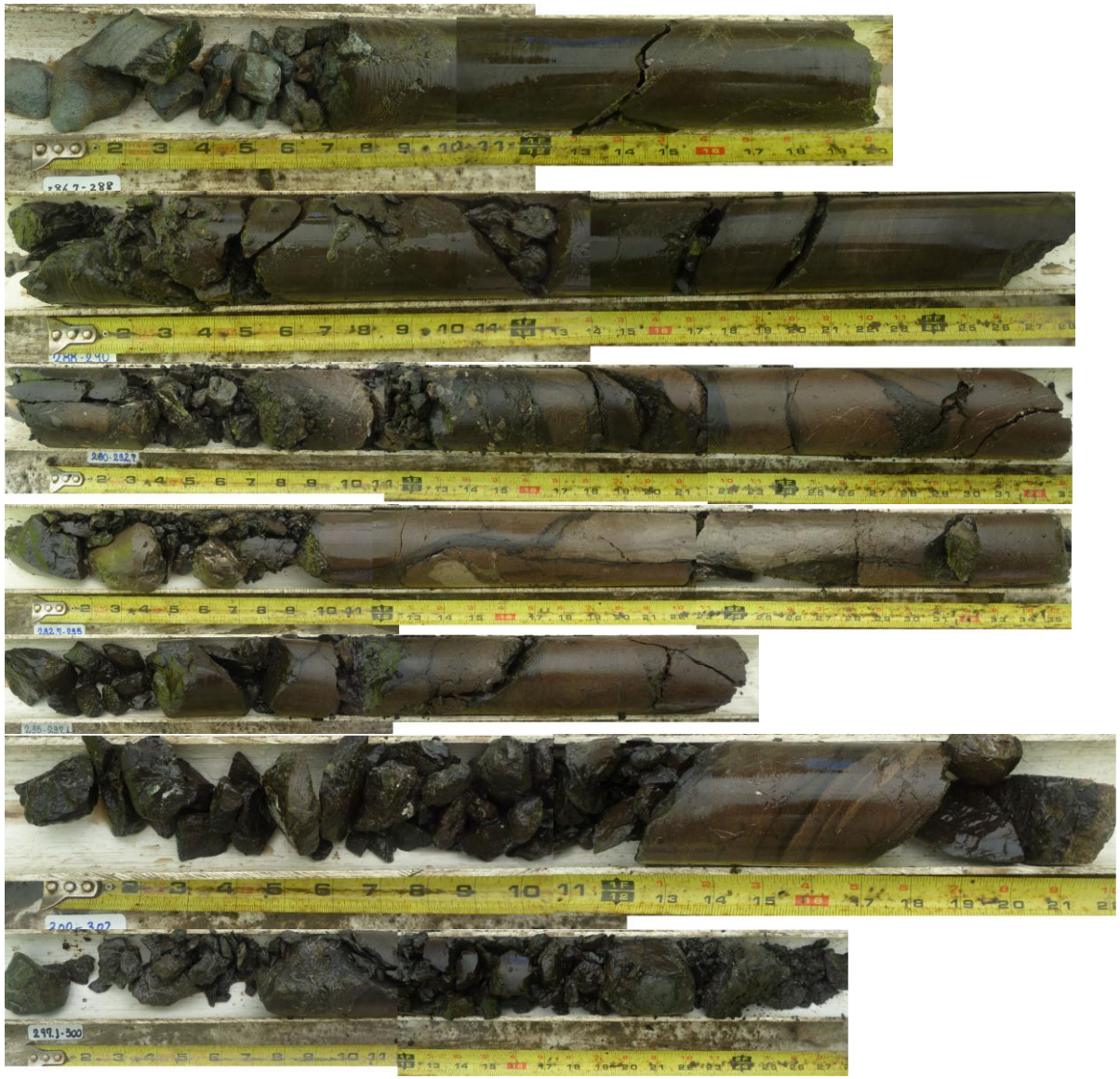

Appendix 6 - Core Images _WF5

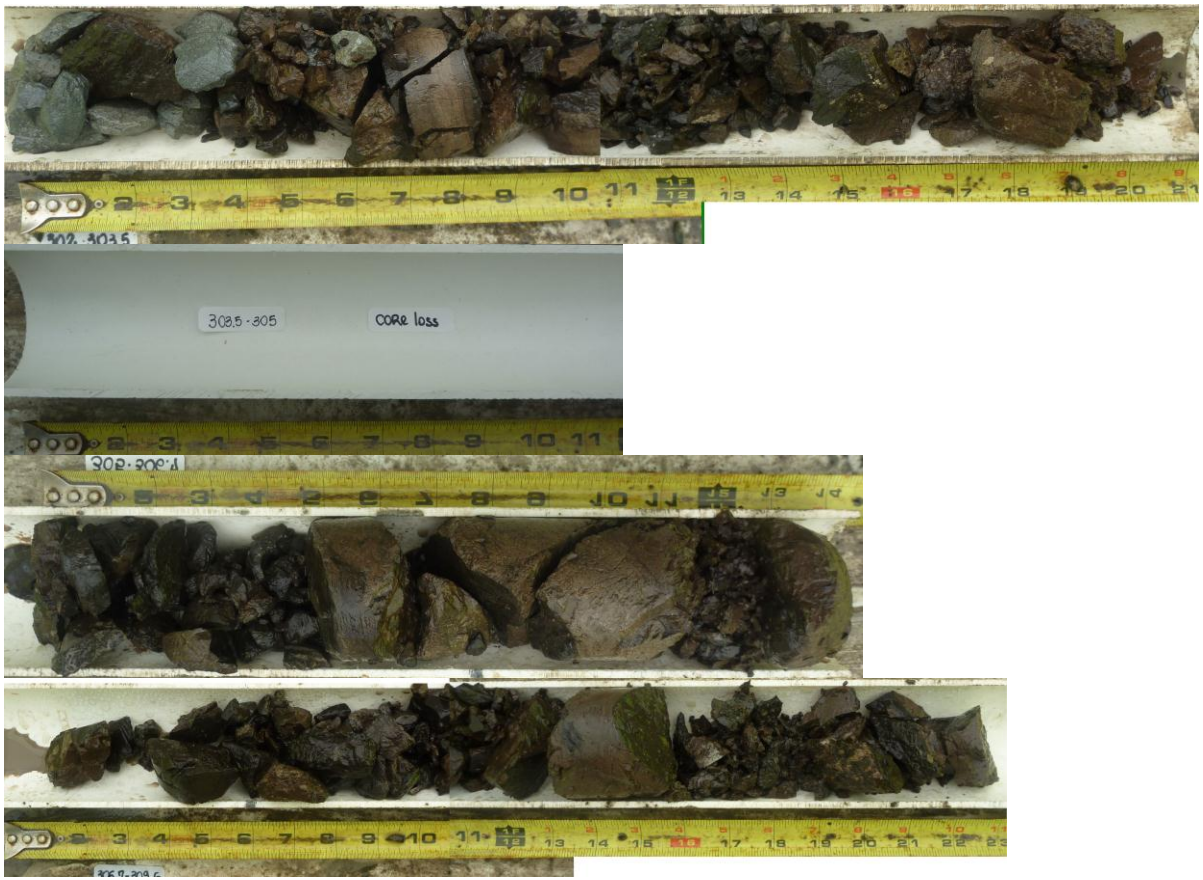

Appendix 6 - Core Images _WF5

Appendix 6 - Core Images _WF5

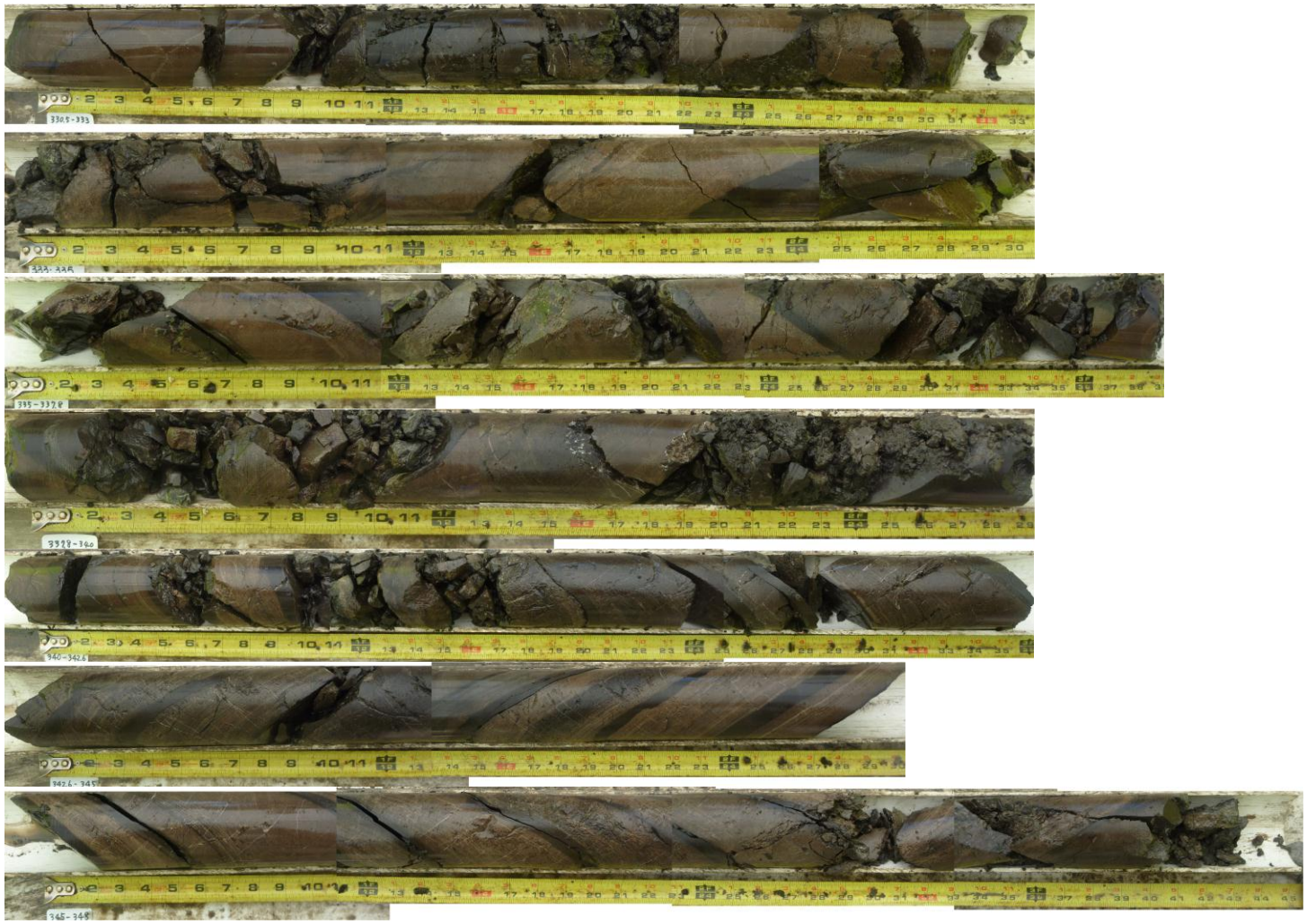

Appendix 6 - Core Images _WF5

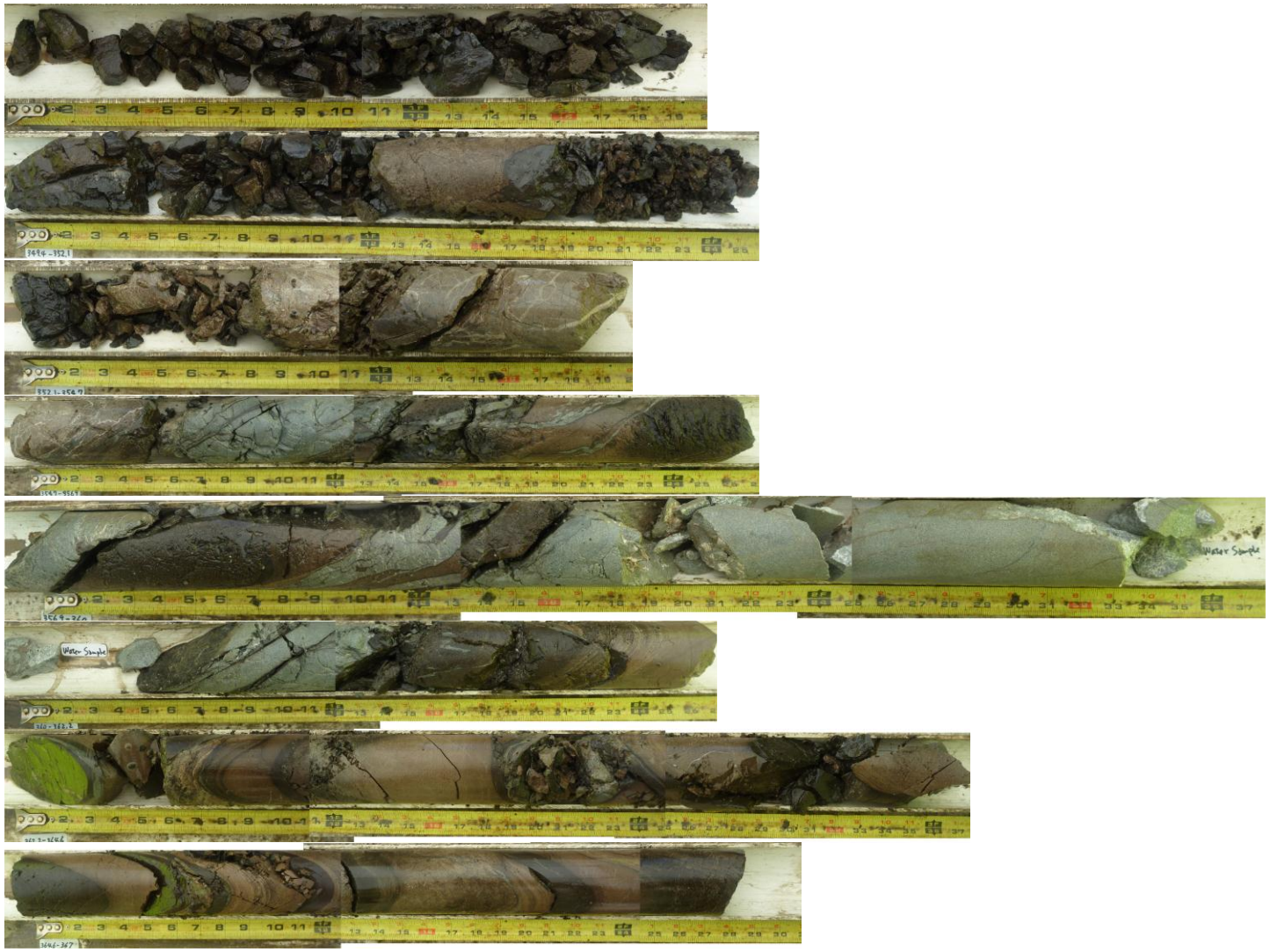

Appendix 6 - Core Images _WF5

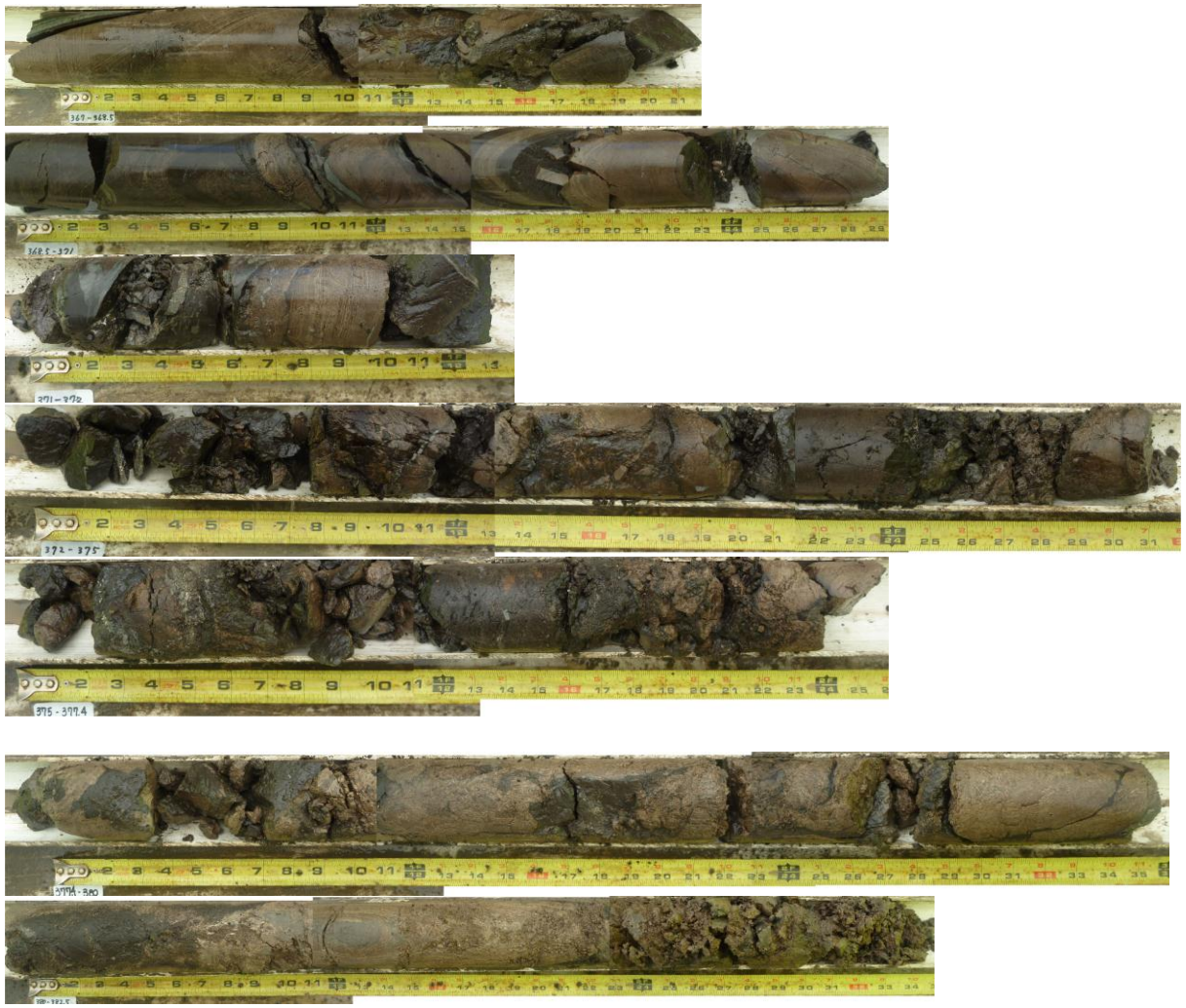

Appendix 6 - Core Images _WF5

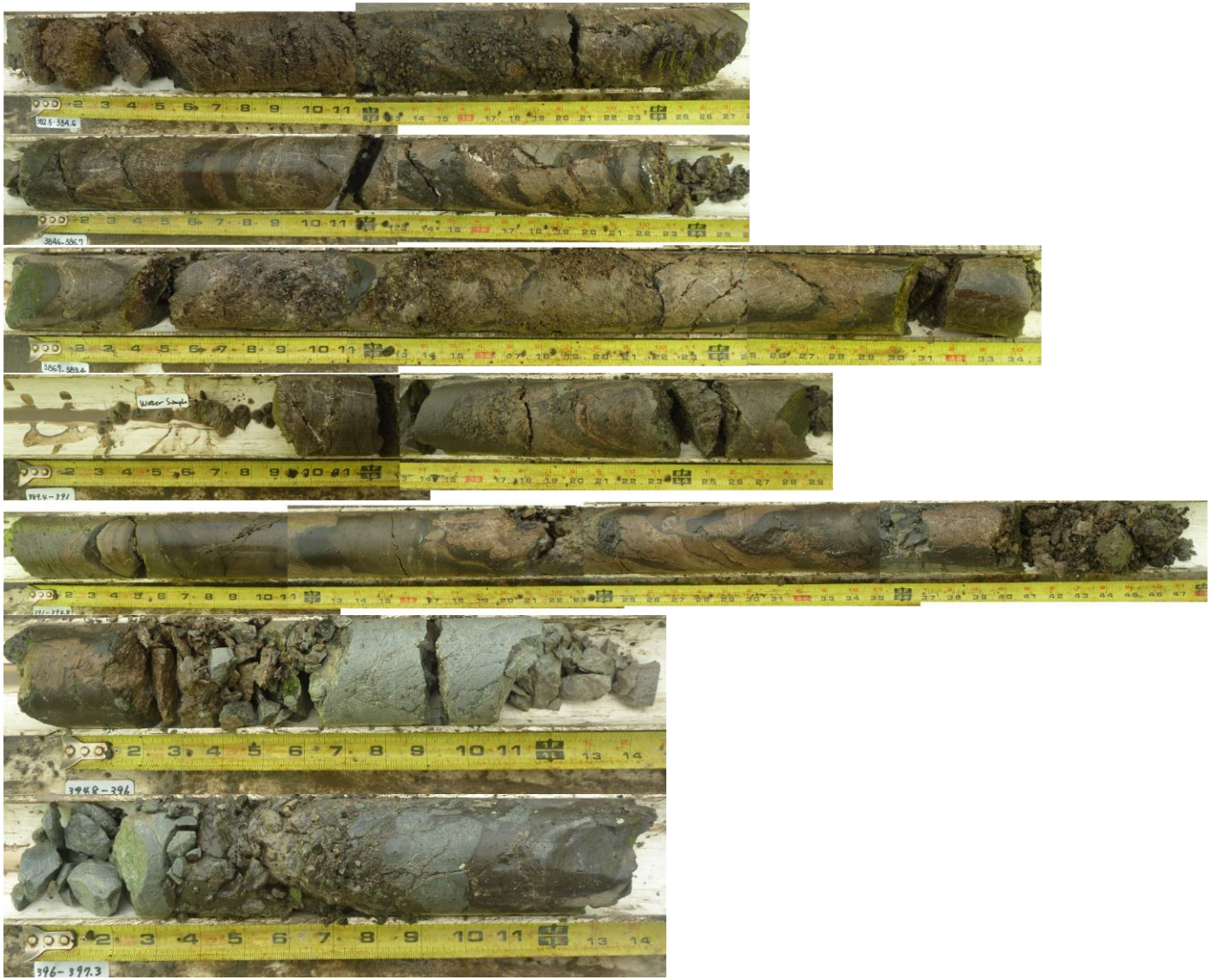

WF5_ 410-411ft or 415-416ft?

Possible 5 ft core loss

WF5_416-418.3ft

Fault

WF5_420-423ft core loss

WF5_428.5-431ft core loss

Orientation Line

WF5_ 438-441.5ft

WF5_449.4-452ft

Appendix 6 - Core Images _WF5

468 - 470.2
CORE LOSS
470.2 - 471.1
CORE LOSS
470.2 - 471.1
CORE LOSS
471.1 - 492.4
492.4 - 494.4
494.4 - 497
497 - 498.7

Appendix 6 - Core Images _WF5

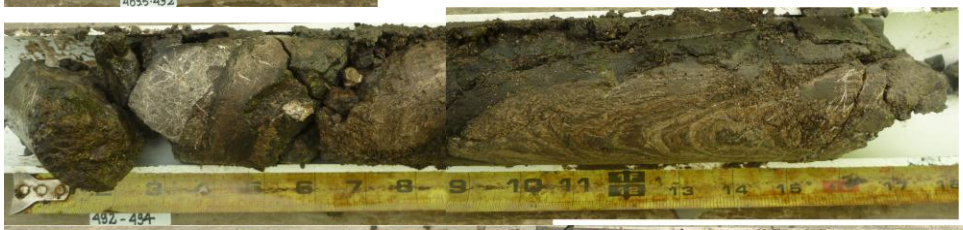

Appendix 6 - Core Images _WF5

WF5_528.3-530 ft core loss

Appendix 6 - Core Images _WF5

Appendix 6 - Core Images _WF5

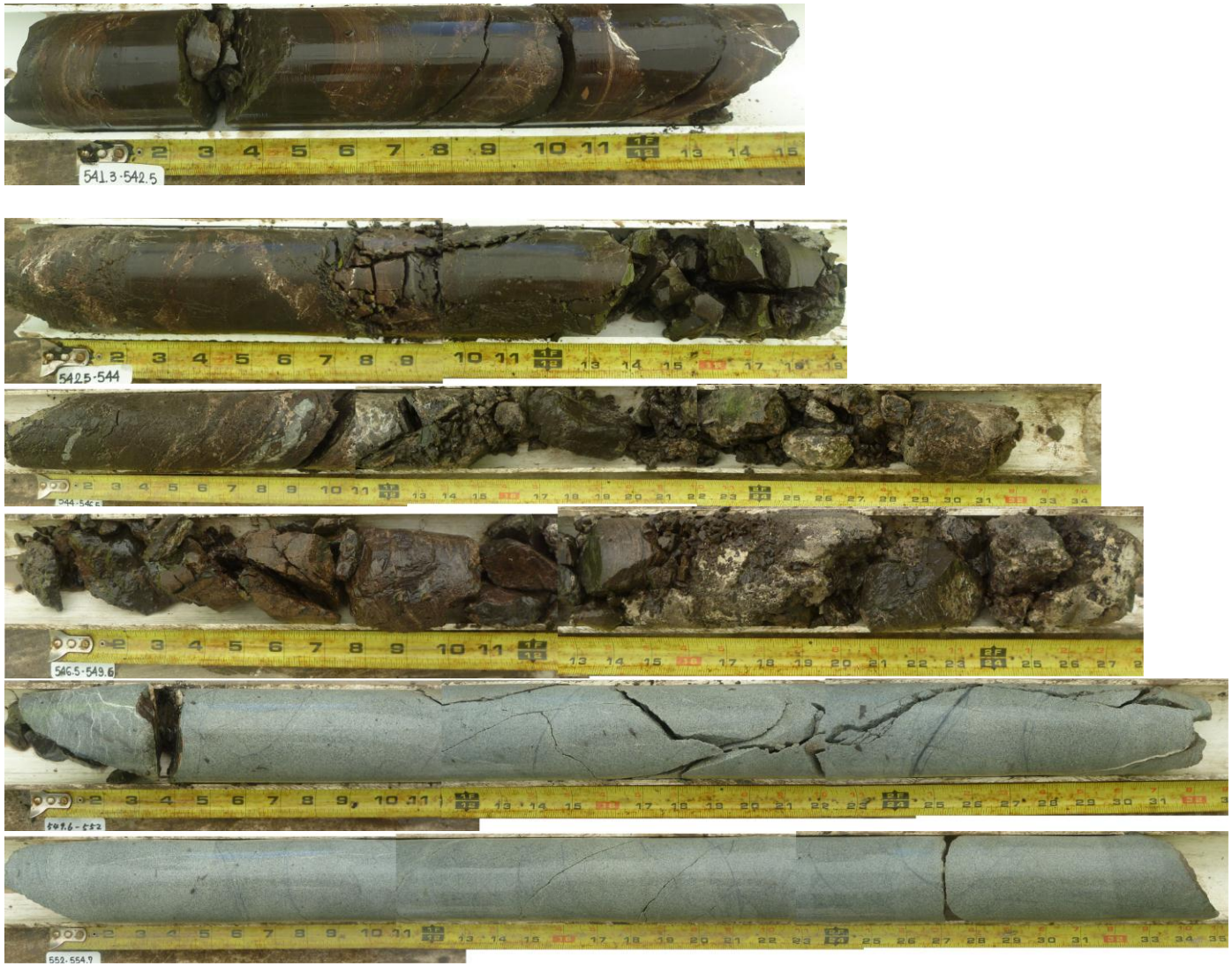

WF5_561-562.3ft

core loss

569-570

WF5-574-576

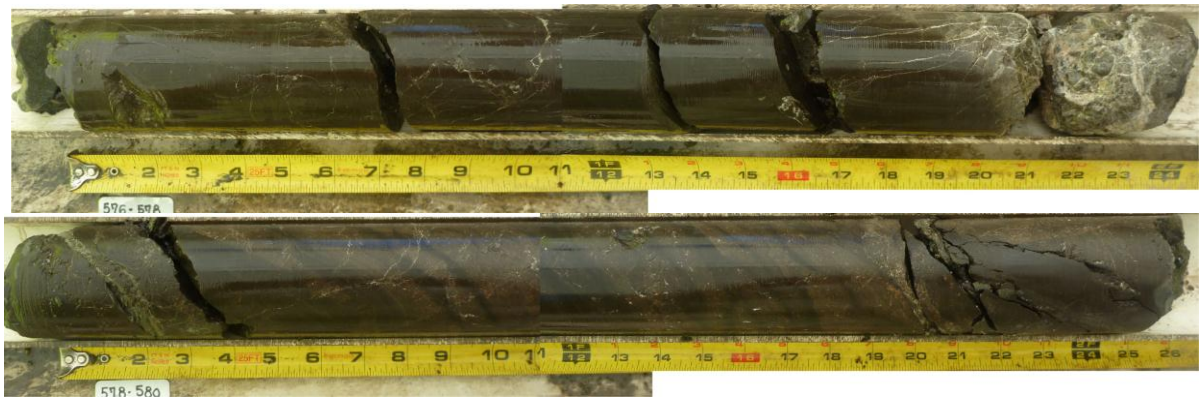

Appendix 6 - Core Images _WF5

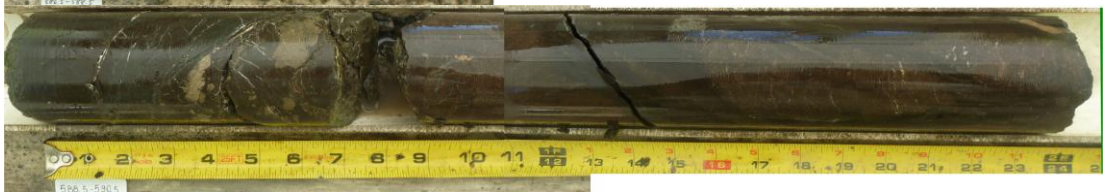

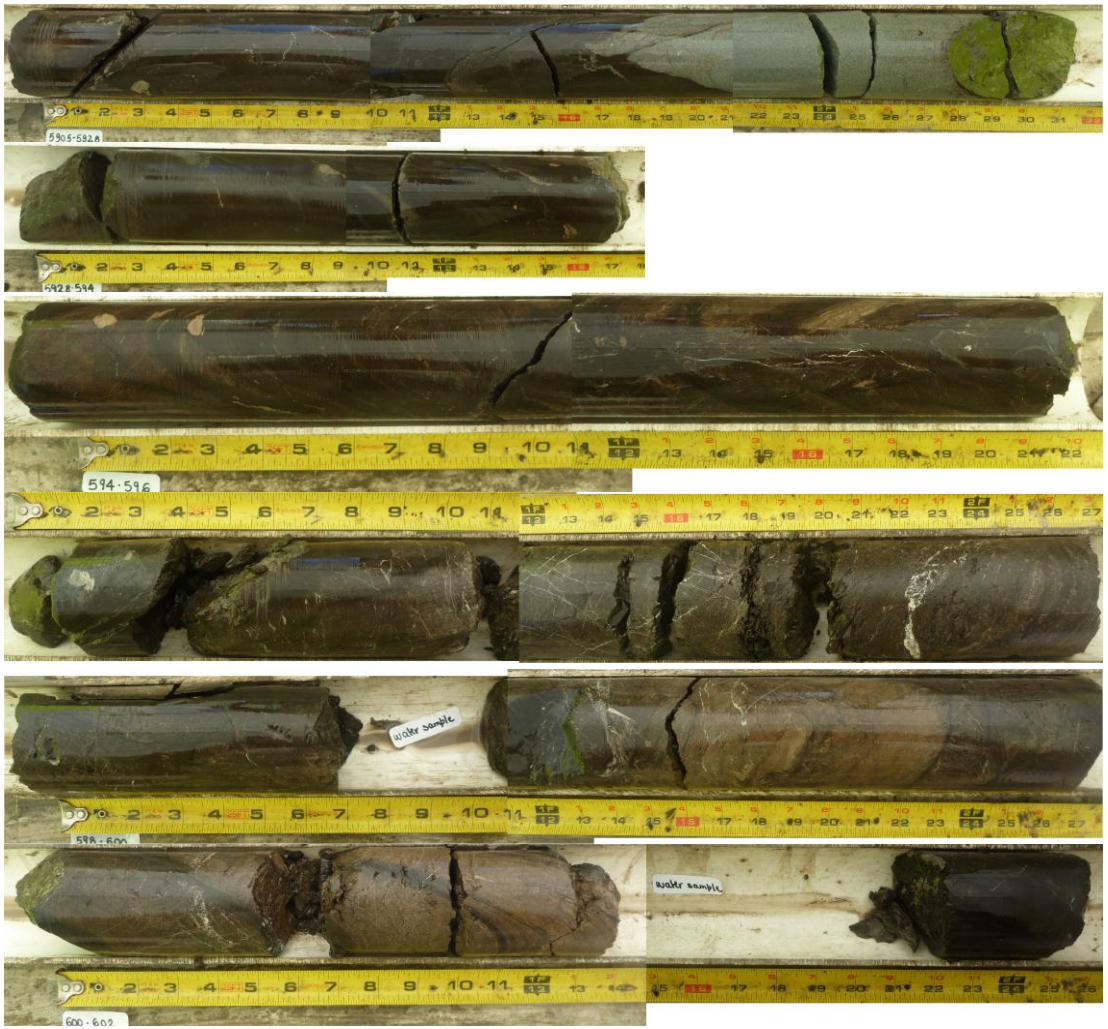

WF5_596-598ft

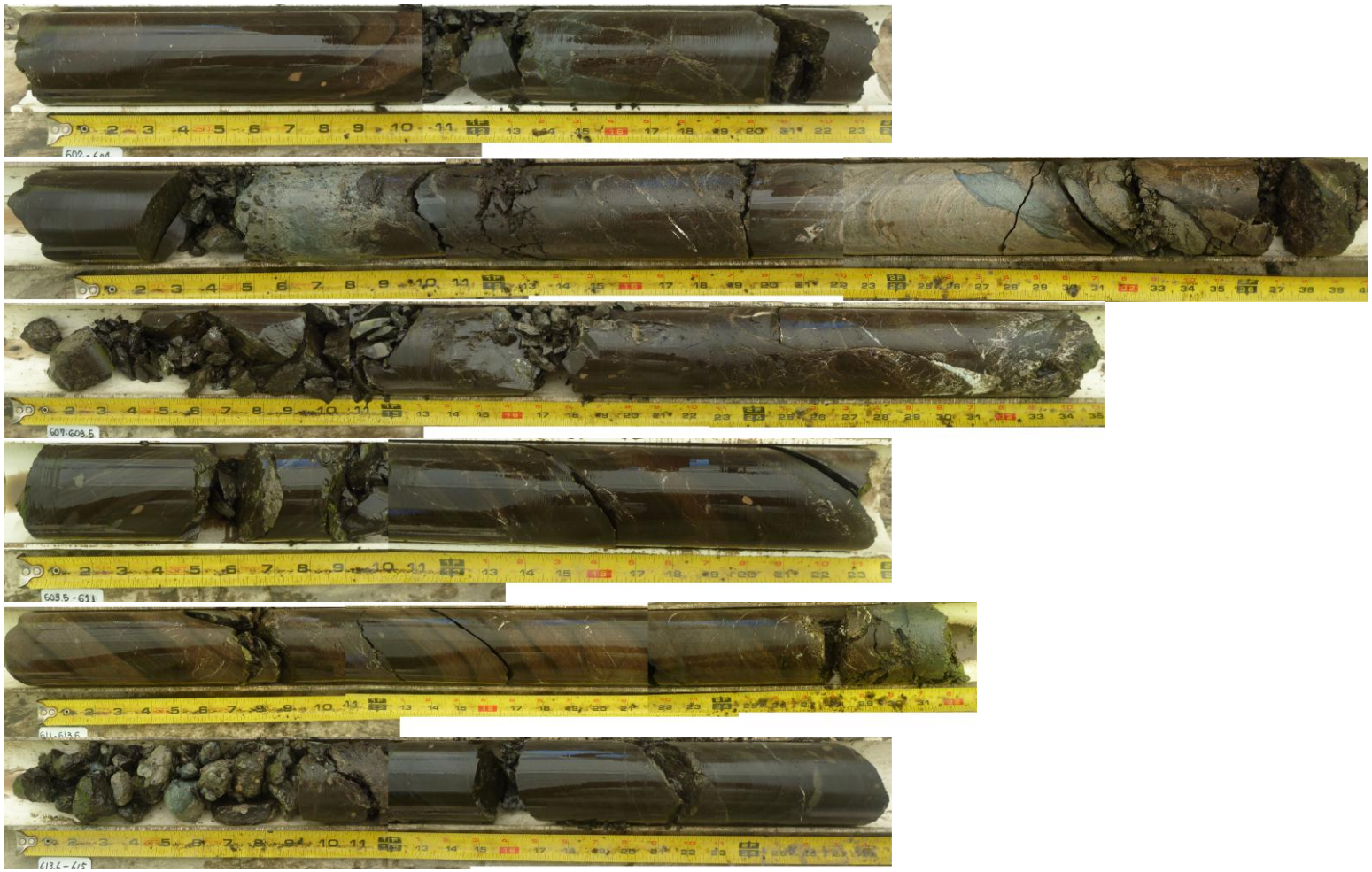
607-608.5
608.5 - 611
611-613.5
613.5-615

615-617.5
617.5-620
620-622.5
622.5-624
624-626
626-628
628-630.5

Appendix 6 - Core Images _WF5

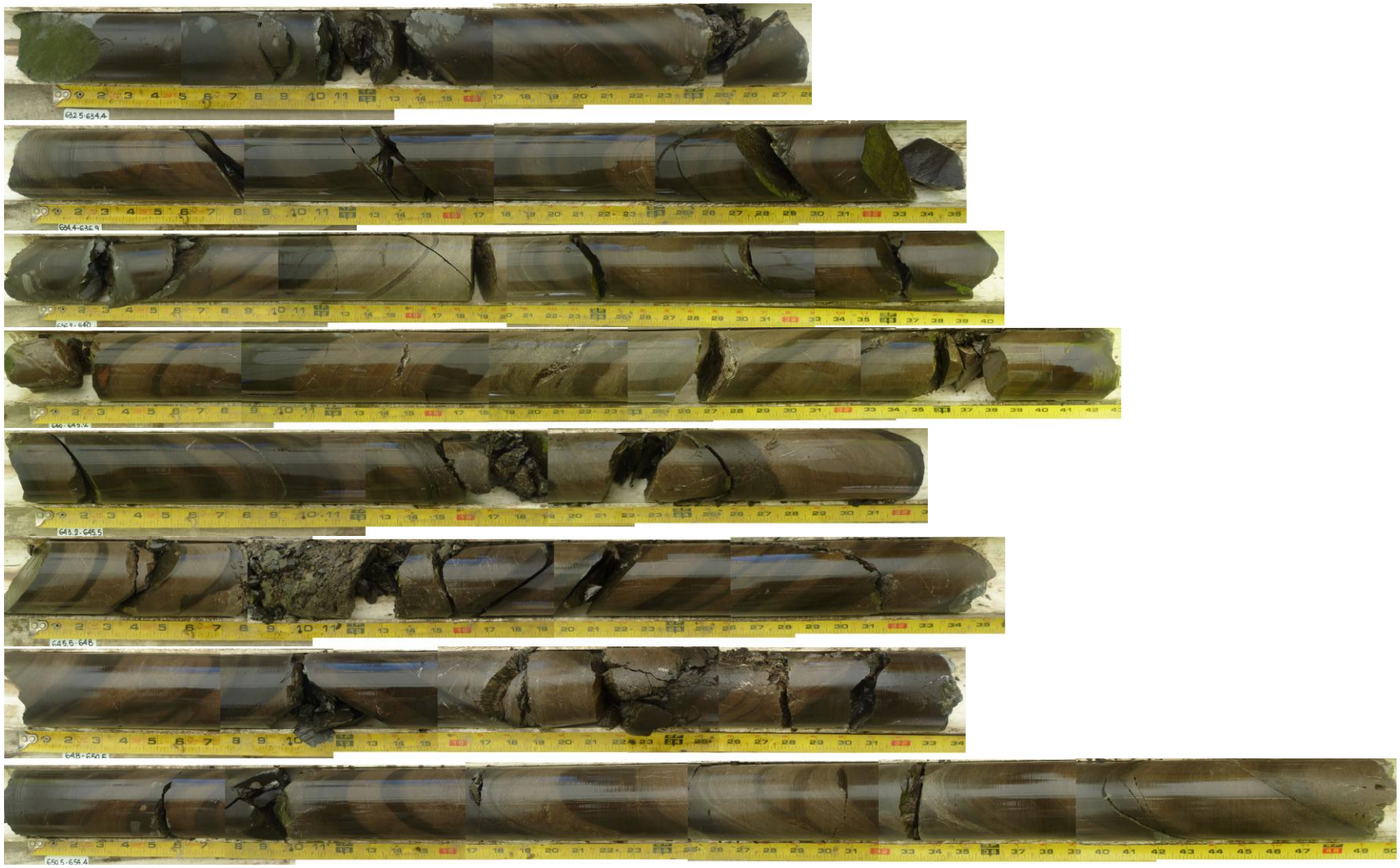

Appendix 6 - Core Images _WF5

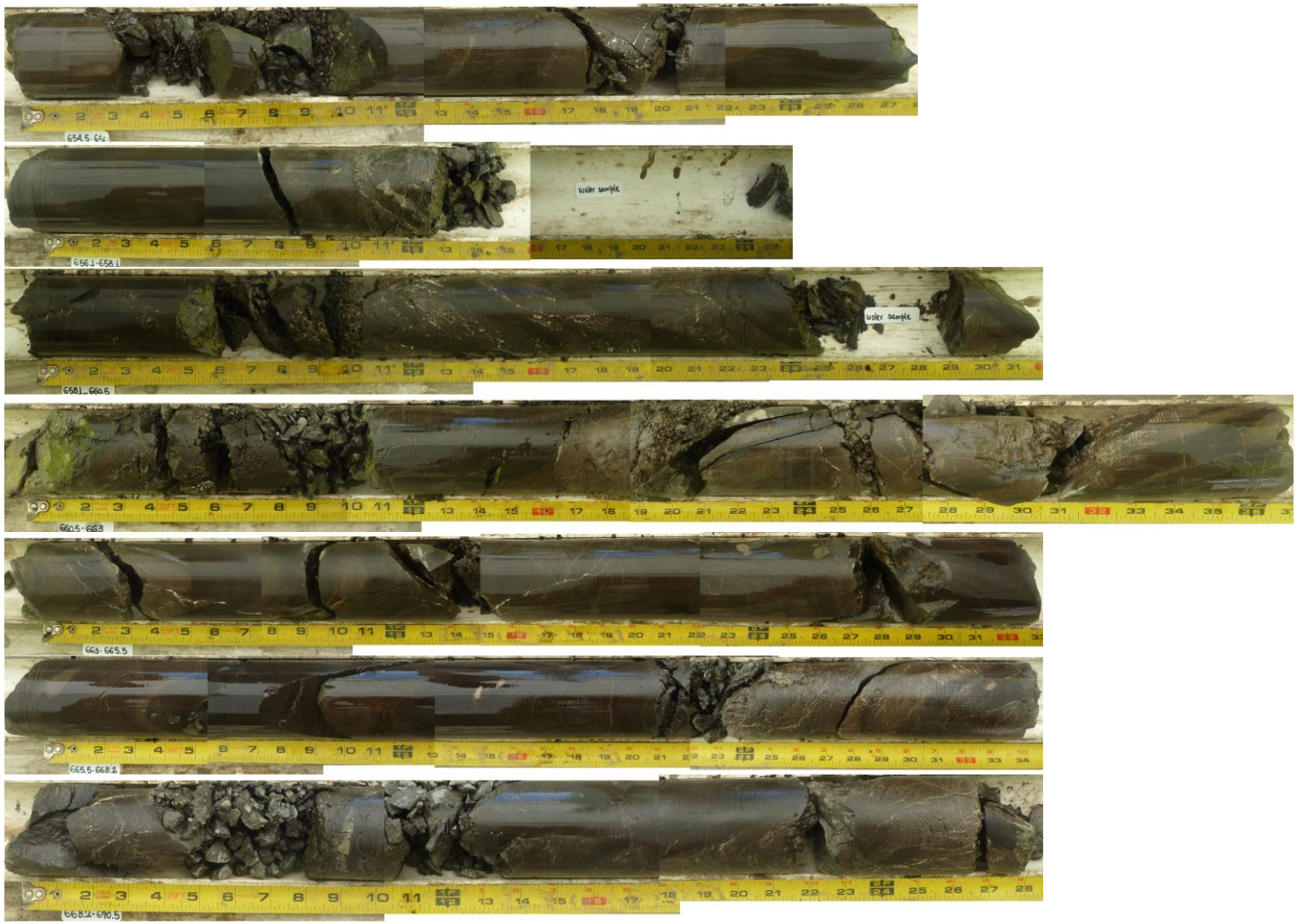

670.5-673.2
673.2-675.5
675.5-678